Transactions of the ASME®

FLUIDS ENGINEERING DIVISION
Technical Editor
DEMETRI P. TELIONIS (1999)
Executive Secretary
PAT WHITE (1999)
Assistant to the Editor
N. W. SCHAEFFLER
Calendar Editor
M. F. ACKERSON

Transactions of the ASME, Journal of Fluids Engineering (ISSN 0098-2202) is published quarterly (Mar., June, Sept., Dec.) for $215.00 per year by The American Society of Mechanical Engineers, Three Park Avenue, New York, NY 10016. Periodicals postage paid at New York, NY and additional mailing offices.

POSTMASTER: Send address changes to Transactions of the ASME, Journal of Fluids Engineering, c/o THE AMERICAN SOCIETY OF MECHANICAL ENGINEERS, 22 Law Drive, Box 2300, Fairfield, NJ 07007-2300.

CHANGES OF ADDRESS must be received at Society headquarters seven weeks before they are to be effective. Please send old label and new address.

PRICES: To members, $40.00, annually: to nonmembers, $215.00. Add $40.00 for postage to countries outside the United States and Canada.

STATEMENT from By-Laws. The Society shall not be responsible for statements or opinions advanced in papers or . . . printed in its publications (B7.1, Par. 3).

INDEXED by Applied Mechanics Reviews and Engineering Information, Inc. Canadian Goods & Services Tax Registration #126148048.

Journal of Fluids Engineering

Published Quarterly by The American Society of Mechanical Engineers

VOLUME 121 • NUMBER 3 • SEPTEMBER 1999

Technical Papers

(Contents continued on p. 532)

This journal is printed on acid-free paper, which exceeds the ANSI Z39.48-1992 specification for permanence of paper and library materials. ♾™
♻ 85% recycled content, including 10% post-consumer fibers.

(Contents continued)

Technical Briefs

Announcements and Special Notices

F. Holzäpfel[1]
Scientist.

B. Lenze
Professor.

W. Leuckel
Professor.

Engler-Bunte-Institut der Universität Karlsruhe,
D-76128 Karlsruhe,
Germany

Quintuple Hot-Wire Measurements of the Turbulence Structure in Confined Swirling Flows

The novel quintuple hot-wire measurement technique was used to perform detailed measurements of the mean velocities and Reynolds stresses in an isothermal model combustion chamber at two different levels of swirl. The measured flow quantities are analyzed and described in detail where the emphasis is put on typical swirl-related effects as well as the interaction of rotation and turbulence dynamics. The results provide a well-documented data base for the development and validation of turbulence closures. They also serve to improve understanding of specific characteristics of swirl flows.

1 Introduction

Swirling flows have been subject to extensive research efforts in a wide range of engineering disciplines. Furnaces, gas turbine combustors, and swirl atomizers are only a few examples of applications in combustion technology. The great diversity of governing parameters and their strong interrelations constitute a big challenge for the development of adequate models for numerical simulations of the combustion process. At present, most parametrizations of turbulence are not able to capture completely the influence of Coriolis and centrifugal forces on turbulence dynamics and can, therefore, not be applied universally in different configurations of swirling flows.

It is well known that eddy-viscosity-type two-equation models (k-ϵ theory) can only be applied successfully for certain flows. Hirsch and Leuckel (1996) show that closure assumptions may lead to a overprediction of the shear stress $\tau_{r,\varphi}$ which eventually generates a forced-vortex dominated flow. Therefore, these models succeed fairly well in predicting simple swirling flows with forced-vortex dominated tangential velocity distributions (Armfield et al., 1990; Durst and Wennerberg, 1991; Riahi et al., 1990). On the other hand, they completely fail in predicting complex swirling flows (Döbbeling et al., 1990; Weber et al., 1990), since the tangential velocity distribution essentially determines the pressure field and therewith the structure of the entire flow. The more expensive and elaborate algebraic stress model and the Reynolds stress model usually are much more effective in representing the main features of swirling flows (Weber et al., 1990; Leschziner, 1991), because they correctly take into account the Coriolis-force-related production terms in the Reynolds stress transport equations (Hirsch, 1995; Hirai and Takagi, 1995). Although these models satisfy the linear effects of rotation, the nonlinear effects which modify the characteristics of the spectral energy cascade remain unresolved (Jacquin et al., 1990). First attempts to model technically relevant swirl flows by Large Eddy Simulations yielded promising results (Pierce and Moin, 1998).

A high-quality data base is essential in order to verify and to develop closure hypotheses in turbulence models. Therefore, appropriate measurement techniques are needed. Drawbacks of the widely spread Laser Doppler velocimetry are: the optical access from several directions causes considerable difficulties particularly in confined flows; no high-frequency coincident and time-equidistant data can be sampled in order to calculate for example power spectra. Unfortunately, common hot-wire measurement techniques are also not suitable. They do not provide a sufficient uniqueness domain for resolving all angles of attack occurring in highly turbulent swirling flows. Even four-wire measurement techniques are restricted to the insufficient uniqueness domain of approximately 40 deg half angle of a cone. Considerable progress was achieved by the five-wire technique used in the current study, which was developed by the author and is described in detail in Holzäpfel et al. (1994a). This so-called quintuple technique allows unique measurements for angles of attack comprising the whole hemisphere. Furthermore, it shows an increased angular resolution which improves the accuracy and reduces the calibration effort. For these reasons, the quintuple technique is best suited to overcome the lack of reliable turbulence data for highly turbulent confined swirling flows. A part of this study was presented in a conference (Holzäpfel et al., 1994b).

2 Experimental Apparatus and Measurement Technique

Figure 1 shows the model combustion chamber used in the present experiments. After the swirl is imparted by a movable-block swirl generator, the flow enters the cylindrical test section which is connected with an annular ring outlet. This outlet geometry avoids backflow through the exit section, which otherwise would be induced by the low pressure near the axis of the rotating fluid. It thus provides unique outlet conditions for the numerical modeling of the flow. In addition, the formation of the classical precessing vortex core (Jacobs and Günther, 1975) is obviated, which otherwise could be induced in the shear layer between swirling forward flowing and nonswirling backward flowing fluid sucked in through the outlet. The test section consists of a perspex cylindrical tube, 447 mm in diameter and 765 mm in length. Measurement access is provided in arbitrary axial positions along a vertical opening. The axisymmetry of the swirling flows was checked in advance. Maximum eccentricities of 4 mms were found.

The swirl strength is characterized by the inlet swirl number

[1] Present address: Institut für Physik der Atmosphäre, DLR-Oberpfaffenhofen, D-82234 Weßling, Germany.

Contributed by the Fluids Engineering Division for publication in the JOURNAL OF FLUIDS ENGINEERING. Manuscript received by the Fluids Engineering Division July 3, 1996; revised manuscript received May 17, 1999. Associate Technical Editor: P. R. Bandyopadhyay.

$$S_0 = \frac{2\pi \int_0^R \rho(UW + \overline{uw}) r^2 dr}{2\pi \int_0^R \rho(U^2 + \overline{u^2}) r dr \cdot R},$$

which is defined by the ratio of angular to axial momentum flux in the inlet divided by the outer inlet radius R. Here and in the following, U, V, W, denote the mean velocities in axial, radial, and tangential direction in cylindrical coordinates and, u, v, w, their respective fluctuating portions. In the current paper, a theoretical inlet swirl number $S_{0,theo}$ (Leuckel, 1967) is used which is calculated as a function of the swirl generator geometry and the angle ξ (see Fig. 1)

$$S_{0,theo} = \frac{2\pi}{n\xi_{max}} \frac{\sin\alpha \cos\alpha \xi/\xi_{max}}{(1 - (1 - \cos\alpha)\xi/\xi_{max})^2} \frac{R}{2B}\left(1 - \frac{R^2}{R_i^2}\right).$$

$S_{0,theo}$ is approximately equal to the actual inlet swirl number.

The quintuple hot-wire probe is composed of five 2.5 μm platinum plated tungsten wire sensors which are evenly distributed in angles of 72 deg on the surface of a cone of 45 deg half angle (Fig. 2). The resulting measurement volume amounts to 1.1 mm in diameter and 0.5 mm in height. The main benefit of the five-wire arrangement is to allow unique measurements for all angles of attack in the whole hemisphere with an increased accuracy compared to three and four wire arrangements (Holzäpfel et al., 1994a). The signal equation

$$l_i = c^2 g_i(\psi, \theta); \quad i = 1, 5$$

allows the decoupled description of the flow direction (angles ψ, θ) and the magnitude c of the velocity vector in both calibration and data reduction.

All experiments were conducted with cold air (21°C) at theoretical swirl numbers of $S_{0,theo} = 0.4$ and 0.95 and a volumetric flow rate of $\dot{V} = 426$ m^3/h. Investigations of the nonswirling case were not carried out. The measurements were performed at 26 axial locations including the inlet plane and 37 radial positions per radius (to save room only every second axial location is shown). At each location, 4096 samples of the instantaneous velocity vector recorded with a data rate of 50 Hz, were used to calculate subsequently the three mean velocity components and all six Reynolds stress components.

3 Mean Velocities, Vector Plot, and Streamfunction

The general flowpattern is to a great part determined by the structure of the vortex breakdown. This phenomenon characterizes a sudden divergence of the axial flow which is followed by the creation of an internal recirculation zone (IRZ). This has several different appearances (Sarpkaya, 1971). To give an impression of the flow pattern isolines of the streamfunction are shown for both swirl numbers in Fig. 3. The streamlines are plotted in increments of 10% with respect to the inlet flow rate. In the weak swirl case, the vortex breakdown begins at $x = 80$ mm in the form of a closed recirculation bubble close to the axis. A similar structure is observed further upstream (starting at $x = 0$ mm) for $S_{0,theo} = 0.95$ which is continued with a large ear-shaped recirculation zone and a recirculation tube close to the axis reaching to the bottom of the test section. At $S_{0,theo} = 0.95$ the swirling jet already impinges on the wall at $x = 170$ mm, 60 mm further upstream than for $S_{0,theo} = 0.4$. This is due to the displacement effect of the vortex breakdown bubble appearing immediately after the inlet and the increased centrifugal force. As a result, a smaller outer recirculation zone is formed in the stronger swirling case.

Some of the above details, and particularly the similarity of the basic structure of the vortex breakdown for both swirl intensities, can be seen more clearly in Fig. 4 where the upstream part of the flow is plotted as a vector plot. Every vector represents the sum of the axial and radial velocity components in all measured positions.

Some principle features of the flow can be explained by the manifestation of the Taylor-Proudman theorem (Proudman, 1916) and the concept of criticality originally introduced by Benjamin (1962). Both concepts describe the strong interaction of up- and downstream flow quantities in strongly rotating fluids. The Taylor-Proudman theorem states that axial velocity gradients vanish in stationary, strongly rotating fluids. In addition, if this borderline case is axisymmetric as well, then the circumferential gradients disappear and the flow depends only on the radial coordinate. However, even at moderate swirl numbers, downstream disturbances have a distinct influence on the upstream flow. This can be seen clearly downstream of the vortex breakdown region where a precontraction of the flow anticipates the flow conditions in the annular outlet (see axi-parallel streamlines in Fig. 3). With increasing swirl number, this influence reaches further upstream, whereby even the structure of the vortex breakdown is modified. This is the case for $S_{0,theo} = 0.95$: From $x = 180$ mm to 400 mm the fluid moves toward the axis with a noticable negative axial velocity component. Herewith, the flow complies with the Taylor-Proudman theorem as far upstream as possible and creates the ear-shaped recirculation zone. This is in agreement with results of Escudier and Keller (1985), who also showed that the structure of the vortex breakdown is influenced by the outlet conditions for downstream swirl numbers exceeding a critical value.

In addition, Fig. 3 indicates the formation of weak outer recirculation zones close to the outlet. A closer view reveals that these toroidal vortices do not mate with the "outlet-jet." Their direction of rotation is opposite to that which a jet-driven recirculation zone would have. They are induced by boundary-layer effects at the bottom of the chamber, which disturb the equilibrium between pressure and centrifugal forces. As a result, fluid moves to decreasing radius along the bottom of the chamber and drives the weak counter-rotating recirculation zone. A similar mechanism is also observed in the so-called tea-cup phenomenon (Lugt, 1983).

In Figs. 5 and 6, the mean axial and tangential velocities U, W are plotted for both swirl intensities at 13 chosen axial locations. At $S_{0,theo} = 0.4$ in the inlet plane ($x = 0$ mm), both mean velocity

Nomenclature

c = velocity magnitude, also cross covariance coefficient
B = block height in axial direction
g_i = angular sensitivity function of the ith wire
l_i = linearization function of the ith wire
n = number of radial and tangential channels
r = radial coordinate
R = inner radius of the inlet annulus
R_i = outer radius of the inlet annulus
$S_{0,theo}$ = theoretical inlet swirl number
u = axial fluctuating velocity
U = axial mean velocity
v = radial fluctuating velocity
V = radial mean velocity
$\dot{V}$ = volumetric flow rate
w = circumferential fluctuating velocity
W = circumferential mean velocity
x = axial coordinate
α = angle between tangential and radial channels
θ = angle of attack
ξ = angle of adjustment of movable blocks
ρ = density
τ = time difference, also turbulent stress
ψ = angle of attack
φ = circumferential coordinate
$\bar{}$ = time average

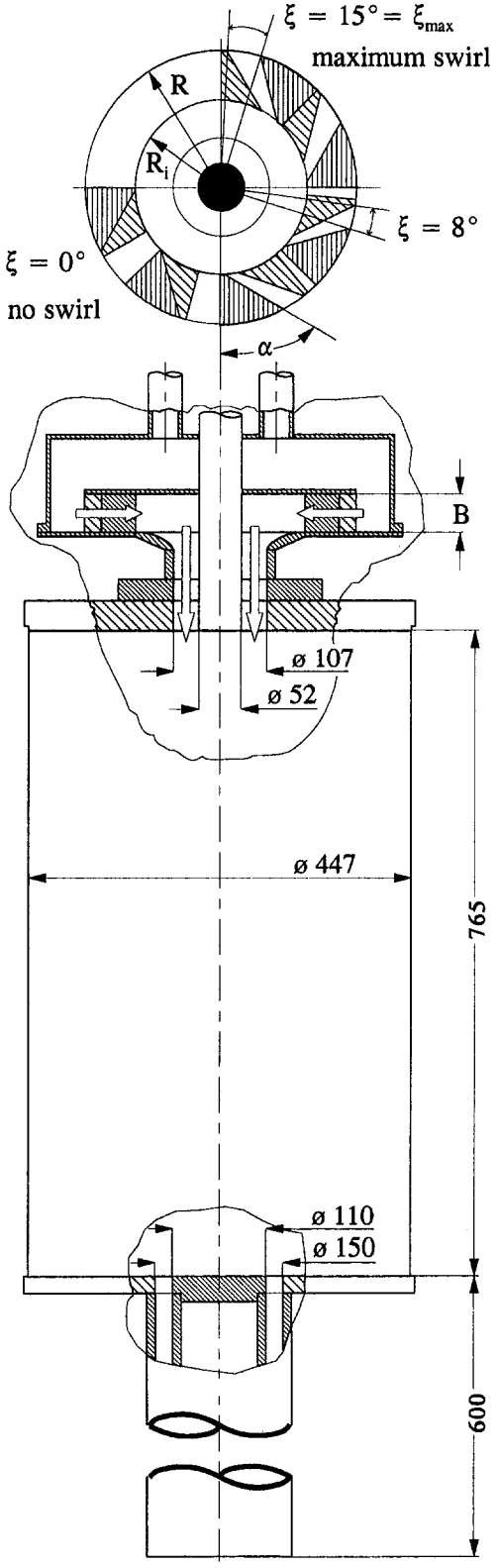

Fig. 1 Isothermal model combustion chamber. Top: movable blocks swirl generator in top and side view.

components are nearly constant, whereas for $S_{0,theo} = 0.95$ both components display a positive slope. The annular jet starts to expand in the combustion chamber. Since the divering swirling jet approximately conserves its angular momentum ($W \cdot r = \text{const}$), the corresponding W-maximum vanishes relatively fast. For $S_{0,theo} = 0.95$, a second maximum becomes visible at $x = 120$

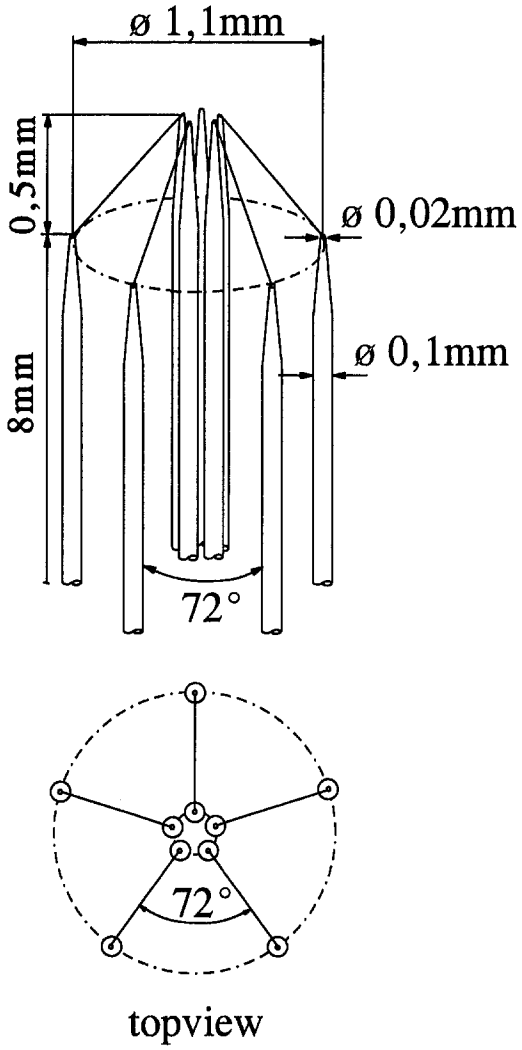

Fig. 2 Sketch of the quintuple hot-wire probe

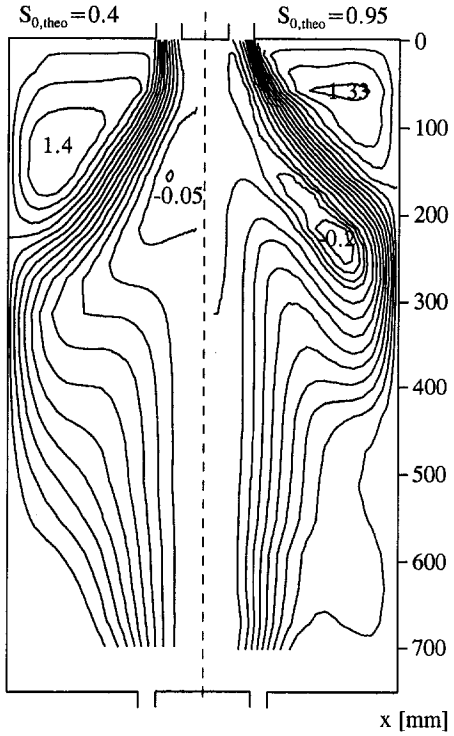

Fig. 3 Isolines of the stream function for both swirl numbers

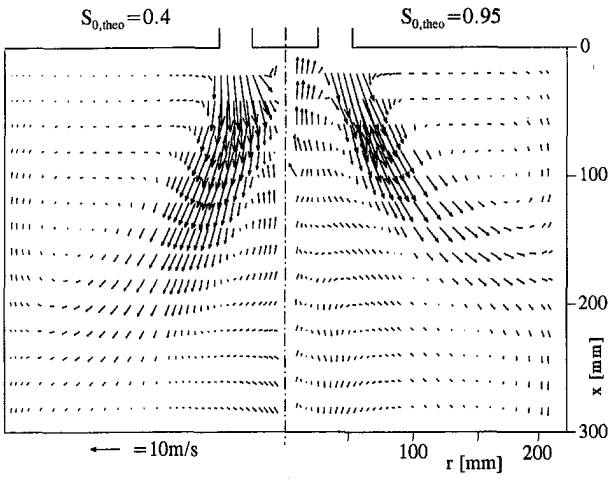

Fig. 4 Vectorplot of the axial and radial mean velocities

mm and r = 35 mm, which corresponds to the maximum of a similarity profile which is well established on three quarters of the chambers length. For $S_{0,theo}$ = 0.4, this similarity profile, consisting of the combined forced-free vortex type, can first clearly be

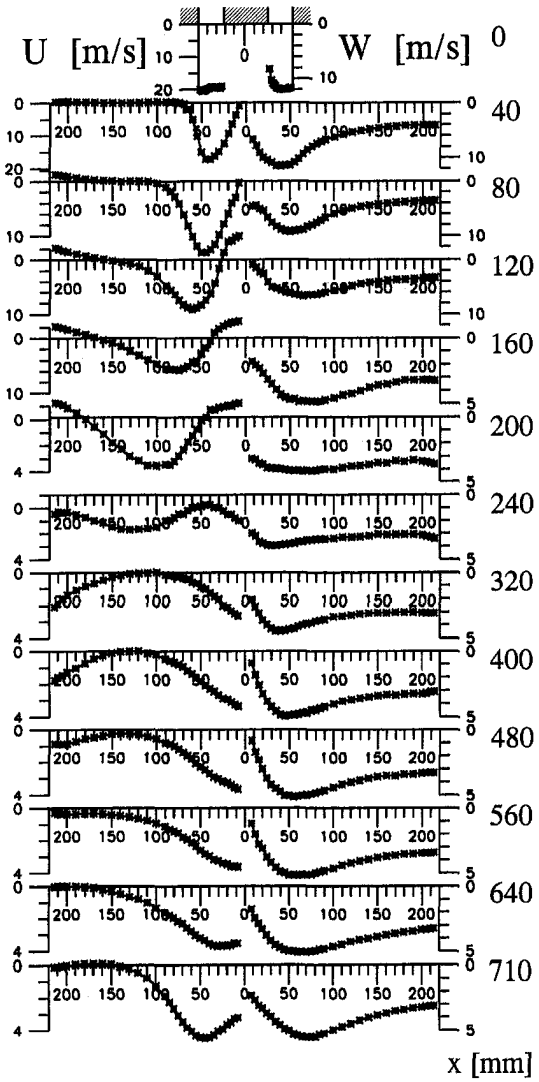

Fig. 5 Mean axial and tangential velocity, $S_{0,theo}$ = 0.4

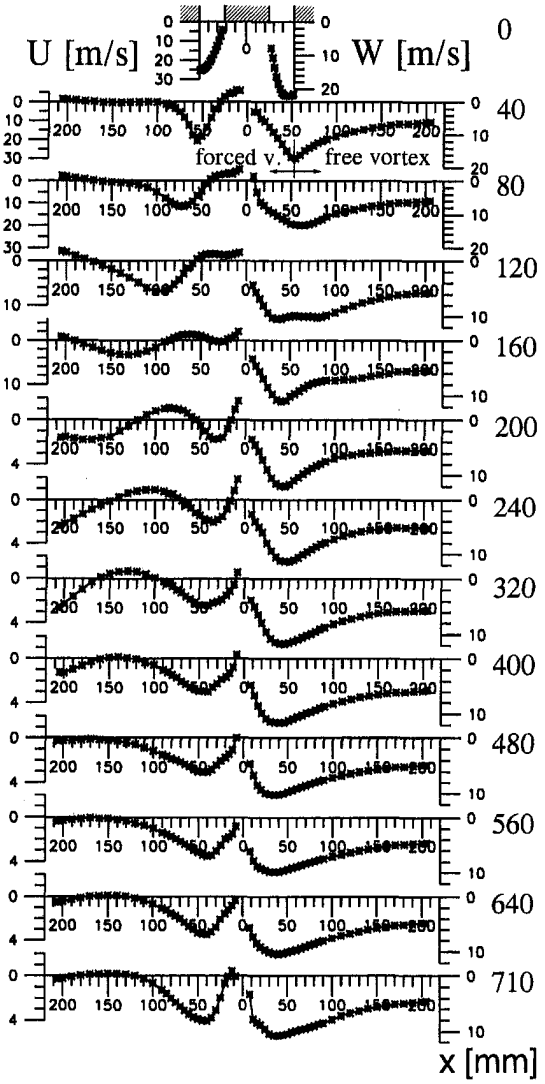

Fig. 6 Mean axial and tangential velocity, $S_{0,theo}$ = 0.95. Forced and free vortex region indicated in x = 40 mm.

identified at x = 320 mm. The generation of the free vortex region indicates a turbulent redistribution process where turbulent eddies conserve partially their angular momentum when exchanging their radial positions (Hirsch, 1995). Correspondingly, the free vortex region can be well approximated by a superposition of solid-body rotation and the potential vortex as expressed by $W(r) = a \cdot r + b/r$. On the other hand, this indicates the influence of the Taylor-Proudman phenomenon, which generally forces the similarity of all velocity profiles. It particularly has great influence on the radial position of the maximum swirl and axial velocities which correspond fairly well with the radial outlet position.

The forced vortex is obviously not resolved for $S_{0,theo}$ = 0.4 between x = 200 mm and 240 mm. Here the fluid moves toward the axis of rotation, which leads, due to the partial angular momentum conservation, to a locally limited displacement of the W-maxima toward the axis of rotation.

4 Turbulence Quantities

Figures 7–12 depict the measured Reynolds stresses for both swirl numbers. The $\overline{u^2}$- and $\overline{v^2}$-profiles for $S_{0,theo}$ = 0.4 (Fig. 7) at x = 40 mm display the maxima which were produced in the swirl generator. Starting at the inlet with almost the same magnitude, $\overline{v^2}$ is strongly damped compared to $\overline{u^2}$, which is in agreement with Rayleigh's stability criterion (1917). Rayleigh's criterion states

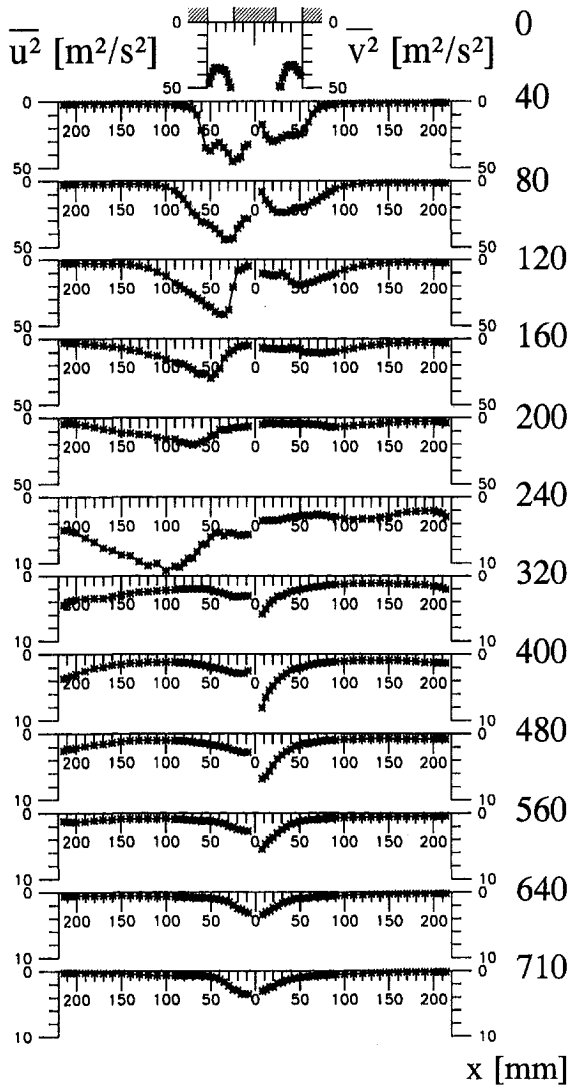

Fig. 7 Reynolds normal stresses $\overline{u^2}$ and $\overline{v^2}$, $S_{0,theo}$ = 0.4

that radial fluctuations are damped for $\partial(W \cdot r)/\partial r > 0$. For $x \leq 160$ mm and $r \leq 50$ mm values of 3 m/s $< \partial(W \cdot r)/\partial r <$ 12 m/s are found. The positions of the $\overline{u^2}$-maxima correspond to the position of the maximum gradient $\partial U/\partial r$ for both swirl numbers up to $x = 140$ mm (Figs. 7, 10), indicating intense local production ($P_{\overline{u2}} \sim \overline{uv}(\partial U/\partial r)$) in the shear zone which is formed by forward and reverse flow in the IRZ. Further downstream, no such steep velocity gradients are found such that $\overline{u^2}$ is convected with the annular jet. This leads to a maximum value of $\overline{u^2}$ in the region where the flow impinges on the wall.

The development of the normal stress $\overline{w^2}$ (Figs. 8, 11) is hardly influenced by its maximum at the inlet. For $S_{0,theo} = 0.4$ (Fig. 8) at $x =$ 40 mm, two maxima at the edges of the annular jet can be observed. The inner maximum arises from production of $\overline{w^2}(P_{\overline{w2}} \sim \overline{vw}(\partial W/\partial r))$. At $S_{0,theo} = 0.95$ an unstable tangential velocity profile ($\partial(W \cdot r)/\partial r \approx -5$ m/s) prevails through the first 30 mm after the inlet at the outer jet boundary and causes a $\overline{w^2}$-maximum (Fig. 11).

It seems noteworthy that the distribution of the turbulence quantities exhibits distinct differences between the forced and the free vortex domain (see Fig. 6). The decay of the normal stresses in the forced vortex region is significantly reduced compared to the free vortex region. This can be demonstrated by a comparison of the decay rates of $\overline{u^2}$ in both flow regions. For $S_{0,theo} = 0.95$, the annular jet reaches the free vortex region ($r > 60$ mm) already at $x = 60$ mm due to its larger spread angle. From $x = 60$ mm to 140 mm, a decay rate $\Delta\overline{u^2}/\Delta x$ ten times higher than in the weaker swirling flow can be observed, whose $\overline{u^2}$-maximum remains in the corresponding axial distance in the forced vortex region ($r < 60$ mm). This decreased decay of turbulent kinetic energy in the forced vortex region is observed for all normal stresses and will be discussed in detail below.

A discussion of the measured shear stresses concludes the current section. The shear stresses $\overline{uv}$ in the jet-dominated domain are mainly a consequence of the gradient $\partial U/\partial r$ and correspondingly become zero at the U-maxima positions (Figs. 8, 11). In doing so, $\overline{uv}$ forces the spreading of the annular jet until the similarity profile for the axial velocity has been developed. Then the magnitude of $\overline{uv}$ is reduced considerably. Despite its minor magnitude in the downstream area, $\overline{uv}$—especially in the lowest measuring position—is still related to the corresponding gradient and therefore contributes to the spreading of the "outlet-jet" (see Fig. 8), which is formed according to the Taylor-Proudman phenomenon.

The shear stress $\overline{vw}$, which is responsible for the turbulent radial transfer of angular momentum, displays the smallest values of all shear stresses in almost the whole flow (Figs. 9, 12). Only in areas where the W-profiles are modified by the diverging annular jet, $\overline{vw}$ displays larger values, which reduce the deviations from the similarity profile. For instance, at $S_{0,theo} = 0.95$, $\overline{vw}$ is negative close to the axis at $x = 40$ mm, creating therewith a more perfect forced

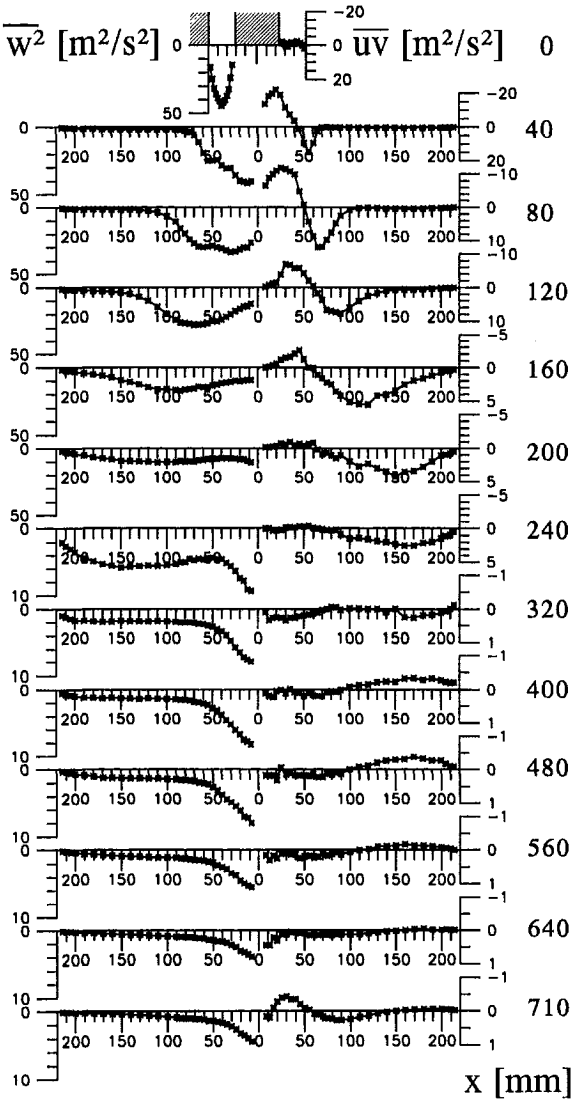

Fig. 8 Reynolds normal stress $\overline{w^2}$ and shear stress $\overline{uv}$, $S_{0,theo}$ = 0.4

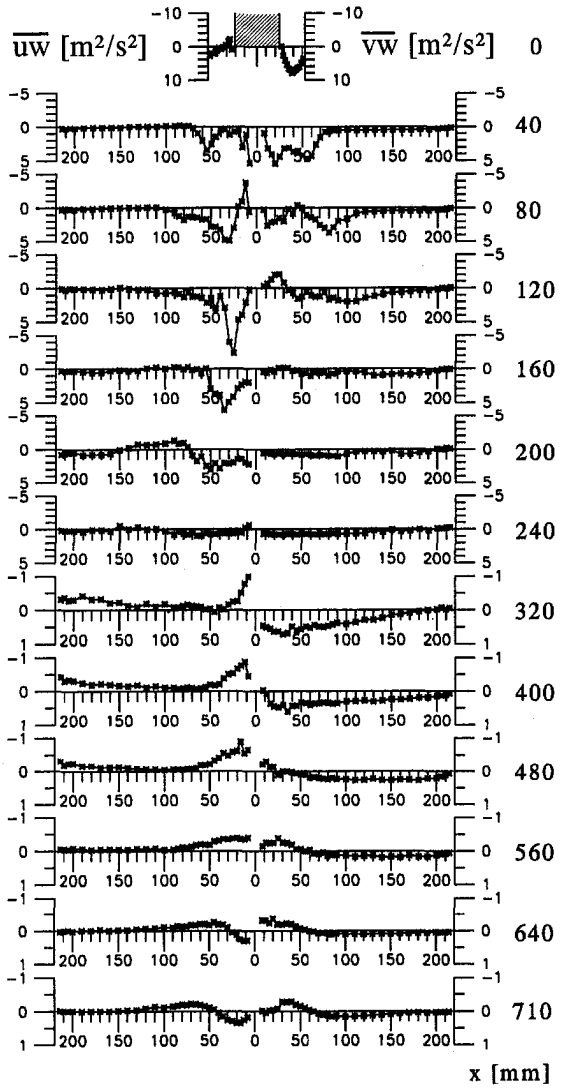

Fig. 9 Reynolds shear stresses $\overline{uw}$ and $\overline{vw}$, $S_{0,theo} = 0.4$

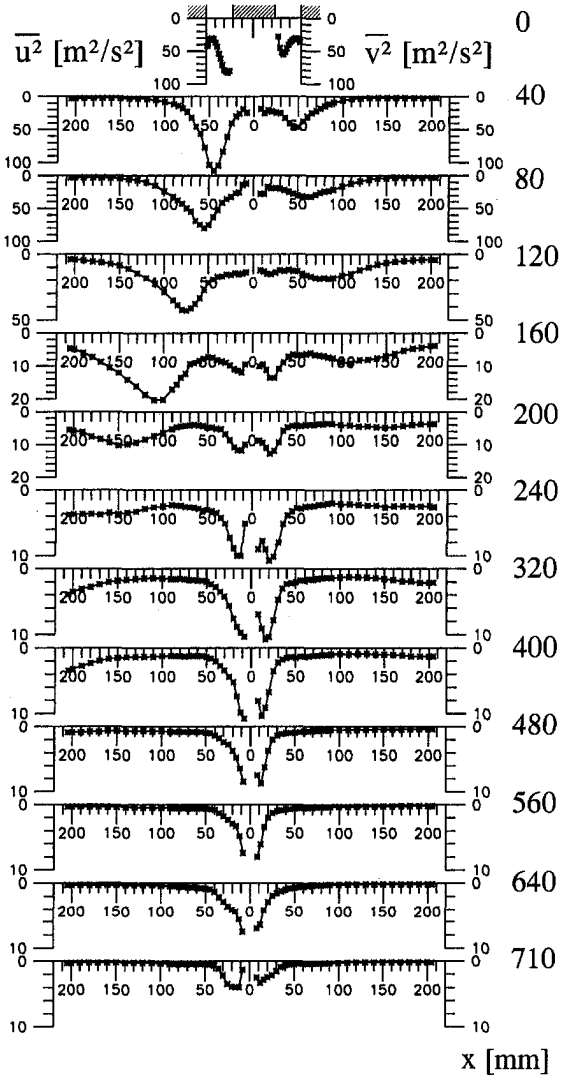

Fig. 10 Reynolds normal stresses $\overline{u^2}$ and $\overline{v^2}$, $S_{0,theo} = 0.95$

vortex. Downstream of the vortex breakdown, small positive values of $\overline{vw}$ indicate a transfer of circumferential momentum to the wall, thereby compensating wall friction losses. Close to the outlet, the $\overline{vw}$-profiles display distributions similar to the $\overline{uv}$-profiles which work against the displacement of the W-maximum toward the radial position of the outlet.

5 Superimposed Unsteady Effects

Basically, swirling flows tend to exhibit hyperbolic behavior. Therefore, it is not surprising that power spectra, computed from linearized single-hot-wire measurements, display many peaks of different frequencies over the flowfield. Because of the minor magnitudes of most peaks, these are of secondary importance and will not be discussed here.

However, the significantly enhanced normal stress levels close to the axis of rotation are surprising and indicate the presence of a "pseudo turbulence." This is, because in a stationary and axisymmetric swirling flow, minimum turbulence levels are expected to occur close to the axis (Rayleigh's criterion).

The isolines of the normal stresses for $S_{0,theo} = 0.95$ shown in Fig. 13 illustrate that the high levels of the normal stresses downstream of the IRZ are limited to the forced vortex region ($r \lesssim 50$ mm). Moreover, they elucidate that the normal stress levels in the vortex core diminish only gradually in axial direction. Analyses of velocity sequences in the vortex core region (not shown) point out that a random motion of the core with a maximum eccentricity of $\Delta r = 10$ mm prevails. Power spectra indicate a periodic portion of approximately 4 Hz (Fig. 14). Two-point correlation measurements (Fig. 15), taken with two axially displaced single-hot-wire probes, indicate that the vortex core moves nearly as a whole. When both probes are situated in the vortex core ($r = 10$ mm) at an axial distance of $\Delta x = 200$ mm, the cross covariance coefficient achieves a value of $c_{12}(\tau = 0) = 0.2$, which indicates a similarity of both signals without time delay τ. The same similarity can be observed in the free vortex region ($r = 120$ mm) at an axial distance of only 25 mm, whereas at the distance of $\Delta x = 200$ mm, the cross covariance coefficient is zero. These clearly different correlations indicate a strong coupling of the flow quantities in the vortex core and suggest that the vortex core moves nearly as a continuous unit largely independent of the free vortex region. The energy of these movements stems from turbulent fluctuations which converge at the bottom of the IRZ.

This interpretation is in good agreement with the results of examinations concerning the development of homogeneous turbulence in solid body rotation by Jacquin et al. (1990) and Ibbetson and Tritton (1975). These authors show that solid body rotation generally slows down the decay of turbulent kinetic energy, as it was observed here. This effect is linked to a transition toward a two-dimensional turbulence structure (McEwan, 1976), which inhibits the energy transfer mechanism by vortex stretching. Furthermore, they found that the axial correlation of the radial fluc-

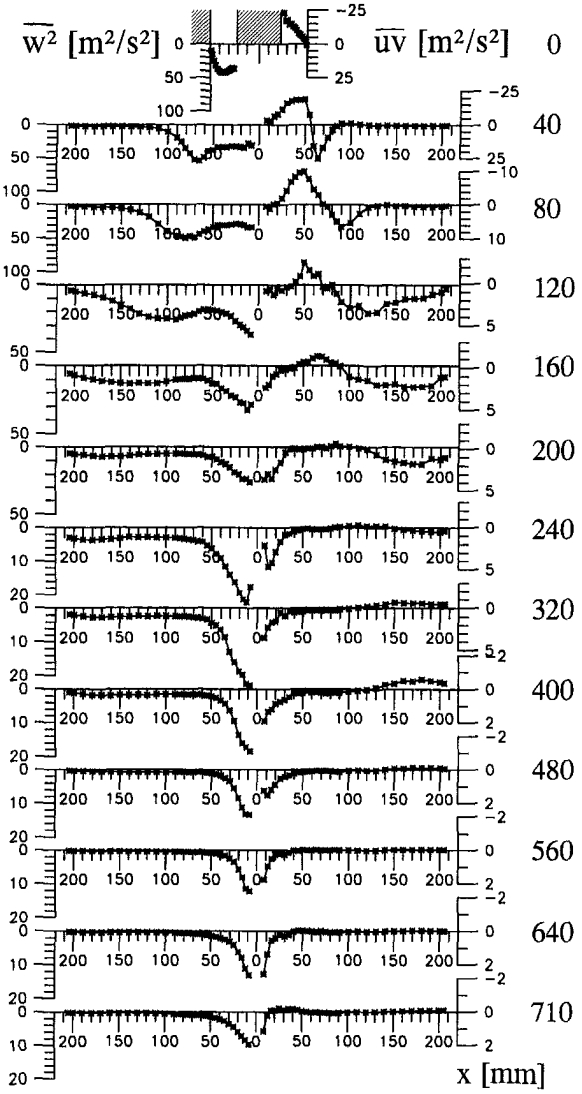

Fig. 11 Reynolds normal stress $\overline{w^2}$ and shear stress $\overline{uv}$, $S_{0,theo} = 0.95$

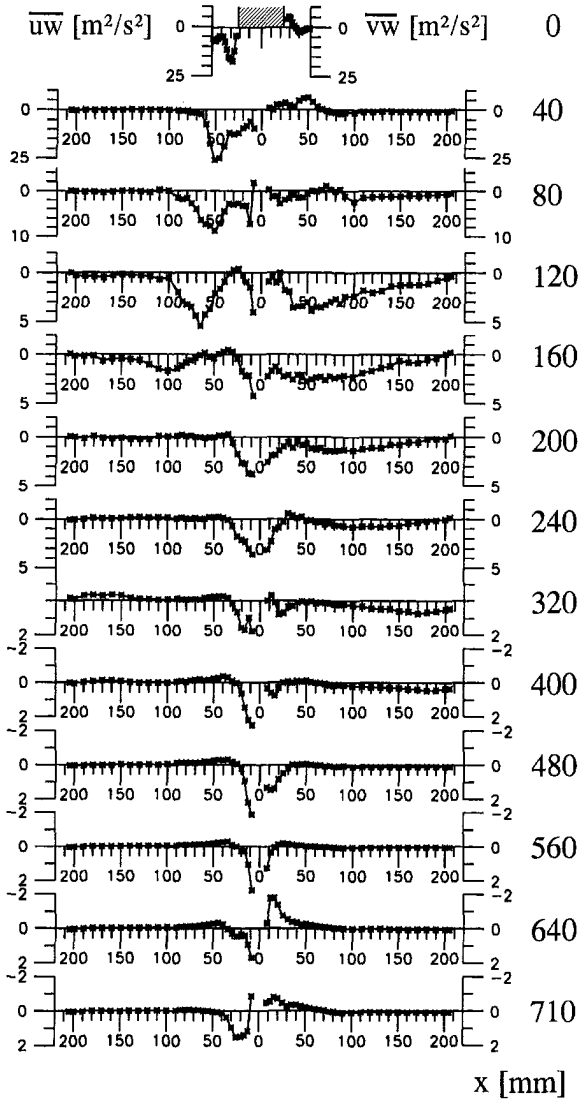

Fig. 12 Reynolds shear stresses $\overline{uw}$ and $\overline{vw}$, $S_{0,theo} = 0.95$

tuating velocity v increases with the rotation rates. Jacquin et al. (1990) connect these findings with Coriolis-force effects, which inhibit transversal movements of radially displaced fluid elements in solid body rotation (Schmid, 1991). They further define a Coriolis lengthscale and state that rotation affects turbulence when the energy-containing eddies become sufficiently large to be influenced by the "transverse confinement" of the Coriolis force.

These arguments allow for a more specific interpretation of the observed vortex core behavior in two respects. First, the quasi-two-dimensional turbulence structure gives an impression on the mechanisms, which are responsible for the strong axial coupling of the fluctuating velocities. This effect can also be interpreted as an extension of the Taylor-Proudman phenomenon for turbulent fluid motions. Second, the sharp restriction of the observed effects on the vortex core domain becomes immediately plausible, since the Coriolis force is distinctly diminished when approaching the free vortex domain.

6 Experimental Uncertainty

The measurement accuracy of the quintuple measurement technique is assessed in detail by Holzäpfel et al. (1994a) and Holzäpfel (1996). Basically, the accuracy decreases with increasing angles of attack of the probe (during the measurements the probe is directed into the mean flow direction). The flow direction of the

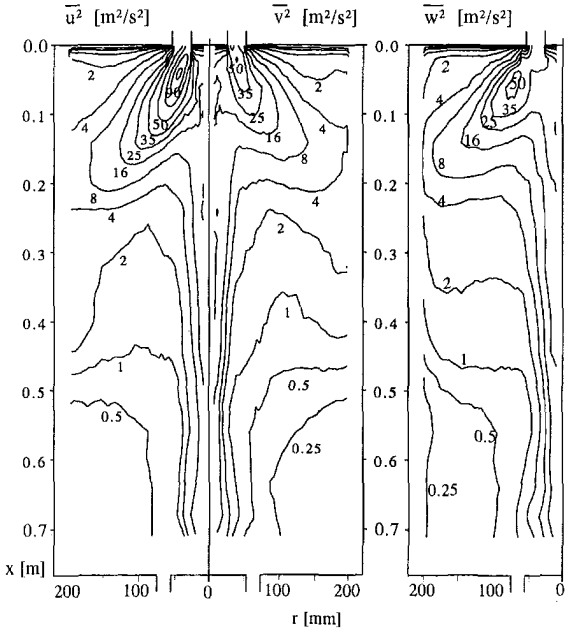

Fig. 13 Isolines of the Reynolds normal stresses, $S_{0,theo} = 0.95$

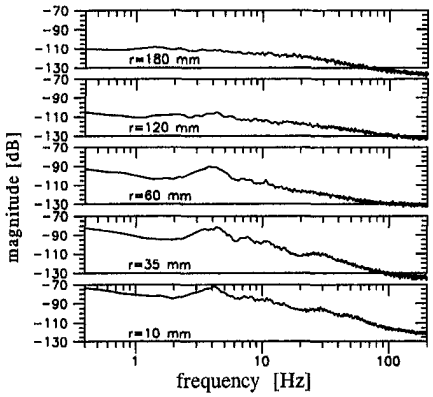

Fig. 14 Power spectra, $S_{0,theo} = 0.95$, $x = 600$ mm

mean velocities is determined with an accuracy of 2 deg for all angles of attack and the standard deviation of the velocity magnitude amounts to 0.1 m/s. For small angles of attack (<20 deg) maximum experimental uncertainties for the Reynolds normal stresses of ±10% and the shear stresses of ±15% are found. Maximum deviations are always below ±20% for the normal stresses and below ±30% for the shear stresses.

Additional uncertainties caused by the superimposed unsteady effects mentioned above are difficult to quantify. The uniqueness domain of the quintuple technique can be exceeded close to the axis ($r \leq 20$ mm) caused by the core motions. This leads to systematic adulterations of all measured flow quantities and particularly the shear stresses. For the shear stresses the uncertainties could reach 100% in the worst case. This would correspond to the case that at $r = 0$ mm the uniqueness domain would be exceeded during the half period of the unsteady vortex core movements. Therefore only results for $r \geq 8$ mm are presented.

7 Conclusions

Detailed measurements of the mean velocities and the complete Reynolds stress tensor were performed with a newly developed five-sensor hot-wire measurement technique in an isothermal model combustion chamber at two different levels of swirl. The distinct smoothness and the reproducibility of the Reynolds stresses elucidate the reliability of the measured data base. The data are listed in Holzäpfel (1996).

The influence of rotation on the turbulent flow is mainly demonstrated by (i) the mean flow topology which is strongly affected by the Taylor-Proudman phenomenon: similarity velocity profiles are enforced far upstream by the outflow pattern, and even modulate the appearance of the internal recirculation zone; (ii) the formation of a similarity tangential velocity profile which is maintained by the reduced turbulent radial transport of angular momentum where the radial transport is governed by the conservation of the angular momentum of radially displaced fluid; (iii) the strong axial coupling of the vortex core region which performs a partially periodic random motion, and adulterates the measured Reynolds stresses.

The measurements show that three-dimensional and time-dependent codes are necessary to correctly predict all features of confined turbulent swirling flows. This is so even when the most dominant unsteady effect, coming from the classical precessing vortex core, can be suppressed in the experiment. The presented flow data can be used for validation purposes of two-dimensional codes, because the most relevant features of practical swirling flows are not altered by unsteady fluid motions.

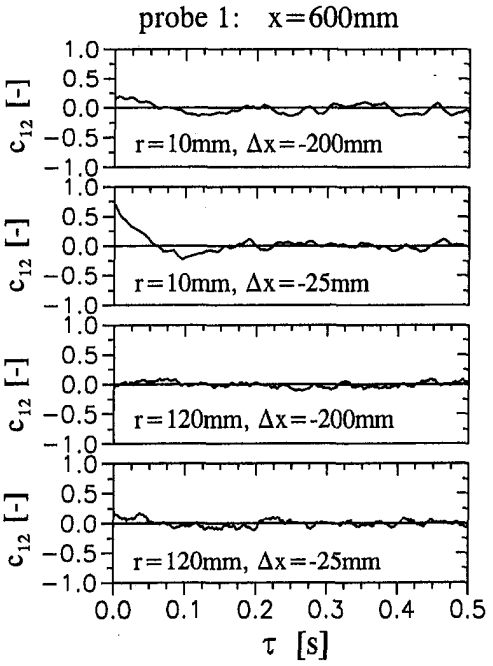

Fig. 15 Cross covariance coefficients, measured with two axially displaced single hot-wire probes, $S_{0,theo} = 0.95$

Acknowledgments

The work of C. Schuler and D. Guyot, former students at the University of Karlsruhe and H. Klette, who manufactured the hot-wire probes, is gratefully acknowledged. This work was supported by the Deutsche Forschungsgemeinschaft, SFB 167, Hochbelastete Brennräume-stationäre Gleichdruckverbrennung, TP A10.

References

Armfield, S. W., Cho, N. H., and Fletcher, C. A. J., 1990, "Prediction of Turbulence Quantities for Swirling Flow in Conical Diffusers," *AIAA Journal,* Vol. 28, pp. 453–460.

Benjamin, T. B., 1962, "Theory of the Vortex Breakdown Phenomenon," *Journal of Fluid Mechanics,* Vol. 14, pp. 593–629.

Döbbeling, K., Lenze, B., and Leuckel, W., 1990, "Computer-Aided Calibration and Measurements with a Quadruple Hotwire Probe," *Experiments in Fluids,* Vol. 8, pp. 257–262.

Durst, F., and Wennerberg, D., 1991, "Numerical Aspects of Calculation of Confined Swirling Flows with Internal Recirculation," *International Journal for Numerical Methods in Fluids,* Vol. 12, pp. 203–224.

Escudier, M. P., and Keller, J. J., 1985, "Recirculation in Swirling Flow: A Manifestation of Vortex Breakdown," *AIAA Journal,* Vol. 23, pp. 111–116.

Hirai, S., and Takagi, T., 1995, "Parameters Dominating Swirl Effects on Turbulent Transport Derived from Stress-Scalar-Flux Transport Equation," *International Journal of Heat and Mass Transfer,* Vol. 38, pp. 2175–2182.

Hirsch, C., 1995, "Ein Beitrag zur Wechselwirkung von Turbulenz und Drall," Dissertation, Universität Karlsruhe.

Hirsch, C., and Leuckel, W., 1996, "A Curvature Correction for the k-ϵ Model in Engineering Applications," *Proceedings 3rd International Symposium on Engineering Turbulence Modelling and Measurements,* Heraklion-Crete, pp. 71–80.

Holzäpfel, F., Lenze, B., and Leuckel, W., 1994a, "Assessment of a Quintuple Hotwire Measurement Technique for Highly Turbulent Flows," *Experiments in Fluids,* Vol. 18, pp. 100–106.

Holzäpfel, F., Lenze, B., and Leuckel, W., 1994b, "Quintuple Hot-Wire Measurements in Highly Turbulent Confined Swirl Flows," *Proceedings 2nd International Conference on Fluid Dynamic Measurements and Applications,* Beijing, pp. 338–343.

Holzäpfel, F., 1996, "Zur Turbulenzstruktur freier und eingeschlossener Drehströmungen," Dissertation, Universität Karlsruhe.

Ibbetson, A., and Tritton, D. J., 1975, "Experiments in Turbulence in a Rotating Fluid," *Journal of Fluid Mechanics,* Vol. 68, pp. 639–672.

Jacobs, J., and Günther, R., 1975, "Periodische Störungen in Drallströmungen," *Forschung im Ingenieur-Wesen,* Vol. 41, pp. 85–91.

Jacquin, L., Leuchter, O., Geffroy, P., and Mathieu, J., 1990, "Homogeneous Turbulence in the Presence of Rotation," *Journal of Fluid Mechanics,* Vol. 220, pp. 1–52.

Leschziner, M. A., 1991, "Modelling Strongly Swirling Flows with Advanced Turbulence Closures," *Advances in Numerical Simulation of Turbulent Flows,* FED-Vol. 117, ASME, Portland, Oregon.

Leuckel, W., 1967, "Swirl Intensities, Swirl Types and Energy Losses of Different Swirl Generating Devices," IFRF Doc G 02/a/16, IJmuiden.

Lugt, H. J., 1983, *Vortex Flow in Nature and Technology,* Wiley, New York, p. 141.

McEwan, A. D., 1976, "Angular Momentum Diffusion and the Initiation of Cyclones," *Nature,* Vol. 260, pp. 126–128.

Pierce, C. D., and Moin, P., 1998, "Large Eddy Simulation of a Confined Coaxial Jet with Swirl and Heat Release," AIAA 98-2892, ,29th AIAA Fluid Dynamics Conference, Albuquerque, NM.

Proudman, J., 1916, "On the Motion of Solids in Liquids Possessing Vorticity," *Proceedings of the Royal Society,* Series A, Vol. 92, p. 408.

Rayleigh, Lord, O. M., 1917, "On the Dynamics of Revolving Fluids," *Proceedings of the Royal Society,* Series A, Vol. 93, pp. 148–154.

Riahi, A., Salcudean, M., and Hill, P. G., 1990, "Computer Simulation of Turbulent Swirling Flows," *International Journal for Numerical Methods in Engineering,* Vol. 29, pp. 533–557.

Sarpkaya, T., 1971, "On Stationary and Traveling Vortex Breakdowns," *Journal of Fluid Mechanics,* Vol. 45, pp. 545–559.

Schmid, C., 1991, "Drallbrenner-Simulation durch Starrkörperwirbel-Strömungen unter Einbeziehung von drallfreier Primärluft und Verbrennung," Dissertation, Universität Karlsruhe.

Weber, R., Visser, B. M., and Boysan, F., 1990, "Assessment of Turbulence Modeling for Engineering Prediction of Swirling Vortices in the Near Burner Zone," *International Journal for Heat and Fluid Flow,* Vol. 11, pp. 225–235.

Turbulent Boundary Layers Subjected to Multiple Strains

Andreas C. Schwarz[1]
Graduate Research Assistant.

Michael W. Plesniak[2]
Associate Professor.

S. N. B. Murthy
Senior Researcher.

School of Mechanical Engineering,
Maurice J. Zucrow Laboratories,
Purdue University,
West Lafayette, IN 47907-1288
email: plesniak@ecn.purdue.edu

Turbomachinery flows can be extremely difficult to predict, due to a multitude of effects, including interacting strain rates, compressibility, and rotation. The primary objective of this investigation was to study the influence of multiple strain rates (favorable streamwise pressure gradient combined with radial pressure gradient due to convex curvature) on the structure of the turbulent boundary layer. The emphasis was on the initial region of curvature, which is relevant to the leading edge of a stator vane, for example. In order to gain better insight into the dynamics of complex turbulent boundary layers, detailed velocity measurements were made in a low-speed water tunnel using a two-component laser Doppler velocimeter. The mean and fluctuating velocity profiles showed that the influence of the strong favorable pressure augmented the stabilizing effects of convex curvature. The trends exhibited by the primary Reynolds shear stress followed those of the mean turbulent bursting frequency, i.e., a decrease in the bursting frequency coincided with a reduction of the peak Reynolds shear stress. It was found that the effects of these two strain rates were not superposable, or additive in any simple manner. Thus, the dynamics of the large energy-containing eddies and their interaction with the turbulence production mechanisms must be considered for modeling turbulent flows with multiple strain rates.

Introduction

With an increased emphasis on higher thrust-to-weight propulsion systems (e.g., Integrated High Performance Turbine Engine Technology, IHPTET), accurate prediction of heat transfer for effective blade cooling has become increasingly important. It is well known that the flow through a turbine blade passage is highly complex, due in part to interactions of streamwise curvature effects and longitudinal strains arising from pressure gradients. Because of these complexities, it is necessary to understand the dynamics of the turbulent boundary layer (TBL) in order to develop and test appropriate turbulence models for these flow fields.

Although there have been relatively few studies concerning multiple additional rates of strain, a number of experiments have been performed to study the influence of single additional rates of strain in TBLs, e.g., convex or concave curvature (cf. So and Mellor, 1973; Gillis and Johnston, 1983; Barlow and Johnston, 1988a, b; and Schwarz and Plesniak, 1996a, b), as well as adverse and favorable streamwise pressure gradients (cf. Kline et al., 1967; Narasimha and Sreenivasan, 1979; Nagano et al., 1991; and White and Tiederman, 1990).

In recent work, Spalart and Shur (1997) modeled the effects of additional strain rates by using an equation governing the total rate of change of the angle of the principal axes of the strain-rate tensor with respect to an inertial frame of reference. Unlike the traditional "extra" strain rate parameter, i.e., $-\bar{U}/R$, their quantity is Galilean-invariant and unifies rotation and curvature effects. They hypothesized that turbulence is enhanced under weak rotation or curvature if the principal axes of the Reynolds stress lead those of the strain rate, and vice versa.

Groundbreaking work on the effects of streamwise pressure gradients on turbulent boundary layer structure was conducted by Kline et al. (1967), who studied the response of a turbulent boundary to zero, adverse and favorable streamwise pressure gradients. They found that turbulent bursts, which result in significant production of turbulence energy and facilitate its exchange with the outer portions of the boundary layer, are affected by streamwise pressure gradients. Adverse pressure gradients were found to make bursting more frequent and violent, while favorable pressure gradients reduced bursting frequency, and, if sufficiently accelerated ($k \approx 3.5 \times 10^{-6}$) the bursting process ceased.

There have been relatively few studies with multiple additional strain rates. One example is the S-shaped duct study by Bandyopadhyay and Ahmed (1993) in which multiple curvatures and pressure gradients are experienced. Other noteworthy studies are those of Baskaran et al. (1991) and Webster et al. (1996), in which a turbulent boundary layer over a curved surface bump or "hill" was examined. A limitation of these studies is that the individual strengths of the radial and streamwise pressure gradients were not independently controllable.

In summary, the effects of single extra rates of strain have been widely studied, but there is a lack of detailed information regarding the turbulence structure of boundary layers that experience *multiple interacting strain rates.* The primary objective of this investigation was to examine how radial and streamwise pressure gradients of various magnitudes interacted with each other, and subsequently to determine their effect on the boundary layer structure and dynamics. This paper is a continuation of previously published work, in which results for a strongly curved TBL were reported (Schwarz and Plesniak, 1996b). The emphasis here is on an entirely new data set (moderate convex curvature as opposed to strong convex curvature), as well as on additional structural details inferred from these time-resolved conditionally-sampled data.

Experimental Facility and Techniques

All data were acquired in a recirculating water channel facility driven by four centrifugal pumps each rated at 5.7×10^{-3} m^3/s (90 gpm). An equilibrium turbulent boundary was developed on the smooth wall of the straight section 1.92 m long upstream of the curved test section. The constant radius ($R = 700$ mm) 90° curved test section was designed to yield a smooth transition in the wall contours. At the onset of curvature ($s - s_o = 0$), the spanwise height of the test section is 200 mm and the width is approximately 110 mm. With an initial boundary layer thickness of $\delta_o \approx 35$ mm, the curvature parameter is $\delta_o/R \approx 0.05$, which comprises moderate curvature. A flexible wall placed between the measurement

[1] Current address: Caterpillar Inc., Corporate Information Services, Product & Process Applications, East Peoria, IL.

[2] Corresponding author.

Contributed by the Fluids Engineering Division for publication in the JOURNAL OF FLUIDS ENGINEERING. Manuscript received by the Fluids Engineering Division November 17, 1998; revised manuscript received June 4, 1999. Associate Technical Editor: D. R. Williams.

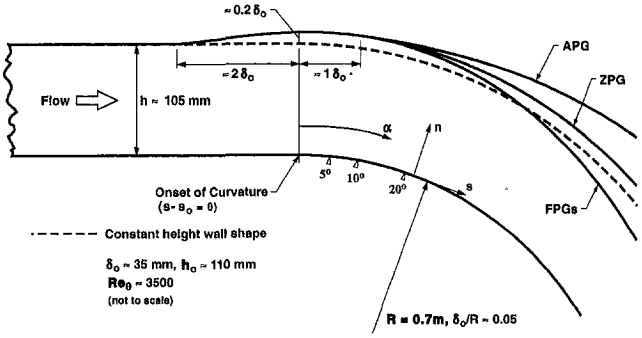

Fig. 1 Schematic of curved test section and wall shapes to achieve desired pressure gradients

and opposite side wall was adjusted to yield a zero pressure gradient (ZPG) in the straight portion and a zero or strong favorable pressure gradients in the curved test section. Figure 1 depicts typical wall shapes used to establish the desired pressure distribution on the convex wall (the exact wall shapes are available in Schwarz, 1998). A region of local acceleration persisted immediately downstream of the onset of curvature ($0 \le s - s_o \le 2\delta_o$), due to the discontinuity in wall curvature, despite widening of the cross-sectional area in that region. For additional details of the test section and pressure distribution see Schwarz (1998) and Schwarz and Plesniak (1996a, b).

Laser Doppler Velocimetry. A two-component laser-Doppler velocimetry (LDV) TSI® model 9100-8 system was employed for simultaneous measurements of the streamwise and wall-normal instantaneous velocity components. The probe volume was 45 μm in diameter and had a spanwise extent of 920 μm, which corresponds to approximately 2 and 40 viscous units, respectively. The probe was oriented with the smaller dimension parallel to the wall for high spatial resolution. In order to enhance the spatial coincidence, a 50 μm pinhole was inserted into the receiving optics, which reduced the effective probe volume length to 12 viscous units. The flow was seeded with 0.3 μm diameter spherical particles from homogenized cream at a concentration of approximately 2.5 ml/m^3.

For the two-component velocity profiles, at least 10,000 and up to 20,000 data points were acquired for each velocity component to ensure converged statistics. Velocity bias, which occurs in LDV measurements of turbulent flows (see McLaughlin and Tiederman, 1973), was eliminated using the fixed-waiting-time sampling method. The inhibit time, which is the time between velocity realizations, was kept at more than ten times the inverse of the validation rate, and the validation rate was maintained (at least five times) in excess of the Kolmogorov frequency, which is representative of the smallest scales in the flow. Typical values for the inhibit time and validation rate were approximately 10–15 msec and 2500 Hz, respectively. The time-resolved measurements, necessary for burst analysis, consisted of 100,000 velocity realizations with the TSI 1980B counter processors operating in the single-point per burst mode. The particle arrival rate was maintained in excess of the viscous frequency of the flow inferred from $f_{vis} = \partial \bar{U}/\partial y|_{y=0} \approx u_\tau^2/\nu$. Typical values of the wall strain rate were 1250 Hz for the zero and 3150 Hz for the strong favorable streamwise pressure gradient.

Burst Detection. The uv_2 "quadrant" technique (Lu and Willmarth, 1973) was used for ejection detection with the probe located at $y^+ \approx 20$. Because there can be one or more ejections per burst, it was also necessary to group multiple ejections appropriately, depending on whether they originated from the same or from different bursts, through the use of a grouping time, τ_g. This grouping procedure was developed by Bogard and Tiederman (1986) and has also been used by other investigators (Barlow and Johnston, 1988b; and Schwarz and Plesniak, 1996a). The reported time between bursts ($\bar{T}_B$) is calculated by simply averaging the values within the threshold-independent range, and the burst frequency, $\bar{f}_B$ is $1/\bar{T}_B$. Details of the grouping procedure and determining the threshold-independent range are discussed by Schwarz and Plesniak (1996a).

Error Analysis. The error analysis for all measured quantities was based on the methodology outlined by Kline and McClintock (1953) and Moffat (1988). A 95% confidence interval for Gaussian (or nearly Gaussian) distributions was assumed.

Calculation of uncertainty estimates for the LDV data followed the procedure used by Yanta and Smith (1973) and Walker and Tiederman (1988), and are reported in Schwarz (1998). The main source of error is the uncertainty in the determination of the beam-crossing angle, which affects the fringe spacing calculation. This results in an uncertainty of 0.4 percent for the measured velocity component. In addition, the uncertainty in the estimate of

Nomenclature

B = log-law constant for intercept, $B = 5.0$
$\bar{f}_B$ = mean burst frequency, $\bar{f}_B = 1/\bar{T}_B$, 1/s
f_B^+ = inner-normalized burst frequency, $f_B^+ = \bar{f}_B \nu/u_\tau^2$
f_{vis} = viscous frequency, $f_{vis} = \partial \bar{U}/\partial y|_w = u_\tau^2/\nu$, 1/s
FPG = favorable pressure gradient
k = acceleration parameter, $k = \nu/U_e^2 \cdot dU_e/ds = -\nu/(\rho U_e^2) \cdot dP/ds$
N = number of samples for statistics
P = mean static pressure, Pa
R = radius of curvature, mm; shear stress correlation coefficient in (1.2*b*)
Re_θ = momentum thickness Reynolds number, $\mathrm{Re}_\theta = U_{pw}\theta/\nu$
s = streamwise coordinate, mm
s_o = location of onset of curvature, mm
SFPG = strong favorable pressure gradient
$\bar{T}_B$ = mean burst period, s
$\bar{U}$ = mean streamwise velocity, m/s
U^+ = inner-normalized streamwise velocity, $U^+ = \bar{U}/u_\tau$
U_c^+ = inner-normalized, curvature corrected streamwise velocity, $U_c^+ = (\bar{U}/u_\tau)\cdot(1 + y/R)$
U_e = streamwise velocity at edge of boundary layer, m/s
u^+ = inner-normalized, streamwise RMS velocity
u_τ = shear velocity, $u_\tau = \sqrt{\tau_w/\rho}$, m/s
$\overline{uv}$ = primary Reynolds shear stress (divided by ρ), m^2/s^2
uv^+ = inner-normalized primary Reynolds shear stress, $uv^+ = \overline{uv}/u_\tau^2$
v^+ = inner-normalized, wall-normal RMS velocity
y = wall-normal coordinate, mm
y^+ = inner-normalized wall-normal coordinate, $y^+ = yu_\tau/\nu$
ZPG = zero pressure gradient
α = streamwise angular position in curved test section, deg
δ = boundary layer thickness, mm
δ_o = initial boundary layer thickness (at onset of curvature), mm
κ = von Karman constant, $\kappa = 0.41$
ν = kinematic viscosity, m^2/s
ρ = fluid density, kg/m^3
θ = momentum thickness, mm
τ_g = grouping time for mean bursting period, s
τ_w = wall shear stress, N/m^2
v_i = uncertainty in the quantity i, units of "i"

statistical quantities depends on both the ensemble size and the RMS level for a mean quantity but solely on the ensemble size for a RMS quantity. The following expressions were derived:

$$\frac{v_{\bar{U}}}{\bar{U}} \approx \left[(0.004)^2 + \frac{1}{N}\left(\frac{u'}{\bar{U}}\right)^2 \right]^{1/2}, \qquad \frac{v_{\bar{V}}}{\bar{U}} \approx \left[(0.004)^2 + \frac{1}{N}\left(\frac{v'}{\bar{U}}\right)^2 \right]^{1/2} \quad (1.1)$$

$$\frac{v_{u'}}{u'} \approx \left[(0.004)^2 + \frac{1}{2N} \right]^{1/2}, \qquad \frac{v_{v'}}{v'} \approx \left[(0.004)^2 \left(\frac{\overline{uv}}{v'^2}\right)^2 + \frac{1}{2N} \right]^{1/2} \quad (1.2a)$$

$$\frac{v_{\overline{uv}}}{\overline{uv}} \approx \left[(0.004)^2 \left(1 + \frac{u'^2}{\overline{uv}}\right)^2 + \frac{1}{N}\left(\frac{2}{R}\right)^2 \right]^{1/2} \quad (1.2b)$$

where N is the number of samples and R is the shear stress correlation coefficient. The two terms in each expression in brackets represent the uncertainty in determining the fringe spacing and the statistical uncertainty, respectively.

Typical uncertainties on the RMS and mean velocities are on the order of the plot symbol sizes, i.e. less than 1%, except for the near-wall region ($y^+ \leq 10$). For $y^+ \leq 10$, the measured wall-normal RMS velocity component was significantly overpredicted compared with the direct numerical simulation data by Spalart (1988) and other benchmark data, and hence is not plotted. The increased uncertainty is associated in part with an increased noise level on both LDV channels, and interference from a reflection of the laser beams due to the close proximity of the probe volumes to the measurement wall.

The maximum uncertainty in the shear stress was typically 12 to 13% in the maximum stress region ($y^+ \approx 40$–80). Uncertainty in the shear velocity is less than 1% due to the mean streamwise velocity measurements and approximately 5% due to the additional uncertainty introduced by the Clauser method, which has been used to infer the wall shear stress.[3]

The uncertainty for the pressure gradient parameter, k, is less than 2%.

The uncertainties associated with measuring quantities upon which the burst periods depend are on the order of 1–2%. However, due to the post-processing operations, i.e., choice of thresholds, and determining grouping times to discriminate between ejections originating from the same or different bursts, the ambiguity in the absolute value of $\bar{T}_B$ is typically between 15 and 20% (Schwarz and Plesniak, 1996a; and Schwarz, 1998). Thus, while the absolute magnitudes of burst period are uncertain up to 20%, all of the data sets were processed consistently to minimize the ambiguity and the trends exhibited are faithful to within the measurement uncertainty of 2%.

Experimental Results and Discussion

Two-component velocity data were acquired in a curved test section with moderate convex curvature in the mid-plane of the test surface. Zero and different favorable longitudinal pressure gradients were imposed in the curved test section. Mean and higher-order velocity statistics, as well as bursting frequencies are discussed herein. The velocity profiles presented here were acquired in the initial curved region at locations corresponding to $\alpha = 5$, 10 and 20° (denoted in the figure legends by (05), (10), and (20), respectively). This region is representative of the leading edge suction surface of a stator vane, where the turbulence dynamics has a profound influence on blade cooling design. The data are compared to a ZPG boundary layer upstream of the curved test section, which formed over a flat smooth wall with $\mathrm{Re}_\theta \approx 3250$ (+ symbols) and to the DNS results of Spalart (1988) ($\mathrm{Re}_\theta \approx 1410$) plotted with solid lines. In the strong favorable pressure gradient "corrected" case (SFPGC), the typical value for the streamwise acceleration parameter, $k = \nu/U_e^2 \cdot dU_e/ds$, was $k \approx 1.8 \times 10^{-6}$.

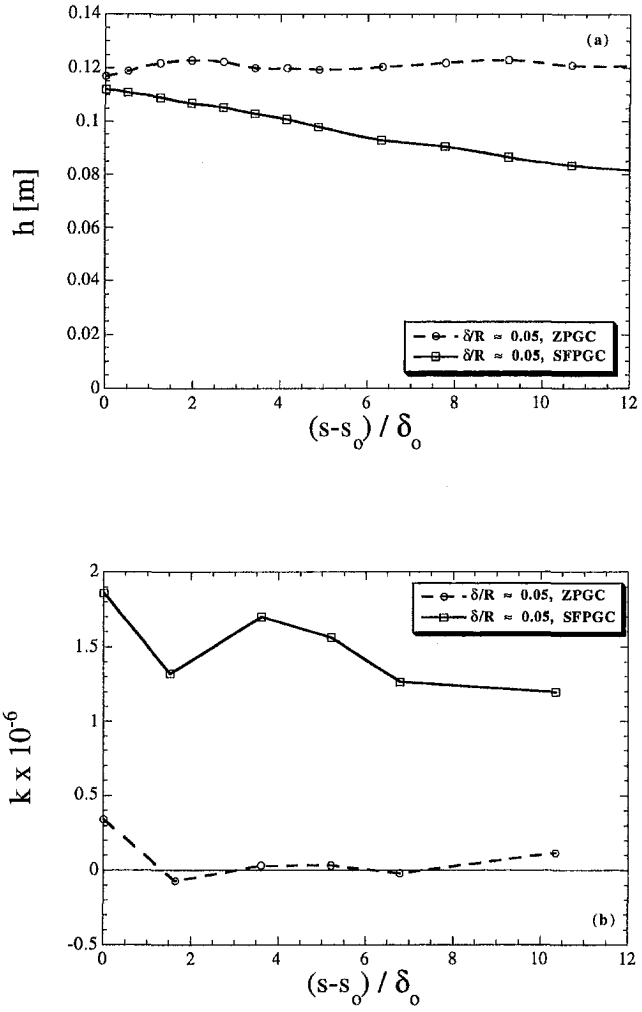

Fig. 2 Streamwise distribution of (*a*) flexible wall shape and (*b*) acceleration parameter for turbulent flow over a convex wall with zero and strong favorable streamwise pressure gradients (uncertainties less than 1% for (*a*) and less than 2% for (*b*))

In Fig. 2, two representative measured wall contours for the moderate curvature case (Fig. 2(*a*)) and the resulting distributions of the streamwise acceleration parameter (Fig. 2(*b*)) are shown. These measured wall positions have an uncertainty of ±0.5 mm (less than the plot symbol size). The goal in establishing the proper wall contours for the desired experimental conditions was to achieve a nearly constant streamwise pressure gradient immediately downstream of the onset of curvature. This was done using an interactive procedure, since the wall contour had to be continuously adjusted while monitoring the streamwise pressure gradient along the measurement wall. The wall shape distributions shown in Fig. 2(*a*) show the necessary variations of the cross-sectional flow areas to achieve zero and strong favorable pressure gradients in the curved portion of the test section. For the ZPGC case, the cross-sectional area remains nearly constant, except for a local area

[3] In flows with curvature and pressure gradient, the constants in the log-law may be different than the universal flat plate values (Schwarz and Plesniak, 1996b; Gibson, 1988; and Gibson et al., 1984). In this study, the classical constants were retained to evaluate the shear velocity, u_τ, primarily because no direct wall shear stress measurements were available and because it facilitates comparison to the vast body of previous work on curved boundary layers. It is estimated that the maximum change in the magnitude of u_τ using the modified constants proposed by Gibson (1988) is 5%. Most importantly, the absolute value of u_τ is not required since only relative magnitudes are compared for the various cases investigated.

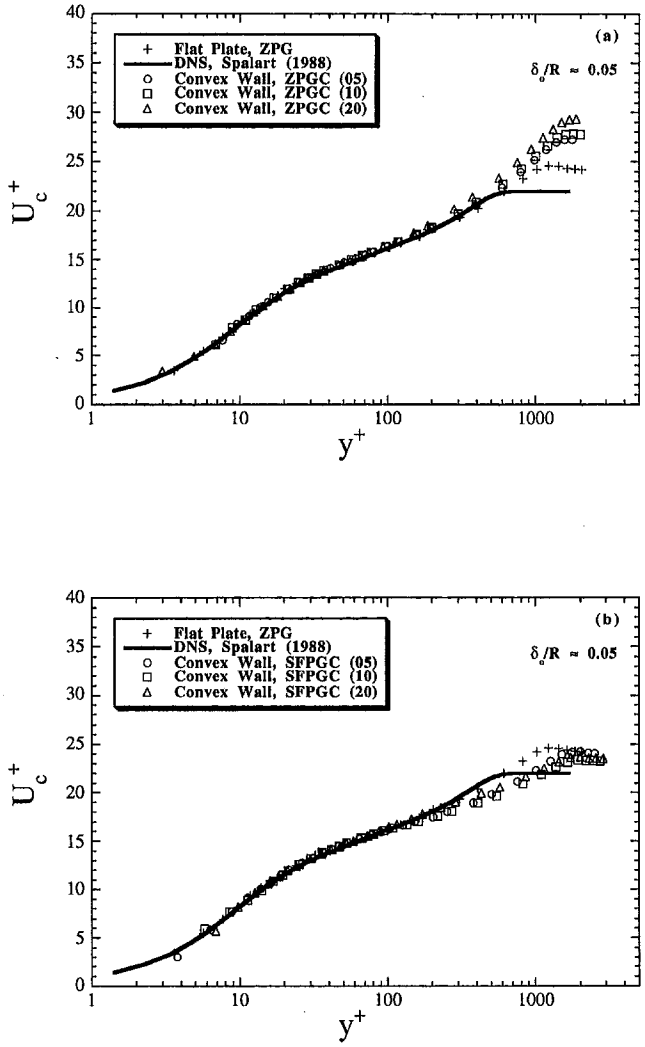

Fig. 3 Inner-normalized mean streamwise velocity for turbulent flow over curved wall with moderate convex curvature under (*a*) zero and (*b*) strong favorable pressure gradient conditions (uncertainties less than 1%)

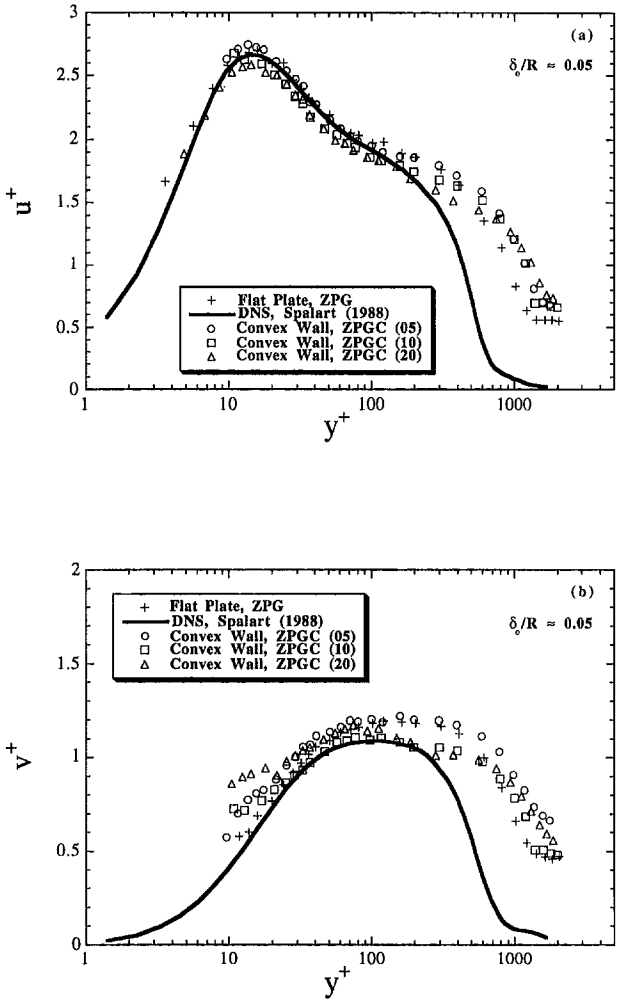

Fig. 4 Inner-normalized RMS (*a*) streamwise and (*b*) wall-normal velocity components for turbulent flow over a convex wall with zero streamwise pressure gradient (uncertainties less than 1%)

increase immediately downstream of the onset of curvature to counteract flow acceleration on the convex wall. On the other hand, the flow area continuously decreases for the SFPGC case. A region of local acceleration still persisted immediately downstream of the onset of curvature ($0 \leq s - s_o \leq 2\delta_o$), due to the discontinuity in wall curvature, despite widening the cross-sectional area there.

Mean Velocity Profiles. In Fig. 3, profiles of the mean streamwise velocity normalized with the shear velocity are shown in the typical inner variable plots for 5, 10, and 20 degrees of curvature and compared to the flat plate profiles. As reported previously by other investigators (e.g., Gillis and Johnston, 1983; Gibson et al., 1988; and Schwarz and Plesniak, 1996b), the extent of the log-law region is reduced ($30 \leq y^+ \leq 100$) due to the presence of the curvature-induced radial pressure gradient. Another effect of convex curvature is the increase of the wake strength. Strong favorable pressure gradient, case SFPGC, on the other hand, had the tendency to oppose the wake-enhancing effect of the stabilizing curvature. Note that the deviation of the wake for the flat plate data set and the DNS result is expected, and entirely attributable to a difference in the Reynolds numbers. Overall, inner variable scaling accounts for the effects of the interacting strain rates in the inner region, and the mean velocity profiles collapse. The largest departures from the baseline flat plate results are observed in the outer portion of the TBL ($y^+ > 100$), where inner scaling is not applicable.

Normal Reynolds Stresses. The streamwise and wall-normal root-mean square (RMS) velocities further illustrate the effects of the interacting extra strain rates. Figure 4 illustrates the zero pressure gradient case, in which all of the RMS velocity profiles are in good agreement with flat plate data throughout the log-law region. The maximum suppression of the wall-normal RMS component (approx. 15%) occurs in the outer portion of the boundary layer (Fig. 4(*b*)). For stronger convex curvature, the measured normal Reynolds stress components are further reduced than in the present case, especially for the wall-normal component (see Schwarz and Plesniak, 1996b). The profiles of u^+ in the curved ZPGC case and straight baseline case are within 5% of each other throughout the entire boundary layer.

In the presence of strong favorable pressure gradient, SFPGC, both RMS velocity components are reduced throughout the entire boundary layer. The inner-normalized RMS velocities, plotted in Fig. 5, each show suppressions of up to 45% with respect to the flat plate baseline. Thus, the strong favorable pressure gradient augments the stabilizing effects of the convex curvature on the turbulence, but does not equally affect each RMS velocity component (or normal Reynolds stress).

Reynolds Shear Stress and Bursting Frequency. Profiles of the primary Reynolds shear stress, $-uv^+$ are shown in Fig. 6, where the effects of the different interacting pressure gradients are

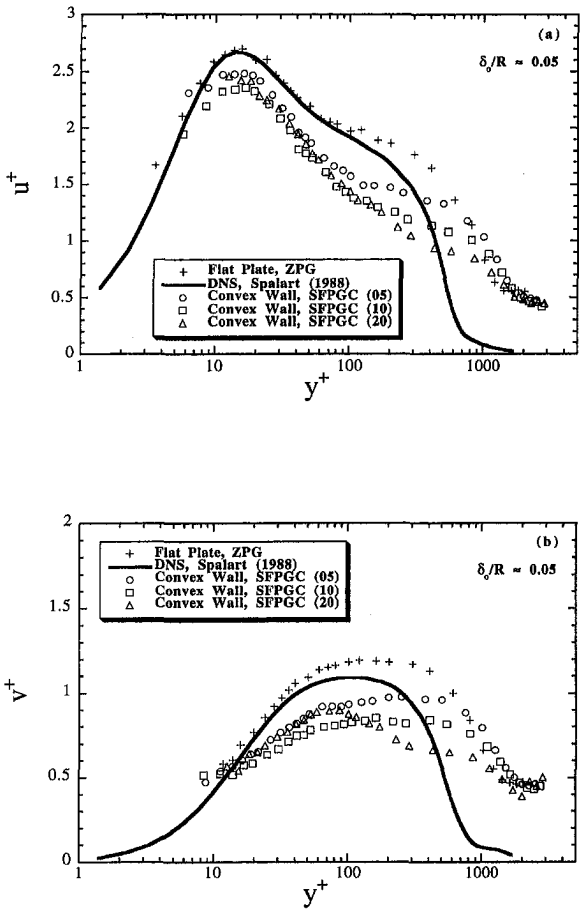

Fig. 5 Inner-normalized RMS (*a*) streamwise and (*b*) wall-normal velocity components for turbulent flow over a convex wall with strong favorable streamwise pressure gradient (uncertainties less than 1%)

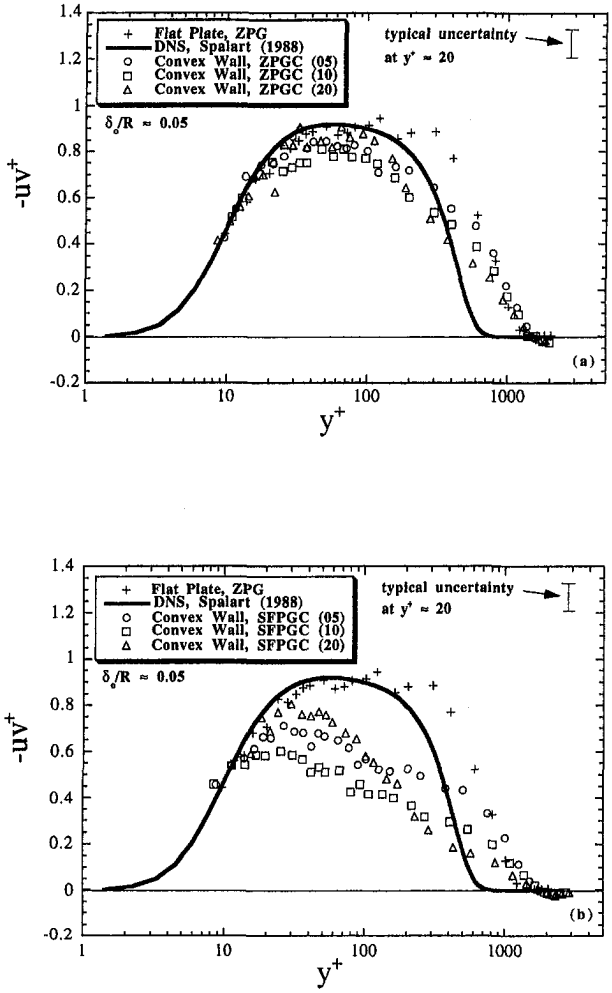

Fig. 6 Inner-normalized primary Reynolds shear stress for turbulent flow over a convex wall under (*a*) zero and (*b*) strong favorable pressure gradient conditions (uncertainties approx. 13% in maximum stress region)

particularly obvious. In the outer portion of the boundary layer, the convex curvature in zero streamwise pressure gradient only causes a slight reduction of the shear stress compared to the flat plate case. In the ZPGC strong convex curvature ($\delta_o/R \approx 0.10$) case (not shown), the reduction of the primary Reynolds shear stress was more pronounced than with moderate curvature shown here (see Schwarz, 1998). It is interesting to note the streamwise evolution of the peak Reynolds shear stress for the ZPGC case (Fig. 6(*a*)), which reaches a local minimum at the second measurement location ($\alpha \approx 10°$), and then at $\alpha \approx 20°$ overshoots the value at first streamwise location. This behavior is believed to be caused by the locally strong favorable streamwise strain rate in the vicinity of the onset of curvature. On the other hand, in the outer layer $-uv^+$ monotonically decreases with streamwise distance. This behavior is consistent with the notion that the streamwise pressure gradient affects the inner region of the boundary layer more than the outer, while curvature affects primarily the outer layer. The interaction of these two effects is not simple. Figure 6(*b*) illustrates that the imposed favorable streamwise pressure gradient, coupled with convex curvature, reduces $-uv^+$ throughout almost the entire TBL, in contrast to the ZPGC curved cases (Fig. 6(*a*)).

In order to investigate this behavior further, the streamwise development of the bursting frequency, which was deduced from time-resolved, two-component LDV measurements, and the maximum Reynolds shear stress, $-uv^+_{max}$, is shown in Fig. 7. The maximum Reynolds shear stress in Fig. 7(*a*) was estimated from the constant stress region of the $-uv^+$ profiles in Fig. 6. Figures 7(*a*) and (*b*) illustrate the correlation between the bursting event, which is a primary contributor to turbulence production, and the primary Reynolds shear stress. The turbulent shear stress generally decreases as the bursting becomes less frequent. However, there is not a one-to-one correspondence between the amount of reduction in the bursting frequency and the Reynolds stress at each particular streamwise location. It is apparent from these data sets, that the sudden onset of curvature (even when "corrected," by widening the test section, to minimize the effect of the naturally-occurring FPG arising from the discontinuity in wall curvature) causes an immediate reduction in the turbulence bursting frequency, which in turn results in a reduction in the maximum Reynolds shear stress. This behavior is much more pronounced when the convex curvature is combined with a strong favorable pressure gradient.

Furthermore, results suggest that the response of the peak Reynolds shear stress and the burst frequency to the sudden application of extra strain rates appears to be sensitive not only to the magnitudes of the "new" strain rates but also to their rate of application. For example, it was found that by changing the rate at which the streamwise pressure gradient was applied in the initial region, the turbulence statistics and bursting could be influenced far downstream. And, in fact, different asymptotic states were achieved for nominally the same flow conditions, with the exception of the wall contour at the onset of curvature. Similar behavior in the more strongly curved case has been reported previously (Schwarz and Plesniak, 1996a) and can be attributed to the history of the large, energy-containing eddies which are affected almost entirely by the mean flow velocity gradient, which in turn depends on the streamwise and radial strain rates (Townsend, 1980). Furthermore, it is expected that the addition of a new strain rate will always have a greater effect than the further application of one to which the flow

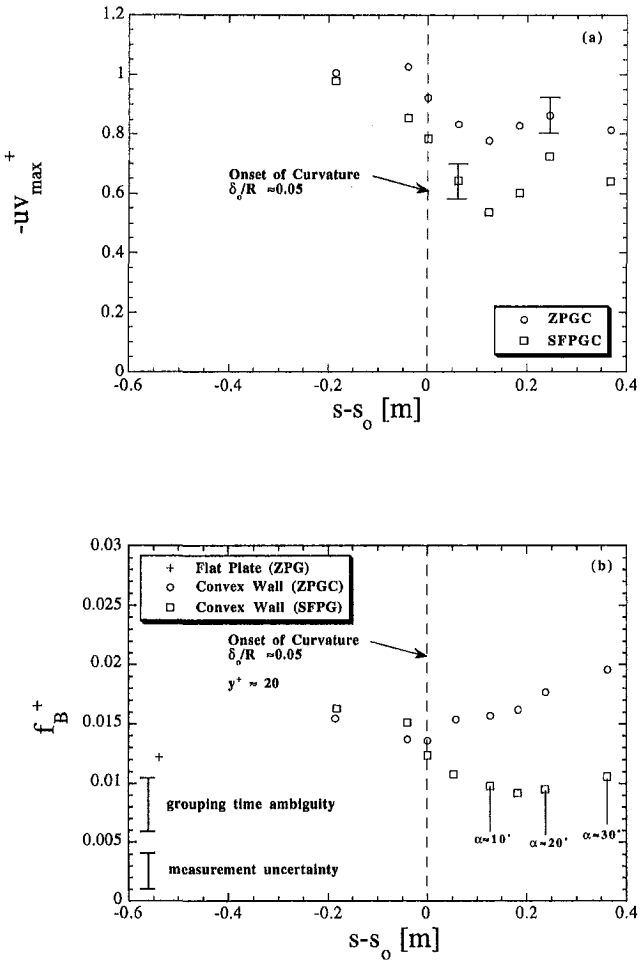

Fig. 7 Downstream development of the (*a*) normalized maximum primary Reynolds shear stress and (*b*) mean bursting period for turbulent flow over a curved wall with moderate convex curvature (uncertainties approx. 13% for (*a*) and 15–20% for (*b*))

structure has already responded to, since the total effective strain experienced by the flow structure is limited by the large-eddy lifetime (Savill, 1987).

Conclusions

Detailed statistical information describing the near-wall turbulent structure was determined from data acquired in a flow facility with straight and convexly curved walls ($\delta_o/R \approx 0.05$) in which longitudinal pressure gradients were imposed. Data reduction and analysis of time-resolved, two-component velocity measurements allowed the response of a TBL to the interacting strain rates to be investigated.

It was found that the stabilizing convex curvature influenced the turbulence structure. This was reflected in the mean and higher order velocity statistics, and in the bursting frequency. The strong favorable pressure gradient ($k \approx 1.8 \times 10^{-6}$) interacting with the radial strain ($\delta_o/R \approx 0.05$) caused further changes in these quantities, especially in the outer region of the TBL. The effect of the additional streamwise strain rate (i.e., case SFPGC) was evident in the following: (i) counteracting the wake-increasing effect of the convex curvature, (ii) reduction of the Reynolds stresses (both normal and shear components) throughout almost the entire turbulent boundary layer, and (iii) continuous reduction in the burst frequency accompanied by a reduction in the peak Reynolds shear stress.

The effects of these multiple strain rates are not additive in any simple manner. In fact, the rate of application of the strain rates, as well as their magnitude affect the turbulence structure far downstream (Schwarz and Plesniak, 1996a; and Schwarz, 1998). Consequently, the dynamics of the large, energy-containing eddies must be closely analyzed in order to incorporate these findings into more reliable nonequilibrium turbulence models. Note that in their study of 3D boundary layers on swept curved wings, Baskaran et al. (1990) found that the interaction of curvature and crossflow was grossly nonlinear, and that the combined effects could not be deduced by considering the action of each effect alone. The current study and that of Baskaran et al. (1990), considerably different flows, demonstrate that the principle of superposition cannot be used to infer the effects of multiple additional rates of strain in turbulent boundary layers.

Acknowledgments

Effort sponsored by the Air Force Office of Scientific Research, Air Force Material Command, USAF, under grant number F 49620-93-1-0003. The U.S. Government is authorized to reproduce and distribute reprints for Governmental purposes notwithstanding any copyright notation thereon.

References

Bandyopadhyay, P. R., and Ahmed, A., 1993, "Turbulent Boundary Layers Subjected to Multiple Curvatures and Pressure Gradients," *Journal of Fluid Mechanics,* Vol. 246, pp. 503–527.

Barlow, R. S., and Johnston, J. P., 1988a, "Structure of Turbulent Boundary Layers on a Concave Surface." *Journal of Fluid Mechanics,* Vol. 191, pp. 137–176.

Barlow, R. S., and Johnston, J. P., 1988b, "Local Effects of Large-Scale Eddies on Bursting in a Concave Boundary Layer," *Journal of Fluid Mechanics,* Vol. 191, pp. 177–195.

Baskaran, V., Pontikis, V. G., and Bradshaw, P., 1990, "Experimental Investigation of Three-Dimensional Turbulent Boundary Layers on Infinite Swept Curved Wings," *Journal of Fluid Mechanics,* Vol. 211, pp. 95–122.

Baskaran, V., Smits, A. J., and Joubert, P. N., 1991, "A Turbulent Flow Over a Curved Hill. Part 2," *Journal of Fluid Mechanics,* Vol. 232, pp. 377–402.

Bogard, D. G., and Tiederman, W. G., 1986, "Burst Detection with Single-Point Velocity Measurements," *Journal of Fluid Mechanics,* Vol. 162, pp. 389–413.

Gibson, M. M., 1988, "Effects of Surface Curvature on the Law of the Wall," *Near-Wall Turbulence,* 1988 Zoran Zaric Memorial Conference, S. J. Kline and N. H. Afgan, eds., Hemisphere.

Gibson, M. M., Verriopoulos, C. A., and Vlachos, N. S., 1984, "Turbulent Boundary Layer Flow on a Mildly Curved Convex Surface," *Experiments in Fluids,* Vol. 2, pp. 17–24.

Gillis, J. C., and Johnston, J. P., 1983, "Turbulent Boundary Layer Flow and Structure on a Convex Wall and its Redevelopment on a Flat Wall," *Journal of Fluid Mechanics,* Vol. 135, pp. 123–153.

Kline, S. J., and McClintock, F. A., 1953, "Describing Uncertainties in Single Sample Experiments," *Mech. Eng.,* p. 3.

Kline, S. J., Reynolds, W. C., Schraub, F. A., and Runstadler, P. W., 1967, "The Structure of Turbulent Boundary Layers," *Journal of Fluid Mechanics,* Vol. 30, Part 4, pp. 741–773.

Lu, S. S., and Willmarth, W. W., 1973, "Measurements of the Reynolds Stress in a Turbulent Boundary Layer," *Journal of Fluid Mechanics,* Vol. 60, pp. 481–511.

McLaughlin, D. K., and Tiederman, W. G., 1973, "Biasing Correction for Individual Realization of Laser Velocimeter Measurements in Turbulent Flows," *Physics of Fluids,* Vol. 16, pp. 2082–2088.

Moffat, R. J., 1988, "Describing the Uncertainties in Experimental Results," *Exp. Thermal Fluid Sci.,* Vol. 3, p. 3.

Nagano, Y., Tagawa, M., and Tsuji, T., 1991, "Effects of Adverse Pressure Gradients on Mean Flows and Turbulence Statistics in a Boundary Layer," *8th Symposium on Turbulent Shear Flows,* University of Munich, pp. 2-3-1 to 2-3-6.

Narasimha, R., and Sreenivasan, K. R., 1979, "Relaminarization of Fluid Flows," *Advances in Applied Mechanics,* Vol. 19, Indian Institute of Science, Bangalore, India, pp. 221–309.

Savill, A. M., 1987, "Recent Developments in Rapid-Distortion Theory," *Annual Review Fluid Mechanics,* Vol. 19, pp. 531–575.

Schwarz, A. C., and Plesniak, M. W., 1996a, "The Influence of Interacting Strain Rates on Turbulence in Convex Boundary Layers," *Physics of Fluids,* Vol. 8, pp. 3163–3171.

Schwarz, A. C., and Plesniak, M. W., 1996b, "Convex Turbulent Boundary Layers with Zero and Favorable Pressure Gradients," ASME JOURNAL OF FLUIDS ENGINEERING, Vol. 118, pp. 787–794.

Schwarz, A. C., 1998, "Response of a Turbulent Boundary Layer to Multiple Strain Rates," Ph.D. thesis, Purdue University, West Lafayette, IN.

So, R. M. C., and Mellor, G. L., 1973, "Experiment on convex curvature effects in turbulent boundary layers," *Journal of Fluid Mechanics,* Vol. 60, Part 1, pp. 43–62.

Spalart, P. R., 1988, "Direct Simulation of a Turbulent Boundary Layer up to $Re_\theta = 1410$," *Journal of Fluid Mechanics,* Vol. 187, pp. 61–98.

Spalart, P. R., and Shur, M., 1997, "On the Sensitization of Turbulence Models to

Rotation and Curvature," *Aerospace Science and Technology,* Vol. 1, No. 5, pp. 297–302.

Townsend, A. A., 1980, "The Response of Sheared Turbulence to Additional Distortion," *Journal of Fluid Mechanics,* Vol. 98, pp. 171–191.

Walker, D. T., and Tiederman, W. G., 1988, "Turbulence Structure and Mass Transport in a Channel Flow with Polymer Injection," Report PME-FM-88-2, Purdue University, W. Lafayette, IN.

Webster, D. R., Degraaff, D. B., and Eaton, J. K., 1996, "Turbulence Characteristics of a Boundary Layer Over a Two-Dimensional Bump," *Journal of Fluid Mechanics,* Vol. 320, pp. 53–69.

White, J. B., and Tiederman, W. G., 1990, "The Effect of Adverse Pressure Gradient on the Turbulent Burst Structure in Low-Reynolds Number Equilibrium Boundary Layers," *Proceedings of the 12th Symposium on Turbulence,* University of Missouri-Rolla, Rolla, MO, pp. A5.1–A5.8.

Yanta, W. J., and Smith, R. J., 1973, "Measurements of Turbulence Transport Properties with a Laser Doppler Velocimeter," AIAA Paper No. 73-169.

H. Mizunuma
Associate Professor.
e-mail: mizunuma@ecomp.metro-u.ac.jp

K. Ueda
Research Associate.

Department of Mechanical Engineering,
Tokyo Metropolitan University,
1-1, Minamiohsawa, Hachioji-shi, Tokyo,
192-0397 Japan

Y. Yokouchi
Mechanical Engineer,
Komatsu Forklift,
110, Yokokura-shinden,
oyama-shi, Tochigi prefecture,
323-8567 Japan

Synergistic Effects in Turbulent Drag Reduction by Riblets and Polymer Additives

Drag reduction was investigated for the combined system of polymer additives and a riblet pipe. The riblet grooves were V-shaped, the spacing of which was 1.3 mm and the height of which was 1.01 mm. For higher h^+, a triangular riblet system including other geometries increases the drag to levels similar to those of normal transient roughness. This drag increase was generally given as a function of h^+. The polymer additives were Aronfloc N-110 and Separan AP-30. The critical shear stress τ^*, at which N-110 started the drag reduction, was approximately eight times higher than τ^* for AP-30. In the combined system, the synergistic drag reduction for higher h^+ was discussed under the assumption that the additives suppressed the drag increase resulting from riblets. Since the additives thicken a wall layer covering the region from a viscous sublayer to a buffer layer, the relative height of h to this wall layer thickness is lowered. In addition, the flow enhancement due to additives relatively suppresses the riblet-induced drag increase. The analysis based on velocity profiles indicated that these effects can produce synergistic drag reduction for higher h^+.

1 Introduction

Dilute polymer solutions show large turbulent drag reduction. One of the drawbacks associated with this method of drag reduction is that the additives do not reduce the drag if the wall shear stress is lower than the critical shear stress. The drag reduction effect caused by riblets has been confirmed for various boundary layer and pipe flows. However, riblets have a narrow range of the effective flow rates and, if a flow rate is higher than this effective range, the riblets increase the frictional drag just like a normal rough wall.

The combined system of polymer additives and riblets is expected to cancel out the drawbacks associated with applying each of these systems and to produce a positive synergistic effect. The effects of the combined system would also help to clarify the respective drag reduction mechanisms of each system. Choi et al. (1989) covered a ship model with riblets and then coated the model with polymer. Measurement of the drag of the model revealed that the combined system represented an approximately 2 percent higher drag reduction than the addition of each system's effect. Rohr et al. (1989) measured the friction factor for dilute polymer solutions in the riblet pipes, and found that the combined system produced the same drag reduction ratio as the polymer additive alone. Similar experiments were carried out by Christodoulou et al. (1991) and Anderson et al. (1993). In both experiments, results obtained for combined systems using Polyox solutions showed that the drag reduction rates were less than the sum of the two systems. In contrast, Anderson observed for a combined system using guar gum that the drag reduction rates were greater than the sum of the drag reduction rates of the individual systems, and that the critical shear stress of the additive was lowered. Koury et al. (1995) carried out a systematic experiment for a combined system of Polyox and a riblet pipe. A positive synergistic effect was observed to occur at moderate additive-induced drag reductions.

Further experiments are needed in order to clarify the combined effects of riblets and polymer additives. Therefore, in the present study, we measured the friction factors for a combined system consisting of polymer additives and a riblet pipe (Section 2). The observed synergistic effects are discussed based on a two-layer model for the turbulent velocity profile (Section 3).

2 Drag Reduction in a Riblet Pipe

2-1 Experimental Setup and Method. The diameter of the riblet pipe was defined as being equal to the diameter of a smooth pipe having the same cross-sectional area. Six cut samples were extracted from the riblet pipe to measure the pipe diameter and the shape of the groove. Measurement was performed using a profile projector. Figure 1 shows one of the cut samples. The mean diameter of the riblet pipe was 50.0 mm, and the precision error limit of the diameter was 0.11 mm. The riblet grooves were 60 deg V-type grooves. The average height h of the riblets was 1.01 mm, and the average interval s was 1.30 mm. The precision error limits of h and s were 0.04 mm and 0.03 mm, respectively. The results obtained for this riblet pipe were compared with those for a smooth pipe of 51.4 mm diameter, the precision error limit of which was 0.02 mm. Both pipes were formed by means of an extrusion process. The length of the pipe test section was 5.94 m. The diameter of the six pressure taps was 3 mm. Pressure loss was measured using a differential-type pressure transducer, the precision error limit of which was 0.34 Pa. Flow rate was measured with an electromagnetic flowmeter, the relative precision error limit of which was 0.5 percent. The fluid was circulated using a bladeless pump, and the flow rate was primarily adjusted by varying the pump rotational speed.

The additives used in the present experiment were Aronfloc N-110 (Toa Gosei Co. Ltd.) of 150 ppm and 300 ppm, and Separan AP-30 (Dow Chemical) of 50 ppm, 100 ppm, 200 ppm, 300 ppm. Both additives are Polyacrylamide. Polymer solution degrades when circulated by a pump. Therefore, the additive solutions were circulated for 30 minutes before measurement after which the degradation was almost complete. In order to examine the effects of the degradation on the experimental results, the experiments were carried out in the following order: smooth pipe (Run-1), riblet pipe (Run-2), smooth pipe (Run-3), riblet pipe (Run-4), smooth pipe (Run-5). Generally, additives of lower concentration are adequate to obtain the drag reduction effect. In the present experiments, additives of high concentration were used in order to

Contributed by the Fluids Engineering Division for publication in the JOURNAL OF FLUIDS ENGINEERING. Manuscript received by the Fluids Engineering Division July 31, 1996; revised manuscript received April 21, 1999. Associate Technical Editor: H. Hashimoto.

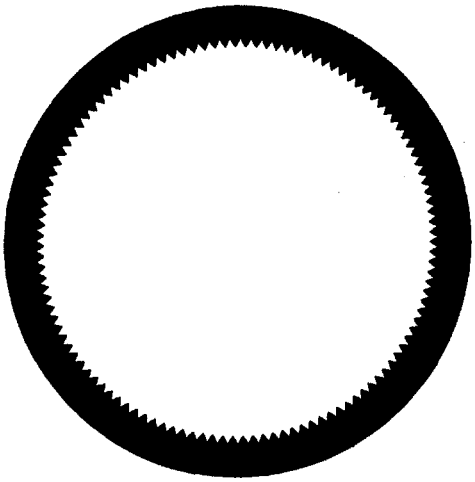

Fig. 1 Cross section of a riblet pipe

compensate for the degradation caused by the pump and the pipe system.

In this concentration range, non-Newtonian viscosity cannot be ignored. Therefore, we used a generalized Reynolds number,

$$\mathrm{Re}^* = \frac{6(3n+1)^{1-n}n^n\rho V^{2-n}D^n}{2^n(2n+1)K}, \quad (1)$$

which is based on a power law model,

$$\tau = K(du/dy)^n. \quad (2)$$

Table 1 shows the model constants n and K, which were obtained using a capillary viscometer. The non-dimensionalized groove interval s^+ was defined as follows,

$$s^+ = \rho u_\tau s/\mu = s u_\tau^{(2/n)-1}(\rho/K)^{(1/n)}, \quad (3)$$

where viscosity μ was calculated from $\mu = \tau_w/(du/dy)_{\text{wall}} = K(K/\tau_w)^{1/n-1}$, and τ_w was obtained from the measurement of the pressure loss. The relative precision error limit of μ was 2.4 percent.

2-2 Experimental Results.

Drag Reduction of Solvent in Riblet Pipe. Figure 2 shows the friction factors and Fig. 3 shows ϵ_r as a function of s^+, where ϵ_r is a relative friction factor change for a solvent in the riblet pipe. Here, ϵ_r also indicates the relative change in wall shear stress, because the pipe diameters are approximately the same in the smooth pipe and the riblet pipe systems. The range of s^+, for which the riblet pipe reduced the friction factors, was from 10 to 30, and the maximum drag reduction attained was approximately 6 percent.

Figure 3 includes the results for other triangular riblets, which were obtained by Nakao (1991) and Anderson et al. (1993). The value of s^+ from which the drag reduction begins is approximately 10. In the region of $s^+ > 20$, ϵ_r increases with s^+. This increase in ϵ_r depends on h/s and, as shown in Fig. 4, ϵ_r is a function of h^+ in the region of $h^+ > 20$. The relationship between ϵ_r and h^+ is given by

$$\epsilon_r = 0.51 \log h^+ - 0.70 (20 < h^+ < 90,\ 0.25 < h/s < 1). \quad (4)$$

Table 1 Rheological constants of the polymer solutions

Additives	AP-30				N-110	
C (ppm)	50	100	200	300	150	300
n	0.918	0.895	0.816	0.740	1.00	0.989
K (Pa·s^n)	2.16×10^{-3}	2.85×10^{-3}	6.32×10^{-3}	1.38×10^{-2}	1.49×10^{-3}	1.92×10^{-3}

Drag Reduction of Additive Solutions in Smooth and Riblet Pipes. The typical examples are shown in Figs. 5 to 7. From these results, the relative friction factor change ϵ was calculated and is shown as a function of wall shear stress τ_w in Fig. 8. The influence of the degradation of the polymer molecules was small. The difference between Run 3 and Run 5 for the smooth pipe was approximately 2 percent for AP-30, and approximately 3 percent for N-110. For AP-30 in the smooth pipe, the Reynolds number at which drag reduction begins is in the transitional region. For N-110, the Reynolds number is about 2×10^4, which is higher than that for AP-30. The critical shear stress of N-110 is approximately 1.1 Pa, which is approximately eight times higher than 0.14 Pa, the critical shear stress for AP-30.

In order to investigate the synergistic effects using Fig. 8, we defined $(\epsilon_{r^+})_{\tau_w}$ as the difference obtained by subtracting the ϵ_p of the additive-system (the average of Run 3 and Run 5) from the ϵ_c of the combined-system (Run 4) as follows,

$$(\epsilon_{r^+})_{\tau_w} \equiv ([\text{combined effect, } \epsilon_c] - [\text{additive effect, } \epsilon_p])_{\tau_w=\text{const.}} \quad (5)$$

$$\therefore (\epsilon_{r^+})_{\tau_w} = ([\text{riblet effect, } \epsilon_r] + [\text{synergistic effect, } \epsilon_+])_{\tau_w=\text{const.}}$$

Figures 9(*a*) and (*b*) show the relationship between $(\epsilon_{r^+})_{\tau_w}$ and s^+. Although the drag reduction produced by AP-30 varies from 7 to 40 percent according to the concentration of AP-30, the range of s^+ for which $(\epsilon_{r^+})_{\tau_w}$ shows its maximum drag reduction is the same as that for the riblets alone. Thus, the drag reduction mechanism of riblets is thought to be different from that of additives, as reported by Anderson et al. (1993) and Koury et al. (1995). Specifically, additives change the scale of the organized turbulent structure. Tiederman et al. (1985) demonstrated that the nondimensionalized spanwise spacing of the streaks increased in accordance with the drag reduction rate. In the present experiment, 200 ppm AP-30 was found to produce a drag reduction of 35 percent at $s^+ = 15$, which would increase the non-dimensionalized streak spacing by approximately 1.8 times, according to Tiederman's

Nomenclature

C_{poly} = concentration of polymer additives
D = pipe diameter
h = height of riblet groove
n, K = a power law model constants
Re = Reynolds number, $\rho DV/\mu$
Re* = generalized Reynolds number based on a power law model
s = interval of riblet grooves
u_τ = frictional velocity
V = average velocity
δ = thickness of a wall layer in turbulent flow
ϵ = $(\lambda/\lambda_0)_{\text{Re=const.}} - 1$, relative friction factor change
κ = von Karman constant, 0.4
λ = friction factor
λ_0 = friction factor for a solvent in a smooth pipe
μ = viscosity
τ^* = critical shear stress in an additive system that includes a smooth pipe
τ_r^* = critical shear stress in a combined system
τ_w = wall shear stress

Subscripts

p = additive system
r = riblet system
c = combined system
$+$ = synergistic effects

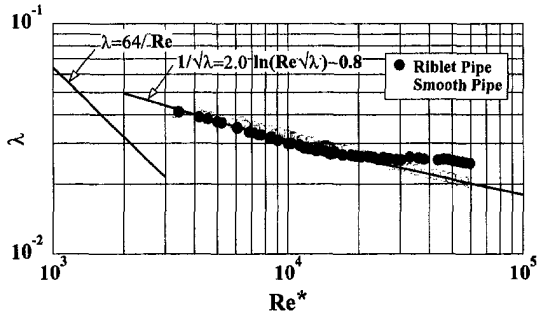

Fig. 2 Pipe friction factors for water. (Maximum uncertainty in λ = 2.5% for a smooth pipe and =2.6% for a riblet pipe. Maximum uncertainty in Re = 2.4% for a smooth pipe and =2.4% for a riblet pipe.)

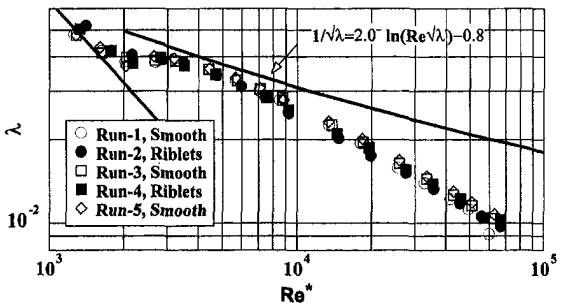

Fig. 5 Relationship between friction factor and Reynolds number for 100 ppm AP-30. (Maximum uncertainty in λ = 1.5% for a smooth pipe and =1.8% for a riblet pipe. Maximum uncertainty in Re = 2.4% for a smooth pipe and =2.4% for a riblet pipe.)

results. However, in the combined system, ϵ_{r+} is a maximum at $s^+ \cong 15$, indicating that no change occurred due to the additives. These results suggest that the performance of the riblets is insensitive to this scale change of the organized turbulent structure.

For s^+ greater than 20, the riblets increase the frictional drag. When τ_w is higher than the critical shear stress τ^*, the synergistic effect occurs and the increase in $(\epsilon_{r+})_{\tau_w}$ is suppressed. The critical shear stress of AP-30 is approximately 0.14 Pa, which is in a turbulent transitional region. In the combined system of AP-30, the synergistic effect cancels out the drag increase caused by the riblets alone. This synergistic effect for $(\epsilon_{r+})_{\tau_w}$ exceeds a value of 10 percent. The critical shear stress for N-110 is approximately 1.1 Pa, which corresponds to $s^+ = 24$ for 150 ppm, and $s^+ = 28$ for 300 ppm. Over this critical shear stress τ^*, the increase in $(\epsilon_{r+})_{\tau_w}$ is suppressed. Similarly, Anderson et al. (1993) reported a beneficial synergistic effect for a combined system using guar gum. In the present study, measurements were performed in a way such that shear degradation was minimized. This is similar to the condition of the Anderson study, because guar gum is resistant to shear degradation. Polyethylene oxide, however, is shear degradable, and Anderson et al. (1993) and Koury et al. (1995) reported a non-beneficial synergistic effect for a combined system using polyethylene oxide. Therefore, the degradation of the additives is supposed to make this synergistic effect non-beneficial.

Another synergistic drag reduction occurs over the limited region $s^+ = 8$ to 20. For the combined system using N-110, the wall shear stress is remarkably lower than τ^* in this region of s^+. This synergistic reduction is less than 5 percent, which is less than the above-mentioned synergistic reduction for the higher s^+. A similar positive synergistic effect was also observed by Koury et al. (1995), although the precise effect was uncertain due to the data scatter. This synergy disappears at $s^+ \cong 20$, at which the increase in drag begins to approach that of a normal rough pipe. If we define τ_r^* as the critical shear stress from which the combined system first causes the drag reduction to occur, τ_r^* is about one order lower than τ^* for N-110. For

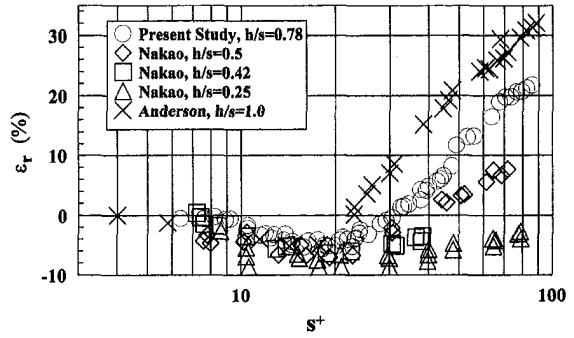

Fig. 3 Relative friction change with respect to s^+ for riblet pipes

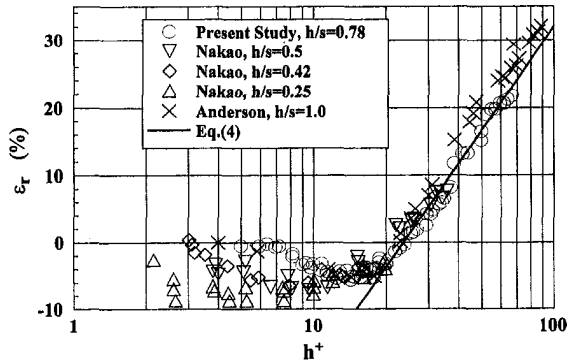

Fig. 4 Relative friction change with respect to h^+ for riblet pipes

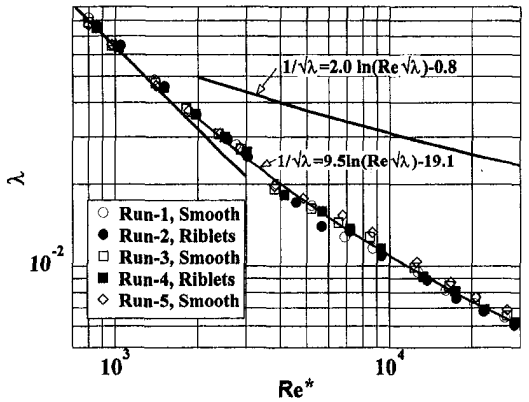

Fig. 6 Relationship between friction factor and Reynolds number for 300 ppm AP-30. (Maximum uncertainty in λ = 1.1% for a smooth pipe and =1.2% for a riblet pipe. Maximum uncertainty in Re = 2.4% for a smooth pipe and =2.4% for a riblet pipe.)

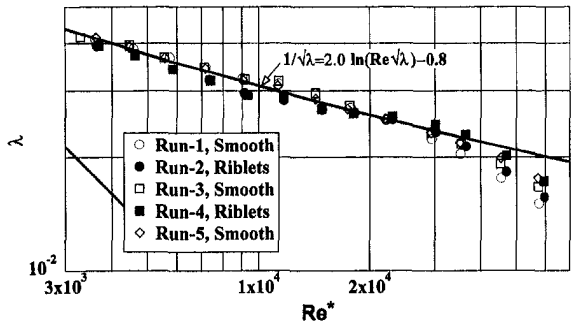

Fig. 7 Relationship between friction factor and Reynolds number for 150 ppm N-110. (Maximum uncertainty in λ = 1.9% for a smooth pipe and =1.9% for a riblet pipe. Maximum uncertainty in Re = 2.4% for a smooth pipe and =2.4% for a riblet pipe.)

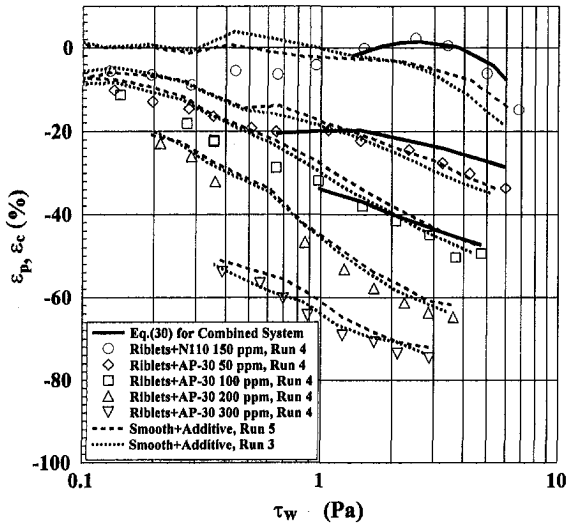

Fig. 8 Relationship between relative friction change and wall shear stress. Runs 3 and 5 for a smooth pipe and Run 4 for a riblet pipe. (Maximum uncertainty in ϵ = 2.1% and in τ_w = 1.0%.)

AP-30, this synergistic effect occurs over the same range of s^+ as N-110. The value of τ_r^* is so small that the synergistic effect begins inside the transitional region.

At the higher concentrations of AP-30, the change in $(\epsilon_{r+})_{\tau w}$ with respect to concentration decreases as the drag reduction approaches saturation. At 300 ppm, the friction factors reach Virk's maximum drag reduction. Figure 9(*a*) indicates the drag increase caused by positive $(\epsilon_+)_{\tau w}$ at $s^+ = 20$. For N-110, the friction factors for 300 ppm are approximately equal to those for 150 ppm. In addition, the combined effect is approximately similar to that for 150 ppm.

Compared to the use of the riblets alone, the combined use of riblets and additive at lower concentrations is characterized as follows:

(1) The region of s^+ at which the riblets show the maximum drag reduction is from 15 to 20, and this region is not affected by additives.

(2) The drag increase caused by riblets is suppressed by the synergistic effect that occurs when τ_w is higher than τ^*.

(3) The beneficial synergistic effect for the drag reduction occurs in the range $8 < s^+ < 20$.

3 Discussion

Anderson et al. (1993) and Koury et al. (1995) have suggested that riblets and polymers reduce drag by separate mechanisms. The result (1) obtained in Section 2 of the present study supports this hypothesis, whereas the synergistic results (2) and (3) indicate that interactions occur between the riblets and the polymers. The polymer additives thicken the buffer layer. For the result (2), the influence of this flow modification on the combined drag reduction effect is discussed using a two-layer model for the turbulent velocity profile. The synergistic effect in the result (3) is less than 5 percent. The limited data obtained in the present study do not provide enough information from which to draw a definite conclusion. The discussion for the third result is described in Appendix.

3-1 Two-Layer Model for Additive Solutions. In this two-layer model, the turbulent velocity profile is divided into a wall layer and a log layer. The wall layer is defined as a layer of thickness δ that covers the region from a viscous sublayer to a buffer layer. The proposed model was introduced assuming similarity of the Reynolds stress distribution in the wall layer. This model is discussed in detail by Mizunuma and Kato (1983). In

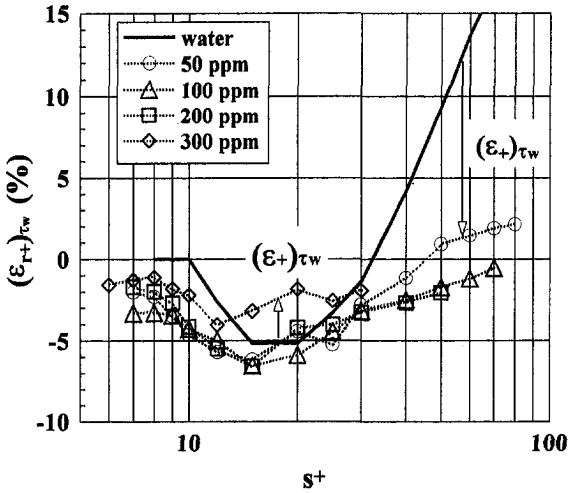

Fig. 9(*a*) AP-30

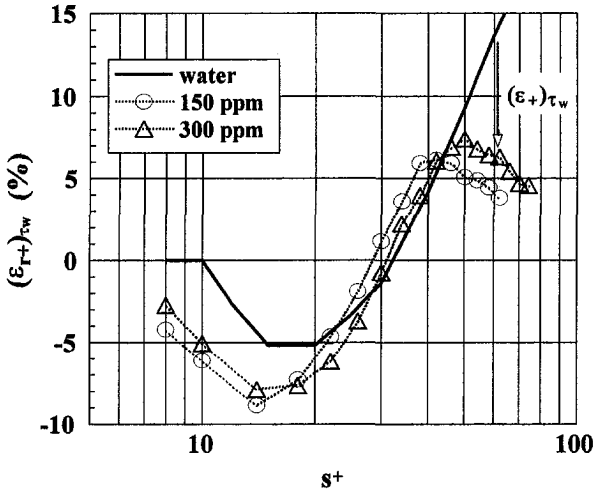

Fig. 9(*b*) N-110

Fig. 9 $(\epsilon_{r+})_{\tau w}$ as a function of s^+. Run 4. (Uncertainty in ϵ_{r+} = 1.8% and in s^+ = 4.0% at s^+ = 10.)

additive solutions over a smooth surface, this two-layer model gives the following velocity profiles.

Velocity profile in wall layer, $y^+ \le \delta^+$:

$$u^+ = y^+ - \delta^+\left(1 - \frac{1}{\kappa\delta^+}\right)\left\{1.0\left(\frac{y^+}{\delta^+}\right)^4 - 0.60\left(\frac{y^+}{\delta^+}\right)^5\right\} \quad (6)$$

Velocity profile in log layer, $y^+ \ge \delta^+$:

$$u^+ = \frac{1}{\kappa}\ln y^+ + 0.60\delta^+ - \frac{\ln \delta^+ - 0.40}{\kappa} \quad (7)$$

Friction factor:

$$1/\sqrt{\lambda} = \frac{0.348}{\kappa}\ln(\mathrm{Re}\sqrt{\lambda}) - 0.311\left[\left\{\frac{1}{\kappa}\ln(4\sqrt{2}\delta^+) + 1.1\right\} - 0.6\delta^+\right] \quad (8)$$

The von Karman constant κ is 0.4, which is equal to that for Newtonian fluids. Reynolds number Re is defined as $\mathrm{Re} = \rho DV/\mu$, and viscosity μ is calculated from the wall shear stress as $K(K/\tau_w)^{1/n-1}$. The non-dimensionalized thickness δ^+ $(=\rho u_\tau \delta/\mu)$

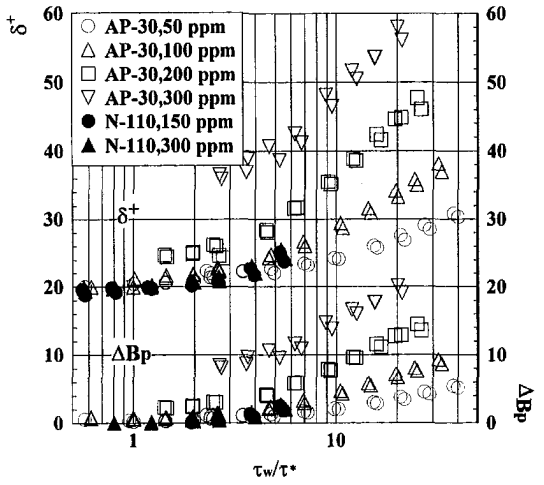

Fig. 10 Calculated wall layer thickness and shift of logarithmic velocity profile for additive solutions in a smooth pipe. Runs 3 and 5.

of the wall layer is related to the shift of the intercept of the logarithmic velocity profile ΔB_p as follows:

$$\Delta B_p = 0.60\delta^+ - \frac{\ln \delta^+ - 0.40}{\kappa} - 5.5. \quad (9)$$

The additives increase the non-dimensionalized thickness δ^+, which results in the positive ΔB_p and produces the turbulent drag reduction. Virk (1975) demonstrated that ΔB_p was a function of the additive concentration C_{poly} and τ_w/τ^*, where the critical shear stress τ^* is characteristic of the additive and is independent of the concentration. Therefore,

$$\tau_w \leqq \tau^* : \Delta B_p = 0, \quad \text{and}$$

$$\tau_w \geqq \tau^* : \Delta B_p = F_0(C_{\text{poly}}, \tau_w/\tau^*). \quad (10)$$

From Eqs. (9) and (10), δ^+ is given as a function of C_{poly} and τ_w/τ^*.

$$\tau_w \leqq \tau^* : \delta^+ = 20, \quad \text{and}$$

$$\tau_w \geqq \tau^* : \delta^+ = F(C_{\text{poly}}, \tau_w/\tau^*) \quad (11)$$

This two-layer model gives the friction factor change ϵ_p by

$$\frac{1}{\sqrt{\lambda_0(1+\epsilon_p)}} = \frac{0.348}{\kappa} \ln\left(\text{Re}\sqrt{\lambda_0(1+\epsilon_p)}\right) - 0.311\left\{\frac{3.23}{\kappa} - (5.5 + \Delta B_p)\right\}. \quad (12)$$

The experimental results of Re and $\lambda_0(1 + \epsilon_p)$ were substituted into Eq. (12) to obtain ΔB_p, and Eq. (9) was used to calculate δ^+. The values obtained for δ^+ were then plotted in Fig. 10. For $\tau_w < \tau^*$, or, for Newtonian fluids, δ^+ is 20, and ΔB_p is 0. Thus, Eq. (12) reduces to the Prandtl-Karman equation,

$$1/\sqrt{\lambda_0} = 2.0 \ln (\text{Re}\sqrt{\lambda_0}) - 0.8. \quad (13)$$

3-2 Logarithmic Law for Riblet Pipes. When the drag is reduced, the riblets produce the upward shift of the logarithmic velocity profile compared to the smooth surface, as reported by Wallance and Balint (1988). Therefore, the logarithmic profile is given by

$$u = \frac{1}{\kappa} \ln y^+ + 5.5 + \Delta B_r, \quad (14)$$

and the relative friction factor change ϵ_r is expressed by

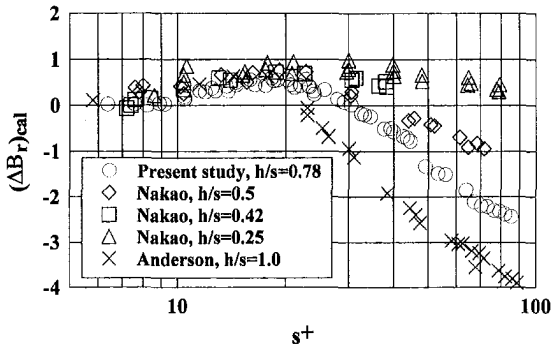

Fig. 11 Calculated shift of logarithmic velocity profile for additive solutions in riblet pipes

$$\frac{1}{\sqrt{\lambda_0(1+\epsilon_r)}} = \frac{0.348}{\kappa} \ln (\text{Re}\sqrt{\lambda_0(1+\epsilon_r)}) - 0.311\left\{\frac{3.23}{\kappa} - (5.5 + \Delta B_r)\right\}. \quad (15)$$

Here, $\kappa = 0.4$, and ΔB_r indicates the shift of the logarithmic profile. Substituting the experimental results of Re and $\lambda_0(1 + \epsilon_r)$ into Eq. (15) gives ΔB_r, values of which are plotted in Fig. 11. If ϵ_r satisfies $|\epsilon_r| \ll 1$, then the subtraction of Eq. (13) from Eq. (15) yields

$$\epsilon_r \cong -\frac{0.622\Delta B_r}{\frac{1}{\sqrt{\lambda_0}} + \frac{0.348}{\kappa}}. \quad (16)$$

Here, ϵ_r is approximately proportional to ΔB_r.

For h^+ between 20 and 90, ϵ_r indicates the increase expressed by Eq. (4). This range of h^+ corresponds to that of transient roughness. For normal transient roughness, Hama (1954) showed that the logarithmic velocity profiles are shifted downward and that the shift of the intercept of the logarithmic profile was expressed by

$$\Delta B = -(1/\kappa) \ln (ku_\tau/\nu) + \text{constant}. \quad (17)$$

Here, k is the roughness length scale. Assuming the increase in ϵ_r for the riblet pipes is also produced by the downward shift of the logarithmic velocity profile, Eq. (16) yields

$$\Delta B_r \cong -\frac{\epsilon_r}{0.622}\left(\frac{1}{\sqrt{\lambda_0}} + \frac{0.348}{\kappa}\right). \quad (18)$$

In our riblet pipe, λ_0 is approximately constant for h^+ between 20 and 90. Therefore, Eqs. (4) and (18) give

$$\Delta B_r \cong -5.8 \log h^+ + 8.0 \quad (20 < h^+ < 90)$$
$$= -(1/\kappa) \ln (hu_\tau/\nu) + 8.0, \quad (19)$$

which results in a form similar to that of Eq. (17) for the transient roughness.

3-3 Synergistic Effect Due to Thickening of the Wall Layer. For the positive synergistic drag reduction, Anderson et al. (1993) hypothesized that a limited polymer influence on the flow structures about the riblet peaks could possibly extend the range of riblet drag reduction. This extension of the range may occur by any of several mechanisms: the enhancement of riblet- or additive-induced drag reduction or the suppression of riblet-induced drag increase as a rough pipe. The additives thicken the wall layer with drag reduction, thus decreasing the relative height h/δ of the riblets. If we assume ΔB_r in Eq. (19) to be a function of h/δ rather than h^+, then ΔB_r is defined as

$$\Delta B_r = G(h/\delta), \tag{20}$$

where $G(h/\delta)$ is a decreasing function of h/δ, similar to Eq. (19). From Eq. (20), the decrease in h/δ due to the effect of the additive appears to suppress the negative shift of ΔB_r and produces the synergistic drag reduction. In this section, this scenario is applied to the synergy that was observed for $s^+ > 20$.

The riblets and the polymer additives produce the parallel shift of the logarithmic velocity profiles, ΔB_p (Eq. (10)) and ΔB_r (Eq. (19)), respectively. For the combined system, we express the shift ΔB as a linear combination

$$\Delta B = \Delta B_p + \Delta B_{r+}, \tag{21}$$

where ΔB_{r+} is the sum of the shift due to riblets and the synergy. The above-mentioned scenario suggests that the additives increase the wall layer thickness δ for τ_w higher than τ^*, which in turn suppresses the negative shift of the intercept ΔB_r. Therefore, from Eq. (20), ΔB_{r+} in Eq. (21) would be given approximately by

$$\Delta B_{r+} \cong \Delta B_r = G(h/\delta). \tag{22}$$

In order to derive the function $G(h/\delta)$, Eq. (19) of the riblet system is modified as follows:

$$\Delta B_{r+} = -5.8 \log (h/\delta_s) + 0.45. \tag{23}$$

Here, δ_s is the wall layer thickness for a smooth surface and is given by Eq. (11). The actual wall layer thickness δ and the definition of wall layer thickness over riblets remain unclear. Therefore, we use δ_s rather than the actual wall layer thickness δ. For a solvent, $\delta_s^+ = 20$, and thus, Eq. (23) can be reduced to Eq. (19). Next, we investigate whether the synergistic drag reduction observed is consistent with Eq. (23).

The log-profile shift ΔB_p is a function of δ_s^+ $(=u_\tau \delta_s/\nu)$ from Eq. (9), and ΔB_{r+} is a function of h/δ_s from Eq. (23). Thus, δ_s is a key parameter that produces this synergistic drag reduction. We define $(\epsilon_{r+})_{\delta_s}$ as a deviation from a polymer system based on common δ_s. Therefore,

$$(\epsilon_{r+})_{\delta_s} = (\epsilon_c - \epsilon_p)_{\delta_s = \text{const.}} \tag{24}$$

From these changes, the friction factor λ is given as follows:

$$\lambda = \lambda_0(1 + \epsilon_c) = \lambda_0(1 + (\epsilon_p)_{\delta_s} + (\epsilon_{r+})_{\delta_s}), \tag{25}$$

and is related to ΔB_p and ΔB_{r+} as follows:

$$\frac{1}{\sqrt{\lambda_0(1 + (\epsilon_p)_{\delta_s} + (\epsilon_{r+})_{\delta_s})}} = \frac{0.348}{\kappa} \ln\left(\text{Re}\sqrt{\lambda_0(1 + (\epsilon_p)_{\delta_s} + (\epsilon_{r+})_{\delta_s})}\right) - 0.311\left\{\frac{3.23}{\kappa} - (5.5 + \Delta B_p + \Delta B_{r+})\right\} \tag{26}$$

Since the additives suppress the riblets to increase the drag to the level of a normal rough surface, $(\epsilon_{r+})_{\delta_s} \ll 1 + (\epsilon_p)_{\delta_s}$. Neglecting the higher-order terms of $(\epsilon_{r+})_{\delta_s}/(1 + (\epsilon_p)_{\delta_s})$, Eq. (26) reduces to

$$\frac{1}{\sqrt{\lambda_0(1 + (\epsilon_p)_{\delta_s})}}\left(1 - \frac{1}{2}\frac{(\epsilon_{r+})_{\delta_s}}{1 + (\epsilon_p)_{\delta_s}}\right) = \frac{0.348}{\kappa}\left\{\ln\{\text{Re}\sqrt{\lambda_0(1 + (\epsilon_p)_{\delta_s})}\} + \frac{1}{2}\frac{(\epsilon_{r+})_{\delta_s}}{1 + (\epsilon_p)_{\delta_s}}\right\} - 0.311\left\{\frac{3.23}{\kappa} - (5.5 + \Delta B_p + \Delta B_{r+})\right\}, \tag{27}$$

and the subtraction of Eq. (12) from Eq. (27) yields

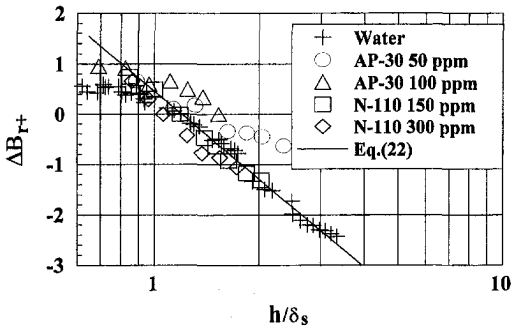

Fig. 12 Calculated shift of a logarithmic velocity profile in combined systems. Run 4.

$$(\epsilon_{r+})_{\delta_s} \cong -\frac{0.622(1 + (\epsilon_p)_{\delta_s})\Delta B_{r+}}{\dfrac{1}{\sqrt{\lambda_0(1 + (\epsilon_p)_{\delta_s})}} + \dfrac{0.348}{\kappa}}, \tag{28}$$

or

$$\Delta B_{r+} = \frac{(\epsilon_{r+})_{\delta_s}}{0.622(1 + (\epsilon_p)_{\delta_s})}\left(\frac{1}{\sqrt{\lambda_0(1 + (\epsilon_p)_{\delta_s})}} + \frac{0.348}{\kappa}\right). \tag{29}$$

In Fig. 12, the ΔB_{r+} calculated from the right-hand side of Eq. (29) was plotted as a function of h/δ_s. The plotted results of ΔB_{r+} agree qualitatively with Eq. (23) in $h/\delta_s > 1$. This agreement suggests that the log-profile shift Eq. (23) is a reasonable approximate extension to the combined system. Furthermore, comparing Eq. (16) and Eq. (28) reveals that additive-induced drag reductions $(\epsilon_p)_{\delta_s}$ suppress the influence of ΔB_{r+} on $(\epsilon_{r+})_{\delta_s}$ by

$$\frac{0.622(1 + (\epsilon_p)_{\delta_s})}{\dfrac{1}{\sqrt{\lambda_0(1 + (\epsilon_p)_{\delta_s})}} + \dfrac{0.348}{\kappa}} \Bigg/ \frac{0.622}{\left(\dfrac{1}{\sqrt{\lambda_0}} + \dfrac{0.348}{\kappa}\right)} \cong (1 + (\epsilon_p)_{\delta_s})^{3/2}.$$

Therefore, the flow enhancement due to additives also contributes to the synergistic effect as well as the decrease in h/δ_s.

From the above-mentioned results, the synergistic drag reduction is given as follows. At first, τ_w $(>\tau^*)$ is given. Next, ϵ_p and δ_s in the additive system are obtained from Figs. 8 and 10. Finally, Eqs. (23) and (28) give ϵ_c for the combined system as follows:

$$\epsilon_c = -\frac{0.622(1 + (\epsilon_p)_{\delta_s})(-5.8 \log (h/\delta_s) + 0.45)}{\dfrac{1}{\sqrt{\lambda_0(1 + (\epsilon_p)_{\delta_s})}} + \dfrac{0.348}{\kappa}} + (\epsilon_p)_{\delta_s} \tag{30}$$

The solid lines in Fig. 8 indicate ϵ_c calculated from Eq. (30) for $h/\delta_s > 1$. The agreement between these values and the experimental results implies that Eq. (23) is a reasonable approximation for the log-profile shift of the combined system.

4 Conclusions

The drag reduction effects were studied for the combined system of a riblet pipe and polymer additives. The additives did not affect the effective range of the non-dimensionalized groove interval, s^+. The range of s^+ for which the riblets showed the maximum drag reduction was from 15 to 20. For s^+ lower than 20 and a sufficiently low additive-induced drag reduction, positive synergistic effects were observed. The synergistic drag reduction was less than 5 percent.

In the region of higher h^+, the riblet pipe increased the drag to levels similar to that of a pipe having normal transitional roughness. For Newtonian fluids, this drag increase appeared for h^+

greater than 20, and the relative friction factor change ϵ_r was found to be a function of h^+. In the combined system, the additives suppressed this increase in drag. This synergistic effect is produced because the additives thicken the wall layer and thus decrease the groove height relative to the wall layer thickness. Another cause of the synergistic effect is the flow enhancement due to additives, which suppresses the riblet-induced drag increase by $(1 + (\epsilon_p)_{\delta s})^{3/2}$. This synergistic effect appears for h^+ greater than δ_s^+. When h^+ is greater than δ_s^+, if an additive having a critical shear stress that satisfies $(\rho h/\mu)\sqrt{\tau^*/\rho} < \delta_s^+$, then τ_w becomes higher than τ^* because $(\rho h/\mu)\sqrt{\tau^*/\rho} < \delta_s^+ < (\rho h/\mu)\sqrt{\tau_w/\rho}$. In additive solutions, δ_s^+ is greater than 20; therefore, this condition for τ^* can be approximately replaced by $(\rho h/\mu)\sqrt{\tau^*/\rho} < 20$. Here, the combined effects almost cancel out the drag increase due to riblets. This synergistic effect exceeds 10%.

Acknowledgments

We wish to thank Dr. S. Nakao of National Research Laboratory of Metrology and the staff of a machine shop in our Faculty of Engineering for their support in setting up the experimental apparatus.

References

Anderson, G. W., Rohr, J. J., and Stanley, S. D., 1993, "The Combined Drag Effects of Riblets and Polymers in Pipe Flow," ASME JOURNAL OF FLUIDS ENGINEERING, Vol. 115, pp. 213–220.

Bechert, D. W., Bartenwerfer, M., and Hoppe, G., 1990, "Turbulent Drag Reduction by Nonplanar Surfaces," *Structure of Turbulence and Drag Reduction,* Springer-Verlag, pp. 525–543.

Choi, H., Moin, P., and Kim, J., 1991, "On the Effect of Riblets in Fully Developed Laminar Channel Flows," *Physics of Fluids A,* Vol. 3, No. 8, pp. 1892–1896.

Choi, H., Moin, P., and Kim, J., 1993, "Direct Numerical Simulation of Turbulent Flow over Riblets," *Journal of Fluid Mechanics,* Vol. 255, pp. 503–539.

Choi, K-S., Pearcey, H. H., Savill, A. M., and Svensson, S., 1989, "Drag Reduction with a Combined Use of Riblets and Polymer Coating," *Drag Reduction in Fluid Flows,* Ellis Horwood, pp. 271–277.

Christodoulou, C., Liu, K. N., and Joseph, D. D., 1991, "Combined Effects of Riblets and Polymers on Drag Reduction in Pipes," *Physics of Fluids A,* Vol. 3, No. 5, pp. 995–996.

Mizunuma, H., and Kato, H., 1983, "Frictional Resistance in Fiber Suspensions," *Bulletin of the JSME,* Vol. 26, No. 219, pp. 1567–1574.

Koury, E., and Virk, P. S., 1995, "Drag Reduction by Polymer Solutions in a Riblet-Lined Pipe," *Applied Scientific Research,* Vol. 54, pp. 323–347.

Nakao, S., 1991, "Application of V Shape Riblets to Pipe Flows," ASME JOURNAL OF FLUIDS ENGINEERING, Vol. 113, pp. 587–590.

Rohr, J., Anderson, G. W., and Reidy, L. W., 1989, "An Experimental Investigation of the Drag Reducing Effects of Riblets in Pipes," *Drag Reduction in Fluid Flows,* Ellis Horwood, pp. 263–270.

Tiederman, W. G., Luchik, T. S., and Bogard, D. G., 1985, "Wall-Layer Structure and Drag Reduction," *Journal of Fluid Mechanics,* Vol. 156, pp. 419–437.

Virk, P. S., 1975, "Drag Reduction Fundamentals," *AIChE Journal,* Vol. 21, No. 4, pp. 625–656.

Wallance, J. M., and Balint, J. L., 1988, "Viscous Drag Reduction using Streamwise Aligned Riblets: Survey and New Results," *Turbulence Management and Relaminarisation,* Springer-Verlag, pp. 133–147.

APPENDIX

Synergistic Effect Due to Reduction of Critical Shear Stress

When $s^+ < 20$ and the additive-induced drag reduction was not at its maximum, the combined system showed a positive synergistic effect, which is discussed here. The valid range of this synergistic effect is from $\tau_w \cong \tau_r^*$ to s^+ $(=u_\tau s/\nu) \cong 20$ in the proposed system, and thus $\tau_r^* < \tau_w < \rho(20\nu/s)^2$.

Generally, the velocity gradient is steeper near the riblet tip and the local wall shear stress τ_{tip} is higher than the average τ_w. Both computations for turbulent flow and laminar flow (Choi et al., 1991, 1993) showed that τ_{tip}/τ_w was approximately 14 for a Newtonian fluid. Even if the shear stress averaged over the entire riblet surface is lower than the critical shear stress τ^* of the additive, the local shear stress near the tip may be higher than the critical shear stress. For the combined system using N-110, the critical shear stress τ_r^* in a riblet pipe was one order lower than τ^* in a smooth pipe. If we assume

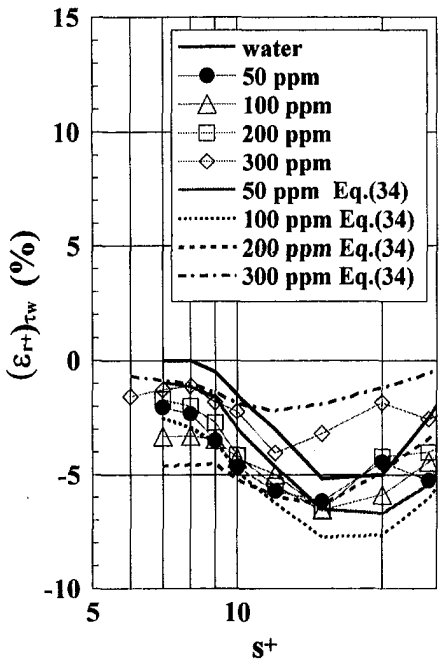

Fig. A1(*a*) AP-30

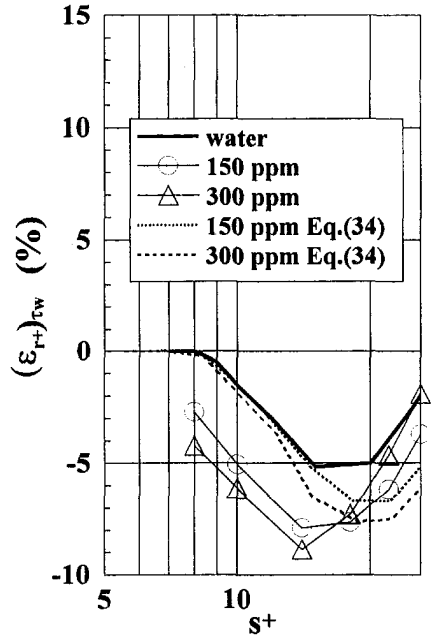

Fig. A1(*b*) N-110

Fig. A1 $(\epsilon_{r+})_{\tau_w}$ as a function of s^+. Run 4. (Uncertainty in ϵ_{r+} = 1.8% and in s^+ = 4.0% at s^+ = 10.)

$$\tau^*/\tau_r^* \cong \tau_{tip}/\tau_w \cong 14 \tag{A1}$$

and $\tau_w > \tau_r^*$, in other word $\tau_{tip} = 14\tau_w > 14\tau_r^* = \tau^*$. That is, $\tau_{tip} > \tau^*$. The condition necessary for the additive drag reduction is locally satisfied. This situation suggests the possibility that the riblets enhance the drag reduction effect of additives. For normal roughness, the rough elements are uniformly distributed on the wall. From these elements, polymeric molecules are subjected to alternately higher and lower shear stress. In contrast, the tips of riblets are aligned in the streamwise direction. Along the riblet tips, the polymeric molecules are temporarily subjected to continuous and higher shear stress. This local high shear over the riblet tips would enhance the molecular alignment and would initiate the

additive drag reduction, even if the averaged shear stress is lower than τ^*. This synergy disappears at $s^+ \cong 20$, where riblets begin to increase the drag to levels that are similar to that of a normal rough pipe.

We examine the influence that this local high shear over the riblet tips exerts on the drag reducing effect of the additives. The shift of logarithmic profile for the combined system can be expressed by the linear combination,

$$\Delta B = \Delta B_r + \Delta B_p + \Delta B_+, \tag{A2}$$

where ΔB_p and ΔB_r are obtained from Figs. 10 and 11, respectively. The synergistic shift ΔB_+ indicates the enhancement of the effect of the additive due to the riblets. This enhancement ΔB_+ appears to be proportional to the shift due to the additive ΔB_p, and is suppressed as ϵ_p approaches the Virk's maximum drag reduction $(\epsilon_p)_{\max}$. Assuming that this suppression is proportional to $\{1 - \epsilon_p/(\epsilon_p)_{\max}\}$, ΔB_+ is given by

$$\tau_w < \tau_r^* : \Delta B_+ = 0,$$

$$\tau_r^* < \tau_w < \rho\left(\frac{20\nu}{s}\right)^2 : \Delta B_+ \cong \alpha \cdot \left\{1 - \frac{\epsilon_p}{(\epsilon_p)_{\max}}\right\} \cdot F_0\left(C_{\text{poly}}, \frac{\tau_{\text{tip}}}{\tau^*}\right).$$

Here, α is an experimental constant. From Eq. (A1),

$$\tau_r^* < \tau_w < \rho\left(\frac{20\nu}{s}\right)^2 : \Delta B_+ \cong \alpha \cdot \left\{1 - \frac{\epsilon_p}{(\epsilon_p)_{\max}}\right\} \cdot F_0\left(C_{\text{poly}}, \frac{14\tau_w}{\tau^*}\right). \tag{A3}$$

Now, if ϵ_p is given as a function of τ_w, as shown in Fig. 8, ΔB_+ is given by Eq. (A3). The shift ΔB_r is obtained as a function of $s^+ (= u_\tau s/\nu)$ from Fig. 11, and ΔB_{r+} is calculated from $\Delta B_r + \Delta B_+$. Because of $(\epsilon_{r^+})_{\tau_w} \ll 1 + (\epsilon_p)_{\tau_w}$, $(\epsilon_{r^+})_{\tau_w}$ is calculated in a manner similar to that used to calculate Eq. (28).

$$(\epsilon_{r^+})_{\tau_w} \cong -\frac{0.622(1 + (\epsilon_p)_{\tau_w})\Delta B_{r^+}}{\dfrac{1}{\sqrt{\lambda_0(1 + (\epsilon_p)_{\tau_w})}} + \dfrac{0.348}{\kappa}} \tag{A4}$$

Figures A1(a) and (b) show the results of $(\epsilon_{r^+})_{\tau_w}$ for $\alpha = 0.07$. For 300 ppm AP-30, ϵ_p approaches $(\epsilon_p)_{\max}$. Equation (A3) gives $\Delta B_+ \cong 0$, and the influence of ΔB_{r^+} ($\cong \Delta B_r$) on $(\epsilon_{r^+})_{\tau_w}$ is approximately suppressed by $(1 + (\epsilon_p)_{\tau_w})$ in Eq. (A4). Therefore, the synergistic effect becomes negative, as shown in Fig. A1(a). The calculated $(\epsilon_{r^+})_{\tau_w}$ agrees approximately with the results measured for AP-30, but not with those measured for N-110. These results suggest that α or τ^*/τ_r^* is not a universal constant and is greater for $\tau_w < \tau^*$ (N-110) than for $\tau_w > \tau^*$ (AP-30). In other words, the effect of the local high shear appears to depend on whether or not polymer molecules are ready for drag reduction. However, this synergistic drag reduction is extremely small (1 to 4%). Thus, the results of the present study should not be considered conclusive.

Drag Reduction in Laminar Flow Between Two Vertical Coaxial Cylinders

Keizo Watanabe
Professor.
e-mail: keizo@ecomp.metro-u.ac.jp

Takashi Akino
Graduate Student.

Tokyo Metropolitan University,
Graduate School of Engineering,
Department of Mechanical Engineering,
1-1 Minami Ohsawa, Hachiooji-shi, Tokyo,
192-0397 Japan

Laminar drag reduction has been shown for the flow of a Newtonian fluid in the space between two vertical coaxial cylinders. Experiments were carried out to measure the torque of a bob with a highly water-repellent wall to clarify the effect of the contact surface of the bob on the flow behavior. The basic material of the highly water-repellent wall is fluorine alkane modified acrylic resin with added hydrophobic silica, and the contact angle of the wall is about 150 degree. The radius ratios of the bob were 0.932 and 0.676. Test fluids were Newtonian aqueous solutions of 60, 70, and 80 wt% glycerin and polymer solutions. The maximum drag reduction ratio was about 12% for 80 wt% glycerin solution at a radius ratio of 0.932. The moment coefficient of the coaxial cylinder in Newtonian fluids was analyzed for fluid slip, and it was shown that the analytical results agreed well with the experimental data. For the case of non-Newtonian fluids, the fluid slip velocity of polymer solutions is not proportional to the shear stress and the relationship is approximated by power-law equations.

Introduction

For simple low-molecular weight fluids such as water or glycerin solution, which are Newtonian fluids, fluid slip at the solid boundary is usually negligible, and the calculated results obtained under the no-slip boundary condition agree well with the experimental results. However, if fluid slip occurs at the solid boundary, we can obtain a new drag reduction for the internal or the external flow of a Newtonian fluid.

One of the authors (Watanabe et al., 1996) first detected the slip velocity of Newtonian fluids at the solid boundary of the highly water-repellent duct wall by investigating pressure losses. The maximum drag reduction ratio for the friction factor of a square duct was about 23% in the laminar flow range. The friction factor was analyzed by applying the fluid slip boundary condition from a macroscopic viewpoint, and the results were found to be in good agreement with those of the experiments. Watanabe et al. (1999) also reported the laminar drag reduction of Newtonian fluids in a circular pipe with a highly water-repellent wall and experimentally clarified the slip velocity of Newtonian fluids at the wall using a hot film anemometer. In addition to the internal flow, Watanabe and Ogata (1998) reported the laminar drag reduction of a rotating disk with a highly water-repellent wall in Newtonian fluids, of which the drag reduction ratio for tap water in an enclosed rotating disk is about 35%. Although fluid slip is the most basic and a very interesting problem in fluid mechanics, there are very few studies on moving wall contact with liquid at this point in time.

On the other hand, rheometrical flow systems which have rotating parts, have been the subject of considerable interest concerning the interaction between liquid and the solid surface, from both experimental and theoretical points of view. The flow between concentric rotating cylinders is well known as a typical example of Couette flow. For the case of the outer cylinder rotating and the inner cylinder at rest, although patterns of alternating laminar and turbulent flow are observed (Coles, D., 1965; Van Atta, C., 1966), the stable flow is obtained at large Reynolds number range. Yamada et al. (1969) showed that in the experimental data of the torque coefficient of two coaxial rotating cylinders. Nouri and Whitelaw (1994) reported measurements of pressure and velocity of two Newtonian fluids and a non-Newtonian fluid in a concentric annulus, at Reynolds numbers up to those of fully turbulent flow and with rotation of the inner shaft. Thus we take note of the flow between vertical coaxial cylinders, which is basically the flow for which viscosity is measured also. The purpose of this study is to clarify the effect of the physical properties of the contact solid wall surface on torque measurement for Newtonian and non-Newtonian fluids flow between two vertical coaxial cylinders.

Consequently, the laminar drag reduction of Newtonian fluid in the space between two vertical coaxial cylinders has been clarified for a bob with a highly water-repellent wall, and the experimental data qualitatively agreed well with the calculated results analyzed using the fluid slip boundary condition. Additionally, experimental data of the slip velocity for polymer solutions, which exhibit viscoelastic and non-Newtonian viscous effects, have been presented in this paper.

Analysis

First we consider two-dimensional Newtonian fluid flow with fluid slip at the wall of the stationary inner cylinder of the two coaxial cylinders shown in Fig. 1. In steady-state laminar flow, the shear stress $\tau_{r\theta}$ and θ-component of the Navier-Stokes equation are given as the following equations,

$$\tau_{r\theta} = \mu\left[r \frac{\partial}{\partial r}\left(\frac{v_\theta}{r}\right)\right] \tag{1}$$

$$0 = \frac{d}{dr}\left[\frac{1}{r}\frac{d}{dr}(rv_\theta)\right], \tag{2}$$

where μ and v_θ are the viscosity and the velocity of the θ-component, respectively. If fluid slip occurs at the wall of the inner cylinder, the boundary conditions are

$$r = \kappa R_o; \quad v_\theta = u_s$$

$$r = R_o; \quad v_\theta = \omega_o R_o, \tag{3}$$

where u_s and ω_o are the slip velocity at the wall of the inner cylinder and the angular velocity of the outer cylinder, respectively.

Contributed by the Fluids Engineering Division for publication in the JOURNAL OF FLUIDS ENGINEERING. Manuscript received by the Fluids Engineering Division October 5, 1998; revised manuscript received May 3, 1999. Associate Technical Editor: J. A. C. Humphrey.

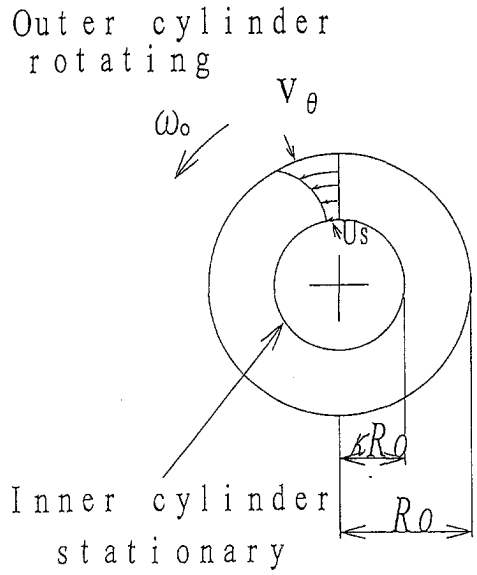

Fig. 1 Flow model

The velocity profile v_θ is calculated using Eq. (2) under boundary conditions, Eq. (3).

$$v_\theta = \frac{\kappa R_o}{r} u_s + \frac{R_o\omega_o - \kappa u_s}{(1-\kappa^2)R_o r}(r^2 - \kappa^2 R_o^2) \tag{4}$$

By substituting Eq. (4) into Eq. (1), we obtain the torque T required to turn the outer shaft.

$$T = 4\pi\mu R_o^2 L\left(\omega_o\kappa - u_s\frac{1}{R_o}\right)\left(\frac{\kappa}{1-\kappa^2}\right) \tag{5}$$

Thus the slip velocity u_s is related to the torque T by

$$u_s = R_o\kappa\omega_o - \frac{T}{4\pi\mu R_o L}\frac{(1-\kappa^2)}{\kappa} \tag{6}$$

By substituting the measured value of the torque T into Eq. (6), we can calculate the slip velocity u_s.

Navier (1816) gives the relationship between the slip velocity at the solid boundary and the shear stress as

$$\tau_{r\theta}|_{r=\kappa R_o} = \beta u_s, \tag{7}$$

where β is the coefficient of sliding friction. Equation (6) is modified, by using Eq. (7), to

$$u_s = \frac{2\mu R_o\kappa\omega_o}{\beta\kappa R_o(1-\kappa^2) + 2\mu} \tag{8}$$

The coefficient of torque acting on the inner cylinder Cm is obtained as

$$Cm = \frac{16\kappa^2}{(\kappa+1)^4}\left(1 - \frac{2}{\frac{\beta R_o}{\mu}\kappa(1-\kappa^2)+2}\right)\Big/ R_\omega \tag{9}$$

where Cm is defined as $Cm = T/2\pi\rho R_m^4\omega_o^2 L$. When fluid slip does not occur, we obtain the following equation by substituting $\beta = \infty$ into Eq. (9)

$$Cm = \frac{16\kappa^2}{(\kappa+1)^4}\Big/ R_\omega = \frac{16(1-\delta/R_o)^2}{2^4(1-\delta/2R_o)^4}\Big/ R_\omega$$

$$= \frac{(1-\delta/R_o)^2}{(1-\delta/R_o+(\delta/2R_o)^2)^2}\Big/ R_\omega$$

where δ is the gap between outer cylinder and bob. In the case of $(\delta/R_o)^2 \fallingdotseq 0$, we obtain $Cm = 1/R_\omega$. For the small gap, the term $(\delta/R_o)^2$ is very small, such as it is approximated by and we have $Cm = 1/R_\omega$.

Second, we analyze non-Newtonian fluid flow with slip fluid. In steady-state laminar flow, the shear stress of a power law model and θ-component of the constitutive equation are given as following equations, respectively,

$$\tau_{r\theta} = K\left[r\frac{\partial}{\partial r}\left(\frac{v_\theta}{r}\right)\right]^n \tag{10}$$

$$0 = \frac{1}{r^2}\frac{\partial}{\partial r}(r^2\tau_{r\theta}) \tag{11}$$

u_s is calculated using Eq. (10) and Eq. (11) under boundary conditions, Eq. (3) as follows,

$$u_s = \kappa\omega_o R_o - \frac{1}{2}n(\kappa R_o)^{1-(2/n)}(1-\kappa^{2/n})\left(\frac{T}{2\pi LK}\right)^{1/n} \tag{12}$$

On the other hand, Cm for no slip is given as following equation by applying $(\delta/R_o)^2 \fallingdotseq 0$,

$$Cm = \frac{2^{2n+2}\kappa^2(1-\kappa^2)}{(1+\kappa)^4 n^n(1-\kappa^{2/n})^n R_\omega^*} \tag{13}$$

By substituting $n = 1$ into Eq. (12) and Eq. (13), they agree with analytical results for Newtonian fluid.

Experimental Apparatus and Method

Experiments were carried out to measure the torque for laminar flow of aqueous glycerin solutions and polymer solutions in the space between two vertical coaxial cylinders, the outer one rotating.

Figure 2 shows the experimental apparatus. The outer cylinder was rotated at rates from 0.9 rpm to 600 rpm by means of a motor connected to a gear. The torque acting on the bob was measured by means of the torsion spring. The shear rate range was 1–1000 s^{-1}.

Nomenclature

Cm = coefficient of torque $\{=T/2\pi\rho r_m^4\omega_o^2 L\}$
K = consistency index
n = exponent in power law
L = length of bob
R_i = radius of bob
R_m = mean radius $\{=(R_o + R_i)/2\}$
R_o = outer cylinder radius
R_ω = Reynolds number $\{=(R_o - R_i)R_m\omega_o/\nu\}$
R_ω^* = modified Reynolds number $\{=R_o(1-\kappa)^2\omega_o^{2-n}/2^{2-n}K\}$
T = torque acting on bob
u_s = slip velocity at bob wall
β = sliding coefficient
γ = shear rate $\{=2\omega_o/(1-\kappa^2)\}$
δ = gap $\{=R_o - R_i\}$
ϵ = drag reduction ratio
κ = radius ratio $\{=R_i/R_o\}$
μ = viscosity
ν = kinematic viscosity
ρ = density
τ_w = wall shear stress
ω_o = angular velocity of the outer cylinder
r, θ, z = cylindrical coordinate

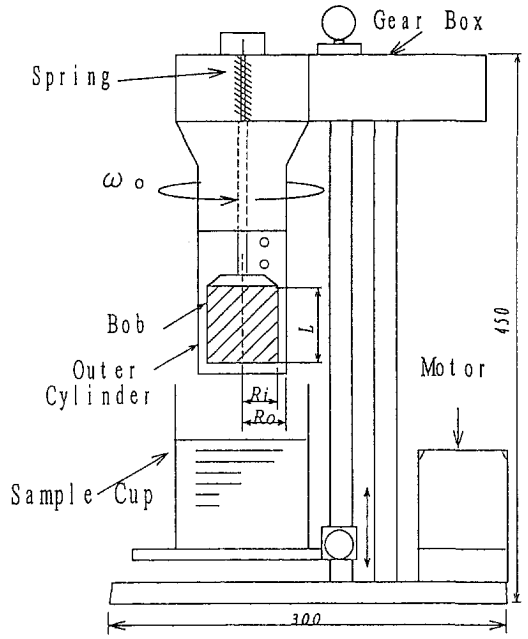

Fig. 2 Experimental apparatus

The surface of the inner cylinder, the bob was coated with the highly water-repellent material, the contact angle of which is about 156 deg with the wall. In general, the largest contact angles recorded for a smooth surface are 112–115 deg (Moilliet, 1963). Thus we need a useful method to produce a surface with a contact angle of 120 deg or larger, since it is necessary not only to reduce the free surface energy but also to change surface morphology.

Figure 3 shows a micrograph of the test highly water-repellent wall observed using a SEM. There are many fine grooves on the surface that raise the water repellency. The basic material of the highly water-repellent coating is fluorine alkane modified acrylic resin with added hydrophobic silica, which was left overnight in air after it was coated to the cylinder wall.

Two bobs, one made of stainless steel and the other of Teflon, the contact angle of which is about 110°, were tested to clarify the effect of the physical properties of the bob surface on the measurement of the torque. Figure 4 shows the shape of droplet of

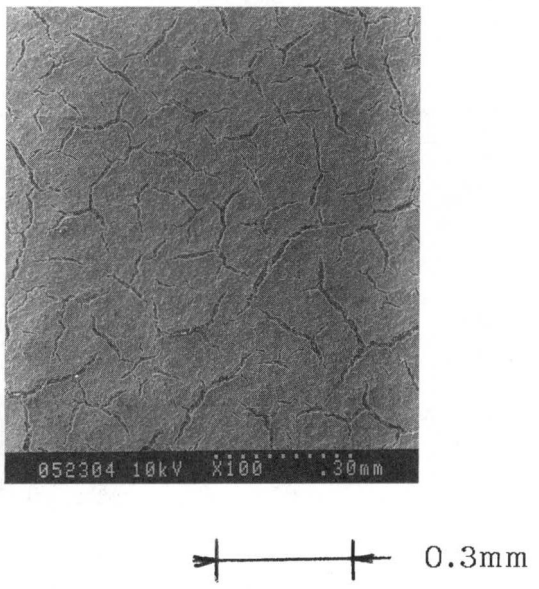

Fig. 3 Micrograph of the highly water-repellent wall observed by SEM

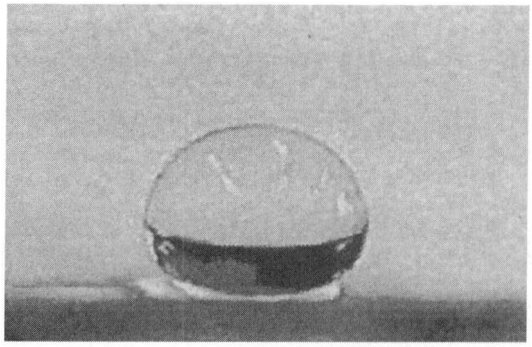

Fig. 4 Shape of a drop of water on the wall

water on the highly water-repellent material used in this study. The dimensions of the bob are listed in Table 1. Test fluids were aqueous solutions of 60, 70, and 80 wt% glycerin. For polymer solutions, tests were conducted using an aqueous polymer solution prepared using tap water as the solvent and polyethylene oxide as the polymer, which is known to be a very effective drag reduction agent in dilute solution. The test fluid has a weight concentration of 2000 and 2500 ppm. The physical properties of the fluids are listed in Table 2. Fluid temperatures were measured using a thermometer. The temperature increase during the experiment was about 2°C.

Figure 5 shows the calibration curve of this experimental apparatus. Measuring the torque acting on the calibration bob by using the weight under the static condition performed the calibration. In Fig. 5, Tcal. and Tex. represent the calculated value of the torque acting the bob under weight and the measured value, respectively. The reported value of the spring constant of the torsion spring is the best estimate for the result, and with 95% confidence, the true value is believed to lie within ±1.25% of the present value of the torque for $T = 2.25 \times 10^{-3}$ N · m.

Experimental Results and Discussion

Figure 6 shows the flow curve for 70 wt% glycerin solution obtained using the present experimental apparatus. The solid line in Fig. 6 shows the experimental result for the Newtonian fluid, obtained using an Ubbelohde viscometer. The secondary flow and the end effects are neglected. The reported values are the best estimates for the results, and with 95% confidence, the true value is believed to lie within ±3.93% of the present value of 70 wt% glycerin solution for the shear rate $\gamma = 318\ s^{-1}$.

Figures 7 and 8 show the effects of viscosity and the radius ratio on the experimental results for the slip velocity calculated by applying Eq. (6), respectively. The reported values are the best estimates for the results, and with 95% confidence, the true value is believed to lie within ±1.7% of the present value of 70 wt% glycerin solution for the slip velocity $Us = 0.03$ m/s in Fig. 7. We note that the relationship between the wall shear stress and the slip velocity is fairly well approximated by the straight line. Therefore the sliding coefficient β, which is obtained as the gradient of these lines, is a constant value. The gradient of the solid lines increases

Table 1 Dimensions of test bob

	Material	Ro(mm)	Ri(mm)	R_i/R_o	L(mm)
Bob1	Stainless Steel / Teflon / Highly water-repellent wall	18.5	17.25	0.932	36.0
Bob2	Stainless Steel / Teflon / Highly water-repellent wall	18.5	12.5	0.676	36.0

Table 2 Physical properties of the aqueous solution of glycerin

	Concentration	Exponent in power law n [-]	Viscosity μ [Pa·s]	Consistency index K [Pa·s^n]	Temperature t [℃]
Glycerin	60%	1.0	14.75×10^{-3}		12.5
	70%	1.0	24.16×10^{-3}		12.5
	80%	1.0	48.24×10^{-3}		12.5
Peo 8	2500ppm	0.97		6.19×10^{-3}	17.0
Peo15	2000ppm	0.77		16.0×10^{-3}	25.0
	2500ppm	0.78		29.9×10^{-3}	16.0
Peo18	2000ppm	0.68		44.5×10^{-3}	17.0
	2500ppm	0.69		68.36×10^{-3}	17.0

with an increase of the viscosity and the radius ratio. β is a physical constant related to the friction between liquid and the solid surface and it is not a nondimensional parameter as shown in Eq. (7). We cannot analytically determine the value because the fluid slip is related to the external friction when the liquid flow on the solid surface. In general, β of the highly water-repellent wall depends on the physical constant of liquid and the characteristics length of the flow field (Watanabe et al., 1999). The range of β is 205–320 Pa · s/m in this experiment. As shown in Fig. 3, the test highly water-repellent wall has many fine grooves which is about 10 μm in a width, such as the surface is fractal. The main reasons for the fluid slip are that the molecular attraction between liquid and the solid surface is reduced because the free surface energy of the solid is very low and the contact area of the liquid is decreased compared with a conventional smooth surface because the solid surface has many fine grooves. Thus it is an important to be in existence the interface between liquid and gas at the solid surface for the mechanism of the fluid slip obtained in this study.

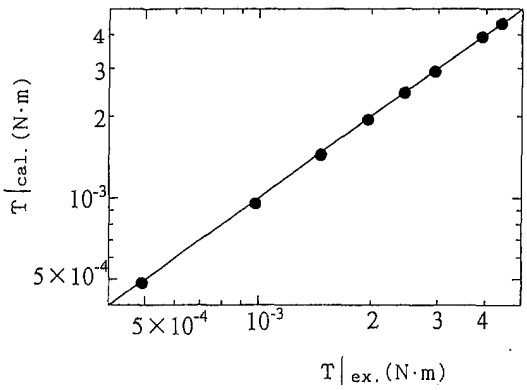

Fig. 5 Calibration curve for torque acting on the inner bob. The maximum uncertainties in Tex. and Tcal. are ±0.05 and ±1.25 percent, respectively.

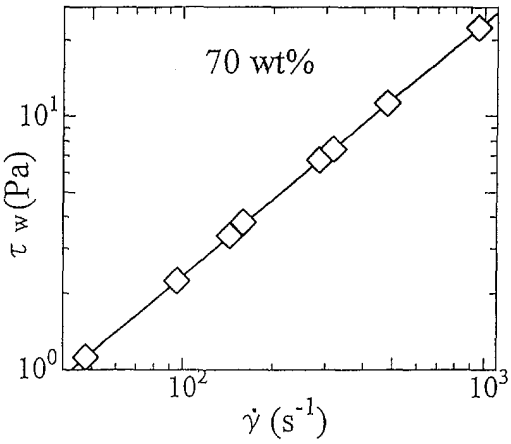

Fig. 6 Flow curve for 70 wt% glycerin solution. The maximum uncertainties in $\dot{\gamma}$ and τ_w are ±0.05 and ±3.93 percent, respectively.

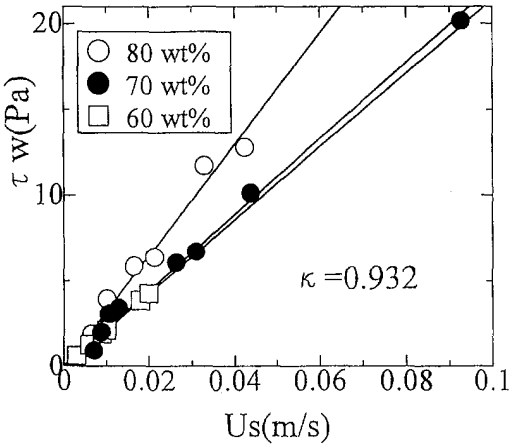

Fig. 7 Effect of concentration of glycerin solutions on slip velocity. The maximum uncertainties in τ_w and *Us* are ±0.05 and ±1.70 percent, respectively.

Figures 9 and 10 show the experimental results of the coefficient of torque rearranged using Eq. (9). In these figures, the solid lines are the results calculated using $Cm = 1/R_\omega$ for no slip at the bob wall. This fits to the experimental result were obtained by Yamada et al. Experimental data for the stainless steel and Teflon bobs fit the solid line, and lay within the scatter of ±2.8% for the stainless steel bob in 60 wt% glycerin solution. The reported values are the best estimates for the results, and with 95% confidence, the true value is believed to lie within ±1.93% of the present value of 70 wt% glycerin solution for the coefficient of torque $Cm = 0.039$ in Fig. 9. A wall with a contact angle greater than 90 deg is generally considered to be water-repellent. Although a Teflon wall is water repellent, it seems to be reasonable to consider that fluid slip does not occur at the wall of the Teflon bob in Newtonian fluid, because the experimental data fit the solid line.

On the other hand, it is seen that the experimental data for the highly water-repellent bob decreases compared to those for the stainless steel and Teflon bobs due to drag reduction in the flow range. For comparison with the data and results reported in the previous paper, it is convenient to use the drag reduction ratio defined as

$$\epsilon = \left| \frac{C_m|_n - C_m|_s}{C_m|_s} \right| \times 100 \quad (\%), \tag{14}$$

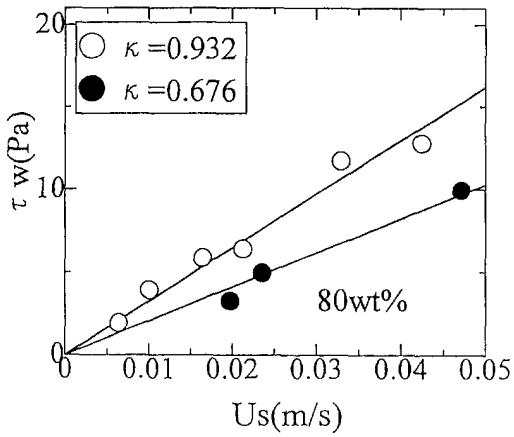

Fig. 8 Effect of radius ratio on slip velocity. The maximum uncertainties in τ_w and *Us* are ±0.05 and ±1.70 percent, respectively.

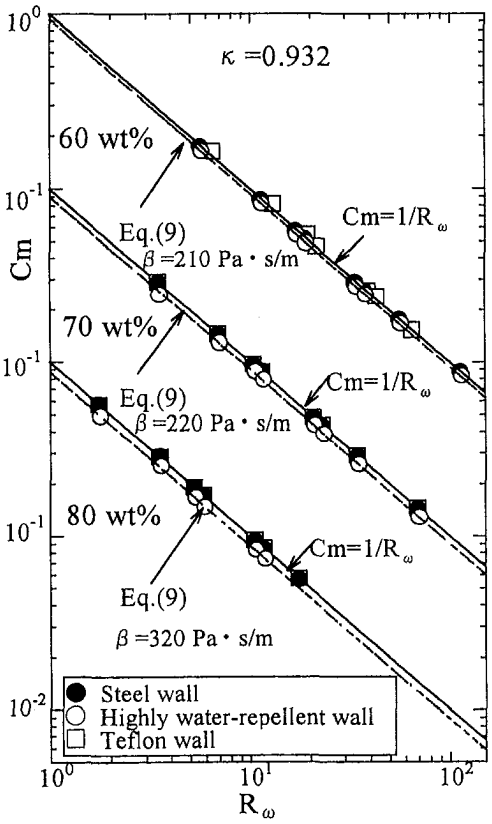

Fig. 9 Moment coefficient of glycerin solutions. The maximum uncertainties in R_ω and Cm are ±0.05 and ±1.93 percent, respectively.

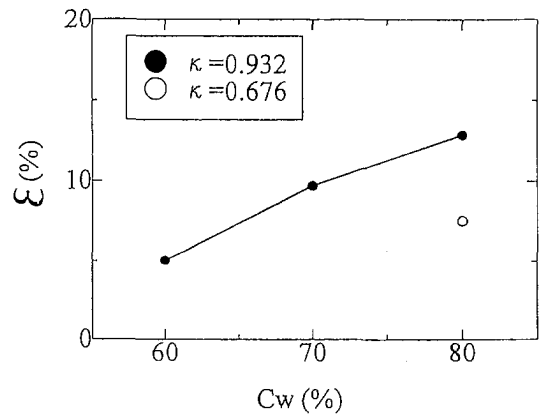

Fig. 11 Effect of concentration of glycerin solutions on drag reduction ratio. The maximum uncertainties in ε is ±3.86 percent.

where subscript n and s indicate the highly water-repellent wall bob and the stainless steel bob, respectively.

Figure 11 shows the drag reduction ratio for glycerin solutions. It is seen that ϵ depends on the concentration of glycerin solutions and the radius ratio, and increases with the increases of those values. This tendency is generally evident in the drag reduction for the flow in a pipe or duct with highly water-repellent walls. The maximum drag reduction ratio obtained in this experiment is about 12% in 80 wt% glycerin solution at $\kappa = 0.932$.

Figure 12 shows the relationship between the sliding coefficient and the concentration of glycerin solution. β increases with an increase of concentration. The coefficient of torque for the bob

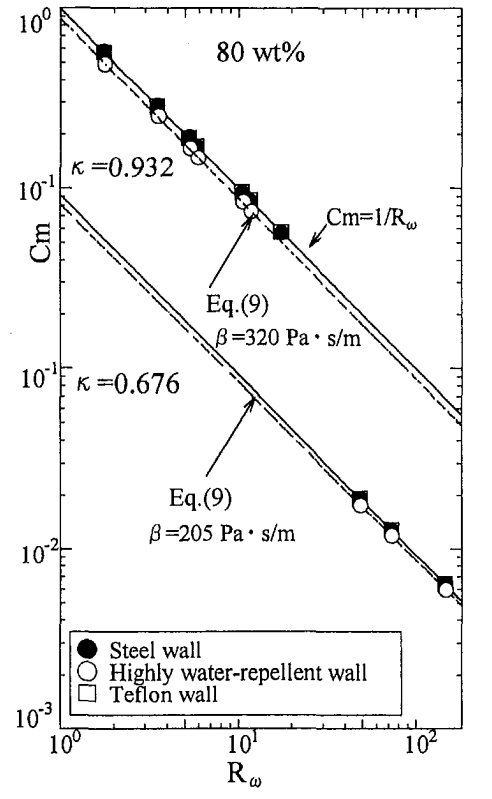

Fig. 10 Effect of radius ratio on moment coefficient for glycerin 80 wt% solution. The maximum uncertainties in R_ω and Cm are ±0.05 and ±1.93 percent, respectively.

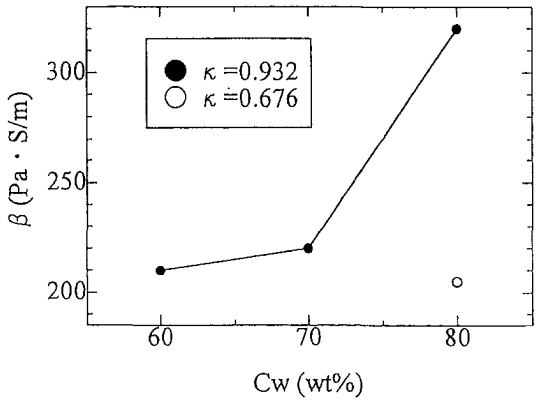

Fig. 12 Effect of concentration of glycerin solutions on sliding coefficient. The maximum uncertainties in β is ±9.58 percent.

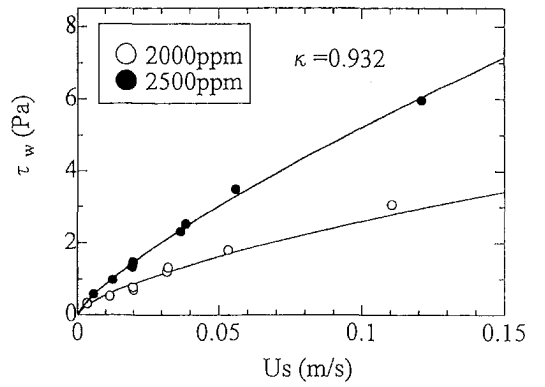

Fig. 13 Effect of concentration of Peo 15 polymer solutions on slip velocity. The maximum uncertainties in τ_w and Us are ±0.05 and ±3.30 percent, respectively.

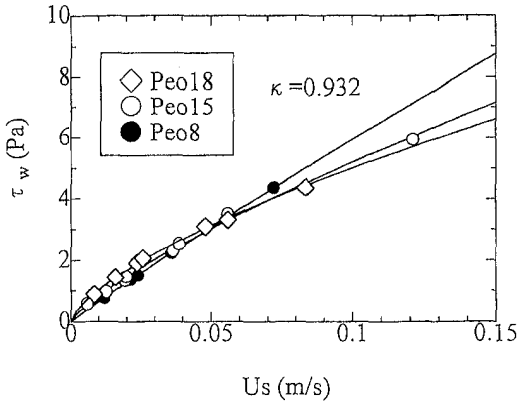

Fig. 14 Effect of molecular weight of polymer solutions on slip velocity. The maximum uncertainties in τ_w and *Us* are ±0.05 and ±3.30 percent, respectively.

with a highly water-repellent wall can be calculated using Eq. (9) if it is possible to examine the value of the sliding coefficient in this flow field. The broken lines in Figs. 9 and 10 indicate the solution given by Eq. (9). Although it is necessary to measure the velocity profile in the case of a circular pipe or a duct flow to determine β, we can easily determine the value of β from Fig. 6 in the case of this flow. Experimental data agree well with the broken line. Therefore, the fact that the slip velocity of Newtonian fluid at the wall is proportional to the wall shear stress, as inferred from Navier's hypothesis, is confirmed also by this experiment.

Figures 13 and 14 show the experimental results for the slip velocity of polymer solutions. The reported values are the best estimates for the results, and with 95% confidence, the true value

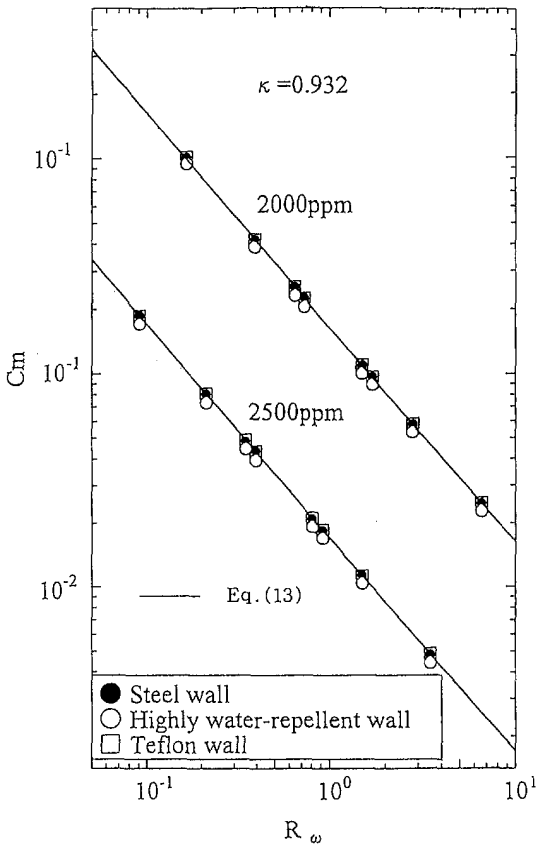

Fig. 15 Moment coefficient of Peo 15 polymer solutions. The maximum uncertainties in R_ω and *Cm* are ±0.05 and ±4.60 percent, respectively.

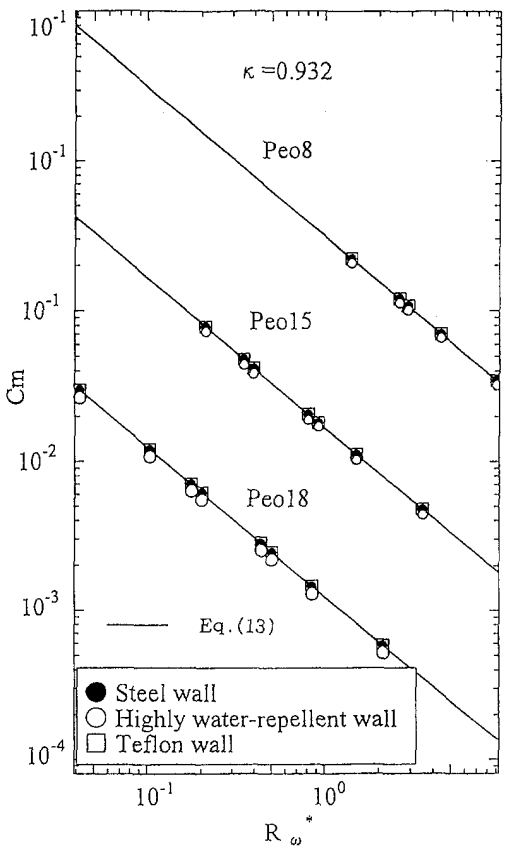

Fig. 16 Effect of molecular weight of polymer solutions on moment coefficient. The maximum uncertainties in R_ω and *Cm* are ±0.05 and ±4.60 percent, respectively.

is believed to lie within ±3.30% of the present value of 2500 ppm PEO15 polymer solution for the slip velocity $Us = 0.038$ m/s in Fig. 13. These figures show that the slip velocity increases with the increase of the concentration of solution and the molecular weight of polymer. And then, we note that the wall shear stress is not proportional to the slip velocity. Thus we can approximate the relationship for polymer solution by the following equation

$$\tau_{r\theta}|_{r=\kappa R_o} = \alpha u_s^N. \tag{15}$$

where α and N are the physical constants. In the case of 2000 ppm PEO15 polymer solution in Fig. 13, we obtained $\alpha = 12.53$ Pa · $(s/m)^n$ and $N = 0.68$.

Figures 15 and 16 show the experimental results for coefficients of torque of polymer solutions. The reported values are the best estimates for the results, and with 95% confidence, the true value is believed to lie within ±4.6% of the present value of 2500 ppm PEO15 polymer solution for the coefficient of torque $Cm = 0.017$ in Fig. 15. It can be seen that fluid slip at the bob wall does not occur with the Teflon bob, since the data for the stainless steel and Teflon bobs almost agree. Although apparent slip flow is known to occur for capillary flow of polymer solutions (Cohen, Y., 1988), the phenomena were not recognized in this experiment because the experimental data for the stainless and Teflon bobs agree well with Eq. (13).

However, we can note that drag reduction occurs with the bob with a highly water-repellent wall. Figure 17 also shows the experimental results of drag reduction ratio of test fluids. The drag reduction ratio is about 8% in 2000 ppm PEO15 polymer solution, which is smaller than that in the case of 80 wt% glycerin solution.

The experimental data show that the values of power-law fluid index n, and N in Eq. (15) are almost equal numerically for 2500 ppm PEO 8, 15 and 18 polymer solutions.

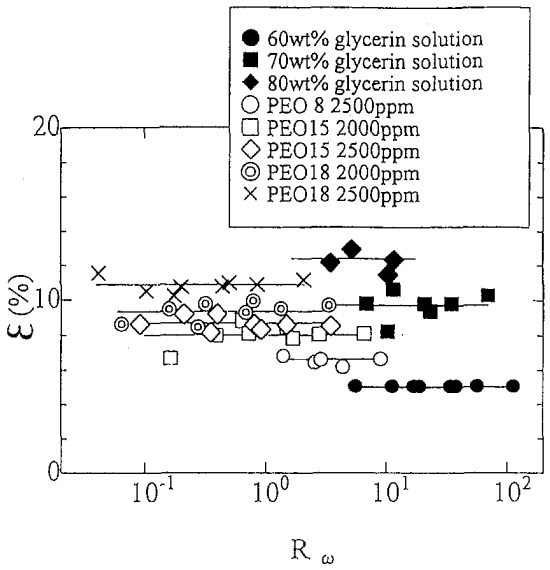

Fig. 17 Drag reduction ratio. The maximum uncertainties in ϵ and R_ω are ±3.86 and ±5.00 percent, respectively.

Conclusions

In this study, the steady Newtonian and non-Newtonian flow in the space between two vertical coaxial cylinders with a highly water-repellent wall which has many fine grooves is experimentally investigated from the macroscopic viewpoint. The results are summarized as

(1) The drag reduction ratio for the coefficient of torque of the bob with highly water-repellent wall in Newtonian fluids increases with increase in the concentration of glycerin solutions and the gap between the two cylinders. In the cases of 80 wt% glycerin solution and 2000 ppm Peo15 polymer solutions at $\kappa = 0.932$, the values of the drag reduction ratio are about 12% and 8%, respectively.

(2) The slip velocity at the wall has been analyzed in Newtonian fluids, and the relationship that the wall shear stress is proportional to the slip velocity was experimentally verified, and the analytical results for the coefficient of torque with fluid slip flow agree well with the experimental data.

(3) The slip velocity of polymer solutions for the bob with highly water-repellent-wall, is approximated by Eq. (15).

Acknowledgment

We wish to thank Messrs. N. Iwasawa, E. Nakatani, Y. Doi and N. Harutani of Kansai Paint Co., Ltd., for their support in setting up the experimental apparatus.

This work was supported financially by the Scientific Research Fund of the Ministry of Education of Japan (B-09450082).

References

Cohen, Y., 1988, "Apparent Slip Flow of Polymer Solutions," *Encyclopedia of Fluid Mechanics,* Vol. 7, Rheology and Non-Newtonian Flows, Chapter 14, Gulf. Pub. Co. pp. 408–457.

Coles, D., 1965, "Transition in Circular Couette Flow," *Journal of Fluid Mechanics,* Vol. 21, Part 3, pp. 385–425.

Moilliet, J. L., 1963, *Water-Repellency,* Elsevier Publishing, Amsterdam, p. 11.

Nouri, J. M., and Whitelaw, J. H., 1994, "Flow of Newtonian and Non-Newtonian Fluids in a Concentric Annulus With Rotation of the Inner Cylinder," ASME JOURNAL OF FLUIDS ENGINEERING, Vol. 116, No. 4, pp. 821–827.

Navier, C. L. M. H., 1816, "Memoires de L'Academie Royale des Sciences de L'Institut de France," Vol. 1, pp. 235–258.

Van Atta, C., 1966, "Measurements in Spiral Turbulence," *Journal of Fluid Mechanics,* Vol. 25, Part 3, pp. 495–512.

Watanabe, K., et al., 1996, "Drag Reduction in Flow through Square and Rectangular Ducts with Highly Water-Repellent Walls," FED-Vol. 237, 1996 ASME FED Conf. Vol. 2, pp. 115–119.

Watanabe, K., et al., 1998, "Slip of Newtonian Fluids at Solid Boundary," *International Journal of JSME,* Series B, Vol. 41, No. 3, pp. 525–529.

Watanabe, K., and Ogata, S., 1998, "Drag Reduction for a Rotating Disk with Highly Water Repellent Wall," *International Journal of JSME,* Series B, Vol. 41, No. 3, pp. 556–560.

Watanabe, K., Yanuar, and Udagawa, H., 1999, "Drag Reduction of Newtonian Fluids in a Circular Pipe with Highly Water Repellent Wall," *Journal of Fluid Mechanics,* Vol. 381, pp. 225–238.

Yamada, Y., et al., 1969, "Viscous Frictional Moment between Eccentric Rotating Cylinders when Outer Cylinder Rotates," *Transaction of JSME* (in Japanese), Vol. 35, No. 269, pp. 89–96.

Hydromagnetic Stability of Current-Induced Flow in a Small Gap Between Concentric Cylinders

Min-Hsing Chang
Assistant Professor,
Department of Mechanical Engineering,
Yung-Ta College of Technology,
Pingtung, Taiwan 909, ROC

Cha'o-Kuang Chen
Professor,
Department of Mechanical Engineering,
National Cheng Kung University,
Tainan, Taiwan 701, ROC

A linear stability analysis has been carried out for hydromagnetic current-induced flow. A viscous electrically conducting fluid between concentric cylinders is driven electromagnetically by the interaction of a superimposed radial current and a uniform axial magnetic field. The assumption of small-gap approximation is made and the governing equations with respect to nonaxisymmetric disturbances are derived and solved by a direct numerical procedure. Both of the two different types of boundary conditions, namely ideally conducting and weakly conducting walls, are considered. For $0 \leq Q \leq 5000$, where Q is the Hartmann number, which represents the strength of magnetic field in the axial direction, it is found that the instability sets in as a steady secondary flow for the case of weakly conducting walls but not for ideally conducting walls. For ideally conducting walls, it is demonstrated that the onset mode is due to nonaxisymmetric rather than axisymmetric disturbances as Q exceeds a certain critical value. The transition of the onset of instability from axisymmetric modes to nonaxisymmetric modes is discussed in detail and the possibility of axisymmetric oscillatory modes is examined. The values of the radial current density required for the appearance of secondary flow are also determined. Furthermore, the predictions of present numerical results are found to be in agreement with previous experimental studies.

Introduction

The stability of a viscous flow between two concentric cylinders was first studied by Taylor (1923). He considered this problem both experimentally and theoretically and obtained a criterion for the onset of a secondary motion in the form of cellular toroidal vortices spaced regularly along the axis of the cylinder. A similar type of instability can also occur when a viscous flow is driven by an azimuthal pressure gradient. This problem was first studied by Dean (1928) for a channel formed by two coaxial cylinders in the small-gap approximation. After Dean's original research, several investigations have been carried out on the stability of this important hydrodynamic flow (Reid, 1958; Walowit et al., 1964; Gibson and Cook, 1974; Finlay et al., 1988).

Another more complicated problem is the stability of hydromagnetic flow where a viscous electrically conducting fluid flows between two concentric cylinders owing to transverse pressure gradient acting around the channel. The transverse pressure gradient can be produced by Lorentz forces due to the interaction of an applied radial current density and a uniform axial magnetic field. It is also of interest in practice to understand the stability characteristics of this flow for the use of liquid metal brushes in high-current homopolar generators. The stability of this flow has been studied theoretically (Chandrasekhar, 1961; Hong and Wilhelm, 1976; Tabeling, 1981; Tabeling and Chabrerie, 1981; Kurzweg and Khalfaoui, 1982) and the critical disturbances are all assumed to be axisymmetric stationary modes. But in the relevant experimental works for ideal conducting walls (Tabeling, 1982; Tabeling and Trakas, 1984), it is found that the onset of instability involves overstability and is in the form of nonaxisymmetric modes at sufficiently large values of the axial magnetic field. Further, in the similar hydromagnetic stability of Taylor-Couette flow, Chang and Sartory (1967) found that the axisymmetric oscillatory modes may become more critical than the stationary modes if the Hartmann number is sufficiently large for the case of ideal conducting walls. So it is necessary to consider the stability of this flow with respect to axisymmetric oscillatory mode and nonaxisymmetric disturbances and how the boundary conditions affect the stability characteristics. The objective of the present paper is to provide this new theoretical information on this flow and compare the results with experiments. It is also desirable for such an investigation to complete the analysis of the stability of this flow because this problem has been studied only with respect to axisymmetric stationary disturbance in all existent investigations.

We consider the stability of thin films of liquid metal between concentric cylinders subjected to a steady externally applied radial current and a uniform axial magnetic field as shown in Fig. 1. A complete linear stability analysis is implemented, in which three-dimensional disturbances including axisymmetric stationary, axisymmetric oscillatory and nonaxisymmetric modes are considered. It is shown that the critical disturbance is always an axisymmetric stationary mode if the cylinders have weakly conducting walls. Then it is demonstrated that the onset mode for the case of ideally conducting walls is a nonaxisymmetric mode when the Hartmann number Q exceeds the critical value. The possible existence of axisymmetric oscillatory mode is also examined. Note that the onset of nonaxisymmetric instability indicates that the instability leads to a weak spiral vortex motion. The transition of azimuthal wavenumber m with Q is discussed. The relationship between critical radial current density and axial magnetic field intensity is also determined.

Formulation and Method of Solution

Let r, θ, and z denote the cylindrical polar coordinates, and let u_r, u_θ, and u_z and H_r, H_θ, and H_z denote the components of velocity and of the magnetic field intensity, respectively. Consider two infinitely long stationary concentric circular cylinders with a

Contributed by the Fluids Engineering Division for publication in the JOURNAL OF FLUIDS ENGINEERING. Manuscript received by the Fluids Engineering Division January 7, 1998; revised manuscript received May 17, 1999. Associate Technical Editor: P. R. Bandyopadhyay.

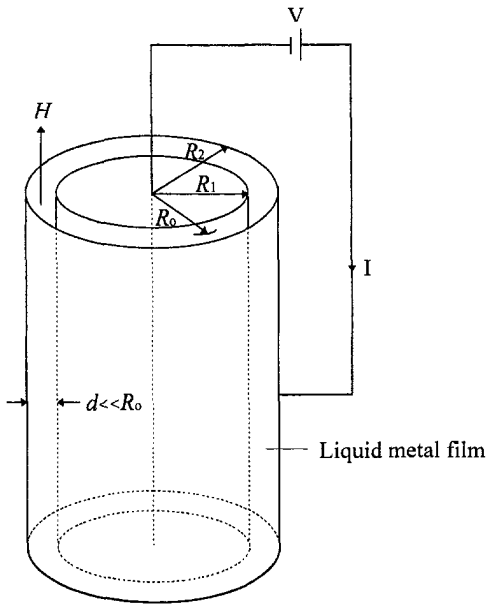

Fig. 1 Sketch of the flow configuration

common z-axis and let the radii of the inner and outer cylinders be R_1 and R_2. The governing equations for a viscous electrically conducting incompressible fluid in the annulus may be found in Chang and Chen (1998). When the fluid is driven by an azimuthal pressure gradient in the presence of a uniform axial magnetic field, the set of governing equations admits a steady solution

$$u_r = u_z = 0, \quad u_\theta = V(r) = \frac{1}{2\rho\nu}\frac{\partial P}{\partial \theta}(r \ln r + Cr + E/r),$$

$$H_r = H_\theta = 0, \quad H_z = H = \text{constant}, \tag{1}$$

where ρ, ν and P are the density, kinematic viscosity and pressure of the basic flow, respectively. The term $\partial P/\partial\theta$ accounts for the azimuthal pressure gradient and the constants are

$$C = -\frac{\ln R_2 - \eta^2 \ln R_1}{1-\eta^2}, \quad E = -\frac{R_1^2}{1-\eta^2}\ln \eta, \tag{2}$$

where $\eta = R_1/R_2$ represents the ratio of the radius of inner cylinder to that of outer cylinder. Assume that the gap between the two cylinders $d = R_2 - R_1$ is much smaller than the mean radius $R_0 = \frac{1}{2}(R_1 + R_2)$. Then after taking the limit $\eta \to 1$ we obtain

$$V(r) = 6V_m x(1-x), \quad V_m = -\frac{d^2}{12\rho\nu R_1}\left(\frac{\partial P}{\partial\theta}\right), \tag{3}$$

where $x = (r - R_1)/d$ and V_m is the mean velocity across the channel. To study the stability of this flow, a general disturbance is superimposed on the basic solution, substitute it into the governing equations and neglect quadratic terms. Since the coefficients in the resultant disturbance equations depend only on r, we can look for solutions of the form

$$u_\theta = V(r) + v(r)\exp[st + i(m\theta + \lambda z)], \tag{4}$$

where $v(r)$ is the azimuthal component of the small disturbance velocity and with similar expressions for the other components. It is assumed that λ be real and m be an integer. Without any loss of generality, the value of m is taken to be zero or a positive integer. The parameter s is complex in general. The derivation of the small gap equations is essentially the same as in previous studies (Chandrasekhar, 1961; Tabeling and Chabrerie, 1981) except that now, we must also consider terms involving differentiation with respect to the circumferential coordinate θ. The proper scaling for θ has been discussed by Krueger et al. (1966).

Now introduce the dimensionless variables

$$\delta = \frac{d}{R_1}, \quad a = \lambda d, \quad \sigma = \frac{sd^2}{\nu}, \quad k = \left(\frac{\delta}{2}\right)^{1/2} m, \quad P_m = \frac{\nu}{\epsilon}$$

$$\Lambda = \frac{72V_m^2 d^3}{R_1\nu^2}, \quad Q = \frac{\mu_0 H^2 d^2}{4\pi\rho\nu\epsilon}, \tag{5}$$

where μ_0, ϵ and P_m represent magnetic permeability, electric resistivity and magnetic Prandtl number, respectively. For liquid metal films, for instance, considering mercury at room temperature, we have $\nu = 1.14 \times 10^{-7}$ m^2/s, $\epsilon = 7.56 \times 10^{-1}$ m^2/s and then $P_m = 1.51 \times 10^{-7}$ which is very small. Hence P_m is set equal to zero (see Chandrasekhar, 1961). After combining the governing equations of perturbations under the small-gap approximation, we obtain the following eighth-order system of ordinary differential equations:

$$[L(D^2 - a^2) + Qa^2]\psi = (1 - 2x)u, \tag{6}$$

$$[L(D^2 - a^2) + Qa^2]u = a^2\Lambda x(1-x)(D^2 - a^2)\psi, \tag{7}$$

where

$$D = \frac{d}{dx}, \quad L = D^2 - a^2 - \sigma - ik\sqrt{\Lambda}\,x(1-x), \tag{8}$$

and ψ represents the azimuthal component of the small disturbance magnetic field. The boundary conditions at $x = 0$ and 1 for nonconducting walls are

$$u = Du = \psi = (D^2 - a^2)\psi = 0 \tag{9}$$

and for ideal conducting walls are

Nomenclature

a = dimensionless axial wavenumber
d = gap between two cylinders
H = uniform axial magnetic field intensity
(H_r, H_θ, H_z) = components of magnetic field intensity
J_0 = radial current intensity
m = dimensionless azimuthal wavenumber
N = dimensionless radial current number
P = pressure of basic state
P_m = magnetic Prandtl number
Q = Hartmann number
R_1 = radius of inner cylinder
R_2 = radius of outer cylinder
(r, θ, z) = polar coordinates system
(u_r, u_θ, u_z) = components of velocity
(u, v, w) = components of amplitude of normal mode for infinitesimal perturbation velocity
V_m = mean velocity of azimuthal Poiseuille flow
$x = (r - R_1)/d$
Λ = dimensionless number
$\delta = d/R_1$
ϵ = electric resistivity
$\eta = R_1/R_2$
μ_0 = magnetic permeability
ν = kinematic viscosity
ξ = electric conductivity
ρ = density of fluid
σ_i = oscillatory frequency
ψ = azimuthal component of amplitude of normal mode for infinitesimal perturbation magnetic field

$$u = Du = D\psi = (D^2 - a^2)\psi = 0 \tag{10}$$

Note that Eq. (9) is even applicable to finite conductivity walls such as stainless steel from the indication of the experimental works by Donnelly and Ozima (1962). Hence, the term "nonconducting walls" is replaced by "weakly conducting walls" based on this empirical observation. While Eq. (10) is valid for thick copper walls and the working fluid is mercury (Tabeling and Chabrerie, 1981). The homogeneous set of Eqs. (6) and (7) with the boundary conditions (9) or (10) determine an eigenvalue problem of the form

$$F(Q, k, a, \sigma, \Lambda) = 0. \tag{11}$$

The corresponding stability problem of hydrodynamic flow is only a special case when Q is set equal to zero. The marginal state is characterized by the real part of σ, σ_r, equal to zero. For a given value of Q, the minimum real positive Λ is sought over real $k \geq 0$ for which there is a solution for (11) with $\sigma_r = 0$. The value of Λ sought is the critical value Λ_c for assigned value of Q. The values of a and m corresponding to Λ_c determine the form of the critical disturbance. Under the small-gap approximation, the value of δ is given 0.05 and the imaginary part of σ, namely σ_i, corresponding to Λ_c determine the frequency of oscillation. For a fixed z, the wave will propagate in the direction of the basic flow with an angular velocity given by $c = -\sigma_i/k\Lambda^{1/2}$. Then we solve the two-point eigenvalue problem defined by (6)–(10) by a shooting technique together with a unit-disturbance method. To be brief, the system of Eq. (6) and (7) can be rewritten as a system of first-order equations. Then a set of four linearly-independent solutions of the first-order equations that satisfy the boundary condition at $x = 0$ can be constructed. Any solution of the system satisfying the boundary condition at $x = 0$ can be represented as a linear combination of these four solutions. A necessary condition is that the linear combination also satisfies the boundary condition at $x = 1$. This determines the characteristic equation. The solutions are obtained by integrating the system of first-order equations by the Runge-Kutta method and evaluating the characteristic equation. Iteration is continued until the root is approximated with sufficient accuracy. Once the root was determined, the process was repeated for a sufficient number of values of a so that the minimum of Λ with respect to a, $\Lambda_c(Q, m)$, could be determined. $\Lambda_c(Q, m)$ and the corresponding values of a and σ_i are determined by quadratic polynomial interpolation with an interval in a of 0.02. Finally, the entire process was repeated for several values of m until the minimum of $\Lambda_c(Q, m)$ was determined for the assigned value of Q. For details of the procedure, the reader is referred to Chen and Chang (1992) and Krueger et al. (1966) for this type of eigenvalue problem.

It is also necessary to estimate the error in the numerical procedures. First, all computations were carried out on a Cray J916 computer with all variables allotted to twelve integer and decimal places. The characteristic equation was evaluated and the root was determined to at least six significant figures. So it is estimated that the round-off error is negligible in comparison with the truncation error. Because the Runge-Kutta method is of order h^4, where h is the step size, the truncation error can be estimated by using the Richardson's extrapolation method. Of course we assume the error in evaluating $F(Q, k, a, \sigma_i, \Lambda)$ is negligible. Then several checks were run using step sizes of $h = 0.025$, 0.0125 and 0.01. For example, for ideally conducting walls and the extreme case $Q = 5000$, $m = 2$ and $a = 2.20$, the corresponding values of Λ were 66105874, 66105663 and 66105575, respectively. The extrapolated values of Λ using the first two and the last two results are 66105649 and 66105569 respectively. These results and other checks indicate that the maximum error in any of the tabulated values is not more than ± 2 in the fifth significant figure for Λ_c and in the fourth figure for a and σ_i, and that a step size of $h = 0.025$ is satisfactory. The error in most cases is considerably less. For the classical Dean problem, ($Q = 0$, $m = 0$, and $\sigma_i = 0$), the present results agree excellently with those given by Gibson and Cook (1974), using a Chebyshev collocation method.

Table 1 The corresponding critical values for assigned values of Q and m for the case of weakly conducting walls

Q	m	a_c	Λ_c	$-\sigma_i$	c
0	0	3.954	92915	0	0
	1	3.956	93056	10.256	0.2126
	2	3.963	93485	20.562	0.2127
	3	3.975	94203	30.970	0.2127
	4	3.992	95220	41.509	0.2127
100	0	3.18	3.6872×10^5	0	0
	1	3.19	3.6986×10^5	19.881	0.2068
	2	3.22	3.7330×10^5	39.966	0.2069
	3	3.27	3.7907×10^5	60.471	0.2070
	4	3.33	3.8728×10^5	81.327	0.2072
1000	0	0.88	3.7059×10^6	0	0
	1	0.90	3.8254×10^6	64.843	0.2083
	2	0.99	4.2274×10^6	133.88	0.2059
	3	1.09	4.8371×10^6	217.90	0.2082
	4	1.46	5.6913×10^6	301.29	0.2056
5000	0	0.43	1.8771×10^7	0	0
	1	0.48	2.0889×10^7	155.19	0.2084
	2	0.76	3.0831×10^7	327.88	0.1866
	3	0.93	3.7381×10^7	538.42	0.1853
	4	1.07	4.7152×10^7	831.19	0.1907

It is noted that the transverse pressure gradient can be produced by the interaction of a superimposed uniform radial current and the uniform axial magnetic field. From the governing differential equations (Tabeling, 1981; Tabeling and Chabrerie, 1981), the azimuthal flow of basic-state can be expressed in another form

$$V(r) = \frac{\mu_0 J_0 H d^2}{2\rho\nu}(x^2 - x), \quad 0 \leq x \leq 1, \tag{12}$$

where J_0 is the applied radial current intensity and produced across the fluid film by an external battery. It is worth noting that the small-gap approximation allows the neglect of terms of order one in which we expand J_0 in powers of d at $r = R_1$. So J_0 is taken to be a constant over the gap. We are interested in determining the values of the current required for the onset of instability. By the aid of Eq. (12), we define a nondimensional current number N in the form

$$N = \frac{J_0 d^2}{\nu}\left(\frac{\delta}{\rho\nu\xi}\right)^{1/2} = (2\Lambda/Q)^{1/2} \tag{13}$$

where ξ is the electrical conductivity. The value of N is used as a measure of the applied radial current. Results for the critical values of N as a function of Q can be found by Eq. (13) when the critical values Λ_c are determined.

Weakly Conducting Walls

The solutions of the eigenvalue problem (11) with the boundary conditions defined by Eq. (9) for the case of weakly conducting walls are shown in Table 1. Calculations have been performed for $0 \leq Q \leq 5000$. The critical values of a_c, Λ_c, as well as the corresponding values of the dimensionless frequency σ_i and the dimensionless angular wave velocity c are tabulated for assigned values of Q and a suitable range of m. We have found that the critical disturbances are always axisymmetric stationary modes in the range of Q considered. The results are also in agreement with those of Chandrasekhar (1961) for the axisymmetric mode $m = 0$. Note that the variation of Λ_c with m for assigned value of Q gradually increases with increasing Q. This implies that the onset mode is always axisymmetric and time-independent when Q tends to infinity. The numerical results also indicate that the principle of exchange of stabilities is a valid method for analyzing this problem for weakly conducting walls. We have mentioned that this problem will reduce to the hydrodynamic case as Q approaches zero and then the flow is driven by external pumping to produce azimuthal pressure gradient. In Table 1, for the case $Q = 0$, the critical

values of Λ of nonaxisymmetric modes are only slightly higher than that of the axisymmetric mode. It is possible that when Λ increases above Λ_c, several equilibrium states are reached and disturbances with different wavenumber may appear. The weakly nonlinear analysis of this flow carried out by Finlay et al. (1988) also found that the principle of exchange of stabilities is valid only for a range of $\Lambda > \Lambda_c$, because this vortex flow will bifurcate to a nonaxisymmetric time-periodic flow at a higher value of Λ. The critical axial wavenumber a_c in Table 1 appears to be a monotone decreasing function of Q. Since the onset mode is always stationary axisymmetric for weakly conducting walls, we will not discuss the functional relationship between the dimensionless radial current density N and the Hartmann number Q because it had been performed by Kurzweg and Khalfaoui (1982) for $0 \leq Q \leq 1000$. But the results for the case of ideal conducting walls are different and will be discussed in the next section.

Ideal Conducting Walls

The eigenvalue problem in Eq. (11) for the case of ideal conducting walls defined by Eq. (10) is considered now. Detailed calculations have also been performed for $0 \leq Q \leq 5000$. In Table 2, the critical values of a_c, Λ_c, σ_i and c with respect to the modes of axisymmetric and nonaxisymmetric disturbances are tabulated for assigned values of Q. It is found that the critical disturbance will be nonaxisymmetric as the Hartmann number, Q, exceeds the critical value which is approximately equal to 606. When Q is less than 606, Λ_c occurs for $m = 0$ and the critical disturbance is an axisymmetric stationary mode. On the other hand, when Q is greater than 606, Λ_c occurs for $m \neq 0$, indicating that the critical disturbance will be of nonaxisymmetric mode. The azimuthal wavenumber m increases to the maximum value of 4 and then decreases gradually with increasing Q, while the oscillation frequency σ_i is a monotonic increasing function of Q if Q is greater than the critical value. To interpret the results in as simple a manner as possible, we denote the appropriate critical Λ by Λ_c^m. In Fig. 2, the ratios of Λ_c^m/Λ_c^0 for different values of m are given for several values of Q. For $Q = 610$, 630, 700, 800, 1000, 2000, and 5000, the critical value of Λ corresponds to a nonaxisymmetric disturbance with 2, 3, 4, 4, 4, 3 and 2 waves travelling in the azimuthal direction respectively.

Note that in Table 2, the critical axisymmetric disturbance is a stationary mode with $a_c = 5.499$ for $Q = 700$. But the critical axisymmetric disturbance is an oscillatory mode with $a_c = 3.559$ for $Q = 1000$. This is due to the neutral curves transition with increasing Q as shown in Fig. 3. In general, a neutral stability diagram is multiple valued at a given value of Q. For axisymmetric stationary modes, Tabeling and Chabrerie (1981) found that the neutral curve has two branches in the plane (Λ, a). When Q is sufficiently large, the two branches intersect each other to form a single loop which rises up and recedes to the right as Q increases (see the circle-solid line). Therefore, they suggest that the critical axial wavenumber tend to infinity with the magnetic field. Now we consider further the possibilities of axisymmetric oscillatory modes. In Fig. 3, it is found that the axisymmetric oscillatory mode begins to appear when Q is large enough (see the triangle-dashed line) and extends with increasing Q. At first, the right loop for axisymmetric stationary mode has a lower minimum than the left branch for axisymmetric oscillatory mode as shown in Fig. 3(a). As Q is increased, the right loop rises and recedes to the right quickly and the left branch gradually dips lower than the right loop. At $Q = 855$ (Fig. 3(b)), both axisymmetric stationary and oscillatory modes become critical simultaneously. As Q increases further, for instance, at $Q = 1000$ (Fig. 3(c)), the left branch for axisymmetric oscillatory mode becomes critical than the right loop for axisymmetric stationary mode. As a result, the value of a_c of the axisymmetric disturbance experiences a change from 6.26 to 3.80 as Q near 855. But by considering the possible existence of nonaxisymmetric modes, we find that the critical mode near $Q = 855$ is nonaxisymmetric with the azimuthal wavenumber $m = 4$.

Table 2 Critical values of a, Λ, σ_i and c for ideally conducting walls with axisymmetric mode ($m = 0$) and nonaxisymmetric mode ($m \neq 0$) for assigned value of Q

Q	m	a_c	Λ_c	$-\sigma_i$	c
0	0	3.954	9.2915×10^4	0	0
	1	3.956	9.3056×10^4	10.256	0.2126
	2	3.963	9.3485×10^4	20.562	0.2127
	3	3.975	9.4203×10^4	30.970	0.2127
	4	3.992	9.5220×10^4	41.509	0.2127
100	0	4.534	4.7824×10^5	0	0
	1	4.537	4.7920×10^5	22.712	0.2075
	2	4.548	4.8209×10^5	45.571	0.2075
	3	4.564	4.8698×10^5	68.728	0.2076
	4	4.587	4.9393×10^5	92.339	0.2077
300	0	4.875	1.8242×10^6	0	0
	1	4.879	1.8292×10^6	42.244	0.1975
	2	4.892	1.8441×10^6	84.849	0.1976
	3	4.914	1.8694×10^6	127.86	0.1971
	4	4.944	1.9058×10^6	172.20	0.1972
600	0	5.229	5.1135×10^6	0	0
	1	5.139	5.1145×10^6	64.305	0.1798
	2	4.875	5.1168×10^6	128.57	0.1797
	3	4.504	5.1244×10^6	194.40	0.1810
	4	4.189	5.1519×10^6	262.21	0.1827
610	0	5.250	5.2510×10^6	0	0
	1	5.149	5.2503×10^6	64.860	0.1790
	2	4.851	5.2477×10^6	129.64	0.1790
	3	4.445	5.2479×10^6	195.70	0.1801
	4	4.121	5.2698×10^6	264.55	0.1822
620	0	5.272	5.3904×10^6	0	0
	1	5.159	5.3879×10^6	65.395	0.1782
	2	4.821	5.3794×10^6	130.68	0.1782
	3	4.381	5.3714×10^6	197.33	0.1795
	4	4.057	5.3872×10^6	266.75	0.1817
700	0	5.499	6.5823×10^6	0	0
	1	5.192	6.5503×10^6	68.716	0.1698
	2	4.282	6.4412×10^6	135.11	0.1683
	3	3.819	6.3421×10^6	207.85	0.1740
	4	3.590	6.3146×10^6	284.18	0.1788
1000	0	3.559	1.1271×10^7	46.593	0
	1	3.238	1.0554×10^7	53.508	0.1042
	2	2.946	1.0073×10^7	150.92	0.1504
	3	2.741	9.7943×10^6	247.70	0.1668
	4	2.641	9.7080×10^6	346.83	0.1760
2000	0	2.609	2.5776×10^7	79.774	0
	1	2.096	2.3436×10^7	78.046	0.1019
	2	1.699	2.1800×10^7	229.95	0.1557
	3	1.617	2.1111×10^7	375.82	0.1724
	4	1.657	2.1431×10^7	529.27	0.1807
5000	0	1.710	7.2508×10^7	98.735	0
	1	1.025	6.0974×10^7	165.59	0.1341
	2	0.914	5.5803×10^7	402.67	0.1703
	3	1.039	5.8916×10^7	662.47	0.1805
	4	1.410	7.4162×10^7	983.33	0.1818

As shown in Fig. 3, the critical value of Λ of the neutral curve for $m = 4$ (square-dashed line) is invariably lower than that of either the axisymmetric stationary or oscillatory mode.

In order to clarify the magnetic field effects on the stability behavior of nonaxisymmetric disturbances, the variation of Λ_c^m/Λ_c^0 with Q for assigned values of m is shown in Fig. 4. For a given value of Q, the lowest point on the set of curves gives the critical value of Λ. Thus, in the ranges $0 \leq Q < 606$, $606 \leq Q < 611$, $611 \leq Q < 648$, $648 \leq Q < 1546$, $1546 \leq Q < 3530$, and $3530 \leq Q \leq 5000$, the critical value of Λ_c corresponds to disturbances with $m = 0$, 2, 3, 4, 3 and 2, respectively. Further, for $Q > 606$, the points at which the critical value of m jumps discontinuously to the next value occur quite quickly at first, but later more slowly. Each curve of m shows a discontinuity in slope at $Q = 855$ which is due to the shift in instability mode for axisymmetric disturbance from stationary to oscillatory mode.

The variation of the critical value Λ_c with Q is shown in Fig. 5, Λ_c is generally a monotonic increasing function of Q which indicates the applied magnetic field has a stabilizing effect on this flow. Although the axisymmetric oscillatory mode will become

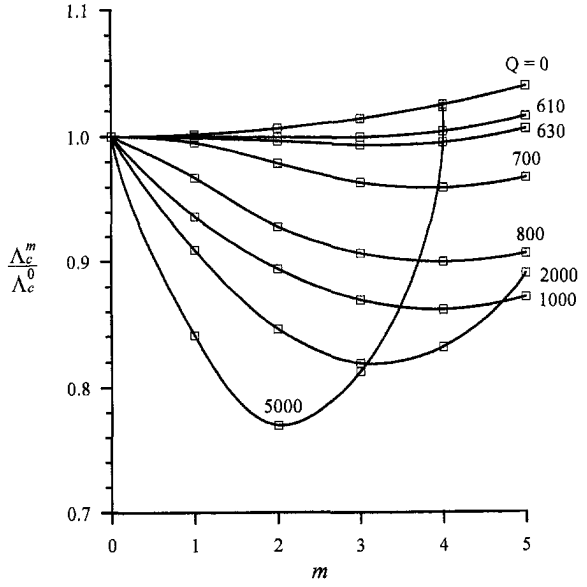

Fig. 2 The variation of Λ_c^m/Λ_c^0 with m for assigned values of Q (ideal conducting walls)

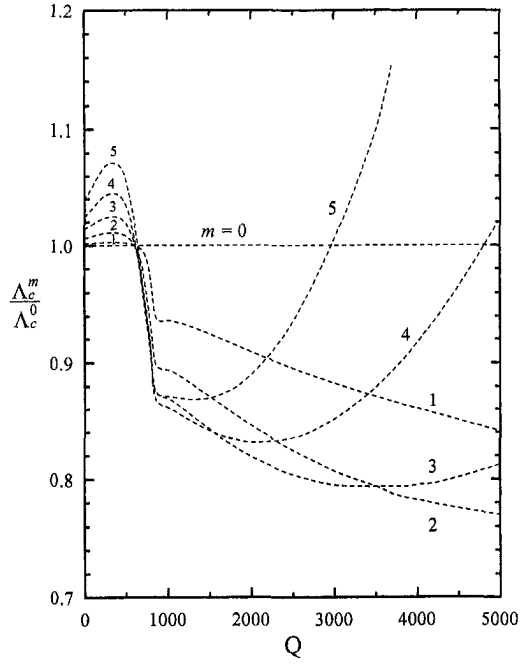

Fig. 4 The variation of Λ_c^m/Λ_c^0 with Q for assigned values of m (ideal conducting walls)

more critical than stationary mode when Q is above 855, the instabilities of this flow have been dominated by nonaxisymmetric modes as Q is greater than 606. The corresponding experimental work has been conducted by Tabeling and Chabrerie (1981) in the range $0 \leq Q \leq 1100$. By measuring the variation of the effective viscosity versus the mean velocity across the channel, they determined the corresponding critical value Λ_c when the effective viscosity has a sharp increase. Then they concluded that the most critical modes are stationary up to $Q = 1100$ and their theoretical predications are in agreement with the experimental results. But later Tabeling (1982) and Tabeling and Trakas (1984) have carried out more refined experiments for this flow. They found that the onset of instability of the laminar state is in the form of nonaxisymmetric modes when the strength of axial magnetic field is sufficiently large. In the ranges $0.95 \leq H \leq 1.14T$ and $1.14 < H \leq 1.25T$ which are approximately equivalent to $764 \leq Q \leq 1100$ and $1100 < Q \leq 1323$, the azimuthal wavenumber m is 4 and 3, respectively. The range of Q that corresponding to the mode $m = 4$ is in agreement with our prediction but not for the mode $m = 3$. However, the curvature ratio δ of 0.026 in their experiments is comparable with $\delta = 0.05$ in the present analysis. In order to compare the results more accurately, the calculations have been carried out again by using $\delta = 0.026$. It is found that the critical value of Λ_c corresponds to the onset mode with $m = 0$, 2, 3, 4, 5, 6, 5, 4 and 3 in the ranges $0 \leq Q < 605$, $Q = 605$, $605 < Q < 611$, $611 \leq Q < 631$, $631 \leq Q < 761$, $761 \leq Q < 947$, $947 \leq Q < 1905$, $1905 \leq Q < 3462$ and $3462 \leq Q < 5000$, respectively. These results are more inconsistent than those of $\delta = 0.05$ in comparison with the experiments. Note that the value of δ has no effect on the solution of axisymmetric mode but affects the behaviors of neutral curves of nonaxisymmetric disturbances. It is predictable from Eq. (5), $\delta = 2(k/m)^2$, that the azimuthal wavenumber of the critical disturbance will increase by decreasing δ and vice versa. Moreover, the discrepancy between theory and experiment may be due to several factors such as end effects, misalignment and eccentricity of the cylinders, and conductivity of the boundary walls. But the present theoretical predication with

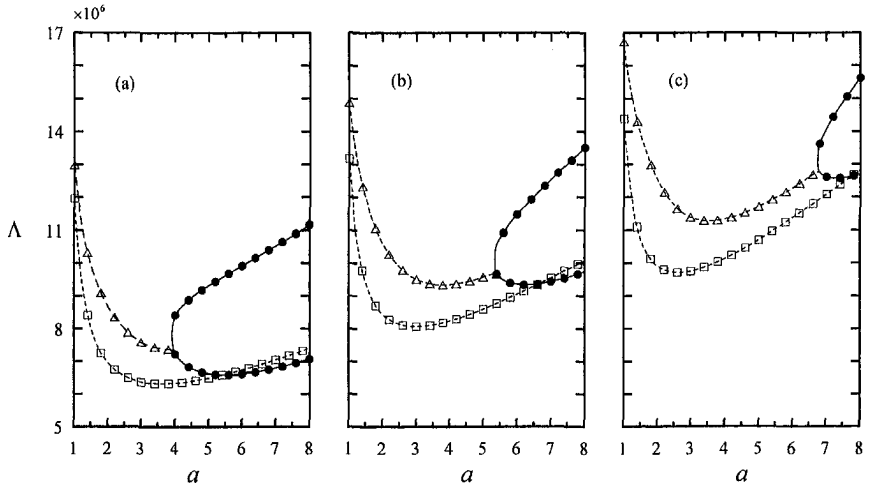

Fig. 3 Neutral curves for various Q (ideal conducting walls): ——●——, axisymmetric stationary mode $m = 0$; ------△------, axisymmetric oscillatory mode $m = 0$; ------□------, nonaxisymmetric mode $m = 4$ (*a*) $Q = 700$, (*b*) $Q = 855$, (*c*) $Q = 1000$

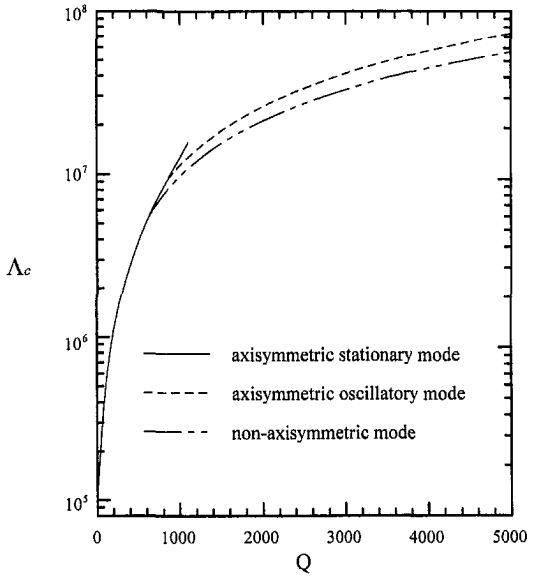

Fig. 5 Variation of Λ_c with Q for ideal conducting walls

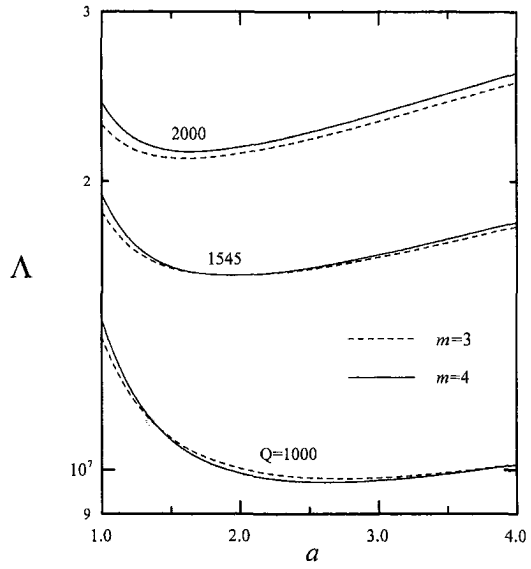

Fig. 7 The transition of neutral curves for various Q (ideal conducting walls)

$\delta = 0.05$ for the transition of onset mode from $m = 4$ to $m = 3$ with increasing Q is consistent with experimental findings. For the same value of Q, the differences for the critical values of Λ_c and a_c between $\delta = 0.05$ and 0.026 are not apparent. Typically for $Q = 2000$, the values of Λ_c and a_c are 2.1111×10^7, 1.617 and 2.1139×10^7, 1.618 for $\delta = 0.05$ and 0.026, respectively. So the results for nonaxisymmetric mode with $\delta = 0.026$ are omitted in Figs. 5 and 6 because the curves for $\delta = 0.05$ and 0.026 are almost overlapped. Note that the differences of Λ_c between axisymmetric and nonaxisymmetric disturbances gradually increase with increasing Q. This indicates that the nonaxisymmetric mode will dominate the flow instability over a wide range of Q as the boundary walls have ideal electrical conductivity.

Figure 6 illustrates the variation of critical axial wavenumber a_c with Q. If we consider axisymmetric disturbances only, a_c will increase initially until $Q = 855$. Then a_c changes abruptly from 6.26 to 3.80 which is due to the mode transition from stationary to oscillatory mode. And then a_c decreases when Q tends to infinity. By considering the existence of nonaxisymmetric disturbances, a_c will have a sudden jump near $Q = 606$ from 5.24 to 4.86, which is due to the mode transition from axisymmetric to nonaxisymmetric mode. This change of a_c is relatively smaller than that of axisymmetric disturbances near $Q = 855$. When Q is greater than 606, a_c also decreases with increasing Q and tends to zero as Q approaches to infinity. Those results are also in agreement with the experimental works of Tabeling (1982) which found the number of cells decreases with Q as Q is above the instability threshold of nonaxisymmetric disturbance. Thus the axial wavelength, $2\pi/\lambda = 2\pi d/a$, will decrease first and then increase. This implies the cells of secondary flow will contract first and then elongate in the axial direction as Q is greater than 606. In the cases for which nonaxisymmetric disturbances occur, the critical value of a is always less than the critical value of a for an axisymmetric disturbance. Note that the curve of nonaxisymmetric mode in Fig. 6 is smooth. This indicates that a_c has no apparent change and is still continuous as the critical mode of nonaxisymmetric disturbance is changing. This can be illustrated by the transition of the corresponding neutral curves in the plane (Λ, a). For example, as shown in Fig. 7, the onset mode is $m = 4$ for $Q = 1000$ and $m = 3$ for $Q = 2000$. Both the neutral curves of $m = 3$ and $m = 4$ become critical almost simultaneously at $Q = 1545$ and the corresponding critical axial wavenumber a_c have approximately the same value. Therefore, the finite jump of a_c will not occur when the critical mode of nonaxisymmetric disturbance changes.

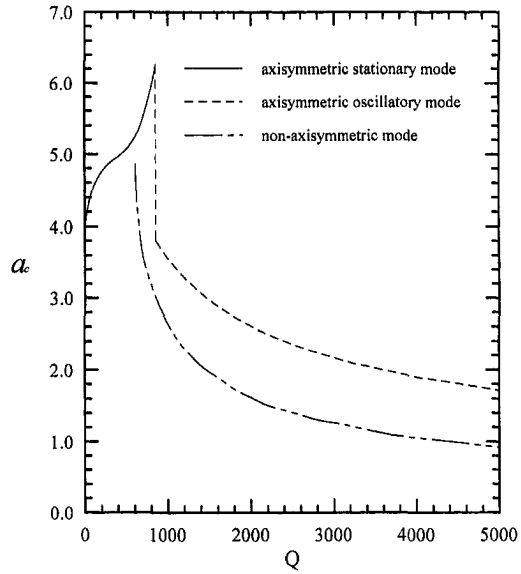

Fig. 6 Variation of a_c with Q for ideal conducting walls

Now, we pay attention to Eq. (13) which represents the relationship between critical radial current density N and Hartmann number Q. Results are shown in Fig. 8. For a given value of Q, the onset of instability will occur as N is equal to the critical value. When Q approaches zero, N tends to infinity, which indicates that the flow is stable when the strength of axial magnetic field is very low. Note that at $Q = 0$ the flow is reduced to hydrodynamic flow and the onset of instability occurs when the flow is driven by external pumping. But here we consider the flow to be driven by the interaction of radial current and axial magnetic field only. It is found that N has a minimum value that is approximately equal to 97.8 as Q nears 100. When Q is greater than 100, the critical value of N increases quickly first. But when the nonaxisymmetric mode begins to dominate the flow instability, N increases slowly and tends to a constant as Q approaches to infinity. Furthermore, the critical value of N corresponding to the onset nonaxisymmetric mode is significantly lower than that predicted by considering axisymmetric mode only. The dimensional critical radial current density J_0 could be calculated from Eq. (13) and Fig. 8 when the

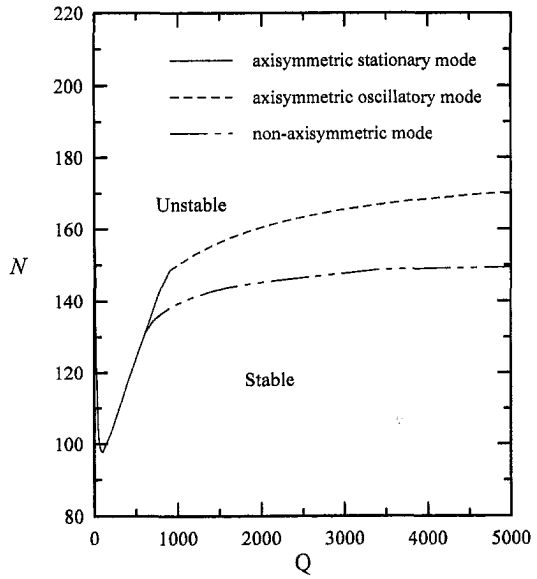

Fig. 8 Critical radial current density N as a function of Hartmann number Q for ideal conducting walls

corresponding properties of the working fluid are known. Some numerical data is provided in Table 3 for mercury in order to facilitate a comparison with future experimental works.

Conclusions

We have conducted an analysis for the onset of secondary motion of current-induced hydromagnetic flow in a small-gap spacing between two infinitely long cylinders subjected to a uniform axial magnetic field and a radial current density. It is usually assumed in the literature that the critical number Λ_c will correspond to an axisymmetric stationary disturbance. However, the relevant experimental works for ideally conducting walls reveal that nonaxisymmetric disturbances will become critical at sufficiently large values of Q. The present study provides new theoretical results and shows that the principle of exchange of stabilities is valid only for weakly conducting boundary walls. For the case of ideally conducting walls, nonaxisymmetric instability modes play an important role once magnetic field effects become significant and the onset of instability will be dominated by nonaxisymmetric disturbances as Q becomes greater than the critical value of 606. The possible existence of axisymmetric oscillatory modes has also been examined. It is found that axisymmetric oscillatory mode will be more critical than stationary mode when Q is above 855 but never become critical than nonaxisymmetric modes in the range of Q we considered. When the critical mode is nonaxisymmetric, the azimuthal wavenumber m first increases rapidly then decreases gradually with increasing Q. The associated frequency of oscillation is a monotonic increasing function of Q. In particular, the critical axial wavenumber a_c will tend to zero as Q approaches to infinity. The variation of the critical radial current density for the onset of instability as a function of Q for ideally conducting walls is also illustrated. Although the theoretical predictions are generally in agreement with previous experiments, the discrepancies should need to be further studied by more detailed experimental work.

Table 3 Some critical values of N and J_0 of the onset mode for mercury ($d = 10^{-3}$ m, $\delta = 0.05$, $\rho = 13.6 \times 10^3$ kg/m^3, $\xi = 1.017 \times 10^6$ mho/m)

Q	m	N	$J_0(A/m^2)$
50	0	101.78	2060
100	0	97.80	1980
200	0	103.11	2087
400	0	117.28	2374
606	2	130.94	2651
611	3	131.17	2655
648	4	132.80	2688
800	4	136.49	2763
1000	4	139.34	2821
1546	3	143.69	2909
2000	3	145.30	2942
3000	3	147.63	2989
3530	2	148.72	3011
4000	2	148.96	3016
5000	2	149.40	3024

Acknowledgments

The financial support for this work from National Science Council of Taiwan through Grant No. NSC 88-2212-E-132-003 and the aid of computer resources from National Center for High-Performance Computing are gratefully acknowledged.

References

Chandrasekhar, S., 1961, *Hydrodynamic and Hydromagnetic Stability,* Clarendon.

Chang, M. H., and Chen, C. K., 1998, "Hydromagnetic Stability of Current-Induced Flow in a Small Gap Between Concentric Rotating Cylinders," *Proceedings of the Royal Society* (London), Vol. A454, pp. 1857–73.

Chang, T. S., and Sartory, W. K., 1967, "On the Onset of Instability by Oscillatory Modes in Hydromagnetic Couette Flow," *Proceedings of the Royal Society* (London), Vol. A301, pp. 451–471.

Chen, C. K., and Chang, M. H., 1998, "Stability of Hydromagnetic Dissipative Couette Flow with Non-Axisymmetric Disturbance," *Journal of Fluid Mechanics,* Vol. 366, pp. 135–158.

Chen, F., and Chang, M. H., 1992, "Stability of Taylor-Dean Flow in a Small Gap Between Rotating Cylinders," *Journal of Fluid Mechanics,* Vol. 243, pp. 443–455.

Dean, W. R., 1928, "Fluid Motion in a Curved Channel," *Proceedings of the Royal Society* (London), Vol. A121, pp. 402–420.

Donnelly, R. J., and Ozima, M., 1962, "Experiments on the Stability of Flow Between Rotating Cylinders in the Presence of Magnetic Field," *Proceedings of the Royal Society* (London), Vol. A266, pp. 272–286.

Finlay, W. H., Keller, J. B., and Ferziger, J. H., 1988, "Instability and Transition in Curved Channel Flow," *Journal of Fluid Mechanics,* Vol. 194, pp. 417–456.

Gibson, R. D., and Cook, A. E., 1974, "The Stability of Curved Channel Flow," *Quarterly Journal of Mechanics and Applied Mathematics,* Vol. 27, pp. 149–160.

Hong, S. H., and Wilhelm, H. E., 1976, "Magnetohydrodynamic Instability of a Cylindrical Liquid-Metal Brush," *Journal of Applied Physics,* Vol. 47, pp. 906–913.

Krueger, E. R., Gross, A., and DiPrima, R. C., 1966, "On the Relative Importance of Taylor-Vortex and Non-Axisymmetric Modes in Flow Between Rotating Cylinders," *Journal of Fluid Mechanics,* Vol. 24, pp. 521–538.

Kurzweg, U. H., and Khalfaoui, A. H., 1982, "Current-Induced Instabilities in Rotating Hydromagnetic Flows between Concentric Cylinders," *Physics of Fluids,* Vol. 25, pp. 440–445.

Reid, W. H., 1958, "On the Stability of Viscous Flow in a Curved Channel," *Proceedings of the Royal Society* (London), Vol. A244, pp. 186–198.

Tabeling, P., 1981, "Magnetohydrodynamic Taylor Vortex Flows," *Journal of Fluid Mechanics,* Vol. 112, pp. 329–345.

Tabeling, P., 1982, "Sequence of Instabilities in Electromagnetically Driven Flows Between Conducting Cylinders," *Physical Review Letters,* Vol. 49, pp. 460–463.

Tabeling, P., and Chabrerie, J. P., 1981, "Magnetohydrodynamic Taylor Vortex Flow under a Transverse Pressure Gradient," *Physics of Fluids,* Vol. 24, pp. 406–412.

Tabeling, P., and Trakas, C., 1984, "Structures spiralees dans une instabilite de Taylor en presence de champ magnetique," *Le Journal De Physique-Lettres,* Vol. 45, pp. L-159–L-167.

Taylor, G. I., 1923, "Stability of a Viscous Liquid Contained Between Two Rotating Cylinders," *Philosophical Transactions of the Royal Society of London,* Vol. A223, pp. 289–343.

Walowit, J., Tsao, S., and DiPrima, R. C., 1964, "Stability of Flow Between Arbitrarily Spaced Concentric Cylindrical Surfaces Including the Effect of a Radial Temperature Gradient," ASME *Journal of Applied Mechanics,* Vol. 86, pp. 585–593.

Todd W. Riddle
Graduate Research Assistant,
Aeronautical Engineering Department,
California Polytechnic State University,
San Luis Obispo, CA 93407

Alan J. Wadcock
Research Engineer,
Sterling Software,
Moffett Field, CA 94035

Jin Tso
Professor.

Russell M. Cummings
Professor.

Aeronautical Engineering Department,
California Polytechnic State University,
San Luis Obispo, CA 93407

An Experimental Analysis of Vortex Trapping Techniques

An experimental verification is presented for the theoretical vortex trapping concept. A suction orifice located along one wall of a water channel test section was used to simulate a point sink to trap spanwise vortices downstream of a backward-facing step and between two parallel fences. Results from the backward-facing step geometry indicated an increase in the sink strength required to hold a vortex as the sink is positioned closer to the step, closely following previous theoretical predictions made using conformal mapping. The experimental data also showed reasonable agreement with the theoretical position for optimum vortex trapping. Flow visualization has shown a three-dimensional cross-stream effect due to bending of the forced-vortex core by suction. Results from the dual-fence geometry, on the other hand, verified the ability to use a lower level of suction for vortex trapping when compared with the backward-facing step.

Introduction

Current concepts for High-Speed Civil Transport (HSCT) aircraft have long fuselages and low aspect ratio wings, which create operational problems when rotating the aircraft for take-off and landing. To counter this problem the lift of the wing must be augmented at low angles of attack without the addition of large amounts of drag. Conventional lift augmentation by means of flap and/or slat systems can add substantial weight penalties and manufacturing costs. Alternative systems, such as streamwise or tangential blowing and suction, are usually only effective in the post-stall regime. Another potential method for increasing aircraft lift at low angles of attack is through the use of vortex trapping, a technique which has not been employed on existing aircraft.

Rossow theoretically investigated the effect of cross-stream suction on the flow behind a single fence placed near the leading edge of a wing (see Fig. 1) (Rossow, 1978). Cross-stream suction was shown to entrain the separated shear layer from the fence and trap a vortex. The trapped vortex increases the effective wing thickness and circulation, thereby enhancing the lift of the wing. Both the theoretical results and some preliminary experiments showed that fairly large values of sink flow rate were required to establish an equilibrium position for the vortex and moderate increases in lift. Unfortunately, further increases in sink flow rate also led to higher drag, as well as other disruptions to the flowfield.

Rossow undertook another theoretical study to find the conditions to alleviate the necessity for a strong sink to trap the vortex (Rossow, 1992). According to these theoretical results the sink flow rate required for equilibrium could be reduced, possibly eliminated, if the streamlines in the vicinity of the trapped vortex had fore and aft symmetry. It was also shown that the required symmetry could be achieved by placing a second fence downstream of the vortex.

An experimental study of vortex trapping was conducted in a water channel based on the theoretical work of Rossow. Two vortex-trapping geometries were studied using laser speckle velocimetry for flow visualization (Wadcock et al., 1991), one with flow over a backward-facing step and another with flow over two fences on a flat plate. In both cases the flowfield was first studied with zero sink strength, and then qualitative and quantitative studies were performed to determine the effect of sink flow rate through a side-mounted suction orifice.

Contributed by the Fluids Engineering Division for publication in the JOURNAL OF FLUIDS ENGINEERING. Manuscript received by the Fluids Engineering Division October 9, 1997; revised manuscript received April 19, 1999. Associate Technical Editor: M. S. Triantafyllou.

Experimental Analysis

Backward-Facing Step.

Apparatus. The experiment was conducted in a closed-circuit water channel at NASA Ames Research Center, as shown in Fig. 2. The water channel facility consists of an upstream reservoir, a 132 cm × 43 cm × 31 cm acrylic test channel, and a downstream reservoir. A secondary acrylic test section placed within the test section held the 23 cm span × 6.4 cm height backward-facing step (Fig. 3). Both the height and position of the step were adjustable, allowing for movement of the step relative to the orifice located in one wall of the secondary test section. The orifice inlet was a bell-shaped, 2.54 cm diameter insert mounted flush with the wall, connected by PVC piping to a 373 W centrifugal pump and two parallel flow meters.

The test section was designed to match the non-dimensional analysis performed by Rossow (1992). To determine the most significant parameters for the vortex-influenced flowfield, the section lift coefficient was expressed as a function of the non-dimensional vortex position coordinates, the suction volume flow rate, and the Reynolds number based on the step height as follows (the backward-facing step configuration is shown in Fig. 4):

$$C_l = f(X_s/h,\ Y_s/h,\ \mathrm{Re}_h,\ C_Q)$$

where h is the step height, X_s and Y_s are the vortex position coordinates, and

$$\mathrm{Re}_h = \rho_\infty U_\infty h/\mu_\infty$$

$$C_Q = Q_s/h^2 U_\infty$$

The aspect ratio of the step (AR = span/h) was limited to a two-dimensional range ($2.25 < AR < 3.60$), and the Reynolds number, Re_h, was kept nearly constant at 3000, which allowed for X_s/h, Y_s/h, and C_Q to be the dominant flow parameters for investigation.

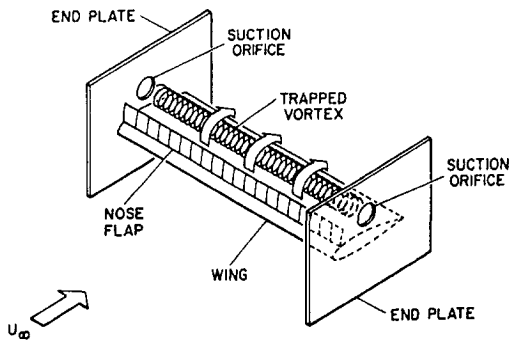

Fig. 1 Trapped vortex on upper surface of a wing (from Riddle et al., 1991)

The flowfield was visualized by illuminating 0.005 cm diameter silver-coated spherical particles (specific gravity = 0.85) with a thin laser-light sheet generated by a 2-Watt argon laser. The laser was deflected and dispersed by a series of plane mirrors followed by a cylindrical lense to create a laser sheet extending about 20 cm down the centerline plane of the test section.

Procedure. The experiment consisted of two phases for each combination of length ratios, X_s/h and Y_s/h. The first phase examined basic flow patterns with no suction applied. These patterns, which included separation and reattachment of the shear layer, were used for comparison with the flowfield when suction was applied. The channel flow rate was varied for each step height in order to maintain a Reynolds number of $\mathrm{Re}_h \approx 3000$. The second phase involved vortex trapping with the sink at various locations (see Table 1 for tested sink locations). The suction flow rate was gradually increased until a marginally stable vortex was observed; a marginally stable vortex is defined as a free vortex with a discernable, though weak, forced-vortex core region.

Dual-Fence.

Apparatus. Using the same water channel and secondary test section, the backward-facing step was replaced with two thin fences (the fence geometry is shown in Fig. 5). The two fences, which spanned the width of the test section, were of fixed height (both 6.4 cm and 3.2 cm fence heights were tested). The position of the fences relative to the sink, X_s/h and Y_s/h, was adjustable.

Procedure. The fences were placed both upstream and downstream of the sink location in order to restrict the streamwise motion of the vortex. Cases with and without suction were tested, as they were for the backward-facing step geometry. The fence and sink arrangements which were tested are listed in Table 2. Geometric arrangements were chosen to simulate the backward-facing step parameters to facilitate a comparison between the two sets of results.

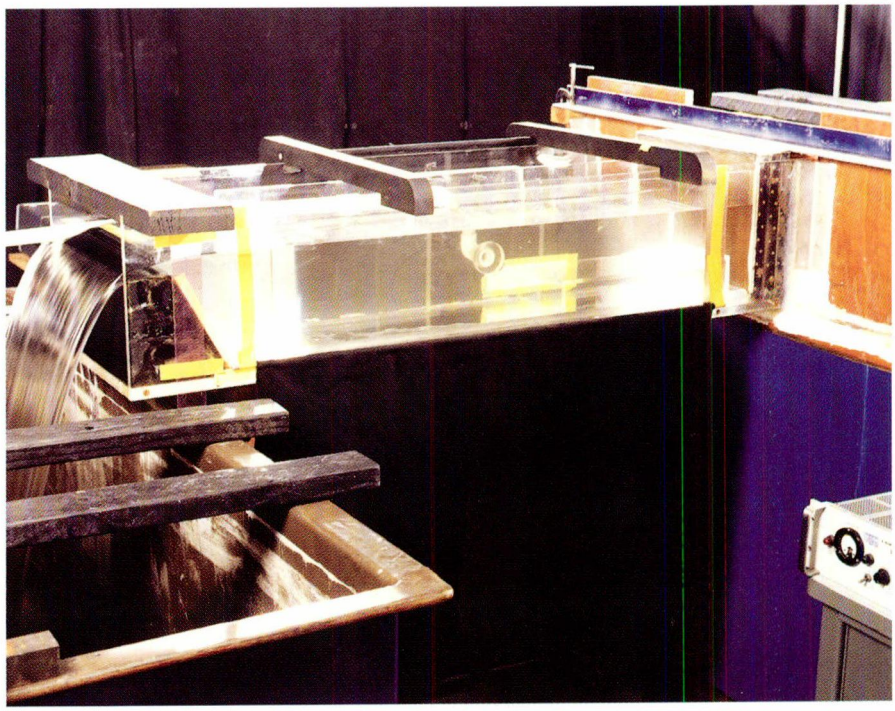

Fig. 2 Experimental facility

Nomenclature

A_s = sink cross-sectional area
AR = step aspect ratio, span/h
C_l = sectional lift coefficient, $l/\frac{1}{2}\rho_\infty U_\infty^2 h$
C_Q = suction coefficient, $Q_s/h^2 U_\infty$
h = step or fence height
l = lift per unit span
$\dot{m}_s$ = sink mass flow rate, $\rho A_s U_s$
Q_s = sink strength (suction volume flow rate), $A_s U_s$
Re_h = Reynolds number based on step height, $\rho_\infty U_\infty h/\mu_\infty$
U = velocity
X, Y = spatial coordinates
μ = fluid dynamic viscosity
ρ = fluid density

Subscripts

f = fence
s = sink
∞ = freestream

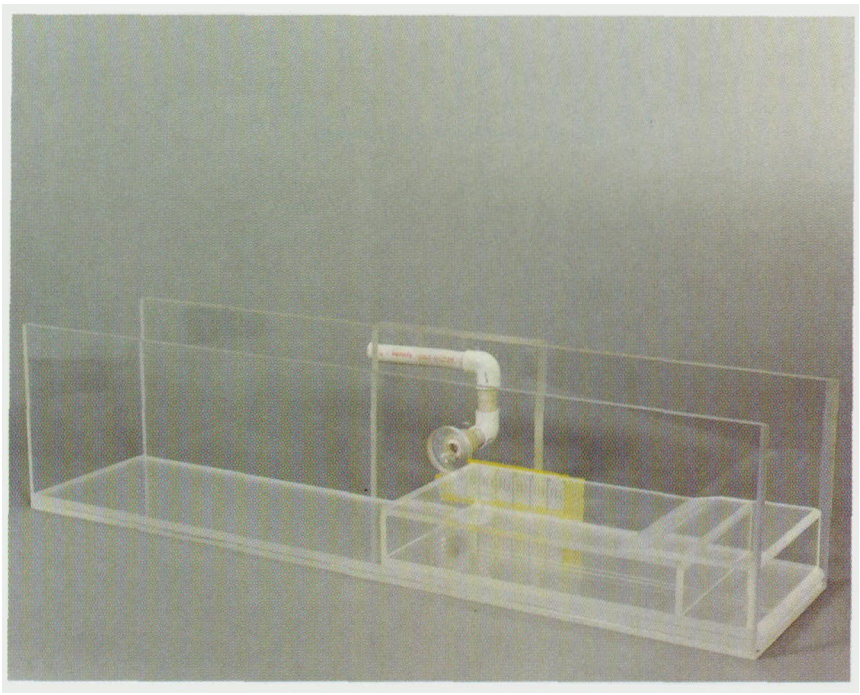

Fig. 3 Test section showing backward-facing step and suction orifice

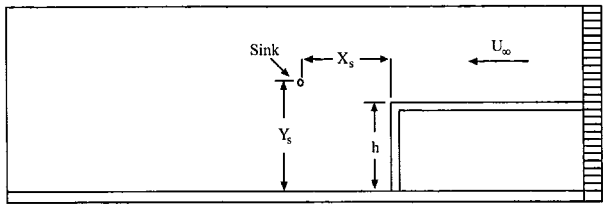

Fig. 4 Backward-facing step and sink configuration

Table 1 Backward-facing step geometry and experimental data; $Re_h \approx 3000$

Case number	X_s/h	Y_s/h	Trapped vortex (Y/N)	C_Q
1	1.14	0.57	N	
2	1.00		N	
3	0.71		N	
4	0.50		N	
5	0.25		N	
6	1.00	0.75	N	
7	0.75		N	
8	0.50		Y	1.31
9	0.25		Y	1.31
10	1.33	1.00	Y	2.01
11	1.00		Y	3.70
12	0.75		Y	2.29
13	0.50		Y	3.70
14	0.25		N	
15	1.25	1.20	Y	2.91
16	1.00		Y	2.60
17	0.75		Y	2.60
18	0.50		Y	2.91
19	0.25		Y	4.20
20	1.50	1.50	Y	5.03
21	1.00		Y	5.03
22	0.75		Y	5.83
23	0.50		Y	6.70
24	0.25		N	

Results and Discussion

Backward-Facing Step. Investigations of the backward-facing step flowfield without suction shows a large region of recirculation, extending one to two step heights downstream of the step. The boundary layer that builds up along the wall upstream of the step forms a shear layer of concentrated vorticity, which propagates and mixes with the freestream flow. The downstream flowfield was observed to return to essentially freestream conditions by approximately ten step heights.

Applying suction at the sink location changes the flowfield by entraining the separating shear layer into a free vortex. A small recirculation region is formed at the base of the step, rotating counter to the trapped vortex. A separation, or bounding, streamline is also evident, which acts as a line of demarcation between the trapped vortex and the external flow. The strength of the trapped vortex is reflected in the downstream position at which the bounding streamline reattaches to the lower wall. Freestream con-

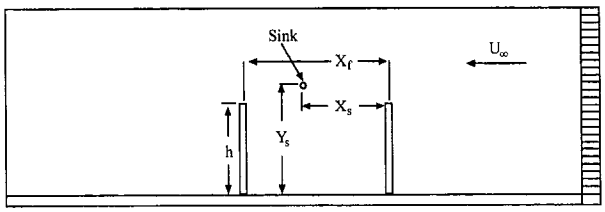

Fig. 5 Dual-fence and sink configuration

Table 2 Dual-fence geometries and experimental data; $Y_s/h = 1.0$, $Re_h = 3800$

Case number	X_f/h	X_s/X_f	Trapped vortex (Y/N)	C_Q
1	1.00	0.50	Y	0.99
2	2.00	0.50	Y	0.99
3	3.00	0.50	Y	4.20
4	2.00	0.25	Y	1.61
5	2.00	0.75	Y	0.99

ditions can be reached in less than five step heights downstream of the step in the presence of a trapped vortex.

Figure 6 summarizes the vortex trapping results observed for flow over the backward-facing step. Distinguishable trapping occurs in about 60 percent of the test cases, with the rest of the cases having no observed vortex trapping for suction flow rates up to the maximum available. Vortex trapping may be possible at higher suction rates for cases such as these, but higher suction rates would make the system impractical and inefficient. All of the cases where the vortex was successfully trapped occurred for suction flow rates of $C_Q > 1.31$, which suggests that the backward-facing step (or the single fence geometry) may not be suitable for optimized (low suction) vortex trapping.

Several general flowfield characteristics can been observed in Fig. 6. No vortex trapping is seen for sink locations either far above, far below, or at the step height for $X_s/h = 0.25$. However, vortex trapping is possible if the sink is located either just above or just below the shear layer, with the minimum suction required for $(X_s/h,\ Y_s/h) = (0.25,\ 0.75)$. As the sink location is moved downstream there are two distinct regions where vortex trapping is relatively efficient, either just above or just below the shear layer.

Rossow showed similar results using a conformal mapping analysis in his potential flow theory (see Fig. 7) (Rossow, 1992). The results showed that a mass sink is required if the vortex is located too close to the step (Fig. 7(*a*)), and a mass source is required if the vortex is too far from the step (Fig. 7(*b*)). In between these two locations, however, he found that the vortex could exist with no mass addition or subtraction (Fig. 7(*c*)). This theoretically optimum location for vortex trapping is at $(X/h,\ Y/h) = (0.82,\ 0.64)$. In the water channel experiments the trapped vortex cores clustered in a region centered by $(X/h,\ Y/h) = (0.65,\ 0.60)$, which is also near the sink location for minimum suction to trap a vortex. Thus there is only a small difference between the experimental and theoretical optimum locations, with the difference probably due to viscous effects in the shear layer.

Another difference between the theoretical development and the experiment was the vortex trapping results for sink locations farther downstream than the optimum location. Conformal mapping results from Rossow, 1992 show that vortex trapping is not possible by suction for sink locations downstream of $X_s/h = 1.0$, and that trapping could only occur if a mass source is added for these locations. The experimental results, however, showed that sink locations farther downstream than $X_s/h = 1.0$, as well as above $Y_s/h = 1.0$, could trap a vortex. In these cases the vortex was not trapped at the location of the sink, however, with the trapped vortices clustering around $(X_s/h,\ Y_s/h) = (0.65,\ 0.60)$,

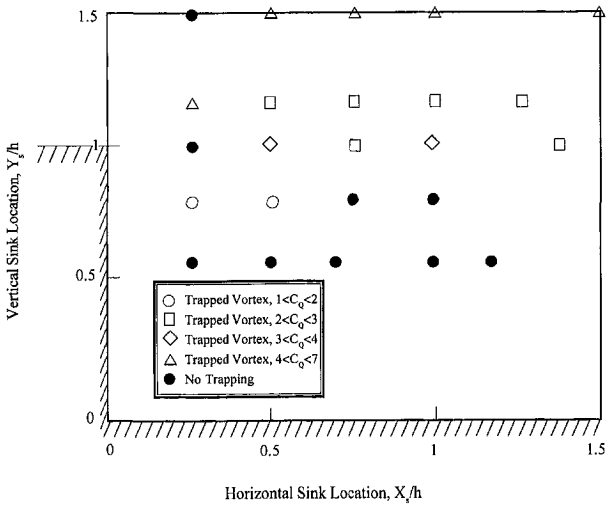

Fig. 6 Required suction levels for trapping a vortex in the backward-facing step configuration

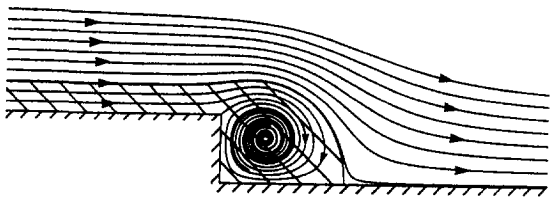

Fig. 7(*a*) $(X_s/h,\ Y_s/h) = (0.25,\ 0.92)$, $\dot{m}_s/hU_\infty = -7.234$

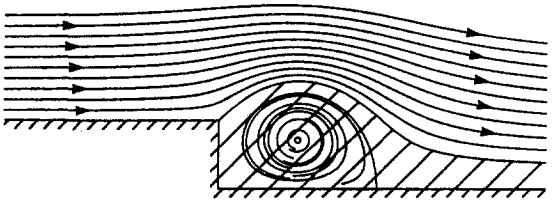

Fig. 7(*b*) $(X_s/h,\ Y_s/h) = (0.59,\ 0.69)$, $\dot{m}_s/hU_\infty = +3.142$

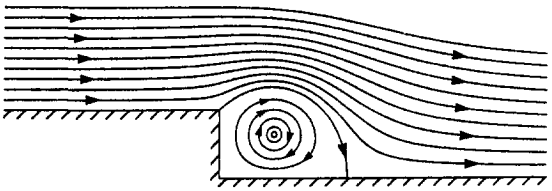

Fig. 7(*c*) $(X_s/h,\ Y_s/h) = (0.83,\ 0.64)$, $\dot{m}_s/hU_\infty = 0.0$

Fig. 7 Conformal mapping of streamline traces (from Rossow, 1992)

as was mentioned earlier. This indicates that the sink imparts a three-dimensional influence on the flowfield, and causes the vortex core to bend across the span of the water channel (which was observed in the experiment) (Ringleb, 1961).

Dual Fence. The dual-fence arrangement was considered as a geometry which could improve vortex trapping by minimizing the required suction. The dual fence geometry was first tested without suction, where the flow was seen to separate from the top edge of the leading fence, with the shear-layer mixing with both the freestream flow and the flow from the inter-fence region. However, the flow between the fences remained largely stagnant. A recirculation zone was evident behind the trailing fence, which extended downstream approximately one-half step heights.

The flowfield became more organized and coherent with the addition of suction. In most cases, the shear layer from the forward fence was pulled by the suction into the inter-fence region and formed a trapped vortex. As a result, very little stagnant fluid was evident in the region between the fences. Freestream flow passed smoothly over the vortex, accelerating due to the circulation of the trapped vortex.

Various fence configurations were examined to study the effect of suction on the formation of the trapped vortex. The distance between the fences, X_f/h, was varied between $1 \le X_f/h \le 3$ fence heights, with the suction applied at various locations between the fences. Table 2 summarizes the dual-fence geometries tested and shows the minimum amount of suction required to form a stable trapped vortex between the fences. All cases are for a sink placed at the same height as the top of the fences ($Y_s/h = 1.0$) and with $\mathrm{Re}_h = 3800$.

Cases 1–3 show the results for a range of fence separation distances, X_f/h, with the sink located midway between the fences ($X_s/X_f = 0.5$). Cases 1 and 2 show the low suction rate required for trapping a vortex between fences located relatively close together ($X_f/h = 1$ and 2, respectively). The trapped vortex was observed to remain stable both horizontally and vertically as the suction coefficient was decreased to $C_Q = 0.99$; for values of

suction coefficient below this level the vortex began to intermittently disappear and breakup. Case 3 demonstrates the problem of separating the fences too far ($X_f/h = 3$), resulting in a much higher suction rate to trap a vortex.

Cases 4 and 5 ($X_f/h = 2$) show the impact of placing the sink fore and aft of the centerline between the fences ($X_s/X_f = 0.25$ for Case 4 and $X_s/X_f = 0.75$ for Case 5). Both cases show better performance than Case 3, with Case 5 requiring the same level of suction as Cases 1 and 2. With the sink located closer to the upstream fence (Case 4) the vortex was initially trapped midway between the fences. As the sink strength was decreased the vortex core moved downstream due to the increased influence of the freestream flow. The same behavior was observed for the sink located near the downstream fence (Case 5). However, as the vortex moved downstream it moved close to the position of the sink, thereby making the sink more effective. Results for other dual-fence configurations can be found in Riddle et al. (1991). The dual-fence system is seen to require much lower suction rates for certain configurations than the backward-facing step.

Conclusions

The trapping of a vortex with a sink and cross-flow fences has been shown to be a viable way to improve the lift of airfoils. The comparative performance of a backward-facing step and a dual-fence configuration has shown the dual-fence to be more effective, due to the restriction of the streamwise motion of the vortex by the fences. The backward-facing step has characteristics which are helpful in understanding the trapped-vortex concept, including: the relation between sink strength and vortex location, the position of the sink for optimum trapping of the vortex, and an indication of the three dimensional nature of the vortex core. The experiment showed the dual-fence configuration to be more efficient than the backward-facing step, which verified previous theoretical predictions, although a zero-suction trapped vortex was never found experimentally. Further experimental study of the trapped vortex concept applied to the upper surface of a wing should be conducted to determine the feasibility and practicality of the concept.

Acknowledgment

This research was supported by NASA Cooperative Agreement NCC-2-684.

References

Riddle, T. W., Wadcock, A. J., Tso, J., and Cummings, R. M., 1991, "Experimental Analysis of Vortex Trapping Techniques," AIAA Paper 91-3271, Sept.

Ringleb, F. O., 1961, "Separation Control in Trapped Vortices," *Boundary Layer and Flow Control,* Vol. 1, G. V. Lachmann, ed., Pergamon Press, pp. 265–294.

Rossow, V. J., 1978, "Lift Enhancement by an Externally Trapped Vortex," *Journal of Aircraft,* Vol. 15, No. 9, pp. 616–625.

Rossow, V. J., 1992, "Two-Fence Concept for Efficient Trapping of Vortices on Airfoils," *Journal of Aircraft,* Vol. 29, No. 5, pp. 847–855.

Wadcock, A. J., Bennett, M. S., and Smith, C. A., 1991, "An Efficient Micro-Computer System for the Analysis of Particle Image Velocimetry Specklegrams," AIAA Paper 91-3246, September.

M. A. Koenders
Professor.

N. Gaspar
Research Student.

E. Liebhart
Research Assistant.
e-mail: e.liebhart@kingston.ac.uk

Department of Chemistry,
Penrhyn Road,
Kingston University,
Kingston upon Thames KT1 2EE,
United Kingdom

The Stress-State in a Torsion Shear Cell Filled With a Newtonian Fluid

The flow in a torsional shear cell is investigated with the purpose of finding a measure for the wall effect due to strongly nonuniform flow in the vicinity of the edge of the top platen. Various laminar flow problems are analysed that are relevant to this set-up. These include pure shearing flow of a single fluid in a both an infinite and finite cell, as well as pure shear of a two-fluid system in a finite cell. For pure shearing flow it is found that the extent of the wall effect is of the order of magnitude of the depth of the fluid layer. For piston flow the wall effect is entirely determined by boundary conditions at the bottom of the cell.

Introduction

The torsional shear cell is a cylindrical cell that has a rotating top platen and a rigid wall. The bottom of the cell can be either permeable porous or impermeable. The permeable version is used for filtration purposes: the cell is filled with a particle fluid mixture and the top platen is pushed down. In this way a particulate cake is formed on the porous septum. When no rotation is applied the device is an ordinary deadend filter cell, which operates pretty well as a one dimensional compression apparatus, subjecting the contents to a uniaxial stress path. Filtration carried out under the combined action of a top pressure and a rotating top platen introduces an extra shear field, which leads to a much more complicated stress field. The purpose of this paper is to determine by theoretical means what the character of that field is and also to characterise the extent of the wall effect associated with the singularity at the edge of the top platen.

For simplicity, calculations are done assuming that the contents of the cell consists of an incompressible Newtonian fluid. To simulate the effect of a separated cake at the bottom of the cell two fluids are considered, the bottom one being much more viscous than the top one. The effect of the shear is mostly felt at the top of the cell and efforts are concentrated to obtain rational solutions in that region. The problem, which is directly relevant to the flow problem near the top platen, is the discontinuity of nonslip boundary conditions at the point where the platen touches the cylinder wall. The two ways in which this problem can be approached are: (1) introducing slipping boundary conditions or (2) permitting a singularity in the velocity, c.q. stress field in any analytical expressions for the solutions. The second method is chosen in this paper.

The fluids that have practical application in filtration are always particle laden. The velocities are always small; the cell is not a "stirred cell" as the formation of a dense cake is often an objective of the experimental procedure. The description of the flow in the cell should therefore in principle involve a diffusion effect due to the shear field. This effect has been reported in the literature and appropriate constitutive laws have been developed for it (McTigue and Jenkins, 1992, Nott and Brady, 1994). In describing the flow as a Newtonian fluid the diffusion effect is ignored. In the near future the analysis will be extended to allow for any non-Newtonian features. For the moment, the principal purpose is to obtain expressions for the spatial variation of the shear field. While assumption of a purely Newtonian constitutive relation for the substance that fills the cell is somewhat primitive, it is reasonable to assume that as a first step it suffices. The slowness of the flow is now a bonus in that a low Reynolds number approximation is appropriate. In certain cases this may be somewhat optimistic.

The internal workings of the traditional dead end cell may be described using a one-dimensional analysis. For the worst case of a Newtonian fluid with a very thin septum and no-slip boundary conditions this has been demonstrated (Koenders and Wakeman, 1995). For the cell with a rotating top platen the one-dimensional approach is not valid: there is a very appreciable radial effect, especially in the shear stress, as well as a substantial variation in the axial direction. It is thus necessary to calculate the whole velocity distribution in the cell, but the simplifying assumption of azimuthal symmetry applies of course. Below, it is demonstrated that all fields for this case can be described analytically in terms of series expansions. These are all fast converging ones, except very close to the top platen itself. Especially at the point where the top platen meets the cylinder wall no satisfactory, computable solution can be obtained. There is, however, the possibility of approximating the solution in this region by assuming that the fluid extends infinitely, in which case the problem has no length scale and a similarity solution can be found. For "piston flow" in a corner this solution is described in Batchelor (1967). Here it is further developed to include shear flow.

In order to attain a degree of completeness of the treatment of the flow problems the following geometries have been analyzed. Two-dimensional flow in a corner, shearing flow in an infinite cylinder, shearing flow in a finite cylinder, shearing flow in a finite cylinder with two fluids of different viscosities and piston flow in a two-dimensional rectangular cell. It is possible to add the two modes of motion: shear and compression, as for a linear flow these are independent. In the case of compressive piston flows the solution presented here is an approximate one, as it is very difficult to arrive at an exact analytical expression. In addition, for this case the boundary conditions include assumptions that must be made about the flow pattern near the bottom of the cell. These will be along the same lines as the ones introduced by Koenders and Wakeman (1995). The procedure followed to calculate the piston flow problem makes use of the exact analytical solutions for corner flow. The latter are perturbed to give an approximation of the flow field in the whole cell. In this way the high gradient flow pattern in the corners is accurately represented, and satisfies the Stokes equation on a small scale. At the same time the large-scale velocity field variations are accounted for and these are largely dominated by the equation of continuity and the global flow pattern as prescribed by the boundary conditions at the ends of the cell.

The paper is structured as follows. To begin with, all mathe-

Contributed by the Fluids Engineering Division for publication in the JOURNAL OF FLUIDS ENGINEERING. Manuscript received by the Fluids Engineering Division June 8, 1998; revised manuscript received May 17, 1999. Associate Technical Editor: J. A. C. Humphrey.

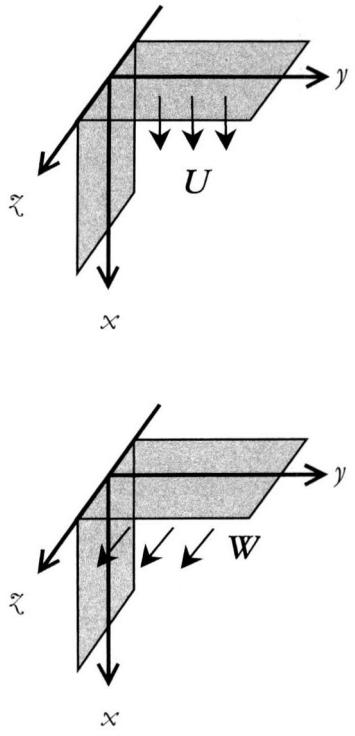

Fig. 1 Definition sketch for corner flow

matical considerations are discussed: first the simple two-dimensional corner flow problems, then the various flows in a sheared cell and finally the piston flow approximation for the normally loaded cell. Then the various solutions are presented graphically for parameter examples relevant to a practical application. These solutions are discussed, with special attention being paid to the position dependence of the shear field in the torsion shear apparatus.

Flow in a Rectangular Corner

The laminar Stokes equation for an incompressible fluid with viscosity μ is solved in Cartesian coordinates. The problem is defined in Fig. 1. The fluid extends infinitely in the region $x > 0$, $y > 0$, $-\infty < z < \infty$. The problem is independent of z. The x, y, z velocity components are denoted by u, v and w. The boundary conditions are $u(0, y) = U$, $u(x, 0) = 0$, $v(0, y) = 0$, $v(x, 0) = 0$, $w(0, y) = W$, $w(x, 0) = 0$.

The problem for u and v has been solved by Batchelor (1967) in polar coordinates using a stream function ψ which satisfies the biharmonic equation. The solution is reproduced here in Cartesian coordinates:

$$\psi(x, y) = \frac{2U}{4 - \pi^2}(\pi y + 2x) \arctan(x^{-1}y) + \frac{4U}{\pi^2 - 4} y \quad (1)$$

The velocities are:

$$u(x, y) = \frac{-\partial\psi}{\partial y} = \frac{2\pi U \arctan(xy^{-1})}{4 - \pi^2} + \frac{2Uy(\pi x - 2y)}{(\pi^2 - 4)(x^2 + y^2)} + \frac{\pi^2 U}{\pi^2 - 4} \quad (2)$$

$$v(x, y) = \frac{\partial\psi}{\partial x} = \frac{2U(2(x^2 + y^2)\arctan(xy^{-1}) - x(\pi x - 2y))}{(\pi^2 - 4)(x^2 + y^2)} \quad (3)$$

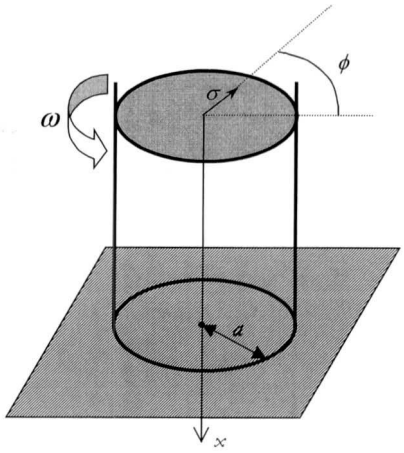

Fig. 2 Definition sketch for shearing flow in a cylinder

The z component satisfies the equation $\nabla^2 w = 0$, which is easily solved to give:

$$w(x, y) = W\left(1 - \frac{2}{\pi}\arctan(xy^{-1})\right) \quad (4)$$

The pressure field is obtained to within a constant p_0:

$$p(x, y) = p_0 + \frac{4\mu U(2x + \pi y)}{(\pi^2 - 4)(x^2 + y^2)} \quad (5)$$

The following stress field components are easily found and reported here for completeness

$$\tau_{xx} = -2\mu\frac{\partial u}{\partial x} = \frac{8\mu Uxy(\pi x - 2y)}{(\pi^2 - 4)(x^2 + y^2)^2};$$

$$\tau_{yy} = -2\mu\frac{\partial v}{\partial y} = -\tau_{xx} \quad (6)$$

$$\tau_{xy} = \tau_{yx} = -\mu\left(\frac{\partial u}{\partial y} + \frac{\partial v}{\partial x}\right) = \frac{4\mu U(x^2 - y^2)(\pi x - 2y)}{(4 - \pi^2)(x^2 + y^2)} \quad (7)$$

$$\tau_{xz} = \tau_{zx} = -\mu\frac{\partial w}{\partial x} = \frac{2\mu Wy}{\pi(x^2 + y^2)^2};$$

$$\tau_{yz} = \tau_{zy} = -\mu\frac{\partial w}{\partial y} = \frac{-2\mu Wx}{\pi(x^2 + y^2)^2} \quad (8)$$

Finally, the dissipation function is determined:

$$-(\tau:\nabla u) = \frac{16\mu U^2(\pi^2 x^2 - 4\pi xy + 4y^2)}{(\pi^2 - 4)^2(x^2 + y^2)^2} + \frac{4W^2}{\pi^2(x^2 + y^2)} \quad (9)$$

Torsional Shear Flow in a Cylinder

The geometry is sketched in Fig. 2; the cylinder has radius a. The top platen rotates with angular velocity ω. Cylindrical coordinates are the obvious choice, the axial coordinate is x, the radial coordinate is σ, and the angular coordinate is ϕ. The problem has azimuthal symmetry and is therefore independent of ϕ. The only velocity component that is relevant is u_ϕ which satisfies the Laplace equation $\nabla^2 u_\phi = 0$:

$$\frac{\partial}{\partial\sigma}\left(\frac{1}{\sigma}\frac{\partial}{\partial\sigma}(\sigma u_\phi)\right) + \frac{\partial^2 u_\phi}{\partial x^2} = 0 \quad (10)$$

This equation has the basic solution $u_\phi \sim J_1(\lambda\sigma)e^{-\lambda x}$ (see Jackson, 1962), where $J_\nu(\cdot)$ is the Bessel function of order ν. The generality of this type of solution in satisfying any boundary conditions has been discussed by Pickett (1944). The boundary

conditions are $u_\phi(0, \sigma) = \omega\sigma$ (top platen), $u_\phi(x, a) = 0$ (no-slip at the cylinder wall) and $u_\phi(x, \sigma)$ remains finite for $x \to \infty$. The latter condition immediately excludes negative λ as well as any solutions involving Neumann functions that have the property that they become infinite as $\sigma \to 0$ (these would be included if the problem pertained to a hollow cylinder). The boundary condition on the cylinder wall is satisfied if λ is chosen such that the Bessel function vanishes there. The $J_1(\cdot)$ has zeros α_n, $n = 1 \ldots \infty$. The solution thus takes the form with $\lambda = \alpha_n/a$ and a set of coefficients ξ_n:

$$u_\phi(x, \sigma) = \sum_{n=1}^{\infty} \xi_n J_1(\alpha_n\sigma/a) e^{-\alpha_n x/a} \tag{11}$$

The condition at the top platen is satisfied if the coefficients ξ_n can be found such that:

$$\omega\sigma = \sum_{n=1}^{\infty} \xi_n J_1(\alpha_n\sigma/a) \tag{12}$$

This is just the representation of a Fourier-Bessel series (see Jackson, 1962) and it is easily seen that the coefficients are:

$$\xi_n = \frac{2\omega a}{\alpha_n J_2(\alpha_n)} \tag{13}$$

The solution is thus completely known in terms of a series. The physical quantities that can be obtained are:

$$u_\phi(x, \sigma) = 2\omega a \sum_{n=1}^{\infty} \frac{J_1(\alpha_n\sigma/a) e^{-\alpha_n x/a}}{\alpha_n J_2(\alpha_n)} \tag{14}$$

$$\tau_{\phi\sigma}(x, \sigma) = \tau_{\sigma\phi}(x, \sigma) = -\mu\sigma \frac{\partial}{\partial\sigma}\left(\frac{u_\phi}{\sigma}\right)$$

$$= 2\omega\mu \sum_{n=1}^{\infty} \frac{e^{-\alpha_n x/a}}{J_2(\alpha_n)} \left\{ \frac{2a}{\sigma\alpha_n} J_1(\alpha_n\sigma/a) - J_0(\alpha_n\sigma/a) \right\} \tag{15}$$

$$\tau_{\phi x}(x, \sigma) = \tau_{x\phi}(x, \sigma) = -\mu \frac{\partial u_\phi}{\partial x}$$

$$= 2\omega\mu \sum_{n=1}^{\infty} \frac{e^{-\alpha_n x/a}}{J_2(\alpha_n)} J_1(\alpha_n\sigma/a) \tag{16}$$

Kim (1981) has also obtained Eq. (14) as a special case of the more general problem of a disk in a cylindrical vessel with a disk/cylinder diameter ratio less than 1.

For calculation purposes the behavior of the terms of these series is determined for large values of α_n. Using the asymptotic expansions (as in Abramowitz and Stegun, 1964) $J_\nu(\eta) \sim \sqrt{2/\pi\eta}\,\{\cos(\eta - (\nu\pi/2) - (\pi/4)) + O(\eta^{-1})\}$ and $\alpha_n \sim (n + \frac{1}{4})\pi - [3/2\pi(4n + 1)] + O(n^{-3})$ it is found that:

$$\frac{J_1(\alpha_n\sigma/a) e^{-\alpha_n x/a}}{\alpha_n J_2(\alpha_n)} \sim \frac{e^{-[n+(\pi/4)]x/a}}{\left(n + \frac{\pi}{4}\right)} \sqrt{\frac{a}{\sigma}} \tag{17}$$

$$\frac{J_0(\alpha_n\sigma/a) e^{-\alpha_n x/a}}{J_2(\alpha_n)} \sim e^{-[n+(\pi/4)]x/a} \sqrt{\frac{a}{\sigma}} \tag{18}$$

$$\frac{J_1(\alpha_n\sigma/a) e^{-\alpha_n x/a}}{J_2(\alpha_n)} \sim e^{-[n+(\pi/4)]x/a} \sqrt{\frac{a}{\sigma}} \tag{19}$$

Convergence of the series is therefore always guaranteed while $x \neq 0$ and the number of terms required to obtain an accuracy of δ is such that $\delta \approx e^{-[N+(\pi/4)]x/a}\sqrt{a/\sigma}\,(1 - e^{-x})$. For $x \to 0$ no convergence is achieved for the stress components. Note that the behavior of the Bessel functions for $\sigma \to 0$ is $J_0(\alpha_n\sigma/a) \to 1$ and $J_1(\alpha_n\sigma/a) \to \alpha_n\sigma/(2a)$.

The finite cylinder has length L and radius a. Fundamentally the same procedure as in the previous section is followed, but the boundary conditions are $u_\phi(0, \sigma) = \omega\sigma$ (top platen), $u_\phi(x, a) = 0$ (no-slip at the cylinder wall) and $u_\phi(L, \sigma) = 0$ (bottom platen). The solution is extended to include a second set of coefficients in addition to ξ_n to accommodate the solution with negative λ; these coefficients are called η_n. The basic form of the velocity field is then conveniently written in the following form:

$$u_\phi(x, \sigma) = \sum_{n=1}^{\infty} J_1(\alpha_n\sigma/a)[\xi_n \cosh(\alpha_n x/a) + \eta_n \sinh(\alpha_n x/a)] \tag{20}$$

The coefficients ξ_n are the same as before, Eq. (13). The coefficients η_n are obtained from the boundary condition at the bottom platen to give:

$$\eta_n = \xi_n \coth(\alpha_n L/a) \tag{21}$$

The following physical parameters are thus obtained:

$$u_\phi(x, \sigma) = 2\omega a \sum_{n=1}^{\infty} \frac{J_1(\alpha_n\sigma/a)}{\alpha_n J_2(\alpha_n)} [\cosh(\alpha_n x/a) - \coth(\alpha_n L/a) \sinh(\alpha_n x/a)] \tag{22}$$

$$\tau_{\phi\sigma}(x, \sigma) = \tau_{\sigma\phi}(x, \sigma) = -\mu\sigma \frac{\partial}{\partial\sigma}\left(\frac{u_\phi}{\sigma}\right)$$

$$= 2\omega\mu \sum_{n=1}^{\infty} \frac{[\cosh(\alpha_n x/a) - \coth(\alpha_n L/a) \sinh(\alpha_n x/a)]}{J_2(\alpha_n)} \times \left\{ \frac{2a}{\sigma\alpha_n} J_1(\alpha_n\sigma/a) - J_0(\alpha_n\sigma/a) \right\} \tag{23}$$

$$\tau_{\phi x}(x, \sigma) = \tau_{x\phi}(x, \sigma) = -\mu \frac{\partial u_\phi}{\partial x}$$

$$= -2\omega\mu \sum_{n=1}^{\infty} \frac{[\sinh(\alpha_n x/a) - \coth(\alpha_n L/a) \cosh(\alpha_n x/a)]}{J_2(\alpha_n)} \times J_1(\alpha_n\sigma/a) \tag{24}$$

The problem is easily extended to give a result for two fluids with different viscosities μ_1 and μ_2. The solution for the velocity has the same basic form as before, Eq. (20), with coefficients $(\xi_n)_{1,2}$ and $(\eta_n)_{1,2}$; the subscripts outside the brackets denoting whether the solution pertains to the top or bottom part of the cell. The fluid interface is plane and located at $x = L_1$; the bottom is at $x = L_2$. We require that the velocity and shear stress across the fluid interface boundary must be continuous.

The basic form of the equations is now:

$$(u_\phi)_1(x, \sigma) = \sum_{n=1}^{\infty} J_1(\alpha_n\sigma/a)[(\xi_n)_1 \cosh(\alpha_n x/a) + (\eta_n)_1 \sinh(\alpha_n x/a)] \tag{25}$$

$$(u_\phi)_2(x, \sigma) = \sum_{n=1}^{\infty} J_1(\alpha_n\sigma/a)[(\xi_n)_2 \cosh(\alpha_n x/a) + (\eta_n)_2 \sinh(\alpha_n z/a)] \tag{26}$$

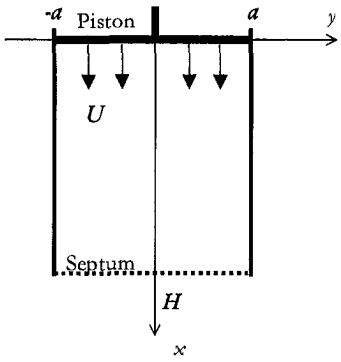

Fig. 3 Definition sketch for piston flow in a rectangular cell

The relations between the coefficients are found from the boundary conditions; they are:

$$(\eta_n)_1 = -(\xi_n)_1 \times \frac{(\mu_1 - \mu_2)(e^{4L_1\alpha_n/a} + e^{2L_2\alpha_n/a}) - (\mu_1 + \mu_2)e^{2L_1\alpha_n/a}(1 + e^{2L_2\alpha_n/a})}{(\mu_1 - \mu_2)(e^{4L_1\alpha_n/a} - e^{2L_2\alpha_n/a}) + (\mu_1 + \mu_2)e^{2L_1\alpha_n/a}(1 - e^{2L_2\alpha_n/a})} \tag{27}$$

$$(\eta_n)_2 = 2(\xi_n)_1 \times \frac{\mu_1 e^{2L_1\alpha_n/a}(1 + e^{2L_2\alpha_n/a})}{(\mu_1 - \mu_2)(e^{4L_1\alpha_n/a} - e^{2L_2\alpha_n/a}) + (\mu_1 + \mu_2)e^{2L_1\alpha_n/a}(1 - e^{2L_2\alpha_n/a})} \tag{28}$$

$$(\xi_n)_2 = 2(\xi_n)_1 \times \frac{\mu_1 e^{2L_1\alpha_n/a}(1 - e^{2L_2\alpha_n/a})}{(\mu_1 - \mu_2)(e^{4L_1\alpha_n/a} - e^{2L_2\alpha_n/a}) + (\mu_1 + \mu_2)e^{2L_1\alpha_n/a}(1 - e^{2L_2\alpha_n/a})} \tag{29}$$

The velocity condition at the top platen determines the coefficients $(\xi_n)_1$ as before.

Piston Flow in a Finite Rectangular Two-Dimensional Cell

Here Cartesian two-dimensional coordinates (x, y) are employed; x is the vertical coordinate, see Fig. 3. The cell has a width of $2a$ and a length H. The boundary conditions are as follows: $u(0, y) = U$; $u(x, \pm a) = 0$; $v(x, \pm a) = 0$; $v(0, y) = 0$; a suitable boundary condition at $x = H$ is furthermore required. The flow for $x > H$ is left unspecified to some extent; analogously to the treatment by Koenders and Wakeman (1995) the problem could be coupled to a Darcyan one in a porous medium at the bottom of the cell. For the approximate solution given here it is sufficient to state the width of the horizontal boundary zone, that is the distance away from the cell wall at which the vertical flow has approximately reached a plateau. The problem of the flow in the vicinity of the region of the lower boundary is further discussed by Koenders and Wakeman (1995), where it is shown that the velocity is completely dominated by the vertical component for the cell and cake dimensions as well as the velocities that prevail in dead-end filtration.

The governing equation for an incompressible Newtonian fluid is the biharmonic equation, from which the velocity field is derived by differentiation:

$$\nabla^2\nabla^2\psi(x, y) = 0 \tag{30}$$

$$u(x, y) = \frac{-\partial\psi}{\partial y}; \quad v(x, y) = \frac{\partial\psi}{\partial x}; \tag{31}$$

The equation of continuity is important for the present problem

$$\frac{\partial u}{\partial x} + \frac{\partial v}{\partial y} = 0 \tag{32}$$

Furthermore, the geometry of the problem imposes the conditions $u(x, -y) = u(x, y)$; $v(x, -y) = -v(x, y)$.

The high order derivatives, such as appear in Eq. (30), are relevant to the corners at the top platen. For this region the solution is already known: formulas (2) and (3). The flow in the two-dimensional rectangular cell is approximated by multiplying the results in the corner with smooth weighting functions, that only have low derivatives so as to not to perturb the high derivative results. Calling the velocity fields in the two corners as obtained from equations (2) and (3) u^+ and u^- for positive y and negative y, respectively, the following approximate form for the flow in the whole cell is put forward:

$$u(x, y) = (u^+(A + Cy + By^3) + u^-(A' + C'y + B'y^3)) \cdot F(x) \tag{33}$$

The coefficients $A \ldots B'$ are adapted to suit the boundary conditions. The ones at $x = 0$ and $y = \pm a$ are used to dertermine A, C, A' and C': $A = A' = \frac{1}{2}$; $C = -C' = -(Ba^2 - \frac{1}{2}a)$. The vertical velocity depends on one parameter: $B = -B'$. It has the form:

$$u(x, y) = \left\{ \left[\frac{2\pi U \cdot \arctan\left(\frac{y-a}{x}\right)}{4 - \pi^2} + \frac{2U(y-a)\cdot(\pi x + 2\cdot(y-a))}{(4-\pi^2)\cdot(x^2 + (y-a)^2)} \right] \cdot \left[\frac{1}{2} + By^3 - \left(Ba^2 - \frac{1}{2a}\right)y \right] + \left[\frac{2\pi U \cdot \arctan\left(\frac{y+a}{x}\right)}{\pi^2 - 4} + \frac{2U(y+a)\cdot(\pi x - 2\cdot(y+a))}{(\pi^2-4)\cdot(x^2 + (y+a)^2)} \right] \cdot \left[\frac{1}{2} - By^3 + \left(Ba^2 - \frac{1}{2a}\right)y \right] \right\} F(x) \tag{34}$$

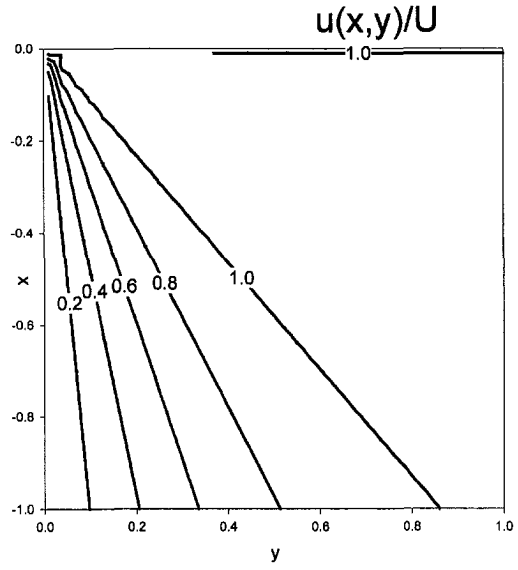

Fig. 4 Contour plot of the vertical velocity component for flow in a corner

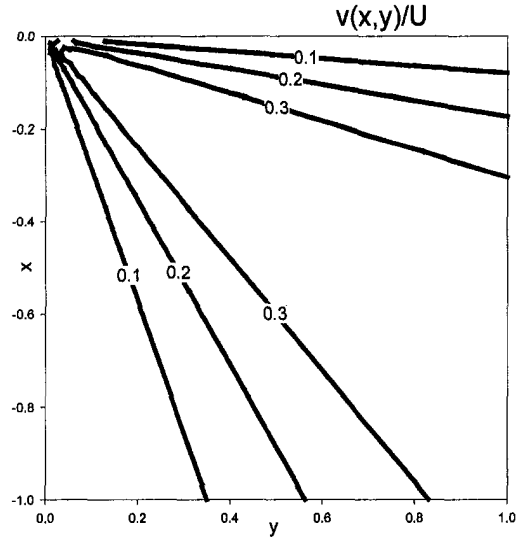

Fig. 5 Contour plot of the horizontal velocity component for flow in a corner

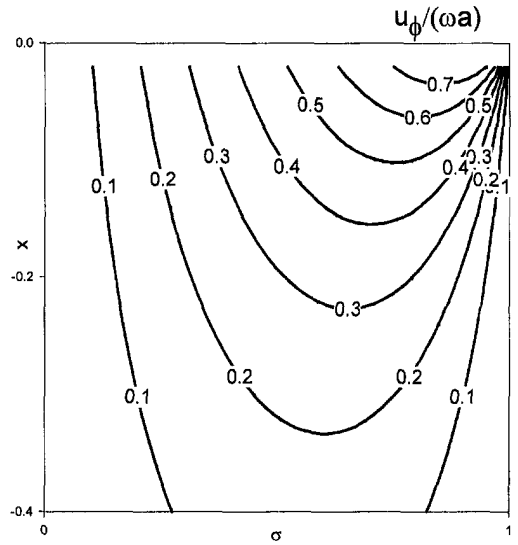

Fig. 7 Contour plot of the shear velocity for shear flow in an infinite cylinder

The function $F(x)$ is derived from the equation of continuity:

$$\int_{-a}^{a} u(x, y)dy = \int_{-a}^{a} u(0, y)dy = 2Ua \tag{35}$$

The result for $F(x)$ is somewhat involved; define the auxiliary functions:

$$G_1(x) = 2x^2(2Bax(x - a) - 4Ba^3 - 1) \ln \frac{x^2}{x^2 + 4a^2} - 2a((4Bax^2 - 1)(4a + \pi x) - Ba\pi x^3)$$

$$G_2(x) = [(Bax^2 - 1)(8ax - 4\pi a^2 + \pi x^2) + 2\pi a(Bx^4 - 4a)] \arctan \frac{2a}{x} \tag{36}$$

Then:

$$F(x) = \frac{2a^2(4 - \pi^2)}{G_1(x) + G_2(x)} \tag{37}$$

The parameter B is used to adapt to the boundary condition at $x = H$. In the discussion below this will be further elucidated. The horizontal velocity field is found from Eq. (32). In the parameter range envisaged here it is of an order of magnitude smaller than the vertical velocity field, except in the corners where Eq. (3) rules.

Piston flow in a cylindrical cell follows very much the same pattern as the flow for a rectangular cell. The mathematical development, however, is somewhat tortuous and is omitted here.

Graphical Presentation of the Results and Discussion

The velocity components for corner flow, Eqs. (2), (3), and (4) are depicted in Figs. 4, 5, and 6. The feature to note here is the singularity in the corner. No length scales need to be investigated, as the whole solution possesses similarity properties. The reason corner flow is investigated is that its intended use is a first order approximation to piston flow.

The findings on shearing flow in a cylinder are reported in Figs.

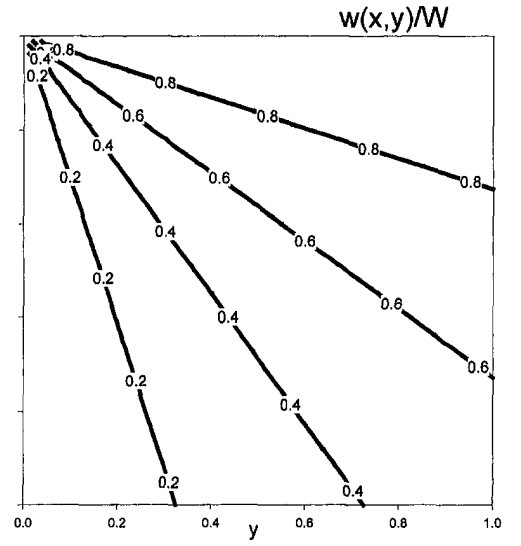

Fig. 6 Contour plot of the shearing velocity component for flow in a corner

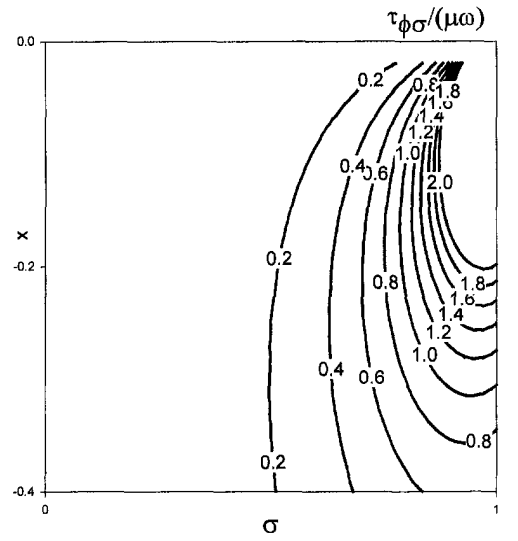

Fig. 8 Contour plot of the shearing radial stress component for shear flow in an infinite cylinder

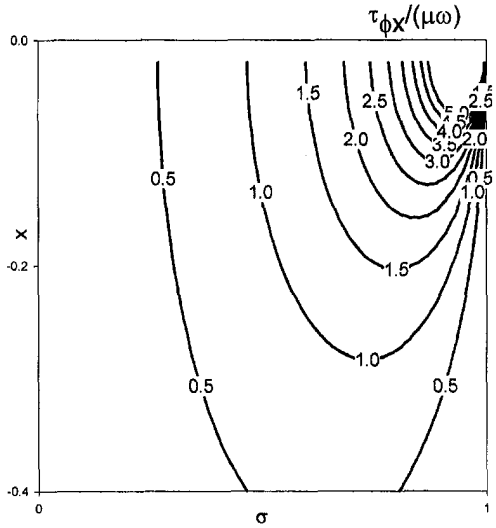

Fig. 9 Contour plot of the shearing axial stress component for shear flow in an infinite cylinder

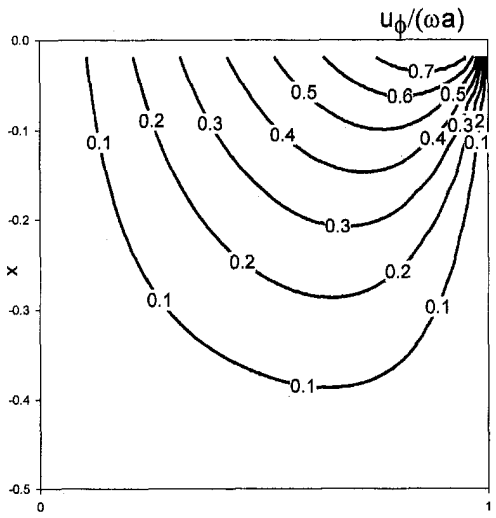

Fig. 10 Contour plot of the shear velocity for shear flow in a finite cylinder with length/radius ratio $L/a = 0.5$

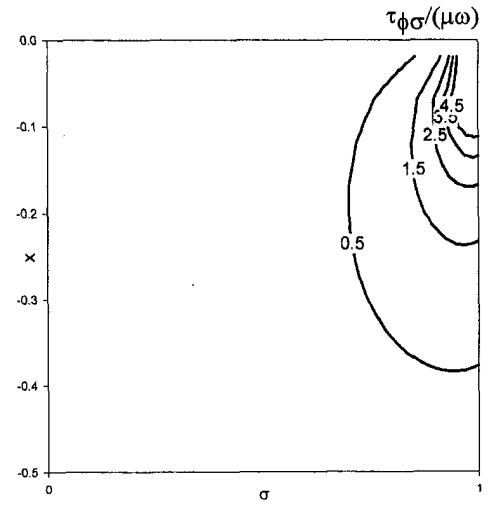

Fig. 11 Contour plot of the shearing radial stress component for shear flow in a finite cylinder with length/radius ratio $L/a = 0.5$

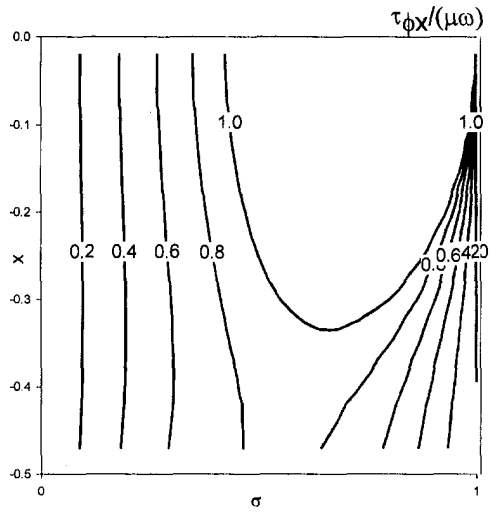

Fig. 12 Contour plot of the shearing axial stress component for shear flow in a finite cylinder with length/radius ratio $L/a = 0.5$

6–15. The result of the velocity field, the shearing radial stress $\tau_{\phi\sigma}(x, \sigma)$ and the shearing axial stress $\tau_{\phi x}(x, \sigma)$ for the infinitely long cylinder, as obtained in expressions (14)–(16) are depicted in Figs. 6–8. The calculation can obviously not be done very close to $x = 0$, nonetheless the singularity in the corner of the apparatus, where the top platen meets the cylinder wall, is clearly seen. It is also seen that near the corner the two stress components are of the same order of magnitude and that they diminish at distances away from the top platen. The typical decay distance is of the order of $0.2a$. In this case the cylinder radius is the only length scale in the problem.

When an extra length scale L is introduced in the form of the finite cylinder, the pattern of the fields changes. Figures 10, 11, and 12 show the fields for a cylinder with $L/a = 0.5$. The notable difference with the infinite cylinder is that the shearing radial stress component only plays a role in the very corner, while the shearing axial stress component is more evident in the rest of the cell. This effect becomes even more important when the length radius ratio is decreased more. Figure 13 shows the shearing axial stress component for $L/a = 0.1$. This stress component is now virtually a linear function of the radius in the region $0 < \sigma < 0.8$ and all other features can be regarded as wall effects. The general con-

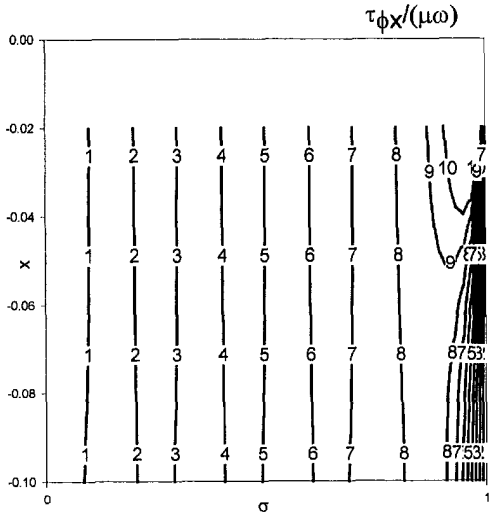

Fig. 13 Contour plot of the shearing axial stress component for shear flow in a finite cylinder with length/radius ratio $L/a = 0.1$

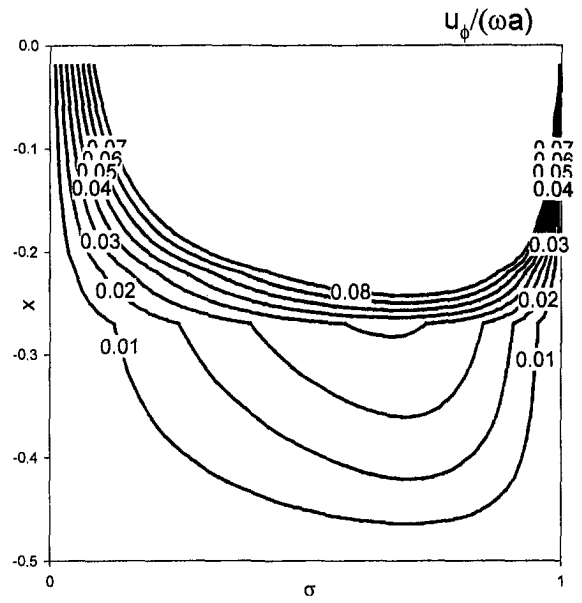

Fig. 14 Contour plot of the shear velocity for shear flow in a finite cylinder filled with two immiscible fluids with length/radius ratio L_2/a = 0.5. The ratio of the viscosities of the fluids is μ_2/μ_1 = 10; the two fluids occupy equal volumes: L_2/L_1 = 2.

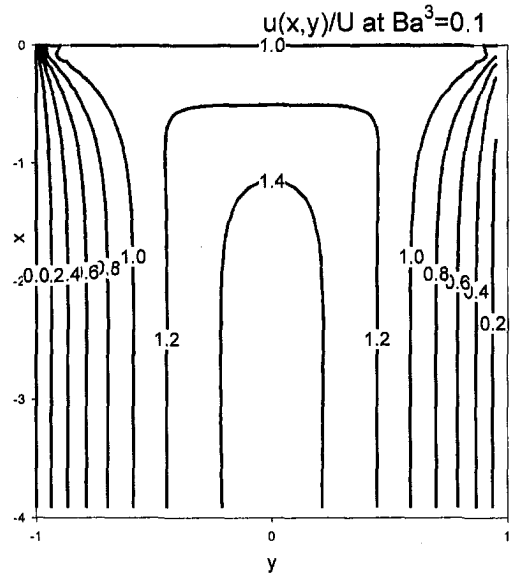

Fig. 16 Contour plot of the vertical velocity for piston flow. The parameter B is chosen such that Ba^3 = 0.1.

clusion is that the shearing axial stress becomes a linear function of the radius, independent of the distance away from the top platen, when the fluid depth is much smaller than the diameter of the cell. The extent of the thickness of the wall effect δ is of the order of $\delta/a \approx 2L/a$.

In reality, the lower part of the cell is filled with a particle fluid mixture that has accumulated on the septum in the form of a "cake." The cake can be modelled as a fluid of high viscosity. Figures 14 and 15 show contour plots of the shear velocity and the shearing axial stress for shear flow in a finite cylinder filled with two immiscible fluids with length/radius ratio L_2/a = 0.5. The ratio of the viscosities of the fluids is μ_2/μ_1 = 10; the two fluids occupy equal volumes: L_2/L_1 = 2. The illustration of the shear velocity shows how all velocity is concentrated in the top region of the cell. Figure 15 gives information on the (continuous) stress field. The linear function of the axial distance is here also observed, similar to the finite cylinder problem. Applying the findings of the finite cylinder to the present problem where the viscosity ratio warrants the assumption of the lower part of the fluid practically speaking immobile (as borne out by the velocity picture). For this case the equivalent ratio $L/a \approx L_1/a$ = 0.25; thus a wall effect of thickness $\delta/a \approx 0.5$ is expected and also found.

The cake formation process is effected to a large extent by piston pressure, rather than shear. The radial dependence of the vertical velocity component is thus important. It has been shown by Koenders and Wakeman (1995) that the radial dependence of the flow depends to a large extent on the septum/cake permeability properties. In practice the departure from one-dimensionality is confined to a region of the order of magnitude of either the septum thickness in the case of a clean filter, or a few particle diameters

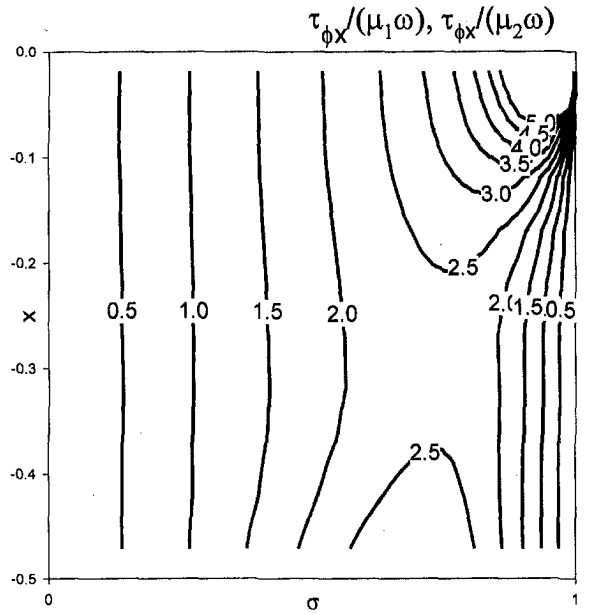

Fig. 15 Contour plot of the shearing axial stress for shear flow in a finite cylinder filled with two immiscible fluids with length/radius ratio L_2/a = 0.5. The ratio of the viscosities of the fluids is μ_2/μ_1 = 10; the two fluids occupy equal volumes: L_2/L_1 = 2.

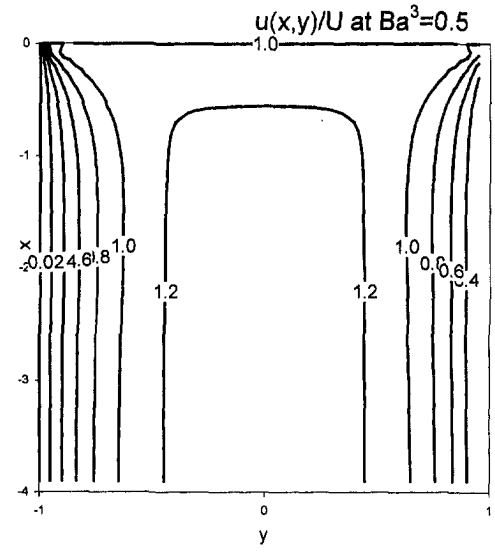

Fig. 17 Contour plot of the vertical velocity for piston flow. The parameter B is chosen such that Ba^3 = 0.5.

when a cake has formed. (The septum thickness is always much smaller than the cell radius.) These conditions prevail at the bottom of the cell. The question that is then whether the singularity at the top platen edge influences the flow pattern to a significant degree. The parameter B in the piston flow approximation (Formula (34)) is the only adaptable constant in that estimate. The flow field is shown in Figs. 16 and 17 for two values of B. It is seen that by varying this parameter the velocity field at the bottom of the cell is influenced; notably the thickness of the shear layer by the wall of the apparatus is controlled in this way. It is also shown quite convincingly that the wall effect is greatest near the bottom of the cell; towards the top the region where the velocity is nonuniform is broader. The flow at the bottom of the cell has been modelled by Koenders and Wakeman (1995); the thickness of the shear layer by the wall of the apparatus has been shown to be dependent on the thickness of the cake.

So it has been shown that the wall effect due to shearing is much more significant than that due to piston flow. For situations where the top platen is close to the septum (or the cake boundary) the wall effect is confined to a small region, but the shearing axial stress is a more or less linear function of the radial coordinate. The shearing radial stress for this case is confined to the region of the wall effect.

The calculations shown here are an excellent basis for the further modelling of cake formation in the torsional shear cell. The extent of the wall effect at all stages of the process can now be estimated, as well as the behaviour of the important shearing axial stress.

Acknowledgments

Financial support from the Engineering and Physical Sciences Research Council, award number GR/L62085 is gratefully acknowledged. Discussions with Em. Prof. Harry "Don" Conway from the Department of Theoretical and Applied Mechanics at Cornell University have been most helpful.

References

Abramowitz, M., and Stegun, I. A., 1964, *Handbook of Mathematical Functions,* Dover Publications, New York.

Batchelor, G. K., 1967, *An Introduction to Fluid Dynamics,* Cambridge University Press.

Jackson, J. D., 1962, *Classical Electrodynamics,* John Wiley, New York.

Kim, M-U., 1981, "Slow Rotation of a Disk in a Fluid-Filled Circular Cylinder," *Journal of the Physical Society of Japan,* Vol. 50, No. 12, pp. 4063–4067.

Koenders, M. A., and Wakeman, R. J., 1995, "Radial Flow Dependence in Filtration Experiments," *Chemical Engineering Science,* Vol. 50, No. 23, p. 3777.

McTigue, D. F., and Jenkins, J. T., 1992, "Channel Flow of a Concentrated Suspension," *Advances in Micromechanics of Granular Materials* H. H. Shen et al., ed., Elsevier Science Publishers BV, Amsterdam, pp. 381–390.

Nott, P. R., and Brady, J. F., 1994, "Pressure Driven Flow of Suspensions: Simulation and Theory," *Journal of Fluid Mechanics,* Vol. 275, p. 157.

Pickett, G., 1944, "Application of the Fourier Method to the Solution of Certain Boundary Problems in the Theory of Elasticity," *Journal of Applied Mechanics,* Sept., p. A-176.

The Effect of Permeability Variations on the Flow in a Heterogeneous Porous Channel Subject to Rotation

Peter Vadasz
Professor of Mechanical Engineering,
University of Durban-Westville,
Private Bag X54001, Durban 4000,
South Africa.
Fellow ASME
e-mail: vadasz@pixie.udw.ac.za

Mark A. Havstad
Mechanical Engineer,
Atomic Vapor Laser Isotope
Separation Program,
Lawrence Livermore National Laboratory,
L-470, Livermore, CA 94550
Mem. ASME

A significant effect of permeability variations on the three-dimensional fluid flow in a heterogeneous porous channel subject to rotation is presented. The results of a numerical solution to the governing equations confirm for the more general case the conclusions from earlier analytical investigations, which suggest that permeability functions be classified corresponding to whether their variation is monotonic or not, and to whether their vertical gradient is positive or not. Unicellular and multiple vortex solutions are obtained for the secondary flow in the plane perpendicular to the imposed axial flow, while their direction is dictated by the corresponding class of permeability function as applicable. The impact of rotation on the imposed axial flow is shown to be significant as well, leading to different axial flow fields depending again on the class of permeability function used. In particular, the rotation impacts significantly in creating axial flow deficiencies in some regions on the cross section.

Introduction

The study of flow in rotating porous media is motivated by its practical applications in engineering such as the food process industry, chemical process industry, centrifugal filtration processes, solidification processes and rotating machinery. A review of the field, including discussion of engineering applications, is presented by Vadasz (1997, 1998). In particular, the macro-level porous media approach is gaining increased interest for solving practical fluid flow an heat transfer problems which are too difficult to solve by using a traditional micro-level approach. Some applications of the porous medium approach are discussed by Nield and Bejan (1999) and Bejan (1995) in comprehensive reviews of the fundamentals of heat convection in porous media. Bejan (1995) mentions among the applications of heat transfer in porous media the process of cooling of winding structures in high-power density electric machines. When this applies to a rotor of an electric machine, say generator (or motor), rotation effects become relevant as well. Investigation of the heat transfer processes requires the understanding and use of the macro-level approach in a rotating device (rotor).

A particular problem of excessive hydrogen consumption in a generator (hydrogen is being used as the cooling fluid in power plant generators) receives current interest in the Duvha coal fired power plant in Witbank, South Africa. In this particular problem the inefficient cooling of hydrogen during a periodic change in load demand triggers occasionally during the peak load (and quite frequently in this power plant) the pressure emergency sensors in the generator, resulting in the need to temporarily exhaust hydrogen. This exhausted amount needs to be refilled at off-peak load, resulting in excessive hydrogen consumption. The heat transfer processes in this problem are divided between the different components in the system. For the rotor, it represents a forced convection heat transfer problem in a rotating porous medium. The flow field needs to be solved prior to solving the forced heat convection problem. Hence the relevance and importance in understanding the fundamental theory behind the flow of fluid in rotating porous channels.

The problem of the effect of rotation on isothermal flow in porous media received relatively little attention. The major reason behind the lack of interest for this type of flow is probably the fact that isothermal flow in homogeneous porous media following Darcy's law is irrotational (Bear, 1972) hence the effect of rotation on this flow is not significant. However, for a heterogeneous medium with spatial dependent permeability or for free convection in a non-isothermal homogeneous porous medium the flow is not irrotational any more, hence the effects of rotation become significant.

The fundamental theoretical aspects of such flows, including the proof of the existence of Taylor-Proudman columns in porous media, and their experimental confirmation, was presented by Vadasz (1997). These results apply to small values of the porous media Ekman number. One of the conclusions from this study was that the flow at high rotation rates (small Ekman numbers) has a tendency toward two-dimensionality leading to a flow in the plane perpendicular to the rotation axis. On the other hand, the effect of rotation on the flow through heterogeneous porous media in a rotating square channel was investigated analytically by Vadasz (1993), for the case of small rotation rates (i.e., large values of the porous media Ekman number), while using an asymptotic method of solution. The major conclusion from this study was that the axial flow in a heterogeneous porous channel is deflected due to rotation and secondary circulation is produced in a plane perpendicular to the imposed axial flow. An investigation of the analytical results indicated that the direction of the circulation in this cross-sectional plane is controlled by the variations of permeability.

Therefore, the objective of the present paper is to report results of a further investigation of the effect of different permeability functions on the three-dimensional flow field in a heterogeneous rotating porous channel. The present results were obtained via a finite difference numerical method while using a particularly useful mesh refinement technique which allows to extend the validity of the numerical solution to extreme values of Ekman number, when boundary layers involving sharp filtration velocity gradients are present. The numerical method of solution as applied to an exponential monotonic variation of the permeability function was presented by Havstad and Vadasz (1999).

Contributed by the Fluids Engineering Division for publication in the JOURNAL OF FLUIDS ENGINEERING. Manuscript received by the Fluids Engineering Division January 9, 1998; revised manuscript received May 14, 1999. Associate Technical Editor: M. N. Dhaubhadel.

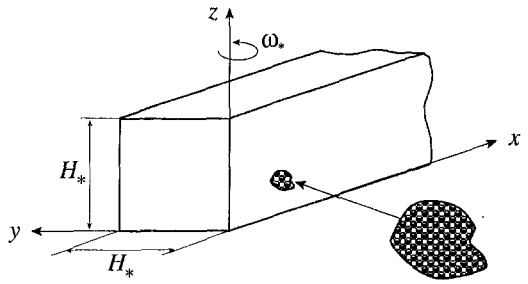

Fig. 1 A heterogeneous fluid saturated porous medium in a rotating square channel

Problem Formulation

The problem of an axial flow through a long rotating square channel filled with fluid saturated porous material is considered. The axial flow is imposed through an axial pressure gradient while the channel rotates about an axis perpendicular to the horizontal walls (Fig. 1). With homogeneous porous medium the permeability is constant throughout the flow domain resulting in a uniform distribution of the filtration velocity and the rotation does not affect the flow. However, for heterogeneous porous media, the permeability is spatially dependent, thus allowing the development of secondary circulation. The particular case where the permeability varies only along the vertical coordinate is considered. This assumption is equivalent with the assumption of developed flow in pure fluids (nonporous domains).

The dimensionless equations governing the flow in a rotating heterogeneous porous media following Darcy's law (extended to include the Coriolis and centrifugal terms) were presented by Havstad and Vadasz (1999) and can be reduced to the following explicit form

$$u^* - k^* v^* = -k^* \frac{\partial p}{\partial x} \tag{1a}$$

$$v^* - k^* u^* = -k^* \frac{\partial p}{\partial y} \tag{1b}$$

$$w^* = -k^* \frac{\partial p}{\partial z} \tag{1c}$$

subject to the scaling

$$\mathbf{q}^* = \frac{\mathbf{q}}{\mathrm{Ek}}; \quad k^* = \frac{k}{\mathrm{Ek}} \tag{2}$$

and the choice $\hat{\mathbf{e}}_\omega = \hat{\mathbf{e}}_z$.

In Eqs. (1)–(2), $\mathbf{q} = u\hat{\mathbf{e}}_x + v\hat{\mathbf{e}}_y + w\hat{\mathbf{e}}_z$ is the dimensionless filtration velocity (Darcy's flux), p is the dimensionless reduced pressure generalized to include the constant centrifugal as well as the gravity terms, $k(\mathbf{X})$ is the dimensionless permeability function, $\hat{\mathbf{e}}_\omega$ and $\hat{\mathbf{e}}_z$ are unit vectors in the direction of the imposed angular velocity and z direction, respectively, and the porous media Ekman number is defined as

$$\mathrm{Ek}_\Delta = \frac{\phi \nu_{c*}}{2\omega_* k_{c*}} \tag{3}$$

where ϕ is porosity, ω_* is the angular velocity of rotation, k_{c*} is a reference value of permeability and ν_{c*} is the kinematic viscosity. The size of the square cross section of the channel, H_*, is used to transform the independent variables to the following dimensionless form $x = x_*/H_*$, $y = y_*/H_*$, $z = z_*/H_*$. The only dimensionless group which appears in the governing equations is, therefore, the Ekman number (Ek_Δ) which controls the significance of the Coriolis effect. In solving Eq. (1) the following impermeability boundary conditions on the solid walls of the channel apply: $\mathbf{q} \cdot \hat{\mathbf{e}}_n = 0$ on the solid walls, where $\hat{\mathbf{e}}_n$ is a unit vector normal to the channel walls.

By applying this particular scaling, the effect of Ek is absorbed entirely in the definition of k^*, which is a function that needs to be provided as input to any particular problem that is considered.

The only assumption we make is the requirement to have a developed flow along the channel, i.e., $\partial \mathbf{q}^*/\partial x = 0$ everywhere in the channel. This requirement limits the choice of possible permeability variations. Variations of k^* only in the z direction are consistent with the condition of developed flow. Therefore $k^* \equiv k^*(z)$, while z is the direction corresponding to the angular velocity of rotation. The condition for developed flow in the channel (i.e., $\partial \mathbf{q}^*/\partial x = 0$) implies in particular $\partial u/\partial x = 0$, thus reducing the continuity equation to the form

$$\frac{\partial v^*}{\partial y} + \frac{\partial w^*}{\partial z} = 0 \tag{4}$$

Equation (4) can be identically satisfied by reformulating the problem via the introduction of a stream function, defined in the form $v^* = \partial\psi/\partial z$, $w^* = -\partial\psi/\partial y$. Substituting this definition into Eqs. (1a–c), taking the z-derivative of Eq. (1b) and the

Nomenclature

Ek = Ekman number, defined by Eq. (3)
$\hat{\mathbf{e}}_x$ = unit vector in the x direction
$\hat{\mathbf{e}}_y$ = unit vector in the y direction
$\hat{\mathbf{e}}_z$ = unit vector in the z direction
$\hat{\mathbf{e}}_n$ = unit vector normal to the solid boundary, positive outwards
$\hat{\mathbf{e}}_\omega$ = unit vector in the direction of the angular velocity of rotation
H_* = the size of the square cross section of the channel
k = dimensionless permeability function
k_{c*} = a reference value of permeability, dimensional
p = pressure, dimensionless
$\mathbf{q}$ = filtration velocity, dimensionless
Q = volumetric flowrate, dimensionless
u = horizontal x component of the filtration velocity
u_o = horizontal x component of the filtration velocity in the absence of rotation
v = horizontal y component of the filtration velocity
w = vertical component of the filtration velocity
$\mathbf{X}$ = position vector, equals $x\hat{\mathbf{e}}_x + y\hat{\mathbf{e}}_y + z\hat{\mathbf{e}}_z$
x = horizontal length coordinate
y = horizontal width coordinate
$\tilde{y}$ = horizontal width coordinate in the transformed space
z = vertical coordinate
$\tilde{z}$ = vertical coordinate in the transformed space
ϕ = porosity
ω_* = angular velocity of the rotating porous domain
ν_{c*} = fluid's kinematic viscosity, dimensional
ψ = stream function

Subscripts

* = dimensional values
c = characteristic values

Superscripts

* = rescaled dimensionless variables, applies to filtration velocity and permeability

y-derivative of Eq. (1c), adding this two equations, and substituting for $\partial p/\partial y$ and $\partial p/\partial z$ their corresponding relationships from 1(b) and 1(c) expressed in terms of ψ, yields

$$\frac{\partial^2\psi}{\partial y^2} + \frac{\partial^2\psi}{\partial z^2} - \frac{d[\ln (k^*)]}{dz}\frac{\partial\psi}{\partial z} = -k^*\frac{du^*}{dz} \tag{5}$$

A constant axial pressure gradient was assumed in order to be consistent with the condition of developed flow, hence $(-\partial p/\partial x)$ = constant and it is convenient to use its corresponding dimensional value as the characteristic pressure gradient, therefore normalising its dimensionless value, in the form $(-\partial p/\partial x) = 1$. The derivative of the horizontal filtration velocity in Eq. (5) can now be evaluated by using Eq. (1a), leading to

$$\frac{\partial^2\psi}{\partial y^2} + [(k^*)^2 + 1]\frac{\partial^2\psi}{\partial z^2} + [(k^*)^2 - 1]\frac{d[\ln (k^*)]}{dz}\frac{\partial\psi}{\partial z} = -k^*\frac{dk^*}{dz} \tag{6}$$

and

$$u^* = k^*\left[1 + \frac{\partial\psi}{\partial z}\right] \tag{7}$$

The method described in this paper applies generally to any permeability variation in the z direction, however the computational examples to be presented used three different vertical distributions of permeability; one monotonic, the other two nonmonotonic, the second having an antisymmetric deviation with respect to the mid-plane $z = 0.5$ and the third having symmetric deviation with respect to this plane, in the form

(i) *Monotonic Variation of Permeability*

$$k = k_o + \gamma \sin\left(\frac{\pi z}{2}\right) \tag{8}$$

(ii) *Nonmonotonic and Antisymmetric Variation of Permeability*

$$k = k_o + \gamma \sin (2\pi z) \tag{9}$$

(iii) *Nonmonotonic and Symmetric Variation of Permeability*

$$k = k_o + \gamma \sin (\pi z) \tag{10}$$

The anticipation was to obtain different flow patterns in the cross sectional $y - z$ plane which according to the approximate analytical results presented by Vadasz (1993) are dependent on whether the vertical permeability variation is monotonic or not, and on the concavity or convexity of the permeability function.

In order to have a global benchmark for the permeability function which will permit comparison of results obtained by using the three different permeability functions, a criterion of setting the values of k_o and γ in Eqs. (8), (9), and (10) in such a way as to produce a unit value of flowrate under conditions of no rotation was adopted. One can easily notice from the original Darcy law extended to include the Coriolis effect (see Eq. (2) in Havstad and Vadasz (1999)) that when the rotation is absent (Ek $\rightarrow \infty$) $u = u_o(z) = k(z)$. Therefore,

$$Q = \int_0^1\int_0^1 u(z)dydz = \int_0^1 dy\int_0^1 k(z)dz = \int_0^1 k(z)dz \tag{11}$$

when Ek $\rightarrow \infty$. For a homogeneous channel $k = 1$ and the flowrate is $Q = 1$. To get the same flowrate with the permeability functions presented in Eqs. (8), (9) and (10) the following conditions on the values of k_o and γ need to be fulfilled

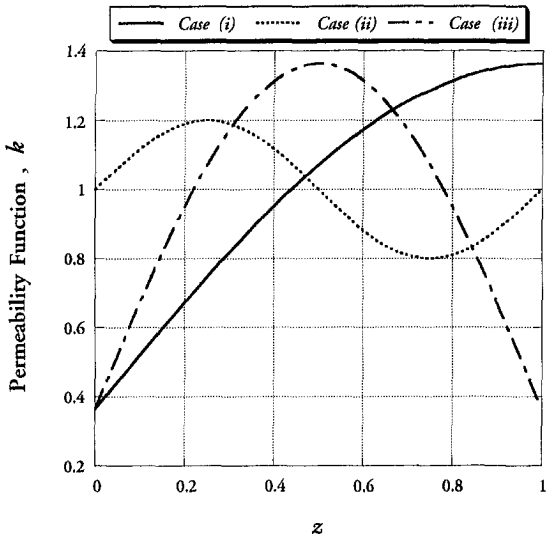

Fig. 2 Graphical description of the permeability variations within the porous channel. (i) Monotonic variation of permeability, Eq. (10); (ii) Nonmonotonic and antisymmetric variation of permeability, Eq. (11); (iii) Nonmonotonic and symmetric variation of permeability, Eq. (12).

(i) *Monotonic Variation of Permeability*

$$k_o = 1 - \frac{2}{\pi}; \quad \gamma = 1 \tag{12}$$

(ii) *Nonmonotonic and Antisymmetric Variation of Permeability*

$$k_o = 1; \quad \gamma < 1 \tag{13}$$

(iii) *Nonmonotonic and Symmetric Variation of Permeability*

$$k_o = 1 - \frac{2}{\pi}; \quad \gamma = 1 \tag{14}$$

The conditions as listed above were obtained by substituting the different permeability functions (8), (9), and (11) into Eq. (11) and equating to 1. There are of course infinitely many solutions of pairs of (γ, k_o) which fulfil this condition. For simplicity we chose $\gamma = 1$ which uniquely determines the value of k_o as listed above, except for case (ii) which is limited by $\gamma < 1$ in order to get a positive permeability throughout the domain. In case (ii), since the value of γ is arbitrary as long as $\gamma < 1$, we chose $\gamma = 0.2$. These three different permeability functions are presented graphically in Fig. 2, where it can be observed that their integral over z between 0 and 1 equals to 1 for each one of them. It is important to point out that the choice of the class of permeability function indicates the anticipated type of secondary flow in the $y - z$ plane which is expected to be consistent with the permeability gradient, i.e., the direction of a single vortex flow is anticipated to be anticlockwise for case (i) corresponding to a monotonic permeability function and a combination of multiple clockwise and anticlockwise vortices in different vertical positions is anticipated for cases (ii) and (iii). This expectation is based on the approximate analytical results presented by Vadasz (1993, 1997). A significant number of computer runs were performed for each of the three different permeability cases, and for each such case subsequent runs identified the best numerical mesh refinement parameters and number of global internal grid points. We present here only a selected number of results to highlight the significant impact of the class of permeability function on the resulting three dimensional flow field. The same unit value of Ekman number was used in all computer runs, i.e., Ek = 1.

Once the function $k(z)$ and the value of Ek are specified ($k^*(z) = k(z)/\text{Ek}$), Eq. (8) is to be solved subject to the boundary

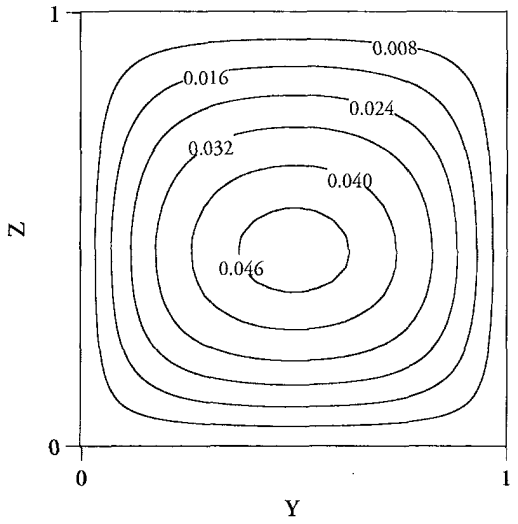

Fig. 3 Graphical description of the secondary circulation flow field in terms of streamlines for a permeability function corresponding to case (i), Eq. (10). The domain was divided into 60 by 60 internal grid points using the mesh refinement transformation parameters $r = 0.4$ and $s = 5$. The maximum value of the stream-function is $\psi_{max} = 0.04824$.

conditions: $\psi = 0$ at $y = 0$, $y = 1$, $z = 0$ and $z = 1$, which are consistent with the impermeability conditions on the channel's solid walls.

Numerical Method of Solution

Here we give a brief outline of the numerical method reported in detail earlier (Havstad and Vadasz, 1999). A mesh refinement technique closely linked to the numerical method of solution was used in order to allow solutions corresponding to wide variations of Ekman number values and to properly represent expected boundary layers. Although in the present cases, where we used $Ek = 1$, this may seem unnecessary, the results indicate that the multiple vortex secondary circulation needs such a mesh refinement if weak vortices are to be detected. The anticipation of getting boundary layers or tertiary vortices in the proximity of all solid walls suggested a transformation allowing very fine and variable discretization near the flow boundaries. The governing equations and boundary conditions suggested a transformation symmetrical around both $y = 0.5$ and $z = 0.5$. Two parameters, r and s in the transformed equations, control the degree and location of mesh refinement, while two scaling constants c_1, c_2 are chosen to keep the transformed domain boundaries between 0 and 1. Of the two parameters, r controls the slope of the distribution at the boundary and s (referred to as the damping factor) controls the rate of departure from a linear distribution.

Application of the transform and the chain rule gives the following governing equation

$$\frac{\partial^2\psi}{\partial\tilde{y}^2}\left[\frac{\partial\tilde{y}}{\partial y}\right]^2 + \frac{\partial\psi}{\partial\tilde{y}}\frac{\partial^2\tilde{y}}{\partial y^2} + [1 + (k^*)^2]\left[\frac{\partial^2\psi}{\partial z^2}\left[\frac{\partial\tilde{z}}{\partial z}\right]^2 + \frac{\partial\psi}{\partial z}\frac{\partial^2\tilde{z}}{\partial z^2}\right] + [(k^*)^2 - 1]\frac{1}{k^*}\frac{dk^*}{d\tilde{z}}\frac{\partial\psi}{\partial\tilde{z}}\left[\frac{\partial\tilde{z}}{\partial z}\right]^2 = -k^*\frac{dk^*}{d\tilde{z}}\frac{\partial\tilde{z}}{\partial z} \quad (15)$$

Solutions of this equation are obtained over a uniformly spaced grid in transform space regardless of the choice of r and s parameters (mesh refinement at the boundaries). Evaluation and substitution of the derivatives of the transforms is straightforward and these are inserted into the numerical scheme in their analytical form. Evaluation and substitution of the derivatives of the spatial dependence of the permeability is easier when done in finite difference form.

The alternating direction implicit method (ADI) (Peaceman and Rachford, 1955) and second order accurate centered finite differences were implemented to solve Eq. (15). A single relaxation parameter was used with the Thomas algorithm solution of each tridiagonal stage. Cyclical usage of a set of relaxation parameters was tried but was slower than use of a single relaxation parameter with repeated reuse of the L-U decomposition. Iteration was terminated when the fractional change in the stream function was less than $1. \times 10^{-7}$ at all grid points.

Results and Discussion

The results representing the graphical description of the secondary circulation in the $y - z$ plane for case (i), corresponding to a monotonic variation of the permeability function (see Eq. (8) and Fig. 2) are presented in Fig. 3 in terms of streamlines. The unicellular flow is counter-clockwise as expected because of the positive permeability gradient in the z direction. The flow field is substantially asymmetric with respect to $z = 0.5$ but perfectly symmetric in the y direction, i.e., with respect to $y = 0.5$. Since the Coriolis effect on the axial flow in the channel, is expressed by the term $(-\boldsymbol{\omega} \times \mathbf{q})$ in the extended Darcy's equation, it is evident that the secondary circulation in the $y - z$ plane is the result of the cross product $(-\hat{\mathbf{e}}_z \times u\hat{\mathbf{e}}_x)$. However, as soon as this secondary flow in the $y - z$ plane is established it affects back the original axial flow in the channel through the Coriolis component $(-\hat{\mathbf{e}}_z \times v\hat{\mathbf{e}}_y)$. Therefore, in order to observe this effect, a three dimensional surface plot of the resulting axial flow field $u^*(y, z)$ for case (i) is presented in Fig. 4(*a*). To observe the isolated effect of the rotation on the axial flow for case (i) we present the results of the deviation of $u^*(y, z)$ from its corresponding value associated with the case without rotation, i.e., $u_o^*(z) \equiv k^*(z)$, in Fig. 4(*b*). It is clear from Figs. 4(*a*) and 4(*b*) that a deficiency in the axial flow results in the top part of the channel (high values of z) while the rotation enhances the axial flow in the bottom part of the channel (low values of z). The streamlines representing the secondary circulation in the $y - z$ plane for case (ii), corresponding to a nonmono-

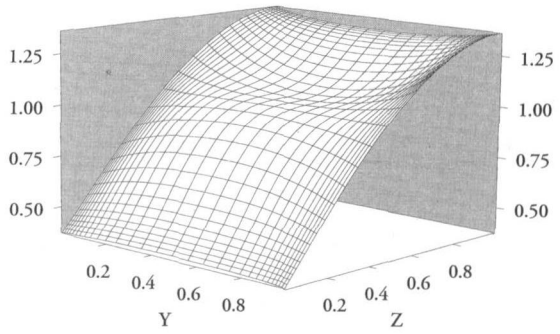

Fig. 4(*a*) Graphical description of the axial flow field $u^*(y, z)$ for a permeability function corresponding to case (i), Eq. (10). The results correspond to a division of the channel cross section into 60 by 60 internal grid points using the mesh refinement transformation parameters $r = 0.4$ and $s = 5$.

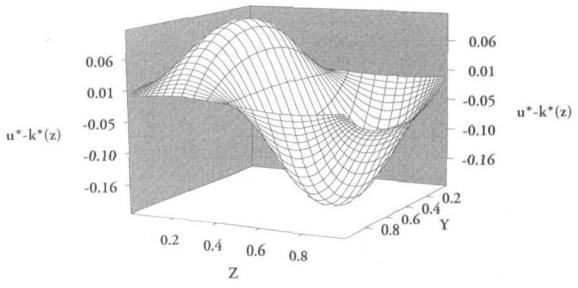

Fig. 4(*b*) Graphical description of the impact of rotation on the axial flow expressed by the deviation of the axial flow field from the corresponding flow in the absence of rotation, i.e., $u^* - u_o^* \equiv u^* - k^*(z)$.

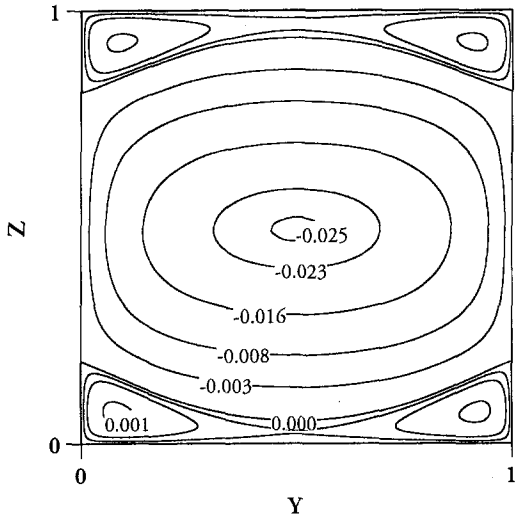

Fig. 5 Graphical description of the secondary circulation flow field in terms of streamlines for a permeability function corresponding to case (ii), Eq. (11). The domain was divided into 120 by 120 internal grid points using the mesh refinement transformation parameters $r = 0.4$ and $s = 5$. The maximum value of the stream-function is $\psi_{max} = 0.007293$ and its minimum value is $\psi_{min} = -0.0256$.

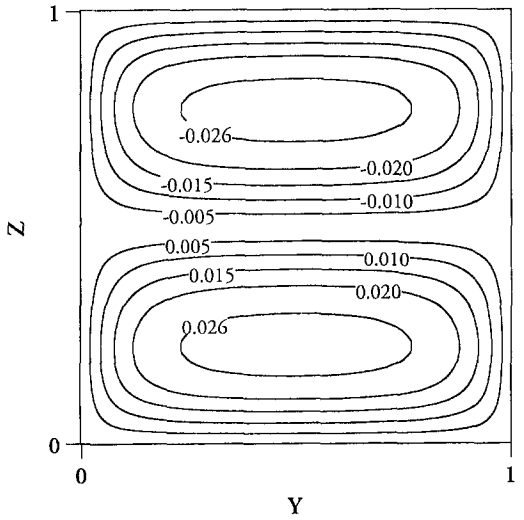

Fig. 7 Graphical description of the secondary circulation flow field in terms of streamlines for a permeability function corresponding to case (iii), Eq. (12). The domain was divided into 60 by 60 internal grid points using the mesh refinement transformation parameters $r = 0.4$ and $s = 5$. The maximum value of the stream-function is $\psi_{max} = 0.02936$ and its minimum value is $\psi_{min} = -0.02936$.

tonic and antisymmetrical variation of the permeability function (see Eq. (9) and Fig. 2) are presented in Fig. 5. The permeability function for this case is characterised by a positive vertical gradient in the close vicinity of the top and bottom walls and a negative vertical gradient in the core region. The results presented in Fig. 5 confirm the expectation of a clockwise circulation in the core region, associated with the negative permeability gradient in the z direction, and tertiary vortices near the top and bottom walls of the channel. The flow direction of these tertiary vortices is counter-clockwise, as dictated by the positive vertical permeability gradient in this region, although their intensity is weaker than the core vortex. The impact of rotation on the axial flow field for case (ii) is presented in Fig. 6(a). The isolated effect of the rotation on the axial flow for case (ii) is better observed in Fig. 6(b) which demonstrates the three dimensional features of the result. When the non-monotonic permeability function is symmetrical with respect

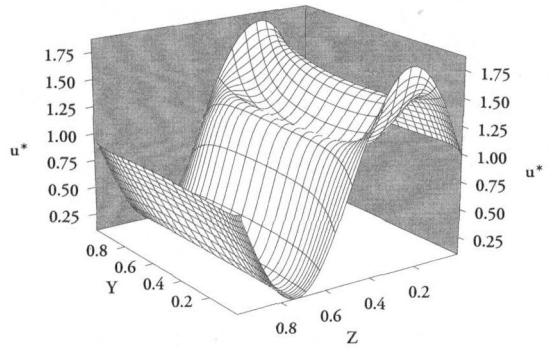

Fig. 6(a) Graphical description of the axial flow field $u^*(y, z)$ for a permeability function corresponding to case (ii), Eq. (11). The results correspond to a division of the channel cross section into 120 by 120 internal grid points using the mesh refinement transformation parameters $r = 0.4$ and $s = 5$.

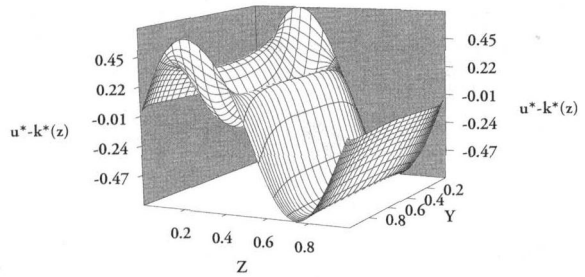

Fig. 6(b) Graphical description of the impact of rotation on the axial flow expressed by the deviation of the axial flow field from the corresponding flow in the absence of rotation, i.e., $u^* - u_o^* \equiv u^* - k^*(z)$.

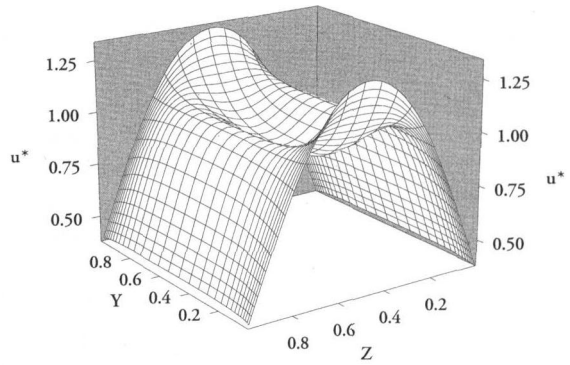

Fig. 8(a) Graphical description of the axial flow field $u^*(y, z)$ for a permeability function corresponding to case (iii), Eq. (12). The results correspond to a division of the channel cross section into 60 by 60 internal grid points using the mesh refinement transformation parameters $r = 0.4$ and $s = 5$.

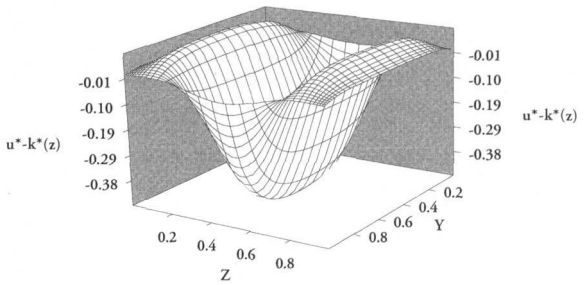

Fig. 8(b) Graphical description of the impact of rotation on the axial flow expressed by the deviation of the axial flow field from the corresponding flow in the absence of rotation, i.e., $u^* - u_o^* \equiv u^* - k^*(z)$

to the mid-plane $z = 0.5$, corresponding to case (iii), the vertical permeability gradient is positive in the bottom part of the domain and negative in the top part (see Eq. (10) and Fig. 2). As a result, a double-vortex circulation, which is symmetrical with respect to $z = 0.5$, is anticipated. The numerical results for case (iii) as presented in Fig. 7 in terms of streamlines confirm indeed this double-vortex flow with an counter-clockwise flow in the bottom half of the domain and a clockwise flow in the top half. The resulting axial flow field as presented in Fig. 8(*a*) is symmetric as well and is demonstrating again the three dimensional effect of rotation on the axial flow field. The isolated effect of rotation on the axial flow for case (iii) is better observed in Fig. 8(*b*) where it is evident that the deficiency in the axial flow is particularly focused in the core region, while the top and bottom parts of the domain contribute to an axial flow enhancement. In all cases considered it is important to stress that occurrence of axial flow deficiency may create hot spots in a corresponding forced heat convection problem and hence should be carefully accounted for, when forced convection is anticipated.

Conclusions

Results of a numerical solution to the problem of fluid flow through a long rotating square channel filled with fluid saturated porous material were presented for three classes of permeability functions varying in the vertical direction. The results and the contextual analysis of the equations indicate that a monotonic permeability function forces a unicellular secondary flow in the plane perpendicular to the imposed axial flow, while the direction of the circulation in this plane is determined by the vertical permeability gradient; a positive permeability gradient leads to a counter-clockwise secondary circulation while a negative gradient causes a clockwise unicellular vortex. For nonmonotonic permeability functions tertiary vortices appear in the corners of the cross-sectional plane in the case of antisymmetric vertical distribution of permeability and a perfectly symmetric double-vortex is obtained when the permeability variation is symmetrical with respect to the mid-plane $z = 0.5$. It was evident that in all cases the axial flow is significantly affected by rotation and its affinity to the class of permeability function as applicable was demonstrated.

Acknowledgment

The authors wish to thank the Foundation for Research Development (South Africa) for partially supporting this study through the Competitive Industry Research Grant (CIPM-GUN2034039).

References

Bear, J., 1972, *Dynamics of Fluids in Porous Media,* Elsevier, New York, pp. 131–132.

Bejan, A., 1995, *Convection Heat Transfer,* 2nd ed., Wiley, New York.

Havstad, M. A., and Vadasz, P., 1999, "Numerical Solution of the Three Dimensional Fluid Flow in a Rotating Heterogeneous Porous Channel," *International Journal of Numerical Methods in Fluids,* in press.

Nield, D. A., and Bejan, A., 1999, *Convection in Porous Media,* Springer-Verlag, New York.

Peaceman, D., and Rachford, H., 1955, "The Numerical Solution of Parabolic and Elliptic Differential Equations," *SIAM Journal,* Vol. 3, pp. 28–41.

Vadasz, P., 1997, "Flow in Rotating Porous Media," *Advances in Fluid Mechanics: Fluid Transport in Porous Media,* J. P. du Plessis, ed., Chap. 4, Computational Mechanics Publications, Southampton, pp. 161–214.

Vadasz, P., 1998, "Free Convection in Rotating Porous Media," *Transport Phenomena in Porous Media,* I. Pop and D. B. Ingham, ed., Elsevier Science, pp. 285–312.

Vadasz, P., 1993, "Fluid Flow through Heterogeneous Porous Media in a Rotating Square Channel," *Transport in Porous Media,* Vol. 12, pp. 43–54.

Vortex Detachment and Reverse Flow in Pulsatile Laminar Flow Through Axisymmetric Sudden Expansions

S. Tavoularis
Professor.

R. K. Singh
Postdoctoral Fellow.

Department of Mechanical Engineering,
University of Ottawa,
Ottawa, Ontario K1N 6N5, Canada
e-mail: tav@eng.uottawa.ca

Incompressible, steady and pulsatile flows in axisymmetric sudden expansions with diameter ratios of 1:2.25 and 1:2.00 have been simulated numerically over the ranges of time-averaged bulk Reynolds number $0.1 \leq Re \leq 400$ and Womersley number $0.1 \leq W \leq 50$. For steady flow, the calculated recirculation zone length increased linearly with an increase in Re, in good agreement with earlier experiments. For pulsatile flows, particularly at higher values of W, the recirculation zone length correlated strongly with the acceleration of the flow and not with the instantaneous Reynolds number; it increased during the deceleration phase and decreased during the acceleration phase. The computed mean velocity and reattachment length were in general agreement with published experimental data. At relatively low W, the computed near-wall, reverse flow region extended along the full domain over part of the cycle, similarly to that in the experiments. At low values of W, the vortex rings created at the expansion remained attached and oscillated back and forth; for an intermediate range of W, they detached and moved downstream; at relatively high W, these vortices became, once more, attached.

Introduction

Laminar flow in an axisymmetric sudden expansion (ASE) is a classical paradigm of a separated flow with recirculation region. Internal flows through ASE and related geometries, both steady and pulsatile, occur in many industrial and biological applications, for example in systems involving positive displacement pumps, in pulsed solid rocket motors, and in blood circulation systems, especially in diseased or injured arteries and in prosthetic devices. In several of these systems, pulsatile flows occur over wide ranges of dynamic flow parameters. In the human circulation system alone, pulsatile blood flow is encountered over the range of Reynolds number (based on peak velocity) from 10^{-3}, in the capillaries, to 4.5×10^3, in the aorta, and over the range of Womersley number (Womersley, 1955; see next section for a definition) from 0.005 to 13.5 (Fung, 1996). The understanding of the ASE flow characteristics is essential to the understanding of mixing, combustion, head loss, and heat and mass transfer in separated flows. Moreover, from a computational point of view, ASE flows can serve as idealized paradigms for the development and validation of numerical models and algorithms that could apply to the large class of engineering flows containing recirculating regions.

Pulsatile flows are known to have features which are quite distinct from those of geometrically similar steady flows. Although there have been numerous investigations of steady flows in ASE configurations (among others, Macagno and Hung, 1967; Back and Roschke, 1972 and 1976; Iribarne et al., 1972; Latornell and Pollard, 1986; and Baloch et al., 1995), there are only few studies of unsteady laminar flows in ASE and related geometries (Ahmed and Giddens, 1984; Ojha et al., 1989; Pedrizzetti, 1996). Most relevant to the present work are the experiments by Budwig et al. (1997; hereafter referred to as BET), which largely supersede those reported by Budwig and Tavoularis (1995).

The main objective of the present study was to investigate separation and reverse laminar flow in ASE over relatively wide ranges of Reynolds and Womersley numbers. In particular, our aim was to establish the pulsatile conditions under which the vortices forming at the ASE detach and travel downstream rather than remaining attached to the ASE, as in steady flows. Another feature that was investigated in detail was the phenomenon of far-field reverse flow near the wall, over part of the cycle, which is due to the pulsatile nature of the flow and is distinct from reverse flow due to the sudden expansion. This behavior has been observed by BET in their experiments in ASE and explained using a theoretical solution of pulsatile pipe flow. Finally, the present computational study provides the distribution of wall shear stress, which has not yet been measured in the available experiments. It may be noted that the wall shear stress magnitude and its gradient have been correlated with the occurrence of vascular disease, as the initial plaque thickening (atherogenesis) in arteries occurs in regions where wall shear stress is low and/or oscillates in direction during the cardiac cycle (Loth et al., 1997).

In the present study, laminar pulsatile flow has been calculated in ASE with diameter ratios of 1:2.25 and 1:2.00. First, the experimental configuration of BET was simulated and the computed results were compared with the measurements. Then, the computations were extended to cover relatively wide ranges of Reynolds numbers and Womersley numbers, which are difficult to attain in experiments. Some preliminary results of these computations have been presented by Singh et al. (1997).

Problem Definition

Figure 1 shows a schematic of the ASE geometry identifying the symbols used in this paper. Two geometrical configurations were considered: "Configuration A," which was meant to simulate the BET experiments, and "Configuration B," which was meant to simulate a new set of experiments. The latter experiments featured a vertical test section, in order to avoid the convective secondary flows that formed in the horizontal test section arrangement used by BET, but, unfortunately, they remain incomplete and cannot be discussed any further.

Configuration A: The diameter ratio for these simulations was $D/d = 2.25$ and the step height was $h = 0.626d$. The length of the downstream tube was $34.6h$. The inlet boundary condition was

Contributed by the Fluids Engineering Division for publication in the JOURNAL OF FLUIDS ENGINEERING. Manuscript received by the Fluids Engineering Division February 5, 1998; revised manuscript received April 19, 1999. Associate Technical Editor: J. A. C. Humphrey.

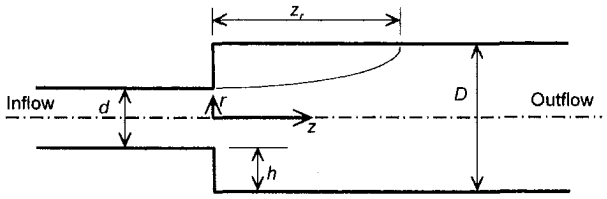

Fig. 1 Schematic diagram of the ASE geometry.

applied at a location $4.72d$ upstream of the expansion, which is where, in the BET experiments, flow entered the small tube through a smooth bell-mouth mounted in the feed tank. The inlet velocity profile was taken to be uniform and the time-dependent inlet velocity was specified to match the experimental waveform presented by BET, which can be approximated as $U(t) = U_o(1 + 0.57 \sin \omega t)$, where U_o is the bulk velocity in the smaller tube, t is the time, and ω is the circular frequency of pulsation in rad/s. The time-averaged, bulk Reynolds number, $\mathrm{Re} = U_o d/v$, was set at 121 (v is the kinematic viscosity of the fluid), so that the pulsatile-amplitude Reynolds number was 69. The Womersley number, $W = (d/2)(\omega/v)^{1/2}$, was set to 5.0.

Configuration B: The diameter ratio for these simulations was $D/d = 2.00$ and the step height was $h = 0.50d$. The length of the downstream tube was $43.4h$. The inlet boundary condition was applied at a location $7.07d$ upstream of the expansion. The time-dependent, uniform, inlet velocity was specified as $U(t) = U_o(1 + 0.50 \sin \omega t)$. A large number of pulsatile flow cases with $0.1 \leq \mathrm{Re} \leq 400$ and $0.1 \leq W \leq 50$ were computed.

Computational Procedures and Accuracies

The computations were performed on an IBM RS6000 workstation, using the commercial CFD code FIDAP (FIDAP 7.6, 1996; Engelman, 1982; Sohn, 1988) to solve the time-dependent Navier-Stokes equations. This method employs Galerkin's weighted residual approach in conjunction with the finite element approximation. Within each element, the different variables are interpolated by functions of order compatible with the set of nodal points and the resulting approximations are substituted into the unsteady Navier-Stokes equations for an incompressible Newtonian isothermal fluid without body forces. The errors resulting from the use of this approximation are reduced by being made orthogonal to the interpolation function for each finite element. Then, the resulting equations are transformed into integral equations using the Green-Gauss theorem to convert the second-order terms and pressure term to first-order terms plus a surface integral. These equations are rewritten as matrix equations with coefficients determined from the quadrature procedure and the successive substitution method is used to solve the resulting global matrix equation. The second-order trapezoidal scheme with implicit time integration was used to solve the unsteady cases.

An axisymmetric finite element mesh was employed, which has substantially lower memory and disk storage requirements than a three-dimensional mesh. Nine-node quadrilateral elements were used in all cases. The element size was reduced smoothly approaching the solid wall and toward the separation region to improve the resolution in areas of high gradients. The boundary conditions applied were the zero radial and azimuthal velocities at the inlet, the no-slip condition at the wall, the zero radial velocity along the axis of symmetry, and a uniform velocity at the inlet to the small tube. The stress-free boundary condition that arises naturally from the application of the finite element method to the flow equations in a truncated domain was maintained as the outflow condition. The time-dependent inlet velocity variation was represented by twelve equally spaced points per cycle. Convergence of the solution for each time step was assumed when the relative changes of the different unknowns and the relative changes in the residuals became smaller than 0.001. Such convergence was usually attained within 2–6 iterations for each time step.

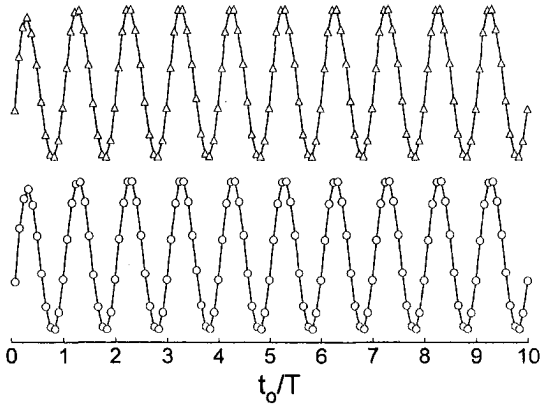

Fig. 2 Variation of flow velocity on the axis and on the ASE plane for Configuration A, computed using 12 time steps per cycle, Re = 121 and W = 5; the numbers of nodes were 4651 (○) and 8929 (△); scales are arbitrary but the same in both plots.

The results reported below were obtained using an axisymmetric mapped mesh with 4989 nodal points for the Configuration A computations and 4569 nodes for the Configuration B computations. Independent computations were carried out to establish that these mesh densities were sufficient. The nearly 100% refinement of the computational mesh for Configuration A from 4651 nodes (1275 elements) to 8929 nodes (2391 elements) produced essentially the same results. As an example, this is illustrated in Fig. 2 by the time history of the velocity on the axis and on the expansion plane; in this figure, as well as in the next two figures, t_o indicates the time from the start of computations. Similar time history plots for several other representative positions in the computational domain, as well as streamline plots at different time steps, were inspected and they all showed indistinguishable differences when comparing corresponding results computed with the coarser and finer meshes.

A test of the sufficiency of the time discretization increment was carried out by repeating the computations for two sets of Re-W combinations using 24 rather than the usual 12 time steps. Representative results shown in Figs. 3 and 4 demonstrate indistinguishable differences in the corresponding time histories.

The pulsatile flows were computed using the corresponding steady flow solution at the same mean Re as the initial condition. An issue of concern was to carry the computations over time sufficiently long for a "periodic" solution (namely a solution that did not change measurably, i.e., by more than 0.1%, from one cycle to the next) to be attained. Figures 2 to 4 show that the velocity on the axis and on the expansion plane reached a periodic

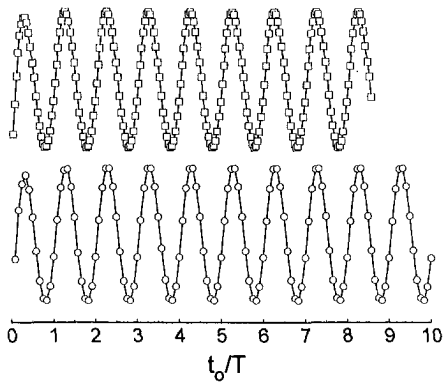

Fig. 3 Variation of flow velocity on the axis and on the ASE plane for Configuration A, computed using 4651 nodes, Re = 121 and W = 5; the numbers of time steps per cycle were 12 (○) and 24 (□); scales are arbitrary but the same in both plots.

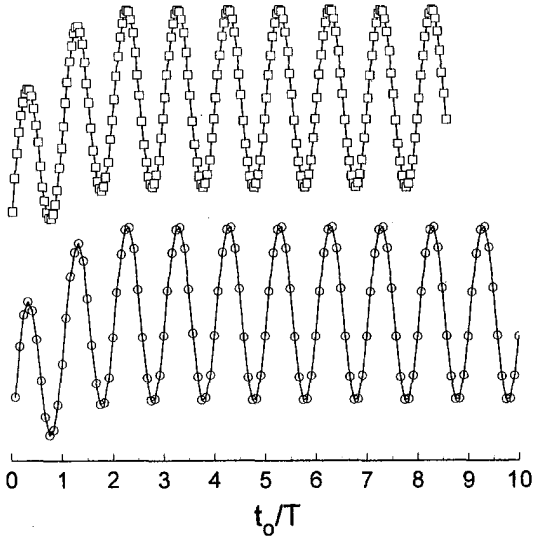

Fig. 4 Variation of flow velocity on the axis and on the ASE plane for Configuration A, computed using 4651 nodes, Re = 300 and W = 15; the numbers of time steps per cycle were 12 (○) and 24 (□); scales are arbitrary but the same in both plots.

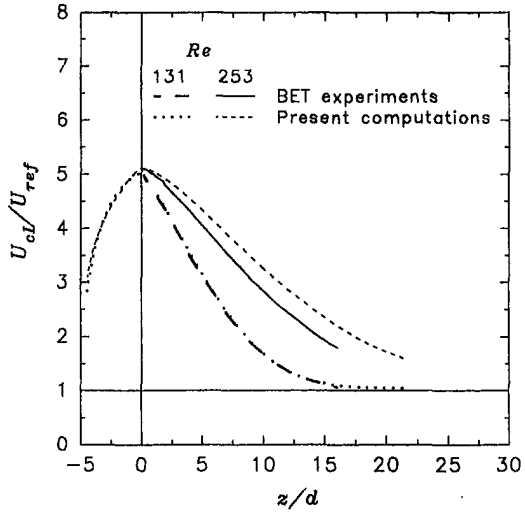

Fig. 5 Axial development of centerline velocity (configuration A). The time averaged centerline velocity in the far-field was U_{ref} = 0.0246 m/s for Re = 131 and 0.0424 m/s for Re = 253.

state within only a couple of cycles. On other locations, periodic solutions took somewhat longer to attain, but never beyond seven cycles. To avoid any chance for transient effects, all reported results correspond to the ninth cycle.

Simulation of the BET Experiments

These preliminary simulations were conducted in order to establish that the present computational study produces realistic results, comparable to the available experimental ones. First, steady flow computations were performed for Configuration A, at Re = 131 and 253, which are identical to those in measurements reported by BET. The recirculation zone length, z_r, was estimated from streamline plots (up to the reattachment point of the separating streamline) as well as from axial velocity contour plots (up to the location of zero wall shear stress). Both methods resulted in nearly the same lengths. The computed dimensionless reattachment lengths (see Fig. 1) at Re = 131 and 253 were z_r/h = 12.1 and 21.6, respectively, somewhat shorter than the experimental values 14.4 and 24.8. However, the reattachment length depends strongly upon the upstream flow condition and the experimental method, and, even for the same expansion ratio, appreciably different results have been found in different studies (Latornell and Pollard, 1986). The agreement between the computed and measured variations of the centerline velocity U_{cL} for steady flow was excellent for Re = 131 and fair for Re = 253, as shown in Fig. 5.

Then, pulsatile flow computations were conducted at conditions simulating those in the BET experiments, namely at Re = 121 and W = 5.0. Figure 6 presents streamlines at eight different dimensionless times t/T (= 0.00, 0.125, 0.25, 0.375, 0.50, 0.625, 0.72 and 0.875) during the ninth pulsatile cycle, which clearly show the existence of several vortices in the flow downstream of the ASE location. As many as three vortices could be easily identified. Some plots have a slight waviness at a location downstream of the third vortex, which is the signature of another vortex that has nearly been annihilated by viscous actions. It was found that, during the first half of the acceleration phase, the recirculation zone decreased, the third vortex disappeared (at $t/T \approx 0.25$), and the first and second vortices were separated, until, finally, the second vortex also disappeared, nearly half way in the acceleration phase. After this, the recirculation zone started growing again. Contours of the axial velocity, not shown here, were used to determine the reattachment length, which, as shown in Fig. 7, was in reasonable agreement with the BET results. BET showed that the variation pattern of this length was quite opposite to the estimated variation in steady flow at the same instantaneous Reynolds number, which demonstrates that quasi-steady estimates

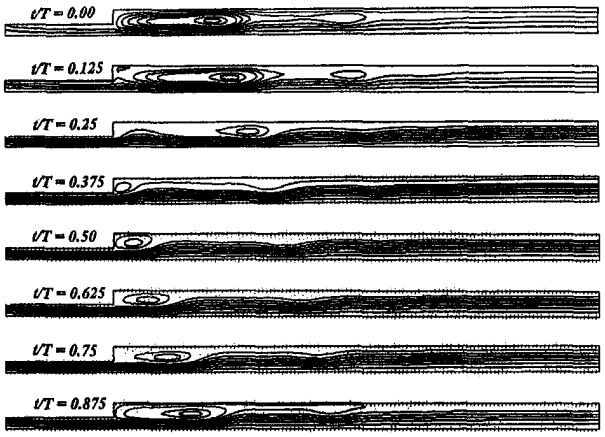

Fig. 6 Streamline plots during a pulsatile flow cycle (Re = 121, W = 5.00; Configuration A).

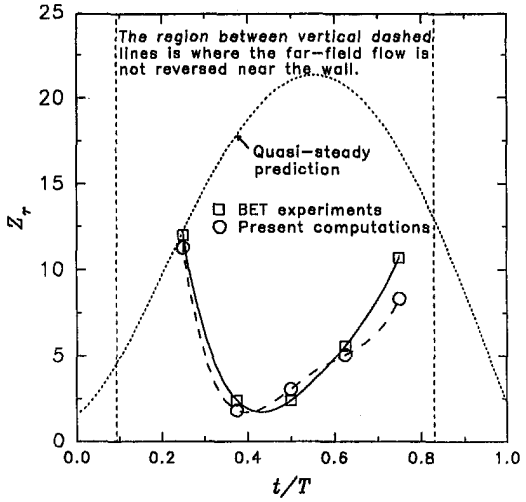

Fig. 7 Reattachment length in pulsatile flow (Re = 121, W = 5.00; Configuration A).

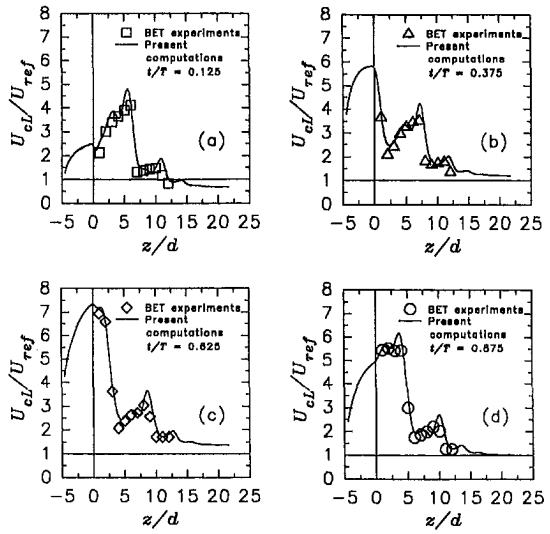

Fig. 8 Axial development of instantaneous centerline velocity in pulsatile flow (Re = 121, W = 5.0; U_{ref} = 0.0224 m/s; Configuration A).

would be totally inappropriate. Another observation in the present computations, as well in the BET experiments, was that, during part of the cycle, the near-wall flow reversed direction not only near the expansion plane, but also far downstream, all the way to the exit plane. As demonstrated analytically by BET, this is not a result of sudden expansion but of flow pulsation, as it would occur even in an infinite-length, circular tube. The boundaries of the time interval for this reverse flow occurrence have been indicated by dashed lines in Fig. 8; obviously, no reattachment length can be defined in this time interval. Vorticity plots, although subjected to considerable uncertainty, also indicated at least three vorticity peaks during part of the cycle. These axisymmetric vortices moved downstream and their energy dissipated until they finally became undetectable. The vortex strength decreased very rapidly once the vortex detached, at the beginning of an acceleration phase. Finally, the variation of the computed centerline velocity was in very good agreement with the BET experimental data, as shown in Fig. 8.

In conclusion, one may assess that the present simulations reproduce faithfully all main phenomena observed by BET and could, therefore, be used for further detailed studies of ASE flows.

Steady Flow Separation and Recirculation

Steady flows with uniform entrance profiles in both configurations were investigated for mean Reynolds numbers from 0 to 400. The lengths of the recirculation zone were found to increase with an increase in Re, in agreement with earlier computations and experiments. The variation of the reattachment length with Re was nearly linear, in agreement with the findings of Latornell and Pollard (1986) and it could be represented by the expression $z_r/h = \kappa$ Re, where the coefficient κ was 0.058 for Configuration A and 0.080 for Configuration B. Latornell and Pollard (1986) have demonstrated that this coefficient depends on the inlet velocity profile and the expansion ratio. In the present computations, a uniform inlet profile was imposed at some location upstream from the sudden expansion, which resulted in a partially developed profile at the plane of expansion. For comparison, in their flow visualization study in an ASE with D/d = 2.0, Latornell and Pollard (1986) estimated that κ = 0.096 for a fully developed, parabolic inlet profile (Re < 920), and κ = 0.068 for a uniform inlet profile (Re < 620). The present value of κ for Configuration B is between the above two values, which is consistent with the notion of flow development.

Vortex Detachment

An important issue concerning mixing and mass transfer in pulsatile flows at ASE is whether the separated region remains attached to the ASE or travels downstream. A large number of computations were conducted for both configurations and different combinations of Re and W. The vortex center was identified visually from streamline plots (such as the ones shown in Fig. 6), and it was generally different from the peak vorticity position, identified from vorticity contour plots. In cases of multiple vortices, the one considered was that closest to the ASE site. A typical set of results, showing the streamwise position of the vortex center for a fixed Re = 100 and different values of W, at different times during the pulsatile cycle, is presented in Fig. 9, which also shows the inlet velocity variation. These results can be classified into three, qualitatively distinct, classes:

(*a*) In the low W-range (W = 0.1, 1 and 2), the vortex oscillated back and forth during the cycle, while remaining attached to the ASE. In this range, the inertia acquired by the vortex during the acceleration phase was not sufficient to detach it and fluid particles trapped within the vortex may remain in the system indefinitely. Although, in this respect, the pulsatile flow resembled steady flow, it was only for the very lowest W value (W = 0.1) that the pulsatile flow patterns were comparable to those in steady flow at the same instantaneous Re. For W = 1 and 2, the oscillation of the recirculating region was non-sinusoidal and out of phase with the inlet velocity variation for both examined Re = 10 and 100.

(*b*) In the intermediate W-range (W = 3, 4 and 5), the vortex moved continuously downstream and was eventually washed out from the downstream end or faded away due to viscous decay. The lines in Fig. 9(*b*) were terminated when a second vortex appeared

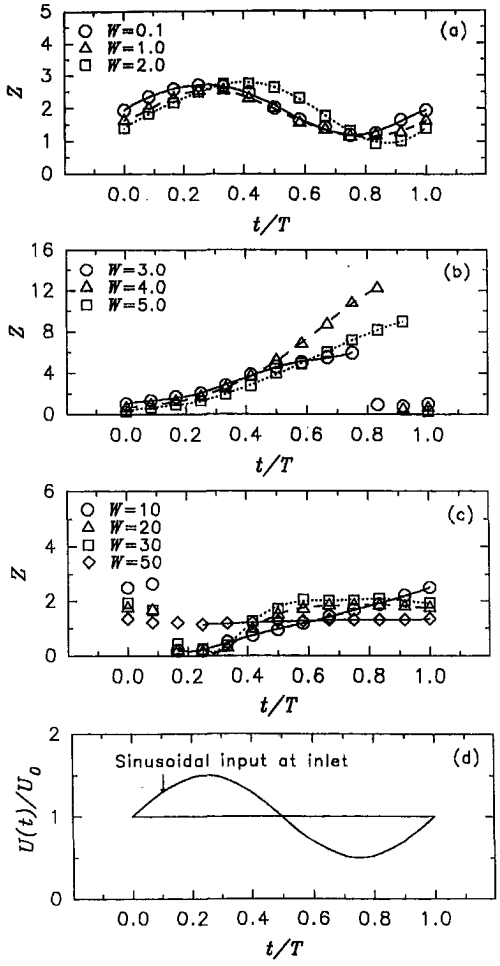

Fig. 9 (*a, b, c*) Position of the vortex center at different W (Re = 100; Configuration B; lines are for visual aid only); (*d*) variation of the inlet velocity.

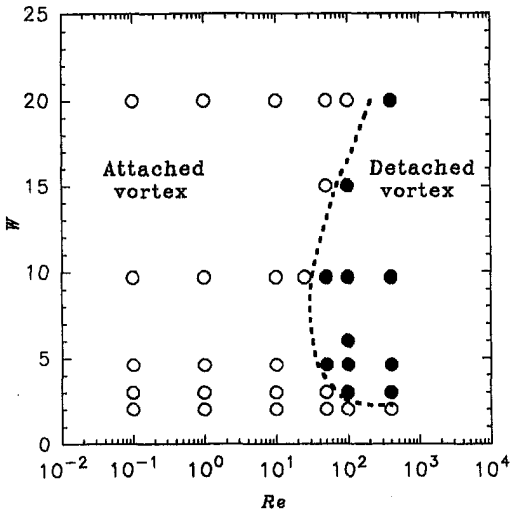

Fig. 10 Vortex detachment in pulsatile ASE flow. Filled symbols indicate a detached vortex (Configuration B).

closer to the ASE, an event that, in those cases, occurred late in the cycle.

(*c*) In the high *W*-range (W = 10, 20, 30 and 50), the vortex pattern gradually changed again. For $W = 10$, the original vortex was detached and travelled downstream but was not detectable for long, as its energy dissipated quickly; in the meantime, a second vortex formed, but, unlike for cases b above, this happened during the initial part of the subsequent cycle. A similar behavior was observed for $W = 15$ (not shown here). For $W = 20$ and 30, a second vortex never appeared and the single vortex oscillated about a mean position close to the plane of expansion. The amplitude of oscillation decreased with increasing W, until, at $W = 50$, the vortex center nearly stabilized at a fixed position, which was comparable to the value $1.7h$ in steady flow at the same Re. This indicates that the vortex could not follow the high frequency pulsations and was essentially steady.

Figure 9 also shows another important feature of vortex formation in pulsatile flows. Let us define the dimensionless vortex inception time, t_i/T, as the moment of the cycle when the vortex closest to the ASE could first be observed. As Fig. 9 shows, the inception time was strongly dependent on the value of W. For $W = 3$, 4, and 5, it was, respectively, 0.83, 0.92, and 1.00, which correspond to parts of the cycle where the flow acceleration was strong and persistent. For higher values of W, the second vortex started during the subsequent cycle. For $W = 10$, $t_i/T = 0.17$, which was still within, although close to the end of, the accelerating phase, and the vortex detached from the ASE. For $W = 20$, 30, and 50, vortex inception occurred at $t_i/T = 0.25$, which is near the start of the deceleration phase; in these cases, the vortex never appeared to detach, because it did not receive the required impulse. In conclusion, vortex detachment depends on whether vortex inception occurs during flow acceleration or flow deceleration, and, therefore, it should also depend on the inlet flow waveform shape.

The results of all relevant computations have been summarized in Fig. 10, which clearly identifies the range of Re-W combinations over which vortex detachment occurs. It may be seen that, at low Re (Re < 25), the vortex remains always attached, irrespective of pulsation frequency, as viscous effects always dominate inertial effects. Furthermore, at very low W, the vortex also remains attached, irrespective of the value of Re (at least within the considered range Re < 400). At low pulsation frequencies, the acceleration is not sufficient to detach the vortex; however, one has to keep in mind that, even in this low W-range, vortex detachment might occur if the pulsatile waveform is such as to cause higher acceleration than the presently considered sinusoidal variation. For Re > 25, the three classes of vortical flows identified above may be observed.

Far-Field Flow Reversal

As mentioned earlier, both the BET experiments and their present simulations have identified a part of the cycle over which reverse flow near the wall extended till the downstream end of the flow domain. This may have important practical implications as it would allow fluid from the discharge reservoir to penetrate into the tube. Reverse flow in ASE may occur for two distinct, although interconnected, reasons: first, due to separation at the ASE, and, second, due to the pulsatile nature of the flow. Reverse flow regions may occur in pulsatile flows even in tubes with a uniform cross section and even when the inlet velocity never reverses direction (Atabek and Chang, 1961; Cho and Hyun, 1990). To resolve the conditions under which far-field reverse flow occurs, the results of the present computations over wide ranges of Re and W were examined carefully. Both streamlines and axial velocity contours were plotted over many time steps for each case. The results have been summarized in Fig. 11, which shows that, for a fixed Re, far-field flow reversal occurs for W higher than a certain value (typically 5 or less) and does not occur when W drops below that value. The critical W appears to decrease somewhat with increasing Re; although we have no results to support this speculation, it is possible that, at sufficiently large Re, no reversal would occur at any W.

Streamwise Length Scale of the Vortices

A dimensionless measure of the pulsatile amplitude of the streamwise motion is the Keulegan-Carpenter number, defined as $Kc = (U_{op}T)/(d/2)$, where U_{op} is the peak bulk velocity in the upstream tube and $T = 2\pi/\omega$ is the time period of the pulsatile flow cycle. This parameter can also be expressed as $Kc = \pi(U_{op}/U_o)(\mathrm{Re}/W^2)$. In the present computations, Kc varied over a very wide range, from 0.005 to 47000, while, for comparison, in the BET experiments, $Kc = 23.9$. In conformity with physical expectation, the vortices were found to become more elongated as Kc increased and, in cases where they were detached, their spacing increased as Kc increased. For example, at a fixed Re = 100 (Configuration B), the distance between the centers of consecutive vortices, normalized by the step height h, took the values 2.9, 7.0 and 10.0, respectively, when $Kc = 5.0$, 13.1, and 22.0 (i.e., when $W = 9.7$, 6.0, and 4.6, respectively). Similar results have been reported by Pedrizzetti (1996) for pulsatile flow in a gradual axisymmetric expansion.

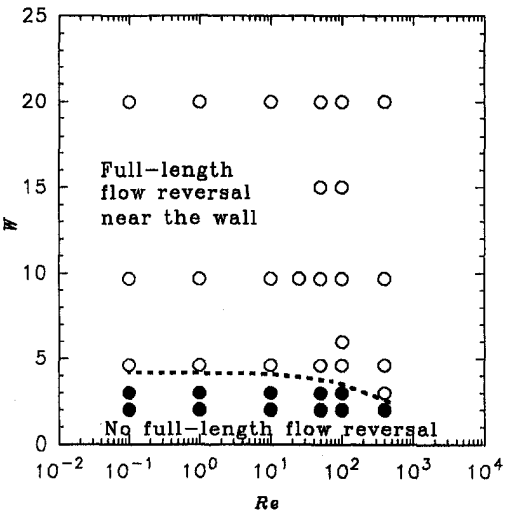

Fig. 11 Full-length, near-wall flow reversal in pulsatile ASE flow. Filled symbols indicate only partial near-wall flow reversal (Configuration B).

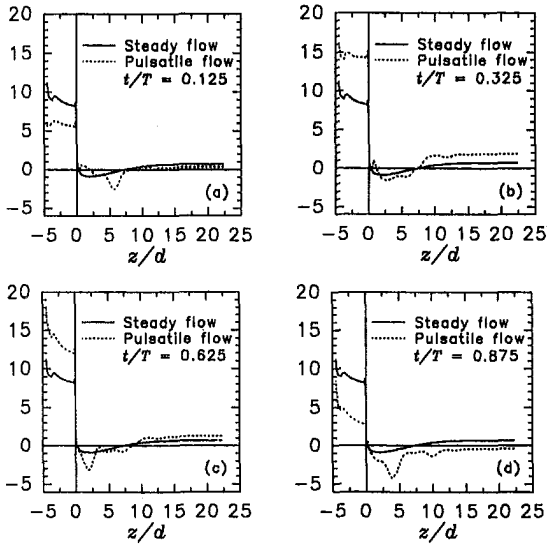

Fig. 12 Computed nondimensional wall shear stress distributions in steady (Re = 121) and pulsatile (Re = 121, $W = 5.0$) flows (Configuration A).

Wall Shear Stress

Examples of the computed wall shear stress variation in both steady and pulsatile flows corresponding to the BET experiments have been presented in Fig. 12, nondimensionalized by the parameter $\mu U_o/d$, where μ is the fluid viscosity. In the upstream tube the pulsatile wall shear stress fluctuated by as much as 70% around the steady value, while in the downstream tube it developed relatively strong instantaneous streamwise gradients. Such issues would be of concern in cardiovascular applications (Kuban and Friedman, 1995).

Conclusions

Numerical solutions to the Navier-Stokes equations have been presented for steady and pulsatile laminar flow through axisymmetric sudden expansions over a wide range of flow and frequency parameters. Both the steady and the pulsatile flow computations were in general agreement with the experimental results of BET. In steady flow the reattachment length was proportional to the Reynolds number. In pulsatile flow, axisymmetric vortex rings formed at the expansion and oscillated back and forth while remaining attached to the expansion site, or detached and moved downstream, depending on the combination of values of Reynolds and Womersley numbers. Near wall reverse flow was found to occur along the full computational domain over part of the pulsatile cycle at all examined Re and sufficiently low W. The longitudinal length scale of flow oscillation decreased rapidly with an increase in W. This study also shows relatively large gradients of the instantaneous wall shear stress in the recirculation region of pulsatile flows.

Acknowledgment

The financial support of the Natural Sciences and Engineering Research Council of Canada is gratefully acknowledged.

References

Ahmed, S. A., and Giddens, D. P., 1984, "Pulsatile Poststenotic Flow Studies with Laser Doppler Anemometry," *Journal of Biomechanics,* Vol. 17, pp. 695–705.

Atabek, J. B., and Chang, C. C., 1961, "Oscillatory Flow Near the Entry of a Circular Tube," *Zeitschrift für Angewandte Mathematik und Physik,* Vol. 12, pp. 185–201.

Back, L. H., and Roschke, E. J., 1972, "Shear-Layer Flow Regimes and Wave Instabilities and Reattachment Lengths Downstream of an Abrupt Circular Channel Expansion," ASME *Journal of Applied Mechanics,* Vol. 39, pp. 677–681.

Back, L. H., and Roschke, E. J., 1976, "The Influence of Upstream Conditions on Flow Reattachment Lengths Downstream of an Abrupt Circular Channel Expansion," *Journal of Biomechanics,* Vol. 9, pp. 481–483.

Baloch, A., Townsend, P., and Webster, M. F., 1995, "On Two- and Three-Dimensional Expansion Flows," *Computers & Fluids,* Vol. 24, No. 8, pp. 863–882.

Budwig, R., and Tavoularis, S., 1995, "Steady and Pulsatile Flows Through an Axisymmetric Sudden Expansion," *Proceedings of the Forum on Unsteady Flows,* ASME FED-Vol. 216, pp. 55–60.

Budwig, R., Egelhoff, C. J., and Tavoularis, S., 1997, "Laminar Pulsatile Flow Through an Axisymmetric Sudden Expansion," ASME JOURNAL OF FLUIDS ENGINEERING, Vol. 119, pp. 208–211 (referred to as BET).

Chebbi, B., and Tavoularis, S., 1990, "Low Reynolds Number Flow in and above Asymmetric, Triangular Cavities," *Physics of Fluids,* Vol. A2, pp. 1044–1046.

Cho, H. W., and Hyun, J. M., 1990, "Numerical Solutions of Pulsatile Flow and Heat Transfer Characteristics in a Pipe," *International Journal of Heat and Fluid Flow,* Vol. 11, pp. 321–330.

Engelman, M. S., 1982, "FIDAP-A Fluid Dynamics Analysis Package," *Advanced Software Engineering,* Vol. 4, p. 163.

FIDAP *Users Manuals,* 1996, Version 7.6, Fluid Dynamics International, Inc., Evanston, USA.

Fung, Y. C., 1996, *Biomechanics, Circulation,* 2nd Edition, Springer-Verlag.

Iribarne, A., Frantisak, F., Hummel, R. L., and Smith, J. W., 1972, "An Experimental Study of Instabilities and Other Flow Properties of a Laminar Pipe Jet," *AIChE Journal,* Vol. 18, pp. 689–698.

Kuban, B. D., and Friedman, M. H., 1995, "The Effect of Pulsatile Frequency on Wall Shear in a Compliant Cast of a Human Aortic Bifurcation," ASME *Journal of Biomechanical Engineering,* Vol. 117, pp. 219–223.

Latornell, D. J., and Pollard, A., 1986, "Some Observations on the Evolution of Shear Layer Instabilities in Laminar Flow through Axisymmetric Sudden Expansions," *Physics of Fluids,* Vol. 29, pp. 2828–2835.

Loth, F., Jones, S. A., Giddens, D. P., Bassiouny, H. S., Glagov, S., and Zarin, C. K., 1997, "Measurements of Velocity and Wall Shear Stress Inside a PTFE Vascular Graft Model Under Steady Flow Conditions," ASME *Journal of Biomechanical Engineering,* Vol. 119, pp. 187–216.

Macagno, E. O., and Hung, T. K., 1967, "Computational and Experimental Study of a Captive Annular Eddy," *Journal of Fluid Mechanics,* Vol. 28, pp. 43–64.

Ojha, M., Cobbold, R. S. C., Johnston, K. W., and Hummel, R. L., 1989, "Pulsatile Flow Through Constricted Tubes: An Experimental Investigation using Photochromic Tracer Methods," *Journal of Fluid Mechanics,* Vol. 203, pp. 173–197.

Pedrizzetti, G., 1996, "Unsteady Tube Flow over an Expansion," *Journal of Fluid Mechanics,* Vol. 310, pp. 89–111.

Singh, R. K., Paquin, S., Boy, J.-M., Deslandes, A., and Tavoularis, S., 1997, "Numerical Simulation of Laminar Pulsatile Flow in Axisymmetric Sudden Expansions," *Proceedings of the Symposium on Separated and Complex Flows,* ASME FED Summer Meeting, paper number FEDSM97-3320.

Sohn, J. L., 1988, "Evaluation of FIDAP on Some Classical Laminar and Turbulent Benchmarks," *International Journal for Numerical Methods in Fluids,* Vol. 8, pp. 1469–1490.

Womersley, J. R., 1955, "Method for the Calculation of Velocity, Rate of Flow and Viscous Drag in Arteries when the Pressure Gradient is Known," *Journal of Physiology,* Vol. 127, pp. 553–563.

Study on Side-Jet Injection Near a Duct Entry With Various Injection Angles

Tong-Miin Liou
Professor.
Fellow ASME
e-mail: tmliou@tmp.nthu.edu.tw

Chin-Chun Liao
Graduate Student.

Shih-Hui Chen
Graduate Student.

Hsin-Ming Lin
Graduate Student.

Department of Power Mechanical Engineering,
National Tsing Hua University,
Hsinchu, Taiwan 30043, R.O.C.

Turbulent flowfields resulting from an oblique jet injecting from a rectangular side-inlet duct into a rectangular main duct with an aspect ratio 3.75 without a forced crossflow are presented in terms of laser-Doppler velocimetry measurements. The main focuses are the effects of the side-jet angle (θ) and side-jet flow rate (Q_s) on the mass entrainment upstream of side-jet port and the flowfield in the rectangular duct. The side-inlet angles investigated were 30, 45, and 60 deg and Reynolds numbers based on the air density, rectangular duct height and bulk mean velocity were in the range of 7.1×10^3 to 3.6×10^4 corresponding to Q_s values of 1×10^3 to 5×10^3 L/min. The present study suggests the presence of a critical side-injection angle θ_c ($30 \leq \theta_c \leq 45$ deg) above which a recirculation zone appears in the rectangular duct, whereas below which the recirculation zone is absent. For the more tangential angle ($\theta = 30$ deg), almost as much fluid is entrained into the main duct as was injected from the side jet. The mean flow field in the rectangular duct is found to be a weak function of the Reynolds-number for the range of Q_s investigated. In addition, a simple linear correlation between the mass entrainment upstream of the side-jet port and side-injection angle is obtained. Complementary flow visualizations and numerical computations with an algebraic Reynolds stress model were also performed. The discrepancies between measured and computed results are documented.

Introduction

The injection of a jet into a uniform or nonuniform crossflow is encountered in many engineering applications, such as the dispersion of exhaust gases from a smoke stack into the wind, the discharge of effluents into a river, the transition from hover to forward flight of a V/STOL aircraft, the film cooling of turbine blades, and the mixing process for the combustor cooling. However, in some cases, for instance, the entrainment of jet pumps and the breath of fresh air in tunnel ventilation, the crossflowing fluid is originally absent but solely induced by the jet. The present study is related to the latter application (Fig. 1). As the jet issues from a nozzle into a forced or induced crossflowing stream, there is a complicated interaction between the jet and the crossflow. The physical mechanisms involved are still not well understood and need further investigation.

Experimental and analytical studies of the jet in a crossflow have been conducted by a number of investigators. A qualitative description of the complex mechanisms occurring in the turbulent jet in a crossflow was presented by Abramovich (1963). Keffer and Baines (1963) studied a jet issuing normally into a uniform velocity crossflow and gave a detailed discussion of the physics imbedded in the jet-crossflow interaction. Bergeles et al. (1976) measured velocity distributions of the jets and found that, for low jet-to-crossflow velocity ratios, the velocity profile across the exit plane of the jet can be considerably nonuniform. A more complete measurement of the mean-flow velocity characteristics in the entire mixing region of a jet in crossflow can be found in Crabb et al. (1981), but their turbulence measurement only included the Reynolds shear stress. Laser-Doppler velocimetry (LDV) was applied to the higher-turbulence upstream region, and hot-wire anemometry to the low-turbulence downstream region. Andreopoulos (1982) presented a study of velocity fluctuation statistics in the jet-pipe flow issuing perpendicularly into a cross stream for various values of jet-to-crossflow velocity ratios.

The jet injection angle investigated by most of the investigators is normal to the crossflow. Experiments on oblique jets have been made by Platten and Keffer (1971) for θ from 45 to 135 deg at 15 deg intervals where θ is the angle between the jet and the crossflow (Fig. 2). Later, Sucec and Bowley (1976) presented a semianalytical prediction of the trajectory of a jet issuing at various angles into a crossflowing stream, and the results agreed well with experimental data over a range of jet to crossflow velocity ratios of 2 to 18.

In all the previous research, the axial flow upstream of the side-jet port is not induced by the side-jet entrainment but exists originally. Fewer investigations have been made about the entrainment effect. Simizu (1987) discussed the entrainment effect when they studied the annular type jet pumps. The main focus of their investigation was the relation between configuration and performance of the jet pumps. A simple empirical correlation between the air entrainment rate and the jet flow rate was developed by Akiyama and Marui (1988). Both of their jet flows are coaxial with the main duct, which differs from the side jet injection of the present work.

The brief survey presented above reveals that most of the above-mentioned studies are concerned with the jet issuing from a nozzle into an unbounded crossflowing stream at a normal angle. To complement these previous works, the present study investigates an oblique jet injecting into an initially quiescent rectangular duct. That is, the crossflowing stream, which does not exist originally, is solely entrained by the oblique jet from a rectangular side-inlet duct. In addition, very few detailed measurements of turbulence quantities and investigations of the relation between the jet injection angle and the flow structure have been reported so far. Hence, the present work measures the mean velocity and turbulence quantities using LDV to characterize the flow field resulting from an oblique jet injected into a rectangular duct without forced cross flow. The main parameters studied are the injection angle and the side-jet flow rate. Moreover, the mass entrainment upstream of the side-jet port, which is believed to be useful for practical applications, is also examined. The entry flow pattern, which is

Contributed by the Fluids Engineering Division for publication in the JOURNAL OF FLUIDS ENGINEERING. Manuscript received by the Fluids Engineering Division November 23, 1998; revised manuscript received May 13, 1999. Associate Technical Editor: Khairul B. M. O. Zaman.

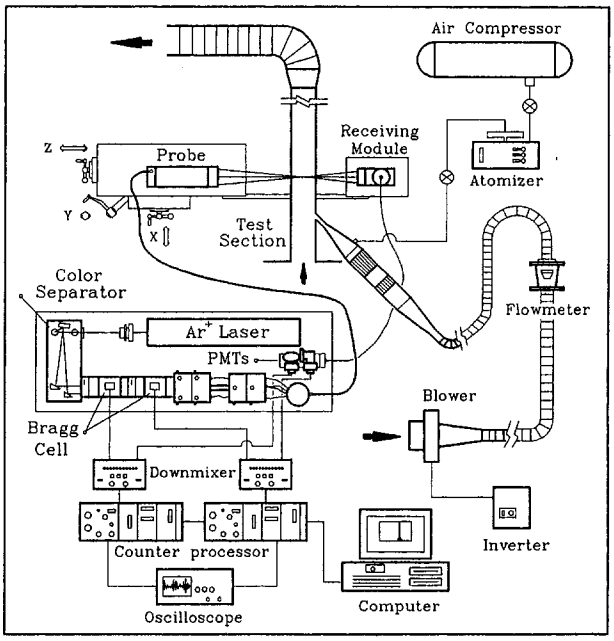

Fig. 1 Schematic drawing of overall experimental system

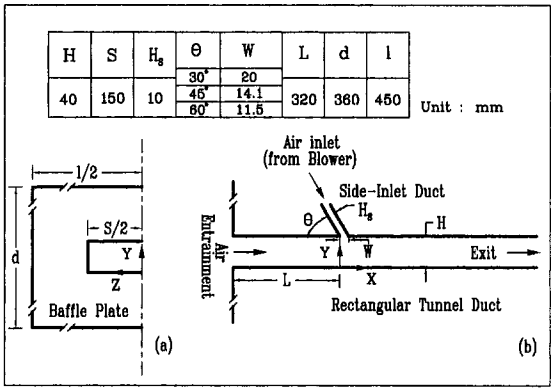

Fig. 2 Sketch of configuration, coordinate system, and dimensions of test model

difficult to measure due to the blockage of the baffle plate (Fig. 2), is complementarily revealed by a numerical computation. Flow visualizations and numerical computations are also performed to complement LDV measurements.

Experimental Apparatus and Conditions

Experimental System. The flow system and LDV experimental setup are shown schematically in Fig. 1. Air was blown into the rectangular test duct through a bellows, a flowmeter, a 1:4 diffuser, a settling chamber with honeycombs and screens, a 10.3:1 contraction, and the side-inlet by a blower (3480 rpm/3 phase/5 hp) at the upstream end. Air upstream of the axial inlet was entrained into the rectangular duct by the shear of the side jet. The side-inlet fluids joining the upstream entrainment fluids flowed through the rectangular duct, a diffuser, and a bellows and was exhausted into the atmosphere.

A two-color, 514.5 nm (green) and 488 nm (blue) lines, four-beam two-component fiberoptic probe LDV system was set up in a forward or off-axis scattering configuration. A 5-W argon-ion laser provided the coherent light source. A Bragg cell was used to cause a 40-MHz frequency shift to eliminate the ambiguity of flow direction and fringe bias. The single-mode polarization-preserving fibers carried the laser power to the probe head, where the light from each fiber was collimated. The four collimated beams were focused into the test model to form a probe volume with two nominally orthogonal sets of fringes. The approximate probe volume dimensions, based on $1/e^2$ extent of light intensity, were 0.181 mm in diameter and 2.601 mm in length (350 mm focal-length lens) or 0.313 mm in diameter and 7.68 mm in length (600 mm focal-length lens). The light scattered from the seeding particles was collected by a receiving optics assembly and finally reflected into a photomultiplier. The detected signals were electrically downmixed to the appropriate frequency shift of 2 to 10 MHz in the present work. Then two counter processors with 1 ns resolution were used to process the Doppler signal. The Doppler signals were monitored on an oscilloscope and the digital outputs of the counter processors were fed directly to a micro-computer for storage and analysis. The seeding particles were introduced into the air stream by six atomizers symmetrically located on the two walls of the settling chamber and an atomizer in front of the baffle. The atomizers were operated by filtered compressed air and salt water to produce particles in the size range of $0.5 \sim 5$ μm. The salt solution was mixed to give a nominal 0.8 μm particle after the droplet dried.

Test Model and Experimental Conditions. Figure 2 depicts the configuration of the test model, coordinate system, and dimensions. The test model consisted of a rectangular side-inlet duct, a rectangular tunnel, and a baffle plate. The rectangular side-inlet duct with a cross-sectional area of 10×150 mm^2 intersected the rectangular tunnel at an angle of θ. The point opposite to the upstream edge of the side-inlet port was taken as the tunnel axial zero-reference point; thus, the axial coordinate downstream of the zero-reference point was positive. The tunnel model having a cross sectional area of 40×150 mm^2 and a length measured 1650 mm was made of 5 mm plexiglass and had a baffle at the upstream end about 320 mm measured from the axial zero reference point. The

Nomenclature

H = rectangular duct height, 40 mm
H_s = rectangular side-inlet duct height, 10 mm
k = turbulent kinetic energy, m^2/s^2
Q_e = entrainment flow rate upstream of side-jet port, L/min
Q_s = side-inlet flow rate, L/min
Q_t = total flow rate in the main duct, L/min
Re = Reynolds number, HU_{REF}/ν
S = rectangular duct width, 150 mm
U = axial mean velocity, m/s
u' = axial turbulence intensity, m/s
U_{REF} = side-inlet duct bulk mean velocity, m/s
U_θ = streamwise mean velocity along the axis of side-jet, m/s
u'_θ = turbulence intensity along the axis of side-jet, m/s
$\overline{uv}$ = Reynolds stresses, m^2/s^2
V = transverse mean velocity, m/s
v' = transverse turbulence intensity, m/s
W = rectangular side-inlet duct width, mm
X = axial coordinate, mm
X^* = dimensionless axial coordinate, X/H
Y = transverse coordinate, mm
Y^* = dimensionless transverse coordinate, Y/H
Z = spanwise coordinate, mm
Z^* = dimensionless spanwise coordinate, Z/H
θ = side-jet angle
ν_t = eddy viscosity

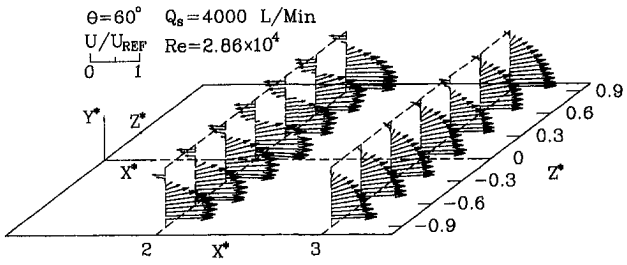

Fig. 3 Measured spanwise and transverse distributions of resultant mean velocity vectors at two selected X^* stations for $\theta = 60°$ and Re = 2.86×10^4 (Uncertainty in $(U^2 + V^2)^{1/2}/U_{REF}$: less than ±3.2 percent)

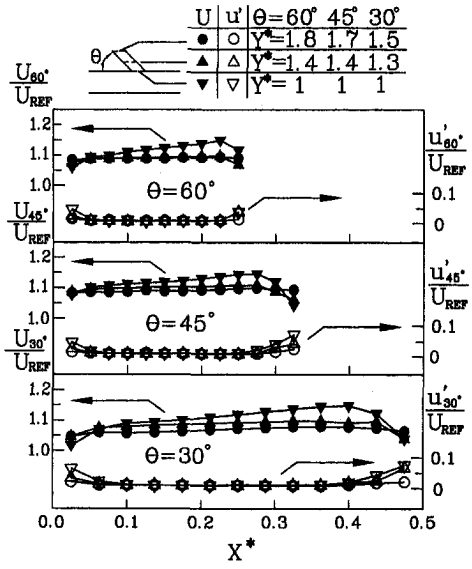

Fig. 4 Measured θ-component mean velocity and turbulence intensity profiles at three Y^* stations in the central plane of the side-inlet duct for Re = 2.86×10^4 or $Q_s = 4 \times 10^3$ L/min (Uncertainty in U/U_{REF}: less than ±3.2 percent, in u'/U_{REF}: less than ±4.4 percent)

baffle plate was made of a 2 mm plexiglass plate with a dimension of 360 mm × 900 mm.

The main parameters investigated were the side-inlet angle (θ) and the side-inlet flow rate (Q_s), which were varied from 30 to 60 deg and 1000 to 5000 L/min, respectively. Velocity measurements were made at 31, 21, and 21 axial stations for $\theta = 60$, $\theta = 45$ and 30 deg, respectively, and at 15 locations per station along the central plane ($Z = 0$) of the test duct. The side-inlet duct bulk mean velocity 55.6 m/s, 44.5 m/s, 33.4 m/s, 22.3 m/s, and 11.1 m/s for $Q_s = 5000$ L/min, 4000 L/min, 3000 L/min, 2000 L/min, and 1000 L/min, respectively, was used as a reference to nondimensionalize the experimental results. The Reynolds numbers based on the air density, rectangular duct height and bulk mean velocity were from 7.1×10^3 to 3.6×10^4 for $Q_s = 1000$ to 5000 L/min.

There were typically 4096 realizations averaged at each measuring location. The statistical errors in the mean velocity and turbulence intensity were less than 1.6 and 2.2 percent, respectively, for a 95 percent confidence level. Representative values of other uncertainty estimates are noted in figure captions. More detailed uncertainty estimates and velocity bias corrections can be found in Liou et al. (1988, 1990).

Two-Dimensionality. Measurements along Z^* direction at 10 selected (X^*, Y^*) positions for each θ were made. It is found that the two-dimensionality for the case of $\theta = 60$ deg is within 2%, 9.9%, 18%, 11%, and 4.8% for the main duct region upstream of the side-inlet port, the side jet region, the separation recirculation flow region (as will be shown below), the region immediately downstream of recirculation bubble, and the far downstream region, respectively. As expected, the three-dimensional effect is largest inside the recirculation zone. The two-dimensionality is improved with decreasing θ due to the decrease in the size of recirculation zone. For $\theta = 30$ deg, the two-dimensionality in the aforementioned regions is within 0.9%, 3.7%, 5.5%, 3%, and 1.2%. Figure 3 depicts an example showing the spanwise (Z^*) and transverse (Y^*) distributions of axial and transverse mean velocity components in terms of resultant velocity vectors at two selected X^* stations across the recirculation bubble for the case of $\theta = 60°$ and Re = 2.68×10^4. It is seen that the vector profiles are rather similar along the spanwise direction.

Results and Discussion

Flowfield in Side-Inlet Duct. Figure 4 depicts the streamwise mean velocity (U_θ/U_{REF}) and turbulence intensity (u'_θ/U_{REF}) distributions at three selected Y^* stations along the central plane ($Z = 0$) of the side-inlet duct for the three θ examined at Re = 2.86×10^4 or $Q_s = 4 \times 10^3$ L/min. For $\theta = 60°$, the U_θ/U_{REF} profile at $Y^* = 1.8$ is quite uniform and symmetric, with deviations within ±0.5%. As the flow proceeds toward the injection port, the U_θ/U_{REF} profile gradually becomes nonuniform near the wall ($Y^* = 1.4$, Fig. 4). When the flow reaches $Y^* = 1$, the U_θ/U_{REF} profile inclines across the side-inlet port due to the asymmetric sudden expansion into the main duct, which results in an imbalance of the main-duct back pressures between the injection induced low-velocity region upstream of the side-jet port ($X^* < 0$, Fig. 5) and the separated recirculation zone immediately downstream of the side-inlet port (Fig. 5). Similar results are found for $\theta = 45°$ and 30°: the farther the fluid flows downstream along the side-inlet duct, the more the mean velocity profile inclines; the degree of inclination increases with increasing side-injection angle due to increased asymmetry in sudden expansion. Notice that the positions where the mean velocity profile is uniform are different for various injection angles; they are $Y^* = 1.8$, 1.7, and 1.5 for $\theta = 60$, 45 and 30 deg, respectively. However, if one calculates the distances along the axis of side-jet, they are all about one H (40 mm) for the three values of θ and the uniformity is all within 3.3% of U_{REF}. The corresponding turbulence intensities for the three cases are mostly less than 1% and rise near the duct wall. The maximum turbulence intensities at $Y^* = 1$ for $\theta = 60$, 45, and 30 deg are 4.8%, 7.2%, and 7.6%, respectively.

Mean Flow Characteristics in the Main Duct. The mean flow patterns in the main duct for the three side-injection angles investigated are shown in Fig. 5 in terms of resultant vector plots.

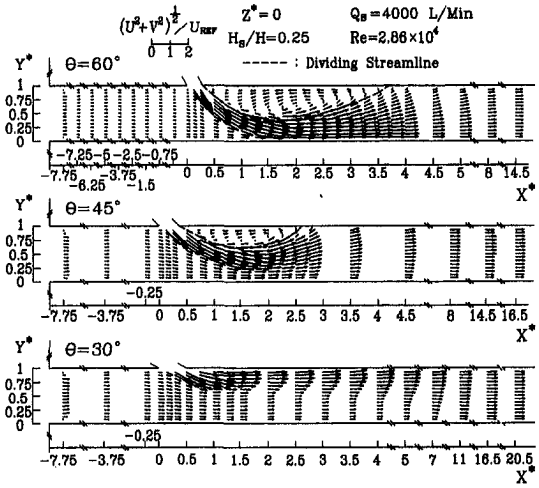

Fig. 5 Mean flow patterns in the main duct in terms of mean velocity vectors for $\theta = 30$, 45, and 60 deg (see Fig. 3 caption)

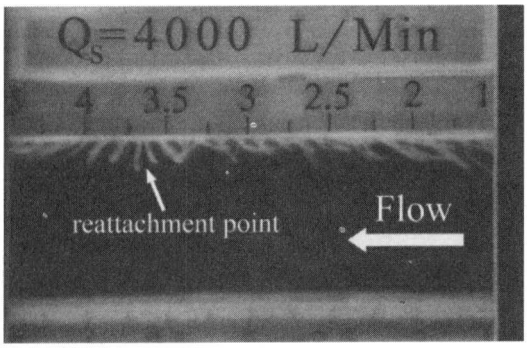

(a)

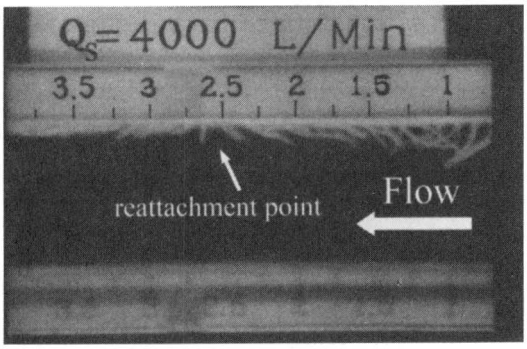

(b)

Fig. 6 Visualization of reattachment zone using surface tufts method for (*a*) $\theta = 60$ and (*b*) $\theta = 45$ deg at Re = 2.86×10^4

The fluid in front of the baffle plate induced into the rectangular main duct by the shear of the side jet moves slowly and uniformly in the region $X^* < 0$, and is subsequently accelerated and entrained into the side-injection flow beyond $X^* = 0$. There exists an obvious velocity demarcation and hence shear layer between the high-velocity jet flow and the low-velocity entrainment flow. For the case of $\theta = 60$ deg, this demarcation extends to the lower wall ($Y^* = 0$), which implies that the side-jet impinges upon the lower wall. As expected, the penetration depth of the side-jet toward the lower wall increases with increasing θ. For $\theta = 60$ and 45 deg, the penetration of the side-jet is deep enough to form a recirculating flow located immediately downstream of the side-jet port. The dashed lines in the velocity-vector diagrams denote the dividing streamlines. For $\theta = 60$ and 45 deg, the reattachment points locate at about $X^* = 3.7$ and 2.6, respectively, and the reattachment lengths, from the downstream edge of the side-jet port to the reattachment point, are 148 mm and 104 mm, or $3.7H$ and $2.6H$, respectively. To check the above LDV measured reattachment lengths for the cases of $\theta = 60$ and 45 deg, a surface tufts method was used to identify the reattachment zone. Typical photographs are shown in Fig. 6 and the visualized reattachment lengths (fluctuating within $\pm 0.06H$) are found to agree very well with those measured by LDV. As for $\theta = 30$ deg, the side-injection angle is too small to form a separated recirculation zone on the upper wall side of the main duct. The above results indicate that the formation of the recirculation zone depends on the side-injection angle and the recirculation-zone size increases with increasing side-inlet angle for the range of θ investigated. In addition, the aforementioned results suggest the presence of a critical side-inlet angle θ_c ($30 \leq \theta_c \leq 45$ deg) above which a recirculation flow will exist in the rectangular main duct, whereas below which there is no noticeable recirculation flow in the main duct. The recirculation flow of $\theta = 60$ deg extends to over half of the cross section of the rectangular main duct. It reduces the space for the air flow passing through the duct and affects the upstream entrainment flow rate. Consequently, the existence of the recirculation zone retards the entrainment of upstream flow and detains part of the fluid in the duct, which substantially influences the application to tunnel ventilation, for instance.

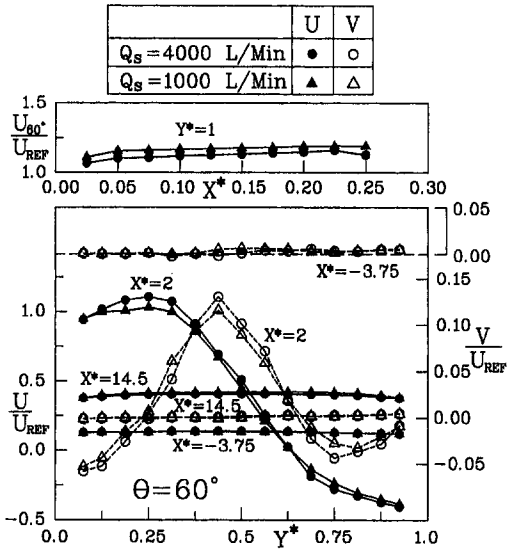

Fig. 7 Axial and transverse mean velocities at four selected stations for $\theta = 60$ deg under different Q_s (Uncertainty in U/U_{REF} and V/U_{REF}: less than ±3.2 percent)

In this study, the nozzle-like zone denotes the region between the edge of the recirculation zone and the lower wall of the main duct. As shown in Fig. 5, the flow is accelerated in the forward half of the nozzle-like zone and subsequently undergoes expansion as it passes through the throat of the nozzle-like zone. The peaks of the mean velocity profiles after the nozzle-like zone diminish gradually and the transverse mean velocity components also gradually disappear, as well. The flow becomes rather unidirectional and finally reaches the fully developed region in the further downstream direction ($X^* > 30$). For $\theta = 60$ deg, the transverse mean velocity is less than 0.5% of U_{REF} at $X^* = 13$, and the flow turns into unidirectional. The difference between the mean velocity profiles at $X^* = 14.5$ and $X^* = 11$ is within 1%, and the flow can be approximately regarded as fully developed. As for $\theta = 45°$ and 30°, the flows are unidirectional at $X^* = 14.5$ and $X^* = 18.5$ and are broadly fully developed at $X^* = 16.5$ and $X^* = 20.5$, respectively.

Reynolds-Number Dependence. In the following the effect of the side-injection flow rate is presented. Four reference planes were selected to investigate the relation between the mean velocity profile and the mean flow rate Q_s or Reynolds numbers. They are $Y^* = 1$ in the side-jet port, $X^* = -3.75$ upstream of the side-jet port, $X^* = 1.5$ or 2 downstream of the side-jet port, and $X^* = 14.5$ or 16.5 in the fully developed zone. The mean velocity profiles of the aforementioned reference stations for two selected side-injection angles and $Q_s = 4000$ and 1000 L/min are depicted in Figs. 7 and 8. These figures show that the mean velocity profiles under different flow rates have the same trend for all three values of θ. The mean axial and transverse velocity profiles are insensitive to the variation of the side-injection flow rates, even in the recirculation zone. The maximum difference at the peaks of the mean velocity profiles in the recirculation zone is only 7.9%. Flow visualizations performed at various Re or Q_s also indicate the weak dependence of the reattachment length on the Re or Q_s. An example is given by comparing Fig. 9 with Fig. 6 for $\theta = 60$ deg. Both figures show that the reattachment lengths are all about $3.7H$. In summary, the mean axial and transverse velocity profiles under different side-injection flow rates are self-similar for the range of Q_s investigated.

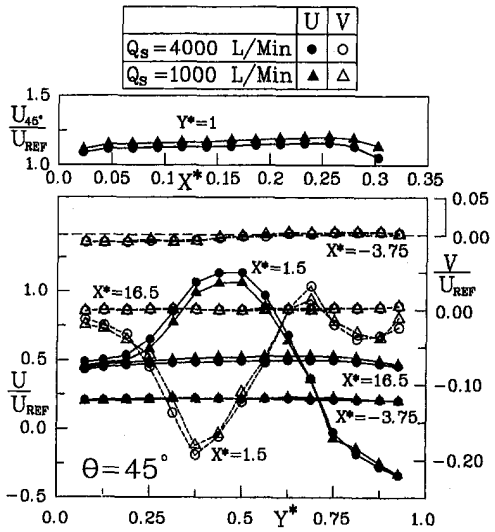

Fig. 8 Axial and transverse mean velocities at four selected stations for θ = 45 deg under different Q_s (see Fig. 7 caption)

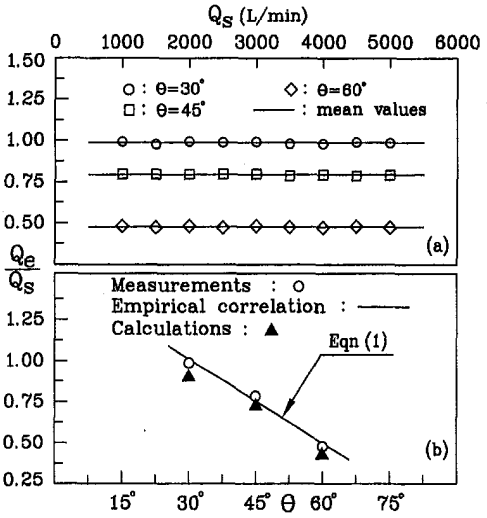

Fig. 11 Q_e/Q_s versus Q_s and θ (see Fig. 10 caption)

Entrainment Effect. The mixing and entrainment in jet streams have been investigated by a number of authors. To our knowledge, however, air entrainment due to a side jet has not been studied to date. In the present study, measurements were made for the entrainment of ambient air in front of the baffle plate into a rectangular duct under different side-injection flow rates (Q_s) and angles (θ). Figure 10 depicts the results of the entrainment flow rate Q_e for various side-injection flow rates and three side-injection angles. It is seen that Q_e increases with increasing Q_s and varies almost linearly with Q_s (Fig. 9) or $Q_e^* = Q_e/Q_s$ attains single values for the three side-inlet angles in the range of Q_s = 1000 to 5000 L/min, as shown in Fig. 11(a). This implies that the normalized entrainment flow rate does not vary with the side-injection flow rate. The solid lines in Fig. 11 indicate the mean values of Q_e^* of the nine measured values. The deviations of Q_e^* from the mean values are within 1.1% for the three values of θ. The mean value of Q_e^* for θ = 60° is 0.48 which reveals that the entrainment flow rate is almost equal to half of the side-injection flow rate. Q_e^* is 0.79 for θ = 45 deg and reaches 0.99 or is almost equivalent to Q_s for θ = 30 deg. Consequently, the air entrainment into the main duct upstream of side-jet port decreases with increasing side-injection angle. Figure 11(b) further shows a linear variation of Q_e^* with the side-inlet angle. As indicated previously, the side-injection angle is the primary factor for entrainment and can now be represented by a linear equation as follows:

$$Q_e^* = Q_e/Q_s = -9.76 \times 10^{-1}\theta + 1.52, \quad (\theta\text{:radian}) \quad (1a)$$

where θ is in radian. If θ is expressed in terms of degree, the above equation becomes

$$Q_e^* = Q_e/Q_s = -1.7 \times 10^{-2}\theta + 1.52, \quad (\theta\text{:degree}) \quad (1b)$$

The empirical correlation of Q_e^* agreed with our measurements to within 5.5% and was also depicted in Fig. 11(b) by the solid line. The air entrainment in the case of a semiconfined coaxial jet has been studied by Akiyama and Marui (1988), an empirical correlation between the rate of air entrainment and the rate of jet flow was also developed. The results of Akiyama and Marui (1988) showed that the ratio of the rate of air entrainment to the rate of jet flow is not dependent on jet flow rate but increases linearly with the ratio of the diameter of cylindrical duct and nozzle. This result parallels to the present one.

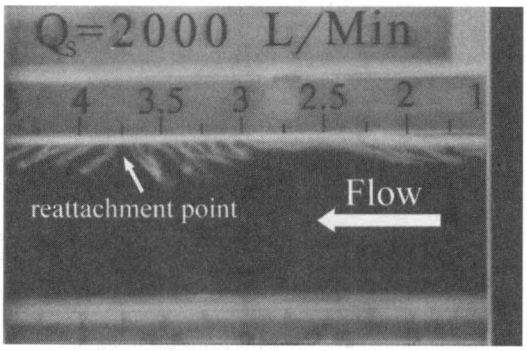

Fig. 9 Visualization of reattachment zone using surface tufts method for θ = 60 deg and Re = 1.43 × 10^4

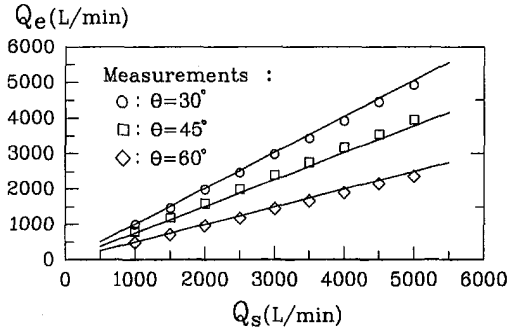

Fig. 10 Entrainment flow rates Q_e versus side-injection flow rates Q_s for various θ (Uncertainty in Q: less than ±1 percent)

Turbulence Intensity. The measured axial and transverse turbulence intensity profiles at a fixed Q_s for two selected side-injection angles are given in Fig. 12. In the θ = 60 deg case, the peaks of the transverse turbulence intensity are larger than those of the axial turbulence intensity in the shear layer between the jet flow and the entrainment flow ($0 < X^* \leq 1$). The reason is that the side-injection turns horizontally after it is injected into the rectangular main duct; the transverse mean velocity therefore decreases rapidly and results in a higher transverse mean velocity gradient. However, the differences between the peak values of the transverse and axial turbulence intensities decrease with increasing X^*, e.g., 14.7% and 1.6% at X^* = 0.125 and X^* = 1, respectively. In contrast, the peaks of the transverse turbulence intensity are smaller than those of the axial turbulence intensity in the edge of the recirculation zone, and the differences of the peak turbulence intensities between the two components are all about 7%. The peak turbulence intensities in the shear layer on the

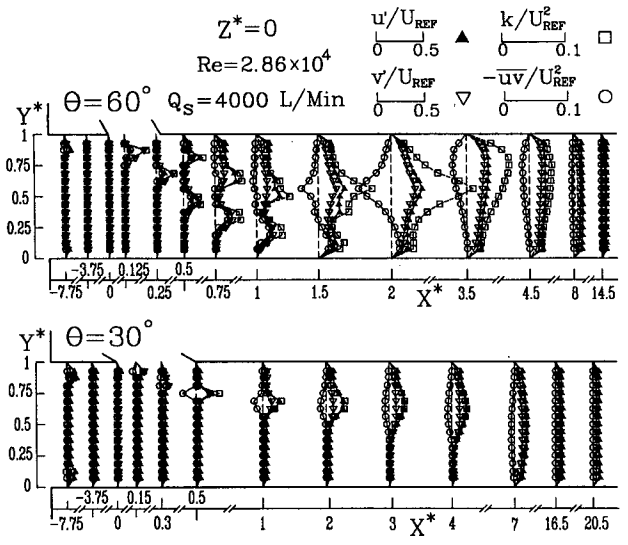

Fig. 12 Measured axial and transverse turbulence intensity, Reynolds stress, and turbulent kinetic energy profiles for θ = 30 and 60 deg (Uncertainty in u'/U_{REF} and v'/U_{REF}: less than ±4.4%, in k/U^2_{REF}: less than ±7.4 percent, in $|-\overline{uv}/U^2_{REF}|$: less than ±4.8%)

entrainment-flow side and in the edge of the recirculation zone can reach values as high as 17.8% and 32.9%, respectively.

Figure 12 further exhibits that turbulence is rather anisotropic and inhomogeneous in most regions of the rectangular duct for the case of θ = 60 deg. The ratios of axial to transverse turbulence intensities are in the range of 1.2 to 1.5 except for the shear layers and near wall regions. The most anisotropic region is in the shear layer near the side-jet port, where the ratio of transverse to axial turbulence intensities could be as high as 3.5. The isotropy of the developing zone ($4 \leq X^* \leq 8$) is better than that of the fully developed zone ($X^* \geq 14.5$). A possible explanation is that the axial turbulence intensity decays faster than the transverse turbulence intensity in the developing zone, which improves the isotropy. All of the three cases examined exhibit the same trend. Similar trend can also be found in the fully developed pipe flow (Laufer, 1955). In other words, the fully developed region is not necessary the most isotropic region. Nevertheless, the fully developed zone is more homogeneous than the developing zone. The measured mean axial and transverse turbulence intensities are 4.9% and 3.4%, respectively, in the fully developed region, whereas they are 8.9% and 7.7%, respectively, in the developing region.

Similar to the case of θ = 60 deg, the turbulence intensities in the axial and transverse directions are fairly anisotropic in the aforementioned two shear layers for θ = 45 deg. The ratio of axial to transverse turbulence intensities can reach a value of 4.1. The peak turbulence intensities in the shear layer on the entrainment-flow side and in the edge of the recirculation zone can reach values as high as 17.8% and 32.9%, respectively. Less degree of anisotropy in turbulence is found for θ = 30 deg, as shown in Fig. 12. The turbulence intensity levels for θ = 30° are smaller than those for θ = 60 and 45 deg. The peak turbulence intensity is only as high as 17%.

Reynolds Shear Stress and Turbulent Kinetic Energy. A common source of energy for turbulent velocity fluctuations is shear in the mean flow. The presence of the shear in the mean flow maintains the energy of the larger eddies which in turn transport energy to the smaller eddies. The distributions of the turbulent kinetic energy and Reynolds stress for θ = 30° and 60° at a fixed Q, are also included in Fig. 12. The turbulent kinetic energy in the present study is expressed in $k = (1/2)(\overline{u'^2} + \overline{v'^2})$. For the case of θ = 60 deg, there are clear peaks of Reynolds stresses existing in the shear layer between the jet flow and entrainment flow; $|-\overline{uv}/U^2_{REF}|$ can reach a value as high as 0.023, which is about 0.44 times the peak value occurring in the shear enclosing the recirculating flow. The above comparison indicates that the main-flow shear supplies more energy to maintain the energy associated with the energy containing eddies in the recirculating flow. When the flow moves downstream to the fully developed zone, $|-\overline{uv}/U^2_{REF}|$ is typically 10^{-4} to 10^{-5} which is comparable to the values found in the fully developed rectangular duct flow by Gessner et al. (1965) and Melling et al. (1976). The Reynolds stress distribution for the case of θ = 45 deg is similar to that for θ = 60 deg. However, the difference between the peak Reynolds stresses in the two shear layers is smaller for the former case than for the latter case. The maximum $|-\overline{uv}/U^2_{REF}|$ is as high as 0.041 for the case of θ = 45 deg. For the case of θ = 30 deg, there is no recirculation flow, so its Reynolds stress levels are smaller than those of θ = 45 and 60 deg. The maximum Reynolds stress is only as high as 0.021 for the case of 30 deg.

The distributions of the turbulent kinetic energy are similar to those of the turbulence intensity. Large values of k/U^2_{REF} are also found in the aforementioned two shear layers. For instance, a value as high as 0.04 occurs at $X^* = 0.75$ in the shear layer between the jet flow and the entrainment flow and a value as high as 0.13 is found at $X^* = 2$ in the edge of recirculation flow for the case of θ = 60°. The values of k/U^2_{REF} are about 10^{-4} in the fully developed zone. The distribution of k/U^2_{REF} for θ = 45° is similar to that of θ = 60 deg, and the values of peaks in the two shear layers are as high as 0.05 and 0.11 at $X^* = 0.75$ and $X^* = 2$, respectively. The turbulence level of θ = 30° is smaller, so the turbulent kinetic energy is smaller in the entire flow field. The maximum turbulent kinetic energy appears at the interface of the jet flow and the upstream entrainment flow and it reaches the maximum value of 0.034. From Fig. 12 it is clear that the maximum turbulent kinetic energy and Reynolds stress in the rectangular main duct increase with increasing side-injection angle for the range of θ investigated. It is also worth noting that for the case of θ = 60 deg turbulent kinetic energy can reach a value as high as 0.04 in the vicinity of the lower wall side at $X^* = 1.5$, as a result of the impingement of the side-jet upon the lower wall. This feature is absent for the cases of θ = 30 deg because of the smaller side-injection angle.

Complementary Computation. The measured mean velocity vector profiles near the axial main duct entrance, for instance: $X^* = -7.75$ in Fig. 5, indicate negligible velocities adjacent to the duct walls, suggesting the possible presence of Vena contracta due to flow separation associated with the sudden contraction. Owing to the blockage of the baffle plate, there exists difficulty in LDV measurements around the axial duct entrance ($X^* < -7.75$). To reveal the entrance flow pattern, a complementary computation was therefore performed to solve the fully elliptic two dimensional Navier-Stokes equations with the algebraic Reynolds stress (ASM) turbulence model (Rodi, 1976). The detailed theoretical formulation has been given in our previous work (Liou et al., 1992) and, hence, is not elaborated on here for the space limitation. In the calculations the Reynolds stresses are decomposed into a Boussinesq part and a deviation part. This is done to reduce the numerical instability inherent from the nonlinearity of the governing equations. The decomposition allows a portion of the Reynolds stresses to be inserted into the diffusion terms of the momentum equation rather than the entire quantity being incorporated into the source terms. The resulted coefficient matrix is found to be more diagonally dominant and, therefore, to converge more quickly. A staggered grid system is employed. The finite difference scheme SCSUDS (Smoothed Hybrid Central/Skew Upstream Scheme) (Liou et al., 1990a) is adopted to reduce numerical diffusion associated with the one-dimensional power-law discretization scheme when large cross-flow gradients exist and the flow cuts across the grid lines at a large angle. The calculated axial entrance flow pattern in terms of mean-velocity vector plot is depicted in Fig. 13 where the boundary conditions are also specified. As expected, there indeed exists Vena contracta with a length of $0.4H$

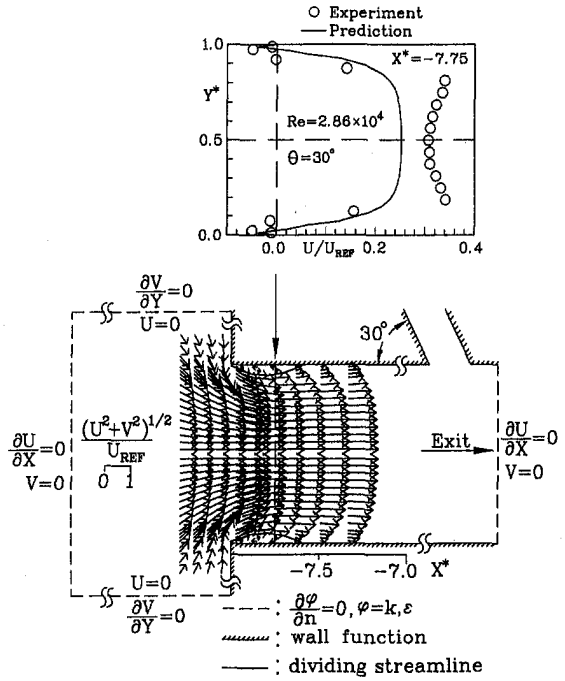

Fig. 13 The calculated axial entrance flow pattern in terms of mean-velocity vector plot in $Z^* = 0$ plane for $\theta = 30$ deg and Re = 2.86×10^4

and a height of $0.06H$. It should be mentioned that the $k - \epsilon$ turbulence model was originally applied to predict the flow field investigated. Nevertheless, owing to the isotropic assumption, the model tends to give the excessive turbulent kinetic energy production around the axial entrance corners resulting in too high eddy-viscosity ν_t or turbulent exchange coefficient. The augmented mixing effect resulting from this high ν_t prevents the occurrence of Vena contracta. The anisotropic features revealed in Fig. 12 are captured to some extent by the ASM model adopted in the present work. More reasonable values of turbulent kinetic energy distributions, about half values of those predicted by $k - \epsilon$ model, around the entrance corners are obtained by the ASM model and thereby the Vena contractas are reproduced. The LDV measurements could be brought to $0.25H$ close to the baffle plate or $X^* = -7.75$. Refined measurements as close as 0.5 mm from the wall were made at $X^* = -7.75$ for $\theta = 30$ deg and the results are plotted in Fig. 13 for verifying the ASM results. It is seen that although the ASM can reproduce the backflow, it underpredicts the velocity magnitudes (within 27 percent of U_{REF}) for the reason given in the following paragraphs.

A validation of computed results downstream of $X^* = 0$ is shown in Fig. 14 for three selected X^* stations. It is found that the

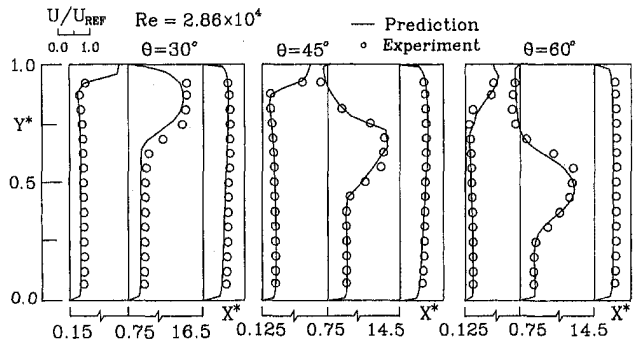

Fig. 14 Comparison between computed and measured axial mean velocity profiles for three θ examined (see Fig. 7 caption)

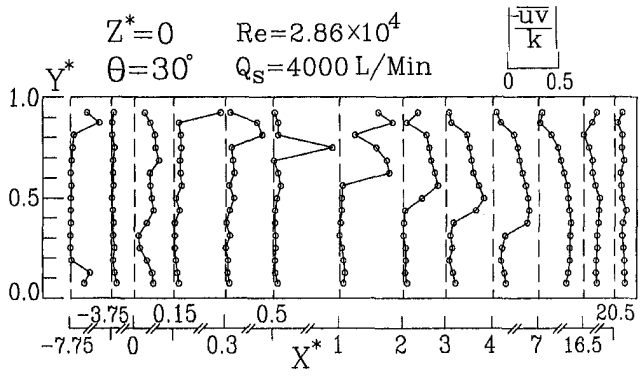

Fig. 15 Measured structure parameter $|-\overline{uv}/k|$ for $\theta = 30°$ (see Fig. 12 caption)

computed axial mean velocity profiles at $X^* = 0.13$ across the side-inlet port, $X^* = 0.75$ across the recirculation flow zone, and $X^* = 14.5$ near the duct exit can capture the measured results. The underprediction in the region immediately downstream of the side-injection port, $X^* = 0.75$ in Fig. 14, is partly due to the assumption of $|-\overline{uv}/k| = \text{constant} = 0.3$ (Harsha and Lee, 1970) or 0.24 (Launder, 1975), i.e., the transport of $-\overline{uv}$ is proportional to the transport of k across the flow field, embedded in the ASM model. However, Fig. 12 ($\theta = 30$ deg) indicates that $-\overline{uv}$ and k vary in different manner. Figure 14 further shows that $|-\overline{uv}/k|$ is not constant across the flow field. Hence, the results from the ASM are unavoidably inaccurate to some degree. Also note that as one takes the average of $|-\overline{uv}/k|$ distribution shown in Fig. 15 over the measured area, a value of 0.114 is obtained and the corresponding values for the cases of $\theta = 45$ and $\theta = 60$ deg are 0.152 and 0.154, respectively. If the average is performed only over the regions downstream of $X^* = 0$, the $|-\overline{uv}/k|$ values are 0.16, 0.21, and 0.21 for $\theta = 30$, 45, 60 deg, respectively.

The computed air entrainment ratios for the three values of θ examined are also compared with the experimental ones in Fig. 11. The trend is approximately predicted and differences between the computation and experiment are 10.5%, 4.1% and 14.8% for $\theta = 30$, 45, and 60 deg, respectively. The underprediction suggests that an improved turbulence model needs to be examined in the future study. In addition, the present experimental investigation was undertaken in a rectangular duct with an aspect ratio of 3.75 and the three-dimensional effect may contribute to the aforementioned differences between experimental data taken along the longitudinal central plane $Z^* = 0$ and two-dimensional computational results presented in Figs. 14 and 11. In fact, the size of the reverse flow zone and the magnitude of the negative mean velocities are largest in the longitudinal central plane $Z^* = 0$ and decreases toward two side walls ($Z^* = \pm 1$), as can be seen from Fig. 3. Consequently, if one takes an average over the spanwise direction, similar to a two-dimensional computation, the spanwise-averaged recirculation zone and negative mean velocity values would be smaller than those measured along the $Z^* = 0$ plane. The above observation provides the rationale for the underprediction of reverse velocities in the separation recirculation zone (Figs. 13–14) and air entrainment (Fig. 11) by the present two-dimensional computations.

Conclusions

Under the present experimental conditions the following main results can be concluded:

1. The axial and transverse mean velocity profiles and reattachment length in the rectangular main duct with a given injection angle are practically independent of the Reynolds number over the range of Reynolds numbers and side-injection rates Q_s investigated.

2. For injection angles $\theta = 60$ and 45 deg, there is a recirculating flow located immediately behind the downstream edge of the side-jet port on the top wall side of the rectangular main duct. The size of the recirculation zone increases with increasing injection angle. In contrast, for $\theta = 30$ deg there is no noticeable recirculation flow in the main duct. As a result, there exists a critical side-injection angle θ_c ($30 \leq \theta_c \leq 45$ deg) for judging the absence or existence of the injection generated separation bubble whose size plays an important role in affecting the cross-stream entrainment rate pertaining to the application such as tunnel ventilation. The above finding is reported for the first time.
3. The entrainment flow rate Q_e is found to increase linearly with increasing Q_s for all three values of θ examined, whereas the ratio Q_e/Q_s decreases linearly with increasing θ. Simple correlations between the mass entrainment into the main duct upstream of the side-injection port and side-injection angle are also presented in this study.
4. The maximum values of turbulence level and Reynolds stress in the rectangular main duct increase with increasing side-injection angle or size of injection induced separation bubble for the range of θ investigated.
5. The complementary flow visualizations support and numerical computations are able to capture the LDV measured results. The underpredictions of numerical simulation are attributed to the three-dimensional effects and the basic assumption embedded in the algebraic Reynolds stress model adopted.

Acknowledgment

Support for this work was provided by the National Science Council under contract NSC-80-0401-E007-02 and by the Environmental Protection Administration, Executive Yuan, Republic of China under contract EPA-79-001-22-175-12.

References

Abramovich, G. N., 1963, *The Theory of Turbulent Jets,* English Translation Published by M.I.T. Press, MA.

Akiyama, T., and Marui, T., 1988, "Entrainment of Ambient Air into a Cylindrical Duct by a Turbulent Jet from a Single Nozzle," *Industrial and Engineering Chemistry Research,* Vol. 27, pp. 1543–1545.

Andreopoulos, J., 1982, "Measurements in a Jet-Pipe Flow Issuing Perpendicularly into a Cross Stream," ASME JOURNAL OF FLUIDS ENGINEERING, Vol. 104, pp. 493–499.

Bergeles, G., Gosman, A. K., and Launder, B. E., 1976, "The Near-Field Character of a Jet Discharged Normal to a Main Stream," ASME *Journal of Heat Transfer,* Aug., pp. 373–378.

Crabb, D., Durao, D. F. G., and Whitelaw, J. H., 1981, "A Round Jet Normal to a Crossflow," ASME JOURNAL OF FLUIDS ENGINEERING, Vol. 103, pp. 142–153.

Gessner, F. G., and Jones, J. B., 1965, "On Some Aspect of Fully-Developed Turbulent Flow in Rectangular Channels," *Journal of Fluid Mechanics,* Vol. 23, pp. 689–713.

Keffer, J. F., and Baines, W. D., 1963, "The Round Turbulent Jet in a Cross Wind," *Journal of Fluid Mechanics,* Vol. 15, pp. 481.

Laufer, J., 1954, "The Structure of Turbulence in Fully Developed Pipe Flow," NACA TR 1174.

Liou, T. M., Chang, Y., and Hwang, D. W., 1990, "Experimental and Computational Study of Turbulent Flows in a Channel with Two Pairs of Turbulence Promoters in Tandem," ASME JOURNAL OF FLUIDS ENGINEERING, Vol. 112, pp. 302–310.

Liou, T. M., Hwang, Y. H., and Chen, L., 1992, "Prediction of Confined Three-Dimensional Impinging Flows with Various Turbulence Models," ASME JOURNAL OF FLUIDS ENGINEERING, Vol. 114, pp. 220–230.

Liou, T. M., and Wu, S. M., 1988, "Flowfield in a Dual-Inlet Side-Dump Combustor," *Journal of Propulsion and Power,* Vol. 4, pp. 53–60.

Melling, A., and Whitelaw, J. H., 1976, "Turbulent Flow in a Rectangular Duct," *Journal of Fluid Mechanics,* Vol. 78, pp. 289–315.

Platten, J. L., and Keffer, J. F., 1971, "Deflected Turbulent Jet Flows," ASME *Journal of Applied Mechanics,* Dec., pp. 756–758.

Rodi, W., 1976, "A New Algebraic Relation for Calculating the Reynolds Stresses," *ZAMM,* Vol. 56, pp. T219–T221.

Simizu, Y., 1987, "Studies of the Configuration and Performance of Annular Type Jet Pumps," ASME JOURNAL OF FLUIDS ENGINEERING, Vol. 109, pp. 205–212.

Sucec, J., and Bowley, W. W., 1976, "Prediction of the Trajectory of a Turbulent Jet Injected into a Crossflowing Stream," ASME JOURNAL OF FLUIDS ENGINEERING, Vol. 98, pp. 667–673.

Nicholas J. Lawson
Research Fellow.

Malcolm R. Davidson
Associate Professor.

G. K. Williams Cooperative Research Centre for Extractive Metallurgy,
Department of Chemical Engineering,
The University of Melbourne,
Parkville, Victoria, 3052, Australia

Crossflow Characteristics of an Oscillating Jet in a Thin Slab Casting Mould

The application of LDA to a transient $\frac{1}{3}$ scale (500 mm wide) water model of a mould, typical of steel thin slab casting, is presented. The characteristics of a crossflow, associated with the oscillating jet emerging from a submerged nozzle (internal diameter 33 mm), were analyzed for a range of casting rates (0–2 m/min), nozzle submergences (20–120 mm) and nozzle-mould wall gap widths (0–21 mm). The frequency of oscillation was found to be primarily dependent on the casting rate of the system, independent of nozzle submergence or gap width, whereas the RMS crossflow velocity depended on all three parameters. Additional crossflow was also observed past the jet below the nozzle exit and this allowed the jet to oscillate even with zero gap width.

Introduction

Continuous slab casting is now a well-established method for producing steel for various applications (Nilles and Etienne, 1991). The technique involves injecting liquid metal into a water-cooled mould as two lateral jets through a Submerged Entry Nozzle (SEN). As the outer edges of the metal cool, they solidify forming a solid shell which increases in thickness as it descends in the mould. The complex nature of the fluid flow in the mould has resulted in significant numerical and physical modelling studies in order to optimise the performance of a given mould geometry. Austin (1992) has surveyed the literature on the modelling of conventional continuous casting and Herbertson et al. (1991) have reviewed the use of mathematical and water modelling.

Recent research has considered thin slab casting aimed at reducing the cost of subsequent hot rolling (Honeyands and Herbertson, 1995). However, the use of a thin mould geometry requires a higher casting speed to achieve the same throughput as a conventional size continuous caster. This results in free surface oscillations of the liquid metal in the mould. These oscillations can cause problems with superheat dissipation and uniformity of shell growth, and can lead to poor product quality (Honeyands et al., 1992; Honeyands, 1994). Similar difficulties occur in the strip casting of aluminium (Espedal et al., 1993). Understanding the fluid dynamics in the mould is necessary for improved efficiency and quality at increased casting speeds.

Studies with water models of thin slab caster moulds (Gupta and Lahiri, 1994; Honeyands, 1994; Honeyands and Herbertson, 1995), based on simple image analysis, free surface measurements and flow visualization, show that the observed surface disturbances at increased casting speeds are associated with an unstable flow pattern which causes the jets emanating from the SEN to oscillate across the broad face of the mould. Honeyands (1994) concluded that the jet oscillation was similar in nature to that which occurs in a blind cavity (Molloy, 1969). The flow oscillation occurred in the presence of a steady supply to the injection nozzle and was thus not being driven by unsteadiness in the delivery system.

Many cavity flows are known to be capable of self-sustained oscillations. Typical configurations involve impinging jets or mixing layers. (See, for example, reviews by Rockwell, 1983 and Rockwell and Naudascher, 1979.) Most studies in this category relate to oscillations driven by the inherent instability of the shear layer. Oscillations which are not generated by shear layer instability have been less well studied. Such oscillations have a much lower frequency and can occur when the shear layer is bounded by a recirculating zone (Rockwell, 1983), as occurs for confined jets (Villermaux and Hopfinger, 1994; Maurel et al., 1996). The oscillation of confined jets in thin slab caster moulds is an example of such a flow. A related example is the confined jet in a fluidic oscillator (Viets, 1975; Shakouchi, 1989; Morris et al., 1992). Indeed, Molloy (1969) interpreted the two-dimensional jet flow into a blind cavity in terms of a fluidic oscillator, as did Honeyands and Herbertson (1995) for flow in a thin slab caster mould.

A common feature of all self-sustaining oscillations is the existence of feedback in which downstream events can influence the flow near the separation point. A jet issuing from a nozzle into a cavity has the features of flow in a duct with a sudden expansion. Such flow in a symmetric channel becomes bistable as the Reynolds number increases, deviating toward one side wall or the other (Cherdron et al., 1978). This is sometimes called the Coanda effect. In the case of a fluidic oscillator, the pressure differences which promote the jet deflection can act to reverse the deflection via a feedback loop linking the flow on each side of the jet, thus creating a self-sustaining oscillation.

For a thin slab caster mould, two feedback routes are possible: (I) the recirculating flow entrained by the jet which links the region near the attachment point with that near the nozzle exit, and (II) the gap between the nozzle shaft and the broad face of the mould wall which links each side of the jet via a crossflow. Route (II) is a direct analogue of the feedback loop in a fluidic oscillator.

Crossflow was reported by Honeyands (1994) who observed it to be necessary for the oscillation to occur; however, he explained the oscillation in terms of feedback mechanism (I) in the manner of Molloy (1969) for a blind cavity (Honeyands and Herbertson, 1995). Honeyands was able to numerically predict sustained oscillation in a two-dimensional blind cavity without crossflow. More recently, Gebert et al. (1998) have numerically predicted single jet oscillation in a two-dimensional mould geometry by incorporating crossflow in the numerical model. Crossflow was required for an oscillation to be predicted in that case, as was observed experimentally by Honeyands (1994). Thus it seems that (II) rather than (I) is the fundamental feedback mechanism for flow oscillation in the thin slab caster mould.

Current results from the numerical modelling of Gebert et al. (1998) are encouraging. However, further development of such computational models of the oscillation is limited by the lack of detailed experimental measurements of the fluctuating flow field. The present paper attempts to address this limitation by investigating the flow field in the crossflow region of an isothermal water

Contributed by the Fluids Engineering Division for publication in the JOURNAL OF FLUIDS ENGINEERING. Manuscript received by the Fluids Engineering Division June 9, 1998; revised manuscript received June 9, 1999. Associate Technical Editor: S. Banerjee.

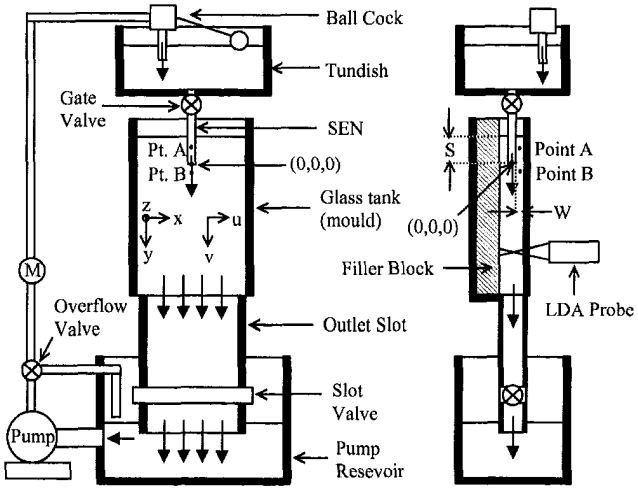

Fig. 1 Schematic of experimental rig (SEN = Submerged Entry Nozzle, *M* = flow meter, *S* = SEN submergence, *W* = SEN-mould wall gap width)

model of a thin slab caster mould. The Laser Doppler Anemometry (LDA) technique (Durst et al., 1981) is used for a single jet flow from an idealised nozzle consisting of a simple pipe. (Twin lateral jet flows from a binozzle, characteristic of industrial practice, will be the subject of a subsequent paper.) The crossflow region in the mould is analysed in detail because of its importance to the oscillation. The aim is to establish the response of the oscillation to changes in casting rate, nozzle-mould wall gap width and nozzle submergence.

Physical Modeling

Experimental Rig. Figure 1 illustrates the design of the experimental rig. The water model of a mould consisted of a rectangular glass tank of dimensions 800 mm × 500 mm × 180 mm with a 200 litre tundish mounted 500 mm above. A 100 mm wide filler block, consisting of polystyrene foam sandwiched between two perspex sheets, was placed inside the glass tank to reduce the geometry to 800 mm × 500 mm × 80 mm for the present experiments. In future experiments the width of the filler block will be adjusted to alter the thickness of the geometry. The broad face of the tank is a third scale of the (full-scale) mould geometry considered by Honeyands (1994). The bottom of the glass tank was fitted with a 300 mm × 500 mm × 100 mm outlet manifold containing an adjustable slot valve for flow control. This results in an effective cavity length of 1100 mm, but with a difference between the thickness of the mould (80 mm) and the thickness of the manifold (100 mm). The effect of this thickness difference on the oscillation was not investigated. Following the top part of the manifold, a 250 mm × 500 mm × 100 mm extension was also added to ensure the flow outlet level was below the water level of the pump reservoir. This was necessary to prevent air entrainment in the slot outlet area. The SEN consisted of a glass tube (38 mm outer diameter) with a wall thickness of 2.5 mm mounted below a gate valve on the tundish. Water flow to the tundish was supplied by a 2 kW centrifugal pump capable of 300 litres/min. A pump overflow was also supplied to the reservoir to prevent the pump stalling. The overflow was controlled by a valve mounted near the pump outlet as shown in Fig. 1.

The manifold was found to be the most critical part of the rig design. A number of designs were tested before reliable jet oscillations were obtained from the rig. Figure 2 illustrates the initial and final designs that were tried. Design 1 consisted of an outlet manifold box connected to the mould through a series of pipes. The outflow was then controlled with three additional pipes mounted onto the sides and bottom of the box as shown in Fig. 2. Each pipe was fitted with a gate valve to regulate the flow.

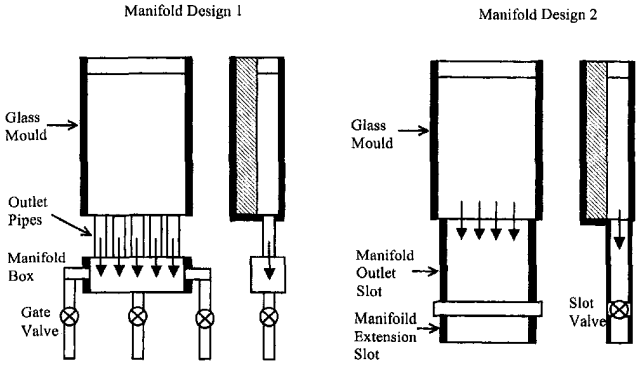

Fig. 2 Manifold designs tested on the slab caster rig

Although this design allowed adequate flow rates, achieving balanced flow out of all three pipes proved too unreliable. These flow mismatches caused the jet to stagnate at a position corresponding to the pipe with the minimum flow. Design 2 overcame these problems by allowing an even flow across the complete manifold section. This was possible by using a slot valve arrangement as shown in Fig. 2. The slot valve system also allowed very high flow rates if required and gave a stable jet oscillation across the complete range of "casting rates" of the system. Here "casting rate" refers to the mean discharge velocity from the manifold.

To control the water flow through the tundish and hence the casting rate, a ball cock system was used in conjunction with a gate valve. The ballcock ensured a constant head was maintained for a given flow rate which was set using the gate valve on the tundish outlet. The ballcock was fitted onto the pump outlet at the top of the tundish while the gate valve was mounted onto the outlet of the tundish. With this system reliable flow control could be achieved for casting rates of between 0.5 and 2.0 m/min (volumetric flow rates between 0.3×10^{-3} and 1.3×10^{-3} m^3/s). To monitor the casting rate, a Coles Palmer electronic turbine flow meter, model 05610-40, was placed 250 mm from the pump overflow valve and calibrated. The calibration procedure consisted of measuring the time taken for the water level in the mould to fall 50 mm for a range of flow meter readings. With the known distance and time, the casting rate in m/min could then be estimated and a calibration curve plotted (not shown).

Measurement System. The LDA measurements were made using a Dantec FibreFlow system and a 58N40 FVA covariance signal processor. A 2D probe was available for measurements which used the green line (514.5 nm) for the horizontal velocity component u and the blue line (488 nm) for the vertical velocity component v from a 4 W Argon Ion laser. The focal length of the probe was set to 250 mm which gave a measurement volume for u of 0.117 mm × 0.117 mm × 1.544 mm and for v of 0.111 mm × 0.111 mm × 1.464 mm. These volumes were considered acceptable for the size of the flow structures expected in the mould. The fluid was seeded with silver-coated hollow glass spheres with a size range of 10–30 μm and a specific gravity of 1.1 as supplied by Fidene Corporation of Australia. To ensure an adequate sampling period for the expected crossflow oscillation frequencies, measurements were taken of the u, v components of velocity for

Table 1 Summary of point A and B measurement conditions

Casting rate R (m/min)	SEN submergence S (mm)	SEN-mould wall gap width W (mm)
2.0	20, 40, 60, 80, 100, 120	21.0
0.5	120	0, 3.0, 6.0, 16.0, 21.0
1.0	120	0, 3.0, 6.0, 16.0, 21.0
1.5	120	0, 3.0, 6.0, 16.0, 21.0
2.0	120	0, 3.0, 6.0, 16.0

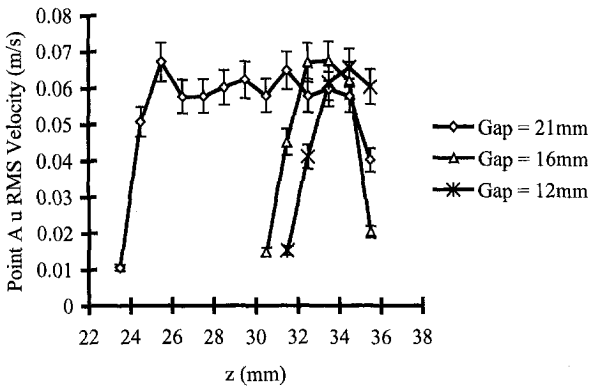

Fig. 3 *z* traverse through point A to illustrate the influence of the jet on the crossflow region (casting rate 2.00 m/min, SEN submergence 120 mm)

up to 250 seconds. Data rates were also set to around of 100 Hz by varying the seeding density and laser power to provide approximately 25,000 samples per data point. This raw data was subsequently resampled for the spectral analysis which is outlined in the data analysis section.

Flow Measurements. The LDA measurements were carried out at points A and B shown in Fig. 1. This allowed the crossflow characteristics of the system to be analyzed from the RMS velocity and crossflow oscillation frequency. Mean crossflow velocity was not considered here due to the sinusoidal nature of the crossflow which consistently gave near-zero mean values. LDA data throughout the region of the jet below the nozzle will be presented in a later paper. The emphasis of the present work is on the crossflow. Three sets of LDA data were recorded in order to isolate different factors which could influence the oscillation. These consisted of varying the SEN submergence S, the SEN-mould wall gap width W and the casting rate R. Table 1 lists all the conditions.

The thickness of the SEN wall was varied to change the resistance to crossflow between the nozzle and mould wall. This was done by placing additional PVC pipes over the original glass SEN. This allowed the gap between the SEN and mould wall to range from 0 to 21 mm. Point A was positioned on the centerline of the broad face of the mould ($x = 0$) and vertically at a midpoint between the free surface and the SEN exit. In the transverse (z) direction, point A is notionally located midway between the SEN and the mould wall, but in practice this position was determined by a z-traverse to coincide with the maximum in the transverse RMS velocity profile where possible. Figure 3 shows these transverse profiles for a number of SEN-mould wall gap widths. Point A was indeed positioned at the mid-transverse point for a SEN-mould wall gap width of $W = 21$ mm as the velocity profile exhibits a broad maximum. For $W = 16$ mm and $W = 12$ mm, the velocity maxima are sharper and the transverse location of point A was adjusted accordingly. However, for $W = 6$ mm and $W = 3$ mm, the position of point A was estimated, since a z-traverse was found to be restricted by poor signal quality caused by back reflections off the SEN wall. Table 2 summarises the point A positions.

The jet requires some distance to expand downstream of the nozzle to fill the cavity. Thus there is the possibility of crossflow in the space between the jet and the mould wall similar to the crossflow between the SEN and the mould wall. To capture this additional crossflow, point B was fixed at $x = 0$, $y = 33.0$ mm, $z = 29.5$ mm. This point is marked on LDA traverses in the y and z directions which are shown in Figs. 4 and 5. The influence of the jet can be seen in the (downwards) y and (transverse) z profiles of RMS velocity to be minimal at positions $y < 60$ mm and $z > 25$ mm. Thus, positioning point B within that range at $x = 0$, $y = 33.0$ mm, $z = 29.5$ mm ensures that additional crossflow below the SEN can be investigated without being influenced by the jet.

Table 2 Summary of point A measurement positions

SEN submergence S (mm)	SEN-mould wall gap width W (mm)	Point A position x, y, z (mm)
20	21.0	0, −10.0, 29.5
40	21.0	0, −20.0, 29.5
60	21.0	0, −30.0, 29.5
80	21.0	0, −40.0, 29.5
100	21.0	0, −50.0, 29.5
120	21.0	0, −60.0, 29.5
120	16.0	0, −60.0, 32.5
120	12.0	0, −60.0, 34.0
120	6.0	0, −60.0, 37.0
120	3.0	0, −60.0, 38.5

Note that changing the SEN-mould wall gap width W does not significantly affect the RMS crossflow velocity over the z-traverse through point B (Fig. 5).

Data Analysis. The u and v velocity data collected from the LDA system was processed into time series, mean and RMS velocity data where the mean and RMS velocities, u_{mean}, u_{rms} and v_{mean}, v_{rms} were calculated using a residence time weighting technique as recommended by Buchhave et al. (1979) to reduce bias effects such that

$$u_{mean} = \frac{\sum_{i=1}^{N_r} u_i \Delta t_i}{\sum_{i=1}^{N_r} \Delta t_i} \quad (1)$$

$$v_{mean} = \frac{\sum_{i=1}^{N_r} v_i \Delta t_i}{\sum_{i=1}^{N_r} \Delta t_i} \quad (2)$$

$$u_{rms} = \frac{\sum_{i=1}^{N_r} (u_i - u_{mean})^2 \Delta t_i}{\sum_{i=1}^{N_r} \Delta t_i} \quad (3)$$

$$v_{rms} = \frac{\sum_{i=1}^{N_r} (v_i - v_{mean})^2 \Delta t_i}{\sum_{i=1}^{N_r} \Delta t_i} \quad (4)$$

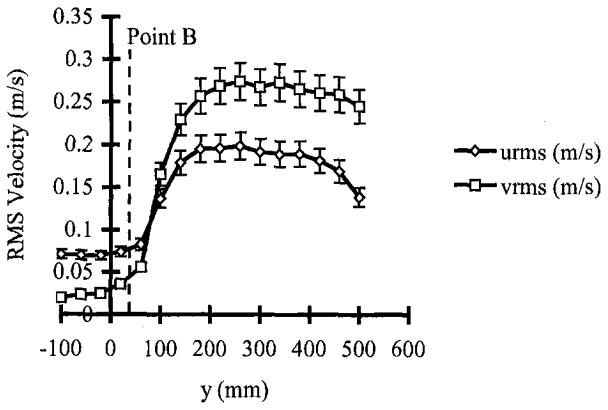

Fig. 4 *y* traverse through point B to illustrate the influence of the jet on the crossflow region (casting rate 2.00 m/min, SEN-mould gap 21 mm, SEN submergence 120 mm)

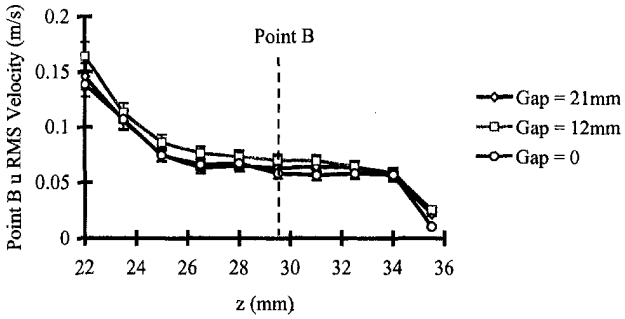

Fig. 5 *z* traverse through point B to illustrate the influence of the jet on the crossflow region (casting rate 2.00 m/min, SEN submergence 120 mm)

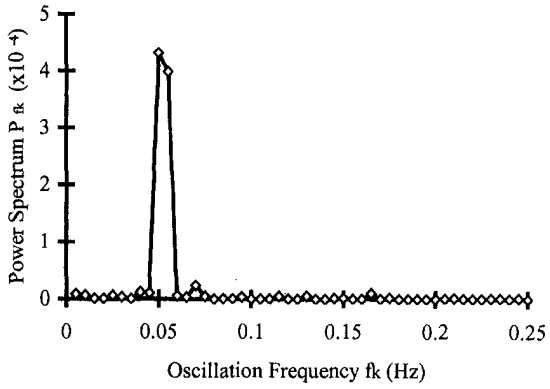

Fig. 7 Power spectrum at point A (casting rate 1.85 m/min, SEN-Mould gap 21 mm, SEN submergence 120 mm)

and where N_r denotes the sample size and Δt_i denotes the residence time of the ith particle in the measurement volume. Error analysis described in the appendix gives an expected error in velocity measurement of between 3.3–8.0%.

Each u velocity component time series measured at points A and B was also processed into a power spectrum to estimate the oscillation period of the jet. This was done by resampling the raw u component data into $N = 4096$ points from an average of the u velocity over the appropriate time increment, Δt_N. Figure 6 shows an example of a resampled time series. These samples were then processed into a power spectrum $P(f_k)$ by using a Fast Fourier Transform (FFT) routine (Press et al., 1992) such that:

$$P(f_k) = \frac{1}{N^2} |U_k|^2 \quad \text{for} \quad k = 1, 2, \ldots, N/2 - 1 \qquad (5)$$

where

$$U_k = \sum_{j=0}^{N-1} u_j e^{2\pi ijk/N} \quad \text{for} \quad k = 0, \ldots, N-1 \qquad (6)$$

$$\text{and} \quad f_k = \frac{k}{N\Delta t_N} \quad \text{for} \quad k = 0, \ldots, N/2,$$

$$\text{with} \quad \Delta t_N = \frac{t_o - t_N}{N}.$$

Here u_j denotes the average velocity at point j in the time series and t_o and t_N represent the times at the start and the end of the sampling period, respectively. A typical power spectrum from point A is shown in Fig. 7. The most dominant peak can be clearly seen and this represents the oscillation frequency of the crossflow at point A. Higher spectral resolution was obtained by using a center of mass estimator on the signal peak region (Alexander and Ng, 1991). Similar analysis was completed on the remainder of the measurement points to calculate the frequency for any given casting rate and SEN-mould gap width. Error analysis described in the appendix gives an expected error in oscillation frequency of between 0.004–0.04 Hz.

Results and Discussion

Crossflow Characteristics. The cyclic behavior of the crossflow is clearly visible from the time series shown in Fig. 6. An oscillating crossflow was always observed to be associated with an oscillation of the jet. The primary crossflow oscillation is seen to be roughly sinusoidal in appearance; the overall period in this case was determined from the calculated power spectrum in Fig. 7 and equals 18.1 s. However, the time series also exhibits velocity fluctuations of much higher frequency over sub-second time intervals. These are illustrated in Fig. 8 which shows a half cycle of the raw data used in Fig. 6. These higher frequencies derive from the turbulent fluctuations which are superimposed on the primary oscillation.

The behavior of crossflow with changing SEN submergence is summarized in Fig. 9. These results at point A and B show the crossflow oscillation frequency to be effectively independent of SEN submergence within the range of experimental error, while the crossflow RMS velocity decreases with increasing SEN submergence. The insensitivity of the oscillation frequency to SEN submergence occurs because the recirculation cells feeding the crossflow are caused by turbulent momentum transfer from the jet. Changing the SEN submergence does not significantly affect this entrainment by the jet, and therefore the oscillation frequency remains unchanged. However, the decrease in RMS velocity occurs because the area between the SEN and the mould wall

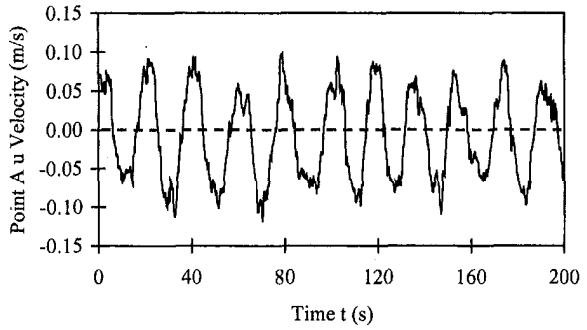

Fig. 6 *u* component time series at point A (casting rate 2.00 m/min, SEN-mould gap 21 mm, SEN submergence 120 mm)

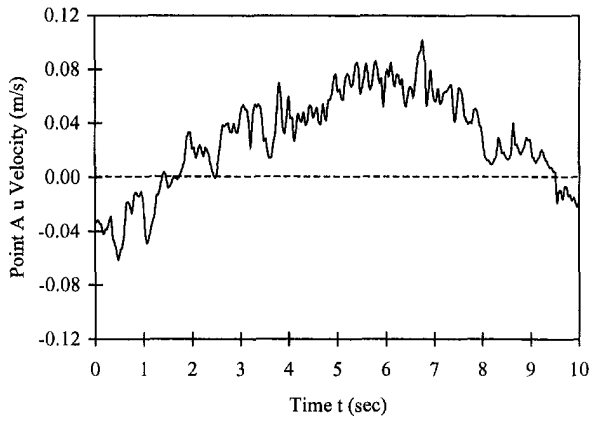

Fig. 8 *u* component time series half cycle at point A (casting rate 2.00 m/min, SEN-mould gap 21 mm, SEN submergence 120 mm)

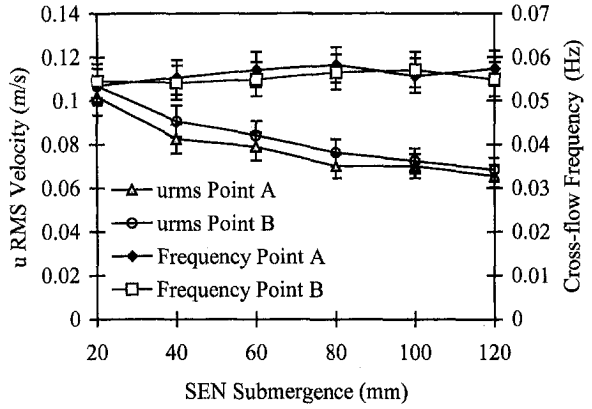

Fig. 9 RMS velocity and frequency of crossflow oscillation vs SEN submergence (casting rate 2.0 m/min, SEN-mould gap width 21.0 mm)

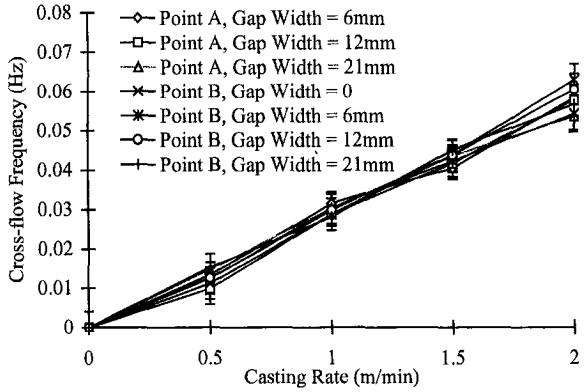

Fig. 11 Characteristics of crossflow oscillation period with casting rate (SEN submergence 120 mm)

available for crossflow increases with increasing SEN submergence.

Figure 10 shows the relationship between crossflow RMS velocity and SEN-mould wall gap width. The gap width was altered by changing the effective outer diameter of the SEN, keeping all other geometric parameters fixed. This only changes the gap available for crossflow past the SEN, leaving that for crossflow past the jet below the nozzle unchanged. Changing the mould thickness (in the z direction), which would alter the gap available for both types of crossflow, will be considered in a subsequent paper.

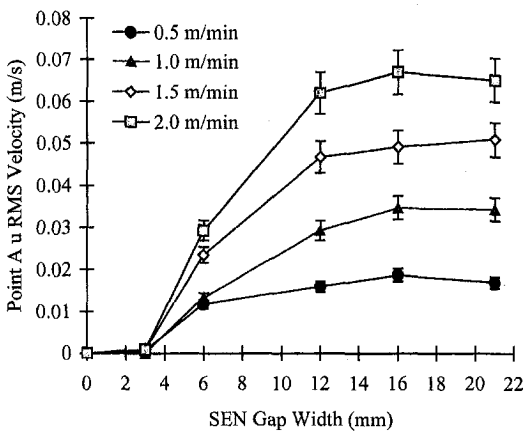

Fig. 10(*a*)

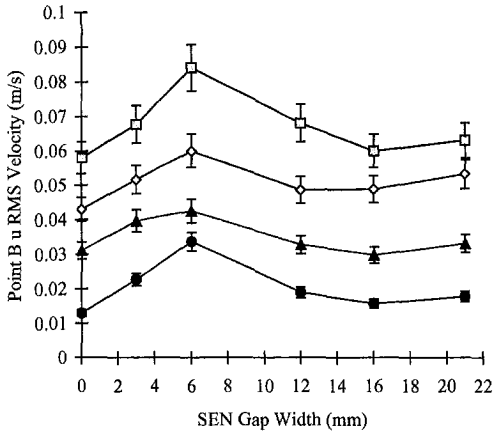

Fig. 10(*b*)

Fig. 10 Characteristics of RMS crossflow velocity with SEN-mould gap width (casting rate 2.0 m/min, SEN submergence 120 mm)

The results in Fig. 10 firstly show crossflow occurring at point B (below the nozzle) for all gap widths. This is possible since a finite distance is required for the jet to expand after exiting the nozzle. The area in the x-z plane adjacent to this expansion zone provides a region for additional crossflow to occur below the SEN exit. As discussed earlier, point B lies in that region. The point B results show that oscillation of the jet can occur even when the gap width between the SEN and the mould wall is reduced to zero. For point A (between the nozzle and the cavity wall) it can be seen that decreasing the gap width results in a decrease of RMS velocity to very small values at a gap width of 3 mm, before falling to zero at zero gap width. This is caused by the increase in flow resistance through the gap as it becomes narrower. However, as the gap width is reduced from the largest values considered here, the crossflow past the jet at point B peaks at a gap width of 6 mm before falling to a non-zero value at zero gap width. This peak in crossflow RMS velocity at point B represents a preferential crossflow between the jet and the mould wall below the SEN exit in the presence of increased flow resistance at point A between the nozzle and the mould wall.

Figures 11 and 12 show the relationships between the crossflow oscillation frequency and RMS crossflow velocity with casting rate for a number of SEN-mould wall gap widths. A linear dependence on casting rate is shown in both cases. In the first case this result is consistent with a dimensionless frequency (Strouhal number), based on a time scale derived from the casting rate (R) and mould width (L), which is independent of casting rate. It is also consistent with other observations of oscillating confined jets for which frequency is proportional to flow velocity (Villermaux and Hopfinger, 1994; Maurel et al., 1996). In the second case, both points A and B show increases in RMS velocity which are proportional to casting rate. This is consistent with a dimensionless flow field

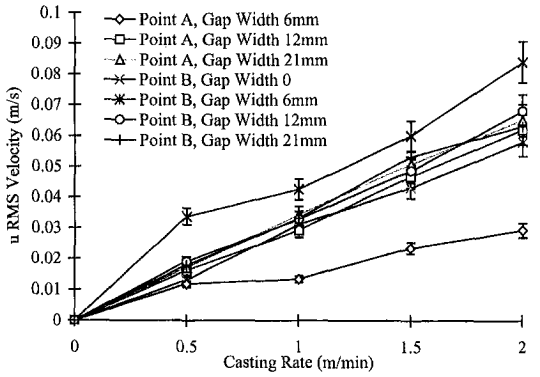

Fig. 12 Characteristics of RMS crossflow velocity with casting rate (SEN submergence 120 mm)

(scaling factor R) which is independent of casting rate. Both results correspond to a Reynolds number independence of the dimensionless flow field (with scaling based on R and L) which is typical of high Reynolds number flows.

The results in Fig. 11 also show that the crossflow oscillation frequency is not sensitive to changes in SEN-mould wall gap width, or vertical location along the gap, within the range of experimental error. The independence of frequency on gap width shows that the instability is determined by the primary confined jet flow in the main body of the mould and not on the resistance to crossflow through the gap. It is interesting to speculate on the possible outcome of a linear stability analysis of the development of small amplitude oscillations from an initial steady flow field without crossflow, such as might occur at very low flow rates (such an analysis is not undertaken here). Consider a two-dimensional theoretical flow model in which the resistance to crossflow is proportional to u^2 in the region of the nozzle (the proportionality constant would depend on gap width), as proposed by Gebert et al. (1998). This resistance term would be of second order in a perturbation analysis and hence would not contribute to predictions of growth rate or frequencies by a linear analysis. In that case, the predicted oscillation frequency would not depend on resistance to crossflow, and hence would not depend on the SEN-mould wall gap width, consistent with the independence of gap width shown in Fig. 11.

From Figs. 10 and 12, the crossflow velocity is seen to be almost the same at both points A and B, and independent of gap widths of 12 mm or more. However, Fig. 12 shows elevated values of u RMS at point B and the reduced values at point A for a gap width of 6 mm compared with corresponding results for other gap widths. The values at B correspond to the peak shown in Fig. 10 for u RMS at point B when gap width is 6 mm. The corresponding values at point A for gap width 6 mm are part way between the zero value when gap width is less than 3 mm (see Fig. 10) and the gap independent values.

Mechanism of Oscillation. Confined jets are characterised by the existence of recirculation zones between the jet and the adjacent walls. Such flows can exhibit self-sustaining oscillations which have a much lower frequency (Strouhal numbers $St \ll 1$) than that associated with the shear layer instability (Rockwell, 1983; Villermaux and Hopfinger, 1994). When the flow is turbulent, as in the present case, additional (turbulent) fluctuations are superimposed on the primary low frequency oscillation. It is generally understood that self-sustaining oscillations of a confined jet are due to a feedback effect related to the confinement and the consequent formation of recirculation cells. In the present case, two feedback pathways are possible. In one, the recirculation cells propagate downstream perturbations upstream to the region near the nozzle. In the other, both sides of the jet are linked via the crossflow through the gap between the nozzle and the cavity wall, and is a direct analogue of the feedback loop in a fluidic oscillator. Since gap width has a significant effect on the amplitude of the oscillation (Fig. 10), crossflow appears to be the primary feedback mechanism in this case.

Figures 13 and 14 show flow visualisation images and schematics for a single oscillation cycle about the centerline of the flow in the mould. Two recirculation cells can be seen on either side of the jet. The cells predominantly move up and down the length of the mould in phase with the crossflow and jet deflection. The movement of these cells in phase with the oscillation of the main jet results in the crossflow around the SEN (Gebert et al., 1998; Lawson and Davidson, 1998). Furthermore, the oscillation frequency of the jet, identified from the flow visualization, is found to be the same as the frequency of the crossflow oscillation. For the case shown in Fig. 13, the period of oscillation is 18 s (however, the image for $t = 18$ s is not shown as it is almost the same as that for $t = 0$).

In a given cycle the two recirculation cells shown in Figs. 13 and 14 will have opposing movements up and down the length of the cavity. At the point in the cycle shown in Fig. 14(a), the

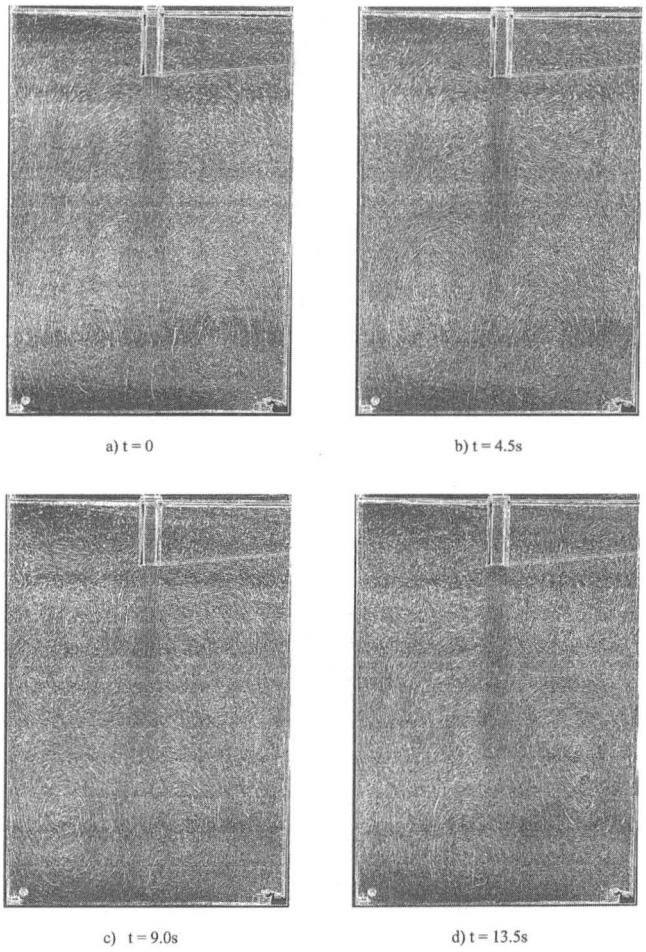

Fig. 13 Flow visualization in the plane $z = 0$ of a single jet oscillation cycle (casting rate 2.0 m/min, SEN-mould gap width 21.0 mm, SEN submergence 120 mm, period 18.1 s)

left-hand and right-hand cells are moving upwards and downwards, respectively, with momentum from the previous cycle. Associated with the cell movement is a crossflow from the left to the right cell which was clearly visible from video imaging of the flow. At this point the pressure in the two cells will be approximately equal. However, as the left cell rises, its angular momentum increases due to the action of the jet shear layer. This causes the pressure in the left cell to decrease. Conversely, the angular momentum of the falling right cell is reduced because of the decaying jet profile, and the pressure in this cell increases. The resulting pressure difference across the jet causes a leftwards deflection of the jet. The same pressure difference across the SEN acts to reduce the crossflow and opposes the motion of the cells as they move up and down the mould face. This adverse gradient eventually reduces the crossflow to zero (Fig. 14(b)) before reversing the crossflow direction. The lower right cell now moves upwards with increasing angular momentum and the upper left cell moves downward with decreasing angular momentum, and the jet moves from left to right, until the pressure difference between the two cells is again almost zero. Now crossflow is from the right to the left cell, with the left cell moving downwards and the right cell upwards, as illustrated in Fig. 14(c). As before, the pressure difference which develops between the cells both displaces the jet (but in the opposite direction) and reduces the crossflow which eventually becomes zero at maximum jet deflection (Fig. 14(d)). The crossflow then moves from left to right, the jet returns to the configuration shown in Fig. 14(a), and a new cycle begins.

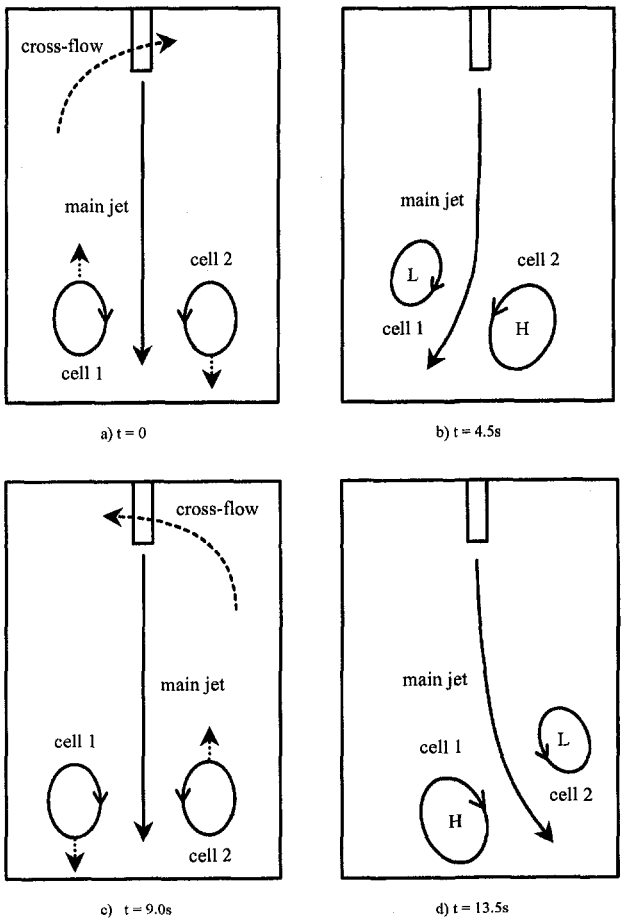

Fig. 14 Flow schematic in the plane $z = 0$ of a single jet oscillation cycle (L-low pressure, H-high pressure)

Conclusion

Oscillatory properties of a $\frac{1}{3}$ scale water model (500 mm wide) of a thin slab continuous casting mould have been successfully characterized by the use of LDA. This application of LDA has allowed oscillatory characteristics of the flow in the mould to be determined over a range of flow rates and geometrical parameters, and in much greater detail, than in previously published work. The fluid crossflow between the SEN and the SEN-mould wall was found to be highly transient due to the turbulent nature of the SEN jet and its adjacent recirculation cells. Both the crossflow oscillation frequency and the RMS crossflow velocity were observed to increase linearly with casting rate. The RMS velocity was found to depend also on SEN submergence (20–120 mm) and SEN-mould wall gap width (0–21 mm), while the frequency was found to be solely dependent on the casting rate (0–2 m/min) for fixed mould geometry and SEN internal diameter. Additional crossflow was also measured in the region below the SEN over the vertical distance required for the jet to expand to fill the space between the broad faces of the mould. The RMS velocity of this additional crossflow past the jet was much less sensitive to SEN-mould wall gap width than that of the primary crossflow past the nozzle. This additional crossflow below the nozzle permitted the flow oscillation to persist even when the primary crossflow was eliminated by reducing the SEN-mould wall gap width to zero.

Acknowledgment

This work was supported by the Australian Research Council using facilities provided by the G. K. Williams Cooperative Research Centre for Extractive Metallurgy, a joint venture between the CSIRO Division of Minerals and the Department of Chemical Engineering.

References

Alexander, B. F., and Ng, K. C. 1991, "Elimination of Systematic Error in Subpixel Accuracy Centroid Estimation," *Optical Engineering,* Vol. 30, pp. 1320–1331.

Austin, P. R. 1992, "Literature Survey on Modelling of Continuous Casting," BHP Research Unrestricted Report BHPR/PMR/R/92/044.

Buchhave, P., George, W. K., and Lumley, J. L. 1979, "The Measurement of Turbulence with the Laser-Doppler Anemometer," *Annual Review of Fluid Mechanics,* Vol. 11, pp. 443–503.

Cherdron, W., Durst, F., and Whitelaw, J. H. 1978, "Asymmetric Flows and Instabilities in Symmetric Ducts with Sudden Expansions," *Journal of Fluid Mechanics,* Vol. 84, pp. 13–31.

Dring, R. P. 1982, "Sizing Criteria for Laser Anemometry Particles," ASME JOURNAL OF FLUIDS ENGINEERING, Vol. 104, pp. 15–17.

Durst, F., Melling, A., and Whitelaw, J. H. 1981, *Principles and Practice of Laser Doppler Anemometry,* Second Edition. London: Academic Press.

Espedal, A. B., and Roder, R. 1993, "Prospects of Thin Gauge High-Speed Strip Casting Technology," *TMS Third Australian-Asian-Pacific Course and Conference on Aluminium Cast House Technology, Theory & Practice,* Nilmani, M., ed., Melbourne, 4–8 July 1993, pp. 303–319.

Gebert, B. M., Davidson, M. R., and Rudman, M. J. 1998, "Computed Oscillations of a Confined Submerged Liquid Jet," *Applied Mathematical Modelling,* Vol. 22, pp. 843–850.

George, W. K., Beuther, P. D., and Lumely, J. L. 1978, "Processing of Random Signals," *Proceedings of the Dynamic Flow Conference, Dynamic Measurements in Unsteady Flows,* Leslie, S. G.; Kovasznay; Favre, A.; Buchave, P.; Fulachier, L.; and Hansen, B. W., Eds., Marseille, September 11–14, 1978; Baltimore, September 18–21, 1978, pp. 757–800.

Gupta, D., and Lahiri, A. K. 1994, "Water Modelling Study of the Surface Disturbances in Continuous Slab Caster," *Metallurgical and Materials Transactions B,* Vol. 25B, pp. 227–233.

Herbertson, J., He, Q. L., Flint, P. J., and Mahapatra, R. B. 1991, "Modelling of Metal Delivery to Continuous Casting Moulds," *Iron and Steel Society,* Vol. 74, 1991 Steelmaking Conference Proceedings, Washington DC, April 14–17, 1991, pp. 171–185.

Honeyands, T. A., Lucas, J., and Chambers, J. 1992, "Preliminary Modelling of Steel Delivery to Thin Slab Caster Moulds," *Iron and Steel Society,* Vol. 75, 1992 Steelmaking Conference Proceedings, Toronto, 5–8 April, 1992, pp. 451–459.

Honeyands, T. A. 1994, *Flow Dynamics in Thin Slab Caster Moulds,* PhD thesis, University of Newcastle, Australia.

Honeyands, T. A., and Herbertson, J. 1995, "Flow Dynamics in Thin Slab Caster Moulds," *Steel Research,* Vol. 66(7), pp. 287–293.

Lawson, N. J., and Davidson, M. R. 1998, "Measurement of Cross-Flow Characteristics from a Transient Water Model of a Thin Slab Casting Mould," IMechE Optical Methods and Data Processing in Heat and Fluid Flow Conference, London, 16–17 April 1998, pp. 301–310.

Marple, S. L. 1987, *Digital Spectral Analysis with Applications,* London: Prentice Hall.

Maurel, A., Ern, P., Zielinska, B. J. A., and Wesfreid, J. E. 1996, "Experimental Study of Self-sustained Oscillations in a Confined Jet," *Physical Review E,* Vol. 54(4), pp. 3643–3651.

Molloy, N. A. 1969, "Oscillatory Flow of a Jet into a Blind Cavity," *Nature,* Vol. 224, pp. 1192–1194.

Morris, G. J., Jurewicz, J. T., and Palmer, G. M. 1992, "Gas-solid Flow in a Fluidically Oscillating Jet," *Trans. ASME,* Vol. 114, pp. 362–366.

Nilles, P., and Etienne, A. 1991, "Continuous Casting Today—Status and Prospects," *Metallurgical Plant and Technology International,* Vol. 6, pp. 56–67.

Rockwell, D., and Naudasher, E. 1979, "Self-sustained Oscillations of Impinging Free Shear Layers," *Annual Review of Fluid Mechanics,* Vol. 11, pp. 67–94.

Rockwell, D. 1983, "Oscillations of Impinging Shear Layers," *AIAA Journal,* Vol. 21(5), pp. 645–664.

Shakouchi, T. 1989, "A New Fluidic Oscillator, Flowmeter, Without Control Port and Feedback Loop," ASME *Journal of Dynamic Systems, Measurement and Control,* Vol. 111, pp. 535–539.

Viets, H. 1975, "Flip-flop Jet Nozzle," *AIAA Journal,* Vol. 13(10), pp. 1375–1379.

Villermaux, E., and Hopfinger, E. J. 1994, "Self-sustained Oscillations of a Confined Jet: A Case Study for the Non-linear Delayed Saturation Model," *Physica D,* Vol. 72, pp. 230–243.

APPENDIX

Error Analysis. For the LDA system, measurement errors originate from a number of sources. The following simplified error analysis will include a velocity error (e_V) due to the seeding response to flow fluctuations, a statistical error (e_S) due to the sampling rate, and a velocity bias error (e_B) due to the particle statistics. If the uncertainty in measurement of the quantities e_V, e_S and e_B is represented by the percentage errors $\delta(e_V)$, $\delta(e_S)$ and $\delta(e_B)$, respectively, then the total percentage error in velocity measurement, $\delta(U)$ can be found from:

$$\delta(U) = \sqrt{[\delta(e_V)]^2 + [\delta(e_S)]^2 + [\delta(e_B)]^2}. \quad \text{(A1)}$$

The error due to the seeding response (e_V) can be simply estimated from previous work by Dring (1982) by using a Stokes number St based on an estimated time scale for the most rapid velocity fluctuations. With the seeding size range of 10–30 μm, specific gravity of 1.1, and a maximum flow fluctuation of 1 kHz, the Stokes number will range from St = 0.06–0.55. This results in a velocity error range of $0 < \delta(e_V) < 5\%$. An estimate of the statistical error (e_S) can be obtained from a previous work by George et al. (1978) for a known integral time scale, sampling period, sample rate, and ratio of standard deviation to mean velocity ($\sigma/\bar{U}$). If the integral timescale is estimated by the oscillation period, it will range approximately from 10–40 s. The sampling period was set to 250 s and the average sampling rate was 100 Hz. For the ratio $\sigma/\bar{U}$, the cyclic nature of the crossflow will result in theoretically zero values of the mean which was found to be the case during the measurements. Therefore a more appropriate quantity must be used to estimate the error. In this case the SEN jet turbulence intensity is used since any momentum transfer into the mould originates from the jet oscillation which generates the crossflow. The average turbulence intensity measured at the jet centerline was 11% which gave a statistical error band of $3.1\% < \delta(e_S) < 6.2\%$. For the bias error estimate (e_B), a comprehensive analysis has been completed by previous workers (see Buchhave et al., 1979) who provide curves to estimate the bias errors. If the turbulence intensity at the jet centerline is used as before, the bias error $\delta(e_B)$, with residence time weighting, will approximately equal 1.0%. Therefore, from equation A1, the total velocity measurement error expected would lie in the range of 3.3–8.0%.

To obtain a simplified estimate of error in the crossflow oscillation frequency, the resolution attainable from the FFT spectral peak analysis will be used. With a time-bandwidth product of one and a sampling period of 250 s, the minimum spectral resolution will be 0.04 Hz (Marple, 1987). Use of the central of mass estimator with sufficient sampling frequency, however, has shown the attainable resolution from the signal peak to be at least one tenth of the discretised resolution (Alexander and Ng, 1991). Therefore the error range for the estimation of oscillation frequency would be expected to lie within the range 0.004–0.04 Hz.

Mean and Turbulence Characteristics of Three-Dimensional Wall Jet on Convex Cylindrical Surfaces

B. H. Lakshmana Gowda
Fluid Mechanics Laboratory,
Department of Applied Mechanics,
Indian Institute of Technology,
Madras-600 036, India

V. S. B. Durbha
Research Fellow,
Fluid Control Research Institute,
Palghat, India

The influence of convex curvature on the mean and turbulent characteristics of three-dimensional wall jet generated from a circular orifice geometry is reported in this paper. Mild, moderate, and strong curvature are considered. Detailed results on a plane surface are also obtained for comparison purposes. Among the mean properties, the decay rate of maximum velocity and the growth of length scales are significantly altered due to curvature effects. The turbulent components, both turbulent normal and shear stresses, show an increase with curvature parameter in a direction normal to the curved surfaces; however, there is very little change in the spanwise direction.

1 Introduction

A wall jet is formed when a jet of fluid strikes a surface at an angle. The angle can vary between 0 to 90 deg. When the angle is 0 deg, i.e., the jet flows over the surface tangentially, the wall jet so formed is called a plane wall jet. When the angle is 90 deg i.e., the jet impinges on the surface normally, the wall jet is called radial wall jet (Glauert, 1956). The geometry of the nozzle from which the fluid issues out onto a flat surface to form a wall jet decides whether the wall jet is two-dimensional, axisymmetric, or three-dimensional. When the aspect ratio of the nozzle from which the jet issues onto a solid boundary is finite, the wall jet becomes three-dimensional (Sforza and Herbst, 1970). In the case of three-dimensional wall jet it is necessary to measure the flow properties both in longitudinal and lateral directions. A typical sketch of a three-dimensional wall jet is shown in Fig. 1 with the various velocity and length scales. The shape of the velocity distribution suggests a possible division of the profile into two regions: (1) the inner region extending from the wall to the point of maximum velocity, (2) the outer region extending from the point of maximum velocity to the periphery of the jet. At the two extremities of the wall jet, the velocity is zero. The velocity scale is usually the local maximum velocity U_m, at any station along the axis of the jet. The length scales are b, the distance from the wall to the point in the outer region where the velocity is half of the maximum velocity at that section (half-width) and $z_{m/2}$ in the spanwise direction (Fig. 1). There are a number of fields of engineering applications where wall jets occur such as the boundary layer control of airfoils, effective film cooling of turbine blades, in the design of air vents for ventilation purposes and in the area of fluidics.

In many of the practical applications of wall jets cited above, curvature effects (particularly convex curvature) occur. Hence, it would be essential to understand the effect of curvature both on mean and turbulence characteristics of wall jets developing on such surfaces. There are quite a few investigations which deal with the influence of curvature on the properties of two-dimensional wall jets (for example: Wilson and Goldstein, 1976; Alcaraz et al., 1977; Dakos et al., 1984; Fujisawa and Shirai, 1987). Comparatively, there is very little information on the development of three-dimensional wall jets on curved surfaces; there appears to be only three studies which deal with this aspect (Patankar and Sridhar, 1972; Catalano et al., 1977; Iida and Matsuda, 1988). Patankar and Sridhar (1972) investigated three-dimensional wall jets on a cylindrical surface; the geometry of the orifice was square. Using a circular geometry, Catalano et al. (1977), and Iida and Matsuda (1988) studied the properties of three-dimensional wall jet on a convex circular cylinder; they presented only $\bar{u}$ and $\bar{v}$ up to a short length from the jet exit of the orifice. Iida and Matsuda (1988) have made measurements up to $25d$ and they reported $\bar{u}$, $\bar{v}$, $\bar{w}$, and $\overline{uv}$ in the plane of symmetry and $\overline{uw}$ in the spanwise direction. In all these cases the measurements were not reported in the fully developed region of a three-dimensional wall jet.

In all the investigations dealing with the study of curvature effects, there are basically two types of approaches, 1. the radius of curvature of the surface is kept constant (Wilson and Goldstein, 1976; Alcaraz et al., 1977; Dakos et al., 1984; Fujisawa and Shirai, 1987), 2. the curvature parameter (b/R; b is the half-width and R, the radius of curvature) is maintained constant along the length of the curved surface (Giles et al., 1966; Kamemoto, 1974; Guitton and Newman, 1977). In the latter case, taking into account the rate of growth of the half width b, the condition of having constant curvature parameter along the length of the surface leads to logarithmic spiral surfaces (the radius of curvature has to vary continuously along the length to obtain the required curvature parameter). In the former case, the surfaces will be cylindrical surfaces. There are advantages and disadvantages in both approaches. In the second case, the influence of a particular curvature parameter on the properties of the wall jet can be seen, whereas in the first case, the properties on a cylindrical surface with a particular radius of curvature are obtained; the curvature parameter will be varying along the length of the cylindrical surface. In practical situations, rarely does one come across a situation where the radius of curvature is changing continuously along the flow direction resulting in a surface with constant curvature parameter. Even if there are changes in the radius of curvature, one could expect long stretches where it will remain constant. Hence, from among the two approaches adopted to study the influence of curvature, the former seems to be nearer to practical situations. This is the approach that has been adopted in the present study.

Investigations have been carried out to determine both mean and turbulence characteristics of three-dimensional wall jets developing on convex surfaces with constant radius of curvature using a circular orifice geometry. Studies are made on three such cylindrical surfaces: 1. Surface with a large radius of curvature (referred

Contributed by the Fluids Engineering Division for publication in the JOURNAL OF FLUIDS ENGINEERING. Manuscript received by the Fluids Engineering Division March 13, 1997; revised manuscript received April 19, 1999. Associate Technical Editor: M. S. Triantafyllou.

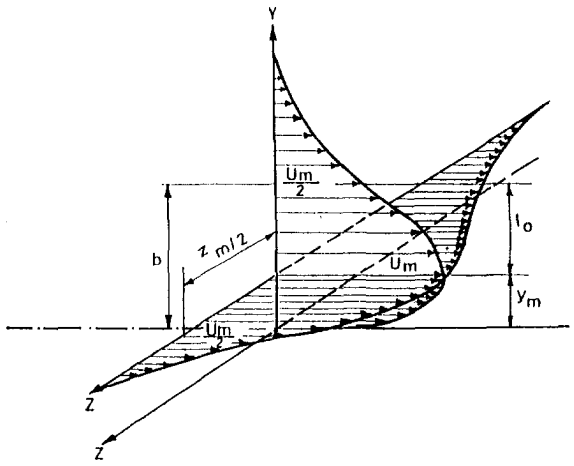

Fig. 1 Definition sketch of a three-dimensional wall jet

to as cylindrical surface 1 or CYS 1) which gives low values of local curvature parameter (b/R varying from 0.01 to 0.03); 2. Cylindrical surface 2 (CYS 2), where the radius of curvature is such that a range of medium local curvature parameters is obtained (b/R varying from 0.025 to 0.12) and 3. A cylindrical surface with a small radius of curvature (CYS 3) which gives high values of local curvature parameter (b/R varying from 0.12 to 1.114). Measurements have been carried out on a plane surface also for obtaining corresponding comparison. Though there are earlier studies on plane surface using circular orifice geometry (e.g., Newman et al., 1972; Padmanabham and Gowda, 1991a, b), the present measurements on plane surface were necessitated to match the lengths employed for the curved surfaces and as the information on detailed mean and turbulent quantities are not available over large distance from the orifice exit.

2 Experimental Procedure

2.1 The Test Setup. All the measurements reported here have been performed using the low speed jet tunnel facility of the Fluid Mechanics Laboratory, Indian Institute of Technology, Madras. It is essentially the same as that employed by Padmanabham and Gowda (1991a and b). Figure 2 shows the schematic diagram of the jet tunnel and the general layout of the experimental arrangement with the flat plate on which the plane wall jet is generated. At the end of the settling chamber an orifice plate made of mild steel (5 mm thickness) having a 10 mm diameter circular orifice was fitted. The orifice plate conforms to Indian Standard specifications (IS:2952, 1964). Before carrying out the wall jet measurements, the characteristics of free jet issuing from the 10 mm dia orifice were determined similar to the results obtained by Padmanabham and Gowda (1991a). The flow field characteristics of the jet corresponded to those of standard free jets (Abromovich, 1963; Schlichting, 1968); the details are given in Durbha (1996). The position of the flat plate and its dimensions are shown in Fig. 2.

A smooth polished plate of size 1.45 m × 2.05 m × 18 mm thick made of teak wood was used to produce the wall jet on the flat surface. The dimensions of the plate were found to be adequate from the preliminary studies. The plate was fixed vertically by brackets on a rigid stand, made of mild steel channels. The stand is provided with levelling screws at the bottom. The leading edge of the plate was chamfered to 45 (to avoid pressure gradient effects due to rounded leading edge) and was placed exactly at the exit of the orifice (flush with the orifice plate) as shown in Fig. 2.

As mentioned in the Introduction, it was planned to carry out measurements on cylindrical surfaces with the curvature parameter varying from a very low value (b/R = 0.01) to a very high value (b/R = 1.1). It was not an easy task to arrive at the various required radii of curvature which would give the necessary range of the curvature parameter. Preliminary measurements were required for that. Measurements were first carried out on the flat surface to obtain the growth rate of the half width (b). Further, it is known and also confirmed in the present study that the turbulent quantities in the case of a three-dimensional wall jet developing on a plane surface attains similarity beyond a distance of 50 times the diameter of the orifice. Hence, it was planned in the present investigation to provide an initial straight portion equal to $60d$ and then introduce the necessary convex curvature. This will ensure that the wall jet profile (both mean and turbulent) is fully developed before it experiences curvature effects.

Based on the value of b obtained on the plane surface, the radii of curvature of the various plates were arrived at to obtain approximately the different ranges of b/R. As the growth rate of b on the curved surfaces were not known before hand, more than the required number of surface plates had to be designed and fabricated. For this purpose totally five plates were designed and prepared. But finally it was found that three of these could give the required range of b/R values. The dimensions of the various plates are shown in Fig. 3. All the plates had a width of 1220 mm in the spanwise direction and a length of 1850 mm. The photograph of one of the plates (CYS3) is shown in Fig. 4(a).

All the measurements reported in this study have been carried out using hot-wire anemometer. The mean velocity measurements were carried out by using a single normal wire probe. The various components of the normal stresses i.e., $\tilde{u}$, $\tilde{v}$, and $\tilde{w}$ and the turbulent shear stresses $\overline{uv}$ and $\overline{uw}$ are measured by using a X-wire probe. The method described by Champagne and Sleicher (1967) has been utilized to calculate the turbulent quantities from the

Nomenclature

R = Radius of curvature
Re_d = Reynolds number ($=U_j d/\nu$)
U = mean velocity in x-direction
U_j = velocity at the exit of the orifice
U_m = maximum velocity in the x-direction at any station
b = y in the outer region of the wall jet at which $U = U_m/2$
d = diameter of the orifice
k = total turbulent kinetic energy ($\overline{u^2} + \overline{v^2} + \overline{w^2}$)/2
n = decay exponent of the maximum velocity
q^2 = $2k$ (k is as defined above)
$\tilde{u}$ = RMS fluctuating velocity in x-direction
$\tilde{v}$ = RMS fluctuating velocity in y-direction
$\tilde{w}$ = RMS fluctuating velocity in z-direction
$\overline{uv}$ = Reynolds shear stress in xy plane
$\overline{uw}$ = Reynolds shear stress in xz plane
x = axial distance reckoned from the exit plane along the jet axis and parallel to the plate
y = coordinate normal to the jet axis, and, normal to the wall
y_m = thickness of the inner region of a wall jet in y-direction
y_0 = position of zero shear stress
z = coordinate normal to the jet axis and parallel to the wall (spanwise direction)
$z_{m/2}$ = velocity half-width (where $U = U_m/2$) in the spanwise direction at a distance $y = y_m$ from the wall
ν = kinematic viscosity
RMS = Root Mean Square
2-d = two-dimensional
3-d = three-dimensional

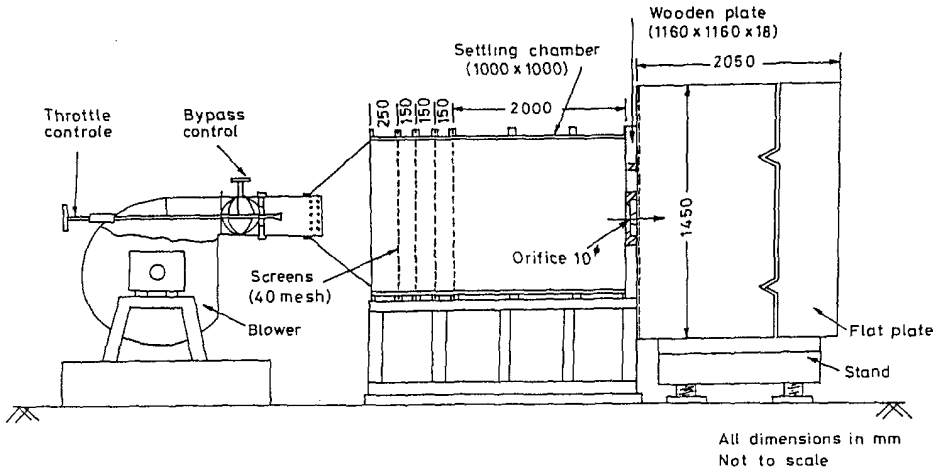

Fig. 2 Experimental setup

measured signals. The constant temperature hot-wire anemometer system DANTEC 56 C with CTA bridges 56C17, linearisers (56N21), signal conditioners (56N20), digital voltmeter (56N10), RMS voltmeter (56N11) and analog processor unit (56N22) are made use of. For single wire measurements, the DISA 55P11 miniature wire probe of 1.25 mm length made of platinum coated tungsten wire 5 μm in diameter is made use of. The cross-wire probe used is DISA miniature-wire probe 55P61 with a wire length of 1.25 mm and a wire separation of 2 mm. The linearisation and calibration of the probes are carried out in two velocity ranges (i) 80 m/s to 8 m/s and (ii) 8 m/s to 0.5 m/s.

The velocity at the exit of the orifice was calibrated against the wall static pressure of the jet tunnel. The tunnel wall static pressure was measured with the help of a Betz manometer from the pressure tapping provided in the side of the settling chamber just upstream of the orifice and this was used to monitor the jet exit velocity over the duration of any run (which lasted for about 4 hours). The change in the temperature of the jet was about 2° to 3°C. However, this variation has been neglected and fluid properties at 30°C have been used in analysing the experimental data. The symmetry of the flow was checked by taking a few measurements on either side of the jet axis at equidistant points from the jet axis. All the measurements have been carried out at a jet exit velocity of 80 m/s. The jet exit Reynolds number based on the diameter of the orifice is 5.48×10^4. On all the cylindrical surfaces it was made sure that the flow is attached to the surface in the range of measurements. This was done using a small tuft probe very close to the surface and noting its direction of motion. Before carrying out the detailed experiments over the cylindrical surfaces, the variation of the centreline static pressure over these surfaces have been measured.

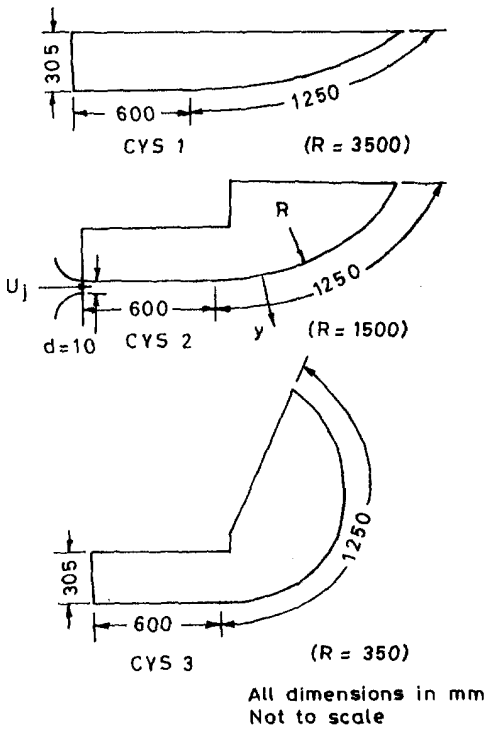

Fig. 3 Details of the curved plates

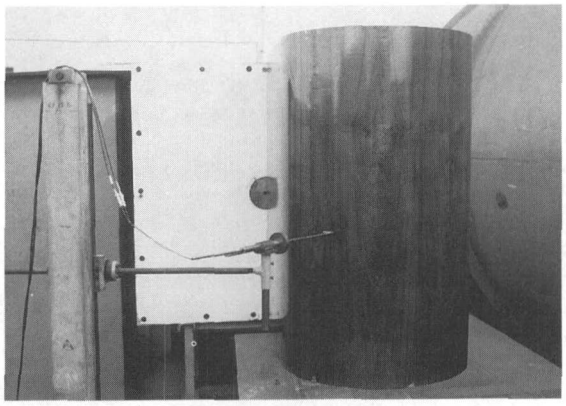

Fig. 4(*a*) Setup with CYS3

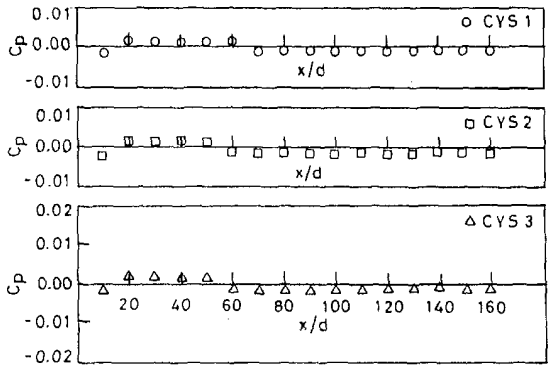

Fig. 4(*b*) Variation of static pressure coefficient along the centreline of the cylindrical surfaces

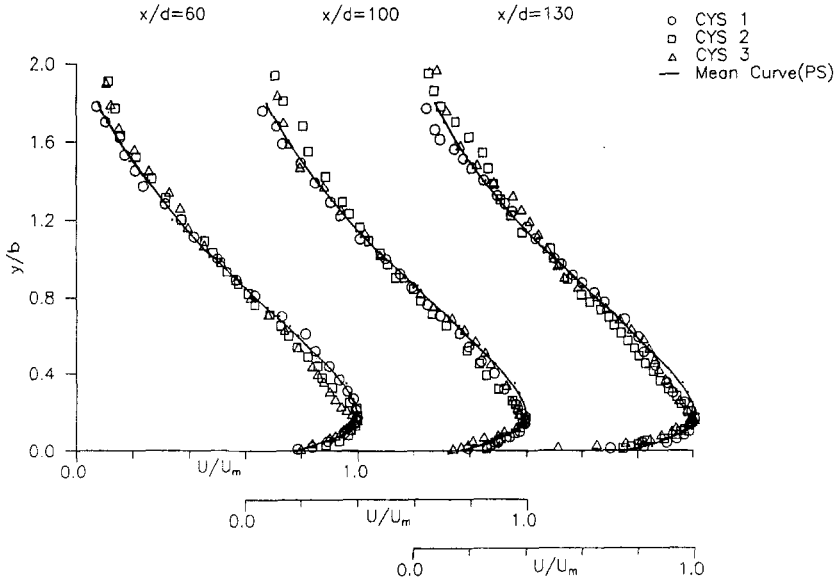

Fig. 5 Normalized mean velocity profiles at three typical axial stations on CYS1, CYS2, and CYS3 in the plane of symmetry (uncertainty in y = 0.5 mm; uncertainty in U = ±1.62 percent at 20:1 odds)

Figure 4(b) shows the variation of the static pressure coefficient $C_p = (p_s - p_a)/\frac{1}{2}\rho U_j^2$ (where p_s = static pressure on the surface; p_a = atmospheric pressure) along the centreline of each model up to a distance of 160 diameters. The pressure tappings are provided at every 10d from the exit of the orifice. From the figure it is seen that the static pressure is slightly negative over the curved portion. Further details such as, fabrication and alignment of surface plates and probes, traversing mechanism, calibration procedure, reduction of data using response equations, comparison of results that can be obtained by the single wire and the cross-wire probes (U and $\tilde{u}$) etc. are given in Durbha (1996).

2.2 Uncertainty Levels. In the present study, the plane and cylindrical surfaces on which wall jets are generated are made of wood (nonconducting) and as such, wall corrections are not applied to the measured data. Bhatia et al. (1982) have found such corrections are not required if the material of the plate is nonconducting. To determine the uncertainty levels in the various quantities measured, the procedure as explained by Kline and McClintock (1953) is adopted. The method is based on a careful specification of the uncertainties in the various primary experimental measurements. The detailed analysis is given in Durbha (1996). The estimated overall uncertainty levels in the various quantities measured, with 20:1 odds are: $U = \pm 1.62\%$; $\tilde{u}/U_m = \pm 1.83\%$; $\tilde{v}/U_m$ and $\tilde{w}/U_m = \pm 2.15\%$; $k = \pm 3.5\%$, $\overline{uv}/U_m^2$ and $\overline{uw}/U_m^2 = 8.71\%$.

The velocity at the exit of the orifice plate was very uniform and the variation was less than 0.5 percent. The uncertainty levels in the measurements are indicated in each of the figures.

3 Results and Discussion

Detailed mean and turbulent quantities on the curved surfaces (CYS1, CYS2 and CYS3) and the plane surface (PS) were measured at internals of 10d along the x-direction. The measurements are carried out normal to the surface plates in the plane of symmetry (z = 0). Also, results are obtained in the spanwise direction at $y = y_m$. The detailed results on each of the plates are given in Durbha (1996). Here, only typical results are presented which bring out the essential features of the characteristics of the flow field considered. The results on the plane surface, as mentioned earlier, were obtained particularly for comparing the turbulent quantities obtained on cylindrical surfaces. The results on the PS were compared with earlier results on plane surface of Swamy and Bandyopadhyay (1975) and Padmanabham and Gowda (1991a and b) and the comparison is seen to be very satisfactory (Durbha and Gowda, 1995). In the present paper, for comparing the results obtained on the curved surfaces with those on the plane surface, only the average curves passing through the experimental results for the plane surface (PS) are shown.

3.1 The Scaling Parameters. Wall jet is a turbulent shear flow and any such flow is in equilibrium in a region if, at every streamwise station in the region, the distribution of mean velocity and the turbulent stresses exhibit similarity with essentially same scales; meaning that in self-preserving flows, the scales that go into the mean velocity are the same as those that go into the Reynolds stresses (Narasimha and Prabhu, 1972).

In a wall jet on a plane surface, the length and velocity scales that have been used are the b and U_m (for two-dimensional case); b, U_m and $z_{m/2}$ when the wall jet is three-dimensional. These are used to normalise the mean flow characteristics. These scales are used for normalising the turbulence quantities also to study if similarity is achieved as the wall jet grows along a plane surface. The same length and velocity scales have been used in respect of two-dimensional wall jet on curved surfaces with varying curvature parameter along the streamwise direction (e.g. Wilson and Goldstein, 1976; Kobayashi and Fujisawa, 1983). In the present study also these length and velocity scales have been used to normalise quantities while presenting both mean and turbulent results. Such a normalisation is expected to indicate the achievement of similarity or otherwise of the various quantities in the wall jet.

3.2 Mean Flow Characteristics. The important overall mean flow characteristics for a three-dimensional wall jet are: 1. mean velocity profile and its similarity form; 2. the rate of decay of the maximum velocity, U_m; 3. the growth of half-widths. These are presented and discussed in what follows.

Among the mean flow characteristics, the least affected due to curvature, appears to be the velocity profiles both normal to the plate and in the spanwise direction. This can be seen from Figs. 5 and 6 where the results at three typical stations i.e., x/d = 60, 100 and 130 for all the cases considered i.e., CYS 1, CYS 2, CYS 3, and PS are shown. Though there appears to be overall agreement in the shape of the mean velocity profiles for the curved surfaces

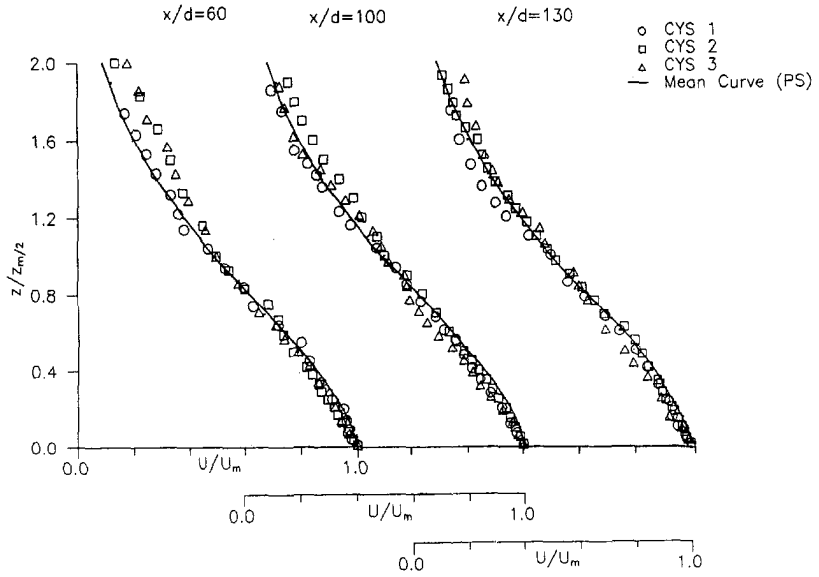

Fig. 6 Normalized mean velocity profiles at three typical stations on CYS1, CYS2, and CYS3 in the spanwise direction at $y = y_m$ (uncertainty in z = 0.5 mm; uncertainty in U = ±1.62 percent at 20:1 odds)

and the plane surface (Fig. 5), a close observation reveals that there is indeed some difference near the point of maximum velocity and near the outer edge. The curvature effects tend to make the shape of the profiles somewhat sharper compared to the plane case. However, in the spanwise direction, hardly any difference is observed between the results for the curved surfaces and the plane surface (Fig. 6).

The mean flow characteristics which are most affected due to curvature effects are the decay rate of the maximum velocity and the growth of half width normal to the plate. In a three-dimensional wall jet, the decay of the maximum velocity in the plane of symmetry can be expressed in a power law form:

$$(U_m/U_j)\alpha(x/d)^{-n}$$

The decay rate for the various cases in the different regions i.e., potential core (PC), characteristic decay (CD) region and radial decay (RD) region (Sforza and Herbst, 1970) are shown in Fig. 7 for all the cases considered. In the PC ($x/d \approx 5$), the CD region ($x/d \approx 20$) and up to $x/d = 60$ in the RD region, the results for the cylindrical and the plane surface are same due to the initial straight portion provided for the former. However, beyond $x/d = 60$, from where the curvature starts, it is observed that the rate of growth can increase by a factor of two due to curvature effects. Such an increase is linked with the increased growth rate of the wall jet normal to the surface i.e., the length scale b. The reasons for the increased growth rate of b is brought out in the following discussion.

The growth of the length scale, b for all the cases is shown in Fig. 8. In addition, the scale in the spanwise direction ($z_{m/2}$) for CYS 3 is also included in this figure. It is clear to see that the convex curvature effects result in a higher growth rate normal to the surface, and this growth rate can even overtake that in the spanwise direction. This is very interesting and significant for the following reason. In a three-dimensional wall jet, the growth in the spanwise direction is much larger than that normal to the plate; the factor can be 5 to 6. Such a feature is attributed to the lateral vortex

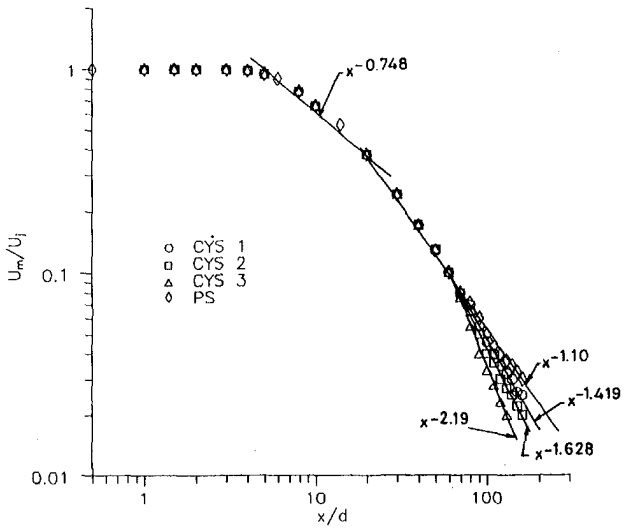

Fig. 7 Decay of the maximum velocity (uncertainty in x = 0.5 mm; uncertainty in U = ±1.62 percent at 20:1 odds)

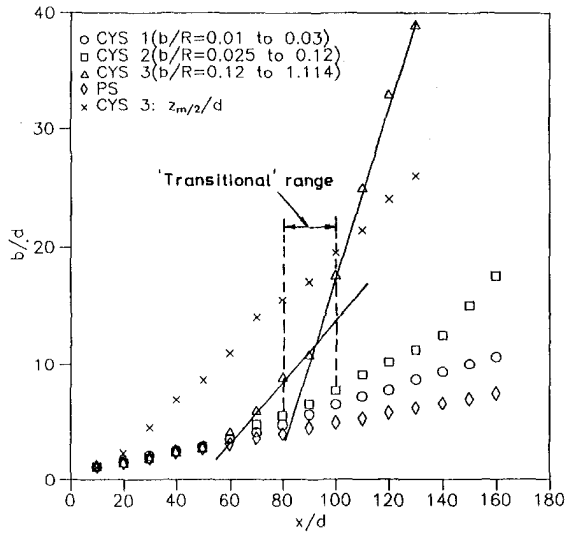

Fig. 8 Growth of half width normal to the surface (uncertainty in y = 0.5 mm; uncertainty in x = 0.5 mm)

Table 1 Growth rates of three-dimensional wall jet on cylindrical surfaces

Investigator	Curvature parameter b/R	Range of measurement x/d	db/dx	$dz_{m/2}/dx$	$\frac{(dz_{m/2}/dx)}{db/dx}$
Present data (PS)	—	0 to 160	0.043	0.25	5.8
Present data					
CYS 1	—	0 to 60	0.043	0.235	5.47
	0.01 to 0.03	60 to 160	0.051	0.235	4.62
CYS 2	—	0 to 60	0.043	0.23	5.34
	0.025 to 0.083	60 to 140	0.110	0.23	2.08
	0.083 to 0.12	140 to 160	0.253	0.23	0.91
CYS 3	—	0 to 60	0.043	0.21	4.88
	0.12 to 0.311	60 to 80	0.220	0.21	0.95
	0.311 to 1.114	100 to 130	0.726	0.21	0.29
Padmanabham and Gowda (PS)	—	0 to 100	0.045	0.216	4.8

stretching that occurs for a three-dimensional wall jet (Newman et al., 1972; Padmanabham and Gowda, 1991a). However, it is seen that due to curvature effects, the growth of the wall jet normal to the plate can increase considerably and even overtake the growth in the spanwise direction. This is seen in the present case for CYS 3. Actually, for CYS 3, there appears to be two ranges i.e., x/d = 60 to 80 and 100 to 130, where the growth rates are different; the rate being steep in the latter range of x/d (i.e., 100 to 130). There is a small intermediate "transitional" range between these two. Such a large growth of wall jet due to curvature effects has also been observed by Wilson and Goldstein (1976) in their study on two-dimensional wall jet on convex cylindrical surface. This is attributed by Wilson and Goldstein (1976) to the large centrifugal force contribution represented by the term

$$2\overline{uv}U/(R + y)$$

For the present case also, the domination of this term through very large observed values of $\overline{uv}$ is seen. This aspect, particularly the link between the large increase in the growth of the wall jet normal to the plate and the turbulent shear stress $\overline{uv}$ is further referred to and discussed at a later stage while presenting the turbulence characteristics. In Table 1, the ratio of the growth rate in the spanwise direction to that normal to the plate i.e., $(dz_{m/2}/dx)/(db/dx)$ for the various cases are summarised. The observation made above is reflected in the values shown in the table.

The effect of the curvature on the growth of the half width ($z_{m/2}$) appears to be only marginal in the spanwise direction as can be seen in Fig. 9. The growth rates for the various cases are listed in Table 1.

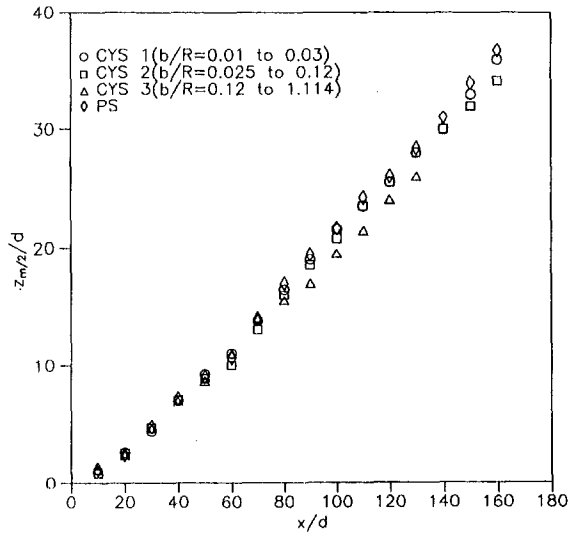

Fig. 9 Growth of half width in the spanwise direction (uncertainty in z = 0.5 mm; uncertainty in x = 0.5 mm)

3.3 Turbulence Characteristics. The detailed variation of the turbulence characteristics on each of the plate are given in Durbha (1996). The main features observed are the increase in the turbulent quantities with curvature and the absence of self presentation. Typical results are presented and discussed.

3.3.1 Variation of Turbulent Normal and Shear Stresses. Figures 10 to 12 show the distribution of turbulent quantities $\tilde{u}$, $\tilde{v}$, $\tilde{w}$, $\overline{uv}$, and k in the plane of symmetry at three different locations over the cylindrical surfaces. The mean curve through the results for the plane surface (PS) is included in all the figures. Figure 10(a) shows the variation of longitudinal turbulence intensity $\tilde{u}$ and at any particular longitudinal station in the plane of symmetry, the turbulence levels increase with increase in the curvature parameter. For CYS 3, at x/d = 130, the levels are nearly 65 percent higher than the plane surface value. The peak value occurs around y/b = 0.6 for all the cases at different stations. The variation of $\tilde{v}$

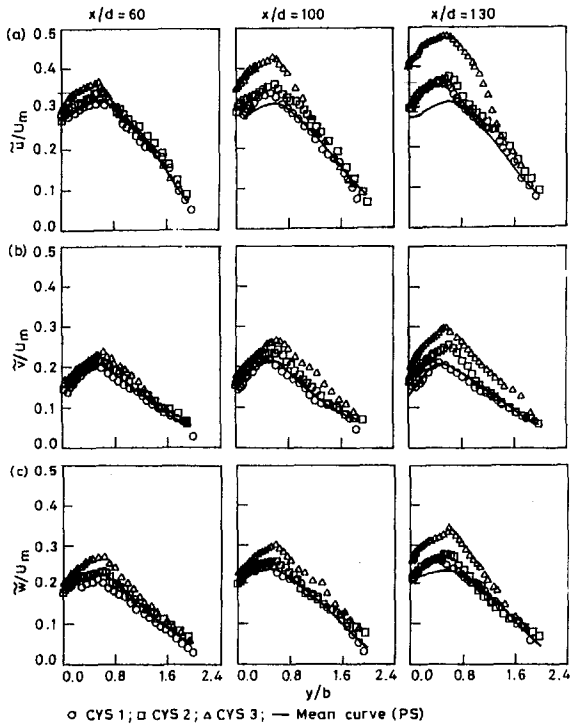

Fig. 10 Distribution of turbulence intensities $\tilde{u}$, $\tilde{v}$, and $\tilde{w}$ across the wall jet at three typical axial stations on CYS1, CYS2, and CYS3 in the plane of symmetry (uncertainty in y = 0.5 mm; uncertainty in $\tilde{u}/U_m$ = ±1.83 percent at 20:1 odds; uncertainty in $\tilde{v}/U_m$ and $\tilde{w}/U_m$ = ±2.15 percent at 20:1 odds)

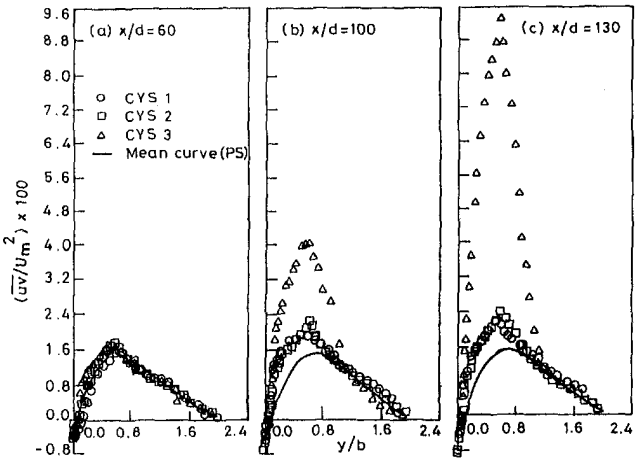

Fig. 11 Distribution of shear stress $\overline{uv}$ at three typical axial stations on CYS1, CYS2, and CYS3 in the plane of symmetry (uncertainty in y = 0.5 mm; uncertainty in $\overline{uv}/U_m^2$ = ±8.71 percent at 20:1 odds)

component is shown in Fig. 10(*b*). Initially, there is a steeper variation observed (compared to $\tilde{u}$) away from the wall with a peak at $y/b = 0.55$ and then the values decrease at a rapid rate. But the overall magnitudes are less than those of $\tilde{u}$ component. In this case also the turbulence levels on CYS 3 are much higher compared to the plane surface values (nearly 35 percent more). Figure 10(*c*) shows the variation of $\tilde{w}$ component. The general trend in the variation of $\tilde{w}$ component is similar to that for $\tilde{u}$ component. The peak values occur at $y/b = 0.6$ and then the values decrease at a rapid rate.

The variation of turbulent shear stress $\overline{uv}$ at the three typical stations shown in Fig. 11 indicate the strong influence of curvature. An important point observed is that the point of zero shear stress moves closer to the wall with increase in the curvature parameter which is discussed in more detail in the next section.

Figure 12 shows the variation of k at three typical axial stations in the plane of symmetry. The peak values are occurring around $y/b = 0.6$ and the values are nearly 2.5 times more than the plane surface values at $b/R = 1.114$.

The distribution of $\tilde{u}$, $\tilde{v}$, $\tilde{w}$, and $\overline{uw}$ at $x/d = 100$ in the spanwise direction are shown in Fig. 13. The mean curve obtained on the plane surface is included in the figure. It is seen that the effect of curvature is marginal in the spanwise direction.

3.3.2 The Counter Gradient Region. An unique feature of wall jets in general is the non-coincidence of the point of maximum velocity and the point of zero shear stress and this leads to regions of counter-gradient between these two points (Padmanabham and Gowda, 1991b). In Fig. 14 are shown the $\overline{uv}$ profiles close to the wall, to a enlarged scale for PS, CYS 1, CYS 2, and CYS 3 at a typical station i.e., $x/d = 100$. In each of these figures, the position of the point of maximum velocity (y_m) and the location of the zero shear stress (y_0) are indicated. It is interesting to observe

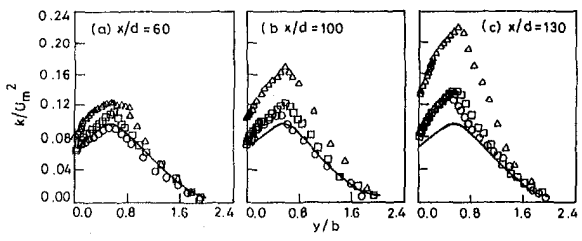

Fig. 12 Distribution of turbulent kinetic energy k at three typical axial stations on CYS1, CYS2, and CYS3 in the plane of symmetry; symbols as in Fig. 11 (uncertainty in y = 0.5 mm; uncertainty in k = ±3.5 percent at 20:1 odds)

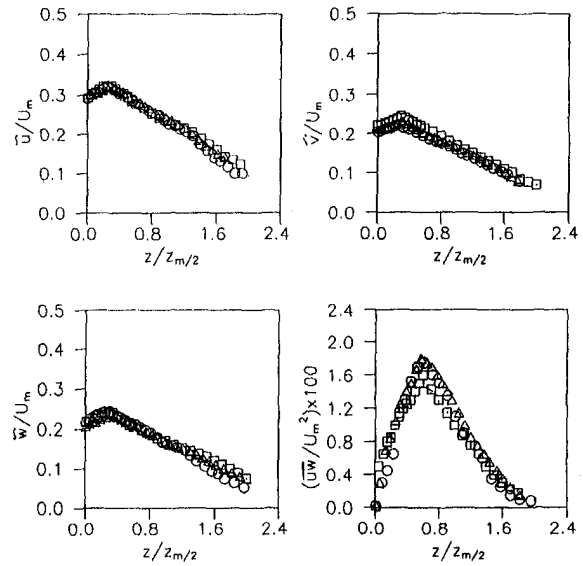

Fig. 13 Locations of maximum velocity (y_m) and zero shear stress (y_0) positions on CYS1, CYS2, and CYS3 at x/d = 100 (uncertainty in y = 0.5 m; uncertainty in $\overline{uv}/U_m^2$ = ±8.71 percent at 20:1 odds)

that the point of zero shear stress moves closer to the wall with increase in curvature. In Fig. 14(*d*), the location of y_0 is very close to the wall and thus almost the entire inner region of the wall jet becomes a region of counter-gradient or negative shear stress. In spite of this, the phenomenon of "energy reversal" i.e., turbulence feeding the mean flow (Palmer and Keffer, 1972) does not occur as for a plane surface. This is because of the considerable contribution from the normal stresses to the turbulent production and a

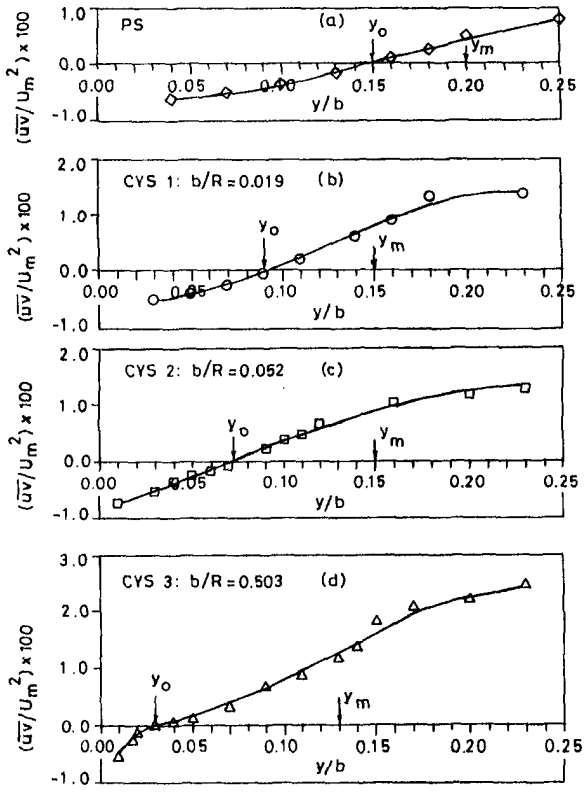

Fig. 14 Distribution of $\tilde{u}$, $\tilde{v}$, $\tilde{w}$, and $\overline{uw}$ at a typical axial station (x/d = 100) at $y = y_m$ in the spanwise direction on CYS1, CYS2, and CYS3; symbols as in Fig. 11 (uncertainty in $\tilde{u}/U_m$, $\tilde{v}/U_m$ and $\tilde{w}/U_m$ as in Fig. 10; uncertainty in uw = ±8.71 percent)

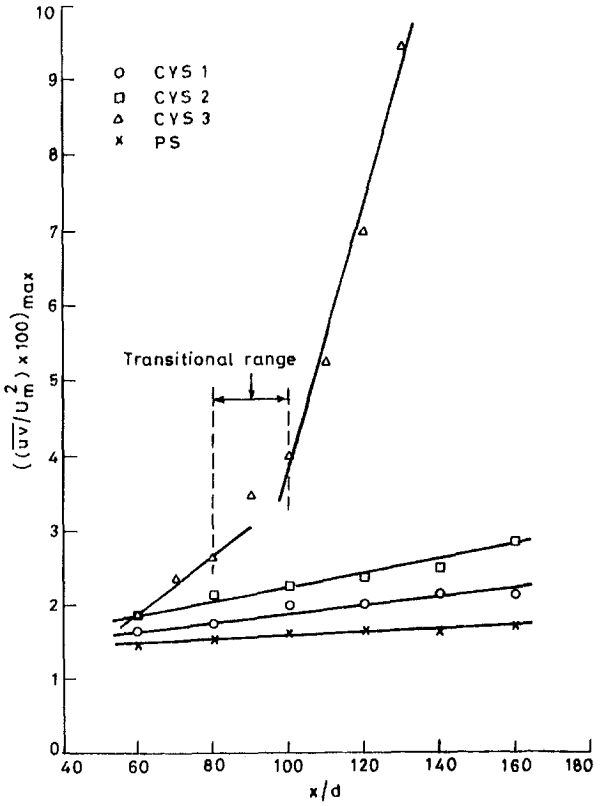

Fig. 15 Variation of maximum value of $\overline{uv}$ along the curved surfaces (uncertainty levels as in Fig. 11)

analysis similar to that carried out by Padmanabham and Gowda (1991b) has been done for the curved surfaces which brings out this feature (Durbha, 1996).

3.4 Centrifugal Instability. The important effect observed due to convex curvature is the increase in the turbulent quantities. The main physical reason for this can be attributed to the conditions of centrifugal instability. When flow takes place on a curved surface, if the conditions are such that the momentum increases in the direction of the radius of curvature, stable conditions prevail giving rise to a reduction in turbulence levels; otherwise instability occurs. This is what happens in the case of a boundary layer on a convex surface (Bradshaw, 1973; So and Mellor, 1973). However, in the case of a wall jet on a convex surface, the inner region is capped by a large outer region. In the outer region, the momentum is decreasing in the direction of the radius of curvature and hence centrifugal instability exists over the large outer region, resulting in high turbulence levels in this region. This is further augmented by the entrainment and the jet-like character of the outer region. A combination of these effects in the outer region, override the stabilising influence of the convex curvature within the inner region of the wall jet, leading to an increase in turbulence levels rather than a decrease unlike for a boundary layer. This is the reason for the increase in the turbulence levels over the entire width of the wall jet on the convex surfaces investigated in the present study.

3.5 Variation of Maximum Shear Stress. Considering the variation of the maximum normalised shear stress values along the three surfaces (Fig. 15), the following interesting feature is observed. On CYS1 and CYS2 the values show a gradual increase with x/d. However, for CYS3 the increase is very sharp and two regions can be indentified similar to that in Fig. 8 ($x/d < 80$ and $x/d > 100$). There is a small "transitional" range between the two (as indicated in Fig. 15). The steep increase in $\overline{uv}$ has a significant effect on the growth of the wall jet normal to the plate (b), which was referred to earlier in Section 3.2. The term

$$2\overline{uv}U/(R + y)$$

is the centrifugal force term, which influences the production of the radial fluctuations (Wilson and Goldstein, 1976) and is largely responsible for the increased rate of growth of the wall jet thickness due to curvature. Such an increase is observed both for three-dimensional case (present study; Section 3.2) and the two-dimensional case (Wilson and Goldstein, 1976). It is very interesting to observe the presence of the "transitional" region in the growth of b/d for CYS 3 in Fig. 8. The region occurs between $x/d = 80$ and 100, which very well corresponds with what is seen in Fig. 14. This is the reason why the growth of the wall jet normal to the curved surface CYS 3, even overtakes that in the spanwise direction as revealed in Fig. 8.

4 Conclusions

1. The similarity of the mean flow velocity profiles normal to the surface in the plane of symmetry appears to be not much affected by the curvature effects. However, there is a marginal shift of the position of the maximum velocity toward the wall due to the curvature effects. Because of this, some differences in the shape of the velocity profile occurs between the profile on the plane surface and that on the curved surfaces. The shape of the velocity profile in the spanwise direction is seen to be unaffected due to curvature.

2. The decay rate of the maximum velocity increases with increase in curvature. On highly curved surfaces, the decay exponent can be as much as twice that on a plane surface.

3. A common feature observed in the case of three-dimensional wall jet on a plane surface is the very large spanwise growth (5 to 6 times) compared to that normal to the surface. The convex curvature appears to reverse this trend, particularly for strong curvature. The growth of length scale normal to the plate can even overtake the growth in the spanwise direction. However, the growth of the length scales in the spanwise direction remain unaltered due to curvature effects.

4. Due to curvature effects, in general, there is an increase in all the turbulent components ($\tilde{u}$, $\tilde{v}$, $\tilde{w}$ and $\overline{uv}$) in the plane of symmetry. This increase becomes larger as the curvature becomes stronger as seen for CYS3.

References

Abramovich, G. N., 1963, *The Theory of Turbulent Jets,* M.I.T. Press, Cambridge, Massachusetts.

Alcaraz, E., Charnay, G., and Mathieu, J., 1977, "Measurements in Wall Jet over a Convex Surface," *The Physics of Fluids,* Vol. 20, pp. 203–210.

Bradshaw, P., 1973, "Effect of Streamwise Curvature on Turbulent Flows," AGARDograph, No. 169.

Catalano, G. D., Mortan, J. B., and Humphris, R. R., 1977, "An Investigation of a Three-Dimensional Wall Jet," *AIAA Journal,* Vol. 15, pp. 1146–1151.

Champagne, F. H., and Sleicher, C. A., 1967, "Turbulence Measurements with Inclined Hot-Wires," Part 2: Hot-wire response equations," *Journal of Fluid Mechanics,* Vol. 28, pp. 177–182.

Dakos, T., Verriopoulos, C. A., and Gibson, M. M., 1984, "Turbulent Flow with Heat Transfer in a Plane and Curved Wall Jets," *Journal of Fluid Mechanics,* Vol. 145, pp. 339–360.

Durbha, V. S. B., 1996, "An experimental investigation of three-dimensional wall jet on convex cylindrical surfaces," Ph.D. thesis, Indian Institute of Technology, Madras, India.

Durbha, V. S. B., and Gowda, B. H. L., 1995, "Turbulence Characteristics of a Three-Dimensional Wall Jet on a Plane Surface," *Proceedings, 22nd National Conference on Fluid Mechanics and Fluid Power,* I.I.T. Madras, India, pp. 124–129.

Fujisawa, N., and Shirai, H., 1987, "Theoretical and Experimental Studies of Turbulent Wall Jet Along a Strongly Concave Surface," *Transactions,* Japan Society for Aero Space Sciences, Vol. 30, pp. 26–37.

Giles, J. A., Hays, A. P., and Sawyer, R. A., 1966, "Turbulent Wall Jets on Logarithmic Spiral Surfaces," *Aeronautical Quarterly,* Vol. 17, pp. 201–215.

Glauert, M. B., 1956, "The Wall Jet," *Journal of Fluid Mechanics,* Vol. 1, pp. 625–643.

Guitton, D. E., and Newman, B. G., 1977, "Self-Preserving Turbulent Wall Jets over Convex Surfaces," *Journal of Fluid Mechanics,* Vol. 81, pp. 155–185.

Iida, S., and Matsuda, H., 1988, "An Experimental Study of Circular Turbulent Wall Jet Along a Convex Wall," *Transactions,* Japan Society of Mechanical Engineering, Series B, Vol. 54, pp. 354–360 (in Japanese).

Kamemoto, K., 1974, "Investigation of Turbulent Wall Jets Over Logarithmic Spiral Surfaces," *Bulletin JSME,* Vol. 17, pp. 335–350.

Kline, S. J., and McClintock, F. A., 1953, "Describing Uncertainties in Single Sample Experiments," *Mechanical Engineering,* Vol. 75, pp. 3–8.

Kobayashi, R., and Fujisawa, N., 1983, "Turbulence Measurements in Wall Jets Along Strongly Concave Surfaces," *Acta Mechanica,* Vol. 47, pp. 39–52.

Narasimha, R., and Prabhu, A., 1972, "Equilibrium and Relaxation in Turbulent Wakes," *Journal of Fluid Mechanics,* Vol. 54, pp. 1–17.

Newman, B. G., Patel, R. P., Savage, S. B., and Tjio, H. K., 1972, "Three-Dimensional Wall Jet Originating from a Circular Orifice," *Aeronautical Quarterly,* Vol. 23, pp. 188–200.

Padmanabham, G., and Lakshmana Gowda, B. H., 1991a, "Mean and Turbulence Characteristics of a Class of Three-Dimensional Wall Jets-Part 1: Mean Flow Characteristics," ASME JOURNAL OF FLUIDS ENGINEERING, Vol. 113, pp. 620–628.

Padmanabham, G., and Lakshmana Gowda, B. H., 1991b, "Mean and Turbulence Characteristics of a Class of Three-Dimensional Wall Jets-Part 2: Turbulence Characteristics," ASME JOURNAL OF FLUIDS ENGINEERING, Vol. 113, pp. 629–634.

Palmer, M. D., and Keffer, J. F., 1972, "An Experimental Investigation of an Asymmetrical Turbulent Wake," *Journal of Fluid Mechanics,* Vol. 53, pp. 593–610.

Patankar, U. M., and Sridhar, K., 1972, "Three-Dimensional Curved Wall Jets," ASME *Journal of Basic Engineering, Transactions ASME,* Vol. 94, pp. 339–344.

Sforza, P. M., and Herbst, G., 1970, "A Study of Three-Dimensional Incompressible Turbulent Wall Jets," *AIAA Journal,* Vol. 8, pp. 276–283.

So, R. M. C., and Mellor, G. L., 1973, "Experiments on Convex Curvature Effects in Turbulent Boundary Layers," *Journal of Fluid Mechanics,* Vol. 60, pp. 43–62.

Swamy, N. V. C., and Bandyopadhyay, P., 1975, "Mean and Turbulence Characteristics of Three-Dimensional Wall Jets," *Journal of Fluid Mechanics,* Vol. 71, pp. 541–562.

Wilson, D. J., and Goldstein, R. J., 1976, "Turbulent Wall Jets with Cylindrical Streamwise Surface Curvature," ASME JOURNAL OF FLUIDS ENGINEERING, Vol. 98, pp. 550–557.

ERRATA

"Some Explicit Analytical Solutions of Unsteady Compressible Flow," by Ruixian Cai, *Journal of Fluids Engineering,* Vol. 120, Dec. 1998, pp. 760–764.

page	line	
762	4th from bottom (left)	$-\rho u^2\{c_1 \exp(-c_2 t)$ $\Rightarrow -\rho u^2\{[c_1 \exp(-c_2 t)$
763	coordinate of Fig. 2	$A \Rightarrow A/A_{x=0}$
764	16th from bottom (left)	$c_5 = 0 = \Rightarrow c_5 = \mathbf{1}$
764	14th from bottom (left)	$\ln (c_o x + c_2)/c_o^2$ $\Rightarrow \ln (c_o x + c_2)/\mathbf{2}c_o^2$
764	Fig. 4	(The streamline slope has to be reduced by half)
764	8th from bottom (right)	Vol. 29 $\Rightarrow$ Vol. **26**

Hydrodynamic Characteristics of a Mechanical Pectoral Fin

Naomi Kato
Professor,
Department of Marine Design and Engineering,
School of Marine Science and Technology,
Tokai University,
3-20-1 Orido, Shimizu,
Shizuoka 424-8610, Japan
e-mail: nkato@scc.u-tokai.ac.jp

This paper describes the use of a mechanical pectoral fin as a new device for maneuvering and stabilizing an underwater vehicle. The mechanical pectoral fin consists of two servo-motors generating a feathering motion and a rowing motion. The hydrodynamic characteristics of the device were analyzed experimentally and theoretically. The mechanical pectoral fin generates a thrust force in a range of phase differences between both motions. The unsteady vortex-lattice method, which takes into account the effects of viscosity, reasonably expresses the unsteady forces acting on the mechanical pectoral fin.

1 Introduction

It is necessary for underwater vehicles to be able to maneuver precisely, including being able to hover and turn at a certain point. This high level of maneuverability enables underwater vehicles not only to survey an intricate seabed, but also to perform dexterous work using multiple manipulators as they float beneath the surface (Kato and Lane, 1996).

Instead of the screw-type thrusters and wings installed in existing underwater vehicles, this study is aimed at examining a new device for maneuvering an underwater vehicle based on observation and experimental analysis of the pectoral fin motion of a fish.

Many previous studies have focused on the fish-fin motion as an oscillating foil for propulsion (Hertel, 1966; Lighthill, 1969; Wu, 1971; Isshiki and Morikawa, 1982; Barrett and Triantafyllou, 1995; Tanaka and Nagai, 1996). However, applying the oscillating foil as the main thruster for underwater vehicles is not straightforward due to the prevalent use of screw-type thrusters. A major drawback of these screw-type thrusters, however, is the sudden generation of a thrust force when the underwater vehicle is hovering, which leads to imprecise control of the position and attitude of the vehicle and its manipulators. Few researchers have considered the utilization of the fish-fin motion to maneuver and stabilize underwater vehicles (Bandyopadhyay et al., 1997). Because many fishes use oscillating pectoral fins for their maneuvers at low swimming speeds (Lindsey, 1978), utilization of the pectoral fin motion could possibly overcome the drawbacks of the screw-type thrusters.

Kinematic studies indicate that pectoral fin movements are variable among species and across a range of swimming speeds with complex fin ray patterns (Webb, 1973; Geerlink, 1983; Gibb et al., 1994; Walker and Westneat, 1997). The author has experimentally analyzed the pectoral fin motion of a black bass (*Micropterus salmoides*) with the intent of developing mechanical pectoral fins (Kato and Furushima, 1996). Webb (1982, 1984) has described the bass as a generalist blessed with the functions of cruiser/sprinters, accelerators and maneuvers. Fin motion like the beating motion of a bird's wings will generally consist of four fundamental motions: (1) a flapping motion in a vertical plane, (2) a rowing motion in horizontal plane, (3) a feathering motion, which denotes a twisting motion of the fin pitch, and (4) a spanning motion, which denotes an alternatively extending and contracting motion of the fin span (Azuma, 1992). In a study carried out by Kato and Furushima (Kato and Furushima, 1996), a rowing motion in the X-Y plane and a feathering motion in the X'-Z' plane or in the X''-Z'' plane, as a rigid paddle, were employed in the analysis of the pectoral fin motion (see Fig. 1). The flapping motion that produces the vertical motion of fish and the spanning motion were neglected because the swimming of the fish being tested was restricted to the horizontal plane, and the pectoral fin was treated as a rigid plate. The study revealed that the combination of the feathering and rowing motions of a pair of pectoral fins is responsible for forward swimming, backward swimming, and turning on the horizontal plane.

This paper deals with the experimental and theoretical analyses of the hydrodynamic characteristics of a mechanical pectoral fin that was designed based on the observation and experimental analysis of the pectoral fin motion of a black bass.

2 Measurement of Hydrodynamic Forces on a Mechanical Pectoral Fin

2.1 Mechanical Pectoral Fin. The mechanical pectoral fin shown in Fig. 2 was constructed in order to test its hydrodynamic characteristics. The fin consists of two servo-motors whose angles are sensed by potentiometers and that are controlled by a personal computer with a proportional and differential control. The two servo-motors control the rowing and feathering motions of the pectoral fin. The fin system can generate any kind of programmed motion within the limitations of the performance of the motors. However, a sinusoidal motion was used in accordance with the observations and experimental analysis of the pectoral fins of a bass (Kato and Furushima, 1996). The pectoral fin model is a flat plate that is 6.2 times larger than the pectoral fin of the observed bass. The plate is made of stainless steel with a thickness of 0.6 mm and a maximum chord length of 0.155 m (see Fig. 2).

2.2 Experimental Setup. An open-water test of the mechanical pectoral fin was carried out in a water-circulating tank measuring 2.2 m long, 1.4 m wide, and 0.9 m deep. The hydrodynamic characteristics were investigated in terms of the phase difference between the rowing motion and the feathering motion as well as the non-dimensional frequency, K, which is defined as follows:

$$K = c \cdot \omega_f / U \tag{1}$$

The inflow velocity was set as 0.162 ± 0.005 m/s, with the variation in motion frequency changing the nondimensional frequency. In this case, the Reynolds number $\mathrm{Re} = U \cdot c/\nu$ is 2.11×10^4. The rowing angle was varied from 0 to 70 deg, and the feathering angle was varied from 0 to -70 deg. The precision error in the control of the rowing angle was in the range of $\pm 5.2\%$, and the precision error in the control of the feathering angle was in the range of $\pm 2.3\%$.

We used a three-component strain gauge to measure the hydrodynamic forces, as defined in Fig. 1, which involved two types of

Contributed by the Fluids Engineering Division for publication in the JOURNAL OF FLUIDS ENGINEERING. Manuscript received by the Fluids Engineering Division April 3, 1998; revised manuscript received April 5, 1999. Associate Technical Editor: P. R. Bandyopadhyay.

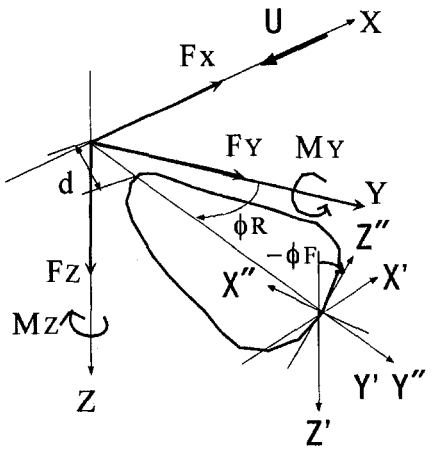

Fig. 1 Definition of coordinate system and notation

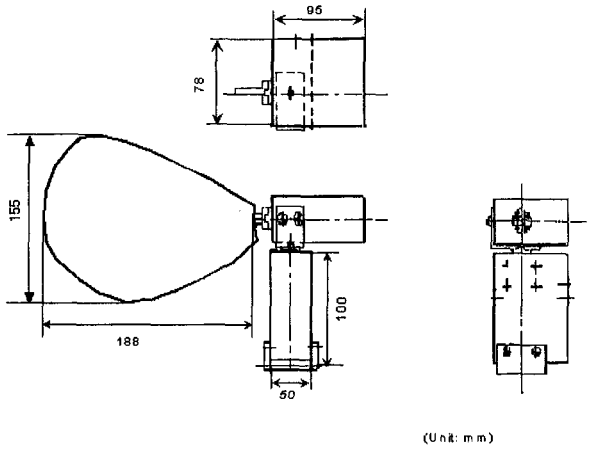

Fig. 2 Mechanical pectoral fin

support setups for the gauge; one for measurement of F_X, F_Z, and M_Y, and the other for F_X, F_Y, and M_Z. Two types of hydrodynamic forces were measured separately. For each type, the hydrodynamic forces on the apparatus without the fin and those with the fin were measured separately because the support setups were submerged in water. To estimate the net hydrodynamic forces on the blade alone, the hydrodynamic forces on the apparatus without the fin were subtracted from those on the apparatus with the fin. The errors in forces and moments from the calibration of the gauge were in the range of ±0.2%.

The hydrodynamic force coefficients are defined as follows:

$$C_X = F_X/(\tfrac{1}{2}\cdot\rho\cdot U^2\cdot S),$$

$$C_Y = F_Y/(\tfrac{1}{2}\cdot\rho\cdot U^2\cdot S),$$

$$C_Z = F_Z/(\tfrac{1}{2}\cdot\rho\cdot U^2\cdot S),$$

$$C_{mY} = M_Y/(\tfrac{1}{2}\cdot\rho\cdot U^2\cdot S\cdot c),$$

$$C_{mZ} = M_Y/(\tfrac{1}{2}\cdot\rho\cdot U^2\cdot S\cdot c) \quad (2)$$

The propeller efficiency of the mechanical pectoral fin is formulated as follows:

Nomenclature

c = maximum chord length of pectoral fin
C_N = normal force coefficient of the two-dimensional flat plate
$\cos n_X$, $\cos n_Y$, $\cos n_Z$ = normal unit vector components in the fixed coordinate system at the control points on the fin
C_X, C_Y, C_Z = coefficients of the hydrodynamic forces
C^*_X, C^*_{mY}, C^*_{mZ} = coefficients of the mean hydrodynamic forces
F_X, F_Y, F_Z, M_Y, M_Z = hydrodynamic forces
F_{X0}, M_{Y0}, M_{Z0} = hydrodynamic forces acting alone on the support setups without the fin
H = length of the two-dimensional flat plate
H_j = length of the jth segment of the two-dimensional flat plate
K = nondimensional frequency
$\mathbf{n}_P$ = normal unit vector to the surface of the pectoral fin
Oe = field out of the pectoral fin
p = pressure on the pectoral fin
$\mathbf{r}_{QP}$ = position vector of point P where the velocity field is calculated from point Q on singularity
$\mathbf{r}_p$ = position vector of point P from point O
Re = Reynolds number, $U\cdot c/\nu$
D, L = drag and lift, respectively, on the two-dimensional flat plate
S = surface area of the flat pectoral fin
Sj = surface area of the jth panel on the pectoral fin
S fin = surface of the pectoral fin
$\mathbf{s}$ = arc vector of the free vortex filament
T = period of motion
t = time
tn = nondimensional time [Eq. (16)]
t_0 = time when a free vortex filament is shed
$\mathbf{T}s$ = strength of the bound vortex sheet on the pectoral fin
U = inflow velocity
$\mathbf{U}$ = inflow velocity vector
$V\omega$ = field of the free vortices
$\mathbf{V}e$ = external velocity field outside the pectoral fin
$\mathbf{V}p$ = velocity vector
ω = induced velocity from a vortex filament
W_{0Y}, W_{0Z} = mean value of the tangential velocity in the Y'' and Z'' directions, respectively, on a pectoral fin normal to the X'' axis
X_{0j}, Y_{0j}, Z_{0j} = the coordinates of the jth control point
(X, Y, Z), (X', Y', Z'), (X'', Y'', Z'') = coordinate systems of the mechanical pectoral fin (Fig. 1)
$\alpha 1$, $\alpha 2$ = angles (Fig. 3)
β = angle of attack of uniform flow to a two-dimensional flat plate
ΔCp = coefficient of the pressure difference
ΔCpj = coefficient of the pressure difference of the jth panel on the pectoral fin
$\Delta\phi$ = phase difference between the rowing motion and feathering motion [Eq. (8)]
Δ_{SB} = length of segments or panels around which bound vortex filaments are arranged

$$\eta = \frac{A}{|B|}$$

$$A = \frac{1}{T}\int_0^T F_X \cdot U dt - \frac{1}{T}\int_0^T F_{X0} \cdot U dt$$

$$B = \frac{1}{T}\int_0^T (M_Z \cdot \dot{\phi}_R) dt + \frac{1}{T}\int_0^T \left(\frac{M_Y \cdot \dot{\phi}_F}{\cos \phi_R}\right) dt - \frac{1}{T}\int_0^T (M_{Z0} \cdot \dot{\phi}_R) dt - \frac{1}{T}\int_0^T \left(\frac{M_{Y0} \cdot \dot{\phi}_F}{\cos \phi_R}\right) dt \quad (3)$$

Here the propeller efficiency of the mechanical pectoral fin is defined as the ratio of mean output power during a period for generating the thrust in the X direction to the mean input power during a period for generating the rowing and feathering motions. In the input power, positive work to generate the pectoral fin motion and the negative work being carried out by the circumferential fluid through the fin during one period are summed. To estimate the net input and output powers on the blade alone, the input and output powers on the apparatus without the fin are subtracted from those on the apparatus with the fin. The moment around the Y' axis for generating the feathering motion is estimated from the Y component of the moment around the Y' axis, M_Y.

3 Hydrodynamic Model of Pectoral Fin Motion

Lindsey (1978) has referred to propulsion by oscillation of pectoral fins as the "labriform mode" after Labridae. Labriform swimming consists of a *drag-based* labriform mode at low swimming speeds (Blake, 1979) and a *lift-based* labriform mode at higher swimming speeds (Webb, 1973). The former is characterized by the rowing action of the pectoral fins at a large angle with relation to the horizontal axis of the fish body. The latter is characterized by the flapping action of pectoral fins at a small angle with relation to the horizontal axis. The propulsion that occurs with a pair of pectoral fins of the bass belongs to the *drag-based* labriform mode.

Separated vortical flow is dominant around a pectoral fin with a drag-based labriform mode because the pectoral fin is at a large angle in relation to the horizontal axis of the fish body in this mode. The author has developed an unsteady vortex lattice method (UVLM) for the theoretical analysis of separated vortical flows.

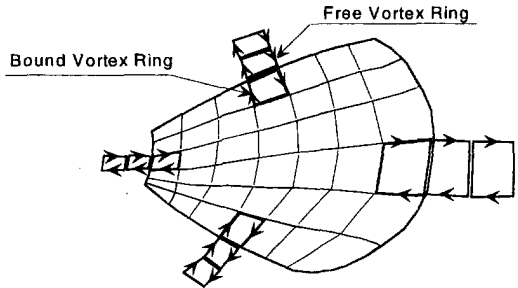

Fig. 3 Arrangements of bound vortex rings on a pectoral fin and free vortex rings shed from the fin

UVLM has been applied to the flows behind a flat plate at a large angle in relation to the uniform flow and around a body of revolution at an angle of attack to the uniform flow (Kato and Yamaguchi, 1985). Here we extend UVLM to the unsteady flow around a pectoral fin with drag-based labriform mode.

3.1 Unsteady Vortex Lattice Method Including the Effects of Viscosity.

3.1.1 Basic Formula. The vortical field around a pectoral fin of a flat plate in inviscid flow can be expressed as follows by applying Green's theorem to the vector potential field:

$$\frac{1}{4\pi}\nabla_P \times \left\{ \int_S \frac{\mathbf{T}s(\mathbf{Q})}{\mathbf{r}_{QP}} dS_Q + \int_{V\omega} \frac{\tilde{\omega}(\mathbf{Q})}{\mathbf{r}_{QP}} dV_Q \right\} = \begin{cases} \frac{1}{2}\{\mathbf{n}_P \times \mathbf{T}s(\mathbf{P})\} + \mathbf{V}e(\mathbf{P}) & P \in S_{\text{fin}} \\ \mathbf{V}e(\mathbf{P}) & P \in Oe \end{cases} \quad (4)$$

The vorticity of free vortices can be approximately expressed by the circulation of free vortex filaments. Therefore, the second term in the left side of Eq. (4) is approximated as:

$$\frac{1}{4\pi}\nabla_P \times \int_{V\omega} \frac{\tilde{\omega}(\mathbf{Q})}{\mathbf{r}_{QP}} dV_Q \approx \frac{1}{4\pi}\int \frac{\Gamma_f\, ds \times \mathbf{r}_{QP}}{\mathbf{r}_{PQ}^3}, \quad (5)$$

which expresses the Biot-Savart law.

The boundary condition on the surface of the fin is expressed as

$$(U - \omega_{\text{fin}} \times r_p + v_p) \cdot n_P = 0 \quad (6)$$

Nomenclature (cont.)

Δt = time step of computation
ϕ_F = feathering angle around the Y' axis (Fig. 1)
ϕ_{FC}, ϕ_{FA} = mean value and amplitude of the feathering angle, respectively
$\dot{\phi}_F$ = angular velocity of the feathering angle
ϕ_R = rowing angle around the Z axis (Fig. 1)
ϕ_{RC}, ϕ_{RA} = mean value and amplitude of the rowing angle, respectively
$\dot{\phi}_R$ = angular velocity of the rowing angle
γ_Y, γ_Z = line density of the bound vortex sheet in the Y'' and Z'' directions, respectively
Γ = circulation around the pectoral fin
Γ_f = circulation of the free vortex filament
Γ_{f0} = circulation of the free vortex filament at the initial stage of generation
ξ = proportional constant in Eq. (11)
η = propeller efficiency [Eq. (3)]
ν = kinematic viscosity
ν_E = effective kinematic viscosity [Eq. (11)]
ρ = fluid density
λ = decay factor [for the] circulation of the free vortex filament in Eq. (12)
ω_f = angular velocity
ω_{fin} = angular velocity vector of the pectoral fin
$\omega_{X\,\text{fin}}$, $\omega_{Y\,\text{fin}}$, $\omega_{Z\,\text{fin}}$ = components in (X, Y, Z) coordinates of the angular velocity vector of the pectoral fin
ϖ = vorticity in $V\omega$
$\times$ = vector product
$|\ |$ = absolute value

Subscripts

$+$ = face side of [the] pectoral fin
$-$ = back side of the pectoral fin

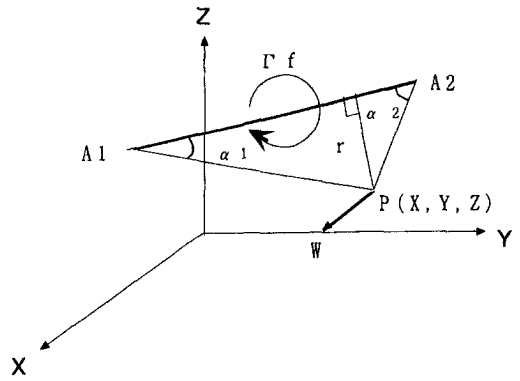

Fig. 4 Induced velocity from a vortex filament

From the unsteady Bernoulli theorem, the pressure difference coefficient is expressed as

$$\Delta C_p = \frac{p_- - p_+}{0.5\rho U^2} = \frac{2}{U^2}\left(W_{0Y}\cdot\gamma_Z - W_{0Z}\cdot\gamma_Y - \frac{\partial\Gamma}{\partial t}\right) \quad (7)$$

3.1.2 Procedure of Computation. We assume that a rigid pectoral fin starts impulsively from rest with an angular velocity, ω_{fin}, of the rowing and feathering motions formulated as follows in a uniform stream having a constant velocity of U:

$$\phi_R = \phi_{RC} - \phi_{RA}\cdot\cos(\omega_f\cdot t)$$
$$\phi_F = -\phi_{FC} - \phi_{FA}\cdot\cos(\omega_f\cdot t + \Delta\phi) \quad (8)$$

In this case, ω_{fin} in Eq. (6) is expressed as follows:

$$\omega_{Z\,\text{fin}} = \phi_{RA}\cdot\omega_f\cdot\sin(\omega_f\cdot t)$$
$$\omega_{XY\,\text{fin}} = \phi_{FA}\cdot\omega_f\cdot\sin(\omega_f\cdot t + \Delta\phi)$$
$$\omega_{X\,\text{fin}} = -\omega_{XY\,\text{fin}}\cdot\sin(\phi_R)$$
$$\omega_{Y\,\text{fin}} = \omega_{XY\,\text{fin}}\cdot\cos(\phi_R) \quad (9)$$

The procedure of computation is as given below:

1) The surface of a pectoral fin is divided into quadrangular panels, as shown in Fig. 10, around which bound vortex rings are arranged.
2) Resultant induced velocity components on each control point located at the center of each panel are computed by the Biot-Savart law. From the boundary condition on the surface of the fin, the strengths of the bound vortex rings are determined.
3) Two vertices of each nascent free vortex ring on one side are shed from the edge of the fin along the induced velocity. Two vertices of the nascent free vortex ring on the other side are arranged at the edge of the plate (see Fig. 3). The circulations of the nascent free vortex rings are taken as the same as those of the bound vortex rings along the edge of the fin. The free vortex rings generated previously are shed along the induced velocity on the vertices.
4) The resultant induced velocity components on each control point located at the center of each panel are computed by applying the Biot-Savart law both to the bound vortex rings and to the free vortex rings. From the boundary condition on the surface of the fin, the strengths of the bound vortex rings are determined by a simultaneous equation.
5) The procedure from 3) to 4) is then repeated.

The reason that bound and free vortex rings are distributed on and around the fin, respectively, is so that the circulation around the flow field can be kept constant at all times.

The free vortices will induce an extremely large velocity on the fin surface when they reattach on the fin surface, because $\mathbf{r}_{PQ}$ in Eq. (5) tends to zero. Therefore, the effect of the diffusion of vorticity due to the viscous effect is taken into account in the Biot-Savart law for free vortices to avoid its numerical problem near the fin surface. It should be noted that the consideration of the effect of the vorticity in the Biot-Savart law leads to an violation of the assumption of an inviscid flow. We express the absolute value of the induced velocity at times after the start of the fin motion from a vortex filament that is shed at time t_0 as follows (see Fig. 4):

$$|w| = \Gamma_{f/4\pi}\cdot|\cos\alpha_1 + \cos\alpha_2|/r \cdot(1 - \exp(-r^2/4\nu_E(t - t_0)) \quad (10)$$

We express ν_E in Eq. (10) in the following form,

$$\nu_E = \xi\cdot\nu \quad (11)$$

The exact solution of Navier-Stokes equations for the diffusion of vorticity in two dimensions (Wieghardt, 1974) is extended to the three-dimensional flow in Eq. (10) assuming that the diffusion of vorticity works uniformly at points at the same radius from the vortex filament center. In addition, the circulations of the free vortex filaments generated along the edge of the fin are assumed to decay with time as shown below.

$$\Gamma_f = \Gamma_{f0}\cdot\exp(-\lambda\cdot(t - t_0)) \quad (12)$$

We obtain the hydrodynamic force coefficients as follows:

$$C_X = \sum_j \Delta Cpj\cos n_{Xj}Sj/S, \quad C_Y = \sum_j \Delta Cpjosn_{Yj}Sj/S,$$
$$C_Z = \sum_j \Delta Cpj\cos n_{Zj}Sj/\text{S},$$
$$C_{mY} = \sum_j (Z0j\Delta Cpj\cos n_{Xj} - X0j\Delta Cpj\cos n_{Zj})\cdot Sj/(Sc),$$
$$C_{mZ} = \sum_j (X0j\Delta Cpj\cos n_{Yj} - Y0j\Delta Cpj\cos n_{Xj})\cdot Sj/(Sc). \quad (13)$$

3.2 Validation of the Computational Method. To validate the proposed computational method, we carried out numerical computations for two-dimensional flow around an inclined flat plate to the uniform flow at an angle of attack. This flow can be regarded as a special case of three-dimensional flow around a pectoral fin because the span of a pectoral fin is taken as infinite and the chord length is taken as uniform in a spanwise direction. It is well known that the characteristics of hydrodynamic forces acting on a two-dimensional flat plate change in conjunction with the angles of attack of the uniform flow to the plate. The drag-based labriform mode of pectoral fin motion generates separate vortical flow with large angles of attack. Therefore, we analyze here flows with large angles of attack having stall phenomena where leading-edge separation occurs. We have compared the computed hydrodynamic forces on the flat plate with the experimental measurements.

3.2.1 Procedure of Computation. We assume here that a flat plate of length H starts impulsively from rest with a constant velocity of U at an angle of attack β. The procedure of computation is given below.

1) The surface of the flat plate is divided into line segments. We arrange a pair of bound vortices with equal absolute values of strength, but in opposite directions, on the edge of each segment.
2) The resultant induced velocity components on each control point, which are located at the center of each segment, are computed by the Biot-Savart law for two-dimensional flow. From the boundary condition on the surface of the flat plate,

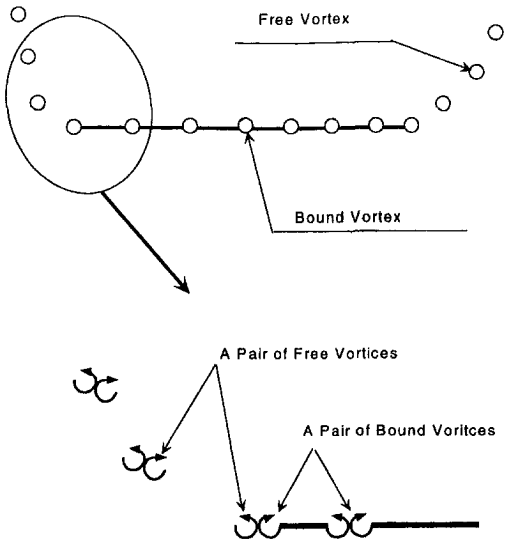

Fig. 5 Arrangements of bound vortices on a two-dimensional flat plate and free vortices shed from the plate

the strength of [the] bound vortices is determined by a simultaneous linear equation.

3) One of a pair of nascent free vortices from each edge of the plate is shed along the induced velocity at each edge of the plate. The other of the pair of nascent free vortices is placed at the edge of the plate (see Fig. 5). The circulation of a pair of nascent free vortices at each edge is taken as the same as the circulation of a pair of bound vortices at the edge of the plate. The pairs of free vortices generated previously are shed along the induced velocity.
4) The resultant induced velocity components on each control point located at the center of each segment are computed by applying the Biot-Savart law both to the bound and the free vortices. From the boundary condition on the surface of the plate, the strengths of the pairs of bound vortices are determined by a simultaneous equation, and
5) The procedure from 3) to 4) is then repeated.

The normal force coefficient to the flat plate is defined as follows:

$$C_N = R_N/(0.5\rho U^2 H) = \sum_j \Delta Cpj Hj/H \qquad (14)$$

3.2.2 Computational Results. The numerical computations were carried out using a 4.0-m long flat plate composed of 20 segments. The velocity of the uniform flow and time step were set as 1.0 m/s and 0.1 s, respectively. Computations were done until $t \cdot U/H = 50$, 50, and 62.5 for angles of attack of 30, 45, and 60 deg, respectively.

Figure 6 shows the time histories of the normal force coefficient in the case of an angle of attack of 30 deg. The values of λ in Eq. (12), ξ in Eq. (11) and ν in Eq. (11) were taken to be 0.005, 1000, and 10^{-6} m^2/s, respectively. Because C_N is oscillatory, as seen in this result, the mean values and the standard deviations of C_N for all cases in this chapter were obtained using the data during the last four periods. Figure 7 shows the vortex pattern at $U \cdot t/L = 50$ in the case of an angle of attack of 30 deg. We can see that a Karman vortex street is generated behind the flat plate, which causes the oscillatory C_N.

Hoerner and Borst (1975) have established the following empirical formula for the normal force coefficient of a two-dimensional flat plate with stall phenomena:

$$1/C_N = 0.222 + 0.283/\sin\beta \qquad (15)$$

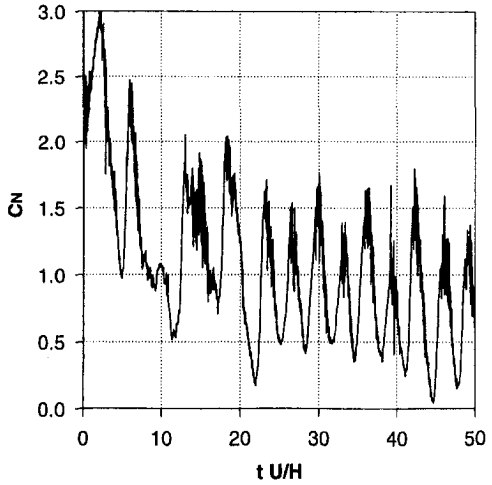

Fig. 6 Time histories of the normal force coefficient of a two-dimensional flat plate at β = 30 deg

Figure 8 shows the computed effect of ξ on C_N compared with the empirical formula. The value of λ was taken to be 0.0, and the values of ξ were taken to be 100, 500, and 2000. The computed hydrodynamic forces with ξ smaller than 1000 and $\lambda = 0$ did not show periodical changes with time. The results indicate that as the value of ξ becomes smaller, the standard deviation becomes larger, and that the effect of ξ on the mean value of C_N varies according to the angle of attack.

Figure 9 shows the computed effect of λ on C_N compared with the empirical formula. The value of ξ was taken to be 1000, and the values of λ were taken to be 0.0 and 0.005. The result shows that the effect of λ is large and that the computed value of C_N in the case of $\lambda = 0.005$ shows better agreement with the empirical formula than in the case of $\lambda = 0.0$. The reason that the normal force is sensitive to the value of λ related to the circulation of each vortex may be that blocks of the vortices with the same sign are formed behind the plate.

The above results validate the use of the proposed unsteady vortex lattice method, although the parameters, λ and ξ used in the method must be tuned according to the flow conditions.

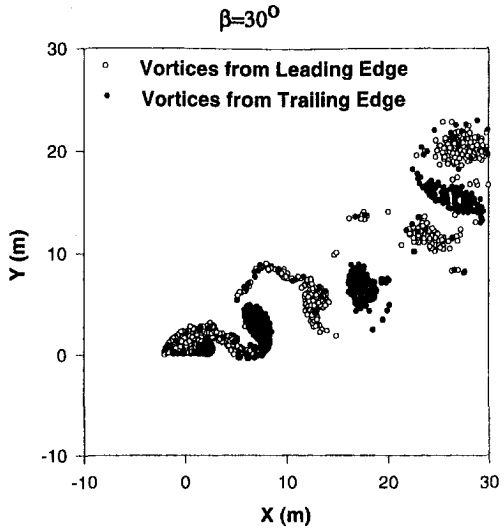

Fig. 7 Vortex pattern at $t \cdot U/L$ = 50

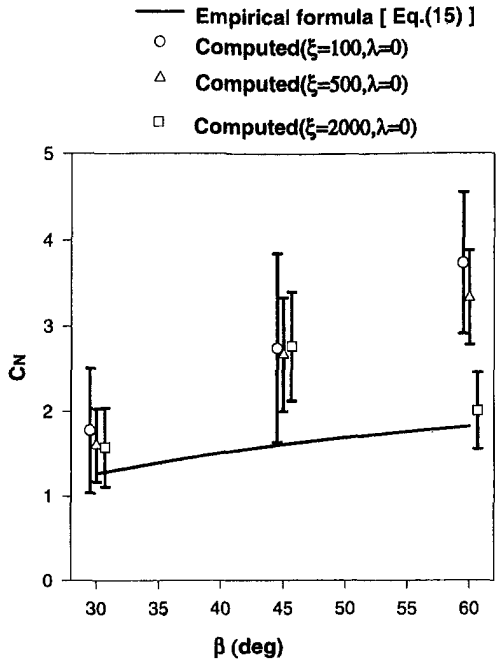

Fig. 8 Effect of the proportional constant ξ on the normal force coefficient of a two-dimensional flat plate

4 Comparison Between Computation and Experiment in Relation to the Hydrodynamic Characteristics of the Mechanical Pectoral Fin

4.1 Computational Conditions. Figure 10 shows the configuration of the pectoral fin for computation with a maximum chord length of 1.55 m and 162 segmented panels. The uniform flow U and time step Δt were set as 1.0 m/s and 0.0405 s, respectively. We define the following nondimensional time tn to verify the value of the time step compared with the two-dimensional case in Section 3.2.

$$tn = \Delta t \cdot U/\Delta_{SB} \tag{16}$$

While tn was 0.5 in the two-dimensional case, tn in the three-dimensional case is approximately 0.47, using a Δ_{SB} of 0.086,

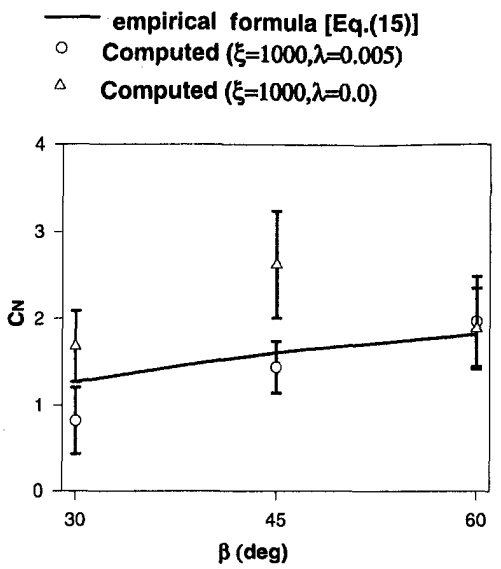

Fig. 9 Effect of the decay factor of the free vortex filament λ on the normal force coefficient of a two-dimensional flat plate

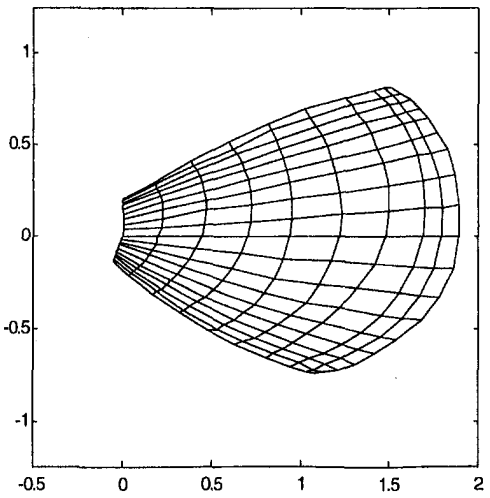

Fig. 10 Configuration of a pectoral fin for computation and the division of its surface

which is the mean value of the panel lengths in a chordwise direction. The computations were performed for three periods for the nondimensional frequency K of 4. The phase values of ϕRC, ϕRA, ϕFC and ϕLA in Eq. (11) were set as 35 deg.

Figure 11 shows the effect of ξ in Eq. (10) on the time history of C_X for three periods, where the values of ξ were taken to be 5000 and 2000. The values of λ in Eq. (9) and ν in Eq. (10) were taken to be 0.0 and 10^{-6}, respectively. The coefficient of hydrodynamic force, C_X, in the case of a ξ of 2000 shows irregular changes with time. The time history of C_X for a ξ of 5000 shows almost regular changes with time. Figure 12 shows an example of the computed flow of streamwise free vortices from the pectoral fin at $t \cdot U/c = 1.57$ using a λ of 0.0 and a ξ of 5000. We can see that the free vortices shed from the leading edge flow near the surface of the fin. We can consider two reasons why the computed hydrodynamic forces on the fin are sensitive to ξ. One is that the changing rate of the effect of diffusion on the vorticity about ξ after one period of the fin motion in this region of ξ is large judging from Eq. (10). The other is that a large velocity from the free vortices near the surface of the fin is induced for $\xi = 2000$.

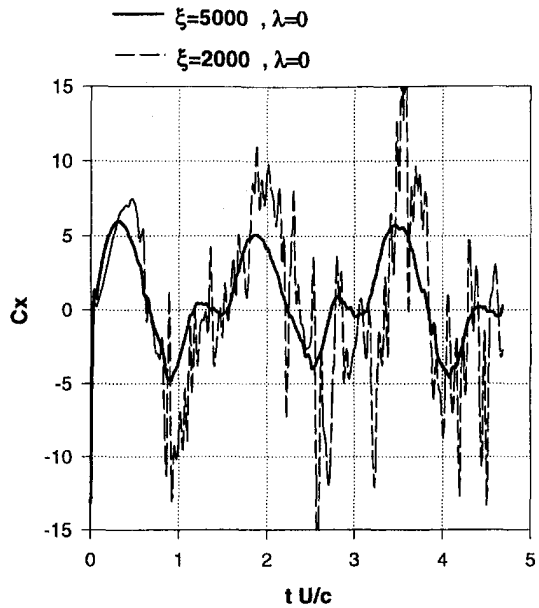

Fig. 11 Effect of the proportional constant ξ on the time history of the thrust coefficient

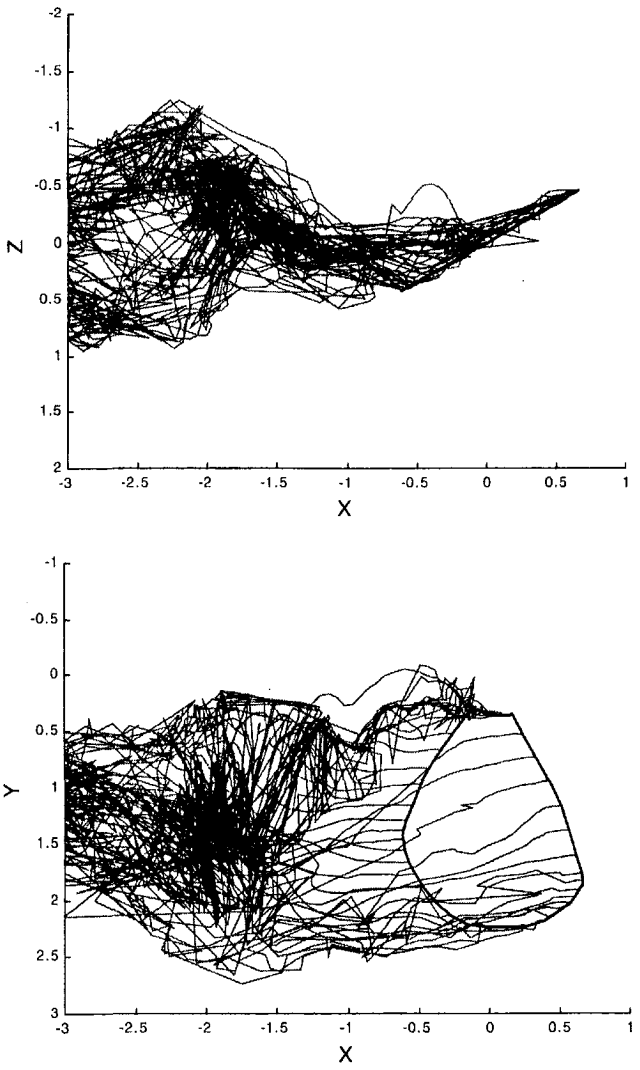

Fig. 12 Computed flow of streamwise free vortices from the pectoral fin at $t \cdot U/c = 1.57$

Although the effect of λ on the time history of C_X was investigated using λ of 0.0 and 0.4 and a ξ of 5000, little difference was observed. For example, the mean values of C_X during the last two periods for λ of 0.0 and 0.4 were 0.7932 ± 0.0856 and 0.7849 ± 0.0463, respectively. Therefore, the λ and ξ values of 0.0 and 5000, respectively, are used in the subsequent discussions. The reason that the computed hydrodynamic forces are insensitive to λ may be that the blocks of vortices with the same sign behind a two-dimensional flat plate as seen in Fig. 7 are not formed in this case due to a three-dimensional flow consisting of vortices flowing in different directions, as shown in Fig. 12.

4.2 Time Histories of Hydrodynamic Forces. Figure 13 shows the experimentally measured time histories of the hydrodynamic force coefficients C_X, C_Y, and C_Z during one period in the case of a phase difference $\Delta\phi$ of 54 deg and a K of 4. The mean values and the standard deviations at each time for the rowing angle, feathering angle, C_X, C_Y, and C_Z were obtained using the data for 4 periods. The thrust force ($C_X > 0$) is generated while the rowing angle varies from its minimum value to its maximum, namely, during the adduction. C_Y and C_Z become minimum shortly after the rowing angle passes its maximum value. The reason that C_Y and C_Z vibrate during one period may be that the pectoral fin model of a flat plate with a thickness of 0.6 mm vibrates.

Figure 14 shows the computed time histories of the hydrodynamic force coefficients during one period in the case of a phase difference $\Delta\phi$ of 60 deg and a K of 4. The mean values at each time on C_X, C_Y, and C_Z were obtained using the data for the last 2 periods. The time histories of the hydrodynamic forces acting on the fin computed by UVLM closely follow the experimentally measured ones. The changes in the computed hydrodynamic forces near the maximum value of the rowing angle are slower than the experimentally measured changes.

4.3 Mean Hydrodynamic Force Coefficients. We discuss here the mean hydrodynamic force coefficients C_X^*, C_{mY}^*, and C_{mZ}^* related to the propeller efficiency.

Figure 15 shows the comparison between the experimentally measured results and the computational results of the mean thrust force coefficient C_X^* during one period versus the phase difference $\Delta\phi$ for a K of 4. The mean values and the standard deviations of C_X were obtained using a method of moving averages during one period among the experimentally measured data for 4 periods and among the computed data for the last 2 periods, respectively. The experimentally measured results show that C_X^* shows a maximum between phase differences of 60 and 90 deg. The standard deviations of the computed results become larger as the phase difference decreases. The computed results agree fairly well with the experimentally measured results except in the region of the phase difference between 90 and 120 deg.

Figures 16 and 17 show the comparisons of the computed mean hydrodynamic force coefficients C_{mY}^* and C_{mZ}^*, respectively, during one period versus the phase difference $\Delta\phi$ for a K of 4 with the experimentally measured results. The mean values and the standard deviations were obtained using the same method as that explained above for C_X^*. There are differences between the experimentally measured results on C_{mY}^* and the computed results. However, the computed results for C_{mZ}^* follow the change in the

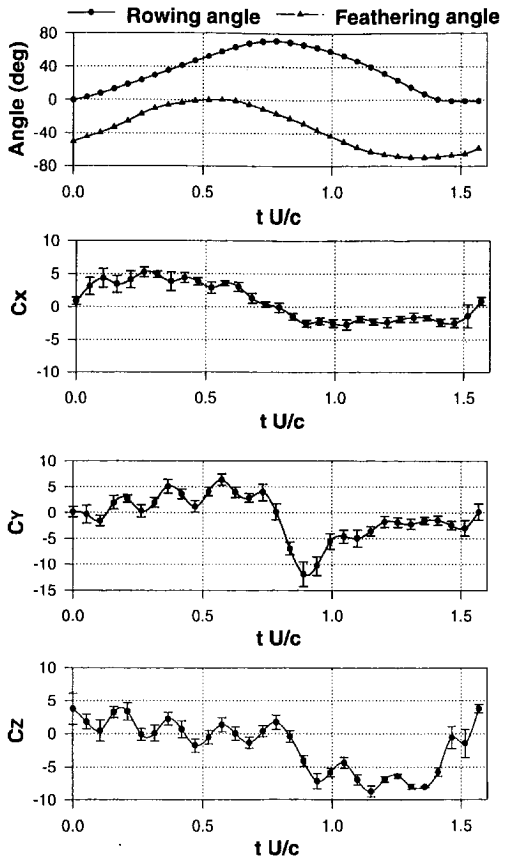

Fig. 13 Time histories of the experimentally measured coefficients of the hydrodynamic forces C_X, C_Y, C_Z

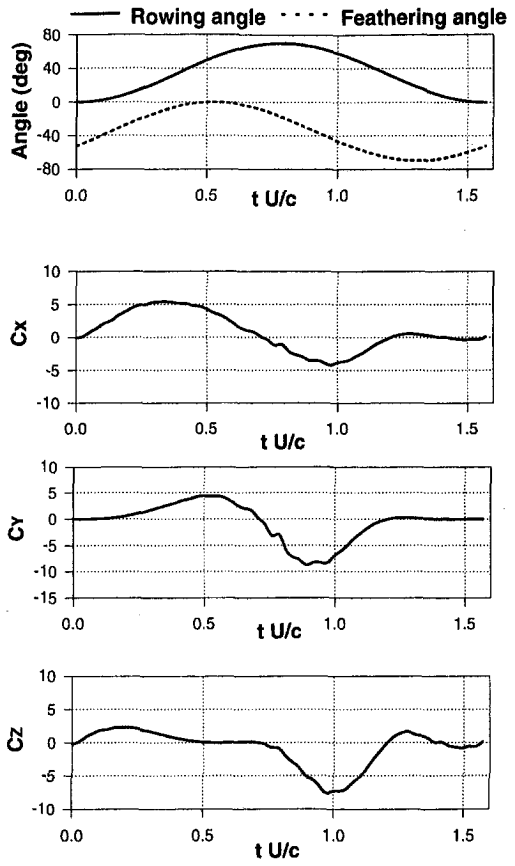

Fig. 14 Time histories of the computed coefficients of the hydrodynamic forces C_X, C_Y, C_Z

experimentally measured results against the phase difference with fairly good agreement.

4.4 Propeller Efficiency. Figure 18 shows a comparison between the experimentally measured results and the computational results for propeller efficiency versus the phase difference for a K of 4. The experimentally measured results show that the phase difference where the propeller efficiency becomes maximum

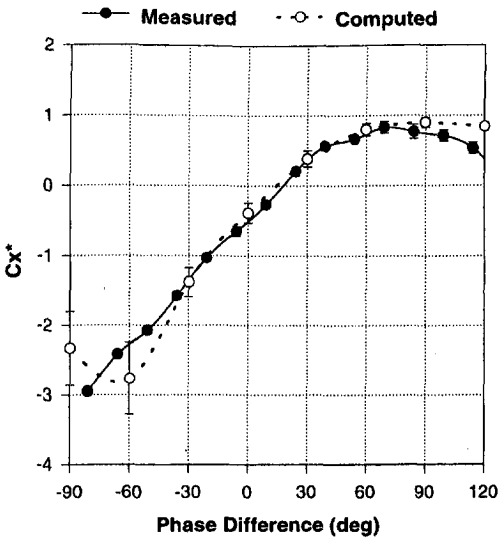

Fig. 15 Comparison between a numerical simulation and the experimental results for the coefficient of mean thrust C_X^*

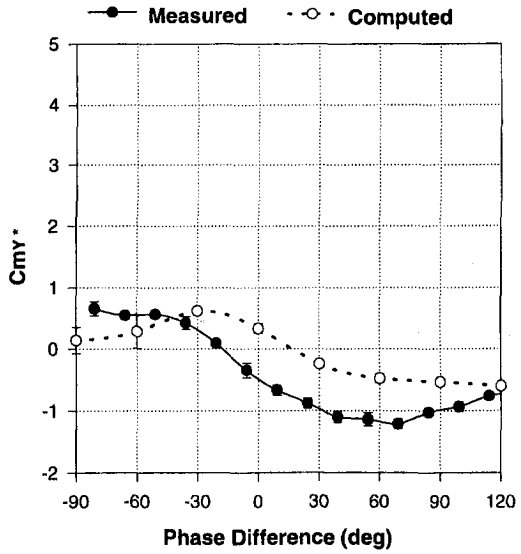

Fig. 16 Comparison between a numerical simulation and the experimental results for the coefficient of mean hydrodynamic force C_{mY}^*

is about 100 deg. The computed results are larger than the experimentally measured results for a phase difference larger than 30 deg. This is mainly due to the differences between the experimentally measured results on C_{mY}^* and the computed values shown in Fig. 16.

5 Conclusions

In this study we examined the hydrodynamic characteristics of a mechanical pectoral fin through experimental and theoretical analyses. The following conclusions have been reached:

1. the mechanical pectoral fin making a feathering motion and a rowing motion generates a thrust force in a certain range of phase differences between these two motions;
2. the unsteady vortex-lattice method, which includes the effects of vortex diffusion and vortex dissipation, was validated by comparisons with measured hydrodynamic forces acting on a two-dimensional flat plate with high angles of attack to the uniform flow;

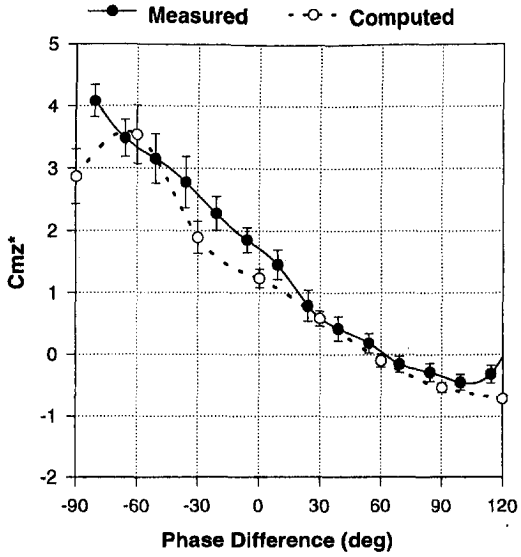

Fig. 17 Comparison between a numerical simulation and the experimental results for the coefficient of mean hydrodynamic force C_{mZ}^*

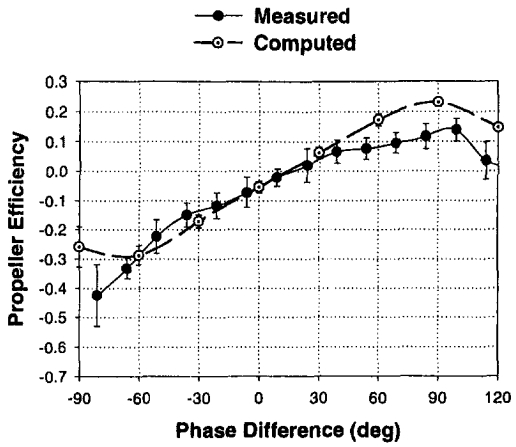

Fig. 18 Comparison between a numerical simulation and the experimental results for the propeller efficiency

3. the unsteady vortex-lattice method, which includes the effect of vortex diffusion, can reasonably express the experimentally measured unsteady forces acting on a mechanical pectoral fin.

Acknowledgments

This research is partially funded by a Grant-in-Aid for Scientific Research of the Ministry of Education, Science, and Culture of Japan. The author is grateful to emeritus professor A. Azuma of the University of Tokyo for his stimulating discussions. The author expresses his thanks to former graduate students M. Furushima and T. Inaba for their contributions to this research.

References

Azuma, A., 1992, *The Biokinetics of Flying and Swimming,* Springer-Verlag, New York.

Bandyopadhyay, P. R., Castano, J. M., Rice, J. Q., Philips, R. B., Nedderman, W. H., and Macy, W. K., 1997, "Low-Speed Maneuvering Hydrodynamics of Fish and Small Underwater Vehicles," ASME JOURNAL OF FLUIDS ENGINEERING, Vol. 119, pp. 136–144.

Barrett, D. S., and Triantafyllou, M. S., 1995, "The Design of Flexible Hull Undersea Vehicle Propelled by an Oscillating Foil," *Proceedings of 9th International Symposium on Unmanned, Untethered Submersible Technology.* (AUSI), Durham, NH, Sept. 25–27, pp. 111–123.

Blake, R. W., 1979, "The Mechanics of Labriform Locomotion I. Labriform Locomotion in the Angelfish (Pterophyllum Eimekei): an Analysis of the Power Stroke," *Journal of Experimental Biology,* Vol. 82, pp. 255–271.

Blake, R. W., 1983, "Median and paired Fin Propulsion," *Fish Biomechanics* Webb, P. W., and Weihs, D., eds., Praeger Publishers, pp. 214–247.

Geerlink, P. J., 1983, "Pectoral Fin Kinematics of Coris Formosa (Teleostei, Labridae)," *Netherlands Journal of Zoology,* Vol. 39, pp. 166–193.

Gibb, A. C., Jayne, B. C., and Lauder, G. V., 1994, "Kinematics of Pectoral Fin Locomotion in the Bluegill Sunfish Lepomis Macrochirus," *Journal of Experimental Biology,* Vol. 189, pp. 133–161.

Hertel, H., 1966, *Structure-Form-Movement,* Reinholds, New York.

Hoerner, S. F., and Borst, H. V., 1975, *Fluid Dynamic Lift,* pp. 21–1.

Isshiki, N., and Morikawa, H., 1982, "Study on Dolphin-Style Fin Ship," (in Japanese), *Bulletin of Society of Naval Architects of Japan,* No. 642, pp. 2–9.

Kato, N., and Yamaguchi, M., 1985, "The Vortex on a Submerged Solid of Revolution," *2nd International Symposium on Ship Viscous Resistance,* Goeteborg, Sweden, Mar. 18–20, pp. 22:1–22:22.

Kato, N., and Lane, D. M., 1996, "Co-ordinated Control of Multiple Manipulators in Underwater Robots," *Proceedings of the 1996 IEEE International Conference on Robotics and Automation,* Minneapolis, MN, Apr. 22–28, pp. 2505–2510.

Kato, N., and Furushima, M., 1996, "Pectoral Fin Model for Maneuver of Underwater Vehicles," *Proceedings of 1996 IEEE Symp. On Autonomous Underwater Vehicle Technology,* Monterey, CA, June 2–6, pp. 49–56.

Lighthill, M. J., 1969, "Hydrodynamics of Aquatic Animal Propulsion," *Annual Review of Fluid Mechanics,* Vol. 1, pp. 413–446.

Lindsey, C. C., 1978, "Form, Function and Locomotion Habits in Fish," *Locomotion Fish Physiology VII* Hoar, W. S., and D. J. Randall, eds., Academic Press, pp. 239–313.

Tanaka, I., and Nagai, M., 1996, *Hydrodynamics of Drag and Propulsion—Learning from High Speed Swimming Performance of Aquatic Animals* (in Japanese), Ship and Ocean Foundation, Japan, August, ISBN 4-916148-00-2 (Not for sale).

Walker, J. A., and Westneat, M. W., 1997, "Labriform Propulsion in Fishes: Kinematics of Flapping Aquatic Flight in the Bird Wrasse Gomphosus Varius (Labridae)," *Journal of Experimental Biology,* Vol. 200, pp. 1549–1569.

Wieghardt, K., 1974, *Theoretishe Stroemungslehre,* B. G. Teubner Stuttgart, pp. 148–152.

Webb, P. W., 1973, "Kinematics of Pectoral Fin Propulsion in *Cymatogaster Aggregata,*" *Journal of Experimental Biology,* Vol. 59, pp. 697–710.

Webb, P. W., 1982, "Locomotor Patterns in the Evolution of Actinopterygian Fishes," *American Zoologist,* Vol. 22, pp. 329–342.

Webb, P. W., 1984, "Body Form, Locomotion and Foraging in Aquatic Vertebrates," *American Zoologist,* Vol. 24, pp. 107–120.

Wu, T. Y. T., 1971, "Hydromechanics of Swimming of Fishes and Cetaceans," Yih, C. S., ed., *Advances in Applied Mechanics,* Vol. II, Academic Press, New York.

Influence of the Flatness Ratio of an Automotive Torque Converter on Hydrodynamic Performance

E. Ejiri
Senior Researcher.

M. Kubo
Research Engineer.

Nissan Research Center,
Nissan Motor Co., Ltd.,
1, Natsushima-cho, Yokosuka-shi 237-8523,
Japan,
e-mail: e-ejiri@mail.nissan.co.jp

Automotive torque converters have recently been designed with an increasingly narrower profile for the purpose of achieving a smaller axial size, which also translates into weight savings. Four torque converters with different flatness ratios were manufactured and tested in order to evaluate the change in their overall performance, including efficiency, stall torque ratio and torque transmission capacity. The experimental results show that the overall performance deteriorates when the flatness ratio is reduced to less than about 0.2. The internal flow characteristics of the torque converters were also investigated by numerical analysis using a CFD code. The computational results indicate that the main cause of this performance deterioration is a reduction in pump efficiency, which is attributed to increases in shock loss in the inlet region, separation loss in the fore half region, and friction loss in the exit region.

Introduction

The torque converter is a kind of turbomachine that is widely used in today's automatic transmissions for automobiles. It consists of three major elements—a pump, a turbine, and a stator. Its functions include damping of engine torque fluctuation, damping of noise and vibration in the drive line, and automatic amplification of torque according to the difference in rotational speed between the input and output shafts without requiring any external control. Internal flow investigations and development of performance prediction methods for the torque converter have been carried out over the years, as its hydrodynamic performance has a significant influence on vehicle fuel economy and driving performance.

Some experimental work has been done to elucidate internal flow characteristics. Unsteady flow between the pump and turbine impellers was measured by hot-film anemometry by Browarzik (1994) in a detailed study of the effect of the pump-turbine interaction on flow fields. Brun et al. (1996) used a laser Doppler velocimeter to investigate the internal flow in the three elements. Complex three-dimensional flow fields in the blade passage were analyzed on the basis of the steady and unsteady velocities measured. Pressure measurements made by Marathe et al. (1995) with high-response pressure transducers showed strong unsteady hydrodynamic interference between the elements. Ejiri et al. (1997) evaluated the performance of each element by measuring flow between any two elements with five-hole Pitot probes. The pump was shown to be the major source of loss in the speed ratio range where vehicles are most frequently operated in everyday driving.

Flows through the pump impeller (By et al., 1995; Tsujita et al., 1996) as well as through the three elements (Cigarini et al., 1995) were computed by using CFD codes. Some of the computational results showed good qualitative agreement with the measured flow patterns. Kubo et al. (1998) applied a general CFD code to a practical in-house CAE system to obtain an improved torque converter design. Some of the design parameters were optimized by using the system and an improvement in efficiency was demonstrated experimentally.

Most passenger cars with small and medium displacement engines have adopted a front-wheel-drive layout in recent years. Torque converters accordingly have been designed with an increasingly narrower profile for the purpose of achieving a smaller axial size, which also translates into weight savings. The literature contains some reports regarding design methods for flat torque converters, as a flatter design reportedly tends to reduce hydrodynamic performance. Sakamoto et al. (1991) introduced a pressure balance analysis method to show that the calculated imbalance between the pressure gradient and the centrifugal force in the direction perpendicular to the meridional stream lines can be correlated by the strength of the visualized secondary flows and the overall performance deterioration. Ejiri (1990) reported a two-dimensional inverse design approach for the stator. It was demonstrated experimentally that this design approach can increase maximum overall efficiency by 2–3 points and transmission torque capacity in the higher speed ratio range by 10 percent without sacrificing performance in the lower speed ratio range. Zangeneh et al. (1997) applied a three-dimensional inverse design approach to the pump and loss was reduced by about 15 percent as a result of eliminating the reverse flow observed in a conventional impeller.

However, there are no reports in the literature of quantitative experimental demonstrations regarding the tendency for performance to deteriorate owing to a flatter design, and its basic mechanism is still not fully understood. In this study, four torque converters with different flatness ratios were manufactured and tested in order to evaluate the change in their overall performance, including efficiency and torque capacity. The internal flow characteristics of the torque converters were also investigated by numerical analysis using a CFD code. A loss analysis was then conducted based on the computed flow results.

Overall Performance Experiment

Test Torque Converters. Torque converters with a 236 mm nominal diameter, D, and four different flatness ratios, defined as L/D in Fig. 1, were used. They are referred to here as Type 1 (a so-called circular type) to Type 4, in decreasing order of their flatness ratio, as shown in Table 1. Their design parameters were unchanged as much as possible except the flatness ratio. The shell (outer channel wall) had an oval shape and the core (inner channel wall) shapes were defined so that the flow passage cross-sectional

Contributed by the Fluids Engineering Division for publication in the JOURNAL OF FLUIDS ENGINEERING. Manuscript received by the Fluids Engineering Division December 4, 1998; revised manuscript received June 13, 1999. Associate Technical Editor: B. Lakshminarayana.

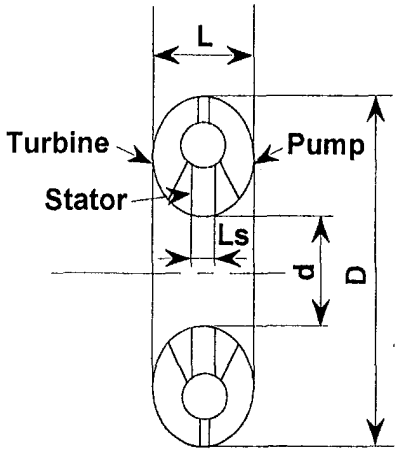

Fig. 1 Dimensions in torus cross section

area would be as constant as possible. As indicated in Fig. 1, d/D had a constant value of 0.417 and the stator axial length, Ls, was proportional to the torque converter axial length, L.

Two different pump impellers, one with a forward exit blade angle (referred to as a high-efficiency type) and the other with a backward angle (referred to as a high-stall-torque-ratio type), were manufactured for each type of torque converter. The high-stall-torque-ratio types are mentioned here only to confirm the consistency of our conventional experimental data and are not discussed in detail in this paper. Their inlet and exit blade angles on the design path, a curve that bisects the flow passage cross-sectional area, are shown in Table 2. The blade angle is defined as an angle from the meridional plane. The minus sign in the table indicates the rotational direction of the impellers. The blade angle was designed at a speed ratio of 0.7 and was constant from the shell to the core at the inlet and the exit. The blade angle distribution from the inlet to the exit in the pump and turbine was defined so that the angular momentum change would be constant along the design path except near the exit. The pump had 31 blades which were 1.0 mm in thickness and the turbine had 29 blades which were 0.8 mm in thickness.

Experimental Apparatus and Procedure. The input and output shafts of the torque converter were connected to DC dynamometers, with tachometers and torquemeters installed in between. These dynamometers were controlled so that the input torque was a constant 98 Nm at a given speed ratio. An ordinary automatic transmission fluid was provided from an external pressure source as the working fluid and controlled so that the inlet pressure was 392 kPaG, the outlet pressure 196 kPaG and the exit temperature 80 ± 1°C for the torque converter.

Table 1 Flatness ratio, L/D

Type 1	Type 2	Type 3	Type 4
0.352	0.297	0.242	0.186

Experimental Uncertainty. The input and output torque were obtained by compensating for mechanical losses in the bearings, the oil seals and the other frictional parts (measured beforehand), disk friction loss between the turbine impeller and the cover, and windage loss (using empirical formulae). Leakage flow was not compensated for either between the elements (within the core) or between an element and the external flow field. The former was estimated as less than 1 percent and the latter as less than 0.1 percent of the circulatory flow according to our LDV measurements. Both the uncertainty of the torque and that of the rotational speed measured with the instruments used in the experiment were estimated at 0.05 percent. Therefore, the uncertainty of the calculated efficiency, torque ratio, and torque capacity coefficient was estimated at 0.2, 0.1, and 0.15 percent, respectively.

Numerical Flow Analysis

Computational Method. Viscous calculations were performed by using a general flow analysis code which employs a finite volume method of discretization. Three-dimensional incompressible time-averaged Navier-Stokes equations were solved with the code. A standard k-ϵ model (Launder et al., 1974) was used for turbulence closure modeling. In discretizing the convection terms of the equations, the QUICK scheme (Leonard, 1979), a third-order upwind differencing scheme, was used to obtain a stable solution while suppressing numerical diffusion. The SIMPLE algorithm (Patankar et al., 1972) was employed to solve the algebraic finite-volume equations resulting from the discretization operation.

To represent the complex geometry of the hydrodynamic elements accurately and distribute the computational meshes in an appropriate fashion, an in-house mesh generation program was used. Mesh-point clustering was performed near the boundary and cell deformity was checked with the program. The computational grid is given in Fig. 2 where one blade passage is shown for each element to illustrate the grid distribution in the computational field when about 68,000 grid cells in total were used. Leakage between

Nomenclature

E = specific energy ($=\omega r V_\theta$)
e = speed ratio ($=N_2/N_1$)
I = rothalpy ($=P/\rho + 1/2\ W^2 - 1/2\ U^2$)
i = incidence angle
N = rotational speed
P = static pressure
P_T = total pressure
r = radius
s = distance along the design path (a curve that bisects the passage cross-sectional area in the meridional plane), starting from the upstream boundary and ending at the downstream boundary of the computation domain of an element
T = torque
t = torque ratio ($=T_2/T_1$)
V = absolute velocity
W = relative velocity
η = efficiency
ρ = density
τ = torque capacity coefficient ($=T_1/N_1^2$)
ω = angular velocity

Subscripts

0 = reference position (design path position at pump exit)
1 = pump
2 = turbine
3 = stator
c = circulatory component (a direction perpendicular to the computation mesh line from the shell to the core in the meridional plane)
0.8 = speed ratio of 0.8
S = stall point (speed ratio of 0)
θ = peripheral component
(i,j) i = 1: pump
= 2: turbine
= 3: stator
j = 1: inlet
= 2: exit

Superscript

* = nondimensional or normalized

Table 2 Blade angle

	pump*	pump**	turbine	stator
inlet	50°	50°	−60°	0°
exit	−40°	19°	60°	−58°

*(**) denotes forward (backward) lean impeller.

the elements and also between an element and the external flow field was disregarded.

The wall function for the velocity vector was used to reduce the grid points near the wall. A cyclic boundary condition was imposed on both peripheral boundaries outside a blade passage. Computations were performed for one element after another along the flow direction in a manner where either the velocity or the pressure was given as the inlet and exit boundary condition of each element, as shown in Fig. 3. For example, the pump flow was computed with the given inlet and exit pressures that had been obtained in the previous iteration inside the turbine and the stator. The turbine flow was computed with the given inlet velocity and the exit pressure, and the stator flow with the given inlet and exit velocities. This manner of imposing boundary conditions significantly reduced the CPU time required for convergence without sacrificing computational stability, compared with the conventional manner where the inlet velocity and the exit pressure were applied to all three elements. Computed pressures and velocities in each iteration were averaged circumferentially, transferred to the adjacent element and used as the boundary condition of the next iteration. The pressure at the core of the pump inlet was reset to zero and all the other pressures were adjusted accordingly in computing the pump flow in each circulatory iteration.

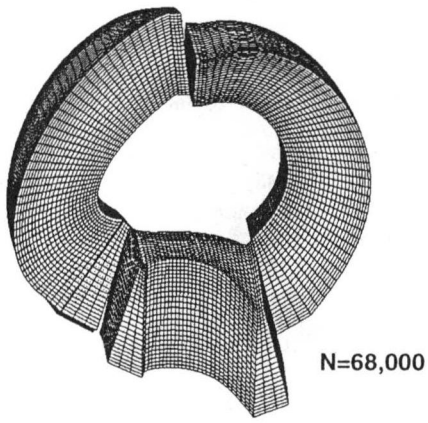

Fig. 2 Computational grid

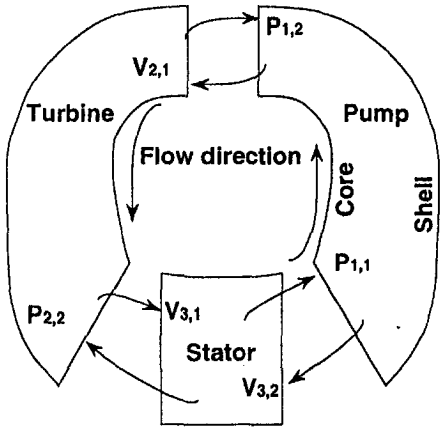

Fig. 3 Interface boundary conditions

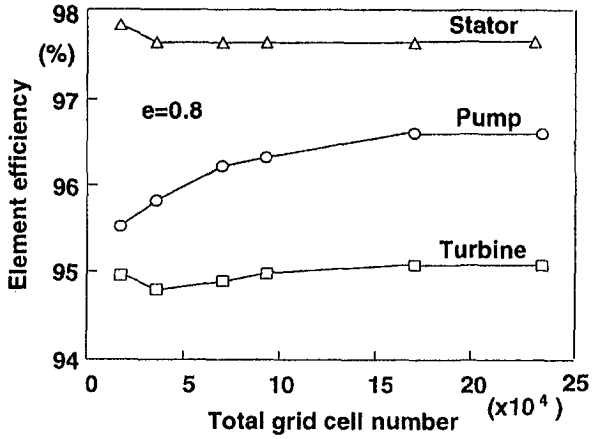

Fig. 4 Grid number dependence of solution

The solution was assumed to have converged when all the normalized residuals in mass and momentum conservation equations were less than 10^{-2} and the rate of change in the mass flow rate in two consecutive circulatory iterations was less than 10^{-3}. Typically, nearly 1000 circulatory iterations and about 12 hours of CPU time were required to obtain a converged solution on a 250 MHz workstation for 166,800 grid cells in total.

Computational Uncertainty. Several types of grid systems were used to evaluate the grid number dependence of the computational results of the circular-type torque converter that was experimentally investigated by Ejiri et al. (1997). Figure 4 shows the grid number dependence of the solution in terms of the element efficiencies. The comparison suggests that a grid-independent solution was obtained with more than about 170,000 grid cells in total.

The standard k-ϵ model and the wall function, both of which are based on high Reynolds number flow, were used in the relatively low Reynolds number turbulent flow in the torque converter. The Reynolds number based on the passage height and the average circulatory velocity at the pump exit was about 7×10^3. This was one source of prediction error. Observe the difference between the computed and the measured circulatory velocity profiles at the pump exit (Ejiri, et al., 1997). Another source of prediction error originated from the transfer of the properties, such as pressure and velocity, at the interface boundary between any two elements. The properties were averaged both in time and space (circumferentially) at the boundary, which means numerical diffusion occurred there. Note that the QUICK scheme almost always gave a more accurate solution than the first-order upwinding for convection terms in the Navier-Stokes equations at the cost of more CPU time.

Uncertainties with these errata were not separately estimated in an exact manner here, however, the overall uncertainty was estimated at around ±5 percent in efficiency and torque ratio, and at ±10 percent in torque capacity at a speed ratio of 0.8 from our previous experience. Figure 5 compares the measured and computed overall performance for the torque converter. Efficiency tended to be overestimated and torque capacity tended to be underestimated in the higher speed ratio range of interest (e = 0.6–0.8).

Efficiency and Loss Evaluation. The individual efficiencies of the pump, turbine, and stator, η_1, η_2 and η_3, are defined by the following expressions:

$$\eta_1 = (P_{T1,2} - P_{T1,1})/\{\rho\omega_1(r_{1,2}V_{\theta 1,2} - r_{1,1}V_{\theta 1,1})\} \quad (1)$$

$$\eta_2 = \rho\omega_2(r_{2,2}V_{\theta 2,2} - r_{2,1}V_{\theta 2,1})/(P_{T2,1} - P_{T2,2}) \quad (2)$$

$$\eta_3 = 1 - (P_{T3,1} - P_{T3,2})/(P_{T1,2} - P_{T1,1}) \quad (3)$$

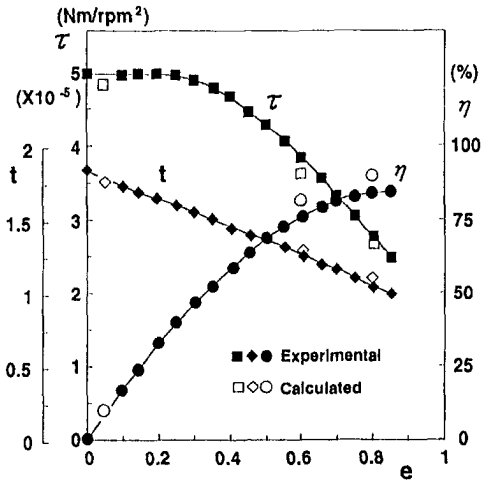

Fig. 5 Overall performance of torque converter

The following relation then holds true between the overall efficiency η and η_1, η_2 and η_3, as the overall efficiency is defined as the ratio of output power to input power, and $P_{T1,2} = P_{T2,1}$, $P_{T2,2} = P_{T3,1}$, and $P_{T3,2} = P_{T1,1}$.

$$\eta = T_2\omega_2/(T_1\omega_1) = \eta_1\eta_2\eta_3 \tag{4}$$

Rothalpy, I, is defined as

$$I = P/\rho + 1/2W^2 - 1/2U^2 \tag{5}$$

and the loss that occurs can be evaluated by this property. The change in rothalpy from the element inlet, ΔI, is nondimensionalized by the change in the theoretical specific energy from the inlet to the exit, ΔE, as follows.

$$(\Delta I)^* = \Delta I/\Delta E \tag{6}$$

If the pump is taken as an example, the following equations hold true for the pump exit position.

$$\Delta E_1 = U_{1,2}V_{\theta 1,2} - U_{1,1}V_{\theta 1,1}(>0) \tag{7}$$

$$(\Delta I_{1,2})^* = \eta_1 - 1 \tag{8}$$

Results and Discussions

Experimental Results. The measured overall performance of the test torque converters is summarized in Fig. 6 in terms of the stall torque ratio, t_s, efficiency at $e = 0.8$, $\eta^*_{0.8}$, and torque capacity coefficient at $e = 0.8$, $\tau^*_{0.8}$. In this figure, $\eta^*_{0.8}$ and $\tau^*_{0.8}$ are

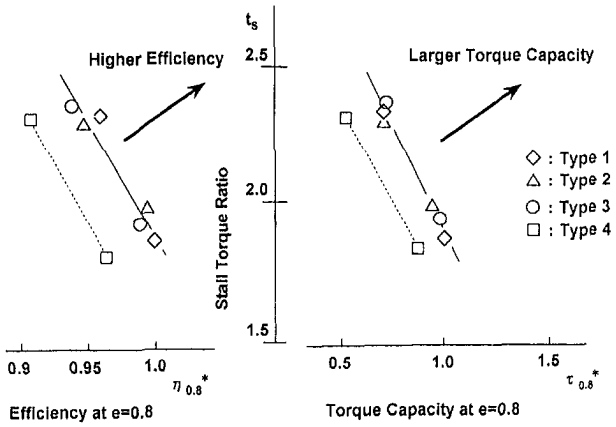

Fig. 6 Measured overall performance at $e = 0.8$

Table 3 Rotational speed of impellers at $e = 0.8$ (rpm)

		Type 1	Type 2	Type 3	Type 4
H-E Type	Pump	1,871	1,919	1,909	2,029
	Turbine	1,493	1,532	1,515	1,622
H-S-T-R Type	Pump	2,190	2,188	2,160	2,570
	Turbine	1,741	1,753	1,715	2,042

the normalized values of $\eta_{0.8}$ and $\tau_{0.8}$ that were obtained by using the corresponding values for the Type 1 unit with a forward lean pump impeller. The lines indicated in this figure are equipotential performance lines the gradients of which were obtained empirically on the basis of our extensive experiments. Similar lines can be derived from data reported in the literature (Jandasek, 1955). The relation of $t_s - \eta^*_{0.8}$ is shown on the left side and the efficiency potential increases in the upper right direction. Shown on the right side is the relation of $t_s - \tau^*_{0.8}$ and the torque capacity potential increases in the same direction. The figure indicates the Type 1 to Type 3 units have almost the same performance potential. However, it is clearly seen that Type 4 shows a significant deterioration in its performance potential. The rotational speeds of the test pumps and turbines at $e = 0.8$ are shown in Table 3 for reference.

Calculation Results. Calculations were performed with 166,800 grid cells (26 × 30 × 80: pitch × span × longitude for

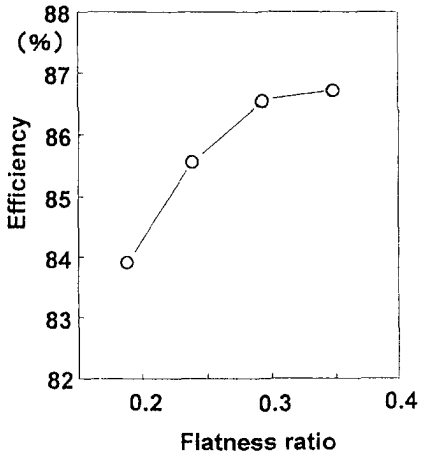

Fig. 7(*a*) Overall efficiency

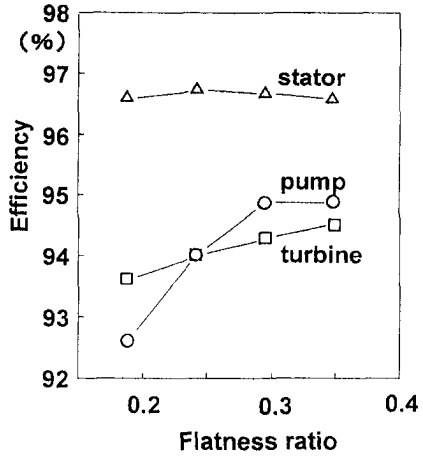

Fig. 7(*b*) Element efficiency

Fig. 7 Computed efficiency at $e = 0.8$

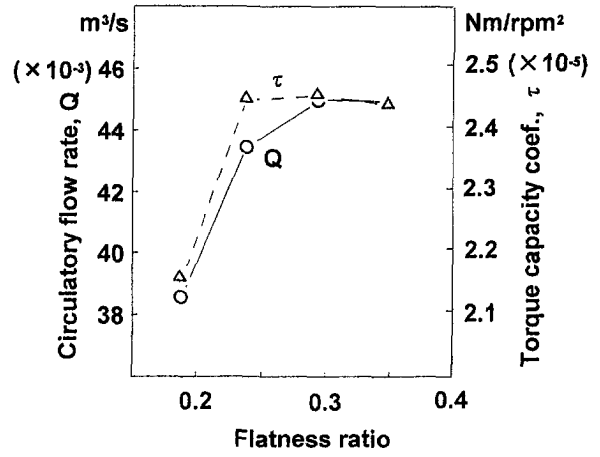

Fig. 8 Torque capacity and circulatory flow rate at $e = 0.8$

the pump and turbine; 28 × 30 × 50 for the stator) at $e = 0.8$ ($N_1 = 2{,}000$ rpm, $N_2 = 1{,}600$ rpm), which is thought to be representative of the speed ratio range where vehicles are operated most frequently in everyday driving. Calculations were performed for all the test torque converters with a forward lean pump impeller.

Figure 7 shows the overall and element efficiencies computed for all four types. Overall efficiency begins to decrease from Type 2 to Type 3 in Fig. 7(*a*). It decreases by no less than 1.6 points from Type 3 to Type 4. The main cause of this decline in overall efficiency is attributed to lower pump efficiency (−1.6 points) in Fig. 7(*b*). Figure 8 shows the computed torque capacity coefficient and circulatory flow rate at $e = 0.8$. The torque capacity begins to decrease from Type 2 to Type 3 and the circulatory flow rate begins to decrease from Type 3 to Type 4. The tendency of the torque capacity coincides relatively well with that of the circulatory flow rate.

As the correlation between overall and pump efficiencies is quite remarkable in Fig. 7, the subsequent discussion will focus on the pump flow and loss. Figure 9 shows the nondimensional rothalpy change mass-averaged in the meridional cross section of the pump. s^* is the distance nondimensionalized by the full length of s. The leading edge corresponds to about $s^* = 0.05$, and the trailing edge corresponds to about $s^* = 0.95$. Compared with Types 1 and 2, Types 3 and 4 show a greater decrease in rothalpy (i.e., suffer a greater loss) in three regions: the inlet region ($s^* = 0.05$–0.1), the fore half region ($s^* = 0.2$–0.6), and the exit region ($s^* = 0.75$–0.95). The cause of the losses is discussed below.

Inlet Region of Pump ($s^* = 0.05$–0.1). Shock loss owing to the incidence angle occurs in this region, and the loss is the largest

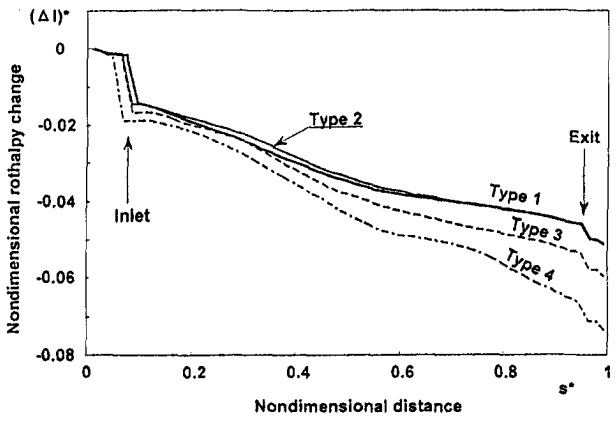

Fig. 9 Rothalpy change from inlet to exit in pump at $e = 0.8$

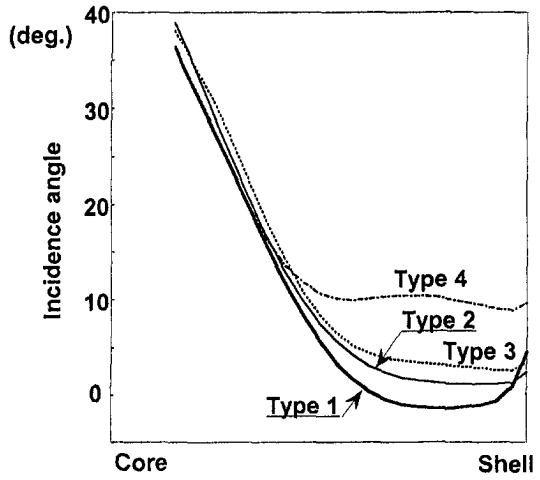

Fig. 10 Incidence angle at pump inlet at =0.8

for Type 4. Figure 10 shows the distribution of the incidence angle i from the shell to the core for the four pumps. The incidence angle for Type 4 is the largest from the center to the shell. Figure 11 shows the distribution of the circulatory velocity from the shell to the core at the pump inlet. It is seen that the circulatory velocity for Type 4 is about 80 percent of that for Type 3 from the center to the shell, through which most of the flow passes. The increase in the incidence angle for Type 4 can be attributed to this flow reduction.

Fore Half Region of Pump ($s^* = 0.2$–0.6). Figure 12 shows the average relative velocity distribution from the inlet to the exit, which has been nondimensionalized by the peripheral velocity at the pump exit in the design-path position. The velocity continues to decline from $s^* = 0.2$–0.6 and the reduction ratio is as low as 0.44 for Type 4. Figure 13 shows the circulatory velocity distribution in the cross section near $s^* = 0.6$. All types exhibit reverse flow on the suction side, however, the area of reverse flow is the largest for Type 4. The reverse flow in this region where the average velocity reduction ratio is the lowest is considered to generate the greatest loss of the four types.

Exit Region of Pump ($s^* = 0.75$–0.95). The average relative velocity accelerates in this region and the average velocity for Type 4 is not as high as for the other types in Fig. 12. Figure 14 shows torus cross-sectional views of Types 3 and 4. Figure 15 shows the circulatory velocity distribution in a cross section near $s^* = 0.8$, where the core has a small round shape in the meridional plane for Type 4 as seen in Fig. 14(*b*). Higher velocity is observed on the core side on the pressure surface, whereas lower

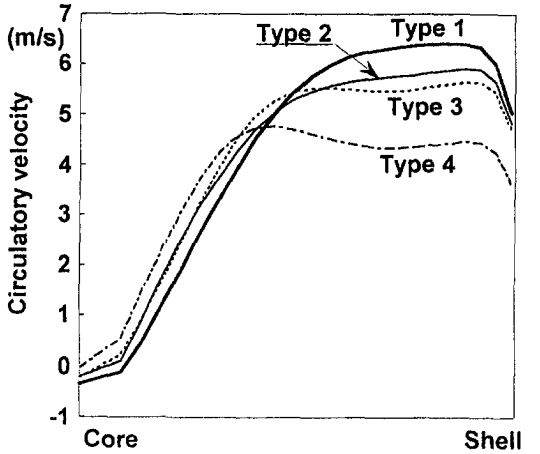

Fig. 11 Circulatory velocity at pump inlet at $e = 0.8$

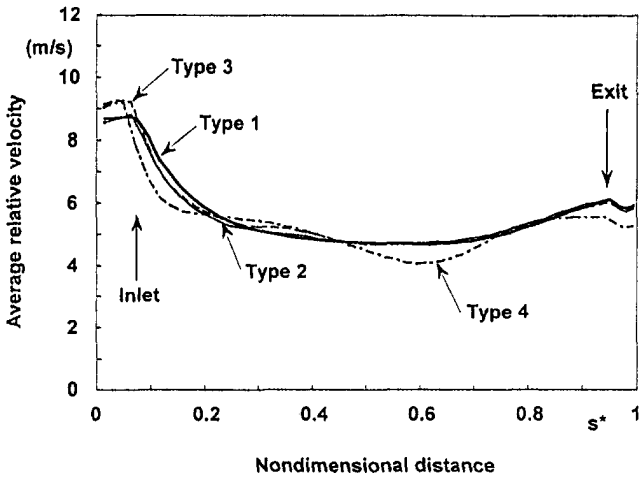

Fig. 12 Average relative velocity in pump at $e = 0.8$

velocity fluid accumulates on the suction surface. This tendency is significant in the Type 4 impeller because the fluid is accelerated by the large wall curvature of the core in the meridional plane. Consequently, a greater loss is generated by the wall friction there. Reverse flow is observed in Type 4, however, it diminishes at the exit because the average flow there is of the acceleration type (not shown). Therefore, it is considered that this reverse flow does not contribute very much to loss generation in this region.

Consideration of Loss Generation in Pump. The greater loss generated in the fore half and exit regions of the Type 3 and Type 4 pump impellers resulted in a lower circulatory flow rate, which, in turn, increased the incidence angle and shock loss in the inlet region. This reduction in the circular flow rate and nonuniformity of the pump exit flow may also affect the turbine and cause greater loss with a flatter design. All these losses noted here would finally reduce transmission torque capacity and also the overall efficiency.

The computational results show a tendency for overall performance to deteriorate relative to the flatness ratio, which coincided reasonably well with the experimental results. Moreover, the computational results predicted not only the elements but also the regions where greater loss occurred with a flatter design.

Concluding Remarks

- Four torque converters with different flatness ratios (0.352, 0.297, 0.242, and 0.186) were manufactured and tested in order to evaluate the effect of this parameter on their overall performance, including efficiency, stall torque ratio and torque capacity. The experimental results show that the overall performance deteriorates significantly with a flatness ratio of 0.186.
- The internal flow characteristics of the torque converters were also investigated by numerical analysis using a CFD code. The computational results also show that the main cause of this performance deterioration with a flatter design is increased pump loss.
- The computational results also show that, with a flatness ratio of 0.186, the pump suffers greater loss than the other pumps in the inlet region ($s^* = 0.05$–0.1), the fore half region ($s^* = 0.2$–0.6), and the exit region ($s^* = 0.75$–0.95).

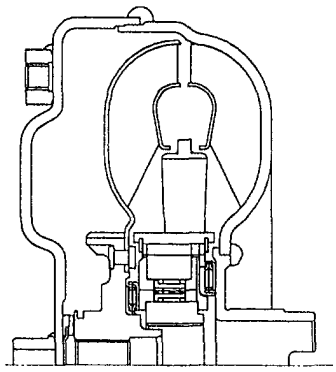

Fig. 14(*a*) Type 3

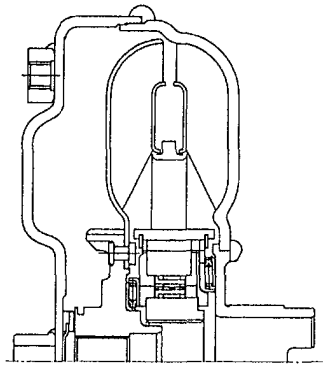

Fig. 14(*b*) Type 4

Fig. 14 Torus cross-sectional views

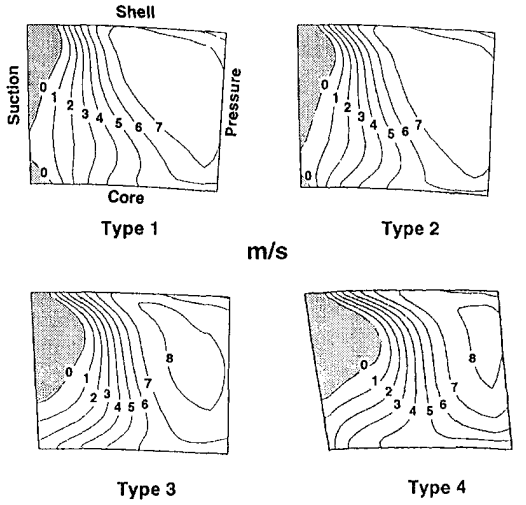

Fig. 13 Circulatory velocity at $s^* = 0.6$ in pump at $e = 0.8$

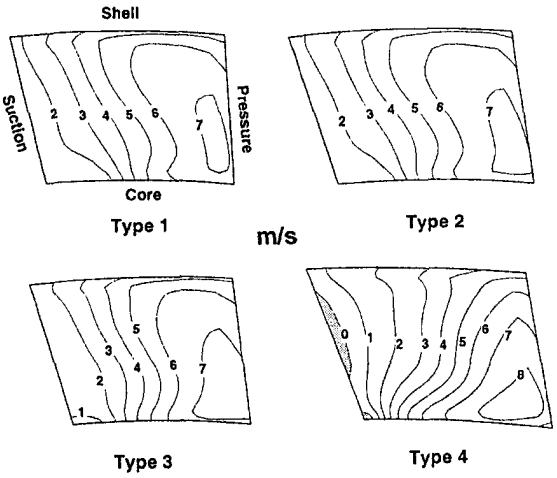

Fig. 15 Circulatory velocity at $s^* = 0.8$ in pump at $e = 0.8$

• The greater loss in the inlet region is attributed to increased shock loss. The greater loss in the fore half region is attributed to a larger reverse flow area caused by a large reduction in velocity. The greater loss in the exit region is attributed to increased wall friction loss as a result of higher velocity at the core with large stream-line curvature in the meridional plane.

Design optimization of the excessively flat torque converter should be possible based on the method and the results presented here, though performance tends to deteriorate as the flatness ratio decreases. As far as the pump design is concerned, the core shape (it is not necessary for the core shape of the pump and the turbine to be symmetric to the center line any more) and the blade loading distribution from the inlet to the exit are the key points. More flexible design methods than conventional ones (Jandasek, 1962, for example) should be effective for these points (see Zangeneh, et al., 1997).

Regarding the prospect of applying CFD to the torque converter, further improvement in the accuracy of performance predictions should be possible if a better turbulence model and more physically reasonable boundary conditions are introduced to allow the transfer of fully three-dimensional unsteady flow information between two elements. Parallel computing using multiple computers will do such a job in a shorter CPU time than a single computer by solving all of the stator-pump-turbine flow fields together with swapping boundary information at each iteration. A tentative research was reported on this subject by Matsuda et al. (1996).

Acknowledgments

The authors would like to thank Nissan Motor Co., Ltd. for permission to publish this paper, as well as Ikuo Aoki for his assistance in performing the computations and Yoshihiko Ishii for his help in conducting the experiments.

References

Browarzik, V., 1994, "Experimental Investigation of Rotor/Rotor Interaction in a Hydrodynamic Torque Converter Using Hot-Film Anemometry," ASME Paper, 94-GT-246.

Brun, K., and Flack, R. D., 1996, "The Flow Field Inside an Automotive Torque Converter: Laser Velocimeter Measurements," SAE Paper, 960721.

By, R. R., Kunz, R., and Lakshminarayana, B., 1995, "Navier-Stokes Analysis of the Pump Flow Field of an Automotive Torque Converter," ASME JOURNAL OF FLUIDS ENGINEERING, Vol. 117, pp. 116–122.

Cigarini, M., and Jonnavithula, S., 1995, "Fluid Flow in an Automotive Torque Converter: Comparison of Numerical Results with Measurements," SAE Paper, 950673.

Ejiri, E., 1990, "A New Approach to Developing More Efficient Torque Converter Stator," SAE Paper, 901765.

Ejiri, E., and Kubo, M., 1997, "Performance Analysis of Torque Converter Elements," *Proceedings of ASME Fluids Engineering Division Summer Meeting,* FEDSM97-3219, (CD-ROM).

Jandasek, S. V., 1962, "The Design of a Single Stage Three Element Torque Converter," *SAE Design Practices-Passenger Car Automatic Transmission,* Vol. 1, pp. 201–226.

Kubo, M., and Ejiri, E., 1998, "A Loss Analysis Design Approach to Improving Torque Converter Performance," SAE Paper, 981100.

Launder, B. E., and Spalding, D. B., 1974, "The Numerical Computation of Turbulent Flows," *Computer Methods in Applied Mechanics and Engineering,* Vol. 3, pp. 269–289.

Leonard, B. P., 1979, "A Stable and Accurate Convective Modeling Procedure Based on Quadratic Upstream Interpolation," *Computer Methods in Applied Mechanics and Engineering,* Vol. 19, pp. 59–98.

Marathe, B. V., Lakshminarayana, B., and Maddock, D. G., 1995, "Experimental Investigation of Steady and Unsteady Flow Field Downstream of an Automotive Torque Converter Turbine and Inside the Stator, Part II: Unsteady Pressure on the Stator Blade Surface," ASME Paper, 95-GT-232.

Matsuda, S., Kobayashi, T., Taniguchi, N., Oshima, M., and Tasaka, T., 1996, "Parallel Numerical Calculation of Turbulent Flow in a Torque Converter with PVM," *SEISAN-KENKYU* (in Japanese), Vol. 48, No. 2, pp. 119–121.

Patankar, S. V., and Spalding, D. B., 1972, "A Calculation Procedure for Heat, Mass and Momentum Transfer in Three-dimensional Parabolic Flows," *Int. J. Heat Mass Transfer,* Vol. 15, pp. 1787–1806.

Sakamoto, H., Suyama, K., and Saka, T., 1992, "Study on Torque Converter Circuit Profile," SAE Paper, 920765.

Tsujita, H., Mizuki, S., and Ejiri, E., 1996, "Analysis of Flow within Pump Impeller of Torque Converter," ASME Paper, 96-GT-404.

Zangeneh, M., Ejiri, E., and Kubo, M., 1997, "On 3D Inverse Design of an Automotive Torque Converter Pump Impeller in Shear Flow," *Proceedings of JSME International Conference on Fluid Engineering,* pp. 201–206.

The Unsteady Pressure Field in a High Specific Speed Centrifugal Pump Impeller—Part I: Influence of the Volute

Kevin A. Kaupert
Turbomachinery Laboratory,
ETH Swiss Federal Institute of Technology,
CH-8092 Zurich, Switzerland

Thomas Staubli
Professor;
Now at HTA Luzern, CH-6048 Horw,
Switzerland.

An experimental investigation is presented regarding the unsteady pressure field within a high specific speed centrifugal pump impeller (ω_S = 1.7) which operated in a double spiral volute. For this, twenty-five piezoresistive pressure transducers were mounted within a single blade passage and sampled in the rotating impeller frame with a telemetry system. The influence of varying volume flux on the pressure transducers was evaluated in terms of pressure fluctuation magnitudes and phase differences. The magnitude information reveals that the pressure fluctuations from the impeller-volute interaction grew as the volume flux became further removed from the best efficiency point and as the trailing edge of the impeller blade was approached. These fluctuations reached 35% of the pump head in deep part load. The upstream influence of the volute steady pressure field dominates the unsteady pressure field within the impeller at all off design load points. Acquired signal phase information permits the identification of the pressure field unsteadiness within the impeller passage as fundamentally synchronized simultaneously with the volute tongue passing frequency. Special emphasis was placed on the volume flux regime where the pump and impeller pressure discharge characteristic undergo hysteresis, as impeller inlet and outlet recirculation commence and cease. A synthesis of the rotating transducers was performed to obtain unsteady blade loading parameters. The value of the unsteady lift coefficient varies on the order of 200% for a single blade in part load operation (at 45% bep), an abrupt fluctuation occurring as the fore running blade suction side passes a volute tongue. The unsteady moment coefficient and center of pressure are also shown to vary significantly during the impeller-volute tongue interaction.

Introduction

Numerical prediction of the pump flow field reduces industries time and construction cost in the design or modification of pump components. Much effort has been spent predicting time averaged flow quantities, obtaining limited success near pump best point efficiency operation (e.g., Staubli et al., 1995). These quantities are useful for pump performance predictions even though agreement in part load is generally poor.

Little success has been reported in the numerical prediction of centrifugal pump unsteady flow fields and associated unsteady forces. This is due greatly to a limited existence of extensive experimental data to perform any validation (Brennen, 1994) and the numerical complexity involved. With pump construction trends moving towards larger output power concentrations (Makay, 1988) and higher heads per stage (Tamatsukuri, 1992), larger unsteady flow field fluctuations within the pump and system are encountered. Experimental validation of numerical simulations and other prediction methods involving unsteady flow fields becomes increasingly necessary.

Test Facility and Instrumentation

Under investigation was a single stage pump designed for the paper industry to transport slurry inhomogeneous substances. The impeller of outlet diameter D_2 = 324 mm operated within a double spiral volute to minimize radial forces. The shrouded pump impeller is shown in Fig. 1. Geometric specifications were:

- 7 blades, shrouded impeller,
- D_1/D_2 = 0.83 impeller inlet tip diameter ratio,
- B_2/D_2 = 0.27 blade outlet breadth ratio,
- D_3/D_2 = 1.22 volute tongues inlet diameter ratio,
- 33° blade outlet back lean angle, 20° blade outlet rake,
- 18°–40° blade inlet angle in relative system.

The experiments were performed at a rotational speed of 750 rpm (u_2 = 12.7 m/s), having a best efficiency point (bep) volume flux of 0.196 m^3/s (ϕ = 0.174) and a pump pressure rise of 0.58 bar (ψ = 0.704).

Water at 18°C for the open pump circuit was drawn from an 80 m^3 reservoir into the pump through a flow straightener to provide uniform inlet flow. The impeller Reynolds number at bep was of the order 10^6 based on the impeller diameter and outlet tip velocity. The measurement locations in the test facility were constructed in accordance to international acceptance norms (ISO, 1987). A booster pump well upstream increased the NPSH to avoid cavitation.

The double spiral volute casing was circumferentially fitted with 32 flush mounted pressure taps, 16 on the casing shroud side and 16 on the casing hub side, near the impeller outlet at r/R_2 = 1.05. The resulting measured pressures were steady quantities in the stationary frame and will be presented here in nondimensional form using a dynamic pressure based on the impeller outlet tip velocity to form the steady pressure coefficient,

$$\overline{C}_p = \frac{\overline{P}_i - \overline{P}_1}{0.5\rho u_2^2}$$

Contributed by the Fluids Engineering Division for publication in the JOURNAL OF FLUIDS ENGINEERING. Manuscript received by the Fluids Engineering Division January 9, 1998; revised manuscript received May 17, 1999. Associate Technical Editor: B. Schiavello.

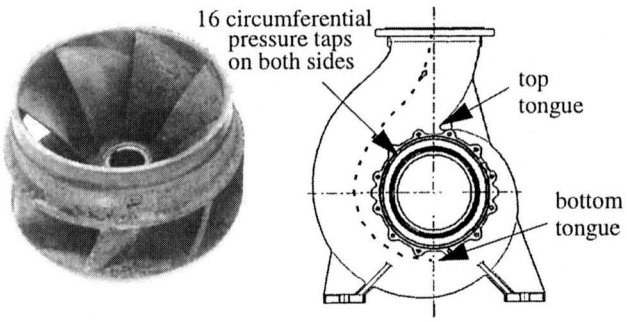

Fig. 1 The pump impeller and double spiral volute

which can be interpreted as a local ψ for the ith pressure tap since an upstream pressure difference is built. In deep part load ($\phi < 0.06$ or 40% bep) this coefficient was affected by the flow prerotation influencing P_1 directly.

On the impeller 25 piezoresistive pressure transducers were mounted within a single blade passage, Fig. 2. Their location was selected to follow the path of two "wall streamlines" on the blade passage pressure side, Pressure Side Hub (PSH) and Pressure Side Shroud (PSS), and two wall streamlines on the blade passage suction side, Suction Side Hub (SSH) and Suction Side Shroud (SSS). Each transducer had a diameter of 4.5 mm with a pressure sensitive zone of 1.3 mm diameter. The eigenfrequency of the transducers was known to be near 100 kHz in air, sufficiently high that the frequencies of interest in water, a maximum of 1 kHz, will not be detrimentally influenced. A static calibration of all transducers was performed to verify manufactures specification. Linearity was within ±0.2% over the full scale of 0 to 5 bar absolute. A dynamic calibration was deemed unnecessary because of the high transducer eigenfrequency and flush mounting of the transducers. The errors in transducer measurements were quantified as ±5% for the steady value, due to the influence of sensor material creep, and ±1% for the unsteady value (Gossweiler, 1993). To reduce the transfer of any mechanical stresses from blade vibration and centrifugal forces the transducers were mounted with an elastic silicon epoxy which received detailed attention before any mounting proceeded (Kaupert, 1997).

A telemetry device was mounted on the pump shaft to send the acquired pressure transducer signals to the stationary system as a high band FM signal, Fig. 3. This permits a wireless connection between the rotating and stationary frame. Since 25 pressure transducers existed each operating point was sampled twice with 16 transducers connected. Repeatability was confirmed with 7 channels measured redundantly. These measurements are unsteady

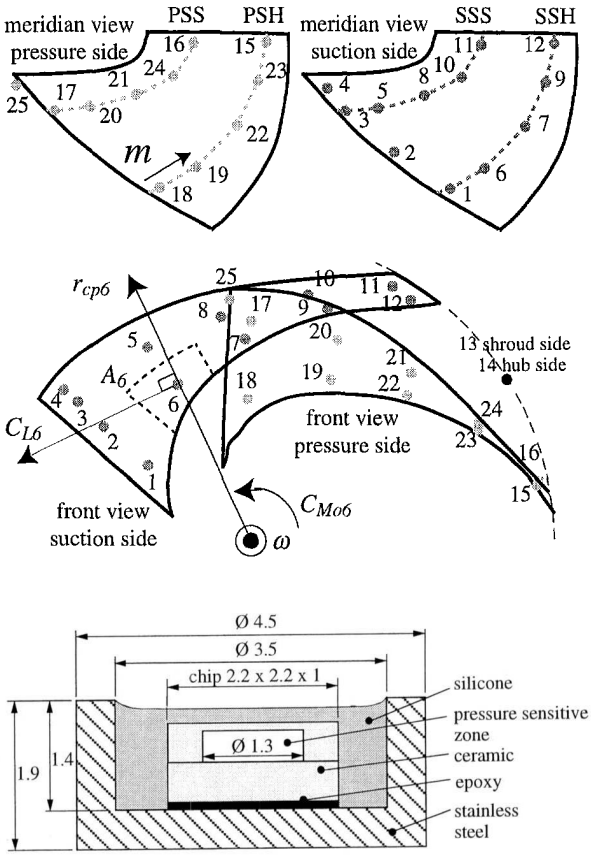

Fig. 2 The location in the meridian and front view of the pressure transducers and the transducer geometry

quantities in the impeller frame and will be presented here in nondimensional form as the unsteady pressure coefficient,

$$\tilde{C}_p = \frac{\tilde{P}_i}{0.5\rho u_2^2},$$

and the combined pressure coefficient,

$$C_p = \frac{\bar{P}_i + \tilde{P}_i}{0.5\rho u_2^2},$$

which make no reference to the upstream inlet pressure.

Nomenclature

A = blade area
C_p = pressure coefficient
L = lift in circumferential direction
m = distance along a wall streamline
Mo = moment about the origin
n = pump shaft harmonic
P_1 = absolute pressure upstream of the pump
P_i = absolute pressure at ith pressure tap
r = radius from impeller origin
r_{cp} = center of pressure with respect to impeller origin
u_2 = impeller outlet tip velocity
δ = transducer meridian plane angle
θ = pump shaft angle
ϑ = transducer front plane angle
ρ = fluid density
σ = statistical standard deviation
ϕ = $c_{m2}/|u_2|$ flow coefficient
φ = phase angle
ψ = $\Delta P_{2-1}/(0.5\rho u_2^2)$
ω = pump shaft angular frequency
ω_S = dimensionless specific speed at bep $\omega Q^{0.5}(gH)^{-0.75}$

Subscripts

i = ith pressure location
1 = upstream pump inlet
2 = impeller outlet

Overscripts

~ = unsteady quantities
¯ = steady quantities

Acronyms

bep = best efficiency point
PSH = Pressure Side Hub distance for transducers
PSS = Pressure Side Shroud distance for transducers
SSH = Suction Side Shroud distance for transducers
SSS = Suction Side Shroud distance for transducers

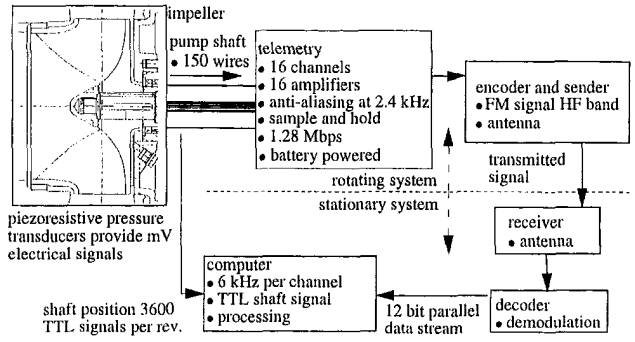

Fig. 3 Telemetry data acquisition from the rotating system

All signal analysis was performed for a sampling set of 2^{17} points per channel sampled at near 6 kHz, slightly more than 270 rotations. The signals were phase averaged using a single shaft position provided by the shaft position encoder. This provided a start point for all analysis to allow phase velocity calculations between transducers.

The pressure discharge characteristic for the pump and the impeller (Kaupert, 1996) is shown in Fig. 4 with an accompanying calculated volute head line based on estimation of the angular momentum in the volute (Lorett and Gopalakrishnan, 1986). This calculation uses the volute throat area, the assumption of free vortex flow in the volute, and the continuity equation to determine c_{u2}. Also shown is a zoom of the characteristic in which a hysteresis loop was found to occur.

Impeller Outlet Flow Distortion

The pump impeller and the double spiral volute exchange fluid to form a matching of the angular momentum exchange, Fig. 4, to determine a best efficiency point ϕ (bep). Any mismatch in this angular momentum exchange causes the flow in the volute to either be accelerated for $\phi > \phi_{bep}$ or decelerated for $\phi < \phi_{bep}$. This simplistic approach can be used to interpret the circumferential pressure distribution measurement of the volute wall pressure taps at $r/R_2 = 1.05$ for four volume fluxes, Fig. 5. At operating points

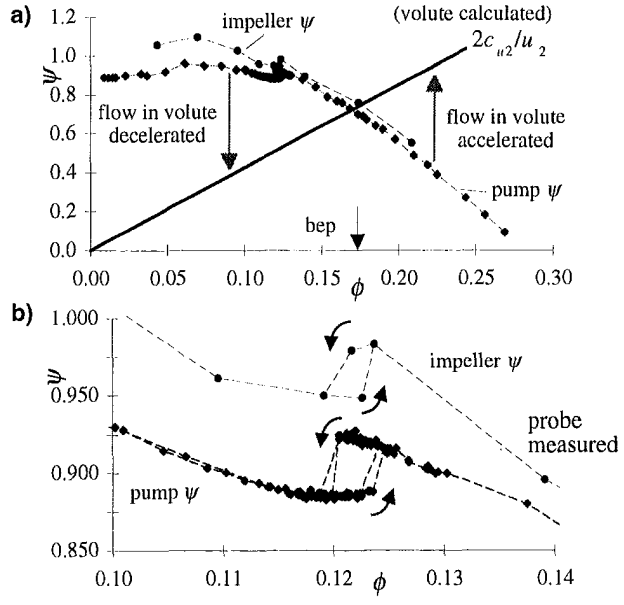

Fig. 4 (*a*) Pump characteristic with a calculated representation of the angular momentum exchange between impeller and volute. (*b*) Zoom of the hysteresis in the characteristic. Uncertainty estimates are ±0.3% for pump measured ψ, ±1.5% for probe measured ψ.

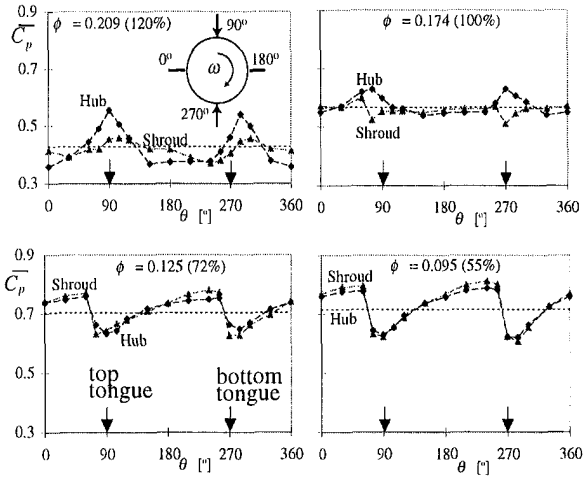

Fig. 5 The circumferential pressure distribution in the volute at four volume fluxes. Uncertainty estimate is ±3% for $\bar{C}_p$.

$\phi < \phi_{bep}$ the value of $\bar{C}_p$ can be seen to rise in the direction of impeller blade rotation with the two volute tongues acting as boundaries to separate the volute flow into two distinct halves. The volute flow was decelerated as the simplistic model predicts. At ϕ_{bep} the variation in $\bar{C}_p$ was smaller while at $\phi > \phi_{bep}$ a reverse tendency to part load was exhibited in the distribution. The volute flow was accelerated as the simplistic model predicts. Figure 5 is in accordance with previously reported experimental results (Adkins and Brennen, 1988, Wesche, 1987) for single spiral volutes. The dotted lines represent the average value for both the hub and shroud side measurements.

Volute Influence on the Impeller Pressure Field

Interpretation of the unsteady pressure field within the impeller must be made keeping the results of Fig. 5 in mind. They represent the average volute pressure a blade passage interacts with as it passes a particular point in the volute. The stationary frame pressure distribution is experienced as an unsteady pressure distribution in the impeller frame. Missing from the measurements of Fig. 5 is the unsteady pressure field in the volute caused by the impeller rotation (i.e., jet-wake flow), this however is mostly steady in the impeller frame.

Figure 6 reveals the phase averaged unsteady pressure for two transducers at 4 operating points over two rotations. The small static pressure head variation per rotation due to the horizontal alignment of the pump was subtracted. A tongue passing frequency is evident at a periodicity of twice per rotation. At bep load the pressure fluctuation in the impeller was small since the volute pressure distribution was uniform. At part load the volute steady

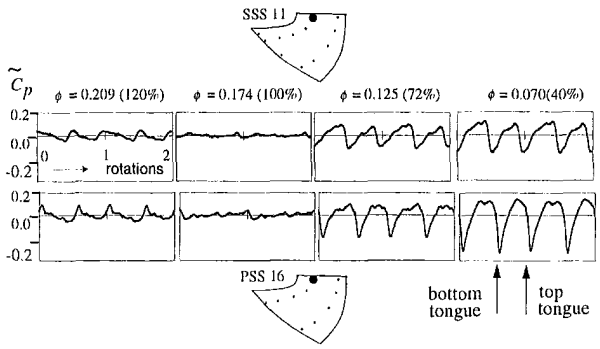

Fig. 6 Phase averaged pressures for two transducers at 4 volume fluxes. Uncertainty estimate is ±0.002 for C_p.

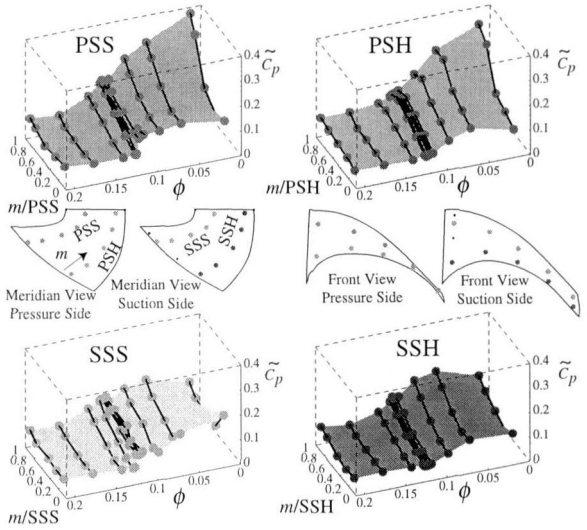

Fig. 7 Pressure signal fluctuation on 4 wall streamlines. Uncertainty estimate is ±0.01 for C_p.

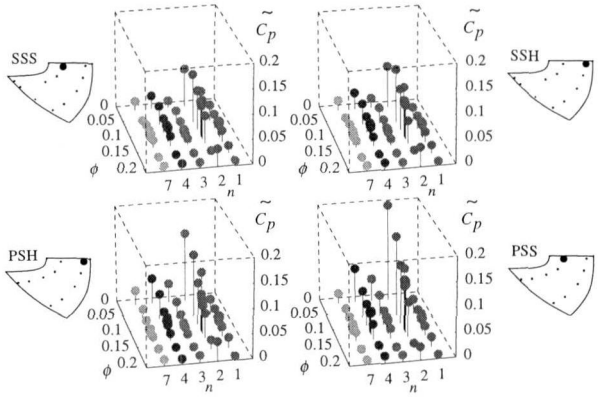

Fig. 8 The magnitude of the pump shaft rotation harmonics for 4 pressure transducer locations. Uncertainty estimate is ±0.015 for C_p.

pressure distribution ($\bar{C}_p$) rises between tongues; this manifests itself in the impeller as a rising pressure fluctuation after the blade passage rotated past a tongue (the arrows show radial alignment between the SSH trailing edge and the tongues). At overload this tendency was reversed as the volute flow had a decreasing pressure between volute tongues, seen in Fig. 5, and thus a decreasing pressure fluctuation in the impeller. The blade passing frequency is not clearly evident but does weakly exist as a result of other blades rotating past the tongue. Of interest is the size of the pressure fluctuation, growing with reduced volume flux in part load to obtain magnitudes of 35% the pump head at 40% bep flow. Other authors (Arndt, 1988) have obtained similar results with even greater fluctuation magnitudes being measured directly at the blade trailing edge.

It has previously been pointed out (Tourret et al., 1989) that pressure fluctuations within a pump impeller grow in magnitude as the volume flux is further removed from the bep and as the trailing edge ($s/L = 1$) of a blade is approached. This was also found in this study as shown in Fig. 7 where the $\bar{C}_p$ is 2 standard deviations of a pressure signal magnitude. At $\phi = 0.174$ (100%) on all four "wall streamlines" the magnitude was a minimum, expected from Fig. 5 where the volute flow circumferential pressure was most uniform. As the volume flux was moved from the best point to the regime where pump impeller characteristic hysteresis was known to occur $\phi = 0.122$ (70%) the fluctuation magnitudes rose. This regime was measured with particularly good resolution in ϕ thus the greater concentration of measuring points and connecting lines. In general it can also be seen that the pressure fluctuation magnitude is greater on the pressure side of the blade channel than on the suction side. On the suction side shroud (SSS) a greater amount of disorder seems to exist which could be caused by a recirculation zone formation in the impeller (Kaupert, 1997).

The circumferentially distorted pressure distribution at the impeller outlet in the stationary frame, influenced the rotating impeller channel in a periodic fashion dominant at the tongue passing frequency. Four pressure transducer locations were selected for supporting this statement, seen in Fig. 8. The harmonic magnitudes from a Fourier analysis are shown where n represents the pump shaft harmonics for various volume fluxes. For the case of a double spiral volute $n = 2$ is the tongue passing harmonic. It can be seen that $n = 2$ was the dominant harmonic at the four pressure transducer positions, a factor of near five greater than the shaft harmonic ($n = 1$) and the blade passing harmonic ($n = 7$). This is typical of all pressure transducer positions in the blade channel excluding a few positions near the impeller inlet where the shaft harmonic ($n = 1$) can reach the same magnitude as the tongue passing harmonic ($n = 2$) but both are then, as seen in Fig. 7, relatively small. This suggests presentation and interpretation of the phase information at the tongue passing harmonic.

The phase information along the 4 wall streamlines are all relative to a single pump shaft position meaning individual phase differences between pressure transducers may directly be interpreted as time lags or leads. Figure 9 reveals the processed phase information from an FFT for the tongue passing harmonic along the four wall streamlines within the impeller blade passage for 13 volume fluxes. The zero phase position occurs when the suction side of the blade passage at the hub trailing edge was radially aligned with the top tongue.

For the two cases $\phi \geq \phi_{bep}$ (100% and 120%) a different tendency is seen than for $\phi < \phi_{bep}$, (80% to 10%) however for the two $\phi \geq \phi_{bep}$ (100% and 120%) cases the pressure fluctuation magnitudes were relatively small, Fig. 7, and thus will not be interpreted. For $\phi < \phi_{bep}$ (80% to 10%) on the blade passage pressure side hub and pressure side shroud (PSH & PSS), the first three pressure transducers in the blade passage have little phase change between them, i.e., slope between them very close to zero.

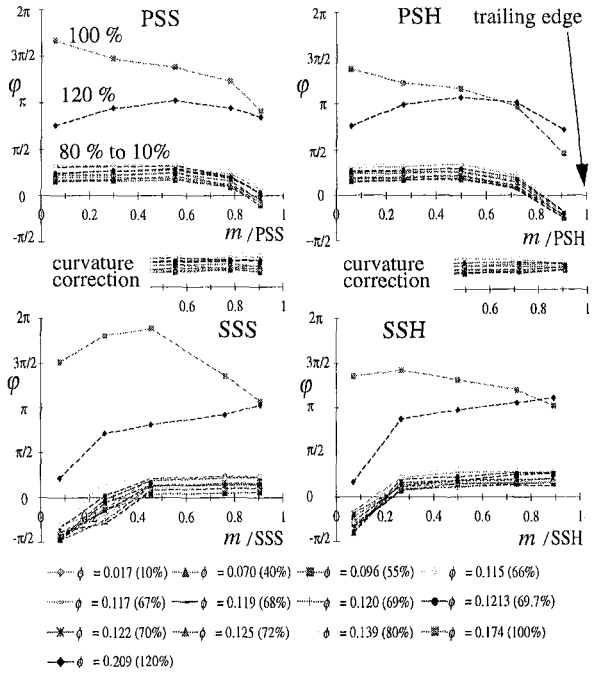

Fig. 9 The phase information for the volute tongue passing ($n = 2$) harmonic along the 4 wall streamlines. Uncertainty estimate is ±0.1 radians for φ.

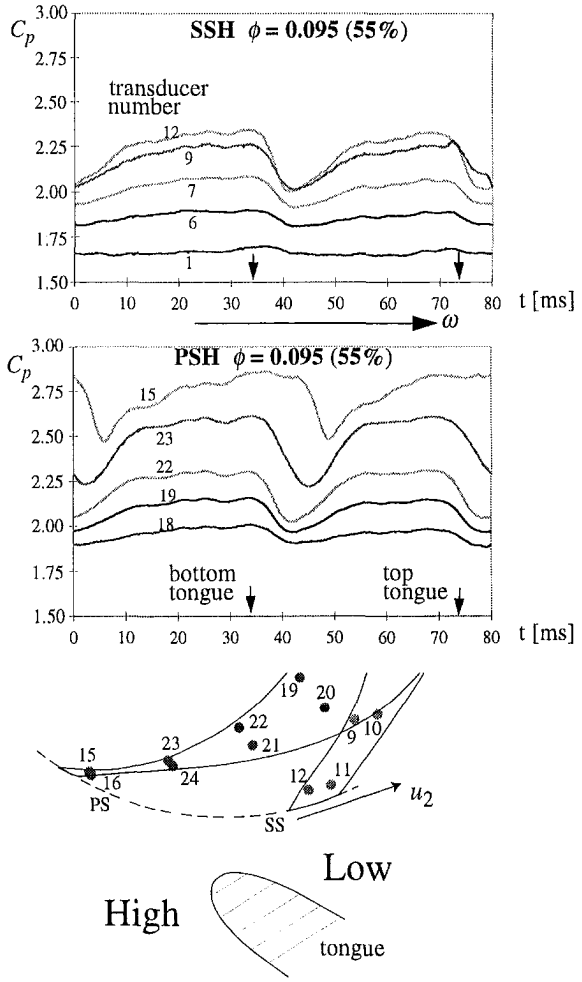

Fig. 10 Two time domain phase averaged signals over one impeller rotation and a sketch of the blade passage as it moves past a volute tongue. Uncertainty estimate is ±0.13 for C_p.

This is an acoustic effect in the blade passage which influences the pressure transducers simultaneously. The acoustic propagation velocity within the test facility was previously measured as 1362 ± 20 m/s in water (note: the water was not deaerated). Both the pump shaft harmonic ($n = 1$) and twice the tongue harmonic ($n = 4$) have also been analyzed and revealed similar, not shown here, phase relations meaning the wave group and phase velocity are both equal to the acoustic velocity. The coherence between transducers was also high (>0.92) indicating little disturbance in the form of noise and nonlinearities (i.e., the system is nondispersive). Near the trailing edge (m/PSH = 1, m/PSS = 1) however, a negative slope occurs in the phase because the trailing edge pressure side transducers arrive at the tongue later due to impeller blade curvature; they experience the change in the pressure field across the tongue at a later time. Along the suction side hub and suction side shroud (SSH and SSS) wall streamlines the phase difference between the pressure transducers in part load was near zero excluding the leading edge. The magnitude of the pressure fluctuation at the leading edge was relatively small and also strongly affected by inlet recirculation with associated prerotation phenomena making interpretation here too abstract. As the entire blade passage suction side rotates through the changing pressure field across the tongue it was immediately exposed to a different pressure field experienced by all the suction side transducers.

To further clarify this explanation Fig. 10 depicts time domain phase averaged pressure signals in part load with a two dimensional sketch of the blade passage and tongue. The arrows at bottom tongue and top tongue represent times when the blade passage suction side hub was aligned with a tongue. Examining the interaction with bottom tongue at:

- t = 30 ms, the suction side of the blade passage approached the bottom tongue, influenced by pressure in region High.
- t = 34 ms, the blade suction side hub passed the bottom tongue, came under the influence of region Low, the entire suction side was immediately influenced by the abrupt change in pressure at the blade passage outlet and reacts with a change in circulation about the blade instantaneously. The blade passage pressure side, however, was now under the influence of the pressure in region High and Low. The first three pressure transducers (18, 19, 22) near the pressure side inlet react to Low while last two transducers (15, 23) near the trailing edge were still, due to blade curvature, in High's influence.
- t = 45 ms, as the blade passage continued to rotate the last two transducers (15, 23) moved past the tongue coming into Low's influence. This blade curvature effect is removed from the phase information of the last 2 pressure side transducers shown in Fig. 9 labelled "curvature correction" to demonstrate the geometrical phase lags.

This simplistic interpretation provides an understanding of the impeller-volute interaction physics represented in the pressure signal phase evaluations and an appreciation for the unsteady flow field during a blade passage—volute tongue interaction.

Synthesis of the Impeller Pressure Field

The circumferentially varying pressure field within the volute caused an unsteady pressure field within the impeller blade passage and was the dominant cause of unsteady blade loading. To quantify this unsteady blade loading coefficients were evaluated where the lifting line of action was taken as the circumferential direction of rotation, Fig. 2. This evaluation involves a summation over the pressure and suction side using Haar function interpolation for each pressure transducer acting over a given surface. Errors were introduced into the evaluation since—

- the surface resolution (i.e., only 25 pressure transducers exist within the blade passage), did not capture any local pressure gradient effects,
- extrapolation was used between transducers and to the wall regions,
- phase averaged pressures were used,
- a single blade passage, not a single blade was investigated. A *shift* of the blade passage suction side data by one blade passage backward was performed to remedy this for single blade loading.

The lift coefficient (C_L) in the circumferential direction, the moment coefficient (C_{Mo}), and the resulting center of pressure (r_{cp}) with respect to the impeller rotational axis, depicted in Fig. 2, were evaluated according to,

$$C_L(\phi, \theta) = \sum_{i=1}^{25} C_p(\phi, \theta) A_i \sin \vartheta_i \cos \delta_i / (\sum_{i=1}^{25} A_i)$$

$$C_{Mo}(\phi, \theta) = \sum_{i=1}^{25} C_p(\phi, \theta) A_i r_i \sin \vartheta_i \cos \delta_i / (R_2 \sum_{i=1}^{25} A_i)$$

$$r_{cp}/R_2 = C_{Mo}(\phi, \theta)/C_L(\phi, \theta)$$

where A_i, ϑ_i, and δ_i are geometrical parameters. The blade outlet radius R_2 was selected as the characteristic length.

The unsteady value $\tilde{C}_L(\phi, \theta)$ is shown nondimensionalised in Fig. 11 using the steady $\overline{C_L}(\phi)$ at a particular ϕ over one impeller rotation. Errors were estimated to be near ±15%. Values in the plot are shown for an impeller angle θ corresponding to the

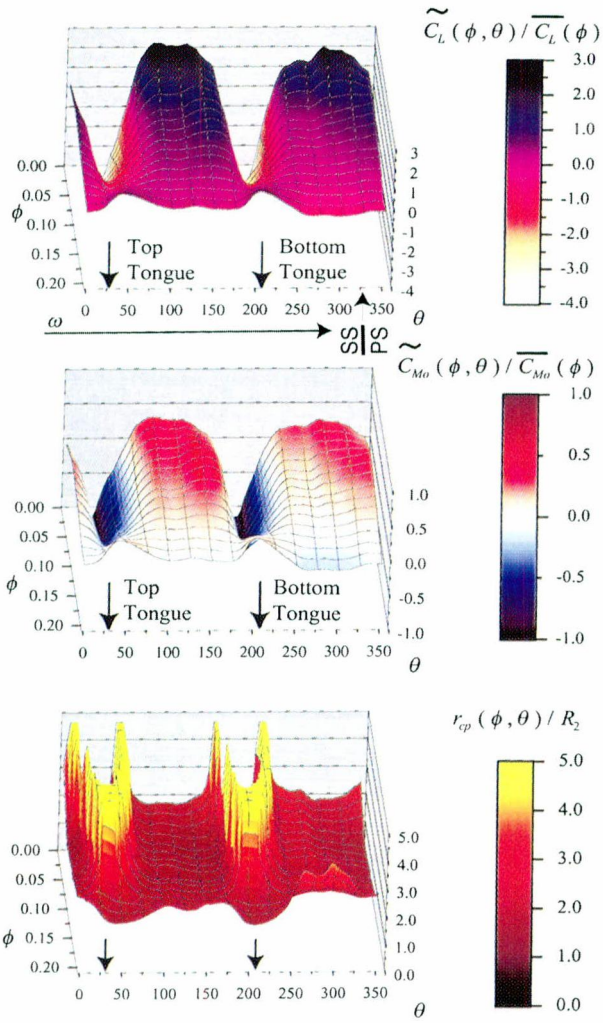

Fig. 11 Unsteady blade loading coefficients for a single impeller blade over one rotation

alignment of the blade suction side at the hub with the volute tongue. At bep $\phi = 0.174$ (100%) the fluctuation in $\tilde{C}_L(\phi, \theta)$ is seen to be small as the volute's circumferential pressure distribution was least distorted, shown in Fig. 5. For lower ϕ the volute's circumferential pressure distribution becomes increasingly distorted as in Fig. 5, having a direct influence on the $\tilde{C}_L(\phi, \theta)$. Between tongues the $\tilde{C}_L(\phi, \theta)$ rose as the pressure in the volute did, reaching a maximum as the suction side of the previous blade was aligned with the volute tongue. Hereafter the blade rotated into the region of influence from the lower pressure region near the tongue, as in Fig. 10, and abruptly experienced the change in impeller outlet pressure fields. Deep in part load (i.e., lower than 45% bep or near $\phi < 0.075$) this phenomenon can be appreciable with $\tilde{C}_L(\phi, \theta)/\overline{C_L}(\phi)$ changing from a value near 2 to -2 in near 20 deg of rotation. For $\phi = 0.209$ (120%) the reverse trend is seen in Fig. 11 to occur, a result of the reverse trend in the volute's circumferential pressure distribution, shown in Fig. 5. The change in $\tilde{C}_L(\phi, \theta)$ across the volute tongue was not as strong as in part load but still appreciable.

The unsteady value of $\tilde{C}_{Mo}(\phi, \theta)$ is also shown in a nondimensionalised form using the steady $\overline{C_{Mo}}(\phi)$. A similar interpretation to that for the $\tilde{C}_L(\phi, \theta)/\overline{C_L}(\phi)$ can be applied with the $\tilde{C}_{Mo}(\phi, \theta)/\overline{C_{Mo}}(\phi)$ for a single blade undergoing a significant change from 0.6 to -0.4 during part load operation at $\phi = 0.075$ (near 45% bep).

Of interest is also the variation of the blade center of pressure $r_{cp}(\phi, \theta)/R_2$. Throughout a greater portion of the plot the value remains relatively constant near a value of 1.7 except during the impeller blade-volute tongue interaction where it becomes comparatively large. These fluctuations can be found in the calculation of $r_{cp}(\phi, \theta)$ to stem from two sources. Firstly the blade pressure side was influenced earlier by the change in pressure across the volute tongue than the blade suction side. Secondly the previously shown phase lag that the trailing edge of the blade pressure side undergoes with respect to the pressure changes, a direct result of the impeller blade passage curvature.

Conclusions

The circumferential pressure variation within the volute of centrifugal pumps resulting from a mismatch of angular momentum exchange is well documented in the literature. This pressure variation is experienced in the rotating system as unsteady, dominated by the tongue passing frequency.

The volute tongue acts as a boundary separating two distinctly different flow regimes providing a pressure gradient responsible for an abrupt flow field fluctuation in the impeller. The magnitude of the flow field unsteadiness grew as the volume flux was further removed from the bep volume flux, particularly below the flow coefficient at which pump characteristic hysteresis occurs. In deep part load the pressure field fluctuations grew to a magnitude of 35% of the pump head. The pressure fluctuation at the impeller outlet propagated upstream through the blade passage at acoustic velocity excluding those locations where blade curvature and rotation provided a phase lag.

The determined unsteady blade loading coefficients provide an indicator of the strong unsteady flow field an impeller blade experiences and reveals the necessity to include these effects in any blade loading considerations.

Acknowledgments

This work was made possible by funding from Sulzer Pumps Ltd. in Winterthur and the Swiss Commission for the Promotion of Applied Research.

References

Staubli, T., Holbein, P., and Kaupert, K. A., 1995, "Verification of Computed Flow Fields in a Pump of High Specific Speed," *International Symposium on Numerical Simulations in Turbomachinery,* ASME-JSME Fluids Engineering Conference, S.C. Aug, No. FED95-NSTM-AH9.

Brennen, C. E., 1994, *Hydrodynamics of Pumps* Concepts ETI and Oxford University Press, pp. 196–204.

Makay, E., 1988, "Power Plant Pump Trouble-Shooting State of the Art Overview," EPRI Report CS-5857, pp. 4.1–4.23.

Tamatsukuri, T., Kikuchi, K., and Satch, J., 1992, "Progress with Ultra High Head Single-Stage Pump-Turbines," Water Power & Dam Construction, Dec., pp. 29–33.

ISO 1987:5198, International Organization for Standardization, *Centrifugal, mixed flow and axial pumps—Code for hydraulic performance test—Precision grade,* Edition 1.

Gossweiler, C., 1993, *Sonden und Messsystem für schnelle aerodynamische Strömungsmessungen mit piezoresistiven Druckgebern,* ETH Zurich Dissertation #10253.

Kaupert, K. A., 1997, *The Unsteady Flow Field in High Specific Speed Radial Pumps,* ETH Zurich Dissertation #12068.

Kaupert, K. A., Holbein, P., and Staubli, T., 1996, "A First Analysis of Flow Field Hysteresis in a Centrifugal Impeller," ASME JOURNAL OF FLUIDS ENGINEERING, Dec. pp. 685–691.

Lorett, J. A., and Gopalakrishnan, S., 1986, "Interaction Between Impeller and Volute of Pumps at Off-Design Conditions," ASME JOURNAL OF FLUIDS ENGINEERING, Vol. 108, pp. 12–18.

Adkins, D. R., and Brennen, C. E., 1988, "Analyses of Hydrodynamic Radial Forces on Centrifugal Pump Impellers," ASME JOURNAL OF FLUIDS ENGINEERING, Vol. 110, pp. 20–28.

Wesche, W., 1987, Messungen am Spiralgehäuse einer Kreiselpumpe, Technische Rundschau Sulzer 2/87, pp. 17–20.

Arndt, N. K. E., 1988, *Experimental Investigation of Rotor-Stator Interaction in Diffuser Pumps,* Dissertation California Institute of Technology, Engineering and Applied Science.

Tourret, J., Kamga, M., Foucher, D., and Kermarec, J., 1989, "Hydraulic Noise Studies from a Centrifugal Pump Through Pressure Pulsations Measurements in the Volute and in the Impeller," Societe Hydrotechnique de France, XX^e Journees de l'Hydraulique, Lyon 4–6 April, Report No. 8.

The Unsteady Pressure Field in a High Specific Speed Centrifugal Pump Impeller—Part II: Transient Hysteresis in the Characteristic

Kevin A. Kaupert
Turbomachinery Laboratory,
ETH Swiss Federal Institute of Technology,
CH-8092 Zurich, Switzerland

Thomas Staubli
Professor;
Now at HTA Luzern, CH-6048 Horw,
Switzerland.

Hysteresis in a pump characteristic results from instability phenomena involving complex three dimensional flow with recirculation. The unsteady flow field on the top and bottom branches of a hysteresis loop in a high specific speed (ω_S = 1.7) centrifugal pump characteristic was experimentally evaluated. A hypothesis for recirculation zones and prerotation as power dissipaters is proposed for explaining the discrepancy in the pressure and shaft power hysteresis. The experimental investigation was performed in both the rotating and stationary frame. In the rotating frame 25 miniature pressure transducers mounted in an impeller blade passage were sampled with a telemetry system. In the stationary frame a fast response probe was implemented. The changing impeller flow field manifested itself between the two branches of the hysteresis with increasing stochastic pressure fluctuations. Using this information the position, size, and strength of the impeller recirculation was quantitatively determined. Theoretically the rate of change of useful hydraulic power in the hysteresis regime during transient pump operation was found to be a function of throttling rate. Quasi-steady behavior existed for slow throttling, $|d\phi/dt| < 0.005\ s^{-1}$. A second-order nonlinear dependence on the throttle rate was determined for the change of useful flow power during the commencement/cessation of the impeller recirculation.

Introduction

The hysteresis in pump characteristics provides an operating regime containing complex flow field changes. Interest in this regime exists because this operational regime often has:

- positive slope characteristics which can lead to system instability (Greitzer, 1981),
- a significant discontinuity in pump efficiency (3% for the pump investigated here),
- increased pressure fluctuations (Stoffel 1991),
- an increased danger of cavitation (Pfleiderer and Petermann, 1990).

The unsteady flow field in the flow regime of the hysteresis is influenced by transient volume flux changes within the pump introducing significant flow field changes. Exact reasons for the abrupt unsteady flow field changes lie in the complex interaction between Coriolis, inertia, viscous, and pressure forces acting on the relative flow. The ω_S = 1.7 pump impeller has a relatively small outlet tip solidity σ_t = 1.4 implying lesser flow guidance, greater secondary flow development, and greater susceptibility to flow recirculation zones often accompanied by characteristic discontinuities. The latter has been previously demonstrated (Hergt and Starke, 1985) with an emphasis on diffuser selection and the dip in the pump characteristic. In striving to obtain increasing efficiencies the volume flux at which these discontinuities occur may move closer to the best efficiency point (bep) (Fraser, 1982). Pump designers and users must evaluate the risks (i.e., dynamic loading, cavitation, flow induced vibrations) involved in the changing unsteady flow field caused by recirculation zones (Makay, 1980) against the cost savings in higher efficiencies. Since recirculation zones are unavoidable over the entire pump operational regime, pump manufactures must design pumps with predictable recirculation zones and a resistance (Stanmore, 1988) to the produced unsteady flow field.

In aerodynamics hysteresis effects in both the steady and unsteady lift coefficients with regard to static and dynamic stall are recognized (McCroskey, 1982) on two-dimensional profiles. This is attributed to flow separation and reattachment occurring at different angles of incidence. Flow separation may also occur within the investigated impeller here also. Hysteresis in the blade lift coefficient would influence blade loading, manifesting itself in the pump characteristics. The three dimensionality, rotation, geometry, and unsteadiness of the pump flow field coupled with transient pump operational load adds to the complexity of the flow making local separation an enlightening interpretation but in an oversimplifying context.

Test Facility and Instrumentation

The single stage pump under investigation was designed to transport slurry inhomogeneous substances. The impeller, depicted in Fig. 1, had an outlet diameter D_2 = 324 mm and operated within a double spiral volute to minimize radial forces.

Experiments were performed at a rotational speed of 750 rpm (u_2 = 12.7 m/s), having a bep volume flux of 0.196 m^3/s (ϕ = 0.174) and a pump head of 5.8 m (ψ = 0.704). The test facility is the same as described in Part I of the article.

Along with standard test rig instrumentation (Kaupert et al., 1996) devices for evaluation of the unsteady flow field were installed. In the stationary system unsteady flow field data were collected using a one hole fast response cylindrical probe. The probe was calibrated in an air free jet facility (Kupferschmied and

Contributed by the Fluids Engineering Division for publication in the JOURNAL OF FLUIDS ENGINEERING. Manuscript received by the Fluids Engineering Division April 9, 1998; revised manuscript received May 17, 1999. Associate Technical Editor: B. Schiavello.

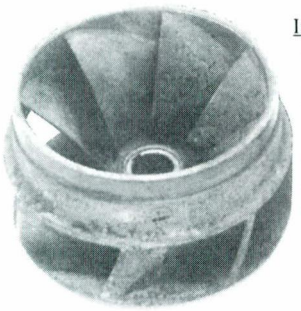

Impeller specifications
- 7 blades, shrouded impeller,
- $D_1/D_2 = 0.83$ inlet tip diameter,
- $B_2/D_2 = 0.27$ blade outle breadth,
- $D_3/D_2 = 1.22$ tongue diameter,
- 33° blade outlet back lean,
- 20° blade outlet rake,
- 18°-44° inlet relative blade angle.

Fig. 1 Test impeller and geometric specifications

Gossweiler, 1992) at the appropriate Reynolds numbers. The probe diameter at the head was 3 mm with a hole of 1 mm being 0.5 mm deep to reach the face of the shaft mounted pressure transducer. The eigenfrequency of the pressure transducer in air was near 100 kHz and was calculated to be near 20 kHz in water which was well above the frequencies of interest, a maximum of 1 kHz. The small cavity in front of the probe pressure transducer revealed no resonance problems near the frequencies of interest.

Flush mounted pressure transducers at the pump inlet and outlet measured the transient pump head during throttling. Their positions were at distances of $2D_2$ upstream and $2D_2$ downstream of the pump. They correspond to the positions of P_1 and P_2, respectively, for the determined pump pressure rise ΔP_{2-1}.

In the rotating system 25 piezoresistive pressure transducers were strategically mounted in an impeller blade passage, Fig. 2. Their location was selected to follow the path of two "wall streamlines" on the blade passage pressure side, Pressure Side Hub (PSH) and Pressure Side Shroud (PSS), and two "wall streamlines" on the blade passage suction side, Suction Side Hub (SSH) and Suction Side Shroud (SSS). Transducers were also placed along the blade suction side leading edge with the anticipation that this region undergoes interesting unsteady flow field changes in the hysteresis loop of the pump characteristic. The transducers were described in Part I of the article.

As in Part I of the article measurement of unsteady quantities in the impeller frame are presented in nondimensionalised form as the unsteady pressure coefficient,

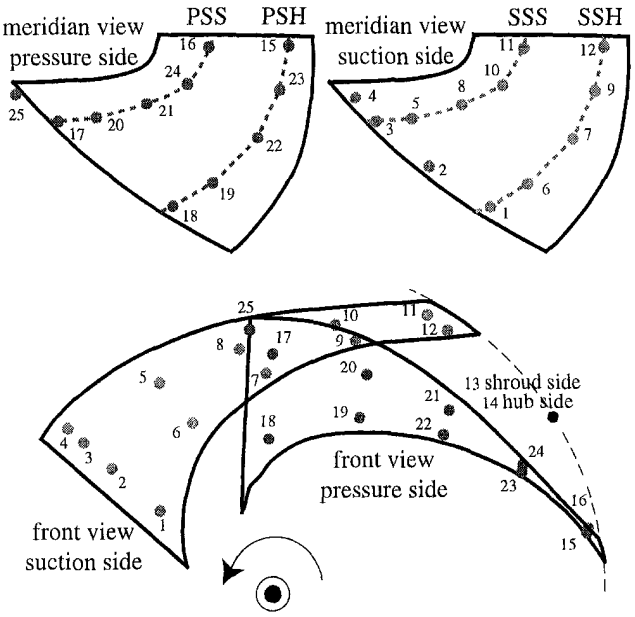

Fig. 2 Pressure transducer positions in impeller passage

$$\widetilde{C}_p = \frac{\widetilde{P}_i}{0.5\rho u_2^2}.$$

Phase averaging of unsteady measured signals is common practice in turbomachinery applications to eliminate the part of the signal often linked to stochastic (i.e., turbulence) effects and to reduce the data size for signal interpretation of the rotational harmonics. However, the remaining signal information after phase averaging not only has the stochastic part of the signal removed but rather everything which is not periodic with the machine rotational speed such as stochastic or transient behavior. This implies a possible loss of valuable signal information in flow instability zones (i.e., recirculation) or any subharmonics (i.e., subsynchronus whirl) the signal may be providing. This is illustrated in Fig. 3 by considering a time domain signal $h(t)$ written as

Nomenclature

A = top branch ϕ operating point without recirculation
B = bottom branch ϕ operating point with recirculation
B_2 = impeller outlet height
C_p = pressure coefficient based on absolute pressure
c_{u1} = impeller inlet tangential velocity, absolute
c_{u2} = impeller outlet tangential velocity, absolute
D_1 = impeller inlet diameter
D_2 = impeller outlet diameter
D_3 = volute tongue inlet diameter
f_o = pump shaft frequency
f_{bp} = blade passing frequency
g = gravitational acceleration
H = pump head
i = index for ith pressure transducers
K_1 = constant throttling rate, $d\phi/dt^*$
K_2 = constant, ϕ_A or ϕ_B at stability limit in hysteresis
K_3 = constant for inhomogeneous equation
L = useful hydraulic power
L_1 = impeller leading edge length
M = pump shaft torque
N = rotations per minute
ΔP_{2-1} = pressure difference across pump
Q = volume flux
S_2 = impeller outlet area ($\pi D_2 B_2$)
s = distance along impeller leading edge ($s = 0$ at hub)
t = time
t^* = time dimensionless, t/T^*
T^* = transition time in hysteresis regime
u_2 = impeller outlet tip velocity
u_1 = impeller inlet tip velocity
η = shaft input efficiency, $(Q\Delta P_{2-1})/(M\omega)$
η_h = hydraulic efficiency
λ = power coefficient, $(M\omega)/(0.5\rho u_2^2 B_2 D_2 u_2)$
ρ = fluid density
σ_t = tip solidity, blade chord/(πD_2/No. blades)
ξ = constant, $K_1/K_2 = (d\phi/dt^*)/\phi$
ϕ = discharge coefficient $(Q/S_2 u_2)$
ϕ_A = discharge coefficient, 0.1213 (69.7% bep)
ϕ_B = discharge coefficient, 0.1225 (70.3% bep)
ψ = pump pressure rise coefficient, $\Delta P_{2-1}/(0.5\rho u_2^2)$
ω = pump shaft angular frequency
ω_s = specific speed dimensionless, $\omega Q^{0.5}/(gH)^{0.75}$

Acronyms

bep = best efficiency point
ISO = international standards organization
PSS = pressure side shroud
PSH = pressure side hub
SSS = suction side shroud
SSH = suction side hub

$$h(t) = \sum_{f_k} A_k e^{i2\pi f_k t} + \sum_{f_j} B_j e^{i2\pi f_j t}$$

information contained: • rotation harmonics • stochastic parts at f_k • instabilities at f_k + • non rotation harmonics • stochastic parts • instabilities

where $f_k = k(N/60)$, $f_j \in \text{Real} | f_j \neq f_k$, $k,j = 1, \ldots \infty$

after phase averaging yields,

$$h_{pa}(t) = \sum_{f_k} A_k e^{i2\pi f_k t}.$$

Fig. 3 The results of phase averaging measured signals

the sum of two Fourier series, The lost signal information *could be* of great value to study unsteady flow fields. In this Part II article signal analysis was performed with no phase averaging on the raw signal data.

Pump Performance

The results of the stationary measured pressure, power, and efficiency coefficient are displayed in Fig. 4 to the right. A zoom of the hysteresis regime in the characteristics is seen to the left. Discontinuities are seen to be found in all three characteristics occurring at the same volume fluxes. Movement from the top to bottom branch of the hysteresis is accompanied by flow field changes consisting of inlet prerotation and impeller inlet and outlet recirculation resulting in flow contraction as the impeller recirculation blocks the larger radius portions of the impeller inlet (Gülich, 1995). For the case of recirculation commencing the impeller experiences a partially blocked inlet flow area at larger radius portions and the resulting through flow experiences a sudden path change resulting in a different energy transfer path.

To provide a physical understanding of the changing flow field in the hysteresis regime the concept of changing power is applied. Along the top branch of the hysteresis for decreasing ϕ at the ψ discontinuity near $\phi = 0.121$ the output power (product $Q\Delta P_{2-1}$, interpreted as the useful hydraulic power transferred to the flow) drops 340W, the λ coefficient (the input power on the pump shaft $M\omega$) drops 250W meaning that after dropping down the discontinuity the flow receives 340W less useful output power for 250W less input power on the pump shaft. Missing are 90W of shaft power not transferred to the useful flow power. Generalizing this case for a $-\lambda_d$ discontinuity in shaft power a $-4/3\ \lambda_d$ discontinuity in the useful flow power occurred. For increasing ϕ a λ_d discontinuity in shaft power results in an $4/3\lambda_d$ increase of transferred useful flow power.

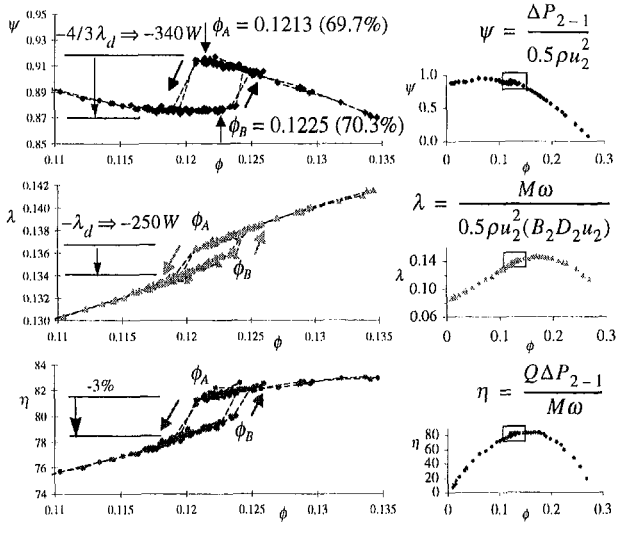

Fig. 4 Steady measured hysteresis in a zoom of the characteristics. Uncertainty estimate is ±0.3% for ψ, λ, η.

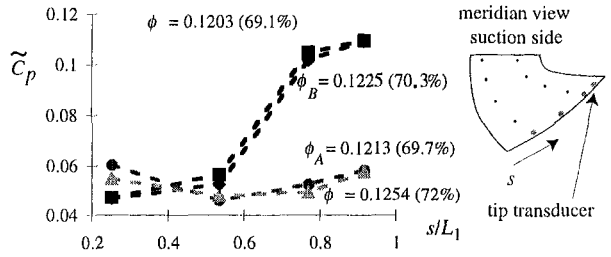

Fig. 5 Unsteady pressure magnitude in the hysteresis loop for the leading edge transducers on the suction side. Uncertainty estimate is ±0.01 for C_p.

To heuristically explain this lost power paradox consider the definition of the shaft efficiency,

$$\eta = \frac{Q\Delta P}{M\omega} = \frac{\eta_h \dot{m}(u_2 c_{u2} - u_1 c_{u1})}{M\omega}$$

where the hydraulic efficiency with the Euler turbomachinery equation has replaced the useful flow output power. Implementation of the Euler equation allows an over simplified though intuitive physical interpretation for the case at hand (i.e., unsteady, three-dimensional, viscous flow). At a characteristic discontinuity η is measured to change and the term $u_2 c_{u2} - u_1 c_{u1}$ changes appropriately with the change in $M\omega$ shaft power. The hydraulic efficiency η_h however also changes. The commencement/cessation of the impeller driven recirculation and prerotation produces a change in the flow field which influences both the input power transferred to the fluid from the impeller and the internal flow losses meaning a change in η_h. In fact the recirculation and prerotation can be considered as power dissipation mechanisms. The fluid rotation of these zones gives rise to viscous stresses and mixing. Once the rotation is established the energy fed into the fluid cells is in equilibrium with dissipation. Thus the discontinuity in the output power $Q\Delta P_{2-1}$ can be larger than the input power $M\omega$ discontinuity through a discontinuity in η_h. An order of magnitude approximation and numerical calculations for power dissipation due to the recirculation and prerotation (Kaupert, 1997) revealed the plausibility of this statement.

The Rotating Frame

Concentrating firstly on the inlet transducers along the blade suction side leading edge the unsteady flow field changes are evaluated for the two branches of the hysteresis. The pressure signal fluctuation magnitude is presented in Fig. 5 (statistically evaluated as two standard deviations of the measured signal magnitude $\tilde{C}_p$) as a function of dimensionless transducer position s/L_1 at 4 values of ϕ in the hysteresis loop. For ϕ values on the top branch of the hysteresis ($\phi \geq \phi_A$) a fairly uniform unsteady pressure magnitude is seen across the leading edge. For ϕ values on the bottom branch ($\phi \leq \phi_B$) the outer two transducers (large s/L_1) were effected by the inlet recirculation with a near doubling of magnitude.

The change in the unsteady inlet flow field is further examined for the tip transducer in Fig. 6 with a Daubechies 8 coefficient wavelet magnitude spectrum (Kaupert, 1996). The ordinate in the time frequency plane is semi log-linear. The top spectrum with no inlet recirculation (ϕ_A) shows a strong pump shaft and second harmonic frequency. The bottom spectrum with inlet recirculation (ϕ_B) shows both the pump shaft and the second harmonic were

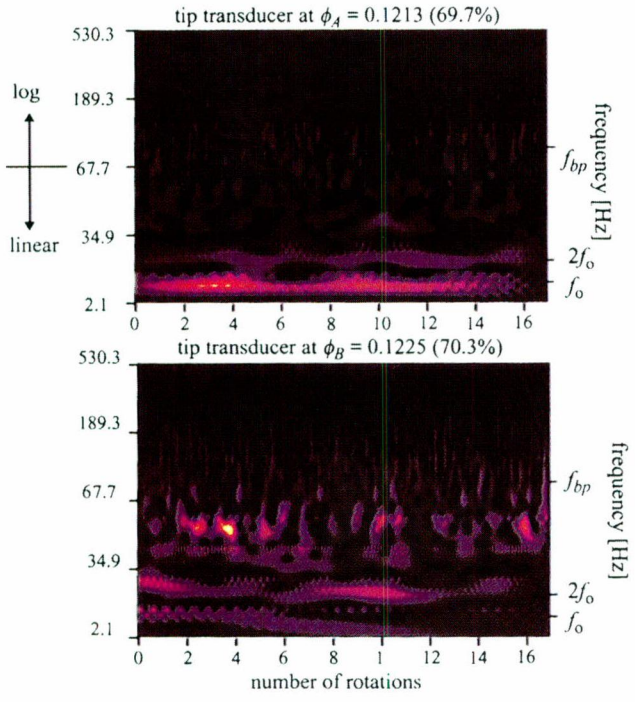

Fig. 6 Unsteady flow field experienced by tip transducer (SS). Uncertainty estimate is ±3 Hz for frequency.

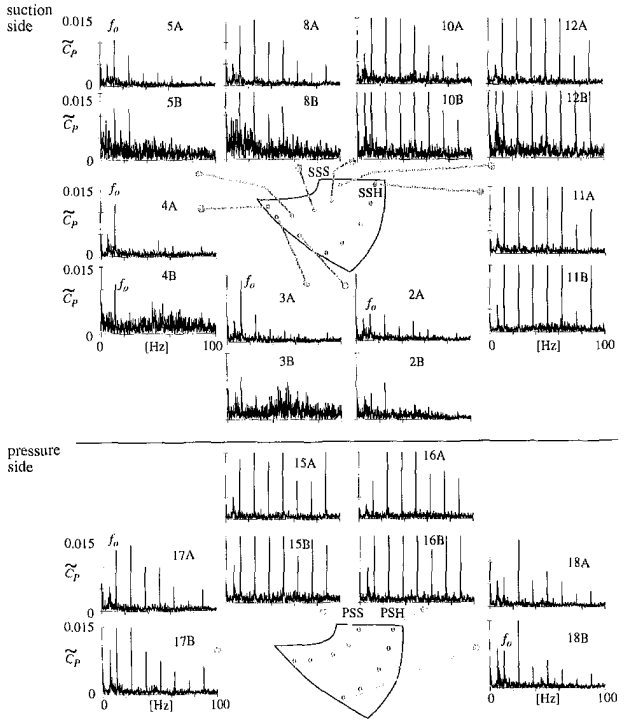

Fig. 7 Fourier magnitude spectra in the rotating impeller without recirculation (*A*), and with recirculation (*B*). Notice the increasing stochastic components on the suction side near the impeller shroud side. Uncertainty estimate is ±0.001 for $\tilde{C}_p$.

present but a frequency band higher (40 to 70 Hz) is seen to exist. This is the frequency band in the vortex arising from modulation of impeller inlet recirculation, influencing the unsteady flow field within the pump.

The coupling of the impeller recirculation behavior with the inlet and outlet influencing each other is examined with the aid of Fourier magnitude spectra shown in Fig. 7. All the Fourier spectra are chopped at a value of 0 to 0.015 to qualitatively compare the stochastic portions of the spectra over a frequency band from 0 to 100 Hz, the f_o = 12.5 Hz being the pump shaft frequency and f_{bp} = 87.5 Hz the blade passing frequency. Table 1 summarizes the observations.

In terms of the frequency spectra and stochastic levels it can thus be stated that the recirculation near the inlet was more intense than near the outlet. It is put forth here that the impeller outlet recirculation was highly transient. In contrast the inlet recirculation was a strong stable flow structure. Perhaps the two recirculations were connected through the impeller but in a highly transient manner (i.e., the two recirculation zones may in fact be one zone of recirculation). This hypothesis has been previously reported with flow visualization tests (Weiß, 1995) on a centrifugal pump of medium specific speed. It implies that the inlet recirculation penetrated downstream to a minimum depth of transducer 8 and fluctuated deeper to transducer 10 and 12. This penetration downstream was enough to register as steady measured impeller outlet recirculation in a previous investigation (Kaupert et al., 1996). Hereto the pressure distribution in the volute of the pump has an upstream influence on the impeller flow which can act on the recirculation zones depth of impeller penetration. In diffuser pumps the selection of a diffuser is known to have a significant influence on the impeller outlet recirculation (Stachnik, 1991, Hergt and Stark, 1985) but lesser on the inlet recirculation.

The Stationary Frame

To qualitatively evaluate the transient behavior of the hysteresis a fast response probe was inserted into the flow near the impeller leading edge tip, Fig. 8 sketch. A link between the transient occurrence of impeller recirculation with prerotation and the ψ discontinuity in the hysteresis loop of the pump characteristic was sought. Figure 8 shows the Haar wavelet transform magnitudes of two unsteady pressure signals acquired by the fast response probe while slowly decreasing (top) and increasing (bottom) ϕ over 40 impeller rotations. The observations for the spectra are summarized in Table 2.

The good ϕ localization provided by a Haar function mother wavelet establishes that $\phi_A \neq \phi_B$. The impeller transient recirculation with prerotation commences at near the location of ψ discontinuity ϕ_A and ceases near the location of ψ discontinuity ϕ_B.

Transient Operation

Typically a pump will not remain at a constant operational point but rather be subjected to transient operation. A connection be-

Table 1 Impeller recirculation observations in rotating frame

operating point	observations in rotating impeller spectra
ϕ_A = 0.1213 (69.7%) • ϕ without inlet recirculation	suction side • shaft frequency f_o and multiples • near leading edge (2A, 3A, 4A, 5A) lower shaft harmonics weak pressure side • shaft frequency and multiples
ϕ_B = 0.1225 (70.3%) • ϕ with inlet recirculation	suction side • increased stochastic level in 3B, 4B, 5B, 8B, 10B, 12B generated by the recirculation zone • 2B shows little change, revealing shroud to hub influence of recirculation • 10B and 12B show decrease in stochastic level compared with 5B, 8B. Deemed the recirculation zones transient area • 11B on hub side shows little change pressure side • 15B, 16B, 17B, 18B no significant change

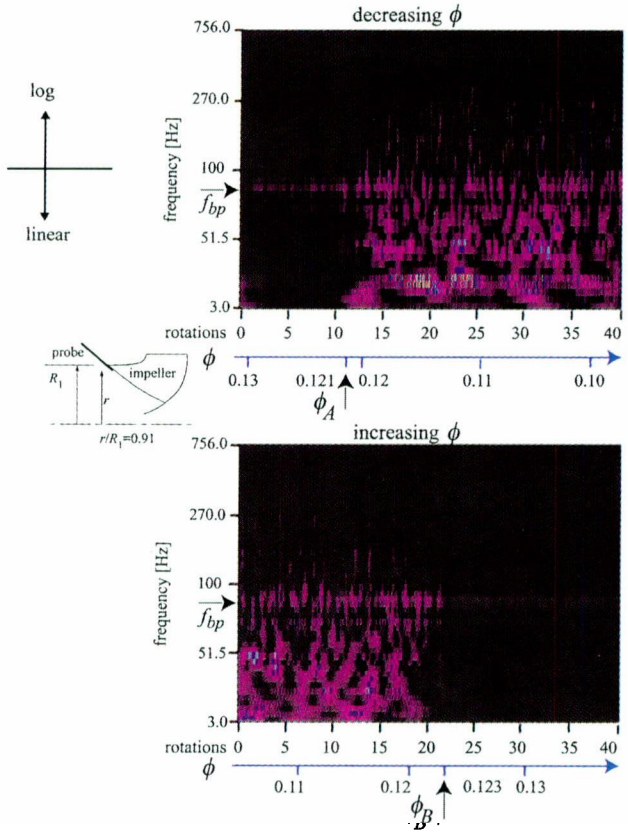

Fig. 8 Determination of the transient inlet recirculation during a slow throttling from unsteady signals. Uncertainty estimate is ±3 Hz for frequency.

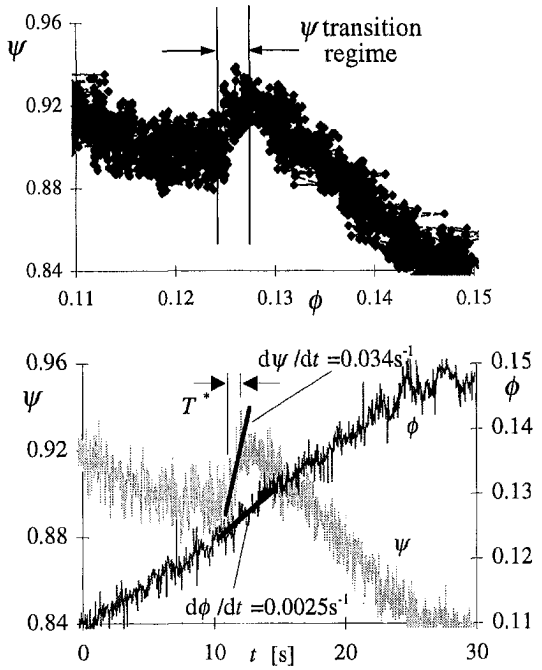

Fig. 9 Transient behavior of ψ at hysteresis discontinuity. Uncertainty estimate is ±0.5% for ψ, ϕ.

tween the transient pump head and the throttling rate in the hysteresis, as recirculation commences/ceases, was sought. For this several tests were performed at various throttling rates.

The quantitative transient behavior of the pump ψ characteristic for increasing ϕ is revealed in Fig. 9, retaining the shape of the steady measured ψ characteristic in Fig. 4 but with points measured along the ψ discontinuity, not possible in the steady case because of the unstable ψ behavior. This is the path ψ takes for increasing ϕ as the impeller recirculation with prerotation ceases. The individual time history of ψ and ϕ is also shown, Fig. 9, within the hysteresis flow regime. The constant T^* is introduced as the hysteresis regime transition time. The sudden transition (jump) in ψ at the stability limit has been quantitatively evaluated with a best fit linear interpolation providing a slope of $d\psi/dt = 0.034\ s^{-1}$ when $d\phi/dt = 0.0025\ s^{-1}$. This evaluation determines the transient behavior of the useful output power transferred to the fluid, proportional to $\phi\psi$, during the cessation of impeller recirculation and prerotation. The behavior is similar, not shown, for the case of decreasing ϕ as flow recirculation with prerotation commences.

The mathematical description of the change in useful hydraulic output power transferred to the flow within the ψ transition regime is,

$$\frac{d(Q\Delta P_{2-1})}{dt} = \frac{dL}{dt}$$

Taking the derivative with the dimensionless coefficients and introducing $t^* = t/T^*$ provides,

$$\frac{S_2\rho}{2}u_2^3\left(\frac{d\phi}{dt^*}\psi + \frac{d\psi}{dt^*}\phi\right) = \frac{dL}{dt^*} \tag{1}$$

at constant rotational speed. This is a quantifying linear differential equation to describe a single aspect of the hysteresis in the ψ transition regime. It appears contradictory since hysteresis is a nonlinear phenomenon in general but for the single quantity, hydraulic output power in the discontinuity it was found to be suitable.

For all the test cases here throttling was performed at a constant rate meaning $d\phi/dt^* = K_1$ within the ψ transition regime, having a linear correlation coefficient greater than 0.97. Note that K_1 is however not the same for each test, rather a constant for a given test. The ϕ at which the ψ transition begins is the stability limit ϕ_A or $\phi_B = K_2$, also a constant so that for a series of tests performed at various K_1 for increasing and decreasing ϕ within the ψ transition regime equation (1) becomes,

$$\frac{d\psi}{dt^*} + \xi\psi = \frac{2}{S_2\rho u_2^3 K_2}\frac{dL}{dt^*} \tag{2}$$

where $\xi = K_1/K_2 = (d\phi/dt^*)/\phi_{A(\text{or}B)}$ and K_2 is taken to be constant over the transition regime (it varies less than 1% depending on increasing or decreasing ϕ). The $t^* = 0$ is defined as the start point of the ψ transition regime. For the case dL/dt constant (assumed here for simplicity to be 340 W/1.5 s from Fig. 4 and Fig. 9) this equation becomes linear and first order,

$$\frac{d\psi}{dt^*} + \xi\psi = K_3$$

where

Table 2 Transient impeller recirculation observations

decreasing ϕ	increasing ϕ
• stability limit at point ϕ_A • above ϕ_A, f_{bp} dominant • below ϕ_A, f_{bp} is smeared, more stochastic signal content • below ϕ_A, transient impeller recirculation and prerotation commence	• stability limit at point ϕ_B • above ϕ_B, f_{bp} dominant • below ϕ_B, f_{bp} is smeared, more stochastic signal content • above ϕ_B, transient impeller recirculation and prerotation cease

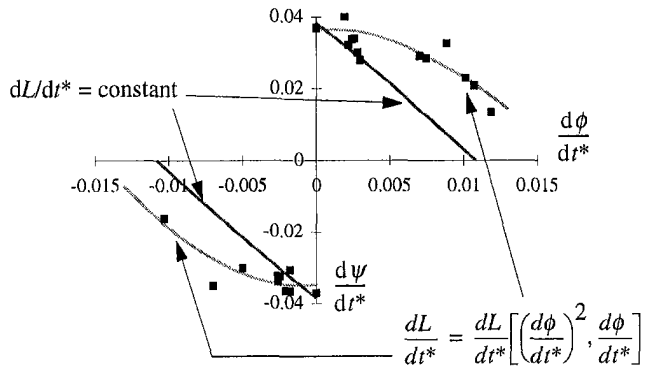

Fig. 10 Results from equation 3 and measurements within the ψ transition regime at $t^* = 1.5$ s. Uncertainty estimate is ±0.001 for $d\phi/dt$, ±0.002 for $d\psi/dt$.

$$K_3 = \frac{2}{S_2 \rho u_2^3 K_2} \frac{dL}{dt^*}$$

and may be integrated to obtain,

$$\psi = (\psi_o - K_3) \exp(-\xi t^*) - \xi^{-1}[T^* \operatorname{sgn}(\xi)\psi_o \exp(-\xi t^*) - K_3]$$

$$\frac{d\psi}{dt^*} = [T^* \operatorname{sgn}(\xi)\psi_o - \xi\psi_o + K_3\xi] \exp(-\xi t^*) \qquad (3)$$

where ψ_o is the steady value of the ψ discontinuity magnitude for an infinitely slow change in ϕ (i.e., $d\phi/dt^* \approx 0$) and sgn (ξ) is the algebraic sign of ξ, positive or negative. For all tests performed $|d\phi/dt^*| \ll \phi_A$ and the ψ transition regime time satisfies the condition $T^* < 2s$ meaning the exponential in Eqs. (3) satisfies $\xi t^* \ll 1$ and further for a given test $d\psi/dt^*$ depends primarily on ξ and only weakly on t^*. This predicts well the nearly constant value for $d\psi/dt$ in the transition regime of Fig. 9.

The results from Eq. (3) revealing the behavior of the pump head during the ψ transition regime are plotted in Fig. 10 for the case $t^* = 1.5$ (as mentioned the model is only weakly dependent on time). The model reveals that as $|d\phi/dt^*|$ increases the $|d\psi/dt^*|$ decreases. The results of various tests are also shown in Fig. 10 as points revealing for small $|d\phi/dt^*| < 0.005$ the model and experiments are in agreement.

The experiments show a greater nonlinearity than found in Eq. (3) which becomes significant for larger $d\phi/dt^*$. Reason for the discrepancy lies in the assumed constant dL/dt^*, which implies that as the impeller recirculation and prerotation commences/ceases the pump useful output power is changing at a constant rate. A parameter variation on the inhomogeneity of Eq. (2) for the case $dL/dt^* = dL/dt^*[(d\phi/dt^*)^2, d\phi/dt^*]$ was performed numerically to quantitatively obtain better agreement and permit physical interpretation. The results are plotted in Fig. 10. The rate of change of useful output power in the hysteresis transient regime during the commencement/cessation of recirculation and prerotation has a nonlinear dependence, due to the exponent 2, on the throttling rate. This characterizes the lost useful hydraulic power due to recirculation and prerotation with a path dependency on $d\phi/dt^*$ (i.e., the throttling rate).

Conclusions

The discontinuities in the pump ψ, λ, η characteristics occur at the same ϕ, resulting in a near 3% change in η, to form a hysteresis loop. The concept of impeller driven recirculation and prerotation as pump power dissipaters was hypothesized to explain the magnitude difference between the characteristic discontinuity in λ and ψ. The inlet recirculation was shown to commence/cease transiently at the exact ϕ values where the ψ discontinuity exists, useful for the interpretation of the transient behavior of ψ.

The recirculation zone at the inlet was a strong phenomenon and its global structure was deemed stable. For the highest ϕ of its existence strong stochastic pressure fluctuations extend through approximately the first half of the impeller passage on the suction side shroud retaining a strong circulating behavior. In the later half of the impeller the recirculation takes on a highly transient form with considerably weaker stochastic pressure fluctuations than at the inlet. Based on the pressure measurements the inlet and outlet recirculation zone are considered one recirculation zone connected transiently through the impeller and are not separable. The outlet recirculation is known to be influenced by the volute configuration and is test configuration dependent.

The behavior of the pump ψ discontinuity in transient operation was experimentally and theoretically evaluated. In particular ψ was found not to undergo a discontinuity but rather had a definite $d\psi/dt$. This was related to the $d\phi/dt$ during increasing and decreasing ϕ tests. The theoretical development bases itself on the change in useful output power the flow receives in the hysteresis flow regime, as the impeller flow recirculation and prerotation was commencing/ceasing.

The faster the throttle is opened the greater the influence on the hysteresis regime of the characteristic. The hysteresis can be viewed as quasi steady for slow changes in ϕ with respect to time (i.e., $|d\phi/dt| < 0.005\ s^{-1}$). For faster changes in ϕ a quasi steady approach to understanding the behavior of the characteristic in the hysteresis regime is no longer suitable.

Acknowledgments

This work was made possible by funding from Sulzer Pumps Ltd. in Winterthur, the Swiss Commission for the Promotion of Applied Research and the precision mechanical work of Mr. H. Suter.

References

Fraser, W. H., 1982, "Recirculation in Centrifugal Pumps," *World Pumps,* pp. 227–235.

Gossweiler, C., 1993, "Sonden und Messsystem für schnelle aerodynamische Strömungsmessungen mit piezoresistiven Druckgebern," ETH Zurich Dissertation Nr. 10253.

Greitzer, E. M., 1980, "The Stability of Pumping Systems—The 1980 Freeman Scholar Lecture," ASME JOURNAL OF FLUIDS ENGINEERING, Vol. 103, pp. 193–242, June.

Gülich, J. F., 1995, "Untersuchung zur sattelförmigen Kennlinien-Instabilität von Kreiselpumpen," Forschung im Ingenieurwesen Bd. 61, Nr 4.

Hergt, P., and Starke, J., 1985, "Flow Patterns Causing Instabilities in the Performance Curves of Centrifugal Pumps with Vaned Diffusers," *Proceedings of the Second International Pump Symposium,* Houston, pp. 67–75.

Hureau, F., Kermarec, J., and Foucher, D., 1993, "Etude de l'Ecoulement Instationnaire dans une Pompe Centrifuge Fonctionnant a Debit Partiel," *Pump Noise and Vibrations,* 1st International Symposium, Clamart France, July.

ISO 1987:5198, International Organization for Standardization, *Centrifugal, mixed flow and axial pumps—Code for hydraulic performance test—Precision grade,* Edition 1.

Kaupert, K. A., Holbein, P., and Staubli, T., 1996, "A First Analysis of the Flow Field in the Hysteresis of a Pump Impeller Characteristic," ASME JOURNAL OF FLUIDS ENGINEERING, Dec., pp. 685–691.

Kaupert, K. A., 1997, *The Unsteady Flow Field in a High Specific Speed Centrifugal Pump,* Dissertation #12068 ETH Zurich, to be published.

Kaupert, K. A., 1996, "Quasi Joint Time Frequency Analysis in Turbomachinery," *Sixth International Conference on Vibrations in Rotating Machinery,* St. Catherine's College, Oxford, England, 9–12 Sept.

Kupferschmied, P., and Gossweiler, C., 1992, "Calibration, Modeling and Data Evaluation Procedures for Pressure Probes," *10th Symposium on Measuring Techniques in Turbomachines,* München.

Makay, E., 1980, "Centrifugal Pump Hydraulic Instability," Electric Power Research Institute Report EPRI CS-1445.

McCroskey, W. J., 1982, "Unsteady Airfoils," *Annual Review of Fluid Mechanics,* Vol. 14, pp. 285–309.

Pfleiderer, C., and Petermann, H., 1991, *Strömungsmaschinen,* Springer-Verlag, Heidelberg, 6th edition.

Stachnik, P., 1991, "Experimentelle Untersuchungen zur Rezirkulation am Ein- und Austritt eines radialen Kreiselpumpenlaufrades in Teillastbetrieb," Dissertation D17, Technische Hochschule Darmstadt.

Stanmore, L. K., 1988, "Field Problems Relating to High-Energy Centrifugal Pumps Operating at Part-Load," IMechE Conference C343/88 Pumps in Part Load.

Stoffel, B., 1989, "Experimentelle Untersuchung zur räumlichen und zeitlichen Struktur der Teillast-Rezirkulationen bei Kreiselpumpen," Forschung im Ingenieurwesen Bd. 55 Nr 5.

Weiß, K., 1995, "Experimentelle Untersuchungen zur Teillastströmung bei Kreiselpumpen," Dissertation D17, Technische Hochschule Darmstadt.

Experimental Measurements of Rotordynamic Forces Caused by Front Shroud Pump Leakage

Robert V. Uy
Graduate Research Assistant.
e-mail:ruy@rand.org

Christopher E. Brennen
Professor.

Division of Engineering and Applied Science,
California Institute of Technology,
Pasadena, CA 91125

Unsteady forces generated by fluid flow through the impeller shroud leakage path of a centrifugal pump were investigated. Different pump shroud geometries were compared, and the effect of leakage path inlet swirl (pump discharge swirl) on the rotordynamic forces was examined for various ratios of fluid throughflow velocity to impeller tip speed. A short axial length leakage path reduced the measured forces, while curvature appeared to increase the destabilizing forces when inlet swirl was present. It was observed that changing the inlet swirl velocity does not appear to significantly affect the measured forces for a given leakage flow coefficient, but any nonzero inlet swirl is destabilizing when compared to cases with no inlet swirl.

Introduction

Previous experimental and analytical results have shown that discharge to suction leakage flows in the annulus surrounding a shrouded centrifugal pump contribute substantially to the fluid induced rotordynamic forces (Bolleter et al., 1987; Adkins and Brennen, 1988). Experiments conducted in the Rotor Force Test Facility (RFTF) at Caltech on an impeller undergoing a predetermined whirl motion have shown that the leakage flow contributions to the normal and tangential forces can be as much as 70% and 30% of the total, respectively (Jery, 1986). Other experiments have examined the consequences of leakage flows and have shown that the rotordynamic forces are functions not only of whirl ratio, but also of the leakage flow rate and the impeller shroud to pump housing clearance. The forces were found to be inversely proportional to the clearance. A region of forward subsynchronous whirl was found for which the average tangential force was destabilizing. This region decreased with increasing flow coefficient (Guinzburg et al., 1994).

Guinzburg et al. (1993) previously examined the difference in rotordynamic forces with and without a prescribed inlet swirl within the leakage path. The tangential force increased in the presence of inlet swirl, and hence the effect of inlet swirl was found to be destabilizing. Later studies by Sivo et al. (1995) examined the effectiveness of anti-swirl brakes in reducing the destabilizing region of forward whirl.

The present research examines differences between the conical leakage path, used by Guinzburg (1992, 1993, 1994) and Sivo (1994, 1995), and leakage paths with more typical geometry. A parametric evaluation of the effect of leakage path inlet swirl on the measured rotordynamic forces is also carried out.

Rotordynamic Forces

Figure 1 shows a schematic of the hydrodynamic forces that act on a rotating impeller whirling in a circular orbit. The unsteady fluid forces acting on the impeller due to the imposed whirl motion (eccentricity ϵ, whirl frequency Ω) are decomposed into a force normal to the direction of whirl motion, F_n, and a force in the direction of forward whirl motion, F_t. The normal and tangential forces are traditionally presented in dimensionless form as functions of the whirl frequency ratio, Ω/ω. More specifically, it is convenient for rotordynamicists to fit F_n to a quadratic function of the whirl frequency ratio, Ω/ω, and to fit the dimensionless tangential force, F_t, to a linear function. These expressions are:

$$F_n = M\left(\frac{\Omega}{\omega}\right)^2 - c\left(\frac{\Omega}{\omega}\right) - K \tag{1}$$

$$F_t = -C\left(\frac{\Omega}{\omega}\right) + k \tag{2}$$

where the dimensionless coefficients are the direct added mass (M), direct damping (C), cross-coupled damping (c), direct stiffness (K), and the cross-coupled stiffness (k). It should be noted that the fluid-induced forces may not always conform to these simple functions of the whirl frequency ratio. However, this assumption is common in the rotordynamics literature. Brennen (1994) and Jery (1986) contain more detailed discussions of the derivation of Eqs. (1) and (2), and the process for experimentally measuring the forces. All five of the force coefficients are directly evaluated from curve fits to the graphs of F_n and F_t against Ω/ω.

In considering rotor stability, a positive normal force F_n will cause the eccentricity to increase and hence be destabilizing. From Eq. (1), a large negative direct stiffness when no whirl motion is present ($\Omega/\omega = 0$) would correspond to such a case. When Ω/ω is positive, a positive tangential force F_t would also be destabilizing as this would drive the forward whirl motion.

A convenient measure of the rotordynamic stability is the ratio of cross-coupled stiffness to the direct damping (i.e., k/C) which is termed the whirl ratio. This defines the range of positive whirl frequency ratios, $0 < \Omega/\omega < k/C$, for which the tangential force is destabilizing.

Figure 2 shows the rotordynamic forces for different flow coefficients as functions of the whirl frequency ratio. A quadratic curve fit for F_n appears appropriate with little loss in accuracy; however a linear fit for F_t would seem to provide an adequate but approximate model of the tangential force.

The magnitude of the forces presented in this study confirm the significance of the shroud forces to the overall rotordynamic forces. For example, Jery (1986) reports stiffnesses for Impeller X/Volute A at design flow of $K = -2.61$ and $k = 1.12$, while using data for $\phi = .009$ in Fig. 2, $K = -.42$ and $k = .62$. Multiplying these by the nondimensionalizing force in both cases, $K = -9.3$ KN/m and $k = 3.99$ KN/m for Jery's tests, while $K = -5.37$ KN/m and $k = 7.92$ KN/m for the current tests. The forces appear to be of similar magnitude, despite significant differences in the geometry and clearance. It is also worth noting that the whirl ratio, k/C, is similar to tests conducted by Jery, but smaller than that reported by Bolleter et al. (1987). Large differences in the

Contributed by the Fluids Engineering Division for publication in the JOURNAL OF FLUIDS ENGINEERING. Manuscript received by the Fluids Engineering Division; revised manuscript received May 15, 1999. Associate Technical Editor: B. Schiavello.

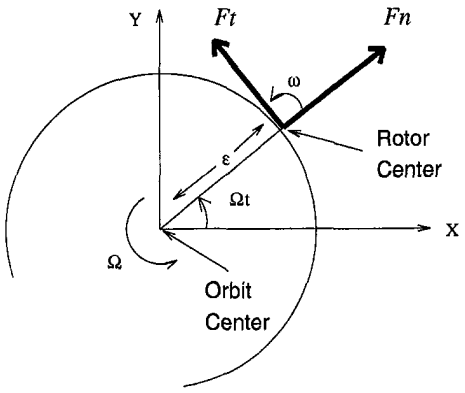

Fig. 1 Schematic of the fluid induced forces acting on an impeller whirling in a circular orbit

leakage path geometry exist between Bolleter and the current tests, most notably in the suction side geometry. The differences in rotordynamic behavior between axial clearance and radial clearance low pressure seals is detailed in Uy et al. (1998).

Test Apparatus

The present experiments were conducted in the Rotor Force Test Facility (RFTF) at Caltech (Jery, 1986). The leakage flow test section of the facility is schematically shown in Figs. 3 and 4. The intention is to isolate the leakage flow forces by using a solid rotor and to generate the flow through the leakage path by an auxiliary pump. The main components of the test section apparatus consist of the solid rotor, a stator (the stationary shroud), the rotating dynamometer (or internal force balance), an eccentric whirl mechanism and a leakage exit seal ring. The working fluid is water. An inlet guide vane is used for the tests with fluid prerotation and appears in Fig. 4.

The rotor is mounted directly to the rotating dynamometer, which in turn is connected to a data acquisition system that permits measurements of the rotordynamic force matrix components (Jery, 1986). The eccentric drive mechanism imposes a circular whirl orbit on the basic main shaft rotation. The radius of the whirl orbit (eccentricity) can be varied but this set of experiments used one eccentricity, $\epsilon = 0.025$ cm. The seal ring at the leakage exit models a wear ring. The clearance between the face seal and the impeller face is adjustable.

The temperature drift of the dynamometer electronics is postulated to be the largest contributor to force measurement errors. The uncertainty in all reported rotordynamic force coefficients is 5% with the exception of the direct stiffness, K, for which the uncertainty is 8%. The uncertainty in the measurement of the flow rate is 1%.

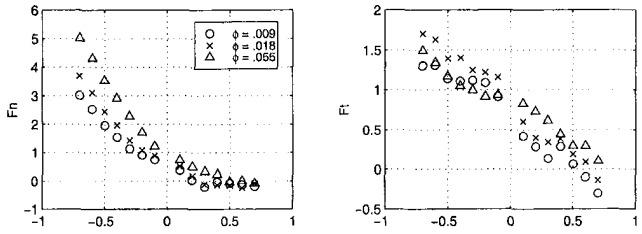

Fig. 2 Experimental rotordynamic forces plotted versus whirl frequency ratio Ω/ω, for indicated flow coefficients

The experimental configurations with the rotor and stator forming the leakage path, are shown in Fig. 3. The conical rotor and shroud with the straight 45 degree leakage path have been extensively tested previously by Guinzburg and Sivo. The contoured rotor was made to match the axial length and eye-to-tip ratio (the ratio of an impeller's inlet diameter to the discharge diameter) of the conic model, but have more typical geometry. The third rotor and stator were made to model the leakage path of the Space Shuttle Main Engine (SSME) High Pressure Oxidizer Turbopump (HPOTP) as closely as possible. It was much shorter in axial length than the previous two impellers and had a much larger eye radius. Both contoured rotors were designed using a third-order polynomial chosen such that the contour was parallel to the centerline at the eye and perpendicular to the centerline at the tip. A matching stator was constructed to maintain a constant clearance, $H = 0.30$ cm, normal to the surfaces of the rotor and stator. The tip radius (corresponding to the discharge radius of a pump) of all of the rotors is the same.

The effect of inlet swirl was investigated by installing guide vanes at the leakage inlet to introduce pre-rotation in the direction of shaft rotation. Figure 4 shows a typical vane consisting of a logarithmic spiral channel with a turning angle of 6 degrees. A series of vanes with angles $\alpha = 1$, 2, and 6 deg were fabricated. The swirl ratio, Γ (the ratio of the leakage flow circumferential velocity to the impeller tip velocity) is varied by changing the inlet leakage flow rate and the turning angle. The swirl ratio depends on the flow coefficient and turning angle according to:

$$\frac{\Gamma}{\phi} = \frac{H}{B \tan \alpha} \tag{3}$$

Nomenclature

B = width of logarithmic spiral channel and swirl vane
C = direct damping coefficient, normalized by $\rho\pi\omega R_2^2 L$
c = cross-coupled damping coefficient, normalized by $\rho\pi\omega R_2^2 L$
F_n = force normal to whirl orbit normalized by $\rho\pi\omega^2 R_2^2 L\epsilon$
F_t = force tangent to whirl orbit normalized by $\rho\pi\omega^2 R_2^2 L\epsilon$
H = normal clearance between impeller shroud and housing
K = direct stiffness coefficient, normalized by $\rho\pi\omega^2 R_2^2 L$
k = cross-coupled stiffness coefficient, normalized by $\rho\pi\omega^2 R_2^2 L$
k/C = whirl ratio, a measure of the destabilizing region of F_t
L = axial length of the leakage path
M = direct added mass coefficient, normalized by $\rho\pi R_2^2 L$
Q = volumetric leakage flow rate
R_2 = radius of rotor and leakage path inlet, in these experiments, 9.366 cm
Re_ω = Reynolds number based on rotational speed, $R_2\omega H/\nu$
Re_{us} = Reynolds number based on fluid through velocity, $u_s H/\nu$
$\mathrm{Re}_{u\theta}$ = Reynolds number based on fluid rotational velocity, $u_\theta H/\nu$
u_s = mean throughflow velocity of fluid at the leakage path inlet, $Q/2\pi R_2 H$
u_θ = mean swirl velocity of fluid at the leakage path inlet
α = angle of logarithmic spiral swirl vane
Γ = leakage inlet swirl ratio, $u_\theta/\omega R_2$
ϵ = eccentricity of whirl orbit
ν = kinematic viscosity
ρ = fluid density
ϕ = leakage flow coefficient, $u_s/\omega R_2$
ω = main shaft radian frequency
Ω = whirl radian frequency
Ω/ω = whirl frequency ratio

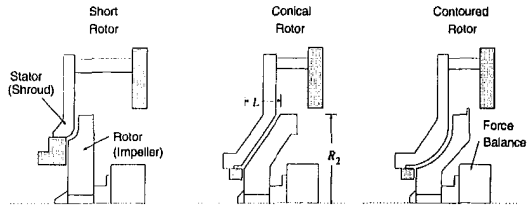

	Short Rotor	Conical Rotor	Contoured Rotor
Path	3rd order	45 degree	3rd order
Eye/tip diameter	.700	.474	.474
Axial length/ tip diameter	.088	.268	.229
L (cm)	1.65	5.02	4.29

Fig. 3 Test matrix of rotor geometries (see Fig. 4 for more detail). Configurations are symmetric about the centerline.

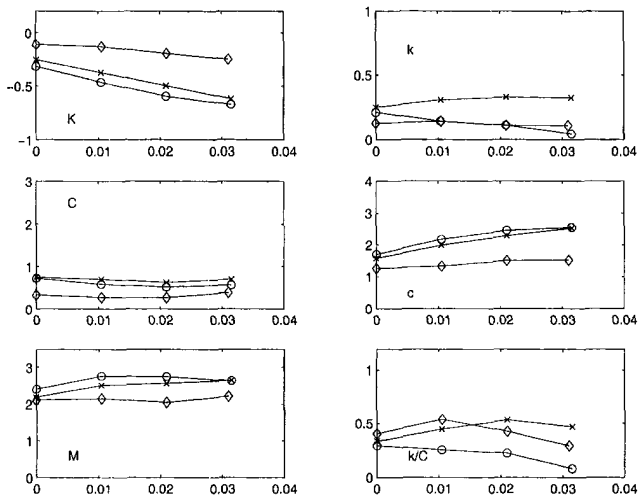

Fig. 5 Experimental rotordynamic coefficients versus flow coefficient, ϕ, for the conical (○), contoured (×), and short (◇) leakage paths ($\Gamma = 0$)

where $B = 0.318$ cm is the width of the logarithmic spiral channel. A derivation of Eq. (3) (which assumes all leakage flow is constrained to follow the vane) is found in Guinzburg et al. (1993). In the present tests it was possible to examine the variation of the forces with α or ϕ while maintaining the same Γ.

Effect of Path Shape

Variations in leakage path geometry were examined using the rotors (dummy impellers) and stators described in the previous section. The conical rotor and stator were tested and compared to the contoured rotor and stator with the same eye diameter, tip diameter, axial length, and leakage path clearance. Results for the short rotor/stator combination are also compared. For these comparisons, a constant main shaft speed, ω, of 1000 rpm was used. A range of leakage flow coefficients from 0 to .033 were studied using flow rates of 0, .19, .37, and .57 l/s; these span the range of leakage flow rates in many industrial applications. The Reynolds numbers for $\phi = .033$ would be $\mathrm{Re}_\omega = 27177$ and $\mathrm{Re}_{u_x} = 896$. A constant leakage path clearance of $H = .30$ cm was also used in comparative tests. The rotordynamic force coefficients were derived from a least squares quadratic and linear fit of the normal and tangential forces, respectively, F_n and F_t, which were measured over the range of whirl frequency ratios, $-0.7 < \Omega/\omega < 0.7$. Figure 5 presents the dimensionless rotordynamic force coefficients as functions of the leakage flow coefficient, and compares the conical and contoured leakage path geometries. In these tests, no guide vane was used and the inlet swirl ratio, Γ, is assumed to be zero.

Except for the cross-coupled stiffness, k, all of the rotordynamic force coefficients are similar (in both trend and magnitude) for the contoured and conical rotors. Thus, the effect of the geometry of the passage is relatively small provided that parameters such as the eye/tip diameter and axial length are the same. The effect of a shorter path length, (which alters the nondimensionalization due to the axial length) with a larger eye/tip diameter ratio, is also clear when all three geometries are compared. The forces for this short rotor are much smaller in magnitude. The coefficients K, c, M, are virtually identical for the conical and contoured geometries, reflecting the fact that the path shape has little effect on the dimensionless normal force, F_n. The normal force coefficients for the short rotor follow the same trends as the other two leakage paths, but are smaller in magnitude across the entire range of flow coefficients.

The contoured rotor has a larger cross-coupled stiffness, k, than the conical rotor over the entire whirl frequency range. The cross-coupled stiffness for the short rotor follows the same trend as the contoured impeller, but with a smaller magnitude. The direct damping, C, seems to be fairly uniform for all three rotors, with the short rotor showing a slightly smaller magnitude. The change in k produces a corresponding change in the whirl ratio, k/C.

Earlier, it was reported by Guinzburg (1992) and Sivo (1995), that, with the conical geometry, the whirl ratio decreased with increasing flow coefficient, and this is confirmed in the present experiments with the conical geometry. However, the contoured geometry produces a k/C which increases with increasing flow coefficient. This trend may reverse at higher flow coefficients (as suggested by the fact that the short rotor exhibits a whirl ratio, k/C, which decreases with ϕ). Indeed, in the tests with inlet swirl described in the next section, the contoured path was subjected to much larger flow rates and the whirl ratio decreased at larger values of ϕ than are shown in this section.

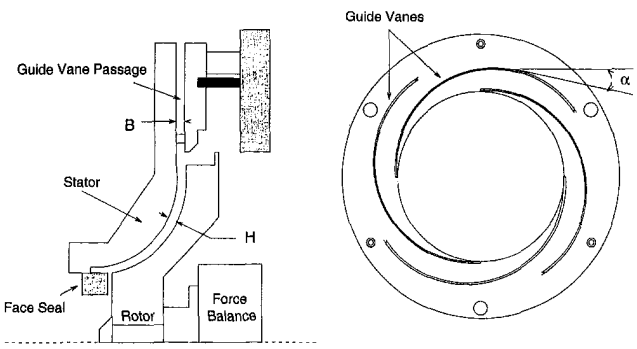

Fig. 4 Inlet guide vane, 6 degree turning angle

Effect of Inlet Swirl

A set of experiments was also carried out to determine the effect of inlet swirl on the unsteady rotordynamic forces in the contoured leakage path. The three swirl vanes of different turning angles were employed to alter the inlet swirl ratio, and a swirl vane with perpendicular channels, ($\alpha = 90$ deg), was used to generate data for zero inlet swirl. In this case, the flow coefficient ranges from $\phi = 0.01$ to 0.066 using flow rates from .17 to 1.15 l/s. The Reynolds numbers for $\phi = .055$ and $\Gamma = .5$ would be $\mathrm{Re}_\omega = 27177$, $\mathrm{Re}_{u_x} = 1494$ and $\mathrm{Re}_{u_\theta} = 13588$. Figure 6 presents plots of the dimensionless rotordynamic force coefficients obtained from the swirl experiments as functions of the leakage flow coefficient. It appears as though the inlet swirl, Γ, has little effect on the forces for any flow rate. However, the effect of swirl is destabilizing compared to the case with no swirl, as K has a larger negative magnitude and k/C is increased. This was previously observed by Guinzburg (1992).

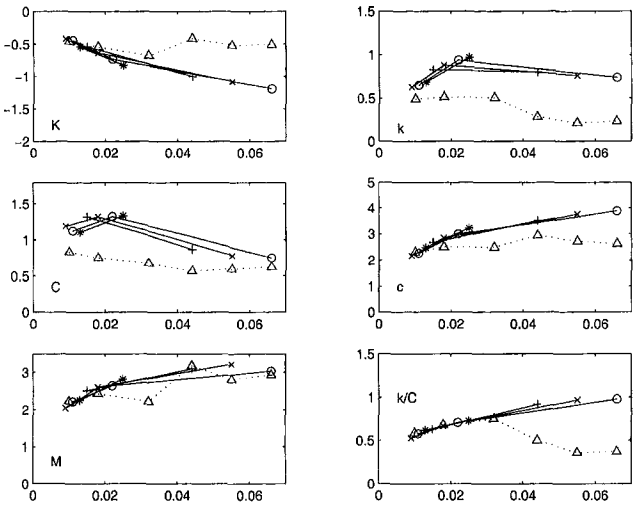

Fig. 6 Experimental rotordynamic coefficients plotted against flow coefficient, ϕ, for tests with inlet swirl, Γ = 0.0 (△), 0.4 (+), 0.5 (×), 0.6 (○), and 0.7 (*), contoured leakage path

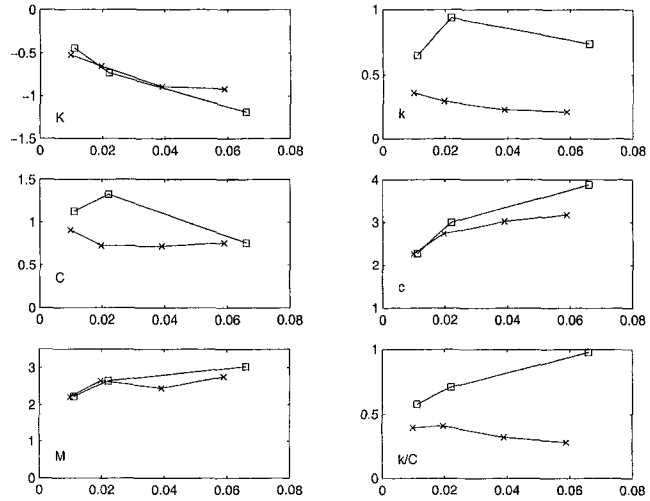

Fig. 7 Experimental rotordynamic coefficients plotted against flow coefficient ϕ for tests with inlet swirl, for the contoured leakage path (□, Γ = .6), and for the conical leakage path (×, Γ variable)

The tangential force coefficients, C and k, are larger when swirl is present than in the absence of inlet swirl. The cross-coupled stiffness with inlet swirl remains at an almost constant level for various values of Γ, while the direct damping shows a tendency to first increase and then decrease slightly with increasing flow coefficient. This leads to a whirl ratio, k/C, that increases with increasing flow coefficient. In the case with no swirl, however, a reduction of the whirl ratio is observed for the contoured dummy impeller at higher flow rates. Some difference in k may be noted between the tests with the 90 deg inlet guidevane and the tests in Fig. 5, where the swirl, Γ, was assumed zero. Clearly the tangential force is highly sensitive to the leakage path inlet conditions, and this discrepancy would indicate that in the cases with no inlet guidevanes present, some pre-rotation of the fluid may be occuring before it enters the leakage path.

Upon examination of the coefficients which determine the normal force, the same trends for M, c, and K observed for the conical rotor by Guinzburg and Sivo are also seen in the present experiments. The added mass does not exhibit an appreciable difference in the cases with and without swirl, but the magnitude of the direct stiffness is higher and the magnitude the cross-coupled damping is smaller with no inlet swirl. In summary, the circumferential fluid velocity induced by inlet swirl affects the rotordynamic behavior significantly if it is nonzero, but the amount of prerotation, Γ, has little influence on the rotordynamics.

The combined effect of inlet swirl and leakage path geometry was also investigated. Figure 7 presents the rotordynamic force coefficients for both the contoured and conical leakage path geometry. The coefficients of the normal force appear to be similar, but there are significant differences in the trend and magnitude of the cross-coupled stiffness and direct damping, leading to substantial differences in the whirl ratio. The contoured rotor exhibits an increasing trend with flow rate, while the conical rotor indicates a decreasing trend.

Discussion and Summary

The experimental data from the current research shows good agreement with previous work in the area of fluid-induced rotordynamic forces in pump leakage paths. The functional dependence of the forces on whirl frequency ratio, Ω/ω, was fairly consistent and allowed quadratic fits to the data and therefore use of conventional rotordynamic force coefficients for meaningful comparisons. Particular attention was paid to the variation in the whirl ratio, k/C, with flow coefficient and with other geometric parameters.

Different leakage path geometries were investigated to evaluate the effects of the front shroud geometry on the forces. A reduced axial length decreases the magnitude of all the rotordynamic force coefficients. As the forces are nondimensionalized by the axial length, this implies that the forces are quite small for the shorter contoured rotor, and that the nondimensionalization with the axial length will not reduce the forces on the rotors with similar profiles to uniform values. The effect of the shroud curvature on rotors of similar axial length was also examined. Only the cross-coupled stiffness for the case with no swirl seems to be affected by the curvature, but both tangential force coefficients, C and k, are affected in the case with inlet swirl. The whirl ratio decreases with increasing throughflow as previously observed for the conical geometry. There are indications that this also occurs with contoured rotors, but at much higher flow rates.

The tests with inlet swirl, Γ, indicate significant fluid effects on the forces. The direct stiffness, direct damping, and cross-coupled stiffness show the greatest change between cases with and without inlet swirl. The magnitude of the fluid pre-rotation, Γ, into the path does not appear to be an important factor on the measured forces. It is postulated that the effect of inlet swirl is largest only at the inlet to the leakage path, and that the viscous effects dominate thereafter. Inlet swirl seems to have very different effects on the tangential force for the conic and contoured geometries, and appears to be more destabilizing with increasing flow rate for the case with curvature.

Concluding Remarks

The effect of front shroud geometry on the rotordynamic forces in shrouded centrifugal pumps has been investigated. Experimental results suggest several options for designers of pumping machinery where fluid-induced rotordynamic forces may be encountered. The short axial length rotor with a larger eye radius experienced rotordynamic forces which were much smaller in magnitude than the longer rotors. Curvature of the leakage path increases the region of forward whirl where the tangential force is destabilizing, and this effect is even more pronounced if inlet swirl is present. The amount of inlet swirl is not a significant factor, but its effect is to increase the magnitude of the rotordynamic forces. Thus, measures to reduce the amount of swirl entering the leakage path may aid stability.

In order to place all of the effects of geometry, inlet swirl, etc., in the context of a coherent prediction methodology, we are currently developing a bulk-flow model which we believe will add to our understanding of the reasons behind many of these fluid mechanical phenomena. The development of this model and the results it yields will be presented in a later companion paper.

Acknowledgments

The authors wish to thank the Advanced Rotating Machinery group of Rocketdyne division of Rockwell Aerospace for financial support and assistance.

References

Adkins, D., and Brennen, C., 1988, "Analysis of Hydrodynamic Radial Forces on Centrifugal Pump Impellers," ASME JOURNAL OF FLUIDS ENGINEERING, Vol. 110, No. 1, pp. 20–28.

Bolleter, U., Wyss, A., Welte, I., and Sturchler, R., 1987, "Measurement of Hydraulic Interaction Matrices of Boiler Feed Pump Impellers," ASME *Journal of Vibrations, Stress, and Reliability in Design,* Vol. 109, pp. 144–151.

Brennen, C., 1994, *Hydrodynamics of Pumps.* Concepts ETI and Oxford University Press.

Guinzburg, A., 1992, "Rotordynamic Forces Generated By Discharge-to-Suction Leakage Flows in Centrifugal Pumps," Ph.D. thesis, California Institute of Technology.

Guinzburg, A., Brennen, C., Acosta, A., and Caughey, T., 1993, "The Effect of Inlet Swirl on the Rotordynamic Shroud Forces in a Centrifugal Pump," ASME *Journal of Engineering for Gas Turbines and Power,* Vol. 115, No. 2, pp. 287–293.

Guinzburg, A., Brennen, C., Acosta, A., and Caughey, T., 1994, "Experimental Results for the Rotordynamic Characteristics of Leakage Flows in Centrifugal Pumps," ASME JOURNAL OF FLUIDS ENGINEERING, Vol. 116, No. 1, pp. 110–115.

Jery, B., 1986, "Experimental Study of Unsteady Hydrodynamic Force Matrices on Whirling Centrifugal Pump Impellers," Ph.D. thesis, California Institute of Technology.

Sivo, J., Acosta, A., Brennen, C., and Caughey, T., 1995, "The Influence of Swirl Brakes on the Rotordynamic Forces Generated by Discharge-to-Suction Leakage Flows in Centrifugal Pumps," ASME JOURNAL OF FLUIDS ENGINEERING, Vol. 117, No. 1, pp. 104–108.

Tsujimoto, Y., Yoshida, Y., Ohashi, H., and Ishizaki, S., 1997, "Fluid Force Moment on a Centrifugal Impeller in Precessing Motion," ASME JOURNAL OF FLUIDS ENGINEERING, Vol. 119, No. 2, pp. 366–371.

Uy, R., Bircumshaw, B., and Brennen, C., 1998, "Rotordynamic Forces from Discharge-to-Suction Leakage Flows in Shrouded Centrifugal Pumps: Effects of Geometry," *JSME International Journal: Fluids and Thermal Engineering,* Vol. 41, No. 1, pp. 208–213.

Chao-Tsung Hsiao
Postdoctoral Scholar,
Currently, Research Scientist,
Dynaflow, Inc.,
7210 Pindell School Rd.,
Fulton, MD 20759

Laura L. Pauley
Associate Professor.
e-mail: LPAULEY@PSU.EDU

Mechanical Engineering Department,
The Pennsylvania State University,
University Park, PA 16802

Numerical Computation of Tip Vortex Flow Generated by a Marine Propeller

The uniform flow past a rotating marine propeller was studied using incompressible Reynolds-averaged Navier-Stokes computations with the Baldwin-Barth turbulence model. Extensive comparison with the experimental data was made to validate the numerical results. The general characteristics of the propeller flow were well predicted. The current numerical method, however, produced an overly diffusive and dissipative tip vortex core. Modification of the Baldwin-Barth model to better predict the Reynolds stress measurements also improved the prediction of the mean velocity field. A modified tip geometry was also tested to show that an appropriate cross section design can delay cavitation inception in the tip vortex without reducing the propeller performance.

1 Introduction

The tip vortex flowfield in the vicinity of the tip region is a very complicated three-dimensional viscous flow phenomenon. The flow in the tip region can significantly affect the performance of lifting surfaces in both aerodynamic and hydrodynamic applications. For example, tip vortex cavitation is of major concern for marine propellers since it is an important source of noise. In order to avoid or control tip vortex cavitation, the underlying flow physics needs to be fully understood.

Using advanced flow visualization and non-intrusive measurement techniques, experimental studies can now reveal the detailed features of the tip vortex flow around a marine propeller configuration. In spite of the success in measurement of many flow features, the pressure field crucial to the prediction of cavitation inception still remained relatively unknown due to the limitations of experimental measurements. Navier-Stokes computations, which can provide a detailed pressure field, have been recently used to predict the tip vortex flow. However, most of the numerical efforts (e.g., Copenhaver et al., 1994; Furukawa et al., 1995; Lee et al., 1996) have studied the tip-clearance flow found in turbomachinery-type geometries while relatively few studies have focused on the open propeller-type tip vortex flow. Unlike the tip-clearance flow, the tip vortex generated by the marine propeller is usually more concentrated and has a tighter structure, which requires a more refined grid within the tip vortex core. For the propeller flow, Stern and Kim (1990) and Kim (1993) presented numerical results for a simplified propeller with infinite-pitch rectangular blades and for a practical propeller model respectively. These works demonstrated how a Navier-Stokes computation can simulate the general features of the propeller flow, but did not provide the detailed features of the tip vortex flow. The numerical calculation of Oh and Kang (1995) is one of the few numerical studies which focus on the propeller-type tip vortex flow. Although Oh and Kang were able to adequately estimate the thrust and torque coefficients in comparison with experimental data, they failed to predict the strength of the tip vortex. It is known that both turbulence model and grid resolution within the tip vortex core have a profound effect on the prediction of the tip vortex. Regardless of the turbulence model used, it is unlikely that they would obtain accurate prediction due to insufficient grid resolution within the tip vortex core since only 0.2 million grid points were used in their numerical calculation.

In the present study, the three-dimensional Navier-Stokes flow solver INS3D-UP developed by Rogers et al. (1991) is used to calculate the flow around a marine propeller configuration. The one-equation turbulence model developed by Baldwin-Barth (1990) is applied to test its accuracy and efficiency on the prediction of the tip vortex flow. In order to validate the numerical predictions, the present numerical method is applied to calculate the David Taylor Propeller 5168 with uniform inflow conditions. Chesnakas and Jessup (1998) carried out extensive experiments for the present geometry using an LDV system in a water tunnel and provided substantial measured data on the flow velocities in the tip vortex. Extensive comparison between calculation results and experimental data is made to demonstrate the capability of the current Navier-Stokes computations to handle propeller flows.

2 Numerical Implementation

2.1 Geometry and Grid Generation. The current study considers a rotating propeller operating in a uniform flow. The propeller model considered is the David Taylor Propeller 5168 which is a five-blade propeller with 15.856 inch diameter. Since the hub and blade root area of the propeller blade are overly complicated, some geometry simplifications are made for the numerical study. The blade flange, root fillets and a root trailing edge cut-out, which produces a gap between the blade and the hub, are ignored. Instead, propeller blades are assumed to be mounted on an infinite constant-radius hub/shaft cylinder. The computational domain is established as one blade-to-blade passage in which there are two side-boundaries (periodic boundaries), one for suction side and one for pressure side, formed by following the inlet flow angle. This grid generation strategy resulted in a spiral-like computational domain. The advantage of this kind of computational domain is that the clustered grid can be easily aligned with the tip vortex and the flow across the periodic boundaries can be minimized. The complete computational domain is constructed by locating the inlet boundary 1.8 propeller radii, R, upstream and locating the outlet boundary two propeller radii downstream of the propeller midplane. The outer boundary in the radial direction is located at two propeller radii while the inner domain is bounded by the hub/shaft surface which is assumed to be a constant-radius cylinder.

To create an appropriate three-dimensional grid inside the computational domain, a combination of algebraic and elliptic grid generation techniques as described in Hsiao and Pauley (1998) is applied. The advantage of this grid generation technique is that one

Contributed by the Fluids Engineering Division for publication in the JOURNAL OF FLUIDS ENGINEERING. Manuscript received by the Fluids Engineering Division July 14, 1998; revised manuscript received June 7, 1999. Associate Technical Editor: P. M. Sockol.

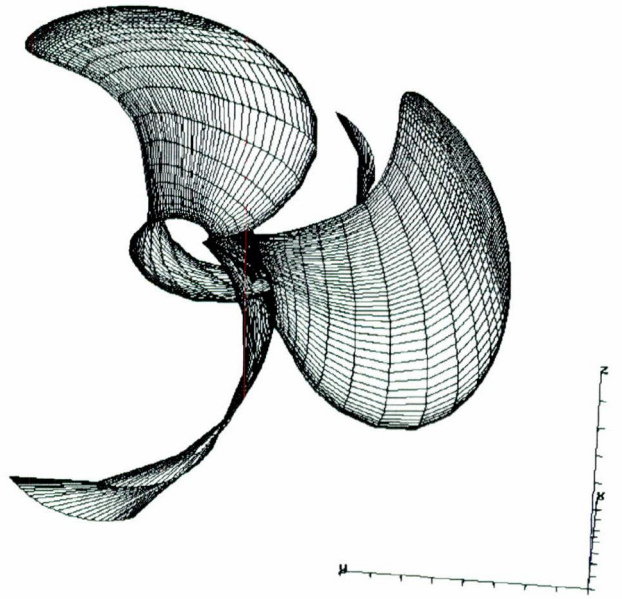

Fig. 1 The blade and hub/shaft surface grid

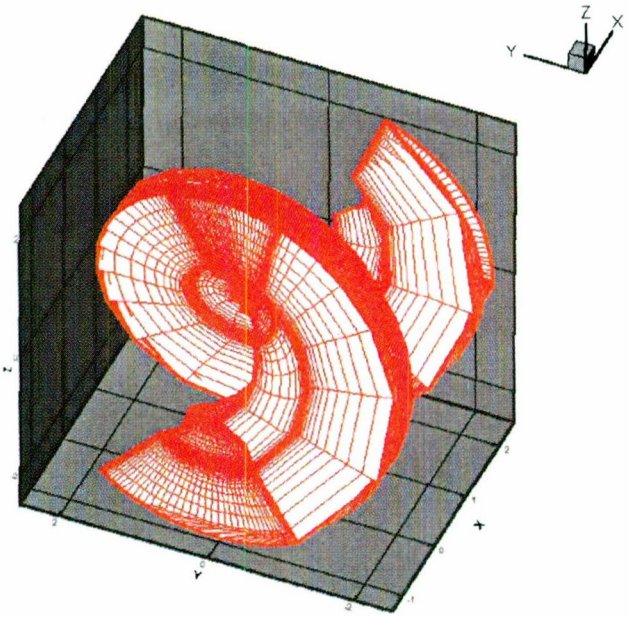

Fig. 2 The complete 3-D view of the computational grid

can easily distribute the initial grid according to the flow field with an algebraic method and then smooth the grid by applying the elliptic smoothing routine. An H-H-type single-block structure grid is generated for the current computational domain. The grid generation procedure starts with generating the surface grid on the blade and hub/shaft surfaces as shown with every other grid line in Fig. 1. A two-dimensional grid is created on each constant-radius plane based on the surface grid. Each two-dimensional grid is generated using only the algebraic method or a combination of algebraic and elliptic methods. The three-dimensional initial grid is established by stacking all two-dimensional grids. Finally, the elliptic smoothing routine is applied to smooth the initial grid. An H-H type grid with a total of 2.4 million points is created for the current computational domain. In this grid, 101 of the 211 streamwise grid points and 81 of 111 radial grid points are used on the propeller blade surface while 101 grid points are used in the blade-to-blade direction. The first grid spacing is specified as 1×10^{-5} and 1×10^{-4} chord length on the blade surface and on the hub/shaft surface respectively. This results in the first grid point at $y^+ < 2$ on all surfaces. As suggested in previous numerical studies of tip vortex flow around a finite-span hydrofoil (Dacles-Mariani et al., 1995 and Hsiao and Pauley, 1998), a grid spacing of at least 15 points across the vortex core is used to obtain a reliable near-field tip vortex flow. Since the present study used the same code and differencing accuracy as Hsiao and Pauley (1998), their observations were used in establishing an appropriate grid for the present study. The overall features of the computational grid and surface grid are shown using every other grid line in Fig. 2.

2.2 Numerical Method. The present computations are conducted on a rotating frame which is fixed on the propeller blade. The steady-rotating reference frame source terms, i.e., the centrifugal and Coriolis force terms, therefore, are added to the Reynolds-Averaged Navier-Stokes equations derived in the inertial frame. The three-dimensional incompressible Navier-Stokes flow solver INS3D-UP, developed by Rogers et al. (1991), is applied to calculate the rotating propeller flow. The INS3D flow solver is based on Chorin's artificial-compressibility approach (1967). In the artificial-compressibility method, a time derivative of pressure is added to the continuity equation to couple it with the momentum equations. As a consequence, a hyperbolic system of equations is formed and can be solved using a time-marching scheme. This method can be marched in pseudo time to reach a steady-state solution. In this code, the first-order Euler implicit difference formula is applied to the pseudo-time derivatives. The spatial differencing of the convective terms uses a fifth-order accurate flux-difference splitting based on Roe's method (1981). A second-order central differencing is used for the viscous terms. The resulting system of algebraic equations is solved by a Gauss-Seidel line-relaxation fully implicit method in which several line-relaxation sweeps through the computational domain are performed before the solution is updated at the new pseudo-time step. In the present study, a steady-state solution is acquired when the maximum residual reduces four orders of magnitude. C_D and C_L both showed four digits accuracy when the maximum residual was reduced four orders.

The INS3D-UP code is accompanied by the Baldwin-Barth one-equation turbulence model (Baldwin and Barth 1990) which is derived from a simplified form of the standard k–ϵ equations. This model is not only simpler than the two-equation model, but also eliminates the need to define the turbulent mixing length which is required in Baldwin-Lomax algebraic model.

2.3 Boundary Conditions. All the boundary conditions are treated in an implicit manner except the outlet boundary. The boundary conditions on each of the boundaries are as follows: free stream conditions are specified for all variables at the inlet and outer radial boundaries; the no-slip condition is applied on the blade and the hub/shaft surfaces; a periodic boundary condition is specified on the side-boundaries. For the outlet boundary, a mass and momentum weighted extrapolation method as suggested by Chang et al. (1985) is adopted. The velocities and pressure obtained by this method will maintain the proper shape of the streamlines and at the same time conserve the mass and momentum fluxes.

3 Results

In the present study the numerical computations were conducted at three different advance coefficients, $J = U_\infty/nD = 0.98, 1.10, 1.27$, where U_∞ is the axial velocity, n is the propeller rotating rate, D is the propeller diameter. $J = 1.27$ is the design condition. These three advance coefficients correspond to three different Reynolds numbers, Re $= 3.40, 4.19, 3.88 \times 10^6$, which are based on the propeller blade chord length at $0.7R$ section and the vector sum velocity of the inflow velocity and the rotational component. The numerical results are extensively compared with the experi-

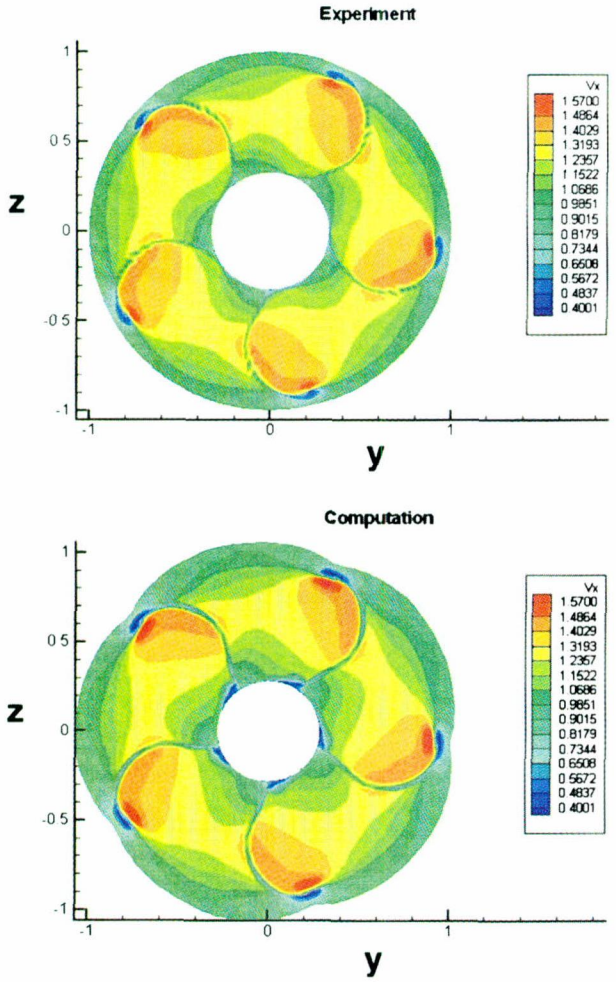

Fig. 3(*a*) Axial velocity V_x from experiment and computation at x/R = 0.2386

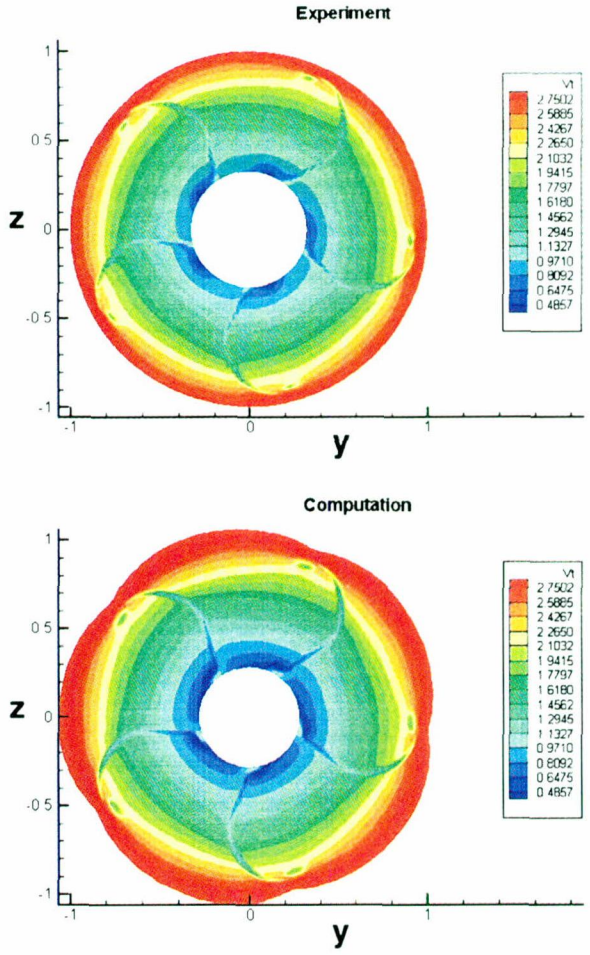

Fig. 3(*b*) Tangential velocity V_t from experiment and computation at x/R = 0.2386

mental data measured by Chesnakas and Jessup (1998) to validate the current numerical method. For the experimental results shown, a fiber-optic LDV system with the probes mounted rigidly together was used to give coincident measurements. The calculated uncertainty within the vortex core was less than 3% of U_∞ for all measured and computed components of the mean velocity. Uncertainties in the Reynolds shear stress terms were estimated to be 0.3% of U_∞^2. The present numerical study also considers a modified tip geometry to investigate its effect on the tip vortex structure.

3.1 Validation. Before comparing the current result with experimental data, some limited domain and grid-independence studies were conducted for the case $J = 1.10$. The domain-independence study was conducted by increasing the inlet and outlet boundaries to 2.3 and 2.5 radii, respectively. In order to maintain the original grid density and minimize grid cell skewing, 10 extra points were added in the streamwise direction with constant grid spacing equal to the original first grid spacing for the 2.3 radii inlet boundary case. A similar grid modification was made for the 2.5 radii outlet boundary case. Our comparison has shown that the results obtained from 2.3 radii inlet boundary and 2.5 radii outlet boundary cases were almost the same as the original domain.

Based on the computation of 2.4 million grid points, the current study also conducted a computation with 2.8 million grid points in which 10 more grid points were added inside the vortex core in both spanwise and blade-to-blade directions. This resulted in at least 26 × 30 grid points within the vortex core while the original grid had at least 16 × 20 grid points. Comparison showed only a slight difference (less than 0.5%) in the velocity field.

Comparison of three velocity components (axial velocity, V_x, tangential velocity, V_t, and radial velocity, V_r) between the present numerical solution and the experimental data for the $J = 1.10$ at the downstream location $x/R = 0.2386$ is shown in Figs. 3(a–c). The axial direction, x, is measured from the propeller midspan at the hub. In Figs. 3(a–c), the experimental data did not include the flow information near the hub/shaft surface and therefore shows a larger white inner circle. From the comparison, it is seen that the current numerical result shows a very good agreement with the experimental data in the tip vortex flow, wake, and blade-to-blade flow. For a better description of the tip vortex structure, a new primary/secondary coordinate system is defined in Fig. 4. In this coordinate system, the primary velocity, V_s, is defined as being in the axial-tangential x-t plane at the propeller pitch angle, ϕ. The secondary velocities (tangential velocity, V_c, and radial velocity, V_r) are the velocity components on the secondary-flow plane which is normal to the primary velocity, V_s. Since the propeller pitch angle varies in the radial direction, the primary and tangential velocities are actually calculated at each radial location by

$$V_s = V_x \sin \phi(r) + V_t \cos \phi(r)$$

$$V_c = -V_x \cos \phi(r) + V_t \sin \phi(r) \quad (1)$$

In this coordinate, the tip vortex axis is virtually normal to the secondary-flow plane and the tip vortex structure such as the size of the vortex core can be better defined. Figure 5 shows a com-

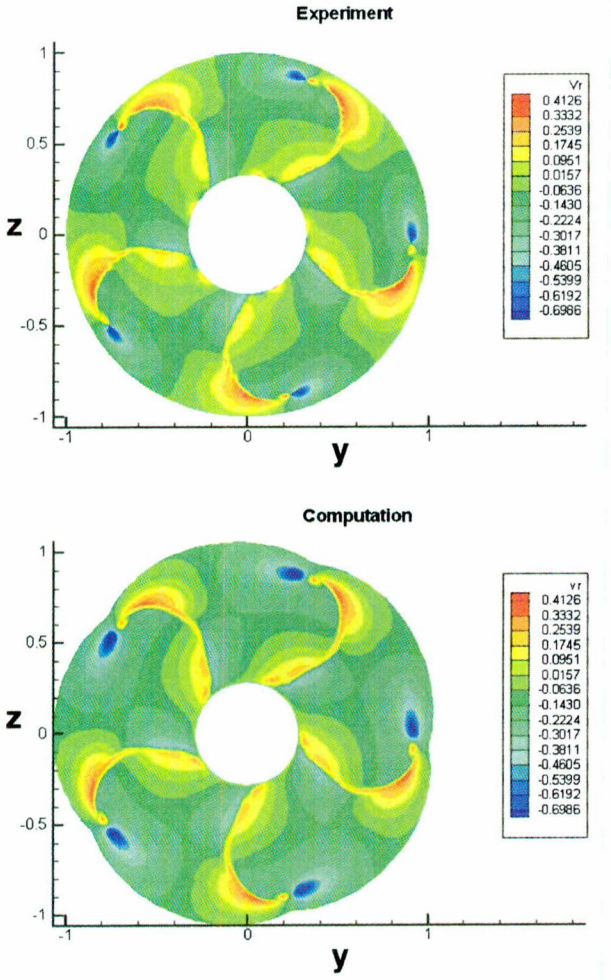

Fig. 3(c) Radial velocity V_r from experiment and computation at x/R = 0.2386

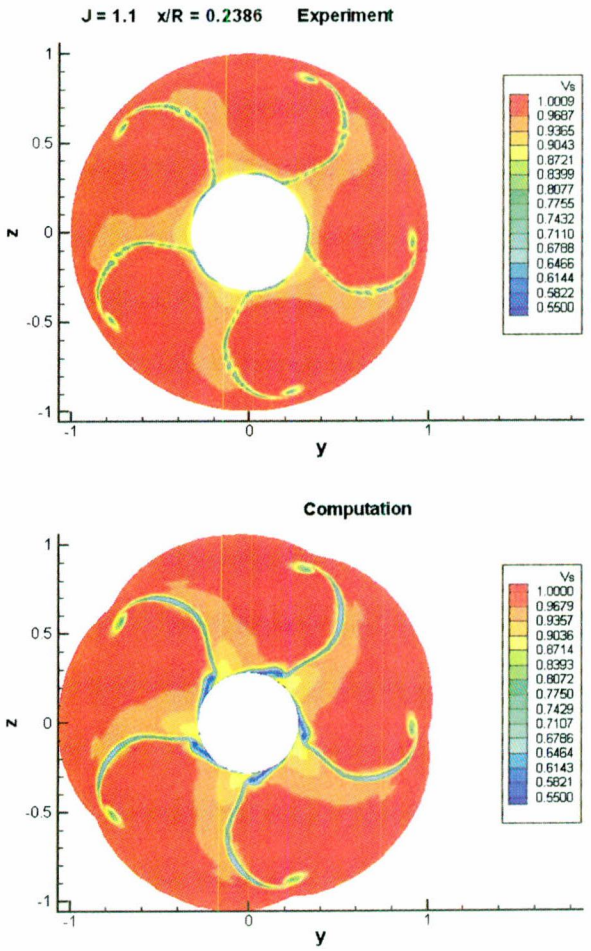

Fig. 5 Primary velocity V_s from experiment and computation at x/R = 0.2386

parison of the primary velocity between the numerical result and experimental data at $x/R = 0.2386$.

The most interesting area of the flow field is the tip vortex. To validate the current prediction of the tip vortex, the close-up view of the tip vortex is compared and shown in Figs. 6 at $x/R = 0.2386$. It is seen that the current numerical result under-predicts the tip vortex strength with about 10% difference in the minimum V_s. For better quantitative comparison between the numerical and experimental results, the line plots of velocities, V_x, V_t, V_r, across the tip vortex center in the tangential direction are shown in Figs. 7 and 8 at $x/R = 0.1756$ ($r/R = 0.934$) and 0.2386 ($r/R = 0.918$). It is noted that the position of the vortex center is specified as $\theta = 0$ in these plots. The vortex center is defined at the location where the minimum V_s occurs within the tip vortex and the experimental data is obtained by averaging the velocities from all five tip vortices. In Figs. 7 and 8, from left to right the first valley of V_x and V_t corresponds to the wake while the second valley is associated with the tip vortex. It is seen that the tip vortex is better predicted at the location closer to the propeller while the wake is better predicted at the farther location. This may indicate that the eddy viscosity calculated from the turbulence model is too large within the tip vortex and leads to an overly diffusive and dissipative tip vortex. Since the current grid has at least 16 × 20 points within the tip vortex core, which has shown to be adequate for resolving the tip vortex flow in the current limited grid-independence study, the discrepancy between the numerical and experimental results is likely caused by the one-equation turbulence model used in the current study. Further discussion on the turbulence modeling will be given in next section.

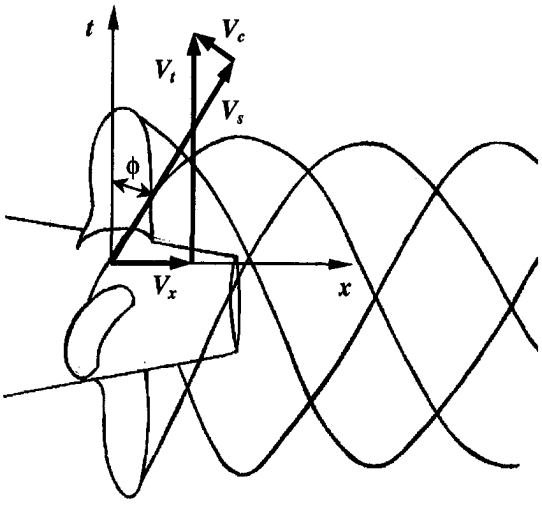

Fig. 4 The primary/secondary coordinate system

The numerical pressure distribution along the tip vortex core is of interest in the study of cavitation inception since the experimental study is unable to directly provide this information with a non-intrusive measurement. To show the pressure distribution along the tip vortex core, we define the vortex core as the location where the local minimum pressure coefficient occurs at the local

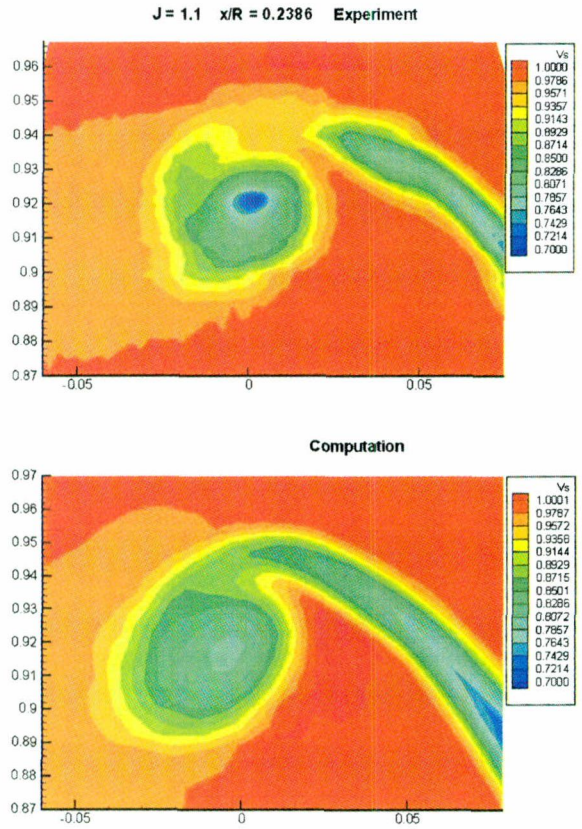

Fig. 6 Close-up view of V_s in the tip vortex from experiment and computation at $x/R = 0.2386$

cross plane normal to the axial direction. The pressure coefficient along the tip vortex core, as shown in Fig. 9, indicates that the location of the minimum pressure coefficient, C_{pmin}, is very close to the tip trailing edge. This also implies that the tip vortex cavitation inception will also occur near the tip trailing edge. It is seen that the negative minimum pressure coefficient increases as the advance coefficient is decreased, i.e. the propeller loading is increased. Although real flow effects such as random turbulent fluctuation, water quality, etc. are known to influence cavitation inception, it is expected that the $-C_{pmin}$ and cavitation inception number, σ_i, should be comparable. Table 1 shows a comparison between $-C_{pmin}$ from the computations and σ_i measured by Jessup for three different advance coefficients. Also listed is x/R, the streamwise location of C_{pmin}. The experimental uncertainty for σ_i is ± 0.4.

Since the performance of the marine propeller is usually deter-

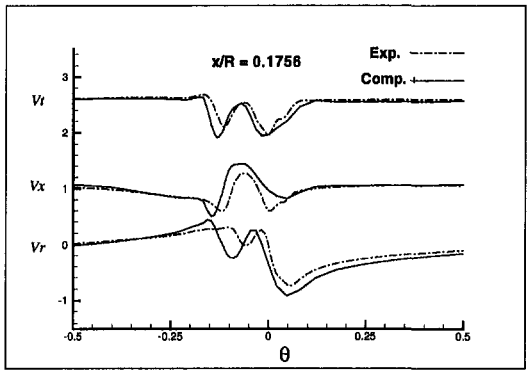

Fig. 7 The line plot of velocity, V_x, V_r, V_t, across the tip vortex center in the tangential direction at $x/R = 0.1756$

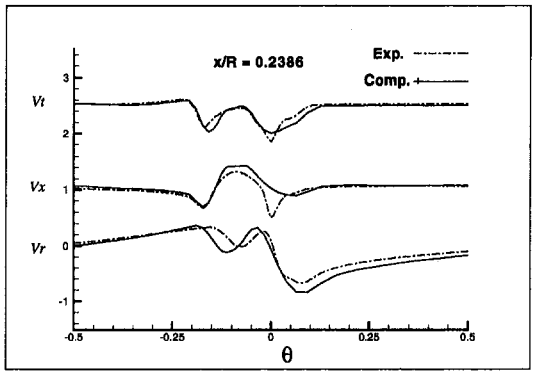

Fig. 8 The line plot of velocity, V_x, V_r, V_t, across the tip vortex center in the tangential direction at $x/R = 0.2386$

mined by the thrust and torque, it is also of interest to compare the thrust coefficient, K_t, and the torque coefficient, K_q. The K_t and K_q are defined as

$$K_t = \frac{T}{\rho n^2 D^4}, \quad K_q = \frac{Q}{\rho n^2 D^5} \tag{2}$$

where T and Q are the thrust and torque acting on the propeller in the axial direction. The computation of thrust and torque includes the surface friction. The experimental data of the thrust and torque coefficient for Prop 5168 were measured in an open water test. Comparison of K_t and K_q between numerical and experimental results are shown in Table 2 for three different advance coefficients. It is seen that current numerical result predicts K_t and K_q accurately for higher advance coefficient, but the discrepancy increases as the advance coefficient is decreased.

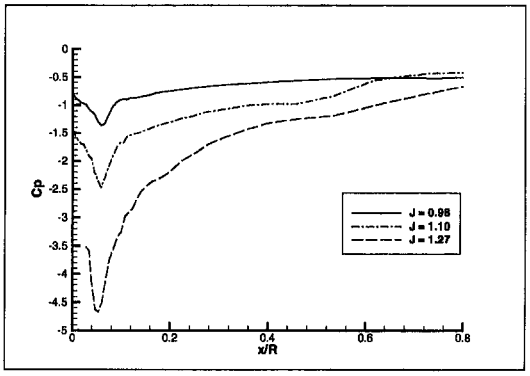

Fig. 9 The distribution of pressure coefficient, C_p, along the tip vortex core for three different advance coefficients

Table 1 Comparison between $-C_{pmin}$ and σ_i for three different advance coefficients J

J	Re	$-C_{pmin}$	σ_i	x/R
0.98	3.40×10^6	4.67	4.88	0.054
1.10	4.19×10^6	2.46	2.04	0.058
1.27	3.88×10^6	1.36	1.11	0.059

Table 2 The comparison of K_t and K_q for three different J

J	Comp. K_t	Exp. K_t	Comp. K_q	Exp. K_q
0.98	0.404	0.371	0.0901	0.0888
1.10	0.333	0.313	0.0781	0.0783
1.27	0.238	0.229	0.0606	0.0618

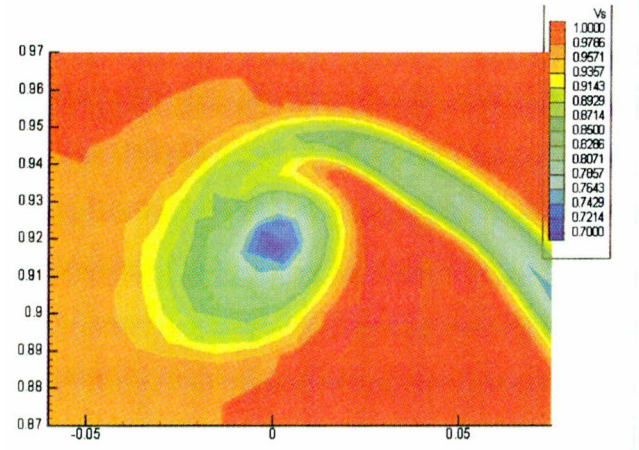

Fig. 10 V_s contour around the tip vortex for modified production term case at $x/R = 0.2386$

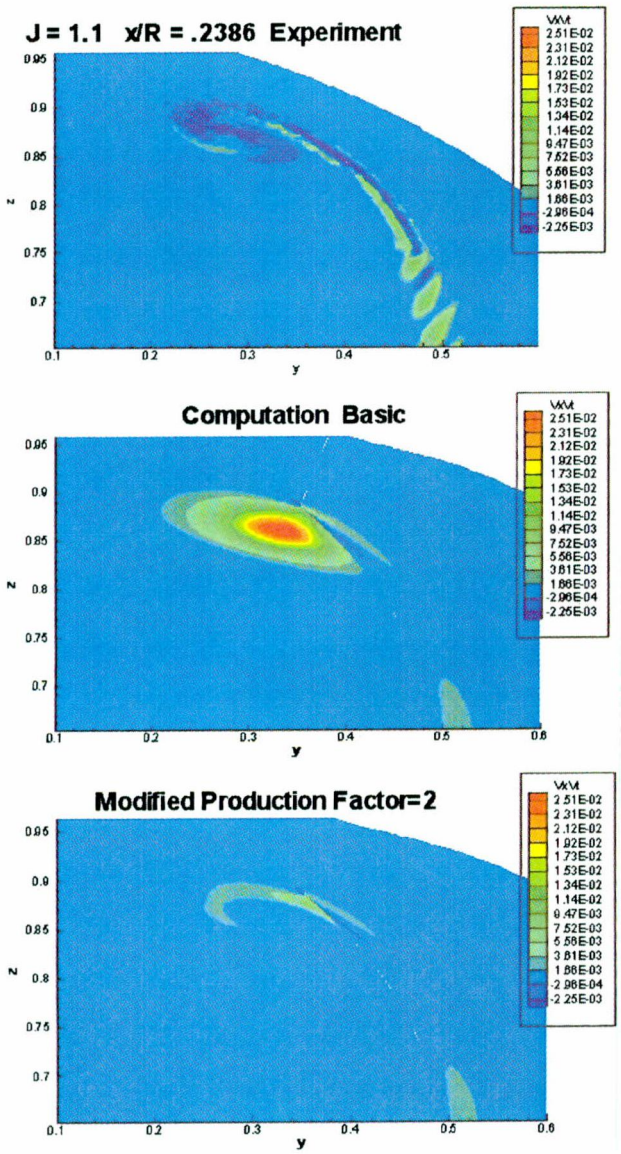

Fig. 11 Comparison of the Reynolds stress component at $x/R = 0.2386$

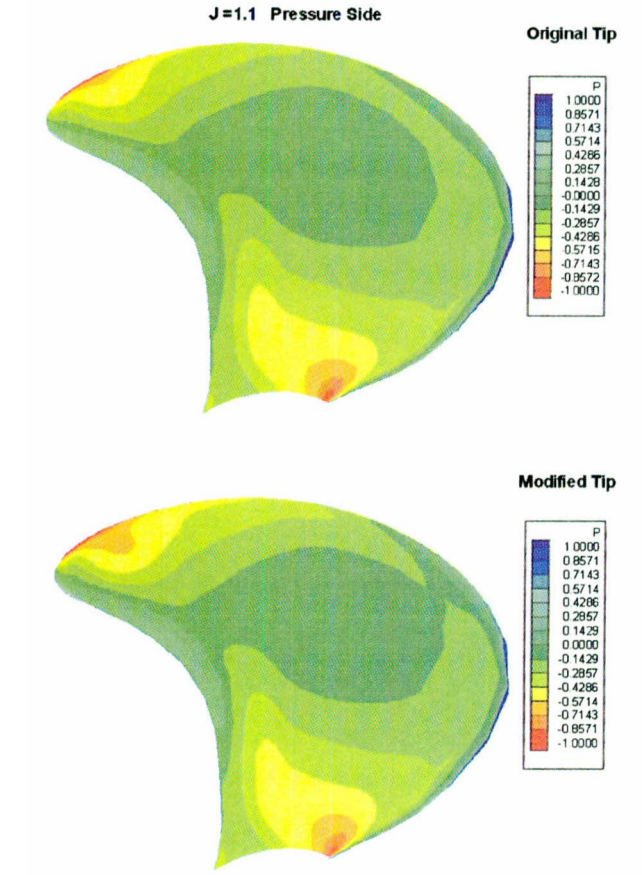

Fig. 12(*a*) Surface pressure coefficient on the pressure side for the original and modified tip geometries

3.2 Modification of Turbulence Model. From comparison of Fig. 6, it is seen that the present computation over-predicted the level of eddy viscosity in the vortex core which leads to an overly diffusive and dissipative tip vortex. To demonstrate the effect of eddy viscosity on the solution a simple modification of the Baldwin-Barth one-equation model as described by Dacles-Mariani et al. (1995) is applied. In the standard Baldwin-Barth one-equation model the production term P is approximated by

$$P = C_1 \nu R_\tau S \tag{3}$$

where C_1 is a constant, ν is the laminar viscosity, R_τ the turbulent Reynolds number, and S is a scalar measure of the deformation tensor. Since S is approximated by the magnitude of vorticity $|\omega|$ in the Baldwin-Barth model, it is expected that the eddy viscosity will be over-predicted if the flow conducts pure solid body rotation such as in the vortex core. To reduce the eddy viscosity in the region where the vorticity exceeds the strain rate, Dacles-Mariani et al. modified the production term as

$$P = C_1 \nu R_\tau (|\omega| + c \min(0, |s| - |\omega|) \tag{4}$$

where $|s|$ is the strain rate and c is an arbitrary constant. Since the factor c is chosen arbitrarily, this modification only represents an attempt to empirically adjust the production term for vortex-dominated flow. Figure 10 shows the primary velocity V_s around the tip vortex for $c = 2$. As compared to Fig. 6, one can see the prediction of minimum of V_s is significantly improved. To show the influence of the modification on the eddy viscosity, one of the Reynolds stress components $\overline{\nu_x \nu_t}$ is shown in Fig. 11 for experimental and numerical results. It was found that although the magnitude of the Reynolds stress is improved with the modification, the distribution of strain rate is not predicted well. This

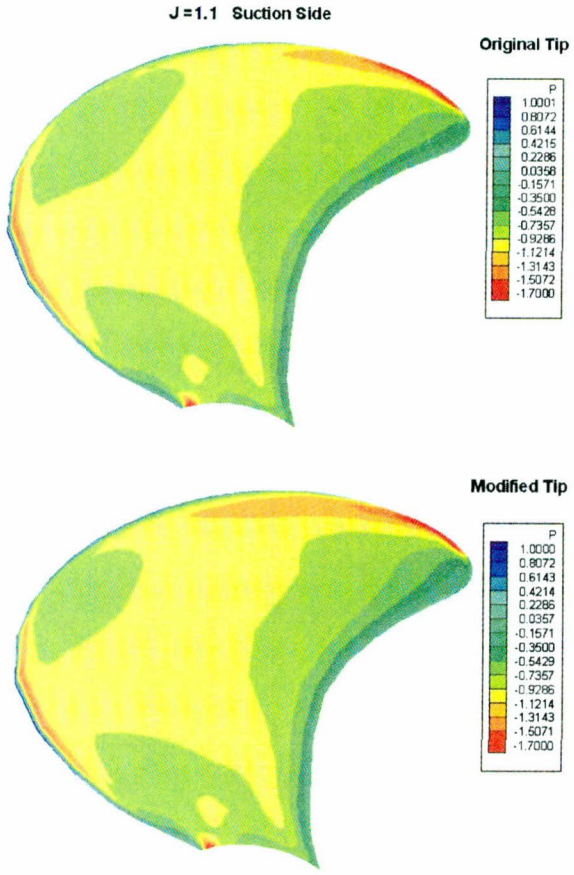

Fig. 12(*b*) Surface pressure coefficient on the suction side for the original and modified tip geometries

indicates that it is difficult to accurately model the Reynolds stress for a vortex-dominated flow using a simple eddy viscosity turbulence model. Since the turbulence around a tip vortex is thought to be highly anisotropic and the Coriolis force in the rotating propeller can also induce anisotropic turbulence, anisotropic turbulence models such as Reynolds-stress models may, therefore, be required to resolve accurately the tip vortex of the rotating propeller.

3.3 Effect of Modified Tip. Previous experimental studies (Fruman et al., 1991; Pauchet et al., 1993) have confirmed that the hydrofoil cross section has a profound influence on the tip vortex cavitation inception and desinence. Hsiao (1996) further numerically studied the cross section effect on the pressure distribution along tip vortex core and on the hydrofoil surface. It was found that the cross section which induces an early tip vortex rollup will entrain more low momentum boundary layer flow into the tip vortex and attenuate the tip vortex strength. They concluded that an appropriate hydrofoil cross section can be designed to delay cavitation inception both on the hydrofoil surface and in the tip vortex.

In the present study, a modified tip geometry designed by Jessup in ONR's progressive research of propeller tip vortex flow is numerically investigated. The modification was made by increasing the thickness of the blade tip about 50% gradually from $0.8R$ section to the tip. The computation for the modified tip case was conducted at $J = 1.10$. The pressure distribution on the blade surface is shown in Fig. 12(a–b) for the original and modified tip geometry cases. From the pressure distribution on the suction side, one can see that the modified tip has a larger low pressure region near the tip trailing edge, which indicates that the tip vortex rollup position moved further upstream for the modified tip case. Comparison of the pressure distribution along the tip vortex as shown in Fig. 13 confirms that this earlier tip vortex rollup reduces the negative minimum pressure coefficient in the tip vortex core. Since the K_t and K_q are almost the same for both cases (less than 1% difference), it is concluded that an appropriate cross section design can delay the cavitation inception in the tip vortex without reducing the propeller performance.

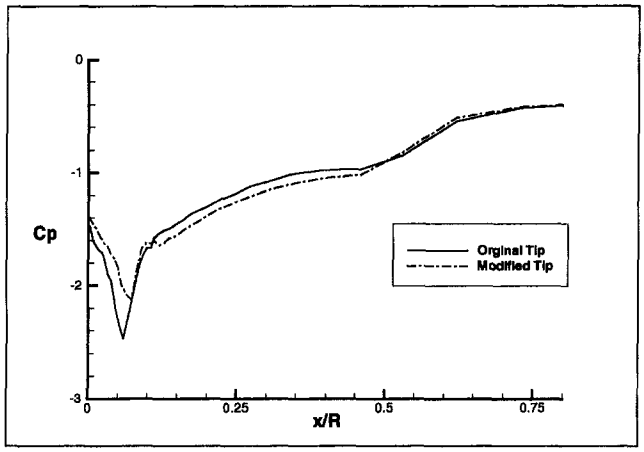

Fig. 13 Pressure coefficient, C_p, along the tip vortex core for the original and modified tip geometries

4 Conclusions

The tip vortex flow generated by a marine propeller was numerically studied using Reynolds-Averaged Navier-Stokes computations with a Baldwin-Barth turbulence model. An spiral-like computational grid was constructed between two blades with two side boundaries formed by following the local inlet flow angle at each radian section. Such computational grid allows easy alignment of the clustered grid with the tip vortex and minimizes the flow across the periodic boundaries. The general characteristics of the propeller flow including the blade-to-blade flow, wake, and tip vortex are well predicted by the present numerical method and computational domain. The close-up view of the tip vortex, however, shows that the numerical result slightly under-predicts the tip vortex strength. Modifying the turbulence model to better match the experimental measurements of the Reynolds stresses also improved the prediction of the mean velocity field.

The numerical computation of the modified tip geometry shows that increasing the thickness of the blade cross section near the tip will induce earlier tip vortex rollup and result in a weaker tip vortex without reducing the propeller performance.

Acknowledgments

This research has been supported by the Office of Naval Research under contract N00014-96-I-1149 monitored by Dr. Edwin P. Rood. Computational facilities were provided by the NAVOCEANO Supercomputer Center and the CEWES High Performance Computing Center. These contributions are gratefully acknowledged.

References

Baldwin, B. S., and Barth, T. J., 1990, "A One-Equation Turbulence Transport Model for High Reynolds Number Wall-Bounded Flows," NASA TM 102847.

Chang, J. L. C., Kwak, D., Dao, S. C., and Rosen, R., 1985, "A Three-Dimensional Incompressible Flow Simulation Method and Its Application to the Space Shuttle Main Engine, Part I—Laminar Flow," AIAA Paper 85-0175.

Chesnakas, C. J., and Jessup, S. D., 1998, "Propeller Tip-Vortex Measurements Using 3-Component LDV," *22nd Symp. on Naval Hydrodynamics,* Washington DC, Aug. 9–14.

Chorin, A. J., 1967, "A Numerical Method for Solving Incompressible Viscous Flow Problems," *Journal of Computational Physics,* Vol. 2, pp. 12–26.

Copenhaver, W. W., Mayhew, E. R., and Hah, C., 1994, "The Effect of Tip Clearance on a Swept Transonic Compressor Rotor," ASME Paper 94-GT-363.

Dacles-Mariani, J., Rogers, S., Kwak, D., Zilliac, G., and Chow, J. S., 1995, "Numerical/Experimental Study of a Wingtip Vortex in the Near Field," *AIAA Journal,* Vol. 33, No. 9, pp. 1561–1568.

Fruman, D. H., Dugue, C., and Cerruti, P., 1991, "Tip Vortex Roll-Up and Cavitation," ASME *Cavitation and Multiphase Flow Forum,* FED-Vol. 109, pp. 43–48.

Furukawa, M., Saiki, K., and Inoue, M., 1995, "Numerical Simulation of Three-Dimensional Viscous Flow in Diagonal Flow Impeller," ASME *Symposium on Numerical Simulation in Turbomachinery,* FED-Vol. 227, pp. 29–36.

Hsiao, C.-T., 1996, "Numerical Study of the Tip Vortex Flow Over a Finite-Span Hydrofoil," Ph.D. thesis, Department of Mechanical Engineering, The Pennsylvania State University. Adviser L. L. Pauley.

Hsiao, C.-T., and Pauley, L. L., 1998, "Numerical Study of the Tip Vortex Flow Over a Finite-Span Hydrofoil," ASME JOURNAL OF FLUIDS ENGINEERING, Vol. 120, pp. 345–353.

Kim, H. T., 1993, "Navier-Stokes Computation of Incompressible Propeller Flowfield," *Proc. 2nd Japan-Korea Joint Workshop on Ship and Marine Hydrodynamics,* Osaka, pp. 9–22.

Lee, Y.-T., Hah, C., and Loellbach, J., 1996, "Investigation of Tip Clearance Vortex Structures Through Numerical Flow Visualization," ASME Fluids Engineering Division Conference, FED-Vol. 229, pp. 157–165.

Oh, K.-J., and Kang, S.-H., 1995, "Numerical Calculation of the Viscous Flow Around a Propeller Shaft Configuration," *International Journal for Numerical Methods in Fluids,* Vol. 21, pp. 1–13.

Pauchet, A., Briancon-Marjollet, L., and Fruman, D. H., 1993, "Recent Results on the Effect of Cross Section on Hydrofoil Tip Vortex Occurrence at High Reynolds Numbers," ASME *Cavitation and Multiphase Flow Forum,* FED-Vol. 153, pp. 81–86.

Rogers, S. E., Kwak, D., and Kiris, C., 1991, "Steady and Unsteady Solutions of the Incompressible Navier-Stokes Equations," *AIAA Journal,* Vol. 29, No. 4, pp. 603–610.

Roe, P. L., 1981, "Approximate Riemann Solvers, Parameter Vectors, and Difference Schemes," *Journal of Computational Physics,* Vol. 43, pp. 357–372.

Stern, F., and Kim, H. T., 1990, "Computation of Viscous Flow Around a Propeller-Shaft Configuration with Infinite-Pitch Rectangular Blades," *Proc. 5th Int. Conf. On Numerical Ship Hydrodynamics,* Hiroshima, pp. 553–569.

Air Influence on Hydraulic Transients on Fluid System With Air Valves

T. S. Lee
Mechanical and Production Engineering Department,
National University of Singapore,
Singapore 119260
e-mail: mpeleets@nus.edu.sg

A study is made on the pressure surges on a fluid system with air valves. The effects of the presence and distribution of air on the system response are studied. Several distinct pressure transient characteristics were observed through this investigation. Investigations showed that air valves with high inflow characteristics installed at peak locations of a fluid system with entrapped air may reduce the magnitude of the extreme negative pressure surges. However, for near zero air entrainment levels, air valves with higher outflow characteristics tend to result in higher positive pressure surges. The effectiveness of the air valves installed for the purpose of surge protection depends not only on the physical configuration of the fluid system, the physical properties of the pipeline and the fluid, but significantly also on the characteristics of the air valves and the distribution of air in the system. The results of the investigations in the present work were confirmed through field observations and measurements.

Introduction

In the earlier studies on an air release valve designed to remove air from pipelines, Tullis (1971) revealed that the use of very small air release valves could aid in the reduction of pressure rise due to the exhaustion of air under pressure. Campbell (1983) similarly showed that nonreturn air valves are capable of cushioning slams that result from negative surges and thereby allow the omission or substantial reduction of surge vessels or other expensive surge protection devices. Tullis (1971), however, also revealed that the use of large automatic air release valves may result in severe undesirable occurrences with large pressure surges. In a more recent study by Devine and Creasey (1997) on the excessive surge pressures in a large twin sewage pumping main, the characteristics of the air valves installed were found to be the main cause. In a study of pressure surges due to rigidity of pipe walls, coatings and surrounding fill, Stephenson (1997) showed that the effects of air on the pipe material is a major factor in water hammer pressure surges. Although the effects of air are to reduce wave speed, increased pressure surges can occur with some pipework configurations. In this study, numerical experiments and field measurements were conducted to investigate the effects of entrapped air on the air valve performances on the pressure surges during a pumping trip in a pumping station.

An Improved Air Entrainment Model

Earlier investigations by Pearsall (1965/66) and Streeter and Wylie (1969) showed that the presence of undissolved gas bubbles in a steady fluid system greatly reduces the wave speed. Lee and Pejovic (1996) and Pejovic and Lee (1996) showed further that the effects on the similarity between model and prototype in a transient fluid flow system. The effect of free air on wave speed is very significant under low-pressure conditions, where the volume of the free air is higher. The variable wave speed model proposed here assumes the initial presence of free entrained air content ϵ_o and dissolved gas content ϵ_g in the liquid at atmospheric pressure. Assumptions were made that: (i) the gas-liquid mixture distribution is homogeneous, (ii) the free gas bubbles in the liquid follow a polytropic compression law with $n = 1.2$–1.3, and (iii) the pressure within the air bubbles during the transient process is in equilibrium with the local fluid pressure. When the computed local transient pressure falls below the fluid gas release pressure p_g, a release of dissolved gas of $\alpha_{gr}\epsilon_g$ is assumed with a time delay of $Ke\Delta t$. The local pressure remains constant and is equal to the vapor pressure. When the computed transient pressure recovers to a value above the gas release pressure, the equivalent amount of gas redissolved into the liquid is observed to be $\alpha_{ga}\epsilon_g$ with a corresponding time delay of $Ka\Delta t$. Since the local pressure remains constant when the computed pressure is below the gas release pressure, the maximum air content has a limit and hence the wave speed also has a lower limit which is consistent with the data observed.

Consider a mass of liquid containing a fractional volume ϵ, of gas in free bubble form. Following the procedures similar to that given by Pearsall (1965/66), Fox (1984), and Wylie et al. (1993), it can be shown that the local wave speed a_i at an absolute pressure p_i and air fraction content ϵ_i is given by

$$a_i^k = \left[\rho_w(1-\epsilon_i^k)\cdot\left(\frac{1}{K}+\frac{\epsilon_i^k}{np_i^k}+\frac{cD}{eE}\right)\right]^{-1/2} \tag{1}$$

For the variable wave speed model proposed here, the initial free air fraction ϵ_o and dissolved gas fraction ϵ_g at a reference absolute pressure p_o must be specified. The initial wave speed variation along a pipeline ($i = 0, 1, \ldots, N$) is then computed through the absolute pressure distribution along the pipeline from Eq. (2) at $k = 0$ (steady state). The transient computation of the above fraction of air content in Eq. (1) along the pipeline depends on the local pressure and local air volume and is given by

$$\epsilon_T^{k+1} = \left(\frac{p_i^k}{p_i^{k+1}}\right)^{1/n}\epsilon_i^k \quad \text{and} \quad \epsilon_o^{k+1} = \left(\frac{p_o}{p_i^{k+1}}\right)^{1/n}\epsilon_o; \tag{2}$$

(a) for $p_i^{k+1} \geq p_g$ and $\epsilon_T^{k+1} \leq \epsilon_o^{k+1} + \alpha_{gr}\epsilon_g$:

$$\epsilon_i^{k+1} = \epsilon_T^{k+1} \tag{2a}$$

(b) for $p_i^{k+1} \geq p_g$ and $\epsilon_T^{k+1} > \epsilon_o^{k+1} + \alpha_{gr}\epsilon_g$ with a time delay of $Ka\Delta t$:

$$\epsilon_i^{k+1} = \left(\frac{p_i^k}{p_i^{k+1}}\right)^{1/n}(\epsilon_i^k - \alpha_{ga}\epsilon_g) \tag{2b}$$

(c) for $p_i^{k+1} < p_g$ and at a time delay of $Ke\Delta t$:

Contributed by the Fluids Engineering Division for publication in the JOURNAL OF FLUIDS ENGINEERING. Manuscript received by the Fluids Engineering Division November 13, 1997; revised manuscript received March 12, 1999. Associate Technical Editor: D. P. Telionis.

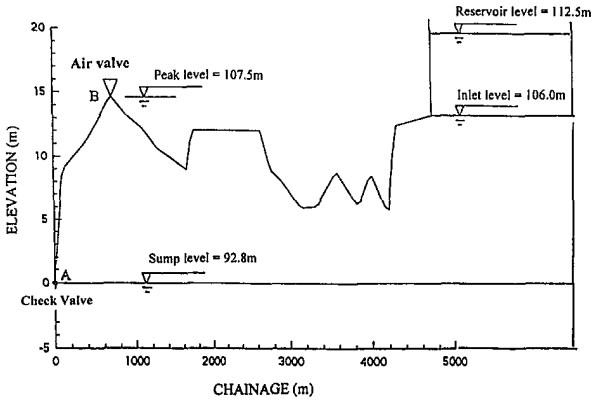

Fig. 1 Pumping station pipeline profile

$$\epsilon_i^{k+1} = \left(\frac{p_i^k}{p_g}\right)^{1/n} (\epsilon_i^k + \alpha_{ga}\epsilon_g), \tag{2c}$$

The present study set the absorption of free gases and the evolution of dissolved gases with a time delay of $Ka\Delta t$ and $Ke\Delta t$, respectively, and an instant cavitation at vapor pressure under transient conditions. Typical values used for Ka and Ke are 1.000. These Ka and Ke values are currently under fine tuning for the better prediction of the pressure transients. For water saturated at atmospheric pressure the gas release pressure head (Pg) approaches that of the vapor pressure (i.e., 2.4 m water absolute). A typical free air content in sewage at atmospheric pressure is about 0.1%; the free gas content evolved at the gas release head is about 2.0% at atmospheric pressure head. The fraction of gas absorption is $\alpha_{ga} \approx 0.3$ and the fraction of gas release is $\alpha_{gr} \approx 0.6$ (Pearsall, 1965; Kranenburg, 1974; Provoost, 1976). For the comparative study of constant wave speed cases, the present study assumed $\epsilon = 0.000$ in the fluid system even when the transient pressure falls below the gas release pressure ($P < Pg$ at any point), i.e., the system is assumed completely free from the influence of entrapped air. The above model expressions in Eqs. (1) and (2) are very significantly different from that obtained by Pearsall (1965/66), Fox (1984), and Wylie et al. (1993).

An Improved Air Valve Model

The flow rate of air through the air valve installed at the peak location B of the pipeline profile as shown in Fig. 1 is assumed here to be dependent on the absolute atmospheric pressure p_o and temperature T_o outside the pipe, as well as the absolute temperature T and pressure p within the pipe. The model air valve used here (Fig. 2) assumed that: (a) air enters and leaves the pipe through the valve under isentropic flow conditions; (b) the air mass within the pipe follows a polytropic law (polytropic index = n); (c) the air admitted to the pipe stays near the valve where it can be expelled; (d) the elevation of the liquid surface remains substantially constant, and the volume of air is small compared with the liquid volume of a pipeline reach; (e) Under all operating conditions, the air valve should retain all liquid in the pipeline without loss of liquid to the atmosphere.

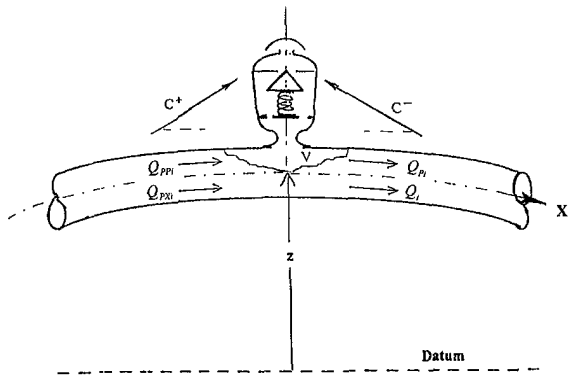

Fig. 2 Air valve at location B

With the above assumptions, flow conditions through the air valve can be classified into four categories:

Subsonic air flow in ($p_o > p > Cr \cdot p_o$):

$$\dot{m} = C_{\text{in}} A_{\text{in}} \sqrt{2\rho_o p_o \left[\left(\frac{p}{p_o}\right)^{2/n} - \left(\frac{p}{p_o}\right)^{1/n+1}\right]} \tag{3a}$$

Critical air flow in ($p < Cr \cdot p_o$):

$$\dot{m} = C_{\text{in}} A_{\text{in}} \frac{Cr\sqrt{n}}{\sqrt{RT_o}} p_o \tag{3b}$$

Subsonic air flow out ($p_o/Cr > p > p_o$):

$$\dot{m} = -C_{\text{out}} A_{\text{out}} p \sqrt{\frac{2}{RT}\left[\left(\frac{p_o}{p}\right)^{2/n} - \left(\frac{p_o}{p}\right)^{1/n+1}\right]} \tag{3c}$$

Critical air flow out ($p > p_o/Cr$):

$$\dot{m} = -C_{\text{out}} A_{\text{out}} \frac{Cr\sqrt{n}}{\sqrt{RT}} p \tag{3d}$$

where A = inflow or outflow nozzle area; C = inflow or outflow coefficients; $\dot{m}$ = rate of air mass flow into or out of air cavity; p = absolute pressure inside the pipeline; p_o = absolute atmospheric pressure outside the pipeline; Q = liquid flow rate within the pipeline into or away from the air valve region; T = temperature in K. As a result of the assumptions made in the present air valve model, the coefficients and indices of the modeled equations are significantly different from those given in the air valve models proposed by Wylie et al. (1993) and Lee and Cheong (1994). In the numerical computation of the pressure variation along the pipeline, when the pressure head in the pipeline at the air valve location is greater than atmospheric and no air is assumed present in the pipe. The boundary condition at a junction of 2 reaches with the installed air valve (Fig. 2) is treated as the usual internal section solution of $H_P(I)$ and $Q_P(I)$. When the pressure head drops below pipe elevation, the air valve opens for air to enter, and the general gas law, $pV = mRT$, is to be satisfied at the end of each time increment of the computation until the admitted air is expelled. With reference to Fig. 2 (Wylie et al., 1993), with $p = \rho g(H_P - z + \bar{H})$ where ρ = density of the fluid, z = pipeline elevation w.r.t. a datum, $\bar{H}$ = atmospheric barometric pressure head, the volume of the air cavity V_i at beginning of time increment Δt is given by

$$p \cdot [V_i - 0.5\Delta t((Q_{PX_i} - Q_i) + (Q_{PP_i} - Q_{P_i}))] = [m_o + 0.5\Delta t(\dot{m}_o + \dot{m})] \cdot RT \tag{4}$$

where Q_{PX_i} = initial fluid inflow into cavity (at start of Δt); Q_i = initial fluid outflow from cavity; Q_{PP_i} = final fluid inflow into cavity (at end of Δt); Q_{P_i} = final fluid flow outflow from cavity; m_o = initial mass of air in cavity; $\dot{m}_o$ = initial rate of air mass flow into or out of cavity; $\dot{m}$ = final rate of air mass flow into or out of cavity. The above equation is to be solved for the end of each time increment when a cavity is present (i.e., $V_i > 0$). The final air flow rate $\dot{m}$ is given by one of the equations in (3).

With the above formulations, solutions for Hp, Qp were initially obtained from the C^+ and C^- characteristic lines for the pressure transient of the general pipeline system. When the local pressure Hp falls below atmospheric pressure, the air valve installed at the low pressure location is activated and the p is determined. The air inflow rate and air volume are then calculated from Eqs. (3) and (4), respectively. During the subsequent pressure

Table 1 Air valve flow characteristics (Lee and Cheong, 1994)

No.	Air valve no.	Model	C_{in}	C_{out}
0	AV0	No Air Valve	0.000	0.000
1	AV1	Wylie, Streeter & Suo (1993)	0.713	1.071
2	AV2	Adams Fig. 75	0.237	0.009
3	AV3	Guest & Chrimes Fig. 4*A*/CR	0.306	0.189
4a	AV4	Biwater Epex Fig. 1291	0.585	0.049
4b	AV4	Standard Biwater Air Valve with Vented Non-Return Valve	0.585	0.045
5	AV5	Guest & Chrimes Fig. 4*A*	0.504	0.744
6	AV6	Standard Biwater Air Valve	0.720	1.361

transient, the condition for inflow or outflow of air from the air valve is determined by the transient p values and the volume of air residued in the pipeline near the air valve location.

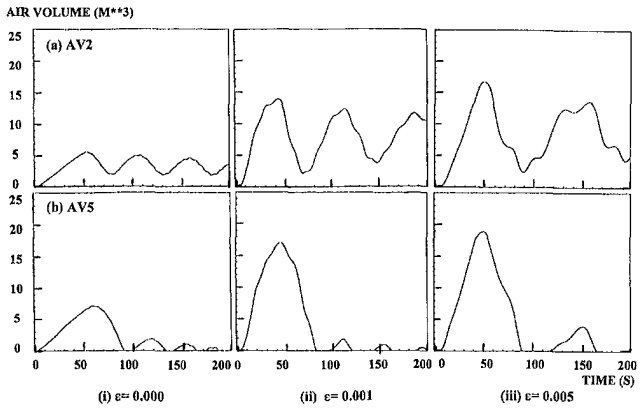

Fig. 4 Effects of air entrainment on air cavity volume at B

Results and Discussions

The characteristics of the six air valves studied here are tabulated in Table 1. The air void fraction ϵ studied were in the range of 0.000 to 0.030. The most severe case of all the pumps in a station fail simultaneously owing to a power failure are study in this work. The changes in pump speed during pump run-down for both normal and turbine modes are modeled (Fox, 1984). The dynamics of the check valves and the flow velocities during the check valves closure were studied in details by Thorley (1989). However, due to lack of physical data on the dynamic behaviors of the check valve used in the present study, the dynamics of the check valve were not modeled in the present analysis and the check valves are assumed closed when the flow reversed. Downstream of the pipeline considered here (Fig. 1) is a constant head reservoir.

Without the air valve installed (Case AV0: C_{in} = 0,00, C_{out} = 0,00), the results obtained in Fig. 3(*a*) serve as a reference for the investigation of the other air valve characteristics on the transient responses of the fluid system. Several distinct features were observed from the above numerical experiments. (i) The pressure peak varies with ϵ and can be higher than that predicted by the constant wave speed calculations, with the transient time that occurs varied. (ii) The damping of the surge pressure is noticeably larger when $\epsilon > 0.000$. (iii) With $\epsilon > 0.000$ the pressure surges are asymmetric with respect to the static head, while the pressure transient for the constant wave speed calculations was symmetric with respect to the static head. (iv) When air was entrained in the system, the pressure transient showed long periods of downsurge and short periods of upsurge when compared with the gas-free constant wave speed case. Surge measurements by Campbell (1983), Kranenburg (1974), and Lee and Cheong (1994, 1998) confirmed that damping is faster in reality, suggesting that energy dissipation mechanisms other than ordinary friction are also operating. (v) The degree of amplification of the first pressure peak is dependent upon the rate of deceleration of the flow and the magnitude of the reverse flow velocity after pump trip.

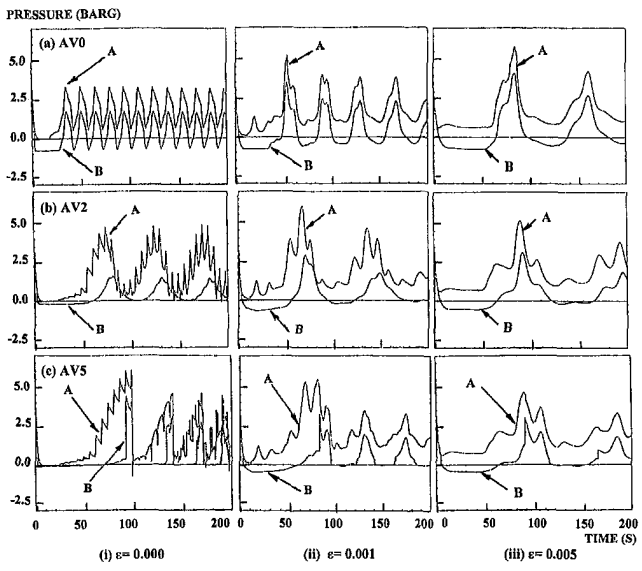

Fig. 3 Effects of air entrainment on pressure transients with various air valves

With an air valve installed at location B, Figs. 3(*b*) and 3(*c*) show the effects of the in-flow and out-flow characteristics of the air valves on the pressure transients at A and B under various air entrainment conditions. During the initial phase of the pump run down, when the transient pressure at B reached subatmospheric pressure, the air valve at B will open and allow air at atmospheric pressure into the pipeline. This minimizes any further drop in pressure within the system. Whenever the transient pressures at B exceeded the atmospheric pressure, air previously entered through the air valve will be vented out. At the point when the air valve closes, the momentum of the reverse flow will be forced to stop at the valve seat. This may result in a rapid build up in pressure at the air valve. Investigations show that the magnitude of this pressure build up depends on very much the air valve inflow/outflow characteristics and the air entrainment content (Figs. 3(*b*)–3(*c*)). This high pressure may cause the pressure head at the air valve to exceed the discharge elevation, setting up a forward hydraulic gradient. Forward flow toward the reservoir is then resumed and a repetitive transient flow process is created. Eventually, friction and turbulent energy dissipation within the pipe system will damped down the subsequent pressures surges over time. Figures 3(*a*)–(*c*) generally show a reduction in the magnitude of the negative line pressure when an air valve was installed at the peak location B.

With higher C_{in} values for the air valve, the rate of air inflow was sufficient to prevent the line pressure from falling below the vapor pressure. The effects of the different C_{in} values on the air flow rates can be seen in the amount of air cavity volume formed in Figs. 4(*a*) and 4(*b*). The corresponding wave speed variations at the check valve location A and at the air valve location B for ϵ = 0.001 and 0.010 are shown in Fig. 5 for air valve AV2 and AV5. These transient wave speed variations follow very closely their local pressure transient (Figs. 3(*b*) and 3(*c*)) at the corresponding points. The magnitude of the maximum wave speed decreases as the air entrainment value is increased. The change in the pressure surge frequencies with respect to the air entrainment values of ϵ can thus be explained through this dominant influence of ϵ on the fluid system wave speed. The above observations are consistent with the available field measurements and observations (Campbell, 1983; Kranenburg, 1974; Lee and Cheong, 1994, 1998; Lee and Pejovic, 1996; Provoost, 1976) of pumps operating near low-water

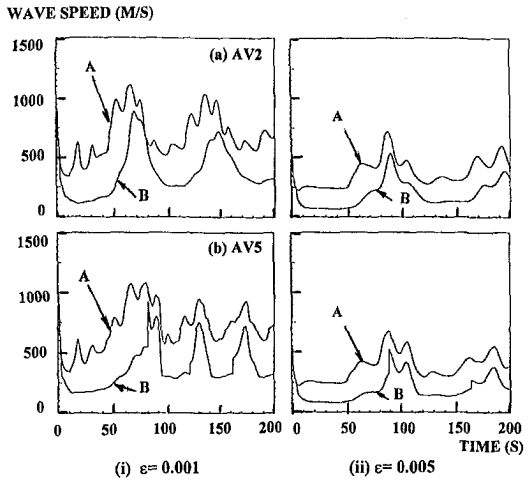

Fig. 5 Effects of air entrainment on wave speed variations

cut-out levels with air entrainment due to falling inflow jets and/or attached surface vortex.

The above results also show that, while installing an air valve at the peak location helps to reduce the magnitude of the negative line pressure, it may on the other hand also result in aggravated positive pressure surges, especially at a low air entrainment level (i.e., higher average system wave speed). The aggravated positive pressure surges worsen with higher values of C_{out} as shown in Fig. 6. After substantial amount of air was admitted into the pipeline to restore the negative line pressure to atmospheric pressure, the admitted air will be expelled to the atmosphere when the positive surge pressure returns. With higher values of C_{out}, the admitted air may be expelled rapidly and completely within a short time interval. This results in a sudden rise in the line pressure when the water at the air-water interface comes into contact with the closing air valve seat. Figure 6 illustrates the sudden rise in the line pressure when the final amount of admitted air was being expelled for a high C_{out} value of 1.361 at zero air entrainment value (Table 1: AV6—Standard Biwater Air Valve). The high pressure resulting from rapid air valve closure can be alleviated by fitting an outflow restriction device to the air valve. This results in the air being vented out more slowly (low C_{out}), reducing the reverse flow rate upon air valve closure and thereby alleviating subsequent high surge pressures. Figure 6 also illustrates a more benign pressure transient for a low C_{out} value of 0.009 (Table 1: AV2—Adams Air Valve) at zero air entrainment value. The positive air cavity volume served as a cushion between the water and the air valve so that a sudden rise in the surge pressure will not occur in the fluid system.

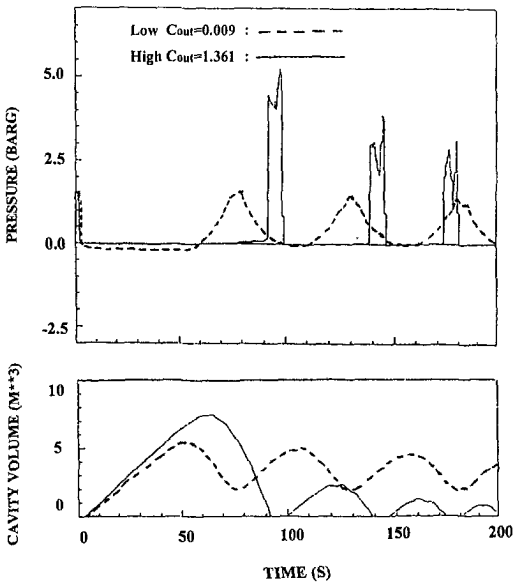

Fig. 6 Effects of air valve characteristics on pressure surges

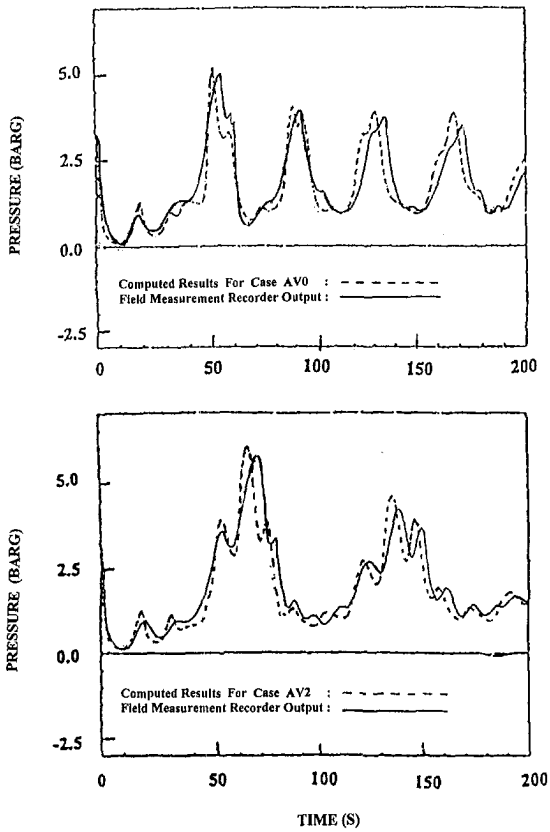

Fig. 7 Comparison with field measurements pressure surges at downstream of check valve location A

In order to reduce the subatmospheric pressure produced upon pump shutdown, it was often conceived that the number of air valves might be increased so that air could be admitted into the pipeline system more rapidly, thus achieving a greater equalization in pressure between atmospheric and the subatmospheric pressures within the pipeline. The present study showed that doubling or quadrupling the air valves has a minimum effect in moderating the subatmospheric pressure further. However, care should be taken here that in doubling or quadrupling the number of air valves used, it has the same effects as increasing the C_{in} as well as the C_{out} values of an equivalent air valve. Thus, additionally, the maximum transient pressures may increase with the number of air valves used as this causes air to be vented more rapidly (high C_{out}), thus causing a greater deceleration in flow when the air valves close. However, high pressure resulting from rapid valve closure (high C_{out}) can be alleviated by fitting an outflow restriction device (lowering the C_{out}). This results in the air being vented out slowly in a controlled manner, reducing the reverse flow rate upon air valve closure and thereby alleviating subsequent high surge pressures. From the above studies, it can thus be concluded that in order to alleviate the problem of increased air outflow (large C_{out}) occurring when using multiple air valves (which leads to rapid air valve closure), vented non-return valves (reducing C_{out}) can be fitted on the air valves to give a restriction in the outflow (low C_{out}) while maintaining satisfactory (higher C_{in}) rate of inflow.

Comparison With Field Measurents

Field measurements (Lee and Cheong, 1998) were carried for two of the simulated cases mentioned in this study in order to verify the validity of the simulations. Monitoring of the transient pressures were conducted at location A (immediate downstream of the check valve of the pump) within the pumping station for the pumping main as shown in Fig. 1. The transducers used are piezoresistive absolute pressure transducers with the capability of measuring sub-atmospheric pressures. Measurements were carried out with simultaneous three pumps trip with the air valve turn on (Adams' Air Valve, AV2: $C_{in} = 0.237$, $C_{out} = 0.009$) and with the air valve isolated (i.e., no air valve, AV0: $C_{in} = 0{,}000$; $C_{out} = 0.000$). The air valve is installed along the pumping system at B as shown in Fig. 1. This air valve can be temporary deactivated (i.e., shut off) during the field measurements. The corresponding transient pressure at a location A of the pumping main obtained through the surge analysis above are reproduced for comparison in Fig. 7 without the air valve (Case AV0) and with an air valve (AV2). The computed results with a specified $\epsilon = 0.001$ value compared very well with the corresponding field measurements. There are proper phasing of the computed pressure surges when compared with the field measurements. The magnitudes of the computed and measure pressure surges are in good agreement. The air entrainment level is estimated to be of the order of $\epsilon \approx 0.001$.

Conclusions

The effects of entrapped air on the air valve performances in a fluid system under transient flow conditions were studied. Field measurements were also made for two selected cases. This study showed that installation of air valves at the high points of the pipeline system with high inflow coefficient C_{in} tend to reduce the magnitude of negative pressure surges. However, if air valves with corresponding high out-flow characteristics are installed, this may result in the rapid and complete exhaustion of the air admitted into the fluid system when the line pressure rises above the atmospheric pressure, resulting in large positive pressure surges in the pipeline. Air valves with a low outflow coefficient C_{out} could ensure that large positive pressure surges due to air valve slamming would not occur.

Acknowledgment

The support of a National University of Singapore research grant (RP3972715) is gratefully acknowledged.

References

Campbell, A., 1983, "The Effect of Air Valves on Surge in Pipelines," *Proc. 4th Int. Conf. on Pressure Surges,* BHRA, Bath, United Kingdom, Paper C1, pp. 89–102.

Devine, J. G., and Creasey, J. D., 1997, "Surge Suppression: Case at all Stages," *Journal of the Chartered Institution of Water and Environmental Management,* Vol. 11, No. 5, pp. 341–345, Oct.

Fox, J. A., 1984, *Hydraulic Analysis of Unsteady Flow in Pipe Networks,* Macmillan, London.

Kranenburg, C., 1974, "Gas Release During Transient Cavitation in Pipes," *J. Hydraulic. Div.,* ASCE, Vol. 100, pp. 1383–1398.

Lee, T. S., and Cheong, H. F., 1994, "Teck Hock Pumping Station: Flow Rate and Pressure Transient Measurements," Johnson Pacific Pte Ltd, Singapore. Dec.

Lee, T. S., and Cheong, H. F., 1998, "Tanjong Rhu Pumping Station—Site Measurement and Analysis of Surge in Pumping Main," Ebara Engineering Singapore Pte Ltd, Singapore, July.

Lee, T. S., and Pejovic, S., 1996, "Air Influence on Similarity of Hydraulic Transients and Vibrations," ASME JOURNAL OF FLUIDS ENGINEERING, Vol. 118, Dec., pp. 706–709.

Pearsall, I. S., 1965,/66, "The velocity of water hammer waves," *Proc. Inst. Mech. Eng.,* Vol. 180, Part 3E, pp. 12–20.

Pejovic, S., and Lee, T. S., 1996, "Similarity of Transient and Oscillatory Flow of Real Fluid," Mechanics, Materials and Constructions (Scientific Meetings of the Serbian Academy of Sciences and Arts, Vol. LXXXIII, Department of Technical Sciences, Book 2, pp. 247–258.

Provoost, G. A., 1976, "Investigation into Cavitation in a Prototype Pipeline Caused by Waterhammer," Proc. 2nd Int. Conf. on Pressure Surges, BHRA, Bedford, United Kingdom, Sept., pp. 35–43.

Stephenson, D., 1997, "Effects of Air Valves and Pipework on Water Hammer Pressures," ASCE, *Journal of Transportation Engineering,* Vol. 123, No. 2, pp. 101–106, Mar.–Apr.

Thorley, A. R. D., 1989, "Check Valve Behaviour Under Transient Flow Conditions: A State-of-the-Art Review," ASME JOURNAL OF FLUID ENGINEERING, June, Vol. 111, pp. 178–183.

Tullis, J. P., 1971, "Control of Flow in Closed Conduits," Fort Collins, CO, pp. 315–340.

Wylie, E. B., Streeter, V. L., and Suo, L., 1993, *Fluid Transients in Systems,* McGraw-Hill.

Rama Subba Reddy Gorla
Professor of Mechanical Engineering,
Cleveland State University,
Cleveland, OH 44115
Mem. ASME
e-mail: gorla@csaxp.csuohio.edu

Larry W. Byrd
Thermal Structures Branch,
Air Vehicles Directorate,
Air Force Research Laboratory,
Wright Patterson Air Force Base, OH 45433
Mem. ASME
e-mail: Larry.Byrd@va.wpafb.af.mil

Effect of Electrostatic Field on Film Rupture

Nonlinear thin film rupture has been analyzed by investigating the stability of films under the influence of a nonuniform electrostatic field to finite amplitude disturbances. The dynamics of the liquid film is formulated using the Navier-Stokes equations including a body force term due to van der Waals attractions. The effect of the electric field is included in the analysis only in the boundary condition at the liquid vapor interface. The governing equation was solved by finite difference method as part of an initial value problem for spatial periodic boundary conditions. The electric field stabilizes the film and increases the time to rupture when a long wavelength perturbation is introduced.

Introduction

The hydrodynamic stability of thin liquid films has attracted much attention in view of many applications in chemical, mechanical and biomedical engineering fields.

The onset of instability of a liquid film flow down a stationary inclined plane was analyzed by Benjamin (1957) and Yih (1963). They showed that the film on a vertical plate is always unstable. The instability manifests itself as gravity-driven surface waves with wavelength much longer than the film thickness. According to Yih (1968), when a horizontal plate is made to oscillate in its own plane, unstable waves synchronous to the plate oscillation can be generated. Control of instability by use of external forcing has attracted attention recently. Coward and Renardy (1995) studied a modulated two-layered problem. Or and Kelly (1996) studied the control of thermocapillary instabilities in a heated layer by external forcing. Woods and Lin (1995) investigated the interaction of the shear waves, surface waves, and Faraday waves in a liquid film on an inclined plate that vibrated in a direction perpendicular to the plate. They found that the amplification rate of the unstable surface waves may be reduced by such an oscillation, but cannot be completely suppressed.

When a liquid layer becomes ultra thin (100–1000 Å), it becomes unstable. The instability is due to the van der Waals potential and results in the rupture of the layer. The rupture of thin liquid films occurs in many industrial applications involving disperse and colloid systems and in biological phenomena. The spontaneous rupture of a liquid film on a planar solid wall was studied by Ruckenstein and Jain (1974). The liquid film was modeled by them as a Navier-Stokes continuum with a potential due to the van der Waals interactions. They used lubrication approximation to obtain the linear dynamic instability results. From this analysis, one can obtain rough estimates for the rupture time, namely, the time needed for the thin film to attain zero thickness at some point. William and Davis (1982) examined the nonlinear evolution equation and numerically treated it as an initial value problem with periodic boundary conditions. Their results indicated that the nonlinearities of the system would accelerate the rupture phenomenon.

Kim et al. (1992) studied the interaction of an electrostatic field with a thin liquid film flowing under gravity down an inclined plane. They did not include the van der Waals force term in their analysis because they were concerned with thicker films. They examined the stability and evolution of the interface in the thin film limit. A discussion was provided on the application of their numerical results to a proposed electrostatic liquid film space radiator. The electrostatic liquid film space radiator was further elaborated by Bankoff et al. (1994).

A review of the literature indicated that no one until now has addressed the question of how the thin liquid film and an electrostatic field interact via van der Waals forces. The present work has been undertaken in order to investigate this problem. We are interested in the specific working regimes of the parameters, where it will be possible to predict rupture or dry out of the thin film. This will be accomplished by solving the equations of thin film motion in the presence of an electric field. A long wave theory is formulated for the nonlinear dynamic instabilities of the thin film.

Analysis

We consider the flow of a thin liquid film down an inclined plane under gravity. The plane is assumed to make an angle β with the horizontal. We choose x and y directions to be parallel and normal to the plane, respectively, as shown in Fig. 1. We assume the characteristic thickness of the film to be d and the length scale parallel to the film to be L. The aspect ratio is given by $\xi = d/L$. If we assume that $\xi \ll 1$, we have a thin film. The distance from the charged foil to the plane is $\hat{H}$. If $d/\hat{H} << 1$ then the charged plate is very far from the plane relative to the thickness of the film. Therefore, to leading order in the ratio of $d/\hat{H}$, we can assume that the charged plate does not see the film and the electrostatic problem for the electric field decouples from the fluid dynamics problem. The ratio $\hat{H}/L$ is assumed to be of order unity. The dimensionless foil height is defined as $H = \hat{H}/d$.

The electric field is determined by solving Laplace's equation.

$$\nabla^2 \phi = 0 \tag{1}$$

where $\phi(x, y)$ is the electric potential. The boundary conditions are

$$\phi(x, \hat{H}) = F\hat{H}\Phi(x); \quad \phi(x, 0) = 0 \tag{2}$$

In this work, we assume $\Phi(x) = 1$ and the length of the plate $L \to \infty$. Along $y = h(x, t)$ we have the boundary conditions that the tangential electric field and the normal displacement field are continuous. It may be noted that $y = h(x, t)$ is unknown, so that solution of the electrostatic problem is coupled to the dynamics of the film.

The liquid film is governed by the Navier-Stokes equations. The liquid layer is assumed thin enough that van der Waals forces are effective ($<\approx 0.1$ μm) and thick enough that a continuum theory of the liquid is applicable.

We assume that the liquid is incompressible. The governing equations and boundary conditions are made dimensionless by using the following scales: length in y-direction $\approx d$, in x-direction $\approx L$, velocity in x-direction $\approx U_0$, velocity in

Contributed by the Fluids Engineering Division for publication in the JOURNAL OF FLUIDS ENGINEERING. Manuscript received by the Fluids Engineering Division January 21, 1998; revised manuscript received April 5, 1999. Associate Technical Editor: M. Sommerfeld.

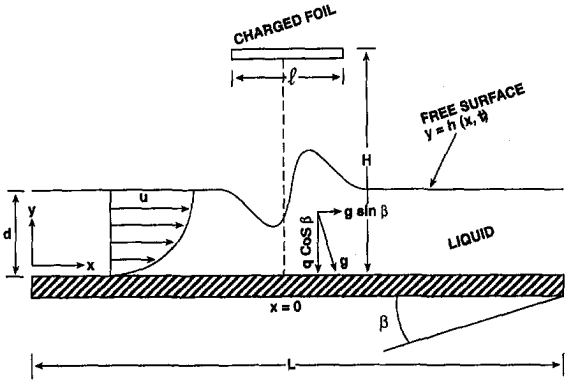

Fig. 1 Flow model for the thin film flow

y-direction $\approx \xi U_0$, unit of time $\approx L/U_0$, unit of pressure $\approx \rho U_0^2$, and unit of electric field $\approx F$. We take ρ as the fluid density, ϵ the dielectric constant and μ the viscosity. The continuity equation becomes

$$\frac{\partial u}{\partial x} + \frac{\partial v}{\partial y} = 0 \tag{3}$$

The momentum equation becomes

$$\xi\left(\frac{\partial u}{\partial t} + u\frac{\partial u}{\partial x} + v\frac{\partial u}{\partial y}\right) = -\xi\frac{\partial p}{\partial x} + \frac{1}{\mathrm{Re}}\left(\xi^2\frac{\partial^2 u}{\partial x^2} + \frac{\partial^2 u}{\partial y^2}\right) + \frac{1}{\mathrm{Fr}^2}\sin\beta - \xi\frac{\partial \psi}{\partial x} \tag{4}$$

$$\xi^2\left(\frac{\partial v}{\partial t} + u\frac{\partial v}{\partial x} + \xi v\frac{\partial v}{\partial y}\right) = -\frac{\partial p}{\partial y} + \frac{\xi}{\mathrm{Re}}\left(\xi^2\frac{\partial^2 v}{\partial x^2} + \frac{\partial^2 v}{\partial y^2}\right) - \frac{1}{\mathrm{Fr}^2}\cos\beta - \frac{\partial \psi}{\partial y} \tag{5}$$

In the above dimensionless equations, u and v represent the velocity components in x and y directions, respectively, p the pressure and ψ the potential function describing the van der Waals forces. We follow Williams and Davis (1982) and write a modified expression for ψ:

$$\psi = Ah^{-3} \tag{6}$$

In the previous equation, the van der Waals forces are represented through the potential function Ψ and A' is the dimensional Hamaker constant. A is related to the Hamaker constant A' as $A = A'/6\pi\rho U_0^2$. We have introduced the Reynolds number, $\mathrm{Re} = \rho U_0 d/\mu$ and the Froude number, $\mathrm{Fr} = U_0/\sqrt{gd}$.

The boundary conditions along the solid plane wall are given by:

$$y = 0; \quad u = v = 0 \tag{7}$$

At the fluid interface, we have the kinematic condition:

$$y = h(x, t) : \frac{\partial h}{\partial t} + u\frac{\partial h}{\partial x} = v \tag{8}$$

Reference may be made to the Appendix for the derivations of Eqs. (9, 10), and (13–16).

The continuity of tangential stress on the interface requires

$$y = h(x, t) : \left[1 - \xi^2\left(\frac{\partial h}{\partial x}\right)^2\right]\left(\frac{\partial u}{\partial y} + \xi^2\frac{\partial v}{\partial x}\right) + 2\xi^2\frac{\partial h}{\partial x}\left(\frac{\partial v}{\partial y} - \frac{\partial u}{\partial x}\right) = 0 \tag{9}$$

The continuity of normal stress at the interface $y = h(x, t)$ becomes

$$\frac{\xi^2}{Ca}\frac{\partial^2 h}{\partial x^2}\left[1 + \xi^2\left(\frac{\partial h}{\partial x}\right)^2\right]^{-3/2} + \frac{\rho U_0 d}{2\mu}Ah^{-3} = -\frac{\mathrm{Re}}{2}p + K\left(\frac{1}{\epsilon_f} - 1\right)\left[(E_n^v)^2 + \epsilon_f(E_t^v)^2\right] + \xi\left[\xi^2\left(\frac{\partial h}{\partial x}\right)^2\frac{\partial u}{\partial x} - \frac{\partial h}{\partial x}\left(\frac{\partial u}{\partial y} + \xi^2\frac{\partial v}{\partial x}\right) + \frac{\partial v}{\partial y}\right] \times \left[1 + \xi^2\left(\frac{\partial h}{\partial x}\right)^2\right]^{-1} \tag{10}$$

where:

$K = \epsilon_0 dF^2/16\pi\mu U_0$
ϵ_f = dielectric constant of the fluid (dielectric constant for vapor is taken as unity)
ϵ_0 = $8.854(10^{-12})$ coul^2/(nt-m^2) electrical permittivity of free space
$E_{n,t}^v$ = dimensionless normal and tangential components of the electric field in the vapor at the interface
$Ca = 2\mu U_0/\sigma$ is the capillary number with σ as the surface tension

We may write:

$E_n^v = H(\partial\phi/\partial y)$
$E_t^v = (\hat{H}/L)(\partial\phi/\partial x)$

Nomenclature

A', A = Hamaker constant (J), $A'/(6\pi\rho U_0^2)$
C = curvature of the interface (m^{-1})
Ca = $2\mu U_0/\sigma$ Capillary number
d = characteristic film thickness (m)
E^v, E' = E'/F dimensionless electric field in vapor, electric field in vapor (V/m)
F = electric field strength (V/m)
Fr = Froude number
g = 9.81 m/s^2 gravitational acceleration
$\hat{H}$ = distance from charged foil to the plate (m)
h = film thickness (m)
K = $\epsilon_0 dF^2/(16\pi\mu U_0)$ constant representing square of electric field strength
L = length of plate (m)
p = pressure (Pa)
q = wave number of disturbance (m^{-1})
Re = $\rho U_0 d/\mu$ Reynolds number
t = time (s)
U_0 = reference velocity (m/s)
u, v = velocity components in x and y directions (m/s)
x, y = coordinate directions parallel and perpendicular to the plate (m)
β = angle made by the plate with horizontal direction
ϕ = electric potential (V)
ξ = d/L aspect ratio
ρ = density of fluid (kg/m^3)
μ = dynamic viscosity (Ns/m^2)
ν = kinematic viscosity (m^2/s)
ψ = Ah^{-3} dimensionless potential function for van der Waals forces
ϵ = dielectric constant
σ = surface tension (N/m)

Subscripts

0, 1 = first-order and second-order perturbations
m = maximum

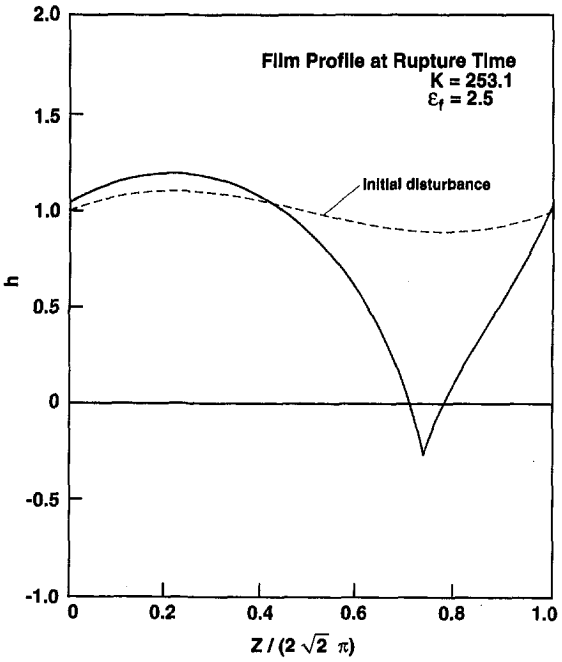

Fig. 2 Film thickness distribution at the rupture time

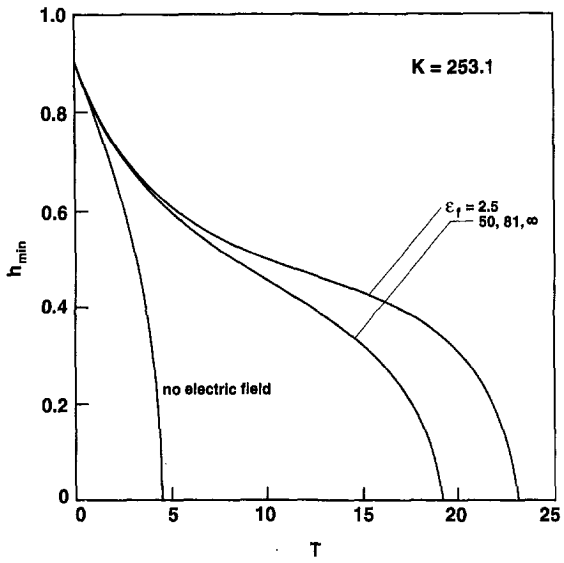

Fig. 3 Minimum film thickness versus time

Equations (3)–(10) determine the motion of the liquid film. An inspection of Eq. (10) reveals that the conditions $K = 0$ and $\epsilon_f = 1$ are equivalent. Our aim here is to solve for the stability of the liquid film while including the effect of van der Waals forces and an applied electric field.

The electric potential is given by Kim et al. (1992) in the following form:

$$\phi_0^f = \frac{y}{\epsilon_f}\left[\frac{1}{\epsilon_f} + H - 1\right]^{-1} \quad \text{for } 0 < y < 1$$

and

$$\phi_0^y = 1 + (y - H)\left[\frac{1}{\epsilon_f} + H - 1\right]^{-1} \quad \text{for } 1 < y < H.$$

We now apply the long-wave theory to study the stability problem. When the layer is thinner than a critical value, small disturbances begin to grow. These waves have wavelengths much larger than the mean thickness of the layer. Defining a small parameter κ that is related to wave number of such disturbances, we may rescale the governing equations:

$$X = \kappa x; \quad Y = y; \quad \tau = \kappa t \tag{11}$$

We assume that $\partial/\partial X$, $\partial/\partial Y$, $\partial/\partial\tau = O(1)$ as $\kappa \to 0$. Given that $u = O(1)$, Eq. (3) indicates that $v = O(\kappa)$. We now let p, $\psi = O(1/\kappa)$ as $\kappa \to 0$.

We now assume the following expansions for the flow field:

$$u = u_0 + \kappa u_1 + \kappa^2 u_2 + 0(\kappa^3)$$

$$v = \kappa[v_0 + \kappa v_1 + \kappa^2 v_2 + 0(\kappa^3)]$$

$$p = \frac{1}{\kappa}[p_0 + \kappa p_1 + \kappa^2 p_2 + 0(\kappa^3)]$$

$$\psi_0 = \kappa\psi = O(1) \quad \text{as} \quad \kappa \to 0 \tag{12}$$

Neglecting the variation of p with y and substituting expressions (12) into Eqs. (1)–(10), we get

$$u_0 = \left[-\frac{\text{Re}}{\text{Fr}^2}\sin\beta + \text{Re}\cdot\xi\cdot\frac{\partial P_0'}{\partial X}\right]\cdot\left[\frac{Y^2}{2} - hY\right] \tag{13}$$

$$v_0 = -\text{Re}\cdot\xi\cdot\frac{\partial^2 P_0'}{\partial X^2}\left[\frac{Y^3}{6} - \frac{hY^2}{2}\right] + \frac{\text{Re}}{2}\left[\frac{-\sin\beta}{\text{Fr}^2} + \xi\frac{\partial P_0'}{\partial X}\right]\left(\frac{\partial h}{\partial X}\right)Y^2 \tag{14}$$

$$p_0 = \frac{2}{\text{Re}}\cdot\left(\bar{K}E'^2 - \frac{\xi^2}{\bar{C}a}\cdot\frac{\partial^2 h}{\partial X^2}\right) - \psi_0 \tag{15}$$

where

$$\bar{K} = K\left(\frac{1}{\epsilon_f} - 1\right)\cdot\kappa; \bar{C}a = Ca/\kappa^3,$$

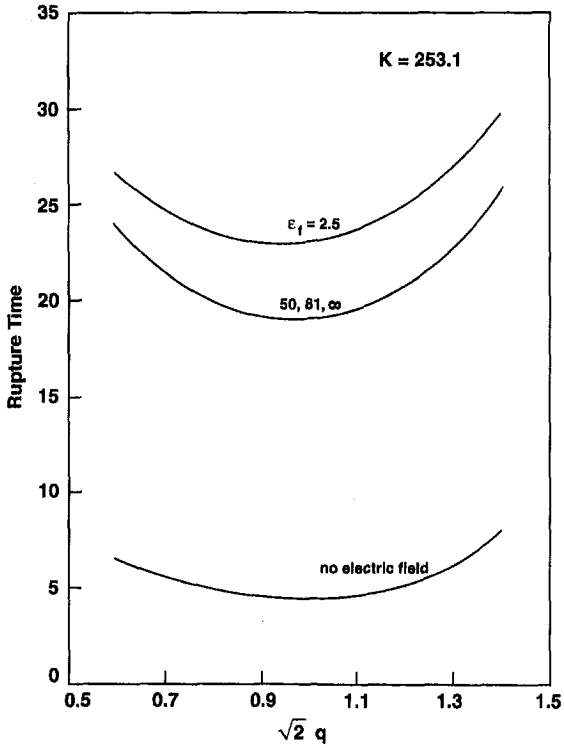

Fig. 4 Rupture time versus q (k = 253.1)

$$P_0' = P_0 + \Psi_0, E'^2 = (E_n^v)^2 + \epsilon_f (E_t^v)^2.$$

Similarly, expressions u_1, v_1, and p_1 may be derived. These expressions are not used in the computations and they are very long. Therefore, they are not reproduced here.

Using Eqs. (13)–(15) we may show that the leading order evolution equation for the film rupture is given by

$$\frac{\partial h}{\partial \tau} - \frac{h^2}{2}\left\{ -\frac{\mathrm{Re}}{\mathrm{Fr}^2}\sin\beta + \mathrm{Re}\cdot\xi\left[\frac{2}{\mathrm{Re}}\cdot\left(-\frac{\xi^2}{\bar{C}a}\cdot\frac{\partial^3 h}{\partial X^3} + \bar{K}\frac{dE'^2}{dX}\right)\right]\right\}\frac{\partial h}{\partial X} = \frac{\mathrm{Re}\xi h^3}{3}\cdot\left\{\frac{2}{\mathrm{Re}}\cdot\left(-\frac{\xi^2}{\bar{C}a}\cdot\frac{\partial^4 h}{\partial X^4} + \bar{K}\frac{d^2E'^2}{dX^2}\right)\right\} \quad (16)$$

subject to initial conditions:

$$h(X, 0) = f(X) \quad (17)$$

Equations (16) and (17) may be solved numerically in order to predict the rupture characteristics.

We now define

$$Z = \left(\frac{Ca}{\xi}\right)^{1/2} X, \quad T = (Ca)\tau \quad (18)$$

Equations (16) and (17) now reduce to the following form:

$$\frac{\partial h}{\partial T} + \frac{h^2}{2}\frac{\partial h}{\partial Z}\left[\frac{\mathrm{Re}\sin\beta}{\mathrm{Fr}^2}\cdot\left(\frac{1}{\xi Ca}\right)^{1/2} - 2K\left(\frac{1}{\epsilon_f} - 1\right)\frac{\partial E'^2}{\partial Z} + 2\xi\frac{\partial^3 h}{\partial Z^3}\right] = -\frac{2\xi h^3}{3}\frac{\partial^4 h}{\partial Z^4} + \frac{2K}{3}\cdot\left(\frac{1}{\epsilon_f} - 1\right)h^3\cdot\frac{\partial^2 E'^2}{\partial Z^2} \quad (19)$$

with initial conditions:

$$h(Z, 0) = g(Z) \quad (20)$$

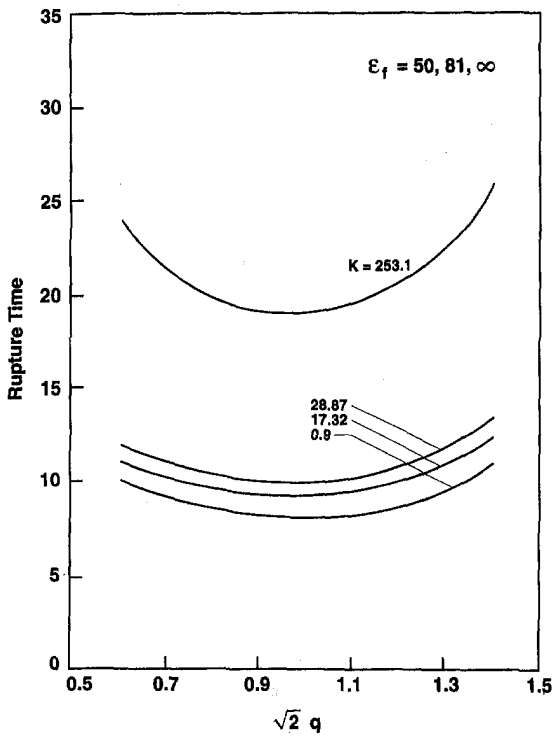

Fig. 5 Rupture time versus q (ϵ_f = 50, 81, ∞)

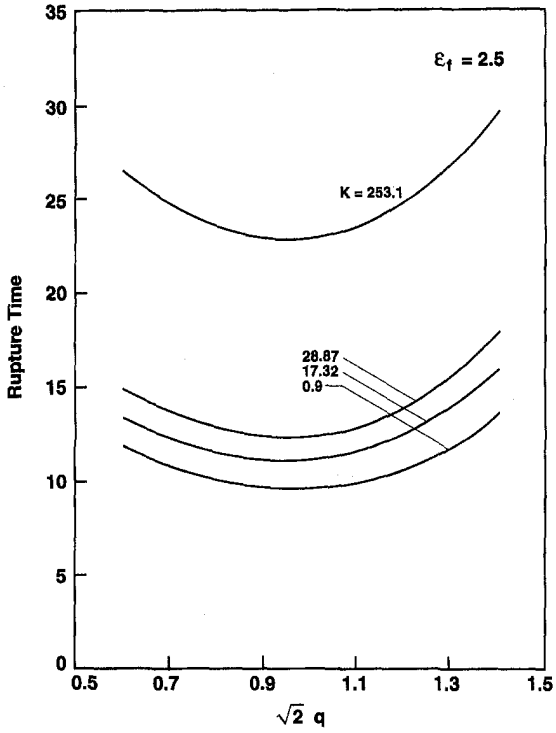

Fig. 6 Rupture time versus q (ϵ_f = 2.5)

Equation (19) governs long wave interfacial disturbances to the static film (having $h = 1$) subject to van der Waals attractions.

Results and Discussion

The nonlinear partial differential Eq. (19) was solved numerically using the finite difference method. Central differences were used for space variable and the midpoint rule was used for time. The Newton-Raphson method was used to solved the resulting system of difference equations. The problem was treated as an initial value problem with spatial periodic boundary conditions within the interval $0 < Z < 2\pi\sqrt{2}$.

In order to obtain a solution independent of the grid size, several computational runs were performed to obtain the optimum step sizes in Z and T directions. The optimization procedure of the grid size includes computing the spatial film thickness distribution at an arbitrary time, employing a given number of grid points in spatial direction. After that the number of grid points is increased gradually, each time, a computer run was performed to compute the film thickness profile. A residue is defined as the absolute difference in film thickness between the two runs. The procedure is continued until the residue approaches a value less than 1×10^{-4}. At this point the spatial grid size is fixed. A similar procedure was followed to choose the optimum time step. Based on these calculations, we used spatial grid points $N = 50$ and time steps $\Delta T = 0.001$ in all the computations.

The initial condition was given by

$$h(Z, 0) = 1 + 0.1\sin(Z/\sqrt{2}) \quad (21)$$

Equation (21) was selected because it provides a check on the accuracy of our computations when compared with those obtained by William and Davis (1982) for the case with no electric field present. All the computations were done for a horizontal plate ($\beta = 0$).

The following parameters were used in the numerical calculations:

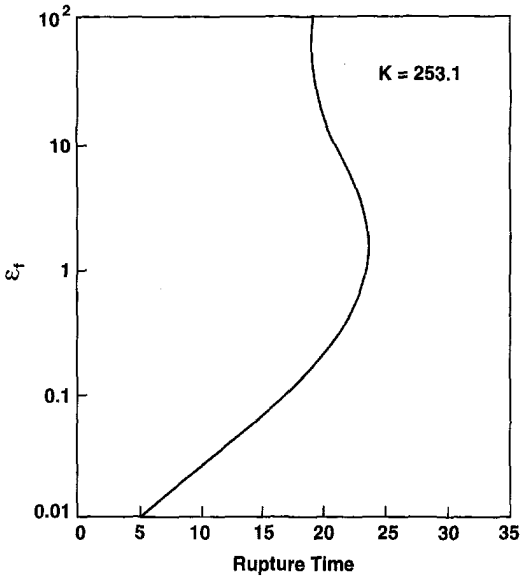

Fig. 7 Rupture time versus ϵ_f

$K = 0.9, 17.32, 28.87, 253.1; \quad \epsilon_f = 2.5, 50, 81, \infty;$

$\mathrm{Re} = 875.2; \quad H = 8; \quad \xi = 0.00025; \quad Ca = 0.0002.$

Figure 2 shows the initial disturbance introduced and the film profile at the time of film rupture. Figure 3 displays the timewise variation of minimum film thickness with and without the imposed electric field effect. When electric field is imposed, the dielectric constant ϵ_f has been chosen as a parameter. It may be observed that the rupture time increases when electric field is imposed. The transient variation of minimum film thickness for $\epsilon_f = 50$(water), 81(glycerin) and ∞ coincide within the scale of the figure. As ϵ_f decreases to 2.5(trichloromonofluoromethane R11), the rupture time increases furthermore.

Figures 4–6 show the variation of the rupture time with the wave number of disturbance, q. From Fig. 4, we observe that the mode of the wave number corresponding to the minimum value of rupture time does not change significantly as the value of ϵ_f changes. The wave numbers of these unstable modes are approximately equal to $1/\sqrt{2}$. When $\epsilon_f = 2.5$, the highest values of rupture times are obtained. As shown in Fig. 4, our results for the rupture time for the case corresponding to no imposed electric field coincide with those reported by William and Davis (1982). This shows that our results are accurate. From Figs. 5 and 6, we observe that for a given fluid, the rupture times increase as the intensity of the electric field strength is increased. Figure 7 shows the variation of rupture time with ϵ_f. The rupture time increases with ϵ_f initially, reaches a maximum around $\epsilon_f = 2$ and then decreases with ϵ_f.

Concluding Remarks

In this paper, we have formulated a long wave theory for the nonlinear dynamic instabilities of a thin liquid film interacting with an imposed electric field. Numerical solutions are obtained for the simplified form of the Navier-Stokes equations governing the dynamics of the liquid film in the presence of an electric field. The results indicate that the film rupture time may be delayed by increasing the electric field strength or using a working fluid with a significantly lower dielectric constant.

Acknowledgments

The authors are grateful to the reviewers for their useful remarks. They are thankful to Mr. Chris Clay, Chief of Thermal Structures Branch at Wright Patterson Air Force Base, for providing the facilities.

References

Bankoff, S. G., Miksis, M. J., Kim, H., and Gwinner, R., 1994, "Design Considerations for the Rotating Electrostatic Liquid Film Radiator," *Nuclear Engineering and Design*, Vol. 149, pp. 441–447.

Benjamin, T. B., 1957, "Wave Formation of Laminar Flow Down an Inclined Plane," *Journal of Fluid Mechanics*, Vol. 20, pp. 505–515.

Coward, A. V., and Renardy, Y. Y., 1995, "Small Amplitude Oscillatory Forcing on a Two-Layer Plane Channel Flow," *Bulletin of American Physical Society*, Vol. 40, pp. 1950–1956.

Kim, H., Bankoff, S. G., and Miksis, M. J., 1992, "The Effect of an Electrostatic Field on Film Flow Down an Inclined Plane," *Physics of Fluids*, Vol. 4, pp. 2117–2130.

Landau, L. D., and Lifshitz, E. M., 1960, *Electrodynamics of Continuous Media*, Pergamon Press, New York, New York.

Or, A. C., and Kelly, R. E., 1996, "Marangoni Convections of a Thin Deformable Layer of Liquid Subjected to Finite-Amplitude Nonplanar Oscillations," *Bulletin of American Physical Society*, Vol. 40, pp. 1949–1954.

Ruckenstein, E., and Jain, R. K., 1974, "Spontaneous Rupture of Thin Liquid Films," Chemical Society, *Faraday Transactions*, Vol. 270, pp. 132–146.

William, M. B., and Davis, S. H., 1982, "Nonlinear Theory of Film Rupture," *Journal of Colloid Interface Science*, Vol. 90, pp. 220–228.

Woods, D. R., and Lin, S. P., 1995, "Instability of a Liquid Film Flow Over a Vibrating Inclined Plane," *Journal of Fluid Mechanics*, Vol. 58, pp. 391–400.

Yih, C. S., 1963, "Stability of Liquid Flow Down an Inclined Plane," *Physics of Fluids*, Vol. 6, pp. 321–326.

Yih, C. S., 1968, "Instability of Unsteady Flows or Configurations, Part 1: Instability of a Horizontal Liquid Layer on an Oscillating Plane," *Journal of Fluid Mechanics*, Vol. 31, pp. 737–742.

APPENDIX

Derivation of Eqs. (9), (10), (13), (14), (15), and (16)

Figure 8 shows the interface coordinate system and a differential element of the interface. The stresses can be written in terms of components tangent and perpendicular to the interface as:

$$i = \mathrm{Cos}\ (\theta)i' - \mathrm{Sin}\ (\theta)j'$$

$$j = \mathrm{Sin}\ (\theta)i' + \mathrm{Cos}\ (\theta)j'$$

$$\bar{\tau}_{yx} = -\tau_{yx}[\mathrm{Cos}\ (\theta)i' - \mathrm{Sin}\ (\theta)j']$$

$$\bar{\tau}_{xy} = \tau_{xy}[\mathrm{Sin}\ (\theta)i' + \mathrm{Cos}\ (\theta)j']$$

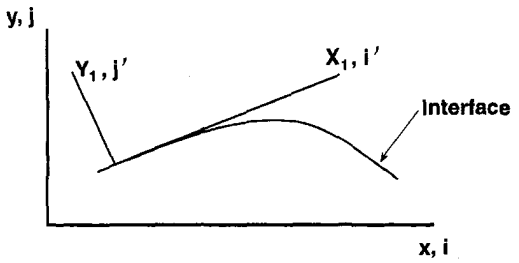

Fig. 8(*a*) Interface coordinate system

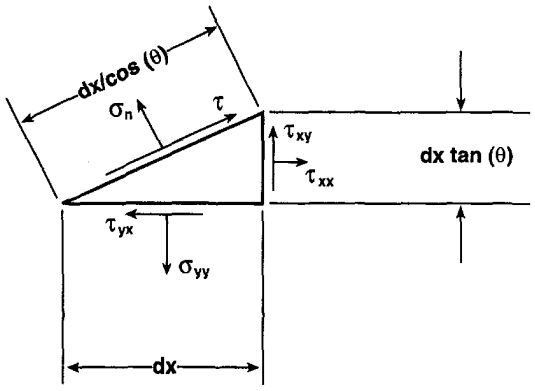

Fig. 8(*b*) Differential element of the interface

$$\bar{\sigma}_{xx} = \sigma_{xx}[\text{Cos}\ (\theta)i' - \text{Sin}\ (\theta)j']$$

$$\bar{\sigma}_{yy} = -\sigma_{yy}[\text{Sin}\ (\theta)i' + \text{Cos}\ (\theta)j'] \quad (22)$$

A force balance in the tangential direction gives:

$$\sum F_i = 0 \quad (23)$$

$$\tau\left[\frac{dx}{\text{Cos}\ (\theta)}\right] + \tau_{xy}\ \text{Sin}\ (\theta)dx\ \tan\ (\theta) + \sigma_{xx}\ \text{Cos}\ (\theta)dx\ \tan\ (\theta) - \tau_{yx}\ \text{Cos}\ (\theta)dx - \sigma_{yy}\ \text{Sin}\ (\theta)dx = 0 \quad (24)$$

If surface tension is assumed constant and the vapor viscosity is neglected, $\tau = 0$ and the force balance reduces to:

$$\tau_{xy}\lfloor -1 + \tan^2\ (\theta)\rfloor + \tan\ (\theta)(\sigma_{xx} - \sigma_{yy}) = 0 \quad (25)$$

Substituting the constitutive equations for an incompressible fluid and equating the slope to tan (θ) gives:

$$\sigma_{xx} = 2\mu\frac{\partial u}{\partial x} - p$$

$$\sigma_{yy} = 2\mu\frac{\partial v}{\partial y} - p$$

$$\tau_{xy} = \mu\left[\frac{\partial u}{\partial y} + \frac{\partial v}{\partial x}\right]$$

$$\tan\ (\theta) = \frac{\partial h}{\partial x} \quad (26)$$

From Eqs. (25) and (26) we get:

$$\left[\frac{\partial u}{\partial y} + \frac{\partial v}{\partial x}\right]\left[1 - \left(\frac{\partial h}{\partial x}\right)^2\right] + 2\frac{\partial h}{\partial x}\left(\frac{\partial v}{\partial y} - \frac{\partial u}{\partial x}\right) = 0 \quad (27)$$

Substituting the dimensionless variables defined in the text, we have:

$$\left[\frac{\partial u}{\partial y} + \xi^2\frac{\partial v}{\partial x}\right]\left[1 - \xi^2\left(\frac{\partial h}{\partial x}\right)^2\right] + 2\xi^2\frac{\partial h}{\partial x}\left(\frac{\partial v}{\partial y} - \frac{\partial u}{\partial x}\right) = 0 \quad (9)$$

Continuity of the normal stress can be written as:

$$\sigma_n\frac{dx}{\text{Cos}\ (\theta)} + \tau_{xy}\ \text{Cos}\ (\theta)\ \tan\ (\theta)dx - \sigma_{xx}\ \text{Sin}\ (\theta)\ \tan\ (\theta)dx - \sigma_{yy}\ \text{Cos}\ (\theta)dx + \tau_{yx}\ \text{Sin}\ (\theta)dx = 0 \quad (28)$$

where σ_n is the normal stress due to surface tension, electric field and disjoining pressure.

This is mathematically represented as $\sigma_n = \sigma_c + \sigma_e + \sigma_d$ where

σ_c = stress due to surface tension

$$= \sigma C = \frac{\sigma\dfrac{\partial^2 h}{\partial x^2}}{\left[1 + \left(\dfrac{\partial h}{\partial x}\right)^2\right]^{3/2}} \quad (29)$$

where C is the curvature of the interface and σ is the surface tension.

σ_e = stress due to electric field
σ_d = stress due to the disjoining pressure.

The stress tensor in an isotropic fluid due to the electric field is given by Landau (1960) as:

$$\sigma_{e,ik} = -\frac{E^2}{8\pi}\epsilon\delta_{ik} + \frac{\epsilon E_i E_k}{4\pi} \quad (30)$$

where

$E^2 = \text{E}_\text{n}^2 + \text{E}_\text{t}^2$
ϵ = permittivity

Here, n and t denote the normal and tangential components of the electric field. The disjoining pressure term is given by:

$$\sigma_d = Ah^{-3}. \quad (31)$$

Substituting Eqs. (29), (30), and (31) into the stress Eq. (28) we get:

$$\left[\frac{\sigma\dfrac{\partial^2 h}{\partial x^2}}{\left[1 + \left(\dfrac{\partial h}{\partial x}\right)^2\right]^{3/2}} - \frac{\epsilon_v E_v^2}{8\pi} + \frac{\epsilon_v E_n^{v^2}}{4\pi} - \left(-\frac{\epsilon_f E_f^2}{8\pi} + \frac{\epsilon_f E_n^{f^2}}{4\pi}\right) + Ah^{-3}\right]\left(\frac{1}{\text{Cos}\ \theta}\right) = \tau_{xy}(-2\ \text{Sin}\ (\theta)) + \sigma_{xx}\frac{\text{Sin}^2\ (\theta)}{\text{Cos}\ (\theta)} + \sigma_{yy}\ \text{Cos}\ (\theta) \quad (32)$$

The sub/superscripts v and f stand for vapor and liquid, respectively. Substituting the constitutive equations for the stresses and using the interfacial relations

$$E_t^f = E_t^v$$

$$\epsilon_f E_n^f = \epsilon_v E_n^v$$

and $\tan\ (\theta) = \partial h/\partial x$ gives upon rearrangement:

$$\frac{\sigma\dfrac{\partial^2 h}{\partial x^2}}{\left[1 + \left(\dfrac{\partial h}{\partial x}\right)^2\right]^{3/2}} + Ah^{-3} = \frac{1}{8\pi}\left\{E_n^{v^2}\left(\frac{\epsilon_v^2}{\epsilon_f} - \epsilon_v\right) - E_t^{v^2}(\epsilon_f - \epsilon_v)\right\} - p + \frac{2\mu}{\left[1 + \left(\dfrac{\partial h}{\partial x}\right)^2\right]} \times \left[-\left(\frac{\partial u}{\partial y} + \frac{\partial v}{\partial x}\right)\frac{\partial h}{\partial x} + \frac{\partial u}{\partial x}\left(\frac{\partial h}{\partial x}\right)^2 + \frac{\partial v}{\partial y}\right] \quad (33)$$

Nondimensionalizing the equation as before and in addition normalizing p by $\bar{p}/\rho U_0^2$ and E by $\bar{E}/F$ we have:

$$\frac{\dfrac{\partial^2 h}{\partial x^2}\xi^2}{\dfrac{2\mu U_0}{\sigma}\left[1 + \xi^2\left(\dfrac{\partial h}{\partial x}\right)^2\right]^{3/2}} + \frac{\rho d U_0 A h^{-3}}{2\mu} = \frac{-dF^2\epsilon_v(\epsilon_f - \epsilon_v)}{16\mu U_0\pi\epsilon_f}\left\{E_n^{v^2} + E_t^{v^2}\left(\frac{\epsilon_f}{\epsilon_v}\right)\right\} - p\frac{\rho d U_0}{2\mu} + \frac{1}{\left[1 + \xi^2\left(\dfrac{\partial h}{\partial x}\right)^2\right]}\left\{-\left(\frac{\partial u}{\partial y} + \xi^2\frac{\partial v}{\partial x}\right)\xi\frac{\partial h}{\partial x} + \frac{\partial u}{\partial x}\xi^3\left(\frac{\partial h}{\partial x}\right)^2 + \xi\frac{\partial v}{\partial y}\right\} \quad (34)$$

$$\text{Substitute Re} = \frac{\rho d U_0}{\mu}; \quad Ca = \frac{2\mu U_0}{\sigma}; \quad K = \frac{\epsilon_0 d F^2}{16\pi\mu U_0} \tag{35}$$

where ϵ_0 is the permittivity of free space. Also use ϵ_f as the dielectric constant of the liquid and assuming the dielectric constant of the vapor to be equal to unity gives:

$$\frac{\dfrac{\partial^2 h}{\partial x^2}\xi^2}{Ca\left[1+\xi^2\left(\dfrac{\partial h}{\partial x}\right)^2\right]^{3/2}} + \frac{Ah^{-3}d^{-2}}{2\mu U_0}$$

$$= K\left(\frac{1}{\epsilon_f}-1\right)\{E_n^{v^2}+\epsilon_f E_t^{v^2}\} - P\frac{\mathrm{Re}}{2} + \frac{\xi}{\left[1+\xi^2\left(\dfrac{\partial h}{\partial x}\right)^2\right]}$$

$$\times\left\{-\left(\frac{\partial u}{\partial y}+\xi^2\frac{\partial v}{\partial x}\right)\frac{\partial h}{\partial x}+\frac{\partial u}{\partial x}\xi^2\left(\frac{\partial h}{\partial x}\right)^2+\frac{\partial v}{\partial y}\right\} \tag{10}$$

The boundary conditions given by Eqs. (9) and (10) may also be obtained from Kim et al. (1992) and Landau and Lifshitz (1960).

Substituting expressions in Eq. (12) into the conservation equations, we have by collecting the coefficients of like powers of κ to the leading order:

$$\frac{\partial^2 u_0}{\partial Y^2} = -\left(\frac{\mathrm{Re}}{\mathrm{Fr}^2}\right)\mathrm{Sin}\,\beta + \mathrm{Re}\xi\left(\frac{\partial p_0}{\partial X}+\frac{\partial \psi_0}{\partial X}\right) \tag{36}$$

with boundary conditions:

$$Y = 0\text{: } u_0 = 0$$

$$Y = h(x, t)\text{: } \frac{\partial u_0}{\partial Y} = 0 \tag{37}$$

Therefore, integrating Eq. (36) and using the boundary conditions given by Eq. (37) we have:

$$u_0 = \left[-\frac{\mathrm{Re}}{\mathrm{Fr}^2}\sin\beta + \mathrm{Re}\cdot\xi\cdot\frac{\partial P_0'}{\partial X}\right]\cdot\left[\frac{Y^2}{2}-hY\right] \tag{13}$$

where $P_0' = P_0 + \Psi_0$.

We note from Eq. (5) that $\partial P_0'/\partial Y = 0$ to the leading order.

Substituting Eq. (13) into the continuity equation, namely,

$$\frac{\partial u_0}{\partial X}+\frac{\partial v_0}{\partial Y} = 0 \tag{38}$$

we have:

$$\frac{\partial v_0}{\partial Y} = -\frac{\partial u_0}{\partial X} = -\mathrm{Re}\cdot\xi\cdot\frac{\partial^2 P_0'}{\partial X^2}\left[\frac{Y^2}{2}-hY\right]$$

$$+\mathrm{Re}\left[\frac{-\sin\beta}{\mathrm{Fr}^2}+\xi\frac{\partial P_0'}{\partial X}\right]\left(\frac{\partial h}{\partial X}\right)Y \tag{39}$$

We use the no-slip boundary condition, namely,

$$Y = 0\text{: } v_0 = 0 \tag{40}$$

Upon integrating (39) and using the boundary condition given by (40), we get the following expression for v_0:

$$v_0 = -\mathrm{Re}\cdot\xi\cdot\frac{\partial^2 P_0'}{\partial X^2}\left[\frac{Y^3}{6}-\frac{hY^2}{2}\right]$$

$$+\frac{\mathrm{Re}}{2}\left[\frac{-\sin\beta}{\mathrm{Fr}^2}+\xi\frac{\partial P_0'}{\partial X}\right]\left(\frac{\partial h}{\partial X}\right)Y^2 \tag{14}$$

From Eq. (10), we have for the leading order,

$$p_0 = \frac{2}{\mathrm{Re}}\cdot\left(\bar{K}E'^2 - \frac{\xi^2}{\bar{C}a}\cdot\frac{\partial^2 h}{\partial X^2}\right) - \psi_0 \tag{15}$$

Or, we may write:

$$P_0' = \frac{2}{\mathrm{Re}}\cdot\left(\bar{K}E'^2 - \frac{\xi^2}{\bar{C}a}\cdot\frac{\partial^2 h}{\partial X^2}\right).$$

Substituting expressions for u_0, v_0 and p_0 from Eqs. (13), (14), and (15) into Eq. (8), we have for the leading order:

$$\frac{\partial h}{\partial \tau}-\frac{h^2}{2}\left\{-\frac{\mathrm{Re}}{\mathrm{Fr}^2}\sin\beta\right.$$

$$\left.+\mathrm{Re}\cdot\xi\left[\frac{2}{\mathrm{Re}}\cdot\left(-\frac{\xi^2}{\bar{C}a}\cdot\frac{\partial^3 h}{\partial X^3}+\bar{K}\frac{dE'^2}{dX}\right)\right]\right\}\frac{\partial h}{\partial X}$$

$$= \frac{\mathrm{Re}\xi h^3}{3}\cdot\left\{\frac{2}{\mathrm{Re}}\cdot\left(-\frac{\xi^2}{\bar{C}a}\cdot\frac{\partial^4 h}{\partial X^4}+\bar{K}\frac{d^2E'^2}{dX^2}\right)\right\} \tag{16}$$

The Design of a Droplet Ejector

P. Grassia
Department of Chemical Engineering,
UMIST, PO Box 88,
Manchester M60 1QD, U.K.
e-mail: PAUL.GRASSIA@umist.ac.uk

A model is developed describing a novel ink jet printer driven by a piezoelectric component used to eject a fluid droplet through a rubber valve. The model is analyzed to address specific printer design issues. Rapid droplet production and efficient conversion of piezoelectric energy to droplet kinetic energy are ensured by suitable choices of the ejector geometry and the voltage step used to produce the droplet. A parameter regime is found in which a resonance prevents the valve from closing properly, and this particular regime must be avoided for correct printer operation. By choosing a suitable voltage signal after the production of an ink droplet, the device is returned rapidly to its initial or quiescent state.

1 Introduction

This paper is concerned with the analysis of a novel droplet ejector built for use as a "drop-on-demand" ink jet printing device (Denne, 1990; Denne, 1991; and Grassia, 1994). As in other drop-on-demand printers (Dijksman, 1984) droplets are produced by supplying a driving voltage to a piezoelectric actuator which induces fluid motion along an ink delivery channel. The novel feature of the particular device that we consider is the presence of a rubber valve at the outlet which is used to regulate droplet production. The aims of this paper are (i) to present a simple mathematical model of the device, describing how the valve is coupled dynamically to the piezoelectric actuator and the fluid in the channel, and (ii) to use this model to address specific printer design issues. Design criteria require rapid delivery of droplets, with adequate volumes and speeds, and which are cleanly cut off from the valve.

Side and sectional views of the ejector are shown in Fig. 1(*a*)–(*b*), with relevant geometric, mechanical and electrical parameters for the basic printer design given in Table 1. In the figure, a piezoelectric component called a unimorph is effectively clamped to a rigid vertical back wall. The unimorph has a length l_b and breadth b. It consists of a layer of piezoelectric material known as pzt bonded to an inert glass backing. The pzt has thickness d_p, while the backing has thickness d_b, giving a total thickness d. Relevant mechanical parameters are the Young's modulus of pzt E_p, the effective Young's modulus of the unimorph as a whole $\langle E \rangle$, and the average unimorph density $\langle \rho \rangle$ (Vernitron, c1990; Kaye and Laby, 1973; Weast, 1971–72). The relevant piezoelectric parameter is the strain in free pzt per unit electric field, denoted $|d_{31}|$ by Vernitron (c1990).

Part of the unimorph distant from the clamped end is made to overlie a channel consisting of a rigid base of length l, typically about half of l_b, and with vertical side walls separated by a distance equal to b the breadth of the unimorph. The channel side walls attach to the sides of the unimorph. The channel has height h_0 and is filled with ink of density ρ. At one end the channel communicates with an ink reservoir, and at the other end it is spanned by a rubber valve.

The rubber valve at the end of the channel is shown in Fig. 2. As seen in Fig. 2(*a*), the valve consists of two triangular flaps of rubber of shear modulus μ, attached to the upper and lower boundaries of the channel. When the device is constructed the flaps are pressed together by a precompression pressure p_p, typically comparable with μ, so the valve is firmly closed when the ejector is quiescent.

The device is energized or activated by applying a voltage step V'^s across the thickness of the pzt layer of the unimorph. The unimorph bends to reduce its potential energy, similar to the bending of a bimetallic strip. The polarity of the pzt is assumed to be such that for positive applied voltage, the unimorph will execute an upstroke. Inertia carries the unimorph beyond the minimum potential energy state, and afterwards it commences a return downstroke. The side walls of the channel, to which the unimorph remains attached, deform passively along with the unimorph and have no dynamical effect on its motion. The acceleration of the unimorph induces pressure changes in the ink in the channel. When the unimorph acceleration is downward, positive pressures are induced (relative to the ink reservoir at zero pressure). If these positive pressures are larger than the precompression p_p then the valve will open and an ink jet will be ejected. Note that the unimorph deflection is far too small to lift the valve open in the absence of deforming pressures. A schematic of the open valve is shown in Fig. 2(*b*). Relatively slow moving fluid enters the valve, and is accelerated as it travels into the jet. The height of the jet itself, denoted h_j, is usually small compared to the channel height h_0, which in turn is typically small compared to the channel breadth b. Under these circumstances the jet may be treated as effectively two dimensional where it emerges from the device.

When the valve closes, the jet breaks off from the device to form a droplet. Surface tension driven dynamics cause the shape of the jet and/or droplet to relax to become circular during flight, but the opening and closing of the valve proceeds more rapidly than this. The present paper concerns itself with the unimorph, channel, and valve dynamics in which surface tension plays no role. The actual printhead consists of a number of these ejector devices stacked normal to the plane of Fig. 1(*a*), sufficiently far apart as to ensure no interference between them.

The issues we specifically want to consider are:

- How to ensure rapid droplet production with efficient conversion of electromechanical energy of the unimorph and channel to droplet kinetic energy.
- How to ensure the valve closes cleanly thereby eliminating secondary droplet production and blurred printing.
- After valve closure, how to vary the driving voltage to return the unimorph to its quiescent state ready as quickly as possible so it is ready to produce another droplet.

The structure of the remainder of the paper is as follows. In the next section we derive the simple mathematical model for the droplet ejector. After this we turn to the specific engineering design issues listed above. In Section 3 we demonstrate how to change the channel height h_0 and the driving voltage step V'^s from their base case values reported in Table 1, to guarantee rapid and efficient droplet production. Next in Section 4 we demonstrate the existence of an undesirable resonance which causes the valve to nearly close but then reopen. We isolate the parameter regime in which this occurs, with a view to avoiding it. In Section 5 we estimate the time taken to return the printer to its quiescent state

Contributed by the Fluids Engineering Division for publication in the JOURNAL OF FLUIDS ENGINEERING. Manuscript received by the Fluids Engineering Division September 3, 1997; revised manuscript received April 19, 1999. Associate Technical Editor: S. Banerjee.

and how this interval can be shortened. Conclusions are offered in Section 6.

2 Model for the Droplet Ejector

In this section we derive the model describing the coupled unimorph, channel and valve system. We define a coordinate x along the unimorph with $-\frac{1}{2}l_b \le x \le \frac{1}{2}l_b$ which places the origin at the entrance to the channel. The unimorph position relative to its quiescent position is denoted by $\zeta(x, t)$, while the deflection of the unimorph tip $\zeta(\frac{1}{2}l_b, t)$ is denoted by $a(t)$. If a voltage V' is applied, the equilibrium unimorph configuration is a parabolic shape denoted $\zeta^V(x)$, with an equilibrium tip deflection denoted a^V,

$$a^V = \frac{3d_b l_b^2 E_p}{\langle E\rangle d^3} V'|d_{31}|, \quad \zeta^V = \left(\frac{x}{l_b} + \frac{1}{2}\right)^2 a^V, \qquad (2.1)$$

these results being derived from standard formulae for the deflection of beams (Landau and Lifschitz, 1970). Table 1 gives the value of a^V corresponding to the base printer design values, and demonstrates that the unimorph tip deflection is very small compared to the channel height h_0. If $\zeta \neq \zeta^V$, a bending moment will be present, which must be balanced by the effects of fluid pressure p and unimorph inertia

$$\frac{\langle E\rangle d^3}{12}(\zeta_{xx} - \zeta^V_{xx}) = \int_x^{l_b/2} (x' - x)(p(x', t) - d\langle\rho\rangle\zeta_{tt}(x', t))dx', \qquad (2.2)$$

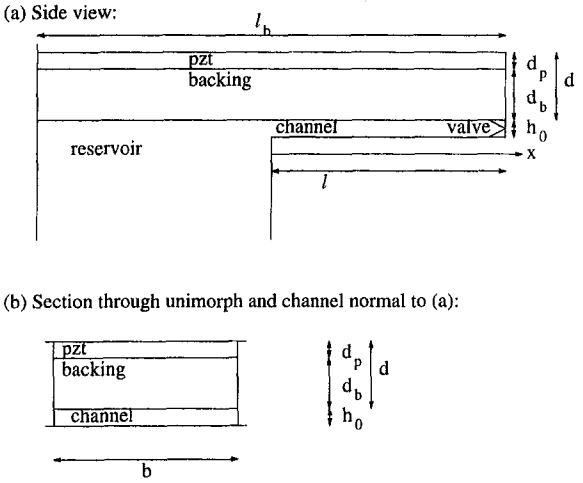

Fig. 1 The ink jet printing device. (*a*) Side view: A unimorph of length l_b consists of a top layer of piezoelectric pzt of thickness d_p, bonded to an inert backing underneath of thickness d_b, to give a total thickness d. One end of the unimorph (far left of the figure) is effectively clamped to the vertical back wall of the device. The unclamped end of the unimorph (right of the figure) overlies a channel of length $l \approx \frac{1}{2}l_b$, filled with fluid to a depth h_0. One end of the channel communicates with a fluid reservoir (lower left), while the other (lower right) contains a rubber valve, consisting of triangular rubber flaps on the top and bottom of the channel. For convenience, an x axis is defined along the channel, with the origin located at the channel entrance, and the valve at $x = l$. (*b*) Section through unimorph and channel normal to (*a*): The unimorph (pzt and backing) of total thickness d and breadth b overlies the fluid filled channel of breadth b and depth h_0. The channel side walls (left and right) attach to the sides of the unimorph. Distances in this figure are not to scale.

Nomenclature

a = unimorph tip deflection
a^V = equilibrium unimorph tip deflection in the presence of an applied voltage
A = dimensionless unimorph tip deflection
$A^{(0)}$, $A^{(1)}$ = terms in perturbation expansion for A
A_c = dimensionless unimorph tip deflection on valve closing
$\dot{A}_c$ = dimensionless unimorph tip velocity on valve closing
$|\ddot{A}|_{max}$ = maximum allowed downward acceleration for unimorph tip
b = unimorph breadth (identical to channel breadth)
d = unimorph thickness
d_b = backing thickness
d_p = pzt thickness
$|d_{31}|$ = piezoelectric parameter
$\langle E\rangle$ = unimorph Young's modulus
E_p = pzt Young's modulus
F_1 = numerical constant in Eq. (2.4)
F_2 = numerical constant in Eq. (2.5)
F_3 = numerical constant in Eq. (2.5)
$\mathcal{F}$ = reservoir fluid flux
$\mathcal{F}^{(0)}$, $\mathcal{F}^{(1)}$ = terms in perturbation expansion for $\mathcal{F}$
h_0 = channel height
h_j = jet height
H_0 = dimensionless channel height
H_j = dimensionless jet height
k = empirical constant for valve compliance
K' = empirical constant for valve stiffening
l = channel length
l_b = unimorph length
p = fluid pressure
p_e = fluid pressure at channel end/valve entrance
p_p = valve precompression pressure
P = dimensionless fluid pressure at channel end/valve entrance
$P^{(1)}$ = term in perturbation expansion for P
P_p = dimensionless valve precompression pressure
P_0 = numerical constant in Eqs. (2.9)–(2.10)
t = time
u = fluid speed at channel end/valve entrance
u_j = jet speed
U = dimensionless fluid speed at channel end/valve entrance
$U^{(0)}$, $U^{(1)}$ = terms in perturbation expansion for U
U_j = dimensionless jet speed
V' = applied voltage
V'^s = applied voltage step
V = dimensionless applied voltage
V^s = dimensionless applied voltage step
x = longitudinal coordinate in channel
x' = dummy coordinate
x'' = dummy coordinate
$\delta\tau$ = short time interval for resetting voltage following valve closure
μ = valve shear modulus
ρ = ink density
$\langle\rho\rangle$ = unimorph density
τ = dimensionless time
τ_c = dimensionless valve closing time
τ_o = dimensionless valve opening time
τ_{tot} = total ejector cycle time
ξ = dummy integration variable in Eq. (4.5)
ζ = unimorph shape
ζ^V = equilibrium unimorph shape in the presence of an applied voltage
Ω_0 = numerical constant in Eqs. (2.9)–(2.10)
Ω_∞ = numerical constant in Eqs. (2.9)–(2.10)

Table 1 Parameter values for the base design of the ejector. The values of voltage step V'^s and channel height h_0 are marked by * to indicate that they will be varied from their base values in the course of the paper. The equilibrium unimorph tip deflection a^V, proportional to V'^s will also vary.

Unimorph properties			
Geometry	Length	l_b	4 mm
	Breadth	b	0.2 mm
	Pzt thickness	d_p	0.25 mm
	Backing thickness	d_b	0.6 mm
	Total thickness	d	0.85 mm
Mechanical parameters	Pzt Young's modulus	E_p	61 GPa
	Unimorph Young's modulus	$\langle E\rangle$	60 GPa
	Unimorph density	$\langle\rho\rangle$	3800 kg m^{-3}
Piezoelectric parameter		$\lvert d_{31}\rvert$	271×10^{-12} m V^{-1}
Applied voltage step		V'^s	155 V*
Equilibrium tip deflection		a^V	2 μm*
Channel properties			
Geometry	Length	l	2 mm
	Breadth		as per unimorph
	Height	h_0	50 μm*
Ink density		ρ	1000 kg m^{-3}
Valve properties	Shear modulus	μ	0.05 MPa
	Precompression	p_p	0.05 MPa
	Empirical constant	k	0.1
	Empirical constant	K'	1.4

a result which again follows from beam theory (Landau and Lifschitz, 1970).

Unimorph deflection induces fluid velocities in the channel, and we suppose there may be an additional velocity $u(t)$ of fluid leaving the channel and entering the valve. The high aspect ratio of the channel, l/h_0 being typically 40 from Table 1, allows us to adopt a one-dimensional model to describe the fluid mechanics. Viscous drag can be neglected despite the narrowness of the channel, owing to the large unsteady inertial forces at the envisaged frequency of operation. The linearised, inviscid momentum equation gives the pressure loading in the channel as

$$\frac{p(x,\,t)}{\rho} = -\frac{1}{h_0}\int_0^x \int_{x'}^{l_b/2} \zeta_{tt}(x'',\,t)dx''dx' - xu_t(t), \quad (2.3)$$

with negligible pressure in the reservoir. The term involving ζ_{tt} in this pressure formula acts as an additional inertia term $O(l_b^2\rho/h_0 \times \zeta_{tt})$ in the equation for unimorph bending. The ratio of this "fluid loading inertia" to the actual unimorph inertia $d\langle\rho\rangle\zeta_{tt}$ is $O(l_b/h_0 \times l_b/d \times \rho/\langle\rho\rangle)$. This is usually large, roughly 100 for the data of Table 1, so the unimorph inertia will be neglected henceforth.

Approximate equations governing the time evolution of a and u can be obtained by assuming that $\zeta(x,\,t)$ always maintains a parabolic shape. We can obtain the following equations relating $a(t)$, $u(t)$ and the channel end pressure $p_e \equiv p(\frac{1}{2}l_b,\,t)$,

$$\frac{p_e}{\rho} = -a_{tt}\frac{l_b^2}{h_0}F_1 - \frac{1}{2}l_b u_t, \quad (2.4)$$

$$a_{tt} = -\frac{\langle E\rangle}{\rho}\frac{h_0 d^3}{l_b^6}(a - a^V)F_2 - \frac{h_0}{l_b}u_t F_3, \quad (2.5)$$

where F_1, F_2 and F_3 are numerical constants arising from the assumption of a parabolic unimorph shape: $F_1 = 0.0885$, $F_2 = 7.245$ and $F_3 = 4.528$. When $p_e < p_p$ the valve is closed so that $u \equiv 0$ and Eq. (2.5) can be immediately solved given $a^V(t)$. When $p_e > p_p$ the valve opens and responds quasistatically to the pressure p_e driving it. An empirical relation between the pressure p_e at the valve entrance and the instantaneous height of the emergent jet h_j is adopted (Denne and King, 1991)

$$\frac{h_j}{1 - K'h_j/h_0} = h_0\frac{k}{\mu}(p_e - p_p). \quad (2.6)$$

Here recall μ is the shear modulus, whereas K' and k are constants depending on valve geometry, with values $K' = 1.4$ and $k = 0.1$ for the particular valves that we have considered. The factor $1/(1 - K'h_j/h_0)$ on the left-hand side of the above equation represents a nonlinear stiffening of the valve with $K'h_j/h_0$ being a measure of the valve strain. The ratio k/μ represents an effective elastic compliance for the valve deformation. We write the speed of the fluid entering the jet as u_j. This can be related to u and h_j by matching the flux entering the valve to that entering the jet (mass conservation) and by using the Bernoulli equation between the entrance to the valve and the jet

$$uh_0 = u_j h_j, \quad \frac{p_e}{\rho} + \frac{1}{2}u^2 = \frac{1}{2}u_j^2. \quad (2.7)$$

Viscous forces remain negligible in the jet and moreover a *steady* Bernoulli equation is employed, justified by the small longitudinal extent of the valve and by the relatively large ratio of jet speed to channel fluid speed.

Equations (2.4)–(2.7) form a complete set for the open valve given $a^V(t)$.

2.1 Dimensionless Equations. We make t, a, V', p_e, h_j and both u and u_j dimensionless using the scales $(k\rho/\mu)^{1/2}l_b$, $\mu/k\langle E\rangle \times l_b^4/d^3$, $\mu/kE_p \times \frac{1}{3}l_b^2/d_b|d_{31}|$, μ/k, h_0 and $(\mu/k\rho)^{1/2}$, and we denote the dimensionless analogues of these variables by τ, A, V, P, H_j, U, and U_j. We also identify three dimensionless groups: dimensionless voltage step V^s, dimensionless channel height H_0, and dimensionless precompression P_p.

$$V^s = \frac{E_p k}{\mu}\frac{3d_b|d_{31}|}{l_b^2}V'^s, \quad H_0 = \frac{\langle E\rangle k}{\mu}\frac{d^3 h_0}{l_b^4}, \quad P_p = \frac{p_p k}{\mu}. \quad (2.8)$$

Based on the dimensional values $V'^s = 155$ V, $h_0 = 50$ μm and $p_p = 0.05$ MPa reported in Table 1, and other data given in that table, typical dimensionless values are $V^s = 0.5757$, $H_0 = 14.39$, and $P_p = 0.07$.

Rearranging Eqs. (2.4)–(2.5) gives

$$\ddot{A} = H_0\Omega_\infty^2\left(-(A - V) + \left(1 - \frac{\Omega_0^2}{\Omega_\infty^2}\right)\frac{P}{P_0}\right), \quad (2.9)$$

$$\dot{U} = \frac{2\Omega_\infty^2 P_0}{\Omega_0^2}\left(A - V - \frac{P}{P_0}\right). \quad (2.10)$$

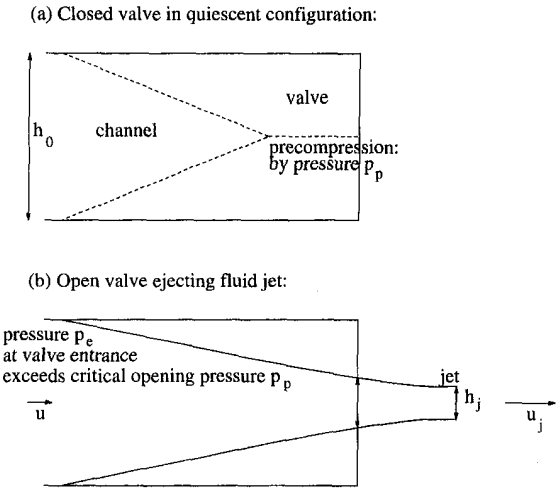

Fig. 2 The valve in detail. (*a*) Closed valve in quiescent configuration: The valve (right side of figure) consists of triangular upper and lower rubber flaps, which are pushed together into contact by a precompression pressure p_p. The height of the valve from top to bottom is h_0. The fluid filled channel extends to the left. (*b*) Open valve ejecting fluid jet: Owing to the precompression, the two flaps of the valve only cease to be in contact when the pressure exerted by the channel fluid at the valve entrance p_e exceeds p_p. Fluid enters the valve with velocity u (left side of the figure), and accelerates through the valve orifice. A parallel jet of height h_j and velocity u_j results (right side of the figure).

Here Ω_0, Ω_∞ and P_0 are numerical constants, which for the assumed parabolic unimorph shape are $\Omega_0 = F_2^{1/2} = 2.691$, $\Omega_\infty = F_2^{1/2}/(1 - 2F_1F_3)^{1/2} = 6.047$, and $P_0 = F_1F_2 = 0.641$.

When $P < P_p$ the valve is closed and $U \equiv 0$. In Eqs. (2.9)–(2.10) this implies

$$P/P_0 = A - V \Rightarrow \ddot{A} = -H_0\Omega_0^2(A - V), \qquad (2.11)$$

which must be solved with initial conditions $A = \dot{A} = 0$. When $P > P_p$ the valve opens and we can show from Eqs. (2.6)–(2.7)

$$U = \frac{\sqrt{2P}}{\sqrt{1 - \left(\dfrac{P - P_p}{(P - P_p)K' + 1}\right)^2}} \times \frac{P - P_p}{(P - P_p)K' + 1}, \qquad (2.12)$$

which must be used to determine P given U. Once P and U are known, Eq. (2.7) gives

$$H_j = \frac{U}{\sqrt{2P + U^2}}, \quad U_j = \sqrt{2P + U^2}. \qquad (2.13)$$

2.2 Driving Voltage Signal. In Eqs. (2.9)–(2.10) and (2.11) we must specify the applied voltage $V(\tau)$. For simplicity we assume that V is held constant at the voltage step value V^s until after the droplet is ejected and the valve has closed. The valve opening and closing times will be denoted τ_o and τ_c. After τ_c, $V(\tau)$ must be varied so that the unimorph returns to the quiescent state. The aim is to accelerate the unimorph as quickly as possible to the quiescent state, subject to the constraint that the valve remains closed $P \leq P_p$. From the closed valve Eq. (2.11) it follows $\ddot{A} = -H_0\Omega_0^2P/P_0$, so that downward accelerations correspond to positive pressures. Hence the maximum allowed downward acceleration $|\ddot{A}|_{max}$ is

$$|\ddot{A}|_{max} = H_0\Omega_0^2P_p/P_0. \qquad (2.14)$$

The constant downward acceleration needs to be driven by a constant unimorph bending moment, meaning that voltage changes are tied to unimorph motion, according to Eq. (2.11)

$$V(\tau) = A(\tau) - P_p/P_0. \qquad (2.15)$$

The downward acceleration reduces A but will tend to increase the downward unimorph speed $|\dot{A}|$. When A reaches the neighbourhood of zero, V can be switched to a large positive value to halt the unimorph essentially impulsively. Then A and $\dot{A}$ vanish simultaneously, and if V is switched to zero, the quiescent state is achieved.

In our calculations we realized the downward acceleration phase by changing V in a sequence of small steps and ramps reset on intervals $\delta\tau = 0.2/H_0^{1/2}\Omega_0$. This kept $|\ddot{A}|$ very close to the maximum $|\ddot{A}|_{max}$ at all times. The final "impulsive" voltage was applied for a duration not exceeding $2\delta\tau$, with a finite voltage value chosen according to duration.

The equations are solved by an explicit midpoint scheme far from the times of valve opening and closing, but by an implicit scheme near τ_o and τ_c to ensure that these points coincide with the end of a time step. Equation (2.12) is solved for P by Newton's rule. At the point of opening we can show that $\dot{U}$ vanishes in addition to U, so a formula for $\ddot{U}$ needs to be deduced to retain accuracy in the vicinity of $\tau \approx \tau_o$.

2.3 Droplet Volume, Speed, and Energy. Droplet production is regulated by valve opening and closing, not by the surface tension effects in the emergent jet. The volume and momentum flux in the jet between τ_o and τ_c can be used to predict the dimensionless droplet volume and speed to be $H_0\int_{\tau_o}^{\tau_c} U d\tau$ and $\int_{\tau_o}^{\tau_c} UU_j d\tau / \int_{\tau_o}^{\tau_c} U d\tau$ respectively. A useful energy equation can be derived in the usual way from the equations of motion,

$$\frac{F_1\Omega_0^2}{2F_3}(A - V^s)^2 + H_0\left(\frac{F_1}{2F_3}\frac{\dot{A}^2}{H_0^2} + F_1\frac{\dot{A}}{H_0}U + \frac{1}{4}U^2\right) = \frac{F_1\Omega_0^2}{2F_3}V^{s2} - H_0\int_{\tau_o}^{\tau} UP d\tau, \qquad (2.16)$$

which applies as long as V remains fixed at the value V^s. On the left-hand side the first term represents the potential energy of the unimorph, and the remaining terms describe the kinetic energy of the fluid in the channel, partly induced by the unimorph swing and partly arising from any fluid moving along the channel to the valve. When the valve is closed $U \equiv 0$ and the sum of potential and kinetic energies equals the energy supplied to the system on activation (the first term on the right-hand side). When the valve opens, the second term on the right represents the work done by the unimorph channel system on the emerging jet. Evaluating the work done between times τ_o and τ_c allows us to determine how efficiently the electromechanical energy of the unimorph and channel is converted to droplet kinetic energy.

Another useful quantity is the flux of fluid, denoted $\mathcal{F}$, drawn from the reservoir into the channel which is found to be $\mathcal{F} = 2\dot{A}F_1 + UH_0$. This is again the sum of a part associated with the unimorph swing and another part due to the valve flux. The dimensionless analogue of Eq. (2.4) gives

$$2H_0P = -2\ddot{A}F_1 - \dot{U}H_0 \equiv -\dot{\mathcal{F}}, \qquad (2.17)$$

which says that pressure differences between the valve region and the zero pressure reservoir are responsible for decreasing the net flux drawn from the reservoir. We shall make use of this result later in the paper.

3 Selecting Good Operating Parameters

Now we perform a parametric study of the model subject to variation of the dimensionless voltage step V^s and channel height H_0. For simplicity we fix the dimensionless precompression $P_p = 0.07$, as in Section 2.1. Initially we also consider a fixed value $H_0 = 14.39$ as in Section 2.1 corresponding to the nominal values of Table 1. We shall find that V^s must be large enough to guarantee adequate valve opening, but that excessive values of V^s should be avoided as they unnecessarily increase the total operation time of the ejector and also, as we shall see, give undesirable valve behavior. After this we consider an H_0 value ten times larger than before. This has the desirable effect of decreasing the fluid loading allowing for faster droplet production.

3.1 The Effect of Changing Voltage Step V^s. We have performed calculations for dimensionless voltage steps V^s of 0.143, 0.5757, 1.0 and 1.2, which we shall call cases A–D. The corresponding dimensional voltages V'^s are 38.6 V, 155 V, 269 V and 323 V. Case B corresponds to the data of Table 1.

In Fig. 3, the driving voltage V is plotted against τ for each case we consider. The valve closing point τ_c is characterized by a small downward step in voltage, following which V varies in an apparently continuous curve, corresponding to a downward unimorph acceleration $|\ddot{A}|_{max}$. Next there is an impulsive positive V which halts the unimorph, and then V is restored to zero. For the present section and the one following we are concerned with the dynamics only up to time τ_c for which V is the constant V^s. In this case, prior to valve opening at time τ_o, the unimorph executes simple harmonic motion of amplitude V^s. The pressure P here is $(A - V^s)P_0$, so from Eq. (2.11) the valve can only open when $P_p/P_0V^s < 1$. Note that P_p/P_0V^s ranges from 0.763 to 0.091 for the data considered here so valve opening is guaranteed in all cases.

The results for the unimorph tip deflection A vs time τ are plotted in Fig. 4 with analogous results for the pressure at the valve entrance P vs τ in Fig. 5. The valve opening and closing points for A are marked by crosses in Fig. 4. Note that P exhibits discontinuities whenever the applied voltage is discontinuously changed,

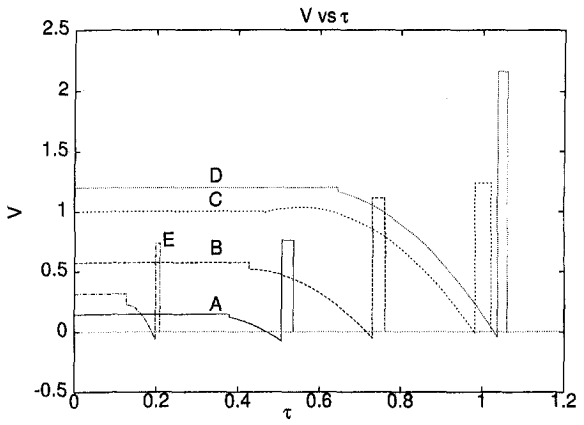

Fig. 3 Varying voltage signal V versus time τ for various values of dimensionless voltage step V^s and dimensionless channel height H_0. Continuous line $V^s = 0.143$, $H_0 = 14.39$ (case A); long dashes $V^s = 0.5757$, $H_0 = 14.39$ (case B); intermediate dashes $V^s = 1.0$, $H_0 = 14.39$ (case C); short dashes $V^s = 1.2$, $H_0 = 14.39$ (case D); dot-dash line $V^s = 0.316$, $H_0 = 143.9$ (case E). In all cases the valve opening pressure P_p is 0.07. Voltage signal V is held fixed at V^s until valve closure at time τ_c. Upon closure V is switched discontinuously to $A - P_p/P_0$ and then is changed in a sequence of short steps and ramps, which appears to be a curved line in the figure. This corresponds to a stage of downward unimorph acceleration. Finally, V is switched discontinuously to a large positive value, thereby decelerating the unimorph, and then to zero as the quiescent unimorph state is achieved. One unit of V corresponds to a voltage of 269 V and one unit of τ is 0.179 ms.

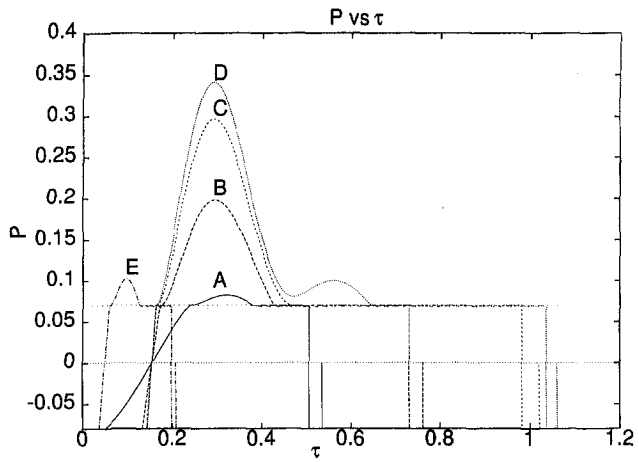

Fig. 5 Valve pressure P versus time τ for various values of dimensionless voltage step V^s and dimensionless channel height H_0. Continuous line $V^s = 0.143$, $H_0 = 14.39$ (case A); long dashes $V^s = 0.5757$, $H_0 = 14.39$ (case B); intermediate dashes $V^s = 1.0$, $H_0 = 14.39$ (case C); short dashes $V^s = 1.2$, $H_0 = 14.39$ (case D); dot-dash line $V^s = 0.316$, $H_0 = 143.9$ (case E). The valve opening pressure $P_p = 0.07$ is shown by dots. Valve opening occurs when $P = P_p$, at which point the P curves show a discontinuous slope. Valve closure occurs when P falls back to P_p. After valve closure P is determined by the varying voltage signal applied to the unimorph. The signal is such that P at first remains roughly P_p, but later P switches to a large negative value, and then finally switches to zero, when the quiescent unimorph state is achieved. One unit of P corresponds to a pressure of 0.5 MPa and one unit of τ is 0.179 ms.

and has slope discontinuities when $P = P_p$ on valve opening and closing. As long as the valve stays open, the data for $P - P_p$ are qualitatively similar to those for U, U_j, and H_j, so we have not supplied plots of these latter quantities. In Table 2 we have also summarized some of the important properties for each of cases A–D. These include the peak pressures encountered, the peak valve strains given by $K'H_j$ (which by Eq. (2.6) can never exceed unity), information about the droplet volume, speed and energy, plus the total time taken during the ejector cycle.

It is clear from the graphs that A and P cease to be harmonic upon valve opening and indeed P/P_0 falls below $A - V^s$ as U grows according to Eq. (2.10). Observe that Eq. (2.9) describes oscillations for A with angular frequency $H_0^{1/2}\Omega_0$ when $P/P_0 = A - V^s$, but with a larger angular frequency $H_0^{1/2}\Omega_\infty$ when P/P_0 is negligible. The actual situation after valve opening should be between these two extremes, but in general we can expect the graph of A vs τ to become more tightly curved after the valve opens. This is as observed in Fig. 4.

The degree of anharmonicity experienced after time τ_o is correlated with the amount of valve opening. Anharmonicity can be measured by comparing the peak positive P to the peak negative pressure swing P_0V^s which occurs on application of the voltage step. The comparison is given in Table 2. For case A the ratio of these pressures is 0.898, which is relatively near unity, meaning the departure from harmonic motion is small. Larger departures are observed for cases B–D, the ratios of the pressure swings then being 0.536, 0.462, and 0.443. In Table 2 low anharmonicity corresponds to small valve strains, as well as small droplet volumes and kinetic energies. For instance, case A exhibits valve strains about nine times smaller than case B, droplet volumes more than 20 times smaller and droplet energies more than forty times

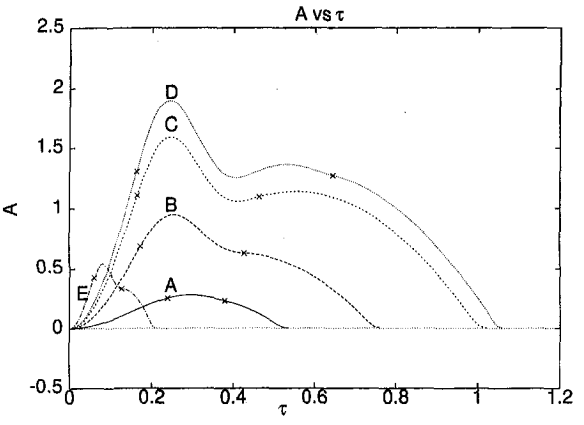

Fig. 4 Unimorph tip height A versus time τ for various values of dimensionless voltage step V^s and dimensionless channel height H_0. Continuous line $V^s = 0.143$, $H_0 = 14.39$ (case A); long dashes $V^s = 0.5757$, $H_0 = 14.39$ (case B); intermediate dashes $V^s = 1.0$, $H_0 = 14.39$ (case C); short dashes $V^s = 1.2$, $H_0 = 14.39$ (case D); dot-dash line $V^s = 0.316$, $H_0 = 143.9$ (case E). The valve opening and closing points are marked ×. In all cases the valve opening pressure P_p is 0.07. For the parameter values we have quoted in Sections 1–2, one unit of A corresponds to a tip height of 3.47 μm and one unit of τ is 0.179 ms.

Table 2 Numerical predictions of ink jet printer performance for various values of driving voltage step V'^s and channel height h_0. The dimensionless analogues of these variables, namely V^s and H_0, are also quoted in the table to facilitate comparison with Figs. 4–5. In all cases, the dimensionless precompression P_p is equal to 0.07 while $P_0 = 0.641$ is a numerical constant. Volumes, speeds, energies, and times have been converted back to dimensional variables by multiplying the dimensionless quantities by $\mu/k\langle E\rangle \times bl_b^5/d^3$, $(\mu/k\rho)^{1/2}$, $\mu/k \times \mu/k\langle E\rangle \times bl_b^5/d^3$, and $(k\rho/\mu)^{1/2}l_b$.

	Case A	Case B	Case C	Case D	Case E
Input Parameters:					
V'^s voltage step (V)	38.6	155	269	323	85.3
V^s	0.143	0.5757	1.0	1.2	0.316
h_0 channel height (μm)	50	50	50	50	500
H_0	14.39	14.39	14.39	14.39	143.9
Deductions:					
maximum value of P	0.0824	0.1979	0.2962	0.3411	0.1020
(maximum P)/P_0V^s	0.898	0.536	0.462	0.443	0.503
maximum strain in valve	0.0171	0.1519	0.2405	0.2751	0.0429
droplet volume (10^{-12} m^3)	0.0164	0.3803	0.7895	1.0508	0.2066
droplet speed (m s^{-1})	8.93	13.04	15.70	16.36	9.74
droplet energy (μJ)	0.0007	0.0324	0.0966	0.1405	0.0099
% energy conversion	32.2%	99.1%	98.1%	99.1%	99.8%
total time taken (ms)	0.0958	0.1364	0.1828	0.1898	0.0373

smaller. Case A also corresponds to inefficient conversion of electromechanical energy of the channel and unimorph to droplet kinetic energy, with only 32.2% of the energy being converted. Energy conversion for cases B–D averages around 99%.

Case D in Figs. 4 and 5 is interesting in that two peaks are observed for each of A and P *while the valve remains open.* We refer to this behavior as a "multiple peak cycle." This implies that the valve will open, nearly close and then open up again, which is undesirable as it could lead to secondary droplets and thereby blurred printing. We consider the physical reasons for this behavior and ways to avoid it in Section 4.

It is desired that the ejector produce droplets as quickly as possible. Although the valve opening time τ_o decreases as V^s increases as seen on Figs. 4 and 5, the valve stays open for longer, and the valve closing time τ_c is actually an increasing function of V^s. The time between τ_c and the attainment of the final quiescent state also increases with V^s. This is because the unimorph deflection A on closing is greater for large V^s, and we are only allowed to apply a maximum downward acceleration $|\ddot{A}|_{\max}$ to restore the unimorph to its quiescent zero deflection position. From Table 2 droplets are produced at a rate of roughly 10 kHz for case A, falling to 5 kHz for case D. From this parametric study, we conclude that P_p/P_0V^s must be small enough to guarantee valve opening with efficient energy conversion to the droplet, but not so small as to produce undesirable multiple peak cycles or to increase greatly the cycle time for the ejector.

3.2 The Effect of Changing Channel Height H_0. The effect of increasing the dimensionless channel height H_0 is to decrease the fluid loading inertia, and thereby to give a faster ejector response, with droplet ejection time scaling as $H_0^{-1/2}$. In Figs. 4–5 and Table 2 we consider a data set called case E for which $H_0 = 143.9$, corresponding to $h_0 = 500$ μm for our data, giving a channel height ten times larger than cases A–D. The ejector can now produce droplets at a frequency roughly 25 kHz, i.e. much higher than cases A–D. We have chosen a value $V^s = 0.316$ for case E corresponding to $V'^s = 85.3$ V which happens to give a particularly efficient conversion of energy to the droplet 99.8%. This parameter combination also avoids the undesirable multiple peak cycles found in case D. Although the droplet volumes and speeds for case E are less than for cases B–C say, the differences are less than an order of magnitude. According to the model case E gives better operating conditions than any of cases A–D.

We have included only fluid loading inertia in the model and ignored unimorph inertia. The relative importance of these two effects is $O(l_b/h_0 \times l_d/d \times \rho/\langle\rho\rangle)$. For the data of Table 1 with $h_0 = 50$ μm as in cases A–D this ratio is about 100, whereas for for case E with $h_0 = 500$ μm it is only about 10. Further increases in h_0 would give higher frequency ejector responses in the model, but in the actual device unimorph inertia must eventually become important and an upper limit on frequency will result. The one-dimensional model of the fluid mechanics also loses validity as the aspect ratio l/h_0 falls, and for case E we note this ratio is only 4 and the applicability of the model is questionable.

4 Regime of Improper Valve Closure

The purpose of this section is to analyze the occurrence of multiple peak cycles, with the objective of determining the parameter values required to avoid them. We shall find these cycles arise in a parameter regime where the valve barely manages to close, but a resonant perturbation then contrives to keep it open. This regime must be avoided for successful ejector operation.

Recall from Section 2.3 that the flux $\mathcal{F}$ drawn from the reservoir has one part associated with the unimorph swing $2\dot{A}F_1$ and another associated with the flow through the valve UH_0. Consider the case when fluid flux drawn from the reservoir remains very nearly constant after valve opening, but is simply redistributed between the two components. From Eq. (2.17) we see that the effect of pressure P must be very weak here. This occurs in the parameter regime $V^sH_0 \gg 1$, as we verify by the following argument. Remembering that F_1, Ω_0, Ω_∞, and P_0 are $O(1)$ numerical constants, we see immediately that the solutions of Eqs. (2.9)–(2.10) will vary on time scales typically $O(H_0^{-1/2})$, and hence we estimate $\dot{A}$ and UH_0 as both $O(V^sH_0^{1/2})$. If we impose the condition $P_p^{3/2} \ll V^sH_0^{-1/2}$ then we can neglect P_p in Eq. (2.12). For *mathematical* convenience we shall additionally assume $V^sH_0^{-1/2} \ll 1$, and then with $K' = O(1)$ Eq. (2.12) reduces to

$$P = U^{2/3}/2^{1/3}. \tag{4.1}$$

It is then apparent that $P = O(V^{s\,2/3}H_0^{-1/3})$, implying that for $V^sH_0 \gg 1$, $\dot{\mathcal{F}} \equiv -2H_0P$ is smaller than either $2\ddot{A}F_1$ or $\dot{U}H_0$ by a factor $(V^sH_0)^{-1/3} \ll 1$. From Eq. (2.17) the reservoir flux $\mathcal{F}$ is nearly constant to within this factor as long as the valve is open.

We adopt a perturbation expansion when the valve is open

$$\begin{aligned} A &= A^{(0)} + (V^sH_0)^{-1/3}A^{(1)} + \ldots, \\ U &= U^{(0)} + (V^sH_0)^{-1/3}U^{(1)} + \ldots, \\ \mathcal{F} &= \mathcal{F}^{(0)} + (V^sH_0)^{-1/3}\mathcal{F}^{(1)} + \ldots, \\ P &= (V^sH_0)^{-1/3}P^{(1)} + \ldots. \end{aligned} \tag{4.2}$$

The leading order solutions are found to be

$$A^{(0)} = V^s\left(1 + \frac{\Omega_0}{\Omega_\infty}\sin H_0^{1/2}\Omega_\infty(\tau - \tau_o)\right),$$

$$U^{(0)} = V^sH_0^{-1/2}\frac{2P_0}{\Omega_0}(1 - \cos H_0^{1/2}\Omega_\infty(\tau - \tau_o)). \tag{4.3}$$

Using Eq. (2.17) and noting from Section 2.1 that $F_1 \equiv P_0/\Omega_0^2$, we deduce $\dot{\mathcal{F}}^{(0)} = V^sH_0^{1/2} \times 2P_0/\Omega_0$ and therefore $\dot{\mathcal{F}}^{(0)} \equiv 0$. Observe that $U^{(0)}$ falls to zero at a time $\tau_o + 2\pi/H_0^{1/2}\Omega_\infty$, but the valve only barely manages to close since $\dot{U}^{(0)}$ also vanishes at this point.

The pressure $P^{(1)}$ can be determined by substituting $U^{(0)}$ into Eq. (4.1), to obtain

$$P^{(1)} = V^s\frac{2^{1/3}P_0^{2/3}}{\Omega_0^{2/3}}(1 - \cos H_0^{1/2}\Omega_\infty(\tau - \tau_o))^{2/3}. \tag{4.4}$$

This in turn can be substituted into Eqs. (2.9)–(2.10) to derive $A^{(1)}$ and $U^{(1)}$. The details are complicated but the key result is that $P^{(1)}$ has a component varying at frequency $H_0^{1/2}\Omega_\infty$, so that $A^{(1)}$ has a resonant response. The phase relationship of the resonance causes the unimorph to be moving upward *slower* at time $\tau_o + 2\pi/H_0^{1/2}\Omega_\infty$ than at time τ_o.

As $P^{(1)}$ is always positive by Eq. (4.4), the reservoir flux at first order $\mathcal{F}^{(1)}$ is a decreasing function of time according to Eq. (2.17). However, the resonant decrease in unimorph flux $2\dot{A}^{(1)}F_1$ between times τ_o and $\tau_o + 2\pi/H_0^{1/2}\Omega_\infty$ *more than compensates* the decrease in reservoir flux between these times. The flux discrepancy must then be diverted to the valve.

If we evaluate $U^{(1)}$ when $\tau = \tau_o + 2\pi/H_0^{1/2}\Omega_\infty$ we obtain

$$\begin{aligned} &U^{(1)}(\tau_o + 2\pi/H_0^{1/2}\Omega_\infty) \\ &= V^sH_0^{-1/2}\frac{P_0^{2/3}}{\Omega_0^{2/3}\Omega_\infty}\left(\frac{\Omega_\infty^2}{\Omega_0^2} - \frac{7}{2}\right) \\ &\times \int_0^{2\pi} 2^{4/3}(1 - \cos\xi)^{2/3}(-\cos\xi)d\xi \\ &= 5.828\ V^sH_0^{-1/2}\frac{P_0^{2/3}}{\Omega_0^{2/3}\Omega_\infty}\left(\frac{\Omega_\infty^2}{\Omega_0^2} - \frac{7}{2}\right). \end{aligned} \tag{4.5}$$

Since $\Omega_\infty^2/\Omega_0^2 = 5.047 > \frac{7}{2}$, Eq. (4.5) gives a positive value. Thus even though the valve barely closes at time $\tau_o + 2/H_0^{1/2}\Omega_\infty$ for the leading order solution $U^{(0)}$, the resonant unimorph motion

$(V^s H_0)^{-1/3} A^{(1)}$ keeps $(V^s H_0)^{-1/3} U^{(1)}$ positive there, meaning the valve stays open. After time $\tau_o + 2\pi/H_0^{1/2}\Omega_\infty$, $U^{(0)}$ grows giving a second peak for the $U(\tau)$ curve. Depending on the parameter values yet more peaks could occur before the valve finally closes.

The above analysis demonstrates the existence of multiple peak cycles when $V^s H_0 \gg 1$ at least for $P_p^{3/2} \ll V^s H_0^{-1/2} \ll 1$. Increasing P_p should make valves close more readily and hence eliminate multiple peak cycles. Increases in V^s or decreases in H_0 both lead to increases in $V^s H_0^{-1/2}$, and thereby larger U values for which Eq. (4.1) loses validity. The equation is most strongly violated near the peak $U^{(0)}$ where nonlinear stiffening of the valve leads to increases in the peak $P^{(1)}$. This can actually increase the likelihood of multiple peak cycles as it gives stronger resonances for $A^{(1)}$ and $U^{(1)}$. In fact, for fixed $P_p = 0.07$, the critical V^s for onset of multiple peak cycles is found numerically to be a slowly increasing function of H_0, taking the value 1.03 for $H_0 = 14.39$ and rising to 1.45 for $H_0 = 143.9$.

5 Time to Achieve Final Quiescent State

In Section 2.2 we described the voltage signal required to return the unimorph to its quiescent state consisting of an initial downward acceleration $|\ddot{A}| = |\ddot{A}|_{\max} \equiv H_0\Omega_0^2 P_p/P_0$, followed by an essentially impulsive upward acceleration. In all cases considered, the latter phase is of negligible duration compared to the former (see e.g., Fig. 3). The cycle time for the ejector, denoted τ_{tot} say, is therefore roughly the sum of the valve closing time τ_c and the downward acceleration period.

If the unimorph position and velocity on closing are A_c and $\dot{A}_c$ then we have

$$\tau_{\text{tot}} \approx \tau_c + \frac{P_0\dot{A}_c}{H_0\Omega_0^2 P_p} + \sqrt{\left(\frac{P_0\dot{A}_c}{H_0\Omega_0^2 P_p}\right)^2 + \frac{2P_0 A_c}{H_0\Omega_0^2 P_p}}. \quad (5.1)$$

If the unimorph velocity on closing is negligible we have $\tau_{\text{tot}} \approx \tau_c + (2P_0A_c/H_0\Omega_0^2P_p)^{1/2}$. Since A_c can be expected to scale like V^s, this is an increasing function of V^s, but it is a decreasing function of H_0. In the limit $P_p \to 0$ the quiescent state can only be reattained if $\dot{A}_c < 0$ and Eq. (5.1) reduces to $\tau_{tot} \approx \tau_c + A_c/|\dot{A}_c|$.

In summary, large H_0 values reduce the period $\tau_{\text{tot}} - \tau_c$ since they permit larger downward accelerations owing to lesser fluid loading. Excessive V^s values are undesirable since a given acceleration is required to move the unimorph tip over a larger distance.

6 Conclusions

The simplified model of the droplet ejector makes the following predictions. Faster droplet production can be ensured by increasing the channel height h_0 which decreases the fluid loading inertia. This mechanism will operate up to $h_0 = O(\rho/\langle\rho\rangle \times l_b^2/d)$, at which point unimorph inertia, which has been excluded from our analysis, becomes comparable with the fluid loading inertia. The valve will only open if the dimensionless voltage step V^s satisfies $P_p/P_0V^s < 1$ or equivalently if $V'^s > \frac{1}{3}P_0 \times p_p/E_p \times l_b^2/d_b|d_{31}| \equiv 0.520\ p_p/E_p \times l_b^2/d_b|d_{31}|$. The dimensionless voltage step V^s must not, however, become too large because the large V^s asymptotics, with P_p assumed negligible, predict improper valve closure and multiple peak cycles owing to a resonance. After valve closure, the unimorph tip must be accelerated downward. The quiescent state is achieved most rapidly if this downward acceleration is as large as possible without reopening the valve. The maximum allowed dimensionless acceleration $|\ddot{A}|_{\max} = H_0\Omega_0^2P_p/P_0$ requires a dimensionless voltage equal to $V(\tau) = A(\tau) - P_p/P_0$. This corresponds to a dimensional acceleration $|a_{tt}^V| = \Omega_0^2/P_0 \times p_p h_0/\rho l_b^2 \equiv 11.3\ p_p h_0/\rho l_b^2$ and a voltage $V'(t) = \langle E\rangle/3E_p \times d^3a(t)/d_b l_b^2|d_{31}| - \frac{1}{3}P_0 \times p_p/E_p \times l_b^2/d_b|d_{31}| \equiv \langle E\rangle/3E_p \times d^3a(t)/d_b l_b^2|d_{31}| - 0.520\ p_p/E_p \times l_b^2/d_b|d_{31}|$.

Acknowledgment

The author acknowledges financial support from a Hackett Studentship awarded by the University of Western Australia, from CCE Contract CI*-CT91-0947 awarded by FONDECYT in Chile, and from NASA grants NAG3-1475-S1 and NAG3-1943. The author thanks Dr. W. Denne of Domino Printing Services PLC for inviting him to study the printing device. Dr. Denne and Mr. M. King have supplied experimental results. The assistance of Dr. E. J. Hinch of Cambridge University and Prof. G. M. Homsy of Stanford University is also acknowledged.

References

Denne, W. of Domino Printing Services PLC, 1990, *Ink Jet Nozzle/Valve, Pen and Printer,* International patent classification B41J 2/14. International publication number WO 90/12691.

Denne, W., 1991, *Slit Printer Technical Manual (1.0),* Domino Printing Services.

Denne, W., and King, M., 1991, Personal Communication.

Dijksman, J., 1984, "Hydrodynamics of Small Tubular Pumps," *Journal of Fluid Mechanics,* Vol. 139, pp. 173–191.

Grassia, P., 1994, *The Design of an Ink Jet Printer,* Ph.D. thesis. University of Cambridge.

Kaye, G., and Laby, T., 1973, *Tables of Physical and Chemical Constants,* Longman.

Landau, L., and Lifschitz, E., 1970, *Theory of Elasticity,* Pergamon Press Ltd.

Vernitron Division, c1990, *Piezoelectric Ceramics,* Morgan Matroc Ltd.

Weast, R. (ed.), 1971–72, *CRC Handbook of Chemistry & Physics,* The Chemical Rubber Co.

Unsteady Deformation and Internal Circulation of a Liquid Drop in a Zero Gravity Uniform Flow

Mohammad Farshchi
Assistant Professor,
Mechanical Engineering Department,
Sharif University of Technology,
Tehran, Iran

Mohammad Hassan Rahimian
Assistant Professor,
Mechanical Engineering Department,
University of Tehran,
Tehran, Iran
e-mail: rahimyan@chamran.ut.ac.ir

Numerical simulation of the internal and external flow fields of a liquid drop moving in the surrounding gas are considered. The present work is concerned with the time accurate numerical solution of a two phase flow field at the low Mach number limit with an appropriate volume tracking method to capture motion and deformation of a liquid drop. In particular, deformation of a liquid drop moving with a coflowing gas stream in a zero gravity field is simulated. The effects of the gas flow Reynolds number and drop Weber number on the deformation dynamics of the drop have been investigated. There appears to be a critical gas stream Reynolds number, at moderate drop Weber numbers, below which the coflowing drop takes on an oblate cap shape and above which it forms an arrow head shape. It has been shown that an observer moving with the average velocity of the liquid drop sees interesting recirculatory flow patterns inside the drop.

Introduction

Dynamics of drops and bubbles are of great importance in a wide range of scientific and engineering applications. Design of variety of devices, from liquid rocket motors to blood pumping machines requires detail knowledge of drop and bubble dynamics in a fluid flow. There is a large body of work dealing with this subject, under the general heading of multi-phase flows. Here, deformation dynamics of single relatively large drop moving with a coflowing fluid flow in zero gravity field is of interest. However, being motivated by the desire to eventually analyze vaporization and combustion of a large deforming drop, two major areas of work were reviewed. The first area is mainly concerned with deformation dynamics of drops and bubbles. Clift et al. (1978) have presented a comprehensive collection of research in this area. Most of the work collected in their book are qualitative experimental results and very few computational work are presented. Rallison (1984) and Acrivos (1987) have reviewed relatively recent work concerned with the deformation of drops and bubbles in idealized creeping shear flows. Bently and Leal (1986) studied drop deformation in pure straining and simple shearing flow fields and used perturbation theory to develop a model for drop deformation in such flow fields. Yiantsios and Higgins (1989) also used the Stokes flow approximation to simulate the formation of two-dimensional drops due to a Rayleigh-Taylor instability in a thin viscous film for fluids of equal viscosity. More recently Kennedy et al. (1994) used boundary element method to simulate three-dimensional deformation of a drop in a Stokes simple shearing flow. Numerical methods used in the above studies can not be applied to drop deformation calculations at a finite Reynolds number, where inertia effects play a major role.

Stationary bubble deformation in a steady finite Reynolds number liquid flow was simulated by Ryskin and Leal (1984) and Christov and Volkov (1985). Ryskin and Leal used finite difference method with boundary fitted coordinate system to solve vorticity-stream function formulation of the Navier-Stokes equations for the steady rise of a deformable inviscide axisymetric bubble. The viscosity and density of the bubble were neglected and flow field inside the gas bubble was not solved for. Their solutions encompass Reynolds and Weber numbers in the range, $1 < We < 20$, and $1 < Re < 200$, and show variety of shapes and flows. Dandy and Leal (1989) extended this method to study buoyancy driven steady rectilinear motion of an axisymmetric bubble through a quiescent liquid. Their simulations for the first time pointed to the important role of the Reynolds number, indicating that at lower Reynolds numbers the shape of the bubble tends toward a spherical cap with increasing Weber number, but at higher Reynolds numbers the bubble becomes more disk shaped with increasing Weber number.

Unsteady numerical simulation of the initial deformation of a two-dimensional bubble moving under gravity in an inviscid incompressible liquid, using boundary integral method, was conducted by Baker and Moore (1989). There was a qualitative agreement between their results and experimental results of Walter and Davidson (1962), producing an approximately two dimensional air bubble in thin vertical slab of water. Unverdi and Tryggvason (1992) used an unstructured grid moving through a stationary grid to successfully simulate unsteady two and three dimensional rise of a buoyant bubble and bubbles collision.

A large number of experimental investigations, as well as the above numerical studies, have led to a reasonably good understanding of the motion and deformation of single buoyant bubble rising in an ambient fluid. However, we are not aware of any work concerning the dynamics of a drop set on motion by a coflowing fluid stream. On the other hand, application of the above methods to numerical simulation of a combusting drop would be either theoretically very difficult or computationally inaccessible.

The second body of work reviewed here is concerned with numerical methods used to study combustion of liquid drops. The early combustion researchers assumed the drop to be either stationary or moving at a very low speed such that the dominant Reynolds number values were much less than one. Consequently, the convective effects were negligible leading to a considerable simplification of the drop burning problem. Sadhal and Ayyaswamy (1983) attempted to improve this restriction by application of perturbation theory to low Reynolds number drop motion. At the same time other researchers, notably Sirignano (1983), used the boundary layer theory to analyze the flow field around a moving drop at much larger Reynolds numbers. In this method, an inviscid external velocity field is imposed on a laminar boundary

Contributed by the Fluids Engineering Division for publication in the JOURNAL OF FLUIDS ENGINEERING. Manuscript received by the Fluids Engineering Division July 26, 1998; revised manuscript received April 19, 1999. Associate Technical Editor: P. M. Sockol.

layer surrounding a spherical drop. The chemically reacting boundary layer equations are solved for a fixed geometry drop. This solution is used to obtain boundary calculations needed to solve the drop's internal flow field. This method can capture major physical processes occurring during the vaporization and combustion of a hydrocarbon drop.

Numerical investigation of unsteady vaporization and combustion of a hydrocarbon drop was conducted by Dwyer and Sander (1986). They solved the complete set of momentum, energy and species equations for ignition and burning of a drop. Detailed description of this approach is given by Dwyer (1989). All of the above researchers assumed that the drop retains its original shape and that motion through the gaseous flow field would not change the shape of the drop.

Given the above background a simple and computationally accessible method was sought that can capture the deformation dynamics of a large drop and at the same time be compatible with approaches used to study the combustion of a drop. Therefore a conventional volume tracking method using a marker function, see Hirt and Nichols (1981), along with an efficient interface curvature determination technique proposed by Ashgriz and Poo (1991), are used to capture deformation of a liquid drop subjected to a convective gaseous flow field. Consistent and complete balancing of kinematics and dynamic conditions at the liquid-gas interface is used to obtain the desired solution. A time implicit fractional step type method is used to capture pressure and velocity fields with proper coupling at a low Mach number limit.

The theoretical formulation and the low Mach number solution method are presented in following sections. Next the numerical solution method is considered followed by discussion of the surface tracking technique. Finally the results obtained for convection and deformation of a liquid drop in a coflowing gas field at a wide range of Reynolds and Weber numbers are presented.

Theoretical Formulation

The governing transport equations for a low Mach number flow field consisting of a gaseous flow around a liquid drop can be presented by the continuity and momentum equations at each point of the flow field. These equations and related boundary conditions are nondimensionalized using the diameter, d, of an undeformed drop as the characteristic length scale, the uniform streaming gas velocity at infinity, U_0, as the characteristic velocity scale, and $\rho_g U_0^2$ as the pressure scale with ρ_g being the gas density. The dimensionless equations, neglecting gravitational force, are given as

Gas field:

$$\nabla \cdot \vec{V} = 0 \tag{1}$$

$$\frac{\partial \vec{V}}{\partial t} + \vec{V} \cdot \nabla \vec{V} = -\nabla P + \mathrm{Re}_g^{-1} \nabla^2 \vec{V} \tag{2}$$

$$\text{B.C.} \begin{cases} \vec{V} = \hat{\vec{V}} & \text{at drop interface} \quad (3) \\ \vec{V} \rightarrow \vec{e}_x & \text{at far field} \quad (4) \end{cases}$$

where $\vec{e}_x$ is the unit vector in the x-direction

Liquid field:

$$\nabla \cdot \hat{\vec{V}} = 0 \tag{5}$$

$$\frac{\partial \hat{\vec{V}}}{\partial t} + \hat{\vec{V}} \cdot \nabla \hat{\vec{V}} = -\frac{1}{\zeta} \nabla \hat{P} + \mathrm{Re}_l^{-1} \nabla^2 \hat{\vec{V}} \tag{6}$$

$$\text{B.C.} \begin{cases} \hat{\vec{V}} = \vec{V} & \text{at drop interface} \quad (7) \\ (\vec{\vec{T}} - \hat{\vec{\vec{T}}}) \cdot \vec{n} = \dfrac{\zeta}{\mathrm{We}} \left(\dfrac{1}{R_1} + \dfrac{1}{R_2} \right) \vec{n} & (8) \end{cases}$$

where $\vec{\vec{T}}$ is the gas field dimensionless stress tensor defined as

$$\vec{\vec{T}} = -P\vec{\vec{I}} + \mathrm{Re}_g^{-1} (\nabla \vec{V} + \nabla \vec{V}^+) \tag{9}$$

and $\hat{\vec{\vec{T}}}$ is the liquid field dimensionless stress tensor defined as

$$\hat{\vec{\vec{T}}} = -\hat{P}\vec{\vec{I}} + \zeta\, \mathrm{Re}_l^{-1} (\nabla \hat{\vec{V}} + \nabla \hat{\vec{V}}^+) \tag{10}$$

and $\vec{n}$ is unit normal to the interface, defined to be positive when pointing into the gas field. R_1 and R_2 are the dimensionless radii of curvature of the interface in any two orthogonal planes containing $\vec{n}$, being reckoned positive when the corresponding center of curvature lies on the side of the interface to which $(-\vec{n})$ points, see Batchelor (1970). Four independent dimensionless groups appearing in the above transport equations and the corresponding boundary conditions are defined as: $\mathrm{Re}_g = \rho_g U_0 d/\mu_g$, $\mathrm{Re}_l = \rho_l U_0 d/\mu_l$, $\mathrm{We} = \rho_l U_0^2 d/\sigma$, and $\zeta = \rho_l/\rho_g$ where σ is the liquid surface tension and subscripts l and g refer to the liquid and gas fields respectively. Superscript $\hat{}$ refers to the nondimensionalized liquid field variables. Gas field variables have no superscripts.

Here a two-dimensional drop is considered. However, it is straightforward to extend the method to three dimensions. Therefore, the governing equations are expanded in a two-dimensional rectangular coordinate system. In a two-dimensional space, i.e., for a cylindrical drop, one of the radii of the curvature goes to infinity and the remaining radius of the surface curvature can be given by

$$\frac{1}{R} = \frac{|Y_{xx}|}{(1 + Y_x^2)^{3/2}} \tag{11}$$

where $Y(x)$ is the parametric representation of the interface curve. Equation (8) represents the vectorial continuity of the stresses across the drop interface. Tangential stress continuity condition is then given as

$$\zeta\, \mathrm{Re}_l^{-1} \frac{\partial \hat{V}_t}{\partial n} = \mathrm{Re}_g^{-1} \frac{\partial V_t}{\partial n} \tag{12}$$

and the normal stress continuity condition is given as

$$\hat{P} - 2\zeta\, \mathrm{Re}_l^{-1} \frac{\partial \hat{V}_n}{\partial n} = P - 2\, \mathrm{Re}_g^{-1} \frac{\partial V_n}{\partial n} + \frac{\zeta}{\mathrm{We}} R^{-1} \tag{13}$$

Exact pressure field specification in single phase low Mach number flow field is not necessary, since it is the pressure gradient that drives the flow field and not the level of absolute pressure. However, for two phase flows the pressure and velocity field inside the drop are caused by the external gas field shear and normal stresses and pressure. Therefore the exact level of pressure inside the liquid drop must be specified. To obtain the dynamic balance between the gas and liquid flow fields the complete set of governing equations are solved. First given the velocity at the liquid surface in the previous time step, as boundary condition for the gas field, velocity and pressure in the gas are solved. Using the gas velocity and pressure around the liquid, stress boundary conditions given by Eqs. (12) and (13), and the equality of the normal component of the interface velocity, given by Eq. (7), the flow field inside the liquid drop is solved. This leaves equality of the tangential component of the interface velocity, given by Eq. (7), to be satisfied. In order to do this, iterations are required. That is, the gas and liquid fields and above conditions should be iterated until the tangential components of gas and liquid velocities are equated. This means that converged solution, satisfying all boundary conditions, has been obtained at a given time step. Next the deformation of the liquid is obtained for the given complete flow field dynamics.

Low Mach Number Solution Method

Calculation of the velocity and pressure fields is a major obstacle for low Mach number flow solvers. As the Mach number goes to zero for incompressible flow fields, the speed of sound (pressure

wave) goes to infinity with respect to the flow velocity, causing a stiffness in the velocity-pressure fields. This means that pressure is no longer coupled, through density, to the velocity field and is merely a driver, or a source term, for the momentum field. The correct pressure field is the one resulting in a divergence free velocity field. The fact that there is no direct pressure transport equation necessitate the consideration of the continuity equation as a means to obtain the correct pressure field. To overcome this difficulty one can presume that the velocity field reaches it's final value in two stages. The first stage is designed to account for transport terms. The second stage is to correct the obtained velocity field for the pressure effects, whereby assuring a divergence-free velocity field. This results in a Poisson equation for the pressure field. The corrected pressure distribution is then used to correct the velocity field. This fractional step type method ensures proper velocity-pressure coupling for incompressible flow fields. For detail discussion see Farshchi et al. (1995).

Numerical Solution Method

Governing equations should be integrated in space using a numerical method. The first step is to choose an appropriate spatial cell network over which flow variables would be evaluated. Two dimensional problems require determination of two components of the velocity vector and pressure at each point in the flow field. Traditionally, to avoid pressure field decoupling between adjacent cells in the grid network, staggered cells are used, Patankar (1980). Staggered cell system uses three overlapping cells for two components of velocity and pressure. This is done such that for a given pressure cell, pressure is defined at the cell center and the x and y components of velocity are defined at the x and y faces of that cell. This method is naturally well suited to the physics of the flow field where over any velocity cell, velocity is driven by the pressure gradient across that cell and pressure should be given at the cell surface. However, the complexities introduced by the staggered grid system in a two phase flow problem and the need to track the liquid surface, necessitates the use of a single cell network for all variables and a collocated specification of variables at center of each cell.

The collocated specification of flow variables requires a special technique to prevent pressure decoupling between adjacent cells. The Rhie and Chow (1983) method is used here. This method subtracts the central difference pressure gradient term from the solution of the intermediate step velocity field, then instead adds a pressure gradient term to the pressure Poisson equation. This sequence has the identical effect as using a staggered grid.

Flow fields around rigid obstacles are usually transformed from the physical space to a computational space. This transforms the curvilinear, non uniform mesh of the physical space to a rectangular uniform spacing grid, in which the rigid bodies' complex geometrical surfaces become simple surfaces on the boundary of computational space. This method is not well suited to problems with moving boundaries, such as a liquid drop problem, in which the obstacle is not rigid and its boundary changes with time. Regriding of the physical domain and a new transformation is required at every time step. This is very time consuming and not practical. The method presented here subdivides the whole flow field, including the liquid drop, using single mesh system. The cells that are filled, with liquid are distinguished from the gas field cells by a void fraction parameter, F. The value of this parameter is unity for liquid filled cells and goes to zero for purely gas filled cells, $0 < F < 1$. Boundary cells at the gas-liquid interface must be identified in the flow field calculations. If a gas-liquid boundary cell has a void fraction, F, larger than one-half, it is considered a liquid cell and liquid properties are assigned to it. If the void fraction value is less than one-half the cell is considered a gas cell and gas properties are assigned to it. The volume tracking method, discussed later, also uses this parameter to capture the liquid surface movement.

Numerical solution of the momentum transport equation requires integration of momentum diffusion and convection terms. The momentum diffusion terms are handled with an alternating direction implicit (ADI) method. The differencing of the convective terms requires special attention to flow regions with cell Reynolds numbers greater than two, Patankar (1980). To obtain a stable and oscillation free solution with a high order of accuracy several modern methods have been advanced in recent years. A simple treatment is to use second-order central differencing at cells with cell Reynolds numbers less than two, and first-order upwind differencing at cells with higher local Reynolds number. This is known as hybrid method and it's application does not provide satisfactory results. A three point interpolation scheme called QUICK (Quadratic Upwind Interpolation for Convective Kinematics), see Leonard (1979) is used here. This method provided satisfactory results presented in the next section.

Surface Tracking Method

A conventional volume tracking method using a marker function, see Hirt and Nichols (1981), along with an efficient interface curvature determination technique called, the Flux Line Segment Model for Advection and Interface Reconstruction (FLAIR) proposed by Ashgriz and Poo (1991), are used to capture the liquid surface. To track the moving and deforming liquid surface a void fraction marker function is defined over the entire flow field. The method requires an evenly spaced grid intervals resulting in a square cell two-dimensional mesh. The value of the void fraction function ranges from zero for fully gas filled cells to one for fully

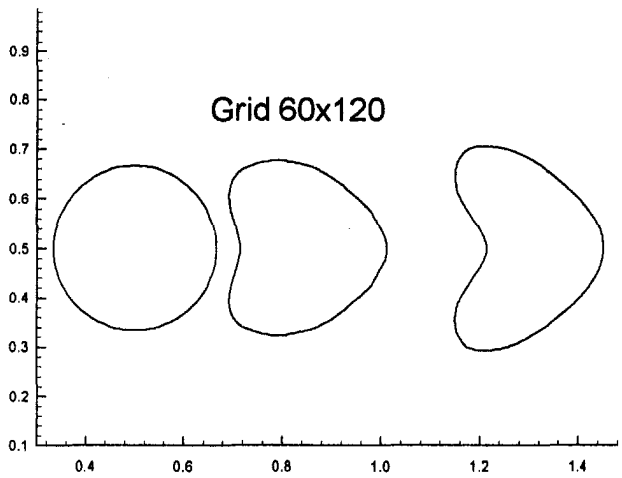

Fig. 1(*a*) Drop deformation sequence at t = 0, 0.24, 0.6

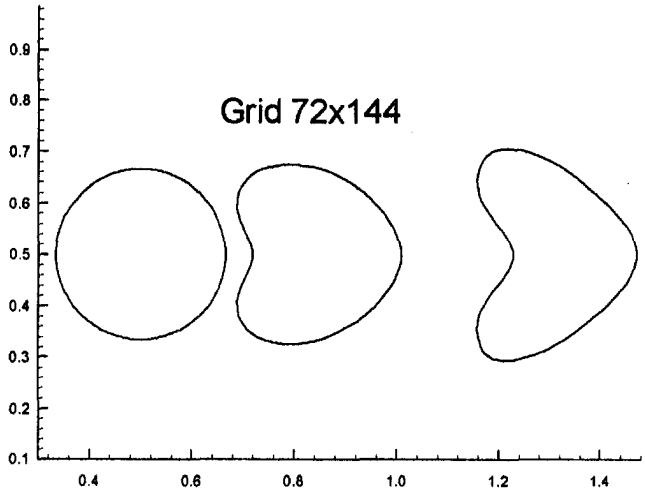

Fig. 1(*b*) Drop deformation sequence at t = 0, 0.24, 0.6

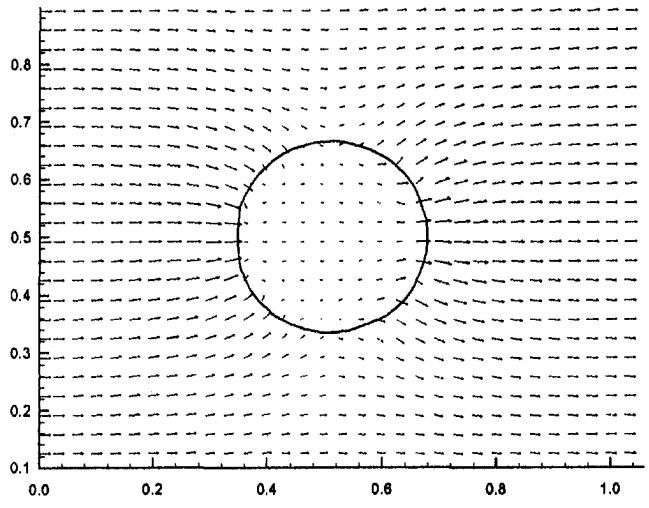

Fig. 2(*a*) Velocity vector field at $t = 0.02$ $Re_g = 20$, $Re_l = 200$, We = 8, $\zeta = 400$

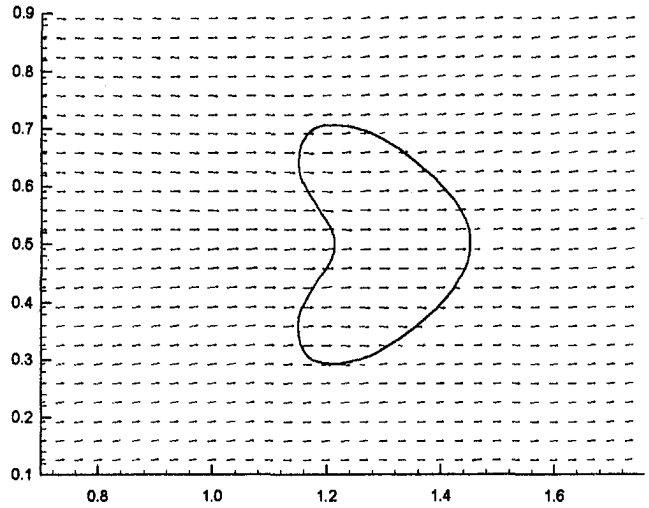

Fig. 2(*b*) Velocity vector field at $t = 0.6$ $Re_g = 20$, $Re_l = 200$, We = 8, $\zeta = 400$

liquid filled cells. The liquid drop geometry provides the means by which the value of the void fraction function is determined in each cell. The liquid surface line in a drop boundary cell determines the fraction of the space occupied by the liquid. This is the value of the void fraction function in that cell. The advection of these surface line segment through the flow field determines the liquid drop deformation. All possible surface line position between two adjacent cells are considered and an algorithm for relating advection of liquid from one cell to it's neighboring cell is obtained through the solution of the transport of the void fraction function in the flow field, governed by the equation $\partial F/\partial t + \vec{V} \cdot \nabla F = 0$. Ashgriz and Poo (1991) provides a complete description of the theory and application of this method.

Results and Discussion

To show the general robustness of the flow solver several different flow fields at a wide range of Reynolds numbers have been considered. The interested reader is referred to Farshchi et al. (1995) for detail discussion of the above results. Here the transient translation and deformation of a liquid drop in a uniform gas stream, as a function of the four aforementioned dimensionless parameters of the problem are studied. To do this an idealized situation, in which a stationary drop is swept away by a uniform gas stream moving from left to right, is considered. The gas flow over the liquid drop initiates its motion and deformation. An undeformed liquid drop with diameter d and surface tension σ is placed in a gas stream with uniform velocity U_0. Time is nondimensionalized using the free stream velocity and the drop diameter. Drop locations and respective deformations are presented for different values of this nondimensionalized time scale. The calculations are started with the whole flow field being at rest except for the inflow plane, which moves with the uniform velocity U_0. Nonreflecting boundary conditions are used at top and bottom of the gas flow domain, allowing appropriate out flux. The left boundary condition is a uniform inflow, and the right boundary condition is an out flow condition. A personal computer with an Intel Pentium (200 MHz) CPU and 32 Meg RAM is used to perform the computational work. An average run takes one and half hours on the above computer. To evaluate grid dependency of the results, deformation of a typical liquid drop with We = 8, $Re_g = 20$, $Re_l = 200$, and $\zeta = 400$, at three different time levels, are calculated on a 60×120 and a 72×144 points grid networks and compared in figures (1*a*) and (1*b*). The 44 percent increase in the number of grid points has not caused a noticeable change in the results. Therefore 60×120 points grid network is used for the rest of calculations.

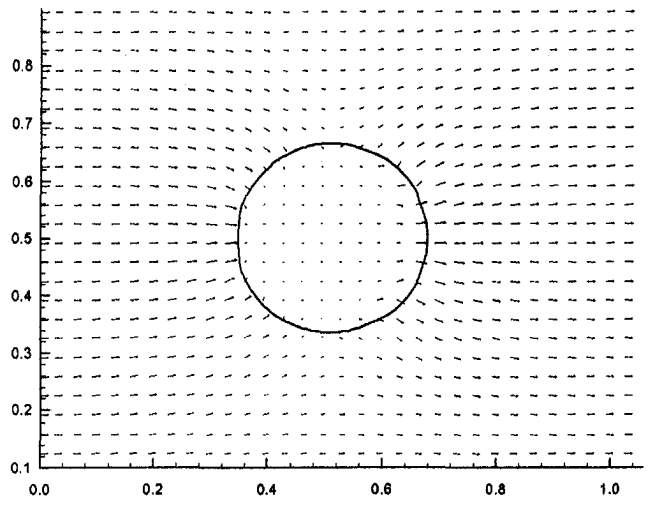

Fig. 3(*a*) Velocity vector field at $t = 0.02$ $Re_g = 1$, $Re_l = 200$, We = 8, $\zeta = 400$

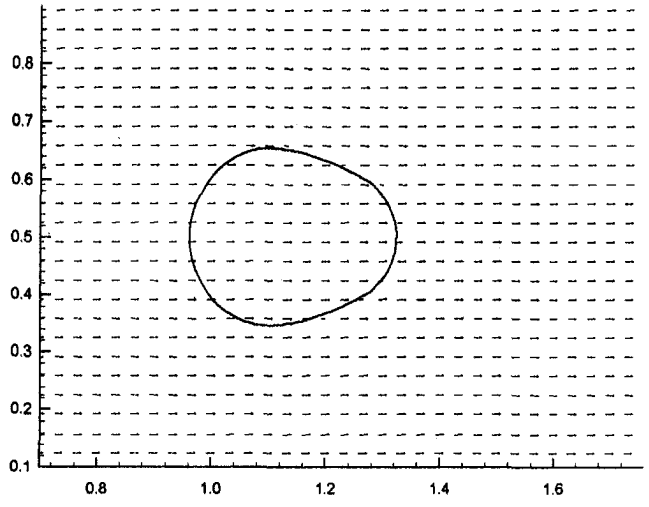

Fig. 3(*b*) Velocity vector field at $t = 0.6$ $Re_g = 1$, $Re_l = 200$, We = 8, $\zeta = 400$

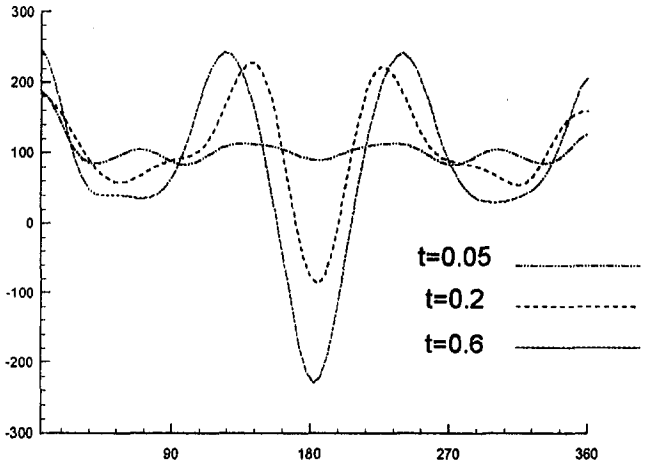

Fig. 4 Pressure difference at drop surface, $Re_g = 20$

The time accurate numerical method used here provides the ability to capture the drop's internal as well as external flow fields simultaneously. Therefore two important issues can be addressed and analyzed. One is the deformation dynamics of the accelerating drop, and the other is the internal flow field of the drop as it accelerates in the gaseous flow field. The internal dynamics of the drop can provide some insight into the drop shape changes. The range of values of the controlling dimensionless parameters considered here are as follows:

$$0.1 \leq Re_g \leq 50, \quad 100 \leq Re \leq 300,$$

$$0.25 \leq We \leq 32, \quad 85 \leq \zeta \leq 400$$

Examination of velocity vector field for the reference case of $Re_g = 20$, $Re_l = 200$, $We = 8$, and $\zeta = 400$ indicates that at normalized time $t = 0.02$ very little deformation has taken place and the gas velocities near the liquid surface are much larger than the velocities inside the drop, causing large pressure gradient across the drop, Fig. 2(*a*). Later, at time $t = 0.6$ the drop has deformed considerably and velocity field across the drop is almost uniform, Fig. 2(*b*). Figures 3(*a*) and 3(*b*) show the same time sequences as above for a gas field with $Re_g = 1.0$, causing less displacement and far less deformation of the drop in this case. The difference between the liquid and gas pressure across the drop surface, according to Eq. (13), are shown in Figs. 4 and 5 at times $t = 0.05$, 0.2, and 0.6 for above cases respectively. Horizontal

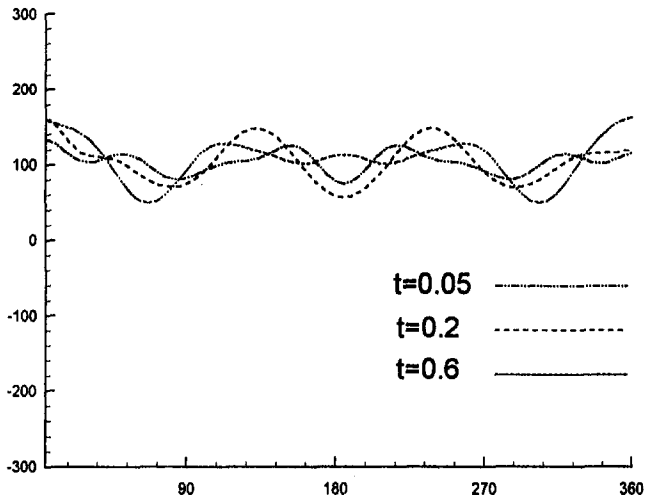

Fig. 5 Pressure difference at drop surface, $Re_g = 1$

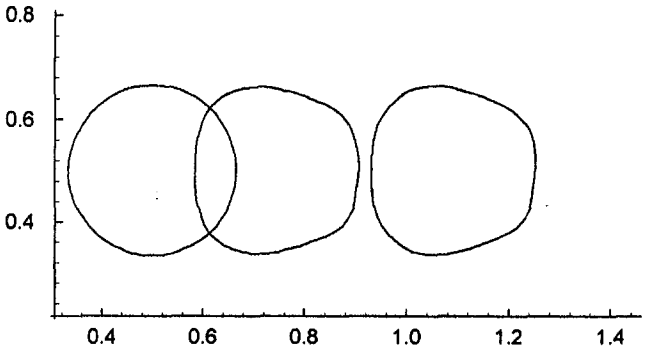

Fig. 6 Drop deformation sequence at $t = 0$, 0.24, 0.6 $Re_g = 0.1$, $Re_l = 200$, $We = 8$, $\zeta = 400$

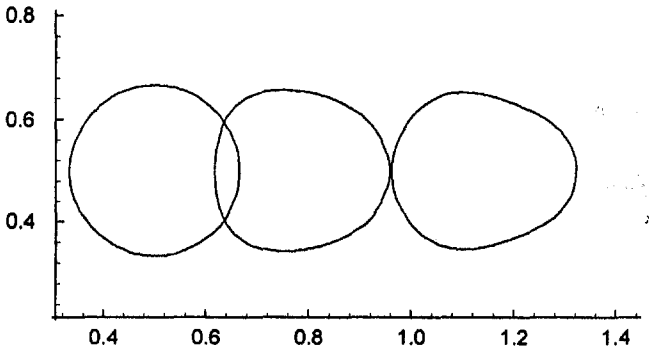

Fig. 7 Drop deformation sequence at $t = 0$, 0.24, 0.6 $Re_g = 1.0$, $Re_l = 200$, $We = 8$, $\zeta = 400$

coordinates of these figures indicate the measuring angle, initiating from the most right hand side point of the drop and traveling counter clockwise around the drop. Surface tension is by far the dominant term, for the range of values of dimensionless parameters used in the above examples, and the pressure difference distribution closely follows the surface tension distribution. Figure 4 indicates that for the case of $Re_g = 20$ surface tensions behind the drop at times $t = 0.2$ and $t = 0.6$ have large negative values resulting in a much larger gas pressure than the liquid pressure in the caved-in region of the drop. In the case of $Re_g = 1.0$ the drop shape is preserved and liquid pressure is greater than the gas pressure everywhere. In neither case a recirculatory flow field is observed inside the drop. Drop particles are accelerated in the same direction as the gas particles. Viewed from an inertial laboratory reference system no internal recirculatory motion is observed. We shall consider this in more detail later.

To study the effect of the gas Reynolds number on the deformation of the liquid drop, the Weber number, the liquid drop Reynolds number and the liquid to gas density ratio are held fixed

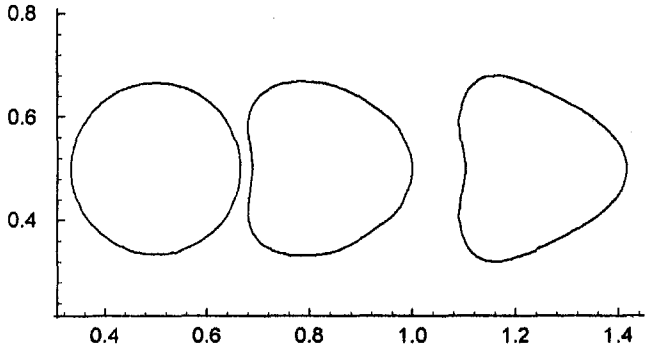

Fig. 8 Drop deformation sequence at $t = 0$, 0.24, 0.6 $Re_g = 10$, $Re_l = 200$, $We = 8$, $\zeta = 400$

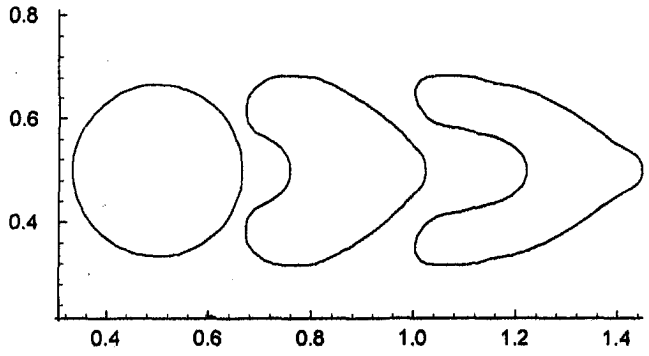

Fig. 9 Drop deformation sequence at $t = 0, 0.24, 0.6$ $Re_g = 50$, $Re_l = 200$, We = 8, $\zeta = 400$

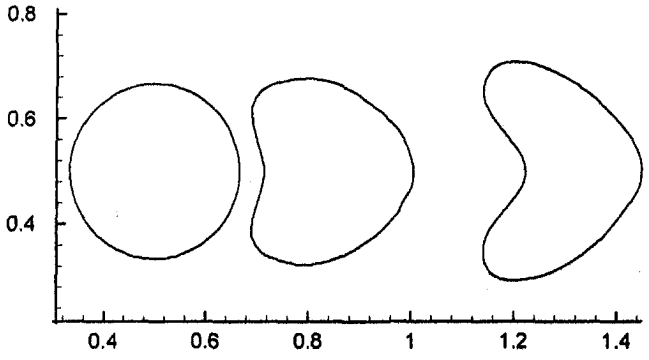

Fig. 10 Drop deformation sequence at $t = 0, 0.24, 0.6$ $Re_g = 20$, $Re_l = 200$, We = 16, $\zeta = 400$

and the gas Reynolds number is varied via decreasing the value of the gas viscosity. Very interesting result is obtained. Figures 6 to 8 show the initial shape and the deformation of the drop at two different time levels for gas Reynolds number values ranging from one tenth to ten. In all these cases the drop takes on an oblate cap shape as it moves down the gas field. Figures 1(*a*) and 9 show the same time accurate development for gas Reynolds numbers of twenty and fifty. At these gas Reynolds numbers the deformation of the drop is developing differently and the drop is taking an arrow head shape as it moves down the gas field. Apparently for the case of a two-dimensional cylindrical drop studied here, deformation of a drop goes through a transition as the gas Reynolds number is increased above ten, for the Weber number equal to eight. At low gas Reynolds numbers the drop assumes an oblate cap shape and its back flattens as it moves down the stream. At high Reynolds numbers situation is changed such that back of the drop caves in, and the front of the drop stretches out and an arrow head shape drop develops. This behavior is not changed by decreasing the drop surface tension, as can be seen from Fig. 11.

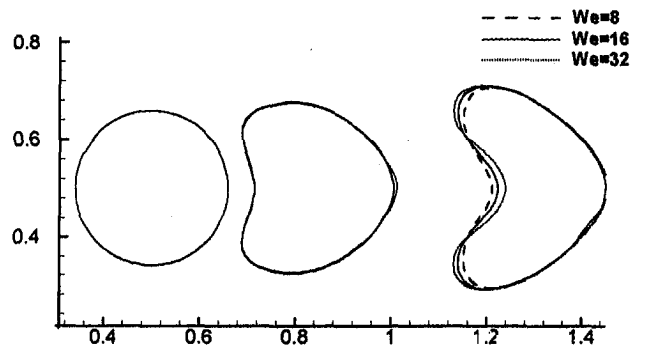

Fig. 11 Drop deformation sequence at $t = 0, 0.24, 0.6$ $Re_g = 20$, $Re_l = 200$, $\zeta = 400$

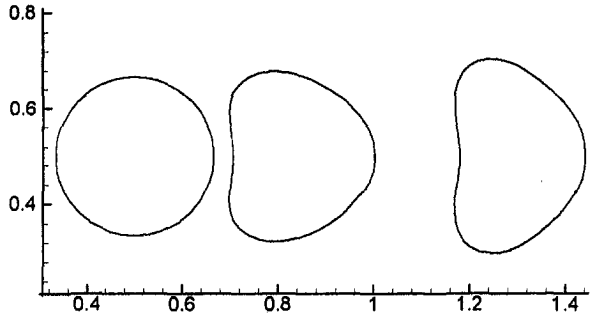

Fig. 12 Drop deformation sequence at $t = 0, 0.24, 0.6$ $Re_g = 20$, $Re_l = 200$, We = 2, $\zeta = 400$

Comparison of these figures indicates that as surface tension decreases the drop retains arrow head shape, however it deforms more rapidly.

Figures 12 and 13 show the effect of increasing surface tension. As expected the decreasing value of the Weber number correspond to less drop deformation. Figure 13 indicates that even at very high surface tension value the drop still deforms in a high Reynolds number gas field. By lowering the gas Reynolds number at low Weber number values the inertia effect becomes negligible and the drop retains its circular shape.

The range of the liquid Reynolds numbers considered in this study was rather narrow and the comparison of Fig. 14 with Fig. 1(*a*), and Fig. 15 with Fig. 7 indicate that limited liquid viscosity variation does not play an important role in the liquid drop deformation. Clearly it can be seen from Eq. (13) that large variation of the liquid Reynolds number could drastically change the dynamics of the forces exerted on the drop surface.

The liquid-gas density ratio for all the cases discussed above was held fixed at 400. The effect of the variation of this parameter on the liquid drop deformation can be seen by comparing Figs. 1 and 16. Density ratio for the case of Fig. 16 was decreased to 85, while all other parameters were held fixed. As it can be seen there is little difference between above figures.

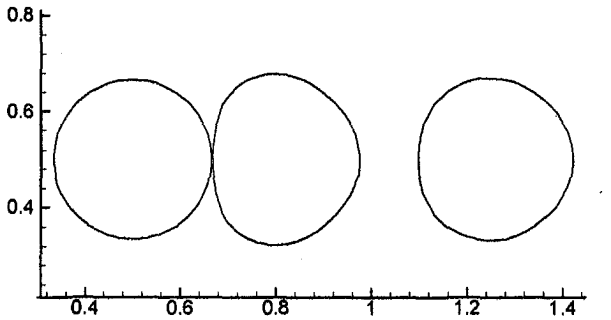

Fig. 13 Drop deformation sequence at $t = 0, 0.24, 0.6$ $Re_g = 20$, $Re_l = 200$, We = 25, $\zeta = 400$

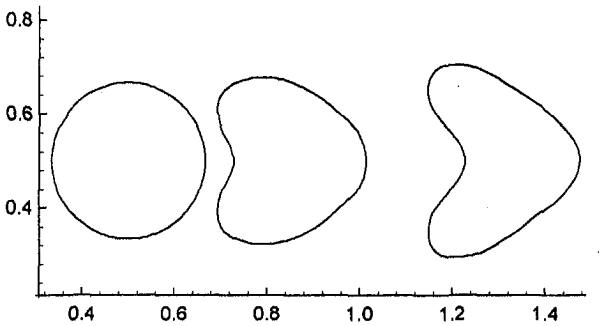

Fig. 14 Drop deformation sequence at $t = 0, 0.24, 0.6$ $Re_g = 20$, $Re_l = 100$, We = 8, $\zeta = 400$

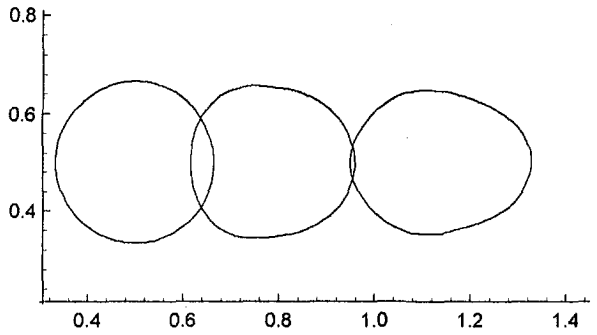

Fig. 15 Drop deformation sequence at t = 0, 0.24, 0.6 Re_g = 1.0, Re_l = 100, We = 8, ζ = 400

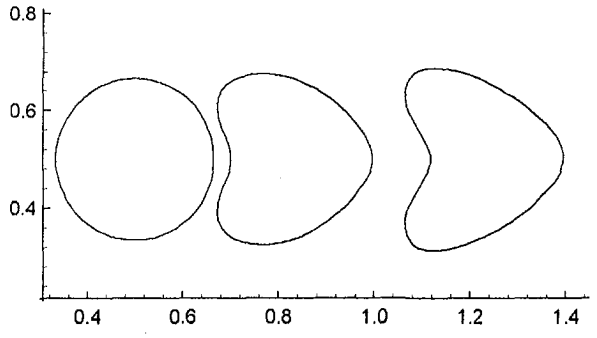

Fig. 16 Drop deformation sequence at t = 0, 0.24, 0.6 Re_g = 10, Re_l = 200, We = 8, ζ = 85

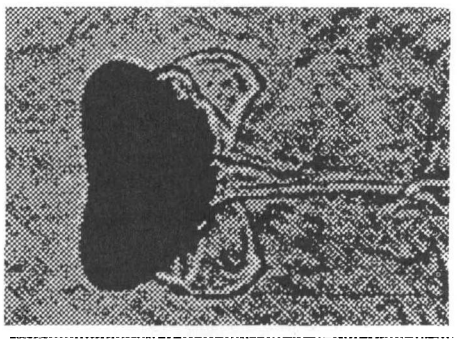

Fig. 17 Deformation of nitrobenzene in coflowing water

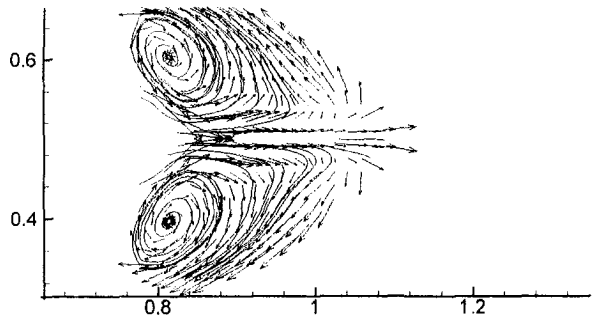

Fig. 18 Drop internal flow field, t = .02 Re_g = 20, Re_l = 200, We = 8, ζ = 400

It was pointed out earlier that an observer fixed to the laboratory reference system does not see any recirculatory motion inside the drop. However, if one views the flow field from a nonstationary reference system fixed to the drop, a different picture emerges. To do this an average liquid drop velocity is calculated and subtracted from the local velocities of the gas stream and the liquid drop. Void fraction weighted average of the axial component of velocity

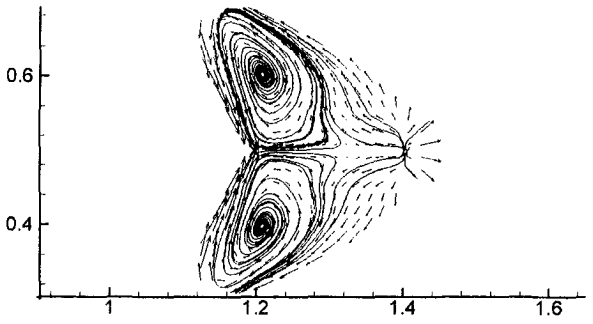

Fig. 19 Drop internal flow field, t = 0.6 Re_g = 20, Re_l = 200, We = 8, ζ = 400

in the flow field is indicated as the average liquid drop velocity. Figures 18 and 19 show the flow field inside the drop as seen by an observer moving with the drop's average velocity. Strong recirculating regions are observed inside the drop. Recirculation paterns are highly transitory and dependent on the four dimensionless parameters governing the dynamics of the problem. Detail analysis of the flow recirculation dynamics, inside and outside of the drop is given by Rahimian and Farshchi (1998).

Clift et al. (1978) present a number of interesting photos of drops and bubbles. Unfortunately, cases matching the range of dimensionless parameters used in this paper were not found in their work. However, they have presented experimentally observed behavior of a falling nitrobenzene drop in water flow, Fig. 17. Qualitative comparison indicates that features of the numerical solutions appear to be in accord with expectations and experimental observations.

Conclusion

A time accurate numerical solution technique for low Mach number, two phase flow fields is used to capture the motion and deformation of a liquid drop moving with a co-flowing gas stream in a zero gravity field. Four controlling dimensionless parameters are identified and the effects of the gas Reynolds number and the drop Weber number on the deformation dynamics of the drop have been investigated in details. The effect of the surface tension is rather predictable and at very low Weber numbers the drop deformation is prohibited. However, at moderate and high Weber numbers the gas Reynolds number variation results in a nonlinear drop deformation behavior. There appears to be a critical gas stream Reynolds number, at moderate Weber numbers, below which the co-flowing cylinderical drop takes on an oblate cap shape and above which it forms an arrow head shape. Numerical simulations show that the contribution of the gas normal stress term at the drop surface, for the range of parameters considered here, is negligible in comparison with the surface tension term. Therefore it is the coupling of the convection of the gas, and its influence on the transport of the void fraction, with the pressure boundary condition that decides the drop shapes presented here. It has also been shown that an observer moving with the average velocity of the liquid drop sees interesting recirculatory flow patterns inside the drop.

References

Acrivos, A., 1987, "The Deformation and Break-up of Single Drops in Shear Fields," *Physicochemical Hydrodynamics, Interface Phenomena,* Plenum, New York.

Ashgriz, N., and Poo, J. Y., 1991, "FLAIR: Flux Line Segment Model for Advection and Interface Reconstruction," *Journal of Computational Physics,* Vol. 93, No. 2, p. 449.

Baker, G. R., and Moore, D. W., 1989, "The Rise and Distortion of a Two-dimensional Gas Bubble in an Inviscid Liquid," *Physics of Fluids A,* Vol. 1, No. 9, p. 1451.

Bentley, B. J., and Leal, L. G., 1986, "An Experimental Investigation of Drop Deformation and Break up in Steady, Two Dimensional Linear Flows," *Journal of Fluid Mechanics,* Vol. 167, p. 241.

Clift, R., Grace, J. R., and Weber, M. E., 1978, *Bubbles, Drops, and Particles,* Academic Press, New York.

Christov, C. I., and Volkov, P. K., 1985, "Numerical Investigation of the Steady Viscous Flow Past a Stationary Deformable Bubble," *Journal of Fluid Mechanics,* Vol. 158, p. 341.

Dandy, D. S., and Leal, L. G., 1989, "Buoyancy-Driven Motion of a Deformable Drop Through a Quiescent Liquid at Intermediate Reynolds Numbers," *Journal of Fluid Mechanics,* Vol. 208, p. 161.

Dwyer, H. A., 1989, "Calculation of Droplet Dynamics in High Temperature Environments," *Progress in Energy and Combustion Science,* Vol. 15, p. 131.

Dwyer, H. A., and Sander, B. R., 1986, "A Detailed Study of Burning Fuel Droplets," *21 st Symposium in Combustion* (Int.), The Combustion Institute Pittsburgh, p. 633.

Farshchi, M., Rahimian, M. H., and Ashgriz, N., 1995, "Chemically Reacting Liquid Droplet Flow Field Calculation," *Transport Phenomena in Combustion,* S. H. Chan, ed., Vol. 1, p. 872, Taylor & Francis, San Francisco.

Kennedy, M. R., Pozrikidis, C., and Skalak, R., 1994, "Motion and Deformation of Liquid Drops, and the Rheology of Dilute Emulsions in Simple Shear Flow," *Computers and Fluids,* Vol. 23, p. 251.

Leonard, B. P., 1979, "The QUICK Algorithm: A Uniformly Third-order Finite Difference Method for Highly Convective Flows," *Computational Methods in Applied Mechanical Engineering,* Vol. 19, p. 59.

Patankar, S. V., 1980, *Numerical Heat Transfer and Fluid Flow,* Hemisphere, Washington.

Rahimian, M. H. and Farshchi, M., 1998, "On the Internal Circulation of a Liquid Drop Moving with the Surrounding Gas," *Proceedings of the CFD98 Conference,* Canada.

Rallison, J. M., 1984, "The Deformation of Small Viscous Drops and Bubbles in Shear Flows," *Annual Review of Fluid Mechanics,* Vol. 16, p. 45.

Rhie, M., and Chow, W. L., 1983, "Numerical Study of the Turbulent Flow Passed an Airfoil with Trailing Edge Separation," *AIAA Journal,* Vol. 21, No. 11, p. 19.

Ryskin, G., and Leal, L. G., 1984, "Numerical Solution of Free-Boundary Problems in Fluid Mechanics, Part 3. Bubble Deformation in an Axisymmetric Straining Flow," *Journal of Fluid Mechanics,* Vol. 148, p. 37.

Sadhal, S. S., and Ayyaswamy, P. S., 1983, "Flow Past a Liquid Drop with a Large Non-uniform Radial Velocity," *Journal of Fluid Mechanics,* Vol. 133, p. 65.

Sirignano, W. A., 1983, "Fuel Droplet Vaporization and Spray Combustion Theory," *Progress in Energy and Combustion Science,* Vol. 9, p. 291.

Unverdi, S. O., and Tryggvason, G., 1992, "A Front-Tracking Method for Viscous, Incompressible, Multi-Fluid Flows," *Journal of Computational Physics,* Vol. 100, p. 25.

Walters, J. K., and Davidson, J. F., 1962, "is "The Initial Motion of a Gas Bubble Formed in an Inviscid Liquid; Part 1. The Two-Dimensional Bubble," *Journal of Fluid Mechanics,* Vol. 12, p. 408.

Yiantsios, S. G., and Higgins, B. G., 1989, "Rayleigh-Taylor Instability in Thin Viscous Films," *Physics of Fluids A,* Vol. 1, No. 9, p. 1484.

Kenneth J. Ruschak
Senior Research Associate.

Steven J. Weinstein
Research Associate.

Manufacturing Research and Engineering Organization,
Eastman Kodak Company,
Rochester, NY 14652-3701
e-mail: kruschak@kodak.com

Viscous Thin-Film Flow Over a Round-Crested Weir

Gravity-driven flow over a round-crested weir is analyzed for viscous flow. An equation for the entire flow profile is obtained by simplifying the equations for slowly varying film thickness, assuming a velocity profile, and integrating across the film. Solution of the resulting first order, ordinary differential equation requires a boundary condition generated at a critical point of the flow, beyond which waves cannot propagate upstream. Results for the relationship between head and flow rate are consolidated on a dimensionless master curve represented by an empirical equation.

Introduction

Weirs are commonly used in hydraulics to measure flow rate or to control the level of a reservoir; such large-scale water flows are usually turbulent. Weirs are also used in coating operations; these smaller scale flows of viscous liquids may be laminar. A coating process requires a means to distribute the coating composition across the width of the surface receiving the coating. Most simply, the distributor in a coating process is a pan, and the liquid distributes by gravitational leveling; drawbacks of pans include gravitational separation, long residence times, and skimming. For demanding applications, elaborate dies are used; these solve the problems of pans at considerable expense. Intermediate options for distributing liquid include the weir; for a modest increase in cost, a weir can reduce the problems of pans. Additionally, weirs are used in various manufacturing processes to form a free-falling sheet of liquid called a curtain to wet or coat objects.

The design of a weir distributor requires a relationship between the depth of an essentially stagnant pool and the flow rate over the face of the weir. Analyses of weirs typically treat high Reynolds number flow because most applications involve flow of water in relatively large channels. In most coating applications, however, viscous effects are significant because the layer is thin. However, treatments of hydraulic flows (e.g., Dressler, 1949; Fox and McDonald, 1992, pp. 519–21) point the way to analyzing viscous flow by suggesting that a critical point is present and that smooth passage through the critical point constrains the flow. At a critical point, waves move in the downstream direction but are stationary in the upstream direction. In the pool, flow is subcritical, and conditions at the crest propagate upstream to determine the depth far from the weir. On the other hand, what happens downstream of the critical point can have no bearing on conditions in the pool. So, conditions at the critical point propagate upstream and downstream to determine the flow profile.

In the following analysis, the crest of the weir is taken to be circular in shape. Such a smooth shape inhibits boundary layers and turbulent flow. In coating flows, surface-tension effects are commonly significant because film thickness and interfacial curvature can be significantly smaller than the capillary length of the liquid, the characteristic dimension of capillary hydrostatics that is usually a millimeter or two. Here, however, the radius of the crest of the weir is supposed several times larger than the capillary length. Capillary pressure gradients are then small compared to gravitational gradients. So, through choice of shape and scale of the crest, surface tension can be safely neglected and the relationship between head and flow rate simplified.

Flow from the pool and over the crest spans regions of disparate length scales when, as is presumed, the film thickness is significantly smaller than the radius of the crest. Then, the liquid in the pool is nearly hydrostatic. The disparity is addressed in the following analysis by retaining those terms that are significant in either the pool or film regions (Ruschak, 1978). The working equation is then a composite applicable to the entire flow field. Matched asymptotic expansions can be considered in such circumstances, but that approach is more restrictive and difficult.

A crest of relatively large radius also ensures that changes in film thickness are gradual, and as a result the Navier-Stokes equation can be greatly simplified. The equations are further reduced by assuming a parabolic velocity profile and integrating across the film to obtain a first order, ordinary differential equation. This standard approach for boundary layers of all types (Schlichting, 1979; Kakac and Yenner, 1995) has long been exploited for free-surface flows. The flat velocity profile commonly employed in analyses of open channel water flows is a prevalent example; a parabolic profile is a common choice for viscous, laminar flows.

Time-dependence is retained in the simplified equations to predict the speeds at which waves propagate and thereby determine the necessary condition for a critical point. Then, requiring that the flow pass smoothly through the critical point generates an initial condition from which the differential equation is integrated in both the upstream and downstream directions. The location of the critical point is found to depend on Reynolds number.

Finally, the results of numerous integrations are used to determine a dimensionless correlation between head and flow rate. The correlation is fitted to an empirical equation that is convenient for applications.

Description of the Flow

Newtonian liquid with viscosity μ, density ρ, and surface tension σ flows over a round-crested weir of radius R as sketched in Fig. 1. The origins of a Cartesian coordinate system (z, x) and a cylindrical coordinate system (r, θ) are located at the center of the circular section. The coordinate z increases vertically upward, and x increases horizontally outward from the pool. The angle θ is measured from vertical and increases in the flow direction.

Upstream from the weir, the liquid surface becomes horizontal at a vertical distance H above the crest of the weir; H is referred to as the head. The volumetric flow per unit width is denoted q and is viewed as imposed, as in coating applications. In hydraulic operations, the head is viewed as imposed rather than the flow rate.

Flow in the film is more naturally described by a radial coordinate $y = R - r$ that is zero at the surface of the weir; the position of the free surface is given by $y = h(\theta)$. A length scale for film thickness is chosen that reflects a balance between gravitational and viscous forces, $h_c = (\mu q/\rho g)^{1/3}$. The dimensionless radial coordinate is then $\eta = y/h_c$ and the dimensionless film thickness is $\zeta = h/h_c$. The dimensionless groups employed are the Reynolds

Contributed by the Fluids Engineering Division for publication in the JOURNAL OF FLUIDS ENGINEERING. Manuscript received by the Fluids Engineering Division May 22, 1998; revised manuscript received May 31, 1999. Associate Technical Editor: P. W. Bearman.

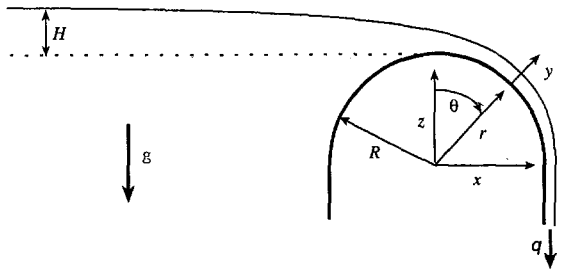

Fig. 1 Definition sketch

number for two-dimensional flow, Re, the ratio of the film-thickness length scale to the weir radius, δ, and the ratio of the capillary length $\sqrt{\sigma/\rho g}$ to the weir radius, γ:

$$\mathrm{Re} = \frac{\rho q}{\mu}; \quad \delta = \frac{h_c}{R}; \quad \gamma = \frac{\sqrt{\sigma/\rho g}}{R} \tag{1}$$

Capillary pressure gradients can be estimated as σ/R^2 and gravitational gradients as ρg; the ratio of capillary to gravitational gradients is presumed small ($\gamma^2 \ll 1$) to suppress surface tension effects. Similarly, the estimated film slope is presumed small ($\delta \ll 1$), and as a result the flow is quasi-rectilinear.

The pressure P and velocity components V_r, V_θ are scaled for gravity-driven flow with slowly varying film thickness. Their dimensionless counterparts, p, u, and v are related by

$$P = \rho g R p; \quad V_\theta = \frac{q}{h_c} u; \quad V_r = \delta \frac{q}{h_c} v \tag{2}$$

Although the flow of interest is steady, wave propagation is deduced from time-dependent flow, and a dimensionless variable τ is related to time t through a characteristic time for flow over the crest of the weir

$$t = \frac{R}{q/h_c} \tau \tag{3}$$

Existing Theory for Inviscid Liquid

In hydraulic applications the Reynolds number is large and the flow is turbulent. Viscous losses related to turbulence are customarily captured as a correction to inviscid theory in the form of a discharge coefficient (Ackers et al., 1978; Brater et al., 1996; Fox and McDonald, 1992, pp. 530–535). Bernoulli's equation, or a macroscopic balance of momentum or mechanical energy, is employed to suggest the form of a relationship. Applying Bernoulli's equation between the pool and the crest of the weir gives

$$\tfrac{1}{2}\rho U^2 = \rho g(H - h) \tag{4}$$

in which h is film thickness at the top of the crest and U is the velocity, constant across the film. Continuity provides a second equation

$$q = Uh \tag{5}$$

A third relationship is required to close the problem. One observation is that the flow will pass from subcritical in the pool to supercritical in the descending, accelerating film (Rouse, 1938, pp. 379–381); it has been argued that the critical point is at the peak of a broad-crested weir (Whitaker, 1968, pp. 379–81). At the critical point, waves propagating against the flow are stationary; the additional relationship is therefore

$$U = \sqrt{gh} \tag{6}$$

where $\sqrt{gh}$ is the speed of small waves in shallow liquid at rest. Solution of Eqs. (4)–(6) gives (Rouse, 1938, p. 283)

$$h = \left(\frac{q^2}{g}\right)^{1/3}; \quad H = \frac{3}{2}\left(\frac{q^2}{g}\right)^{1/3}; \quad U = (gq)^{1/3} \tag{7}$$

An alternative argument leading to the same result (Ackers et al., 1978, pp. 34–36) is that the head is the minimum possible for a specified flow rate, or equivalently, that the flow rate is the maximum possible for a specified head.

Equations

The flow field has two regions disparate in scale. In the film region, the gravitational force drives flow, while in the pool region, the gravitational force is balanced by essentially static pressure. One approach to this situation is to find a single equation applicable in both regions that can smoothly join them. The Navier-Stokes equation and boundary conditions are simplified for each region separately, and a composite equation is formed by combining all terms significant in either region (Ruschak, 1978).

The Navier-Stokes equation is written in dimensionless, component form, and terms of order δ or $\mathrm{Re}\delta^2$ and smaller are neglected. The exceptions are terms describing a hydrostatic pressure field that become order unity in the pool region. The resulting θ and η components of the Navier-Stokes equation are

$$\mathrm{Re}\delta\left[\frac{\partial u}{\partial \tau} + u\frac{\partial u}{\partial \theta} + v\frac{\partial u}{\partial \eta}\right] = -\frac{\partial}{\partial \theta}[p + (1 + \delta\eta)\cos(\theta)] + \frac{\partial^2 u}{\partial \eta^2} \tag{8}$$

$$0 = -\frac{\partial p}{\partial \eta} - \delta\cos(\theta) \tag{9}$$

The pressure variation across the layer is hydrostatic. The simplified continuity equation is

$$\frac{\partial v}{\partial \eta} + \frac{\partial u}{\partial \theta} = 0 \tag{10}$$

Because the film is thin, the geometry on the scale of the film thickness is nearly planar, and so the equations aside from the gravitational terms are identical to those for flow on a flat surface.

At the free surface, the stress boundary conditions are

$$p = 0; \quad \frac{\partial u}{\partial y} = 0 \quad (\eta = \zeta) \tag{11}$$

and the kinematic condition is

$$v = \frac{\partial \zeta}{\partial \tau} + u\frac{\partial \zeta}{\partial \theta} \quad (\eta = \zeta) \tag{12}$$

Finally, the no-slip boundary condition for the solid surface is

$$u = v = 0 \quad (\eta = 0) \tag{13}$$

Boundary conditions in θ are not standard and are treated later.

The equations are further simplified by eliminating p and by integrating the θ-component of momentum across the film. The velocity profile is approximated by a parabola and so is consonant with fully developed viscous flow; a more general approach better treating flow at high Reynolds number is part of ongoing work.

$$p = \delta(\zeta - \eta)\cos(\theta) \tag{14}$$

$$u = A\frac{3}{\zeta^3}\left[\zeta\eta - \frac{\eta^2}{2}\right]; \quad A = \frac{Q}{q} \tag{15}$$

Here Q is instantaneous flow rate and A is dimensionless flow rate; for steady flow, $A = 1$. The continuity equation determines v. Substituting for p, u, and v in Eq. (8) and integrating across the film leads to

$$\frac{\mathrm{Re}\delta}{\zeta}\left[\frac{\partial A}{\partial \tau}+\frac{6}{5}\frac{\partial}{\partial \theta}\left(\frac{A^2}{\zeta}\right)\right]$$

$$=(1+\delta\zeta)\sin(\theta)-\delta\cos(\theta)\frac{\partial \zeta}{\partial \theta}-\frac{3A}{\zeta^3} \quad (16)$$

Similarly, u and v can be eliminated from the kinematic boundary condition, Eq. (12)

$$\frac{\partial \zeta}{\partial \tau}+\frac{\partial A}{\partial \theta}=0 \quad (17)$$

Wave Propagation

The speed of waves of small amplitude according to the Eqs. (16) and (17) is straightforward to derive. First, these equations are formally linearized about the steady solution $A = 1$ and $\zeta = \bar{\zeta}(\theta)$ by considering perturbations $A' \ll 1$ and $\zeta' \ll \bar{\zeta}$.

$$A=1+A'; \quad \zeta=\bar{\zeta}+\zeta' \quad (18)$$

The linearized equations can be combined by relating A' and ζ' through a function ψ defined by

$$\zeta'=\frac{\partial \psi}{\partial \theta}; \quad A'=-\frac{\partial \psi}{\partial \tau} \quad (19)$$

so that Eq. (17) is satisfied. A second-order partial differential equation for ψ remains.

$$a\frac{\partial^2\psi}{\partial\tau^2}+b\frac{\partial^2\psi}{\partial\tau\partial\theta}+c\frac{\partial^2\psi}{\partial\theta^2}+d\frac{\partial\psi}{\partial\tau}+e\frac{\partial\psi}{\partial\theta}=0$$

$$a=-\mathrm{Re}\delta$$

$$b=-\frac{12\,\mathrm{Re}\delta}{5\bar{\zeta}}$$

$$c=\delta\bar{\zeta}\cos(\theta)-\frac{6\,\mathrm{Re}\delta}{5\bar{\zeta}^2}$$

$$d=\frac{12\,\mathrm{Re}\delta}{5\bar{\zeta}^2}\frac{\partial\bar{\zeta}}{\partial\theta}-\frac{3}{\bar{\zeta}^2}$$

$$e=\frac{12\,\mathrm{Re}\delta}{5\bar{\zeta}^3}\frac{d\bar{\zeta}}{d\theta}-(1+2\delta\bar{\zeta})\sin(\theta)+\delta\cos(\theta)\frac{d\bar{\zeta}}{d\theta}-\frac{6}{\bar{\zeta}^3} \quad (20)$$

The standard classification scheme (Weinberger, 1965, Ch. 9) turns on the sign of the following expression

$$b^2-4ac=4\,\mathrm{Re}^2\delta^2\left[\frac{6}{25\bar{\zeta}^2}+\frac{\bar{\zeta}\cos(\theta)}{\mathrm{Re}}\right] \quad (21)$$

Because the sign is always positive, Eq. (20) is hyperbolic. The speeds of the characteristics, which correspond to the wave speed c, follow as

$$c=\frac{d\theta}{d\tau}=\frac{b\pm(b^2-4ac)^{1/2}}{2a}$$

$$=\frac{6}{5\bar{\zeta}}\pm\left[\frac{6}{25\bar{\zeta}^2}+\frac{\bar{\zeta}\cos(\theta)}{\mathrm{Re}}\right]^{1/2} \quad (22)$$

At a critical point $c = 0$ for the slower wave, and the necessary condition for a critical point follows as

$$\frac{6\,\mathrm{Re}}{5\bar{\zeta}^3}-\cos(\theta)=0 \quad (23)$$

The speeds of waves at a critical point are then

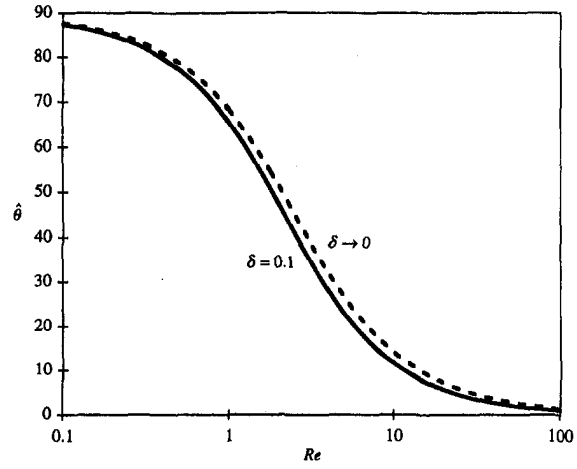

Fig. 2 Angular position in degrees of the critical point versus Reynolds number: dashed line, asymptotic result for $\delta \to 0$, Eq. (28); solid line, numerical result for $\delta = 0.1$

$$c=\frac{6}{5\bar{\zeta}}\pm\frac{6}{5\bar{\zeta}} \quad (24)$$

Steady Solution

For the case of steady flow, Eqs. (16) and (17) reduce to

$$\frac{d\bar{\zeta}}{d\theta}=\frac{N}{D} \quad (25)$$

with $\bar{\zeta}$ again representing the steady-state solution and with N and D defined by

$$N=(1+\delta\bar{\zeta})\sin(\theta)-\frac{3}{\bar{\zeta}^3} \quad (26)$$

$$D=\delta\left[\cos(\theta)-\frac{6\,\mathrm{Re}}{5\bar{\zeta}^3}\right] \quad (27)$$

To integrate this equation, the film thickness must be specified at one location, but there is no obvious condition to apply.

The inviscid analysis recited previously suggests that the flow passes through a critical point. It follows from the necessary condition for a critical point derived in the previous section, Eq. (23), that $D = 0$ there. For the solution to pass smoothly through the critical point, it is therefore necessary that $N = 0$ at the critical point as well and that N/D have a finite limit giving the slope. Such an approach is taken, for example, by Dressler (1949). Press et al. (1992) treat the numerical aspects of internal boundary conditions.

The equations $N = 0$ and $D = 0$ determine the film thickness $\hat{\zeta}$ and angular position $\hat{\theta}$ at the critical point. These nonlinear algebraic equations are iteratively solved by Newton's method; an approximate solution valid as $\delta \to 0$ is readily obtained and provides initial values.

$$\hat{\theta}\to\arctan\left(\frac{5}{2}\frac{1}{\mathrm{Re}}\right) \quad (\delta\to 0) \quad (28)$$

$$\hat{\zeta}\to\left(9+\frac{36}{25}\mathrm{Re}^2\right)^{1/6} \quad (\delta\to 0) \quad (29)$$

These asymptotic results are not accurate enough to start the numerical integration for finite values of δ. Figure 2 shows a plot of $\hat{\theta}$ against Re; the approximate result, Eq. (28), is also shown. As Re increases, $\hat{\theta}$ decreases from $\pi/2$ to 0, and the position of the critical point ranges over an entire quadrant. Figure 3 is similarly a plot of $\hat{\zeta}$ versus Re together with a plot of Eq. (29).

With $\hat{\theta}$ and $\hat{\zeta}$ determined, the corresponding slope of the

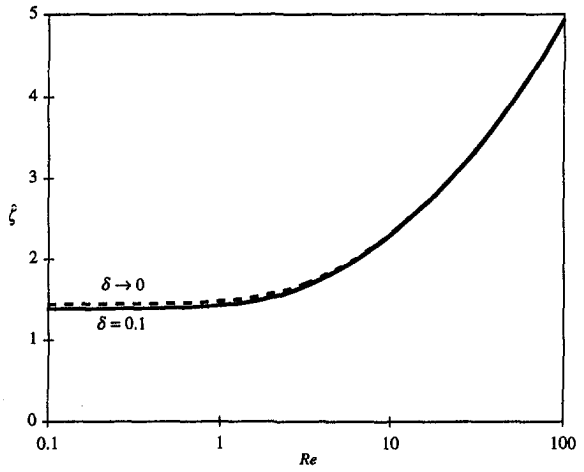

Fig. 3 Dimensionless film thickness $\hat{\zeta}$ at the critical point versus Reynolds number: dashed line, asymptotic result for $\delta \to 0$, Eq. (29); solid line, numerical result for $\delta = 0.1$

interface for use in starting the numerical integration can be found through local expansions of N and D. The slope at the critical point is a root of the quadratic equation

$$\frac{18\ \mathrm{Re}\delta}{5\hat{\zeta}^4}\left(\frac{d\bar{\zeta}}{d\theta}\right)^2 - \left[2\delta \sin(\hat{\theta}) + \frac{9}{\hat{\zeta}^4}\right]\frac{d\bar{\zeta}}{d\theta} - (1 + \delta\hat{\zeta}) \cos(\hat{\theta}) = 0 \quad (30)$$

The numerical integration proceeds from the critical point in both directions.

The solution for $\mathrm{Re} \to \infty$ can be written in closed form. In that limit the conditions at the critical point are

$$\hat{\theta} = 0 \quad (31)$$

$$\hat{\zeta} = \left(\frac{6}{5}\mathrm{Re}\right)^{1/3} \Rightarrow \hat{h} = \left(\frac{6}{5}\frac{q^2}{g}\right)^{1/3} \quad (32)$$

Moreover, the expression for wave speed c, Eq. (24), leads to

$$c = \sqrt{\tfrac{6}{5}g\hat{h}} \quad (33)$$

The complete film profile is given by

$$\frac{3\ \mathrm{Re}\delta}{5}\left(\frac{1}{\hat{\zeta}^2} - \frac{1}{\zeta^2}\right) = (1 + \delta\zeta) \cos(\theta) - (1 + \delta\hat{\zeta}) \quad (34)$$

and the head follows as

$$H = \frac{3}{2}\left(\frac{6}{5}\frac{q^2}{g}\right)^{1/3} \quad (35)$$

Equations (32), (33), and (35) would be precisely the classical, inviscid result at Eq. (7) were the fraction $\frac{6}{5}$ unity instead; the fraction descends from the imposed parabolic velocity profile that is not accurate at high Re. Equation (31) is a derived result supporting the standard supposition that the critical point is at the crest for inviscid flow.

At small Re the conditions at the critical point limit to

$$\hat{\theta} \to \frac{\pi}{2}; \quad \hat{\zeta} \to 3^{1/3} \Rightarrow \hat{h} \to \left(\frac{3\mu q}{\rho g}\right)^{1/3} \quad (36)$$

The film thickness is that corresponding to fully developed viscous flow on a vertical wall. The complete profile cannot be written in closed form, however, and as a result the head cannot be written explicitly.

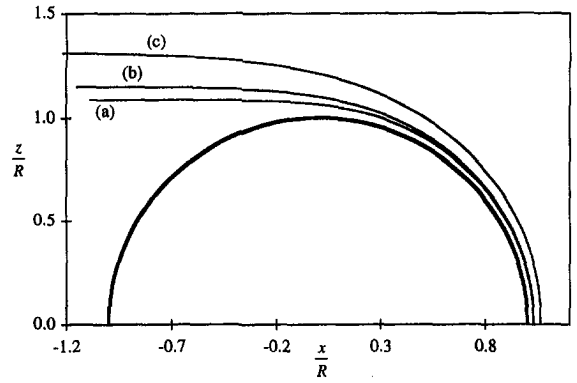

Fig. 4 Film profiles for $\delta = 0.02$ for three values of Reynolds number: curve (*a*), Re = 10; (*b*), Re = 100; (*c*), Re = 1000

Results

Example profiles are shown in Fig. 4. At low and moderate Re, the flow becomes fully developed on the downstream side of the crest; thus, the profiles for Re = 10 and 100 approach one another. At high Re, however, inertia controls the entire profile as that for Re = 1000 illustrates.

Many runs were made to determine the relationship between head and flow rate. Working with these results led to asymptotes at low and high Re and finally to a master curve for all the data. For the correlation, the head is normalized with the inviscid result, H_i, given by Eq. (7). A dimensionless group Po is introduced

$$Po = \frac{\rho}{\mu}\sqrt{gR^3} \quad (37)$$

that is related to the other groups by $\mathrm{Re} = Po^2\delta^3$. The normalized head is plotted against

$$\chi = \frac{\delta Po^n}{k} \quad (38)$$

in which n and k are constants. The master curve can be represented by the following empirical expression

$$H = \frac{3}{2}\left(\frac{q^2}{g}\right)^{1/3}\left[c_o + \frac{c_1}{\chi^{c_2}}\exp(-c_3\chi^{c_4})\right] \quad (39)$$

The following constraints were imposed to ensure the correct asymptotic behavior

$$c_o = \sqrt[3]{6/5}; \quad nc_2 = 2/3 \quad (40)$$

Nonlinear regression achieves the correlation shown in Fig. 5 corresponding to the following values

$$n = 0.57951; \quad k = 1.25135$$

$$c_1 = 1.06459; \quad c_2 = 1.15039$$

$$c_3 = 3/2; \quad c_4 = 4/3 \quad (41)$$

The constants c_3 and c_4 were rounded to rational numbers for convenience.

From Eqs. (39) and (40), the head at small Re is given by

$$H \to \frac{3c_1k^{c_2}}{2\delta^{c_2-1}}\left(\frac{\mu q}{\rho g}\right)^{1/3} \approx \frac{2.07}{\delta^{0.15}}\left(\frac{\mu q}{\rho g}\right)^{1/3} \quad (\mathrm{Re} \to 0) \quad (42)$$

Concluding Comments

The necessary condition for a critical point, namely that wave propagation upstream is stationary, is not enough to close the problem, and an additional constraint is required to determine the

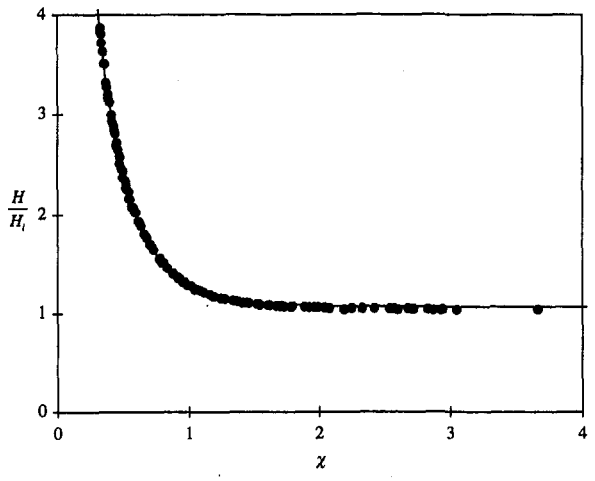

Fig. 5 Master curve for dimensionless head versus χ (Eq. 38): filled circles, results of numerical survey; solid line, empirical curve Eq. 39

location of the critical point. Location follows by requiring smooth passage through the critical point. The resulting constraint propagates in both the upstream and downstream directions to determine the entire flow. The location of the critical point has been found to depend on Reynolds number, and the results support the supposition made in previously cited work that the location of the critical point is at the crest in the limit of inviscid flow. The crest of a weir is sometimes given a horizontal land that is long relative to layer thickness to ensure the absence of curvature effects (e.g., Rouse, 1938, p. 321); the present analysis predicts that a flat is not necessary as long as the curvature of the crest is large relative to film thickness.

An even more remarkable example of the influence of a critical point occurs in a free-falling liquid curtain across which a pressure drop is imposed (Finnicum et al., 1993). Requiring that the curtain pass smoothly through the critical point determines the entire profile of the curtain if flow is initially subcritical, and in particular, the initial angle of the trajectory from vertical is determined independently of the geometry from which the flow issues.

The removal of the ostensible singularity in Eq. (25) directly justifies a constraint inside the flow domain. More formally, the application of a boundary condition at the critical point can be justified through Eq. (20), the hyperbolic equation describing the time evolution of small departures from steady state. The number of boundary conditions, and the regions of the flow that they can influence, must be consistent with the number of characteristics and their propagation, or equivalently, with the number and speed of waves in the film. By Eq. (22), there are two characteristics, and the critical point determines the farthest downstream location where one of these can propagate upstream. The theory of hyperbolic equations, therefore, dictates that the critical point is a location where a single boundary condition is applied because just one characteristic emanates in both the upstream and downstream directions. The steady state can be viewed as the evolution of a transient, and so the boundary condition of the steady formulation must be consistent with that in the time-dependent formulation. The time-dependent formulation clearly indicates the necessity of applying a boundary condition at the critical point based on the regions of influence. Weinstein et al. (1997) analyzed transients for the cited problem of a liquid curtain, which has nearly the same mathematical structure as the flow considered here.

References

Ackers, P., White, W. R., Perkins, J. A., and Harrison, A. J. M., 1978, *Weirs and Flumes for Flow Measurement,* Wiley, New York.

Brater, E. F., King, H. W., Lindell, J. E., and Wei, C. Y., 1996, *Handbook of Hydraulics,* 7th ed., McGraw-Hill, New York.

Dressler, R. F., 1949, "Mathematical Solution of the Problem of Roll-Waves in Inclined Open Channels," *Communications on Pure and Applied Mathematics,* Vol. 2, pp. 149–194.

Finnicum, D. S., Weinstein, S. J., and Ruschak, K. J., 1993, *Journal of Fluid Mechanics,* Vol. 255, pp. 647–665.

Fox, R. W., and McDonald, A. T., 1992, *Introduction to Fluid Mechanics,* 4th ed., Wiley, New York, pp. 519–521.

Kakac, S., and Yenner, Y., 1995, *Convective Heat Transfer,* 2nd ed., CRC Press, Boca Raton.

Press, W. H., Teukolsky, S. A., Vetterling, W. T., and Flannery, B. P., 1992, *Numerical Recipes in Fortran: the Art of Scientific Computing,* 2nd ed., Cambridge University Press, Cambridge, U. K.

Rouse, H., 1938, *Fluid Mechanics for Hydraulic Engineers,* 1961 reissue, Dover Publications, New York.

Ruschak, K. J., 1978, "Flow of a Falling Film into a Pool," *AIChE Journal,* Vol. 24, pp. 705–710.

Schlichting, H., 1979, *Boundary-Layer Theory,* McGraw-Hill, New York.

Weinberger, H. F., 1965, *A First Course in Partial Differential Equations,* Wiley, New York.

Weinstein, S. J., Clarke, A., Moon, A. G., and Simister, E. A., 1997, "Time-Dependent Equations Governing the Shape of a Two-Dimensional Liquid Curtain, Part 1: Theory," *Physics of Fluids,* Vol. 9, pp. 3625–3636.

Whitaker, S., 1968, *Introduction to Fluid Mechanics,* 1992 reissue, Krieger Publishing, Malabar, FL.

Bill Peck[1]
Postdoctoral Fellow.

Lorenz Sigurdson
Professor.

Department of Mechanical Engineering,
University of Alberta,
Edmonton Alberta, Canada T6G 2G8

Geometry Effects on Free Surface Vorticity Flux

Effects of geometry on the flux of vorticity from a free surface are discussed. Special attention is paid to situations where curvature-dependent contributions to the vorticity flux can be neglected. The geometry of vortex lines embedded in the surface is discussed in this context. These results show that vortex lines can be straight and geometry-induced vorticity flux is produced; conversely vortex lines can be curved and no geometry-induced vorticity flux is produced. A convenient method for assessing vorticity flux from a steady surface based on Gaussian curvature is derived.

1 Introduction

This paper discusses effects of complex surface geometries on the vorticity flux $\mathbf{\Phi}$ from an arbitrary two-dimensional free surface embedded in three-dimensional Euclidian space $\mathbb{R}^3$. Most previous analyses of free surface vorticity flux have been restricted to one-dimensional surfaces where the motion is steady.[2] Examples[1] are the free surfaces of plane waves and axisymmetric flows such as rising bubbles. Recent advances in experimental techniques have allowed analysis of complicated two-dimensional surface geometries, Dabiri (1997). In these experiments, complete understanding of geometric effects are essential for correct interpretation of vorticity levels at free surfaces and vorticity flux from free surfaces.

The idea of a vorticity flux was introduced by Lighthill (1963) to describe introduction of vorticity into a bulk fluid from rigid boundaries. Here, diffusion of linear momentum was written in terms of vorticity gradients normal to the boundary. Since vorticity is diffused in the same manner as momentum, the smoothing action of viscosity will try to equalize the level of vorticity where a gradient exists. This results in a flux of vorticity either from or to the surface.

Prediction of vorticity flux was extended to free surfaces by Lugt (1987) who used local series expansion about points on the free surface. More recently, Rood (1995, 1994) and Wu (1995) have interpreted the vorticity flux from free surfaces in a more general sense. We direct the reader to the cited papers by Rood for a thorough discussion of the physical significance of vorticity flux at a free surface. Lundgren and Koumoutsakos (1997) have constructed numerical schemes to predict the creation of vorticity at a free surface using the vorticity flux. For a review of recent work on the dynamics of free surfaces we refer the reader to Sarpkaya (1996). These papers are generally restricted to simple surface geometries and do not discuss the effects of surface geometry in detail. The present paper addresses complex geometric considerations and clears up some misinterpretations in the literature, Rood (1994).

Our paper is organized as follows. Several formulas used in this paper's derivations are presented in Section 2. The level of vorticity required to satisfy free surface boundary conditions is reviewed in Section 3. General expressions for the vorticity flux are derived in Section 4. Here, we also discuss the geometry of vortex lines at the surface. Some results in this section are useful for calculating $\mathbf{\Phi}$ from a rigid boundary. A vorticity flux equation specialized for steady surfaces is derived in Section 4.3.

2 Preliminary Formulas

We begin by presenting definitions and deriving formulas used to describe two-dimensional surfaces embedded in three-dimensional Euclidian space $\mathbb{R}^3$. Equations requiring results from differential geometry are derived with added detail.

2.1 Geometry. The tensor product of two arbitrary vectors $\mathbf{a}, \mathbf{b}$ is defined as $(\mathbf{a} \otimes \mathbf{b})\mathbf{c} = \mathbf{a}(\mathbf{b} \cdot \mathbf{c})$ where $\mathbf{c}$ is an arbitrary vector. Spatial forms of $\nabla \cdot (\ )$, $\nabla \times (\ )$, $\nabla(\ )$ are denoted div $(\ )$, curl $(\ )$, grad $(\ )$. With this convention grad$\mathbf{a}$ $\mathbf{b}$ and grad $\mathbf{a}^T\mathbf{b}$ replace $\mathbf{b} \cdot \nabla\mathbf{a}$ and $\nabla\mathbf{a} \cdot \mathbf{b}$ which some readers may be more familiar with. We refer readers unfamiliar with our chosen notation to Chadwick (1976) and Kosiński (1986) for further details.

We construct a convected coordinate system θ^α that maintains fixed correspondence with particles embedded in the material surface $\mathcal{S}$. Greek indices are understood to range over (1, 2); summation on repeated indices is implied.

A point on $\mathcal{S}$ is located relative to a fixed basis in $\mathbb{R}^3$ with the position vector $\mathbf{r} = \mathbf{r}(\theta^\alpha, t)$. Partial derivatives of $\mathbf{r}$ with respect to surface coordinates θ^α give the covariant basis vectors $\mathbf{a}_\alpha$ along θ^α; $\mathbf{r}_{,\alpha} = \mathbf{a}_\alpha$. Partial differentiation with respect to surface coordinates is represented with a comma and Greek subscript. The subscript 3 is reserved for differentiation with respect to θ^3 which is directed along the surface normal. The covariant derivative is denoted with a vertical bar and subscript $(\ )|_\beta$. For arbitrary contravariant components of a vector $\mathbf{c}$ the covariant derivative is

$$c^\alpha|_\beta = c^\alpha_{,\beta} + \Gamma^\alpha_{\gamma\beta} c^\gamma. \tag{2.1}$$

The surface Christoffel symbol appears in Eq. (2.1) and is defined by

$$\Gamma^\alpha_{\gamma\beta} = \mathbf{a}^\alpha \cdot \mathbf{a}_{\gamma,\beta}. \tag{2.2}$$

For further details we refer the reader to Kreyszig (1991).

The vectors $\mathbf{a}_\alpha$ span the tangent plane and can be used to calculate the surface normal $\mathbf{n} = (\mathbf{a}_1 \times \mathbf{a}_2)/|\mathbf{a}_1 \times \mathbf{a}_2|$. The gradient of $\mathbf{n}$ gives the symmetric curvature tensor $\mathbf{b}$,

$$\text{grad}\,\mathbf{n} = -\mathbf{n}_{,\alpha} \otimes \mathbf{a}^\alpha = -b^\beta_\alpha \mathbf{a}_\beta \otimes \mathbf{a}^\alpha = -\mathbf{b} = -\mathbf{b}^T, \tag{2.3}$$

where we have used Weingarten's equation,

$$\mathbf{n}_{,\alpha} = -b^\beta_\alpha \mathbf{a}_\beta. \tag{2.4}$$

Contravariant basis vectors $\mathbf{a}^\beta$ have been introduced in Eq. (2.2) and Eq. (2.3). These are related to $\mathbf{a}_\alpha$ through the surface metric $a_{\alpha\beta} = \mathbf{a}_\alpha \cdot \mathbf{a}_\beta$ by $\mathbf{a}_\alpha = a_{\alpha\beta}\mathbf{a}^\beta$.

We will find it useful to define an orthonormal basis embedded in $\mathcal{S}$, $(\boldsymbol{\xi}, \boldsymbol{\zeta}, \mathbf{n})$ where $\boldsymbol{\xi}$ and $\boldsymbol{\zeta}$ are orthogonal unit vectors in the tangent plane such that $\boldsymbol{\xi} \times \boldsymbol{\zeta} = \mathbf{n}$, Fig. 1. This coordinate system has the advantage that quantities referenced to it will be physical components of that quantity. Quantities referenced to a contravari-

[1] Presently, Center for Turbulence Research Stanford/NASA Ames Research Center, Stanford, CA 94305-3030.

[2] By one-dimensional we mean surfaces which vary in only one parameter.

Contributed by the Fluids Engineering Division for publication in the JOURNAL OF FLUIDS ENGINEERING. Manuscript received by the Fluids Engineering Division March 30, 1998; revised manuscript received June 7, 1999. Associate Technical Editor: D. P. Telionis.

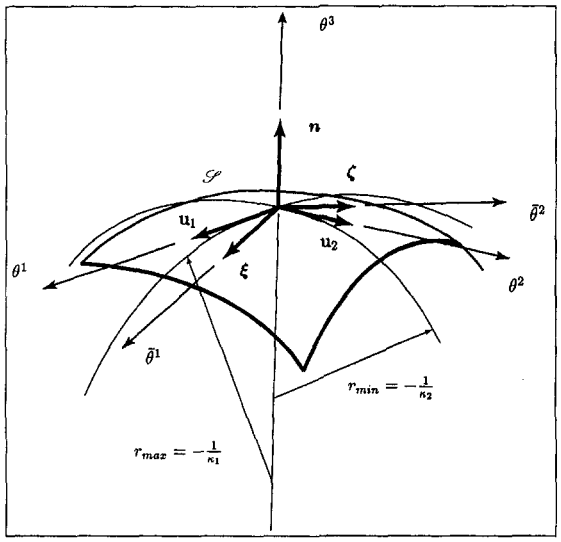

Fig. 1 Two orthonormal coordinate systems embedded in $\mathcal{S}$, $(\theta^1, \theta^2, \theta^3)$ and $(\bar{\theta}^1, \bar{\theta}^2, \theta^3)$

ant or covariant basis may not even have the same physical dimensions as their physical counterpart.

In orthonormal coordinates $\mathbf{b}$ takes on the form,

$$\mathbf{b} = \kappa_\xi \boldsymbol{\xi} \otimes \boldsymbol{\xi} + \kappa_\zeta \boldsymbol{\zeta} \otimes \boldsymbol{\zeta} + \tau(\boldsymbol{\xi} \otimes \boldsymbol{\zeta} + \boldsymbol{\zeta} \otimes \boldsymbol{\xi}). \quad (2.5)$$

Here, $\kappa_\xi = -1/r_\xi$, $\kappa_\zeta = -1/r_\zeta$ are the normal curvatures and τ represents the surface twist at a point $\mathcal{P}$ on $\mathcal{S}$. In some texts τ is called the geodesic torsion since it also represents the torsion of the geodesic curves passing through $\mathcal{P}$ directed along $\boldsymbol{\zeta}$ and $\boldsymbol{\xi}$ (Kreyszig, 1991).

In lines-of-curvature coordinates κ_ξ and κ_ζ correspond to principal curvatures of $\mathbf{b}$ so that $\tau = 0$ and

$$\mathbf{b} = \kappa_1 \mathbf{u}_1 \otimes \mathbf{u}_1 + \kappa_2 \mathbf{u}_2 \otimes \mathbf{u}_2. \quad (2.6)$$

Here κ_1, κ_2 are the principal curvatures and $\mathbf{u}_1$ and $\mathbf{u}_2$ are the principal directions.

We will also use the two scalar invariants of $\mathbf{b}$, the mean curvature $H = \text{div } \mathbf{b}/2 = (\kappa_1 + \kappa_2)/2 = (\kappa_\xi + \kappa_\zeta)/2$ and the Gaussian curvature $K = \det \mathbf{b} = \kappa_1\kappa_2 = \kappa_\xi\kappa_\zeta - \tau^2$.

3 Vorticity at a Free Surface

In this section we briefly discuss the level of vorticity required to satisfy boundary conditions at an arbitrary free surface. Complete derivations of these results are available in Peck and Sigurdson (1998).

Recently, Longuet-Higgins (1998) presented similar results, apparently inspired by Peck and Sigurdson (1998), which is referenced. Longuet-Higgins (1998) used techniques which may be more familiar to some. These techniques are found in texts such as Batchelor (1967). Our derivations rely on a tensor treatment of the surface and results from differential geometry. This is similar, in spirit, to the work of Aris (1962) and Scriven (1960). An immediate advantage of this approach is the obvious physical interpretation of geometry-dependent terms in the resulting equations.

3.1 Model. We assume a two-dimensional material surface $\mathcal{S}$ separates two regions of fluid, $\mathcal{R}^1$ and $\mathcal{R}^2$. Surface tractions $\mathbf{t}_{(n)}$ in one region, say $\mathcal{R}^1$, are assumed to be negligible except for a constant pressure p_o. With these assumptions, the level of vorticity at $\mathcal{S}$ can be calculated by considering the jump in $\mathbf{t}_{(n)}$ across $\mathcal{S}$:

$$[\![\mathbf{t}_{(n)}]\!] = -\rho_{\mathcal{S}}(\dot{\mathbf{v}} - \mathbf{f}_{\mathcal{S}}) + \text{div } \mathbf{S}. \quad (3.1)$$

Here, $[\![\ ]\!]$ denotes a jump in a quantity across $\mathcal{S}$. Body forces acting on surface elements are denoted $\mathbf{f}_{\mathcal{S}}$. An intrinsic surface stress $\mathbf{S}$ is assumed to depend on surface tension γ through the constitutive equation $\mathbf{S} = \gamma \mathbf{a}^\alpha \otimes \mathbf{a}_\alpha$. The velocity of fluid particles embedded in $\mathcal{S}$ is represented with $\mathbf{v}$. The velocity of particles in the bulk fluid is denoted $\mathbf{u}$. In cases where the surface density $\rho_{\mathcal{S}}$ can be neglected the vector-valued tangential component of Eq. (3.1) becomes

$$\mathbf{Dn} - [\mathbf{n} \cdot (\mathbf{Dn})]\mathbf{n} = \frac{1}{2\mu} \text{grad}_{\mathcal{S}}\ \gamma, \quad (3.2)$$

and the scalar-valued normal component becomes

$$2\mu \mathbf{n} \cdot \mathbf{Dn} = p - p_o + 2H\gamma. \quad (3.3)$$

The symmetric portion of the velocity gradient tensor $\mathbf{L}$ is the rate-of-strain tensor $\mathbf{D} = (\mathbf{L} + \mathbf{L}^T)/2$. A surface gradient operator is represented with $\text{grad}_{\mathcal{S}}$.

Equation (3.2) can be rearranged as,

$$\mathbf{Wn} = \dot{\mathbf{n}} + \frac{1}{2\mu} \text{grad}_{\mathcal{S}}\ \gamma, \quad (3.4)$$

where $\mathbf{W} = (\mathbf{L} - \mathbf{L}^T)/2$ is the spin tensor and $\dot{\mathbf{n}}$ is the material derivative of the surface normal. $\mathbf{W}$ is a skew symmetric tensor so that an axial vector $\boldsymbol{\omega}$ exists given by $2\mathbf{Wn} = \boldsymbol{\omega} \times \mathbf{n}$; in this case $\boldsymbol{\omega} = \text{curl } \mathbf{u}$ is the vorticity. Substituting this relation into Eq. (3.4) gives the following expression for the tangential component of vorticity $\boldsymbol{\omega}_t$ on $\mathcal{S}$:

$$\boldsymbol{\omega}_t = 2\mathbf{n} \times \dot{\mathbf{n}} + \frac{1}{\mu} \mathbf{n} \times \text{grad}_{\mathcal{S}}\ \gamma. \quad (3.5)$$

Here, and for the remainder of this text the subscript $(\ )_t$ denotes components of a vector tangential to $\mathcal{S}$.

The material derivative of $\mathbf{n}$ in surface coordinates is

$$\dot{\mathbf{n}} = -\text{grad}_{\mathcal{S}}\ (v) - b^\beta_\alpha v_\beta \mathbf{a}^\alpha = -\text{grad}_{\mathcal{S}}\ (v) - \mathbf{b}\mathbf{v}_t. \quad (3.6)$$

We refer the reader to Naghdi (1972) for this derivation of $\dot{\mathbf{n}}$. Substituting Eq. (2.6) into Eq. (3.6) gives the level of tangential vorticity on $\mathcal{S}$ in lines-of-curvature components,

$$\boldsymbol{\omega}_t = 2\ \text{grad}_{\mathcal{S}}\ (v) \times \mathbf{n} + 2(\kappa_2 v_2)\mathbf{u}_1 - 2(\kappa_1 v_1)\mathbf{u}_2. \quad (3.7)$$

Alternatively, we can express $\boldsymbol{\omega}_t$ with the basis used in Eq. (2.5) where the influence of the surface twist on the level of vorticity is now represented:

$$\boldsymbol{\omega}_t = 2\ \text{grad}_{\mathcal{S}}\ (v) \times \mathbf{n} + 2(\kappa_\zeta v_\zeta + \tau v_\xi)\boldsymbol{\xi} - 2(\kappa_\xi v_\xi + \tau v_\zeta)\boldsymbol{\zeta}. \quad (3.8)$$

If the surface is steady $\text{grad}_{\mathcal{S}}\ v = \mathbf{0}$. Also, in the special case of a steady flow where the velocity $\mathbf{v}_t$ is directed along a principal curvature Eq. (3.7) and Eq. (3.8) reduce to the well-known result appearing in Batchelor (1967),

$$\omega_1 = 2\kappa_2 v_2. \quad (3.9)$$

4 Vorticity Flux

Until now, we have only examined the level of vorticity required to satisfy boundary conditions on $\mathcal{S}$. We can gain insight into the rate at which vorticity enters or leaves the bulk fluid from the surface through expressions for the vorticity flux. In the derivations that follow, most of the equations are valid for any material surface embedded in a fluid. The case of a free surface is examined by directly substituting values required by the free surface boundary conditions into the momentum equation.

In this paper's context, the vorticity flux $\boldsymbol{\Phi}$ is defined by,

$$\boldsymbol{\Phi} = \nu\ \text{grad}\ \boldsymbol{\omega}\mathbf{n} = \nu \frac{\partial \boldsymbol{\omega}_t}{\partial \theta^3} + \nu \frac{\partial (\boldsymbol{\omega}\mathbf{n})}{\partial \theta^3}. \quad (4.1)$$

The first term on the right of Eq. (4.1) represents normal gradients of vorticity tangent to $\mathcal{S}$. The second term on the right represents the normal gradients of vorticity normal to the surface. ω will be used to represent the scalar component of vorticity normal to $\mathcal{S}$ so that $\omega\mathbf{n}$ is the normal vector component of $\boldsymbol{\omega}$.

4.1 Flux of Normal Vorticity. The vorticity flux of normal vorticity $\omega\mathbf{n}$ is readily derived from the vorticity field's solenoidal property:

$$\operatorname{div} \boldsymbol{\omega} = \operatorname{tr} (\operatorname{grad} \boldsymbol{\omega}) = 0. \tag{4.2}$$

To calculate the surface divergence, the vorticity gradient tensor is first calculated in terms of surface coordinates,

$$\operatorname{grad} \boldsymbol{\omega} = \boldsymbol{\omega}_{,\alpha} \otimes \mathbf{a}^{\alpha} + (\omega\mathbf{n})_{,3} \otimes \mathbf{n}. \tag{4.3}$$

After differentiating and grouping terms we obtain

$$\begin{aligned}\operatorname{grad} \boldsymbol{\omega} = {} & (\omega^{\alpha}|_{\beta} - b^{\gamma}_{\beta}\omega)\mathbf{a}_{\alpha} \otimes \mathbf{a}^{\beta} + \omega^{\alpha}_{,3}\mathbf{a}_{\alpha} \otimes \mathbf{n} \\ & + (\omega_{,\beta} + b^{\alpha}_{\beta}\omega_{\alpha})\mathbf{n} \otimes \mathbf{a}^{\beta} + \omega_{,3}\mathbf{n} \otimes \mathbf{n}.\end{aligned} \tag{4.4}$$

Taking the trace of the vorticity gradient tensor yields,

$$\begin{aligned}\operatorname{tr}(\operatorname{grad} \boldsymbol{\omega}) &= \operatorname{tr} [\boldsymbol{\omega}_{,\alpha} \otimes \mathbf{a}^{\alpha} + (\omega\mathbf{n})_{,3} \otimes \mathbf{n}] \\ &= \omega^{\alpha}|_{\alpha} - b^{\alpha}_{\alpha}\omega + \omega_{,3} \\ &= \omega^{\alpha}|_{\alpha} - 2H\omega + \omega_{,3} = 0\end{aligned} \tag{4.5}$$

The mean curvature H appears in Eq. (4.5) which is the arithmetic mean of any two orthogonal normal curvatures at a point on $\mathcal{S}$.

Obtaining an expression for the flux of normally directed vorticity is a simple matter of rearranging Eq. (4.5) and multiplying by ν,

$$\nu \frac{\partial(\omega\mathbf{n})}{\partial\theta^3} = \nu(2H\omega - \omega^{\alpha}|_{\alpha})\mathbf{n} \tag{4.6}$$

It is important to note that the mean curvature is dependent on surface orientation. This means the sign of H is dependent on the direction of the unit normal to $\mathcal{S}$. In the present context $\mathbf{n}$ is assumed to point away from the bulk fluid.

4.2 Flux of Tangential Vorticity. Tangential components of $\boldsymbol{\Phi}$ represent the flux of $\boldsymbol{\omega}_t$ from $\mathcal{S}$. An expression for this can be derived from the momentum equation

$$\rho(\mathbf{a} - \mathbf{g}) = \operatorname{div} \boldsymbol{\sigma}. \tag{4.7}$$

Here $\boldsymbol{\sigma} = -p\mathbf{I} + 2\mu\mathbf{D}$ is the Cauchy stress, $\mathbf{a}$ is the fluid acceleration and $\mathbf{g}$ is the body force; for our purposes $\mathbf{g}$ will only be assumed to represent gravity. We decompose Eq. (4.7) into normal and tangential components as follows,

$$\begin{aligned}\rho\tilde{\mathbf{a}} &= [\mathbf{n} \cdot (\rho\tilde{\mathbf{a}})]\mathbf{n} + \mathbf{n} \times (\rho\tilde{\mathbf{a}} \times \mathbf{n}) \\ &= [\mathbf{n} \cdot (\operatorname{div} \boldsymbol{\sigma})]\mathbf{n} + \mathbf{n} \times (\operatorname{div} \boldsymbol{\sigma} \times \mathbf{n})\end{aligned} \tag{4.8}$$

For convenience $\tilde{\mathbf{a}}$ will be used to represent $(\mathbf{a} - \mathbf{g})$. Using the constitutive equation given above and equating tangential components of Eq. (4.7) gives,

$$\rho\tilde{\mathbf{a}}_t = -\operatorname{grad}_{\mathcal{S}} p - \mathbf{n} \times (\mu \operatorname{curl} \boldsymbol{\omega} \times \mathbf{n}), \tag{4.9}$$

where we have used the identity div grad $\mathbf{u}$ = grad (div $\mathbf{u}$) − curl curl $\mathbf{u}$. Placing our attention on the last right hand side term of Eq. (4.9) we recognize curl $\boldsymbol{\omega}$ as the axial vector of a skew-symmetric tensor formed from (grad $\boldsymbol{\omega}$ − grad $\boldsymbol{\omega}^T$) so that (grad $\boldsymbol{\omega}$ − grad $\boldsymbol{\omega}^T$)$\mathbf{n}$ = curl $\boldsymbol{\omega} \times \mathbf{n}$. Substituting into Eq. (4.9) gives

$$\rho\tilde{\mathbf{a}}_t = -\operatorname{grad}_{\mathcal{S}} p - \mu\mathbf{n} \times (\operatorname{grad} \boldsymbol{\omega}\mathbf{n} - \operatorname{grad} \boldsymbol{\omega}^T\mathbf{n}), \tag{4.10}$$

or, in terms of the vorticity flux:

$$\nu \operatorname{grad} \boldsymbol{\omega}\mathbf{n} = \mathbf{n} \times \tilde{\mathbf{a}}_t + \mathbf{n} \times \frac{\operatorname{grad}_{\mathcal{S}} p}{\rho} + \nu \operatorname{grad} \boldsymbol{\omega}^T\mathbf{n}. \tag{4.11}$$

For our purposes, the last term on the right of Eq. (4.11) is expressed more conveniently using the identity

$$\begin{aligned}\operatorname{grad} \boldsymbol{\omega}^T\mathbf{n} &= \operatorname{grad} (\boldsymbol{\omega} \cdot \mathbf{n}) - \operatorname{grad} \mathbf{n}^T\boldsymbol{\omega} \\ &= \operatorname{grad} (\omega) + \mathbf{b}\boldsymbol{\omega}_t.\end{aligned} \tag{4.12}$$

Since $\mathbf{b}$ is purely a surface tensor it will only operate on a surface vector so $\mathbf{b}\boldsymbol{\omega}$ can be replaced with $\mathbf{b}\boldsymbol{\omega}_t$. Also

$$\operatorname{grad} (\omega) = \operatorname{grad}_{\mathcal{S}} (\omega) + \frac{\partial\omega}{\partial\theta^3}\mathbf{n} \tag{4.13}$$

Substituting Eq. (4.13) into Eq. (4.12) and using this result in Eq. (4.11) yields

$$\nu \frac{\partial\boldsymbol{\omega}_t}{\partial\theta^3} = \mathbf{n} \times \tilde{\mathbf{a}}_t + \mathbf{n} \times \frac{\operatorname{grad}_{\mathcal{S}} p}{\rho} + \nu \operatorname{grad}_{\mathcal{S}} (\omega) + \nu\mathbf{b}\boldsymbol{\omega}_t \tag{4.14}$$

The first term on the right represents tangential acceleration of material elements on $\mathcal{S}$, the second term the tangential pressure gradient. The normal gradients of normal vorticity in Eq. (4.13) cancel those within grad$\boldsymbol{\omega}$ $\mathbf{n}$ so we are left with the third term on the right of Eq. (4.14) which is the surface gradient of the normally directed vorticity. The curvature tensor appears in the last term of Eq. (4.14). This term represents the vorticity flux due to surface curvature acting on the component of vorticity tangential to $\mathcal{S}$.

At this point Eq. (4.14) is simply an alternate expression of the momentum equation tangential to any arbitrary material surface embedded in $\mathbb{R}^3$. No boundary conditions have been imposed to reflect the physical character of $\mathcal{S}$. If a vortex ring were to approach this surface there would be no reason for the vortex ring to be deflected from its path. Thus, the wide variety of phenomena associated with vortex-free-surface interactions such as vortex ring rebound and vortex reconnection are not predicted using this equation without imposing suitable boundary conditions (Sarpkaya, 1996; Bernal and Kwon, 1989). Suitable boundary conditions for a rigid surface can also be used with Eq. (4.14) which produce entirely different phenomena.

We introduce $\boldsymbol{\Phi}_{\kappa}$ to represent the last term on the right of Eq. (4.14)

$$\boldsymbol{\Phi}_{\kappa} = \nu\mathbf{b}\boldsymbol{\omega}_t. \tag{4.15}$$

Interpretation of $\boldsymbol{\Phi}_{\kappa}$ has caused some confusion in the literature (Rood, 1994). The primary purpose of the present paper is to clarify the conditions under which this term can be neglected.

On a free surface, the level of tangential vorticity is set as derived in Section 3. Introducing this boundary condition into Eq. (4.14) provides insight into $\boldsymbol{\Phi}_{\kappa}$. If surface tension gradients are negligible or the ratio γ/μ is negligible we write $\boldsymbol{\omega}_t$ on $\mathcal{S}$ as,

$$\boldsymbol{\omega}_t = 2\mathbf{n} \times \dot{\mathbf{n}}. \tag{4.16}$$

Substituting into Eq. (4.14) gives

$$\begin{aligned}\nu \frac{\partial\boldsymbol{\omega}_t}{\partial\theta^3} = {} & \mathbf{n} \times \tilde{\mathbf{a}}_t + \mathbf{n} \times \frac{\operatorname{grad}_{\mathcal{S}} p}{\rho} + \nu \operatorname{grad}_{\mathcal{S}} (\omega) \\ & + \underbrace{2\nu\mathbf{b}(\mathbf{n} \times \dot{\mathbf{n}})}_{\boldsymbol{\Phi}_{\kappa}}.\end{aligned} \tag{4.17}$$

We may also write $\boldsymbol{\Phi}_{\kappa}$ as

$$2\nu\mathbf{b}\left(\mathbf{n} \times \frac{\dot{\mathbf{n}}}{\|\dot{\mathbf{n}}\|}\|\dot{\mathbf{n}}\|\right) = 2\nu\|\dot{\mathbf{n}}\|\mathbf{b}\mathbf{t} \tag{4.18}$$

where $\mathbf{t}$ is a unit vector directed along the tangential vorticity. $\mathbf{t}$ is calculated from the vector product of $\mathbf{n}$ and the normalized $\dot{\mathbf{n}}$; $\mathbf{t} = \mathbf{n} \times \dot{\mathbf{n}}/\|\dot{\mathbf{n}}\|$.

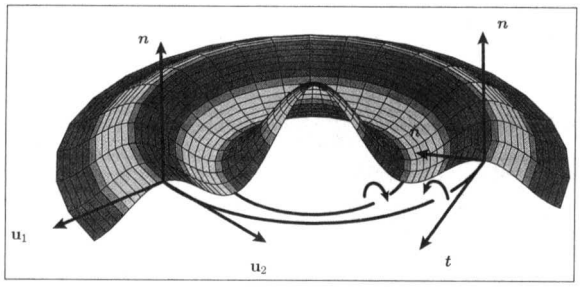

Fig. 2 A surface of revolution formed by rotating a Bessel function around the vertical axis. Radially directed lines are surface meridians, the circular lines are surface parallels. Lines-of-curvature correspond to meridians and parallels. Surface shading indicates the Gaussian curvature's sign. Darkly shaded regions denote hyperbolic regions $K < 0$, lightly shaded regions are parabolic $K = 0$. Unshaded regions are elliptic $K > 0$. The two dark lines are representative vortex lines. The sign of the vorticity is indicated in the figure.

Writing $\mathbf{b}$ in terms of lines-of-curvature components Eq. (4.18) becomes,

$$2\nu\|\dot{\mathbf{n}}\|[\kappa_1(\mathbf{u}_1 \cdot \mathbf{t})\mathbf{u}_1 + \kappa_2(\mathbf{u}_2 \cdot \mathbf{t})\mathbf{u}_2] \tag{4.19}$$

Hence, if $\mathbf{t}$ is directed along a zero-valued principal curvature, $\mathbf{\Phi}_\kappa$ vanishes. This does not imply that vortex lines along $\mathbf{t}$ are straight however. As an example, consider the surface shown in Fig. 2. For this example we have chosen a surface of revolution. The profile curve is a Bessel function, the surface being formed by revolving this curve, shown in Fig. 3, around the vertical axis. The precise function which describes the surface is unimportant, rather the overall qualitative analysis is what we are interested in. On this surface the parallels and meridians are lines-of-curvature so that at each point on $\mathcal{S}$ the principal curvatures are directed along these curves. We denote the principal curvature directed along the surface parallel as κ_π and that directed along the meridians as κ_μ. In the present case $\kappa_\pi = \kappa_1$ and $\kappa_\mu = \kappa_2$. A plot of κ_π, κ_μ and the Gaussian curvature K for the surface in Fig. 2 is shown in Fig. 4. We will see the significance of the Gaussian curvature in Section 4.3. From Fig. 2 and Fig. 4 we see that κ_π, the normal curvature in the direction of the vortex lines vanishes at the local maxima and minima of the generating curves which means that $\mathbf{\Phi}_\kappa$ necessarily vanishes at these points. However, the vortex lines at these points are not straight but form a set of concentric circles about the vertical axis. Hence, the result given in Rood (1994) does not hold: vortex lines can be curved with $\mathbf{\Phi}_\kappa = \mathbf{0}$.

Further complication arises if $\mathbf{t}$ is not directed along a principal direction of curvature. If this is the case $\mathbf{\Phi}_\kappa$ becomes

$$2\nu\|\dot{\mathbf{n}}\|[\kappa_\xi(\boldsymbol{\xi} \cdot \mathbf{t})\boldsymbol{\xi} + \tau(\boldsymbol{\zeta} \cdot \mathbf{t})\boldsymbol{\zeta}]. \tag{4.20}$$

This shows that even if the normal curvature vanishes along $\mathbf{t}$ a component of vorticity flux due to surface twist would still exist:

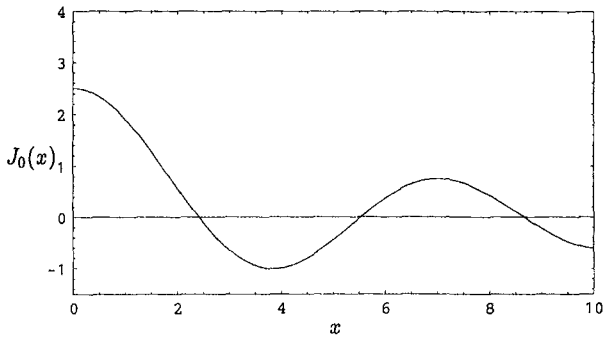

Fig. 3 A Bessel function of the first kind $f(x) = J_0(x)$. This is the generating curve used for the surface of revolution shown in Fig. 2.

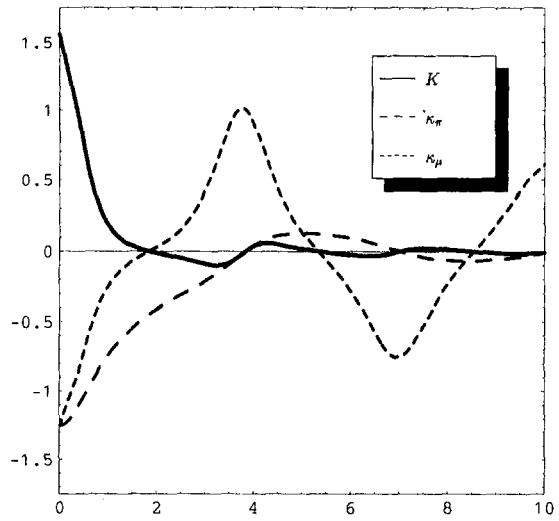

Fig. 4 The value of the principal curvatures κ_π and κ_μ on the surface shown in Fig. 2 as a function of radial distance x from the axis of revolution. The Gaussian curvature K is also shown.

$$\mathbf{\Phi}_\kappa = 2\nu\|\dot{\mathbf{n}}\|\tau\boldsymbol{\zeta}. \tag{4.21}$$

For illustration, we consider the surface shown in Fig. 5. Here we assume vortex lines are directed along rules of the hyperbolic paraboloid shown. The rules of $\mathcal{S}$ are straight lines embedded in $\mathcal{S}$, hence they have no normal curvature and the surface has no normal curvature in that direction. In this case, even though the vortex lines are straight $\mathbf{\Phi}_\kappa$ is nonzero.

4.3 The Vorticity Flux Equation at a Steady Surface. This section describes a convenient means for assessing effects of surface curvature on $\mathbf{\Phi}_\kappa$ from a steady surface. By a steady surface we mean a surface where $\text{grad}_{\mathcal{S}}(v) = 0$. This implies that there is no local rotation of $\mathcal{S}$ in the chosen reference frame. We may also view this as analysis as being that for the steady component of $\mathbf{\Phi}_\kappa$ on an unsteady surface.

With this steady-surface simplification Eq. (3.7) becomes,

$$\boldsymbol{\omega}_t = 2\mathbf{b}\mathbf{v}_t \times \mathbf{n} = 2b^\alpha_\beta v_\alpha \mathbf{a}^\beta \times \mathbf{n} = -2b^\alpha_\beta v_\alpha \epsilon^{\beta\rho}\mathbf{a}_\rho \tag{4.22}$$

Substituting Eq. (4.22) into Eq. (4.15) gives

$$\mathbf{\Phi}_\kappa = -2\nu b^\gamma_\lambda b^\alpha_\beta v_\alpha \epsilon^{\beta\rho}\mathbf{a}_\gamma \otimes \mathbf{a}^\lambda \mathbf{a}_\rho, = -2\nu b^\alpha_\beta b^\gamma_\rho v_\alpha \epsilon^{\beta\rho}\mathbf{a}_\gamma,$$
$$= -2\nu K v_\alpha \epsilon^{\alpha\gamma}\mathbf{a}_\gamma = 2\nu K v \times \mathbf{n}, \tag{4.23}$$

after noting $b^\alpha_\beta b^\gamma_\rho \epsilon^{\beta\rho} = K\epsilon^{\alpha\gamma}$. We can also rewrite Eq. (4.23) in the convenient form

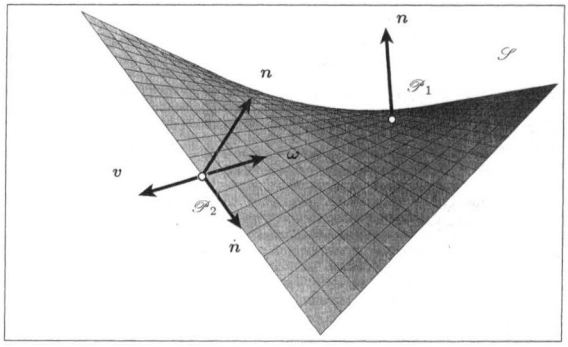

Fig. 5 Local flow on a hyperbolic paraboloid. The fluid velocity v is assumed directed along a rule of the surface. Hence, as a fluid element travels from $\mathcal{P}_1$ to $\mathcal{P}_2$ n rotates due to the surface twist implying the sign of vorticity indicated. In this case the vortex line is straight.

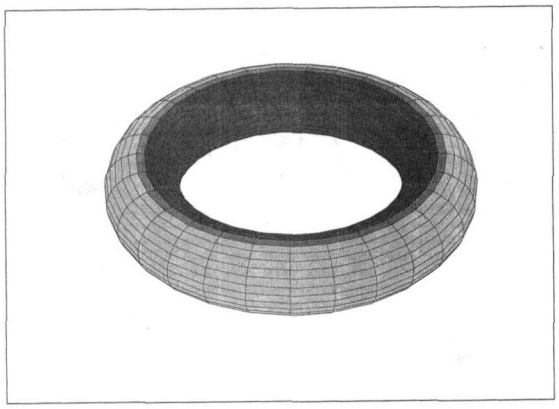

Fig. 6 A torus colored with Gaussian curvature. As with Fig. 2 hyperbolic points are colored with a dark shade, elliptic points with a light shade. The intermediate shade represents parabolic regions.

$$\mathbf{\Phi}_\kappa = 2\nu K q \hat{\mathbf{t}}, \tag{4.24}$$

where $q = \|\mathbf{v}\|$ and $\hat{\mathbf{t}} = \mathbf{m} \times \mathbf{n}$ is a unit vector normal to the plane containing the surface normal and the unit vector $\mathbf{m}$ directed along $\mathbf{v}$.

In Eq. (4.23) and Eq. (4.24) the Gaussian curvature K appears. K is a scalar invariant independent of direction on $\mathcal{S}$. The sign of K characterizes regions of a surface as elliptic $K > 0$, parabolic $K = 0$ or hyperbolic $K < 0$. A developable surface is a surface which is parabolic everywhere.

From Eq. (4.24) we see that determining the sign of $\mathbf{\Phi}_\kappa$ is a matter of assessing the sign of K and knowing the direction of $\mathbf{v}$. Hence if the flow passes from an elliptic region to a hyperbolic region the sign of $\mathbf{\Phi}_\kappa$ will change. This is a convenient method since we do not need knowledge of $\boldsymbol{\omega}_t$. Nor do we require knowledge of the normal curvatures or surface twist beyond what is necessary for calculating K.

Thus, we have a convenient method of determining if the curvature-dependent term will contribute to the vorticity flux in a steady flow. If the Gaussian curvature is nonzero and $\|\mathbf{v}\| \neq 0$ there will be a contribution. If the surface is developable or is locally parabolic there will be no contribution regardless of the flow's direction: $\mathbf{\Phi}_\kappa = 0$.

We consider steady two-dimensional plane waves as an example. Here $\mathcal{S}$ is a surface of translation and the flow is assumed directed along the generating curve. A nonzero level of vorticity occurs at all points on the curve except for points of inflection on the generating curve where the normal curvature vanishes and. Since the principal curvature normal to the generating curve is always zero, the surface is developable and $\mathbf{\Phi}_\kappa$ vanishes. Indeed the direction of the flow is irrelevant to $\mathbf{\Phi}_\kappa$. No matter which way the flow is directed, $K = 0$ and $\mathbf{\Phi}_\kappa = 0$.

The sign of K on surfaces with more complex geometry—even one-dimensional surfaces such as a torus—is not always so obvious. As an example we have illustrated the Gaussian curvature of a torus by shading the surface as shown in Fig. 6. This could represent the geometry of a toroidal bubble rising in water. Here the inner regions of the torus are hyperbolic while the outer regions are elliptic, the dividing region being parabolic. The parabolic region is caused by a vanishing principal curvature directed along the surface parallel. Hence in the parabolic regions $\mathbf{\Phi}_\kappa$ will vanish. Also, if the direction of the flow does not change, the sign of $\mathbf{\Phi}_\kappa$ will change as we move from hyperbolic to elliptic regions.

A still more complex one-dimensional surface shown in Fig. 2 is colored with Gaussian curvature. As in Fig. 6, K vanishes at the local minima and maxima of the generating curve due to vanishing κ_π. The Gaussian curvature is also zero at points of inflection on the generating curve since at these points κ_μ vanishes.

Further simplification of tangential vorticity flux equation is possible if both the surface and flow are steady. First, we rewrite the kinematic expression for the fluid acceleration:

$$\tilde{\mathbf{a}} = \mathbf{a} - \mathbf{g} = \frac{\partial \mathbf{u}}{\partial t} + \mathbf{L}\mathbf{u} - \mathbf{g}. \tag{4.25}$$

Since the flow is assumed steady, $\partial u/\partial t = \mathbf{0}$. Now $\mathbf{a}$ becomes $\mathbf{L}\mathbf{u} = \mathbf{L}^T\mathbf{u} + 2\mathbf{W}\mathbf{u}$ so that

$$\mathbf{a} = \tfrac{1}{2}\,\mathrm{grad}\,(v^2) + \boldsymbol{\omega} \times \mathbf{u} \tag{4.26}$$

after using the relation $\mathbf{L}^T\mathbf{u} = \mathrm{grad}\,(v^2)/2$. If we assume no normal vorticity, the vector product of $\mathbf{n}$ with the Lamb vector $\boldsymbol{\omega} \times \mathbf{u}$ vanishes as does the surface gradient of normal vorticity so that Eq. (4.14) becomes

$$\nu \frac{\partial \boldsymbol{\omega}_t}{\partial \theta^3} = -\mathrm{grad}_{\mathcal{S}}\, \mathcal{H} \times \mathbf{n} - 2\nu K(q\hat{\mathbf{t}}) \tag{4.27}$$

where the surface streamline is assumed directed along $\mathbf{m}$. The total head is $\mathcal{H} = \frac{1}{2}q^2 + p/\rho + \Omega$ and grad $\Omega = -\mathbf{g}$. This is a simple extension of the result Lugt derived for a locally cylindrical surface (Lugt, 1987):

$$\nu \frac{\partial \omega}{\partial r} = \frac{1}{R}\frac{\partial \mathcal{H}}{\partial \theta}. \tag{4.28}$$

Here, r is the radial coordinate and θ is the azimuthal. R is assumed to be a fixed radial distance. Lugt's result holds at points on a locally cylindrical, steady surface since such points are parabolic ($K = 0$) and the effects of geometry-dependent terms can be ignored. Eq. (4.27) extends this result to three dimensions and non-parabolic points.

Surface tension gradients can also be included. Brøns (1994) included surface tension gradient effects and derived an expression for the vorticity flux from a two-dimensional steady flow in the plane. He used a local series expansion technique similar to Lugt's.

To include surface tension gradients in the present analysis, Φ_κ must be modified. First, from Eq. (3.5) and Eq. (4.15):

$$\Phi_\kappa = \nu \mathbf{b}\boldsymbol{\omega}_t = 2\nu K \mathbf{v} \times \mathbf{n} + \frac{1}{\rho}\mathbf{b}(\mathbf{n} \times \mathrm{grad}_{\mathcal{S}}\, \gamma) \tag{4.29}$$

Both terms on the right are zero for flows in the plane. This follows for the first term since K is automatically zero in a two-dimensional plane flow. The second term's zero value follows since $\mathrm{grad}_{\mathcal{S}}\, \gamma$ will lie in the plane of the flow so that $\mathbf{n} \times \mathrm{grad}_{\mathcal{S}}\, \gamma$ is directed along a vector $\mathbf{t}$ out of the plane. Now, considering the whole term $\mathbf{bt}$, a nonzero component of $\mathbf{b}$ would be required out of the plane for this term not to vanish. For a plane flow, the surface is a surface of translation and the out-of-plane curvature is always zero.

The surface tension gradient terms derived by Brøns (1994) were for two-dimensional plane flow. We have shown above that surface tension gradient effects vanish in $\mathbf{\Phi}_\kappa$ for this type of flow. The terms derived by Brøns (1994) appear by rewriting the pressure in $\mathcal{H}$ using the normal component of the surface traction boundary condition Eq. (3.3):

$$\mathrm{grad}_{\mathcal{S}}\, \mathcal{H} = \mathrm{grad}_{\mathcal{S}} \left(\frac{q^2}{2} + 2\nu\lambda + \Omega \right) - 2\frac{H}{\rho}\,\mathrm{grad}_{\mathcal{S}}\, \gamma - 2\,\mathrm{grad}_{\mathcal{S}}\, H\frac{\gamma}{\rho}, \tag{4.30}$$

where we have used $\lambda = \mathbf{n} \cdot \mathbf{D}\mathbf{n}$. In plane flow, $2H$ simply reduces to the normal curvature κ of the bounding plane curve.

Using the results of Eq. (4.29) and Eq. (4.30) with Eq. (4.14) gives the general case for a steady three-dimensional steady flow with surface tension gradients:

$$\nu \frac{\partial \boldsymbol{\omega}_t}{\partial \theta^3} = -\text{grad}_{\mathcal{S}} \left(\frac{q^2}{2} + 2\nu\lambda + \Omega \right) \times \mathbf{n} + 2 \frac{H}{\rho} \text{grad}_{\mathcal{S}}\, \gamma \times \mathbf{n}$$

$$+ 2\, \text{grad}_{\mathcal{S}}\, \mathcal{H} \frac{\gamma}{\rho} \times \mathbf{n} - 2\nu K q \hat{\mathbf{t}} - \mathbf{b}(\mathbf{n} \times \text{grad}_{\mathcal{S}}\, \gamma). \quad (4.31)$$

This is the three-dimensional generalization of Brøns' Eq. (59). On a flat surface $\mathbf{b} = 0$ and $H = K = 0$; hence, all the surface tension gradient dependent terms in Eq. (4.31) become zero.

5 Summary

In this paper we have discussed effects of surface geometry on the flux of vorticity $\boldsymbol{\Phi}$ from a free surface using results from differential geometry. When written in this form, physical interpretation of the equations predicting vorticity flux from an interface becomes obvious. Our analysis has corrected interpretations previously appearing in the literature regarding the effect of surface geometry on the vorticity flux. Our results confirm that if $\boldsymbol{\omega}_t$ is directed along a zero-valued principal curvature the effect of surface curvature can be ignored. However, we have demonstrated with examples that knowing when the principal curvature is zero is not always obvious as demonstrated in Fig. 6. This example shows that a vortex line directed along a zero-valued principal curvature is not necessarily straight. We have also shown that a straight vortex line does not imply a vanishing vorticity flux.

In the special case of a steady interface, the Gaussian curvature can be used as a simple means of determining whether the geometry-dependent vorticity flux term need be included. While Wu (1995) noted this geometry-dependent term, he interpreted his results in terms of $\boldsymbol{\omega}_t$ and the principal curvatures rather than the invariant Gaussian curvature and surface velocity. With our analysis we can easily deduce that if $K = 0$ then $\boldsymbol{\Phi}_\kappa$ vanishes regardless of the level of vorticity at the surface. Hence, on any developable surface this term can be ignored. For example, on a purely two dimensional wave where the free surface is a surface of translation $K = 0$ and the vorticity flux vanishes. However, in a spherical geometry such as a spherical liquid drop or bubble, $K > 0$ and this term must be considered.

We have also given a simple extension to Lugt's result for a steady cylindrical surface that now includes all three-dimensional steady surfaces. The effects of surface tension gradients have also been included extending Brøns (1994) result. Here we found the effects of surface tension gradients on $\boldsymbol{\Phi}_\kappa$ vanish in two-dimensional plane flows.

References

Rutherford, Aris, 1962, *Vectors, Tensors and the Basic Equations of Fluid Mechanics,* Prentice-Hall, Englewood Cliffs, NJ.

Batchelor, G. K., 1967, *An Introduction to Fluid Dynamics,* Cambridge University, New York.

Bernal, L. P., and Kwon, J. T., 1989, "Vortex Ring Dynamics at a Free-Surface," *Physics of Fluids A,* Vol. 1(3), pp. 449–451, Mar.

Brøns, M., 1994, "Topological Fluid Dynamics of Interfacial Flows," *Physics of Fluids,* Vol. 6, pp. 2730–2737.

Chadwick, P., 1976, *Continuum Mechanics,* Wiley, New York.

Dabiri, Dana, 1997, "On the Correlation of the Free-Surface Roughness with the Near-Surface Turbulence," *Bulletin of the American Physical Society,* p. 2162, American Physical Society, Nov.

Kosiński, W., 1986, *Field Singularities and Wave Analysis in Continuum Mechanics.* Wiley, New York.

Kreyszig, Erwin, 1991, *Differential Geometry,* Dover, New York.

Lighthill, M. J., 1963, *Laminar Boundary Layers,* Chapter Introduction, pp. 46–113, Oxford University.

Longuet-Higgins, M. S., 1998, "Vorticity and Curvature at a Free Surface," *Journal of Fluid Mechanics,* Vol. 356, pp. 149–155, Feb.

Lugt, Hans J., 1987, "Local Flow Properties at a Viscous Free-Surface," *Physics of Fluids,* Vol. 30(12), pp. 3647–3652, Dec.

Lundgren, Thomas, and Koumoutsakos, Petros, On the generation of vorticity at a free-surface. In Bulletin of the American Physical Society, page 2163. American Physical Society, November 1997.

Naghdi, P. M., S. Flugge's Handbuch der Physik, volume VIa/2, chapter The theory of plates and shells, pages 425–640. Springer, Berlin, 1972.

Peck, Bill, and Sigurdson, Lorenz, 1998, "On the Kinematics at a Free Surface," *IMA Journal of Applied Mathematics,* Vol. 61, pp. 1–13.

Rood, Edwin P., 1994, "Interpreting Vortex Interactions with a Free-Surface," ASME JOURNAL OF FLUIDS ENGINEERING, Vol. 116, pp. 91–93, Mar.

Rood, Edwin, P., 1995, *Fluid Vorticies,* chapter, "Vorticity Interactions with a Free-Surface," Kluwer Academic.

Sarpkaya, Turgut, 1996, "Vorticity, Free-Surface and Surfactants," *Annual Review of Fluid Mechanics,* Vol. 28, pp. 83–128.

Scriven, L. E., 1960, "Dynamics of a Fluid Interface," *Chemical Engineering Science,* Vol. 12, pp. 98–108.

Wu, Jie-Zhi, 1995, "A Theory of Three-Dimensional Interfacial Vorticity," *Physics of Fluids,* Vol. 7(10), pp. 2375–2395, Oct.

Turbulent Boundary Layers in Low Reynolds Number Shallow Open Channel Flows

Ram Balachandar
Associate Professor.
e-mail: ram_balachandar@engr.usask.ca

Shyam S. Ramachandran
Graduate Student.

University of Saskatchewan,
57 Campus Drive,
Saskatoon, Canada, S7N 5A9

The results of an experimental investigation of turbulent boundary layers in shallow open channel flows at low Reynolds numbers are presented. The study was aimed at extending the database toward lower values of Reynolds number. The data presented are primarily concerned with the longitudinal mean velocity, turbulent-velocity fluctuations, boundary layer shape parameter and skin friction coefficient for Reynolds numbers based on the momentum thickness (Re_θ) ranging from 180 to 480. In this range, the results of the present investigation in shallow open channel flows indicate a lack of dependence of the von Karman constant κ on Reynolds number. The extent to which the mean velocity data overlaps with the log-law decreases with decreasing Re_θ. The variation of the strength of the wake with Re_θ is different from the trend proposed earlier by Coles.

Introduction

In the recent past there has been renewed interest in the characteristics of turbulent, shallow open channel flows (Babarutsi, 1989; Balachandar et al., 1997; Chu et al., 1991). In this context, a shallow flow is defined as the situation where the horizontal length scale (of a typical eddy) is significantly larger than the vertical scale (depth of flow). For example, the tanker Argo Merchant stranded on the Nantucket shoals produced turbulent eddies in the wake region which have a size of about 2000 ft, while the depth of flow at the same location is only about 50 ft (Van Dyke, 1982). Other examples of shallow flows include the wake formed downwind of the mountain in the island of Madeira (Burger and Wille, 1972) and the flow past islands in river systems (Ingram and Chu, 1987; Balachandar et al., 1993). Of particular interest in the area of environmental fluid mechanics is the mixing characteristic of pollutants discharged in shallow flows.

In shallow flows, bed friction effects become very important and are quantified in terms of a friction length scale, which is usually defined as the ratio of the depth of flow (h) to the skin friction coefficient (C_f). Chu et al. (1991) and Balachandar et al. (1997) have defined a bed friction parameter ($S = C_f X/h$) to describe the influence of bed friction in shallow flows. Here, X is a horizontal length scale. Obviously, bed friction effects are expected to be minimized in deep flows. For example, the wake region of a bluff body is quite distinct in a deep flow with the formation of well-known Karman vortex street, while in a corresponding shallow flow, the wake is stabilized due to friction effects and the vortex street is annihilated (Balachandar et al., 1999). To quantify the effect of bed friction in shallow flows, it is important to properly evaluate the skin friction coefficient. Moreover, many of the reported laboratory experiments in open channel flow (shallow or deep), qualify as "low-Reynolds-number flow" in terms of turbulence. Here, Reynolds number is defined as $\mathrm{Re}_\theta = U_e\theta/\nu$, where, U_e is the longitudinal velocity at the edge of the boundary layer, θ is the momentum thickness of the boundary layer and, ν is the kinematic viscosity of the fluid. Specifically, in shallow flows, when experiments are required to be carried out at low Froude numbers (sub-critical range), there is the limitation of working at very low velocities. This results in the occurrence of very low Re_θ. Low-Reynolds-number flows also play an important role in many fluid flow problems including flow through turbomachinery, flow over wings, numerical modeling and model testing in wind and water tunnels.

It is of paramount importance to be able to predict C_f accurately in shallow open channel flows. To evaluate the value of C_f in open channel flows, it has been customary to use any of the methods suggested by the ASCE task force (1963). Others have assumed that Reynolds number effects are minimal and used the semi-empirical laws developed for high Re_θ flows to determine the friction velocity ($u_\tau = (\tau_w/\rho)^{1/2}$), from which C_f can be evaluated. Some standard methods of obtaining u_τ include the Clauser plot technique (Sherman, 1990) and the Preston tube method. However, a source of difficulty in low Re_θ turbulent flows is the accurate determination of the friction velocity. At low Reynolds number flows, there is no rigorous basis for the traditional log-law, $u^+ = \kappa^{-1} \ln y^+ + C$. Here, $u^+ = u/u_\tau$ and $y^+ = yu_\tau/\nu$ are the standard wall variables, u is the mean velocity and y is the distance from the wall. Furthermore, κ and C are constants and generally have values of 0.41 and 5, respectively, at higher values of Re_θ.

Researchers have differing opinions on how the mean flow is dependent on Re_θ. There have been assertions that κ varies with Re_θ (Simpson, 1970) and the logarithmic region disappears below some Reynolds number (Granville, 1977; Preston, 1958; Spalart, 1988; and Landweber, 1973). Preston (1958) has indicated that the log-region disappeared when $\mathrm{Re}_\theta = 389$, while Granville (1977) has determined that the log-region disappeared when $\mathrm{Re}_\theta = 738$. In view of the above assertions, the usefulness of the log-law is reduced and the analysis of turbulent boundary layers such as the one encountered in shallow open channel flow becomes more complex. On the other hand, Coles (1956, 1962) provides the argument that variation of the characteristics of the turbulent boundary layer with Reynolds number is limited to the outer region of the flow and the law-of-the-wall is independent of Reynolds number. He confirmed that $\kappa = 0.41$ and $C = 5$ applied to all values of Re_θ. Simpson (1970) proposed that κ and C varied with Re_θ for $1000 < \mathrm{Re}_\theta < 6000$ and suggested that the reduction of the wake with decreasing Re_θ could be accounted for by varying κ and C, and holding the profile parameter Π constant. This contradicts Coles' assertions. In analyzing duct flow data, Huffman and Bradshaw (1972) provide support to Coles' argument. Their results showed that κ appeared to be a constant and C was Reynolds number dependent. However, they also indicated that the variation of C is likely to be small unless the influence of the outer layer is extremely large. Murlis et al. (1982) have presented mean velocity and turbulence measurements in a zero pressure gradient flow for values of Re_θ ranging from 791 to 4750. Their results

Contributed by the Fluids Engineering Division for publication in the JOURNAL OF FLUIDS ENGINEERING. Manuscript received by the Fluids Engineering Division April 28, 1998; revised manuscript received April 19, 1999. Associate Technical Editor: S. Banerjee.

Table 1 Summary of test conditions

Test #	Depth (h) mm	(U_e) m/s	δ mm	Trip type
A	36.2 ~ 36.0	0.063	29.5 ~ 33.5	Trip I
B	32.0 ~ 31.5	0.151	29.0 ~ 30.0	(Median dia. = 1 mm)
C	20.5 ~ 20.0	0.068	18.5 ~ 19.0	
D	33.8 ~ 33.0	0.066	22.5 ~ 26.0	
E	22.2 ~ 22.2	0.097	19.6 ~ 20.0	Trip II
F	31.4	0.110	26	(Median dia. = 3 mm)
G	50.8	0.110	35.6	
H	31 ~ 30.8	0.057	27.0 ~ 28.2	
I	31.8 ~ 31.4	0.067	18.0 ~ 22.5	

strongly suggest that the log-law applies unchanged down to $Re_\theta \approx 700$. Purtell et al. (1981) conducted extensive measurements for values of Re_θ varying from 465 to 5,200. They confirmed that κ and C did not vary with Re_θ. However, they found that the extent of the log-region to decrease with decreasing Re_θ, but the region did not disappear at low values of Re_θ. Smits et al. (1983) found that the log-region does exist for Re_θ as low as 354.

At low values of Re_θ, there is the additional complication of whether or not a fully developed turbulent flow exists. The often-quoted lowest estimate of Re_θ is about 320. However, Bandyopadhyay (1987) has shown the existence of a turbulent boundary layer at $Re_\theta = 285$. The present study was carried out to estimate C_f in shallow open channel flows at low values of Re_θ ($180 < Re_\theta < 500$) and there by extend the available database. The present study also serves the purpose of validating the usefulness of the traditional log-law.

Experimental Setup and Procedure

The present experiments were conducted in a rectangular cross-section open channel flume. The flume was 0.6 m deep, 0.8 m wide and 10 m long. A contraction and several stilling arrangements used to reduce any large-scale turbulence in the flow preceded the straight section of the channel. The channel bottom was made of brass and the slope was adjustable. In the present tests, the channel bottom was set to be horizontal. The sidewalls of the flume were made of transparent tempered glass to facilitate measurement of velocity using a laser Doppler anemometer. The test section where the present measurements were carried was located 4 m downstream of the contraction. The minimum freestream velocity of flow is about 55 mm/s. At this velocity, the boundary layer in the test section region is expected to be in a state of transition. Consequently, tripping of the boundary layer was required to achieve a developed turbulent regime. Two types of roughness elements were used to trip the boundary layer. The trip was made up of sand particles (median diameters: Trip I—1.0 mm and Trip II—3 mm) and glued on to the bottom of the channel as a 25 mm strip spanning the entire width of the flume. The trip was located 1.76 m upstream of the first measuring station ($X = 0$). Velocity measurements were carried out along the centerline of the flume. A summary of the test conditions is shown in Table 1. For Tests F and G, measurements were carried out at one axial station only ($X = 0$). For the remaining tests, measurements were carried out at $X = 0$, 50 and 100 mm. In Table 1, U_e is the freestream velocity and δ is the boundary layer thickness. The Reynolds number ranged from 175 to 480. The column indicating depth (h) in Table 1 shows the variation of the depth of flow over the region of interest ($X = 0$ to $X = 100$ mm). Similarly, the column δ shows the corresponding change in the boundary layer thickness with increasing axial distance.

The velocity measurements were carried out using a single-component fiber-optic probe laser Doppler anemometer (Dantec Inc.). The present system uses a 300 mW, air-cooled Argon-Ion laser (Ion Laser Technology). A fiber-optic probe fitted with a lens of focal length 400 mm forms the transmitting optics. The laser-Doppler anemometer system was operated in the backward scatter mode and the optical parameters are indicated in Table 2. The fiber optic probe was mounted on a three-dimensional traversing mechanism capable of repeatedly attaining the same location with an accuracy of ±0.1 mm. Each direction of the traversing arrangement was stepper motor driven and controlled by a computer. Detailed descriptions of the laser-Doppler anemometer system and the signal processor used in the present study is available elsewhere and avoided here for brevity (Ramachandran, 1998).

Table 2 Operating parameters of the laser-Doppler anemometer

Wavelength of the laser	514.5 nm
Diameter of the laser beam	1.35 mm
Focal length of the transmitting lens	400 mm
Beam separation	38 mm
Number of fringes	36
Fringe spacing	5.422 μm
Measuring volume dimensions	0.194 × 0.194 × 4.09 mm^3

Preliminary experiments were conducted to examine the variation of the mean velocity profiles in the spanwise direction at $X = 0$. The flow was clearly found to be two-dimensional with a variation of less than 1 percent in the value of U_e.

Determination of u_τ

Since the objective of the present study was to focus on very low Reynolds number flows, the question of "full-development" is important in interpreting the results. To this end, it was necessary to ensure that there would be a convergence of the velocity profiles with increasing axial distance. Moreover, it was necessary to ensure that the flow regime was beyond transition from laminar to turbulent state. Figure 1 shows the variation of the mean velocity for three different flow states. For each test condition, measurements were conducted at three axial stations. In Fig. 1, data are presented using the traditional wall variables. Furthermore, d^+ ($=du_\tau/\nu$) is the Reynolds number based on the depth of flow and H ($=\delta^*/\theta$) is the boundary layer shape factor and δ^* is the displacement thickness. Irrespective of the reliability of the log-law at low Re_θ, a dependable estimate of u_τ can be obtained from the slope of the mean velocity profile in the near wall region using the relation:

$$\tau_w = \mu\left(\frac{\partial u}{\partial y}\right)_{y=0} \tag{1}$$

The usefulness of this equation to estimate the friction velocity by extrapolating the near wall data to the wall has been verified in recent studies by Djenidi and Antonia (1993), Ching et al. (1994), and Neiderschulte et al. (1990). The appropriateness of the method

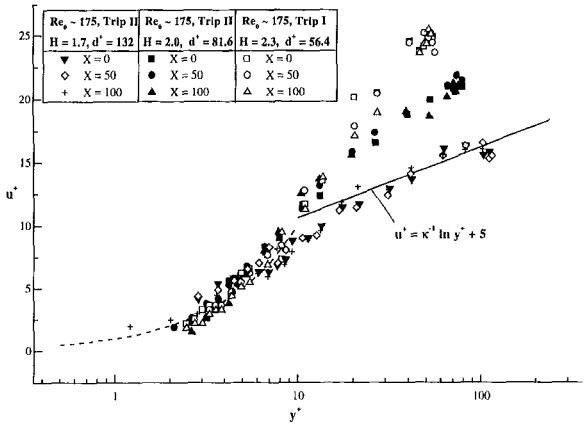

Fig. 1 Mean velocity profiles at very low Reynolds numbers (Uncertainty in u: near wall ±2%, outer region ±1%, uncertainty in y: ±2%)

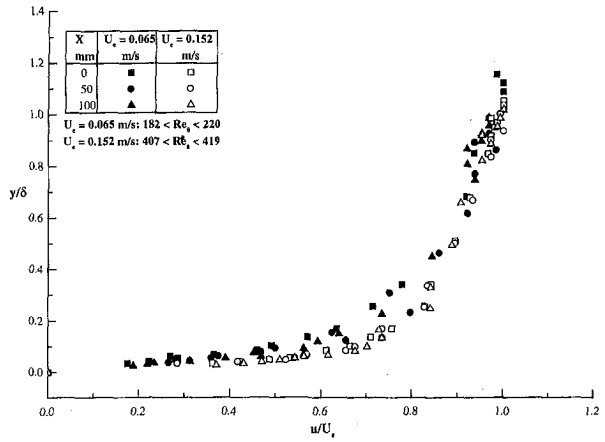

Fig. 2 Verification of convergence of mean profiles to asymptotic state (Uncertainty in u: near wall ±2%, outer region ±1%, uncertainty in y: ±2%)

has also been discussed in an earlier study by Reischman et al. (1975). The use of the above equation would definitely be questionable if one were to consider hot-wire data because of the wall conduction problem. As pointed out by Mazumder et al. (1981), fortunately the near wall LDA data do not suffer from the same difficulty.

A straight line was fit to the data close to the wall and a first estimate of $\mu(\partial u/\partial y)_w$ was obtained. Using this as the value of τ_w, the value of u_τ, and hence u^+ and y^+ were computed. The data of the wall region were once again plotted and the linear fit re-done by weighting the data in the region $y^+ < 3$. For those tests where adequate number of points were not available in the range $y^+ < 3$, the data in the region $y^+ < 5$ was used to re-evaluate the value of u_τ. The change in u_τ was usually less than 3 percent. In their paper, Djenidi et al. (1993) clearly demonstrate in sufficient detail that u_τ can be determined adequately by the procedure adopted in the present study. With the exception of tests F and G (Table 1), the value of C_f and hence u_τ was also computed using the variation of $d\theta/dx$ in the momentum balance equation. A maximum variation of 6 percent was noticed between the two methods.

The data in Fig. 1 clearly indicate that at lower depths and larger values of H, the boundary layer is clearly not turbulent. At $Re_\theta \sim 175$, $d^+ = 132$ and $H = 1.7$, the data indicate a fair resemblance to the traditional log-law data. Comment on the extent of fit with the log-law is made in a later section. Following this preliminary analysis and keeping with the objective of focussing on turbulent boundary layers, a decision was made to conduct tests at values of Re_θ slightly greater than 175. Figure 2 shows two sets of data obtained using trip type I over a range of Re_θ varying from 180 to 420. The data indicate a convergence to an asymptotic state in both the tests.

Results

Figures 3(a) and 3(b) show the variation of C_f and H with Re_θ, respectively. In the range overlapping with previous sets of experimental data (Purtell et al., 1981 and Spalart, 1988), the present data compare favorably. For most part, the present data is an extension of the existing database toward lower values of Re_θ. Figure 4 shows a plot of the mean velocity profiles using the wall variables. Also plotted in Fig. 4 is the log-law using $\kappa = 0.41$ and $C = 5$. The present set of data compares quite favorably with the log-law. For brevity, and to avoid cluttering of data, all the acquired data points at any given Re_θ are not shown in Fig. 4. It should be remarked that the overlap with the log-law generally starts around $y^+ \approx 30$. However, the data does indicate a tendency to overlap with the log-region for a shorter length than that expected at higher Re_θ. Defining L as the extent to which the data overlaps with the log-law, the variation of $L^+ = Lu_\tau/\nu$ with Re_θ is shown as an inset in Fig. 4. For the range of low Re_θ tested in the present study, the data indicate a linear increase with increasing Reynolds number. It should be remarked that the value of L^+ at any Re_θ is obtained by comparing each set of data independently with the log-law. There is a certain degree of uncertainty in the evaluation of L^+ (as high as 10 percent in some cases) as the overlap region was determined visually.

In high Re_θ flows, the values of u_τ/κ can be found by seeking the minimum value of $y(du/dy)$ versus y. Consequently, a goodness-of-fit to the log-law can be evaluated for the present experimental data by verifying the value of κ. Spalart (1988) used the presentation of $y^+(du^+/dy^+)$ versus y^+ in which case the minimum value of the curve will yield the value of κ^{-1}. However, this procedure is very sensitive to noise and direct use of the experimental data to obtain du^+/dy^+ would not be useful. To overcome this difficulty, a fit to the experimental data was used. Figure 5 shows the variation of $y^+(du^+/dy^+)$ with y^+. The present data indicate the existence of a minimum value of 2.44 ($=1/\kappa$) at all values of Re_θ reported. Using the mean velocity data and u_τ reported by Purtell et al. (1981) at $Re_\theta = 465$, the variation of u^+ with y^+ was obtained for their data set. A curve was fit to this data set and the variation of $y^+(du^+/dy^+)$ with y^+ was obtained. This is also shown in Fig. 5. The present set of data compares well with the data of Purtell et al. (1981). Also shown in Fig. 5 is the direct numerical simulation data reported by Spalart (1988) at $Re_\theta = 300$. The present set of data does not conform to the results by Spalart (1988). The data of Spalart (1988) indicate a decrease in the value of κ with decreasing Re_θ. A similar behavior has also been noticed by Ching et al. (1994).

On analyzing the present data in Figs. 4 and 5, one would be tempted to conclude that the log-layer does exist at low Re_θ though the length of the log-layer is very much reduced. The wall and wake regions approach each other and may finally overlap at a very low value of Re_θ. This provides credence to the argument that the log-law may disappear at very low Re_θ. However, the present set of data lends support to Coles' (1962) argument that the value

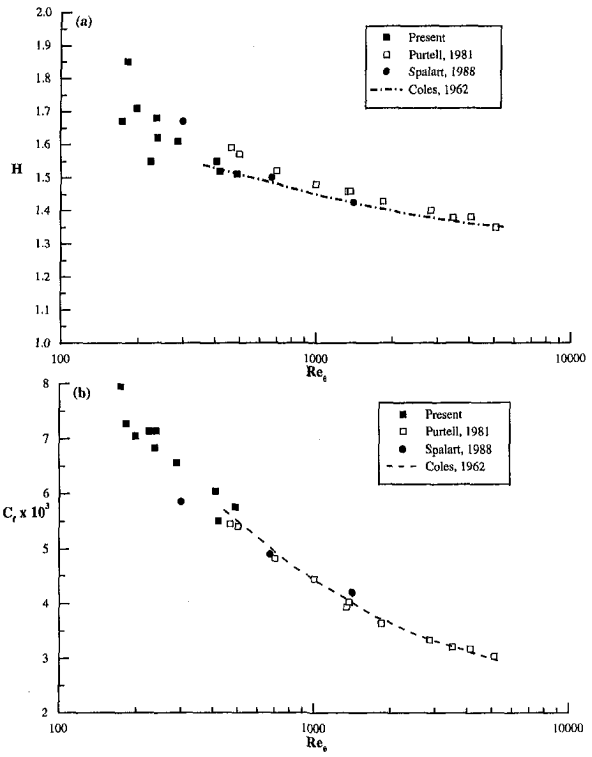

Fig. 3 Variation of H and C_f with Re_θ (Uncertainty in H: ±3%, uncertainty in C_f: ±4%, uncertainty in Re_θ: ±3%)

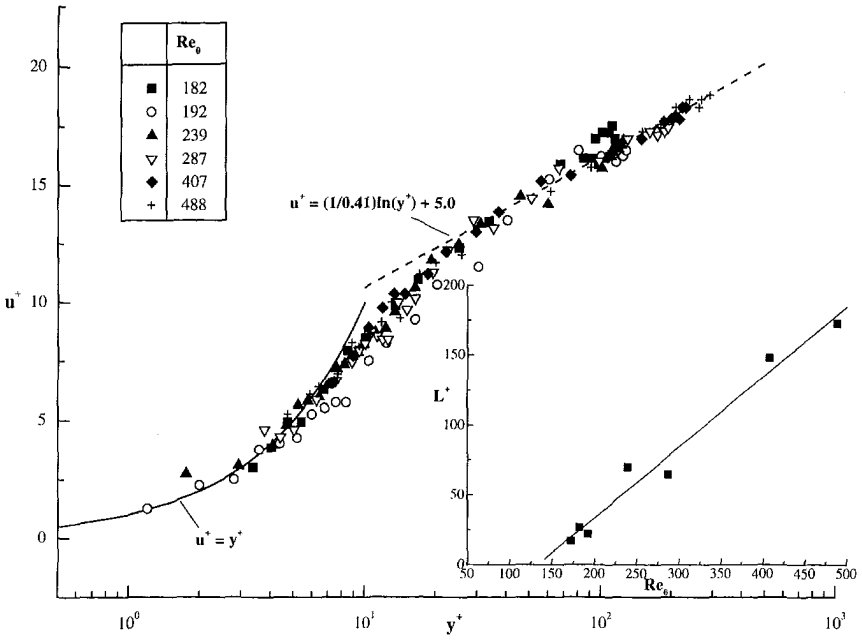

Fig. 4 Mean velocity profiles at various Re_θ (Uncertainty in u: near wall ±2%, outer region ±1%, uncertainty in y: ±2%)

of κ is independent of Re_θ. It has come to be accepted that the larger scales of turbulence become more dominant as the Reynolds number is decreased. Consequently, the low Re_θ flows encountered in shallow open channel flows is expected to be dominated by the larger scales and following Fig. 4, the characteristics of these scales should be independent of Re_θ. Using the smoke visualization studies of Head and Bandyopadhyay (1981), one can conclude that the hairpin eddy structure is the basic element of turbulence in low Reynolds number flows.

The strength of the wake would also provide a method for determining deviations from the log-law and bring out the effects of low Re_θ. Figure 6 shows the variation of Δu^+ with Re_θ. Here, Δu^+ $(=\Delta u/u_\tau)$ is the maximum deviation of a mean profile from the log-law. The relationship suggested by Coles (1962) shows a gradual decrease in Δu^+ from an asymptotic value of about 2.7 at large Re_θ to a value of zero at a very low Re_θ. The present results show an increasing trend with decreasing Re_θ. The present data trend is qualitatively similar to that of Erm and Joubert (1991) and Purtell et al. (1981). The data of Erm and Joubert (1991) indicated in Fig. 6 are the values of Δu^+ that were obtained for three different types of tripping devices at a nominal velocity of 8 m/s. It is worthwhile to note that Δu^+ does not tend to zero as proposed by Coles (1962). The behavior of Δu^+ in the present study shows a clear Reynolds number dependence. In this context, based on a survey of the relevant literature and the present results, one has to reckon with the question if the wake region of a fully developed turbulent boundary layer is dependent on how the boundary layer is generated.

Figure 7 shows the variation of turbulence intensity over the range of Re_θ tested in the present study in terms of the wall

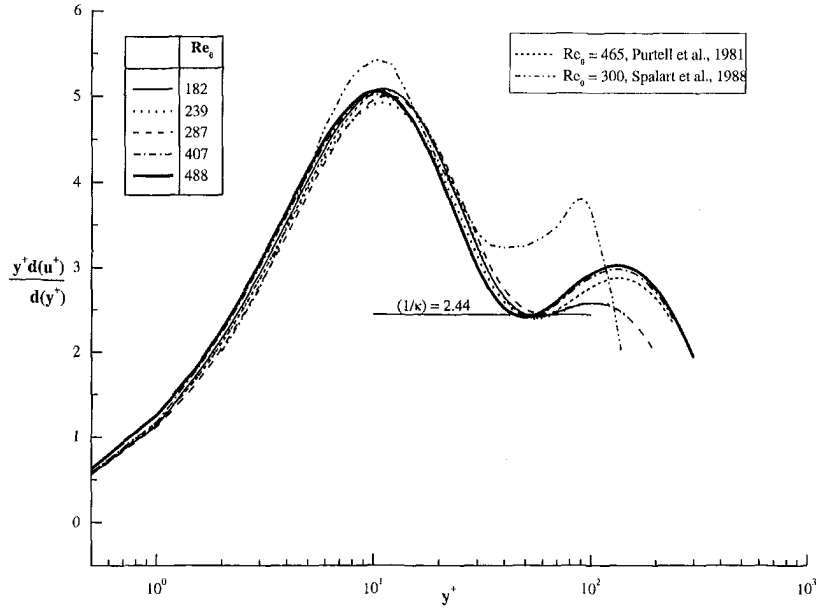

Fig. 5 Mean velocity derivative at various Re_θ

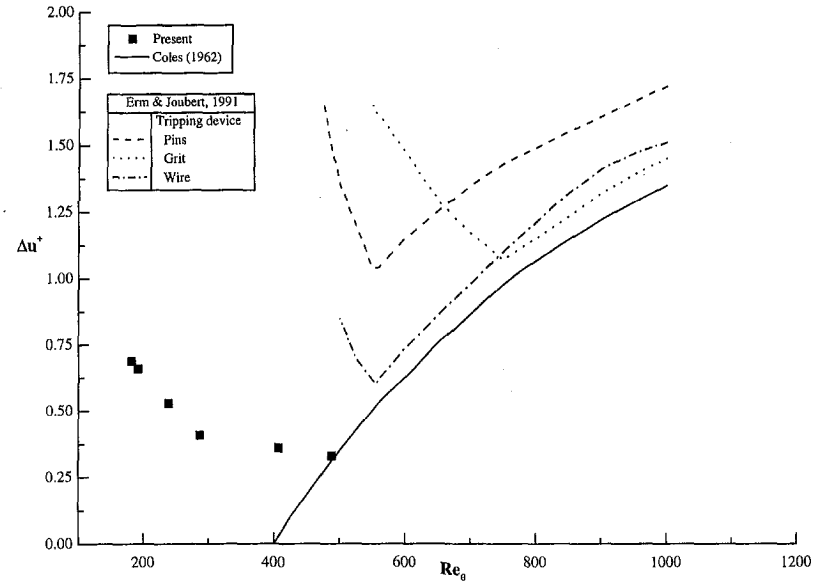

Fig. 6 Variation of Δu^+ with Re_θ (Uncertainty in Δu^+: ±4%, uncertainty in Re_θ: ±3%)

variables. One can notice that a sense of approximate similarity prevails through out the boundary layer. It should be noted that the mean velocity profile showed a near complete similarity and compared to Fig. 4, there is scatter in the turbulence data. However, no systematic variation is noticeable and one can conclude that no discernible Reynolds number effect exists. The u'^+ profiles at all values of Re_θ indicate a peak at $y^+ = 15$. This is consistent with the data reported by Ching et al. (1994) in a Re_θ range of 400 to 1316, and that reported by Purtell et al. (1981) in a Re_θ range of 465 to 5100. The location of the peak is also consistent with the direct numerical simulation (DNS) data of Spalart (1988). The present set of data also indicates that the peak value of u'^+ is in the range 2.5 to 3 and compares favorably with the experimental data of both Ching et al. (1994) and Purtell et al. (1981). However this is in slight variance with the DNS data of Spalart (1988) who found a gradual increase in the peak value with increasing Re_θ. Furthermore, the data of Spalart (1988), Purtell et al. (1981), and Ching et al. (1994) do not indicate similarity for $y^+ > 15$. They noticed a systematic increase in u'^+ with Re_θ any given value of y^+.

Conclusions

The present study extends the available database in turbulent boundary layers toward lower values of Reynolds number. The results of the present experimental investigation in shallow open channel flows indicate a lack of dependence of the von Karman constant κ on Reynolds number based on the momentum thickness. The present study serves to confirm Coles' argument that κ should be independent of Reynolds number at all values of Re_θ. The longitudinal mean velocity and turbulent-velocity fluctuations indicate similarity for Reynolds numbers in the range of 180 to

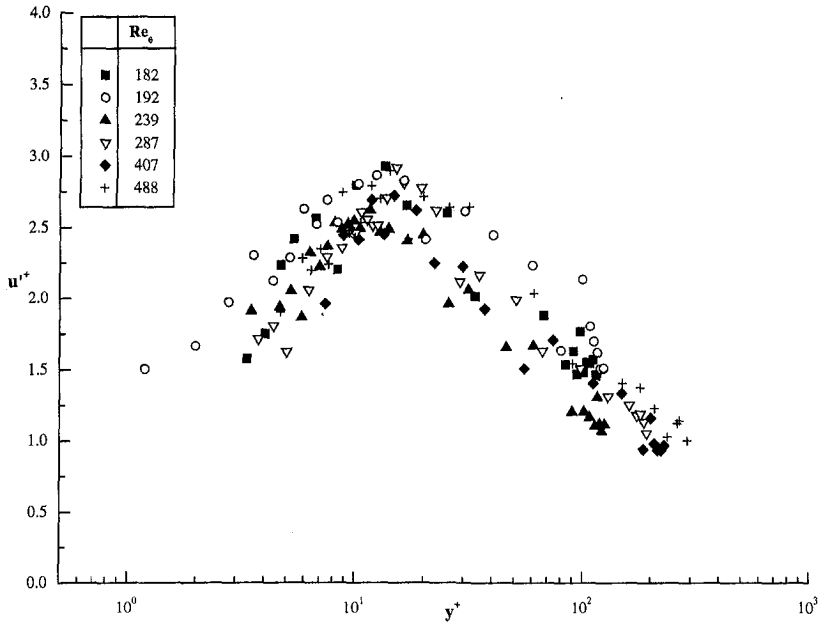

Fig. 7 Turbulence intensity profiles at various Re_θ (Typical uncertainty in u': ±3%, uncertainty in Re_θ: ±3%)

480. The extent to which the data overlaps with the log-law decreases with decreasing Re_θ. Consequently, in shallow open channel flows, caution should be exercised in trying to directly determine u_τ by overlapping the data with log-law. The variation of the strength of the wake with Re_θ is different from the trend proposed by Coles (1962). However, the present results in the wake qualitatively resemble the one presented by Erm and Joubert (1991) for low Re_θ. Besides extending the data to lower Reynolds numbers, in general, the variation of the boundary layer shape parameter and the skin friction coefficient with Reynolds number, resembles the data available in literature.

References

ASCE Task Force, 1963, "Friction Factor in Open Channels," *Journal of Hydraulic Division,* Vol. 89, No. 2, pp. 97–143.

Babarutsi, S., Ganoulis, J., and Chu, V. H., 1989, "Experimental Investigation of Shallow Recirculating Flows," *Journal of Hydraulic Engineering,* Vol. 115, No. 7, pp. 906–924.

Balachandar, R., Zhang, J., and Chu, V. H., 1993, "Quasi-Two Dimensional Turbulence in the Wake of a Normal Flat Plate in Shallow Waters," *Ninth Symposium on Turbulent Shear Flows,* Kyoto, Japan, pp. 16-4-1–16-4-6.

Balachandar, R., Chu, V. H., and Zhang, J., 1997, "Experimental Study of Turbulent Concentration Flow Field in the Wake of a Bluff Body," ASME JOURNAL OF FLUIDS ENGINEERING, Vol. 119, June, pp. 263–270.

Balachandar, R., Tachie, M. F., and Chu, V. H., 1999, "Concentration Profiles in Shallow Turbulent Wakes," ASME JOURNAL OF FLUIDS ENGINEERING, Vol. 121, March, pp. 34–43.

Bandyopadhyay, P. R., 1987, "Resonant Flow in a Row of Small Transverse Cavities Submerged in a Turbulent Boundary Layer," *AIAA Journal,* Vol. 87, pp. 1235.

Burger, E., and Wille, R., 1972, "Periodic Flow Phenomena," *Annual Review of Fluid Mechanics,* Vol. 4, pp. 313–340.

Ching, C. Y., Djenidi, L., and Antonia, R. A., 1994, "Low-Reynolds-Number Effects in a Turbulent Boundary Layer," *7th International Symposium on the Application of Laser Techniques to Fluid Mechanics,* Lisbon, Portugal, pp. 4.1.1–4.1.8.

Chu, V. H., Wu, J.-H., and Kahyat, R. E., 1991, "Stability of Transverse Shear Flows in Shallow Open Channels," *Journal of Hydraulic Engineering,* Vol. 117, pp. 1–19.

Coles, D. E., 1956, "The Law of The Wake in Turbulent Boundary Layer," *Journal of Fluid Mechanics,* Vol. 1, pp. 191–226.

Coles, D. E., 1962, "The Turbulent Boundary Layer in a Compressible Fluid," Rand Report R-403-PR, ARC 24473: Appendix A: A Manual of Experimental Practice for Low-speed Flow.

Djenidi, L., and Antonia, R. A., 1993, "LDA Measurements in Low Reynolds Number Turbulent Boundary Layer," *Experiments in Fluids,* Vol. 14, 280–288.

Erm, L. P., and Joubert, P. N., 1991, "Low-Reynolds-Number Turbulent Boundary Layers," *Journal of Fluids Mechanics,* Vol. 230, pp. 1–44.

Granville, P. S., 1977, "Drag and Turbulent Boundary Layer of Flat Plates at Low Reynolds Numbers," *Journal of Ship Research,* Vol. 21, No. 1, pp. 30.

Head, M. R., and Bandyopadhyay, P., 1981, "New Aspects of Turbulent Boundary Layer Structures," *Journal of Fluid Mechanics,* Vol. 107, pp. 297–338.

Huffman, G. D., and Bradshaw, P., 1972, "A Note on von Karman Constant in Low Reynolds Number Turbulent Flows," *Journal of Fluid Mechanics,* Vol. 53, pp. 45–60.

Ingram, Grant R., and Chu, V. H., 1987, "Flow Around Islands in Rupert Bay: An Investigation of the Bottom Friction Effect," *Journal of Geophysical Research,* Vol. 92, No. C13, pp. 14.521–14.533.

Landweber, L., 1953, "Frictional Resistance on Flat Plates in Zero Pressure Gradient," *Trans. Soc. Naval. Arch., Mar. Eng.,* Vol. 61, No. 5.

Mazumder, M. K., Wauchio, S., McLeod, P. C., Ballard, G. S., Mozumdar, S., and Caraballo, N., 1981, "Skin Friction Drag Measurements by LDV," *Applied Optics,* Vol. 20, 2832–2837.

Murlis, J., Tsai, H. M., and Bradshaw, P., 1982, "The Structure of Turbulent Boundary Layers at Low Reynolds Numbers," *Journal of Fluids Mechanics,* Vol. 122, pp. 13–56.

Neiderschulte, M. A., Adrian, R. J., and Hanratty, T. J., 1990, "Measurements of Turbulent Flow in a Channel at Low Reynolds Numbers," *Experiments in Fluids,* 9, 222–230.

Preston, J. H., 1958, "The Minimum Reynolds Number for a Turbulent Boundary Layer and the Selection of a Transition Device," *Journal of Fluid Mechanics,* Vol. 3, pp. 373–384.

Purtell, L. P., Klebanoff, P. S., and Buckley, F. T., 1981, "Turbulent Boundary Layer at Low Reynolds Number," *Physics of Fluids,* Vol. 24, No. 5, pp. 802–811.

Ramachandran, S. S., 1998, "Laser-Doppler Anemometer," Report-98-002, Department of Mechanical Engineering, University of Saskatchewan, Canada.

Reischman, M. M., and Teiderman, W. G., 1975, "Laser-Doppler Anemometer Measurements in Drag-Reducing Channel Flows," *J. Fluid Mechanics,* Vol. 70, pp. 369–392.

Sherman, F. S., 1990, *Viscous Flow,* McGraw Hill Series in Mechanical Engineering, New York.

Simpson, R. L., 1970, "Characteristics of Turbulent Boundary Layers at Low Reynolds Numbers With and Without Transpiration," *Journal of Fluid Mechanics,* Vol. 42, pp. 769–802.

Smits, A. J., Matheson, N., and Joubert, P. N., 1983, "Low-Reynolds-Number Turbulent Boundary Layers in Zero and Favourable Pressure Gradients," *Journal of Ship Research,* Vol. 27, pp. 147.

Spalart, P. R., 1988, "Direct Simulation of a Turbulent Boundary Layer Up to $R_\theta = 1410$," *Journal of Fluid Mechanics,* Vol. 187, pp. 61–98.

Tachie, M. F., 1997, "Scalar Transport in Intermediate Two-Dimensional Turbulent Wakes," M.Sc. thesis, Department of Mechanical Engineering, University of Saskatchewan.

Van Dyke, M., 1982, *An Album of Fluid Motion,* Parabolic Press, p. 176.

Journal of Fluids Engineering

Technical Briefs

Flow and Noise Characteristics of Notched Elliptic-Orifice Jets

S. B. Verma[1] and E. Rathakrishnan[1]

Introduction

A plethora of investigations of passively controlling the jet characteristics have been carried out for axisymmetric jets (Bradbury and Khadem, 1975; Norum, 1983; Pannu and Johanneson, 1976; Norum and Seiner, 1982; Wlezien and Kibens, 1988; Krothapalli et al., 1990; Samimy et al., 1993). However, not much work seems to report toward enhancement of mixing in noncircular jets. Noncircular jets, due to their nonuniform azimuthal curvature variation spread differently in different planes (Schadow et al., 1989). One important feature of noncircular jets is the process of axis-switching which is responsible for higher mixing rates (Ho and Gutmark, 1987; Hussain and Husain, 1989). Small aspect-ratio (2:1) elliptic jets have been observed to result in higher mixing rates relative to the axisymmetric jets (Ho and Gutmark, 1987; Hussain and Husain, 1989). Also, the presence of sharp corners have been observed to introduce turbulence and higher mixing (Schadow et al., 1988; Quinn, 1988).

The fact that the supersonic jets spread less than their subsonic counterparts is due to compressibility effects creeping in at high Mach numbers (Brown and Roshko, 1974). As such the jet experiences a significant reduction in growth rates and turbulence levels. Further, at off-design Mach numbers, the jet core is dominated by a repetitive shock-cell structure and the shock-associated noise is dominated by a high intensity noise called "Screech" (Powell, 1953) which he found is due to a self-sustaining feedback loop. It has been observed by number of investigators that the source of this noise lies at the end of third to fourth shock-cell (Powell, 1954; Glass, 1968; Hammitt, 1961; Norum, 1983; Krothapalli et al., 1990). Powell found out that, if efficiency of some part of this loop could be reduced, the amplitude of the process would decrease or cease altogether (Powell, 1953). The best way, therefore, is to change the initial conditions of the jet in such a way so as to weaken the shock-structure (Glass, 1968; Powell, 1953). It has been observed by Norum and Seiner (1982) that the choked jet-noise and the screech frequency are primarily dependent on the length of the shock-cells and the shock strength in the shock-cell system. As a result, it has remained a challenging task till date to weaken the shock-structure without much adverse effect on the thrust and other jet characteristics.

The present work reports the results obtained from an experimental study that combines the characteristics of small aspect-ratio (2:1) elliptic jets and sharp corners for the purpose of enhanced mixing and noise attenuation. The basic elliptic shape is modified by introducing two notches, symmetrically along the minor-axis side as shown in Fig. 1. Further, the notch geometry itself is varied to investigate its effect on the jet characteristics.

Experimental Setup and Procedure

The experiments were conducted using a high-speed jet facility at IIT Kanpur, India, which consists of a cylindrical settling chamber, containing three screens for minimizing disturbances at the nozzle exit, and connected to high pressure storage tanks as shown in Fig. 1. Circular aluminium plates of 1.3 mm thickness, with the desired orifice geometry was fixed to the end-plate of the settling chamber. The area-ratio between the settling chamber end-plate and orifice was 100. The settling chamber pressure P_0, which was the controlling parameter in the investigation, was regulated using a pressure regulating valve. All the orifices, i.e., plain and notched, were of equal area, which was equal to the area of a circular orifice of 10 mm diameter and thus the equivalent diameter (D_e) of the noncircular orifices was 10 mm. Each of the notch conformed to 5 percent of the equivalent orifice area. Two notch geometries are investigated. They are, triangular notch with vertex angle of 60° and a square notch configuration. However, it is to be mentioned that the orifices used for the present study are not "sharp edged" as used by Hussain and Husain (Hussain and Husain, 1989) but are "square edged," called "disk nozzle" (Hussain and Ramjee, 1976). Such "disk nozzles" were found by Hussain and Ramjee to be free from the effects of *vena-contracta.* Further, the orifices have negligible boundary layer growth in them and as such have similar initial conditions and hence, can be used for comparative study of mixing characteristics from varying orifice geometries (Hussain and Husain, 1989). The use of orifices instead of nozzles is justified by Gutmark and Schadow (1987) who have shown that an elliptic orifice jet of aspect-ratio 3:1 has large and small-scale characteristics similar to an elliptic jet with well designed contraction. This feature is important for engineering applications where the simplicity of orifice design, especially with noncircular geometries, is advantageous (Gutmark and Schadow, 1987). As such the overall characteristics of orifice jets can be related to jets issuing from nozzles.

The investigation was carried out for two conditions: (1) correctly expanded jets, with sonic velocity at nozzle exit; (2) underexpanded sonic jets at P_0/P_a of 3.86 corresponding to level of underexpansion of 2.0. The Reynolds number based on the equivalent diameter and the equivalent exit velocity (based on M_j, which is defined as the Mach number obtained by correctly expanding the underexpanded jet) for the two conditions ranged from 2.36×10^5 to 3.54×10^5. All the tests were carried out at a room temperature of 30°C and 730 mmHg of pressure averaged over the time taken for the completion of experiments. The variation in temperature was less than 0.1% and that for pressure about 2 percent.

[1] Research Scholar and Professor, respectively, Department of Aerospace Engineering, Indian Institute of Technology, Kanpur-208 016, India.

Contributed by the Fluids Engineering Division of THE AMERICAN SOCIETY OF MECHANICAL ENGINEERS. Manuscript received by the Fluids Engineering Division May 6, 1998; revised manuscript received January 25, 1999. Associate Technical Editor: F. Hussain.

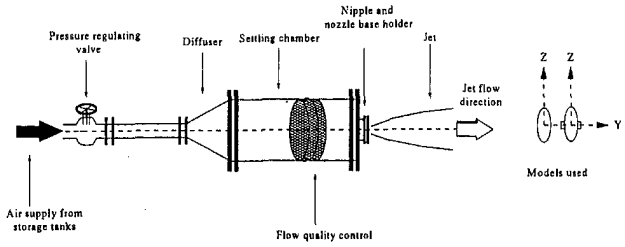

Fig. 1 Schematic of the jet test facility and the test models used

The sensing probe used for obtaining mean flow measurements of the flowfield for the present investigation was a Pitot tube with an internal diameter of 0.40 mm. In addition to this, it was observed that close to the exit, i.e., for $X/D_e = 0.1$, the pressure is nearly constant for 80 percent of the orifice width for all the cases tested. Also, the pressure obtained at the centre was within 2 percent of the total stagnation pressure. It can thus be considered that the magnitudes of the pressures obtained with this probe size relative to the orifice width, were quite accurate. The accuracy of traverse movement along X, Y, Z-directions was ± 0.1 mm. All the pressure measurements were accurate up to ± 1 mm of mercury column and all the measurements were found to be repeatable within ± 3 percent. In all the measurements the sensing probe was oriented parallel to X-axis. The notched plane (minor-axis) is considered as the XY-plane and the unnotched plane (major-axis) as the XZ-plane with its origin on the centreline of the jet.

A $\frac{1}{8}$ in. Larsen & Davis microphone and 800B Model sound level meter was used to obtain the OASPL measurements. The accuracy, according to the manufacturers specifications, was within ± 0.3 dB in the range of 20 Hz to 20 kHz.

Results and Discussions

Jet Half-Width Growth. The location of axis-switching, i.e., the X-location at which the spread in the X-Y and X-Z planes become equal before switching axis, is clearly elucidated in the jet half-width growth plots shown in Fig. 2. The plot clearly indicates the absence of *vena-contracta* effect in the present square-edged orifice jets, where both plain and notched jets show jet growth immediately downstream of orifice exit along minor-axis and notched plane. This is in conformity with the study of Hussain and Ramjee (1976). Switchover location is seen to be $4.0D_e$ for plain ellipse, whereas it is at $1.8D_e$ for square notched ellipse. Also, the spread in the notched/X-Y plane is found to increase considerably after the switchover. This result has earlier been reported for circular nozzles with tabs (Pannu and Johanneson, 1976) and in-plane notches (Bradbury and Khadem, 1975). Spread in the unnotched/X-Z plane is also greater than that in X-Z plane of plain ellipse but the difference is not much.

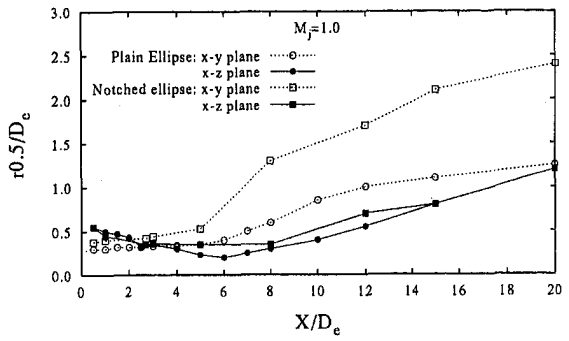

Fig. 2 Comparison of jet half-width growth for plain and notched elliptic slot jets. (The maximum uncertainty in the data presented in this figure is ±1 percent.)

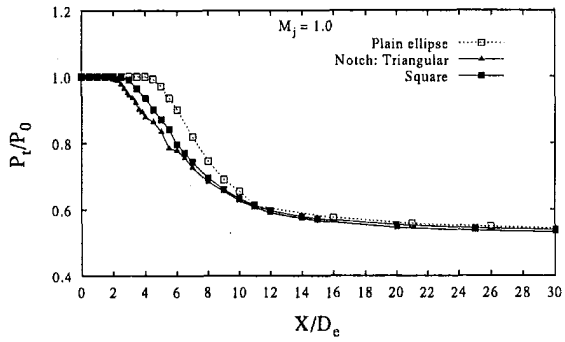

Fig. 3 Centerline pressure decay comparison for the cases investigated. (The uncertainty in the data presented in this figure is ±1.6 percent.)

Centerline Pressure Decay. Figure 3 shows the decay of centreline pressure with axial distance for the three cases investigated at $M_j = 1.0$. The Pitot pressure P_t are divided by the stagnation pressure P_0 and plotted against the non-dimensionalised downstream distance X/D_e. A faster centreline pressure decay is usually a reasonable measure of faster jet spread (Samimy et al., 1993). The plot clearly indicates that under the action of the notch, the jet decays faster than the plain case with the plain ellipse having the least decay followed by square and finally, by the triangular notched ellipse which has the maximum decay. Also, it is evident that the plain ellipse has the longest core-length ($4.0D_e$) followed by the square notched ($2.5D_e$) and finally, by the triangular notched ellipse ($1.7D_e$) which has the shortest core. This observation at full-expansion confirms the flow enhancement brought about by the use of sharp corners in the notch geometry of an elliptic orifice jet as was also observed by Gutmark et al. (1988) for triangular and square nozzle jets. They observed that decreasing the corner angle from 90 deg (for square nozzle) to 60 and 30 deg (vertex angle for triangular nozzle) enhanced the overall mixing which, according to them, is attributed to the improved shedding of small-scale vortices from a sharper corner. This seems to be the prime reason, in the present study, for improved mixing observed by the use of triangular notches than square notches. Beyond $30.0D_e$ all the jets decay at almost the same rate oblivious of the initial geometry.

Azimuthal Directivity. Figure 4 shows the azimuthal variation of far-field OASPL at $\theta = 90°$, $X/D_e = 0.0$, for jets operating at full expansion, $M_j = 1.0$. The measurements were made starting from major-axis side, passing through the minor-axis side (having the notch) and ending up at the other end of minor-

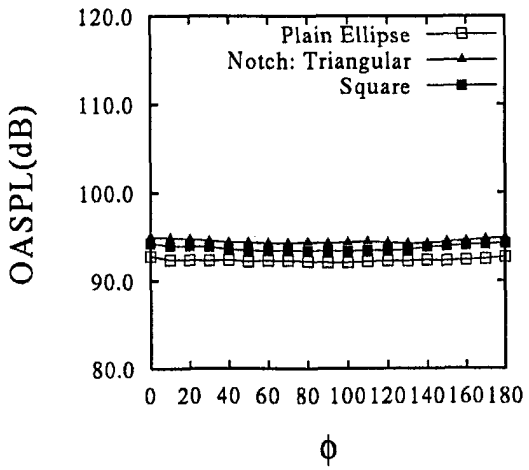

Fig. 4 Azimuthal directivity plot for the cases investigated at full expansion. (The maximum error in the data presented in this figure is ±0.3 dB.)

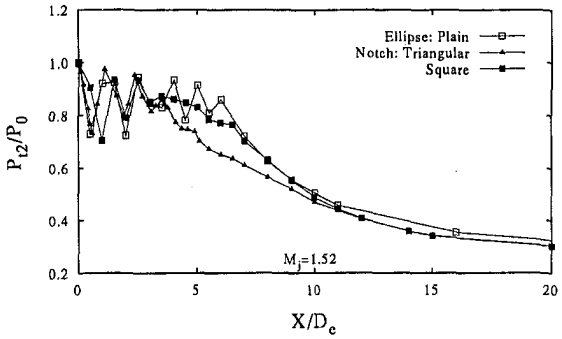

Fig. 5 Centerline pressure decay comparison for the cases investigated at level of underexpansion of 2.0, M_j = 1.52. (The maximum uncertainty in the data presented in this figure is ±5 percent.)

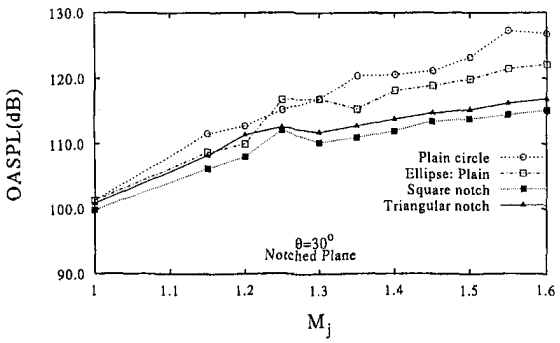

Fig. 7 Overall sound pressure level (OASPL) comparison showing the effect of notches on the shock associated noise. (The maximum error in the data presented in this figure is ±0.3 dB.)

axis side. The microphone was positioned on a fixed aluminium quadrant, mounted on a tripod stand and moved in a circular arc at fixed intervals of 10°, R/D_e = 24. The noise levels for plain and notched orifices is observed to be approximately the same with only a slight increase for notched jets. No significant change in noise levels is seen which is primarily due to the reason that the flow at full expansion is not wave dominated.

Shock-Structure and Far-Field Noise. Figure 5 shows the centreline pressure decay plot for the cases investigated at P_e/P_a = 2.0, M_j = 1.52. The oscillations in the data in the upstream regions are due to the stationary shock structure in the jet. The measurements were not taken at predetermined axial locations but at locations where maxima and minima in pressure were observed. In the supersonic regions of the flow, the measured pitot pressure P_{t2} corresponds to the pitot pressure behind the standing bow shock in front of the pitot probe. In a steady supersonic flow with a single normal shock ahead of the pitot tube, a sharp drop in P_{t2} followed by a rise signifies the presence of a stronger shock wave (Krothapalli et al., 1990). The data presented is, therefore, accurate enough to capture the overall features; e.g., the number of shocks and their spacing etc. (Samimy et al., 1993). As is seen from Fig. 5, the shock cell structure is significantly weakened by the presence of the notch with a reduction in the shock spacing. The plain ellipse exhibits strong shocks in the core region. However, the sharp cornered notches show significant reductions in shock strengths as well as shock spacings in the third and the fourth shock cells. Square notch shows the weakest of such shocks. Figure 6 shows cartoons developed from a shadowgraph picture of notched elliptic orifice jet in both planes. The cartoons show that the notches influences (mostly weakens) the shock-cell system considerably. This is in conformation with Fig. 5.

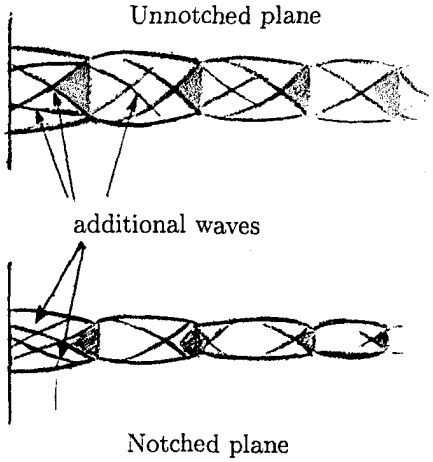

Fig. 6 Cartoons developed from the shadowgraph pictures of notched elliptic orifice jets, M_j = 1.52

The source of noise has been reported by Powell (1953), Hammitt (1961) and Krothapalli et al. (1986) to be located approximately at the end of the third and fourth shock-cell and found that weakening the shock-structure with variation in exit geometry may help to reduce shock-associated noise (Glass, 1968; Powell, 1953). The effect of the notch presence on the far-field noise of an underexpanded elliptic jet can be seen in Fig. 7, which is a plot of the overall sound pressure level (OASPL) against M_j (the correctly expanded Mach number of the underexpanded jets). These measurements are made with the microphone at 30° to the downstream jet axis and placed $50D_e$ away from the jet exit. A significant reduction in OASPL is observed for the notched cases. The plain circle shows an increasing trend from M_j = 1.0 onwards up to M_j = 1.6 relative to all other cases. The plain ellipse shows a considerable reduction in OASPL relative to the plain circle showing the effect of higher mixing in noncircular jets on the far-field noise. A reduction of 5.0 dB at M_j = 1.58 is observed for the plain ellipse relative to the plain circle. Notched elliptic jets further show a reduction in OASPL relative to the plain ellipse. At M_j = 1.6, triangular notched jet shows a 10 dB reduction and the square notched jet a 12 dB reduction in OASPL relative to the plain circle. It may, therefore, be suggested (in accordance with the study of Krothapalli et al., 1990) that the reduction in the magnitude of OASPL is due primarily to the weak shock-cell structure which results in significantly reduced shock-associated noise.

It should be noted that no direct comparison is possible between nozzle and orifice jets. However, the results presented in Fig. 7 can be looked into as a qualitative behavior of jets with passive controls even though they are from nozzles and orifices which have significantly different initial conditions.

Conclusions

A passive control of achieving near-field mixing enhancement in elliptic-orifice jets is demonstrated. The following conclusions can be made from the above observations:

1. Introduction of sharp cornered notches in the minor-axis side help enhance mixing close to the orifice exit ($X/D_e \leq$ 10). The effect also shifts the switchover location upstream which indicates higher bulk-mixing (Hussain and Husain, 1989) in notched cases.
2. The notch geometry seems to be a strong parameter in controlling the mixing characteristics in elliptic jets with the triangular notch showing minimum core-length and maximum decay.
3. The notches in elliptic-orifice jet contribute to a significant noise reduction. The notches perform as silencers because they weaken the shock-cell structure near the orifice exit and thereby reduce shock-associated noise. The square notch configuration seems to be the best for far-field broadband noise reduction.

References

Bradbury, L. J. S., and Khadem, A. H., 1975, "The Distortion of a Jet by Tabs," *Journal of Fluid Mechanics,* Vol. 70, Part 4, pp. 801–813.

Brown, G. L., and Roshko, A., 1974, "On Density Effects and Large Structures in Turbulent Mixing Layers," *Journal of Fluid Mechanics,* Vol. 64, pp. 775–816.

Glass, D. R., 1968, "Effects of Acoustic Feedback in the Spread and Decay of Supersonic Jets," *AIAA Journal,* Vol. 6, No. 10, pp. 1890–1897.

Gutmark, E., and Schadow, K. C., 1987, "Flow Characteristics of Orifice and Tapered Jets," *Physics of Fluids,* Vol. 30, No. 11, pp. 3445–3454.

Hammitt, A. G., 1961, "The Oscillations and Noise of an Overpressure Sonic Jet," *Journal of Aerospace Sciences,* Vol. 28, No. 9, pp. 673–680.

Ho, C. M., and Gutmark, E., 1987, "Vortex Induction and Mass Entrainment in a Small Aspect-Ratio Elliptic Jet," *Journal of Fluid Mechanics,* Vol. 179, pp. 383–405.

Hussain, H. S., and Husain, A. K. M. F., 1989, "Elliptic Jets. Part 1. Characteristics of Unexcited and Excited Jets," *Journal of Fluid Mechanics,* Vol. 208, pp. 257–320.

Krothapalli, A., McDaniel, J., and Baganoff, D., 1990, "Effect of Slotting on the Noise of an Axisymmetric Supersonic Jet," *AIAA Journal,* Vol. 28, No. 12, pp. 2136–2138.

Krothapalli, A., Hsia, Y., Baganoff, D., and Karamcheti, K., 1986, "Role of Screeching Tones in the Mixing of an Underexpanded Rectangular Jet," *Journal of Sound and Vibration,* 106(11), pp. 119–143.

Norum, T. D., and Seiner, J. M., 1982, "Broadband Shock Noise from Supersonic Jets," *AIAA Journal,* Vol. 20, No. 1, pp. 68–73.

Norum, T. D., 1983, "Screech Suppression in Supersonic Jets," *AIAA Journal,* Vol. 21, No. 2, pp. 235–240.

Pannu, S. S., and Johanassen, 1976, "The Structure of Jets from Notched Nozzles," *Journal of Fluid Mechanics,* Vol. 74, Part 3, pp. 515–528.

Powell, A., 1953, "The Noise of Choked Jets," *Journal of Acoustical Society of America,* Vol. 25, pp. 385–389.

Powell, A., 1954, "Survey of Experiments on Jet Noise," *Aircraft Engineering,* Jan., pp. 2–9.

Quinn, W. R., 1988, "Experimental and Numerical Study of a Turbulent Free Square Jet," *Physics of Fluids,* 31(5), May, pp. 1017–1025.

Raman, G., and Rice, E. J., 1994, "Mixing and Noise Benefit Versus Thrust Penalty in Supersonic Jets Using Impingement Tones," *Proceedings of 30th AIAA/ASME/SAE/ASEE Joint Propulsion Conference,* June 27–29.

Samimy, M., Zaman, K. B. M. Q., and Reeder, M. F., 1993, "Effect of Tabs on the Flow and Noise Field of a Axisymmetric Jets," *AIAA Journal,* Vol. 31, No. 4, Apr., pp. 609–619.

Samimy, M., and Elliot, G. S., 1990, "Effects of Compressibility on the Characteristics of Free Shear Layers," *AIAA Journal,* 28(3), pp. 439–445.

Schadow, K. C., Gutmark, E., Koshigoe, S., and Wilson, K. J., 1989, "Combustion-Related Shear-Flow Dynamics in Elliptic Supersonic Jets," *AIAA Journal,* Vol. 27, No. 10, pp. 1347–1353.

Schadow, K. C., Gutmark, E., Parr, D. M., and Wilson, K. J., 1988, "Selective Control of Flow Coherence in Triangular Jets," *Experiments in Fluids,* Vol. 6, pp. 129–135.

Tam, C. K. W., 1988, "The Shock-cell Structures and Screech Tone Frequency of Rectangular and Non-axisymmetric Supersonic Jets," *Journal of Sound and Vibration,* Vol. 121, p. 135.

Wlezien, R. W., and Kibens, N., 1988, "Influence of Nozzle Asymmetry on Supersonic Jets," *AIAA Journal,* Vol. 26, No. 1, pp. 27–33.

Operating Condition and Geometry Influences on Vortex Development in Cyclone

B. Reinhardt,[1] A. Cordonnier,[1] and P. Florent[2]

1 Introduction

FCB develops cyclone preheaters used in cement plants in order to preheat the raw flow that becomes clinker, after the firing stage. These preheaters are composed of cyclones working at high mass load (higher than 1 kg of material per kg of gas) and at high temperature (between 400 and 850°C). Until now, assessments and tests have resulted in an optimized working cyclone design, but there are not a lot of investigations of physical phenomena occurring during separation. However, geometrical optimization of cyclones has to be preceded by the study and the understanding of the suspension vortex flow structure.

Large-sized cyclone investigation (diameter greater than 4 meters) presents the problem of the representativeness of tests made on models having a diameter less than 1 meter. The first part of this study concerns the vortex development in the cyclone with pure air, without material. We study the influence of the cyclone size and operating conditions (inlet velocity, turbulence rate) on aerodynamic profiles. Then the influence of geometrical parameters on vortex development are looked at.

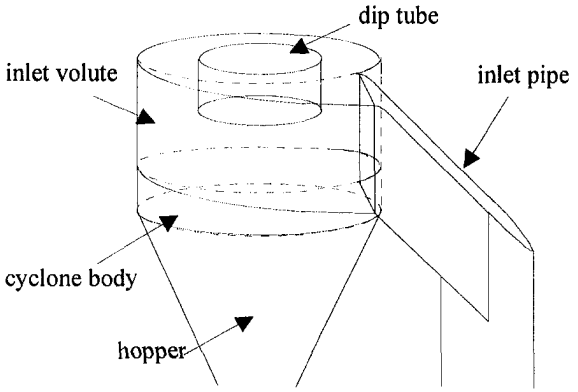

Fig. 1 Cyclone design

2 Cyclone Size Influence

Two homothetical cyclones of 400 and 800 mm diameter are used. This investigation enables the analysis of vortex development in the cyclone in pure air at ambient temperature.

Hot wire anemometry (Perry, 1982) measurements have lead to comparison of tangential and axial velocities and turbulence rate evolutions obtained with both models. Figure 1 shows the cyclone design.

Fluid inlet conditions and then results of vortex characterizations in 400 and 800 mm diameter cyclones are detailed in the following.

2.1 Inlet Conditions. Measurements have been taken for both cyclones for the characterization of inlet conditions according to vertical position, as schematized in Fig. 2.

The flow rate velocity, i.e., velocity V_n normal to the inlet section, the turbulence rate and the angle α between the velocity

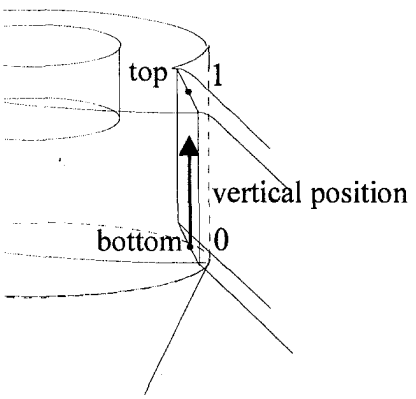

Fig. 2 Inlet conditions characterization

[1] Doctor and Technical Manager, respectively, FCB Research Center, bd de l'usine, BP 2047, 59015 Lille, France. e-mail: FCB.CRCM@WANADOO.FR.

[2] Professor, Fluid Mechanics Laboratory, Le Mont Houy, BP 311, 59304 Valenciennes, France.

Contributed by the Fluids Engineering Division of THE AMERICAN SOCIETY OF MECHANICAL ENGINEERS. Manuscript received by the Fluids Engineering Division February 3, 1998; revised manuscript received March 24, 1999. Associate Technical Editor: S. Banerjee.

References

Bradbury, L. J. S., and Khadem, A. H., 1975, "The Distortion of a Jet by Tabs," *Journal of Fluid Mechanics,* Vol. 70, Part 4, pp. 801–813.

Brown, G. L., and Roshko, A., 1974, "On Density Effects and Large Structures in Turbulent Mixing Layers," *Journal of Fluid Mechanics,* Vol. 64, pp. 775–816.

Glass, D. R., 1968, "Effects of Acoustic Feedback in the Spread and Decay of Supersonic Jets," *AIAA Journal,* Vol. 6, No. 10, pp. 1890–1897.

Gutmark, E., and Schadow, K. C., 1987, "Flow Characteristics of Orifice and Tapered Jets," *Physics of Fluids,* Vol. 30, No. 11, pp. 3445–3454.

Hammitt, A. G., 1961, "The Oscillations and Noise of an Overpressure Sonic Jet," *Journal of Aerospace Sciences,* Vol. 28, No. 9, pp. 673–680.

Ho, C. M., and Gutmark, E., 1987, "Vortex Induction and Mass Entrainment in a Small Aspect-Ratio Elliptic Jet," *Journal of Fluid Mechanics,* Vol. 179, pp. 383–405.

Hussain, H. S., and Husain, A. K. M. F., 1989, "Elliptic Jets. Part 1. Characteristics of Unexcited and Excited Jets," *Journal of Fluid Mechanics,* Vol. 208, pp. 257–320.

Krothapalli, A., McDaniel, J., and Baganoff, D., 1990, "Effect of Slotting on the Noise of an Axisymmetric Supersonic Jet," *AIAA Journal,* Vol. 28, No. 12, pp. 2136–2138.

Krothapalli, A., Hsia, Y., Baganoff, D., and Karamcheti, K., 1986, "Role of Screeching Tones in the Mixing of an Underexpanded Rectangular Jet," *Journal of Sound and Vibration,* 106(11), pp. 119–143.

Norum, T. D., and Seiner, J. M., 1982, "Broadband Shock Noise from Supersonic Jets," *AIAA Journal,* Vol. 20, No. 1, pp. 68–73.

Norum, T. D., 1983, "Screech Suppression in Supersonic Jets," *AIAA Journal,* Vol. 21, No. 2, pp. 235–240.

Pannu, S. S., and Johanassen, 1976, "The Structure of Jets from Notched Nozzles," *Journal of Fluid Mechanics,* Vol. 74, Part 3, pp. 515–528.

Powell, A., 1953, "The Noise of Choked Jets," *Journal of Acoustical Society of America,* Vol. 25, pp. 385–389.

Powell, A., 1954, "Survey of Experiments on Jet Noise," *Aircraft Engineering,* Jan., pp. 2–9.

Quinn, W. R., 1988, "Experimental and Numerical Study of a Turbulent Free Square Jet," *Physics of Fluids,* 31(5), May, pp. 1017–1025.

Raman, G., and Rice, E. J., 1994, "Mixing and Noise Benefit Versus Thrust Penalty in Supersonic Jets Using Impingement Tones," *Proceedings of 30th AIAA/ASME/SAE/ASEE Joint Propulsion Conference,* June 27–29.

Samimy, M., Zaman, K. B. M. Q., and Reeder, M. F., 1993, "Effect of Tabs on the Flow and Noise Field of a Axisymmetric Jets," *AIAA Journal,* Vol. 31, No. 4, Apr., pp. 609–619.

Samimy, M., and Elliot, G. S., 1990, "Effects of Compressibility on the Characteristics of Free Shear Layers," *AIAA Journal,* 28(3), pp. 439–445.

Schadow, K. C., Gutmark, E., Koshigoe, S., and Wilson, K. J., 1989, "Combustion-Related Shear-Flow Dynamics in Elliptic Supersonic Jets," *AIAA Journal,* Vol. 27, No. 10, pp. 1347–1353.

Schadow, K. C., Gutmark, E., Parr, D. M., and Wilson, K. J., 1988, "Selective Control of Flow Coherence in Triangular Jets," *Experiments in Fluids,* Vol. 6, pp. 129–135.

Tam, C. K. W., 1988, "The Shock-cell Structures and Screech Tone Frequency of Rectangular and Non-axisymmetric Supersonic Jets," *Journal of Sound and Vibration,* Vol. 121, p. 135.

Wlezien, R. W., and Kibens, N., 1988, "Influence of Nozzle Asymmetry on Supersonic Jets," *AIAA Journal,* Vol. 26, No. 1, pp. 27–33.

Operating Condition and Geometry Influences on Vortex Development in Cyclone

B. Reinhardt,[1] A. Cordonnier,[1] and P. Florent[2]

1 Introduction

FCB develops cyclone preheaters used in cement plants in order to preheat the raw flow that becomes clinker, after the firing stage. These preheaters are composed of cyclones working at high mass load (higher than 1 kg of material per kg of gas) and at high temperature (between 400 and 850°C). Until now, assessments and tests have resulted in an optimized working cyclone design, but there are not a lot of investigations of physical phenomena occurring during separation. However, geometrical optimization of cyclones has to be preceded by the study and the understanding of the suspension vortex flow structure.

Large-sized cyclone investigation (diameter greater than 4 meters) presents the problem of the representativeness of tests made on models having a diameter less than 1 meter. The first part of this study concerns the vortex development in the cyclone with pure air, without material. We study the influence of the cyclone size and operating conditions (inlet velocity, turbulence rate) on aerodynamic profiles. Then the influence of geometrical parameters on vortex development are looked at.

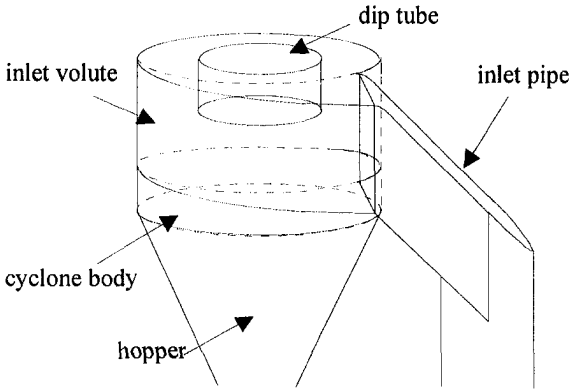

Fig. 1 Cyclone design

2 Cyclone Size Influence

Two homothetical cyclones of 400 and 800 mm diameter are used. This investigation enables the analysis of vortex development in the cyclone in pure air at ambient temperature.

Hot wire anemometry (Perry, 1982) measurements have lead to comparison of tangential and axial velocities and turbulence rate evolutions obtained with both models. Figure 1 shows the cyclone design.

Fluid inlet conditions and then results of vortex characterizations in 400 and 800 mm diameter cyclones are detailed in the following.

2.1 Inlet Conditions. Measurements have been taken for both cyclones for the characterization of inlet conditions according to vertical position, as schematized in Fig. 2.

The flow rate velocity, i.e., velocity V_n normal to the inlet section, the turbulence rate and the angle α between the velocity

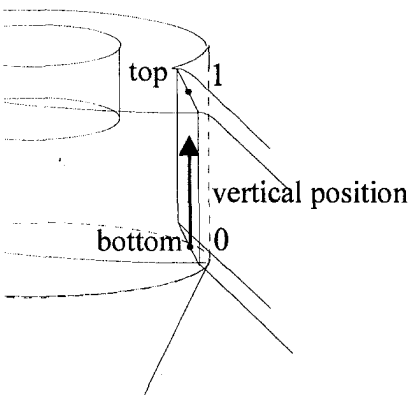

Fig. 2 Inlet conditions characterization

[1] Doctor and Technical Manager, respectively, FCB Research Center, bd de l'usine, BP 2047, 59015 Lille, France. e-mail: FCB.CRCM@WANADOO.FR.

[2] Professor, Fluid Mechanics Laboratory, Le Mont Houy, BP 311, 59304 Valenciennes, France.

Contributed by the Fluids Engineering Division of THE AMERICAN SOCIETY OF MECHANICAL ENGINEERS. Manuscript received by the Fluids Engineering Division February 3, 1998; revised manuscript received March 24, 1999. Associate Technical Editor: S. Banerjee.

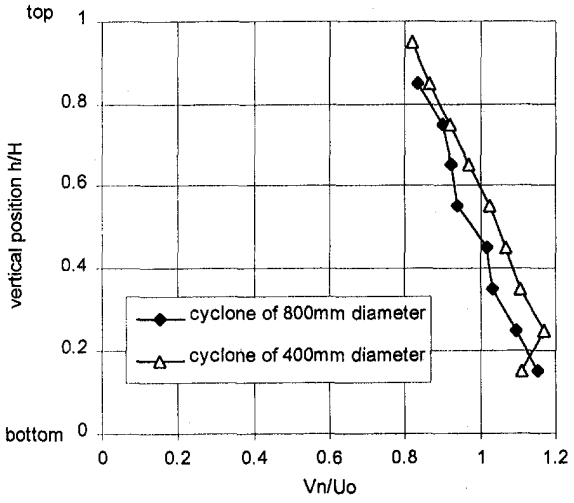

Fig. 3 Dimensionless velocity V_n/U_o versus h/H

vector and an horizontal line characterize the inlet conditions. Angles α measured are the same in both cyclones and vary between 9 deg (at the top section) and 25 deg (at the bottom section) because of the inlet pipe geometry. The flow rate velocity and the turbulence rate for a constant vertical height do not vary significantly along the inlet width.

The ratio of the flow rate velocity, V_n, to the inlet mean velocity, U_o, is represented in Fig. 3 at each vertical position by the average value along the width of the inlet section.

The dip tube and inlet pipe shapes explain the flow rate velocity curves. They are identical for both sizes of cyclone.

With regard to the turbulence level at the cyclone inlet, it is 4% for the 400 mm diameter cyclone and 6% for the 800 mm (Fig. 4). The difference is rather small. We can conclude that both cyclones have the same fluid inlet conditions.

2.2 Vortex Development. The vortex in the cyclone consists of two main flow regions: a solid flow in the central part ($V_t = ar$) and an irrotational flow elsewhere ($V_t = b/r$), where V_t is the tangential velocity, a and b are constants and r is the radial position from the vortex center. The radial position where tangential velocity is maximal is called the viscous core radius, R_{nv}.

The tangential velocity curve obtained is not dependent on the measurement height (inlet volute, cyclone body and hopper) nor on the angular position (position around the cyclone) (Reinhardt, 1996). Moreover, the vortex center is not the cyclone geometrical

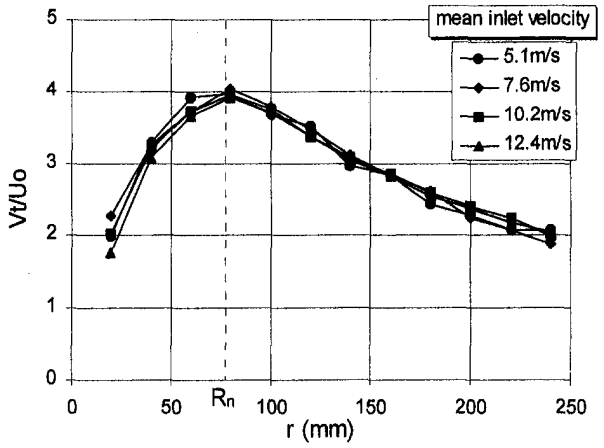

Fig. 5 Dimensionless tangential velocity V_t/U_o curves for different mean inlet velocities

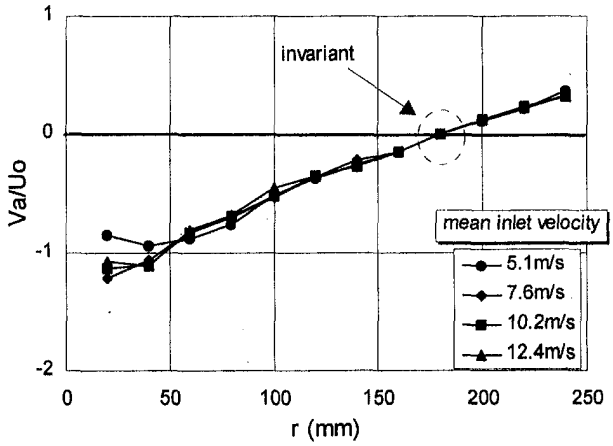

Fig. 6 Dimensionless axial velocity V_a/U_o curves for different mean inlet velocities

center because of the inlet volute geometry, which creates a flow asymmetry. So $r = 0$ corresponds to the vortex center and not to the geometrical center in all following curves.

Figures 5 and 6 show the evolution of the ratio of tangential and axial velocity curves to the inlet mean velocity in the cyclone ϕ800 for several inlet velocities.

The above curves correspond to a 6% mean turbulence rate at the cyclone inlet. Tangential velocity curves are identical and can

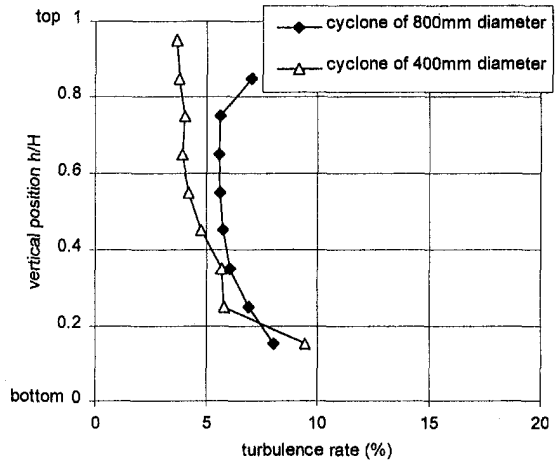

Fig. 4 Turbulence rate versus h/H

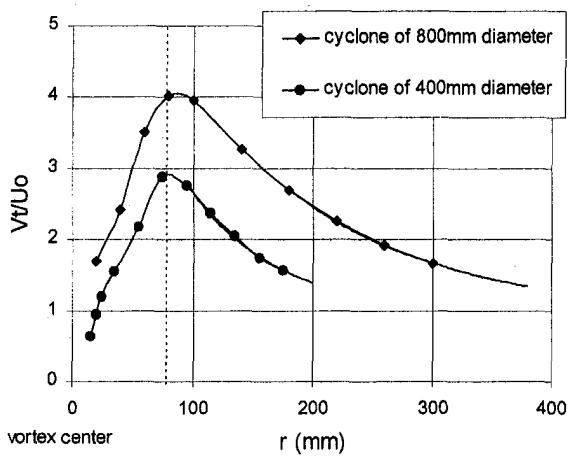

Fig. 7 Dimensionless tangential velocity curves

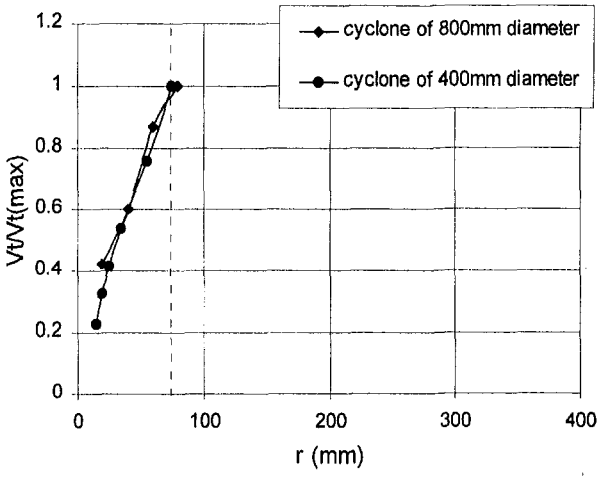

Fig. 8 Dimensionless tangential velocity curves in central flow

be described with a single curve (Fig. 7). The same is true for the axial velocity. The radius corresponding to the zero axial velocity and the viscous core radius are invariant. The ratio of the tangential velocity curves, V_t, to inlet mean velocity U_o, are therefore independent of both the inlet mean velocity and the inlet turbulence rate for both cyclones (Reinhardt, 1996). The viscous core radius does not evolve with the cyclone size. Indeed whatever cyclone diameter we consider, this radius equals 75 mm ± 5 mm (Fig. 7). It can also be noted that a viscous core radius equal to 75 mm, invariant relative to mean velocity, was obtained both by FCB with a 600 and 1200 mm diameter cyclone and by Reydon and Gauvin (1981) with a 1200 mm diameter cyclone.

Equations usually used in fluid mechanics (Navier-Stokes and k-ϵ closure equations) do not reproduce this behavior. Indeed, the dimensionless formulation of these equations leads to two geometrically homothetical flows (Reinhardt et al., 1997). Considering experimental results, we can conclude that a unique similitude does not exist. A first similitude concerns the central rotational flow (Fig. 8), a other one the irrotational flow for which the characteristic size is the cyclone radius; for this reason, in Fig. 9, the tangential velocity curves are the same for both cyclones.

3 Cyclone Geometry Influence

The geometrical parameters of the dip tube presented in Fig. 10 have also been investigated.

In the following, two characteristic parameters are used: $d = d_i/D$ and $h = S/a$. Figures 11 and 12 show results obtained by

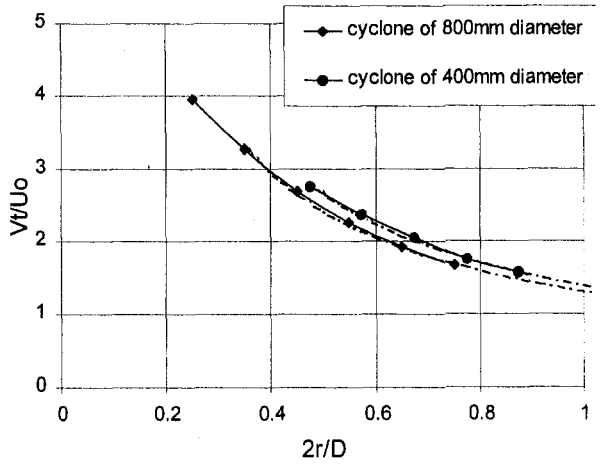

Fig. 9 Dimensionless tangential velocity curves in external flow

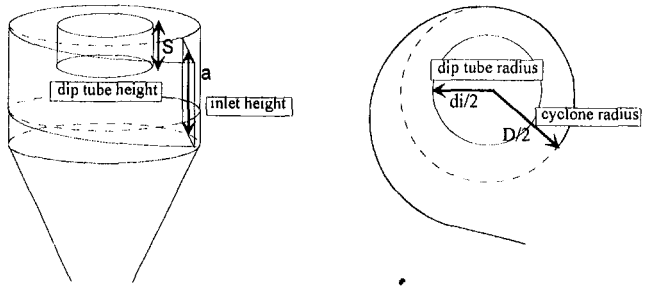

Fig. 10 Geometrical parameters

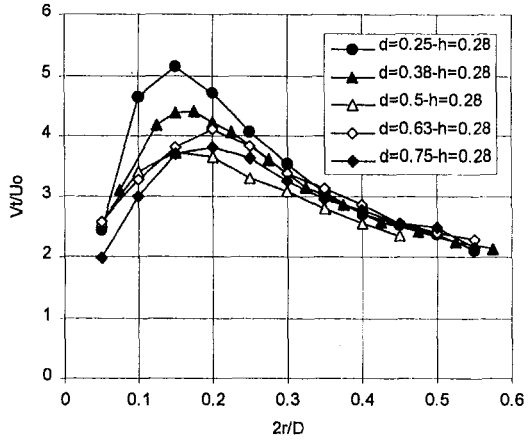

Fig. 11 Dimensionless tangential velocity curves versus dimensionless radius

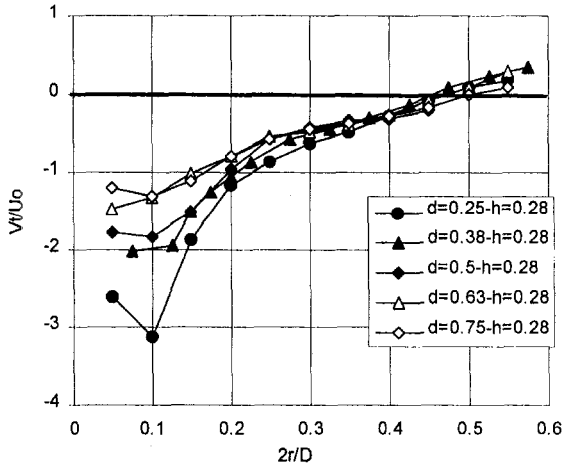

Fig. 12 Dimensionless axial velocity curves versus dimensionless radius

modifying the dip tube diameter. The height influence is presented in Figs. 13 and 14.

Vortex characteristics, viscous core dimension, and maximal tangential velocity, do not evolve as long as the dip tube diameter is above a certain dimension ($d > 0.5$ in this case (Fig. 11)). When the dip tube dimension interferes with the vortex development, the viscous core radius decreases slightly (from 0.2 R to 0.15 R) while the maximal velocity increases (from $4U_o$ to $5U_o$). The decrease in the dip tube diameter obviously involves an axial velocity increase at the cyclone center (Fig. 12). The dip tube height slightly influences the vortex development (Figs. 13 and 14). Vatistas et al. (1986) have studied the influence of the dip tube diameter by using a 152 mm diameter chamber. The viscous core radius evolves from 60 to 90% of the dip tube radius when this latter varies from 20 to 100% of the chamber radius. In small-sized cyclones the viscous core radius is influenced by the cyclone

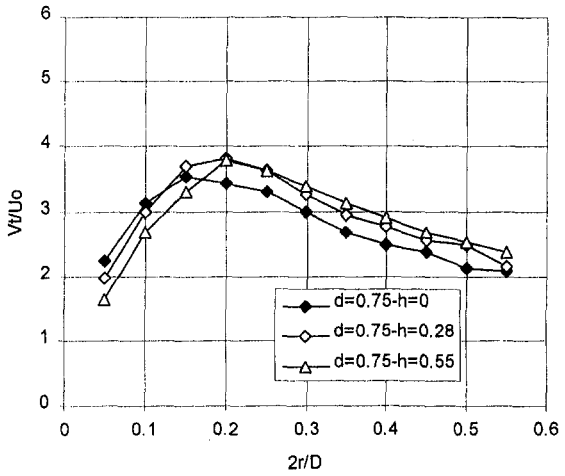

Fig. 13 Dimensionless tangential velocity curves versus dimensionless radius

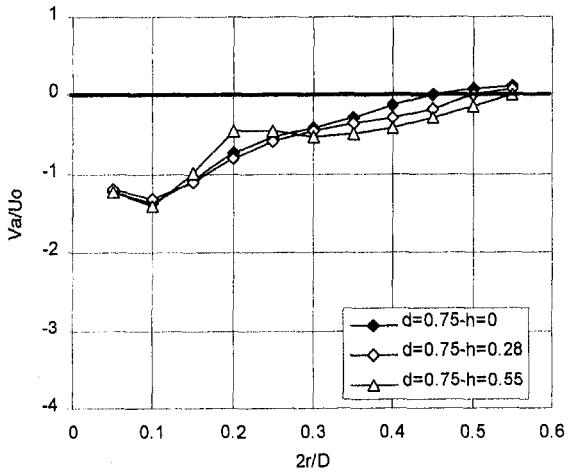

Fig. 14 Dimensionless axial velocity curves versus dimensionless radius

dimensions because the vortex is enclosed in a small space. On the contrary, in large-sized cyclones, this dimension stays constant.

4 Conclusions

Inlet fluid conditions in both homothetical cyclones (flow rate velocity and turbulence rate) are identical. The aerodynamic dimensionless profiles are independent of the inlet mean velocity and turbulence rate for each cyclone. The vortex may then be characterized by unique dimensionless tangential and axial velocity curves for both cyclones.

For both cyclones studied, the viscous core radius, main characteristic of the vortex, does not depend on the cyclone size and is slightly influenced by its geometry. It equals 75 mm $\pm$ 5 mm and seems to be dependent only of physical properties of the carrier fluid as long as the cyclone geometry lets the vortex develop freely. Similitude working of both cyclones of different sizes is thus impossible. But two similitudes exist: the first one for the central rotational flow and the second one for the irrotational flow. In the first domain the characteristic flow dimension is the same for both cyclones while in the second zone it is represented by their radii.

References

Perry, A. E., 1982, *Hot Wire Anemometry,* Clarendon Press Oxford.

Reinhardt, B., 1996, "Compréhension et évaluation du comportement des suspensions gaz-solide à forte charge dans les techniques de séparation aéraulique." Confidential thesis, Valenciennes, France.

Reinhardt, B., Duhamel, P., Cordonnier, A., and Florent, P., 1997, "Développement d'un modèle de turbulence pour modéliser un écoulement vortex." Société française de thermique, Mar. 19.

Reydon, R. F., and Gauvin, W. H., 1981, "Theorical and Experimental Studies of Confined Vortex Flow," Departement of Chemical Engineering, McGill University, Montreal, Quebec, Vol. 59. Feb. pp. 14–23.

Vatistas, G. H., Lin, S., and Kwok, C. K., 1986, "Theorical and Experimental Studies on Vortex Chamber Flows." *AIAA Journal,* Vol. 24, No. 4, Apr.